A Search for Charged Higgs from Top Quark Decay at the CERN $p\bar{p}$–Collider

Dissertation
zur Erlangung des Grades eines
Doktors der Naturwissenschaften
der Abteilung Physik
der Universität Dortmund

vorgelegt von
Emmanuel Tsesmelis B.Sc.(Hons.), M.Sc.
aus Melbourne

– Dortmund, Juni 1992 –

Gutachter : Prof. Dr. Claus Gössling
Prof. Dr. Luigi DiLella

Abstract

An analysis of data collected with the UA2 apparatus at the CERN proton-antiproton ($p\overline{p}$) Collider corresponding to a total integrated luminosity of 13.0 ± 0.7 pb^{-1} at $\sqrt{s} = 630$ GeV is described in this thesis.

The process

$$t \rightarrow H^+b,\ H^+ \rightarrow \tau^+\nu_\tau,\ \tau^+ \rightarrow \text{hadrons} + \overline{\nu}_\tau \qquad (1)$$

and its charge conjugate have been investigated by seeking an excess in the number of τ 's beyond that expected from Intermediate Vector Boson decays in the Standard Model under the assumption of electron - τ universality of couplings to the W boson. No such excess is found allowing the decay chain (1) above to be excluded in new regions of the $m_t - m_{H^\pm}$ plane for two different BR($H^\pm \rightarrow \tau\nu_\tau$) values.

In addition, the ratio of couplings of the τ and electron to the W is measured to be

$$\frac{g_\tau^W}{g_e^W} = 1.02 \pm 0.04\ (\text{stat}) \pm 0.04\ (\text{syst}).$$

Finally, the future prospects for the detection of $H^\pm$ from top quark decay using the proposed EAGLE detector at the future Large Hadron Collider (LHC) at CERN is described. A sensitivity to a $H^\pm$ decaying into τ 's over a large range of the parameter space ($\tan\beta, m_{H^\pm}$) for top quark masses up to about 200 GeV is feasible but only upto low machine operating luminosities of 10^{33} cm^{-2}s^{-1} by using a highly-segmented calorimeter and silicon tracking detector.

A review of top physics and of the Higgs sector in the Standard Model and beyond is given as well as descriptions of the UA2 and the EAGLE detectors and of the dedicated τ trigger and $H^\pm$ Monte Carlo used.

Acknowledgements

I would like to thank my supervisor Prof. Dr. Claus Gössling for his support and guidance and for his good friendship over the last few years. I am particularly grateful to Dr. Joe Incandela for his invaluable assistance and advice and for his good company. I would also like to acknowledge the fine hospitality extended to me by the UA2 Milano group during my visits to Italy and the advice and help of Prof. Dr. Laura Perini and Drs. Donatella Cavalli and Luca Cozzi.

The extensive periods of time spent at CERN have been of immense worth to me since I started on UA2 in February 1989 and I am very grateful to all the members of the UA2 Collaboration for making the experiment so successful. I am particularly indebted to Prof. Dr. Luigi DiLella and Drs. Peter Jenni and Hatti Plothow-Besch for their continual advice and support and to the UA2 silicon group and especially to Dr. Trivan Pal.

Finally, I would like to warmly thank all my friends in Europe and Australia and in particular Ines Kresse for making the last few years unforgettable and my parents, who even though are so far away, have always been my guiding light.

Contents

Chapter 1

Introduction

In this thesis a search for the decay

$$t \rightarrow H^+b,\ H^+ \rightarrow \tau^+\nu_\tau,\ \tau^+ \rightarrow \text{hadrons} + \overline{\nu}_\tau \quad (1.1)$$

and for its charge conjugate in proton-antiproton ($p\overline{p}$) collisions at a centre-of-mass energy of $\sqrt{s} = 630$ GeV and using the UA2 apparatus at CERN is presented.

In Chapter 2 the role of the top quark and the Higgs sector in the Standard Model and beyond is discussed. The Higgs sector in the Standard Model consists of a single doublet of complex scalar fields giving rise to a single scalar boson H^0 whereas in minimally extended models consisting of two such doublets the particle spectrum consists of 5 scalars - H^0, h^0, A^0, and $H^\pm$. In such models the $H^\pm$ couplings are fully specified by its mass, $m_{H^\pm}$, and by the ratio of vacuum expectation values for the two scalar fields, $\tan\beta = \frac{\nu_2}{\nu_1}$ [Gun-90a].

The existence of $H^\pm$ bosons could alter the decay characteristics of top quarks because for $m_t > m_{H^\pm} + m_b$ the decay $t \rightarrow H^+b$ competes with the standard top decay $t \rightarrow W^+b$, (where the W is either virtual or on the mass shell), depending on the values of $m_{H^\pm}$ and $\tan\beta$ [Gla-87]. Since in this case the dominant $H^\pm$ decays are to $\tau^+\nu_\tau$ and $c\bar{s}$, with branching ratios depending on $\tan\beta$, searches for the top quark based on $t \rightarrow be^+\nu_e$ or $t \rightarrow b\mu^+\nu_\mu$, as have been performed by UA1, UA2 and the CDF Collaborations [UA2-90, UA1-90, CDF-91d], would result in a much weaker signal than expected. In particular in the mass range accessible at the CERN $p\overline{p}$ Collider, $m_W > m_t + m_b$, the decay $t \rightarrow H^+b$ is by far the dominant decay mode independent of $\tan\beta$. In

this case the lower bounds on m_t derived from direct searches at hadron colliders are invalidated and a lower bound on the top mass can only be obtained by measuring the W width, Γ_W, and from direct searches at electron-positron machines such as the Large Electron Positron Collider (LEP) at CERN.

The CERN $p\overline{p}$ Collider, which first provided proton-antiproton interactions for physics in 1982, and the UA2 experiment there are described in Chapter 3. The Collider was upgraded between 1985 and 1987, with the addition of the Antiproton Collector (ACOL) to increase the available luminosity by improving the antiproton supply. Concurrently, the UA2 experiment was upgraded to increase the calorimeter coverage thus improving the measurement of the total energy of events and enhancing the electron identification by improving the central tracking detector. In addition, the trigger and readout were significantly improved to take advantage of the increased luminosity available. The remainder of Chapter 3 is devoted to a description of the dedicated τ trigger used in the 1990 runing period to enhance events containing τ 's. (Appendix A describes the calibration of the Inner Silicon detector (ISI) of UA2).

In Chapter 4 the characteristics of the Monte Carlo (MC) simulated events of the type in Equation (1.1) and of the backgrounds from Standard Model processes are described.

Chapters 5 and 6 provide a detailed description of the analysis performed to search for $H^{\pm}$ from top quark decay. The analysis method is based on measuring the electron - τ universality of weak couplings to the W. First, the number of events with a τ or electron are determined from data with a high missing transverse momentum (p_T^{miss}). The number of electron events is then used together with the assumption of electron - τ universality to determine the number of τ 's expected from Standard Model Intermediate Vector Boson (IVB) decays. This prediction is then compared to the data. A statistically significant excess of events in the data would indicate new physics whereas the agreement between data and expectation makes it possible to exclude process (1.1) in some new regions of the model parameter space. These chapters also contain a description of the particle identification procedures in UA2 and of the systematic uncertainties.

Chapter 7 discusses the prospects for detecting a $H^{\pm}$ from top quark decay using the proposed EAGLE apparatus at the future Large Hadron Collider (LHC) at CERN. The assumptions made are that of a detector consisting of a highly-segmented calorimeter and silicon tracking device operating at

$\sqrt{s} \sim 16$ TeV and at a luminosity of 10^{33} $cm^{-2}s^{-1}$.

Finally, the conclusions and outlook are summarized in Chapter 8.

Chapter 2

Theoretical and Experimental Review

2.1 Introduction

The fundamental fermions that experience weak but not strong interactions are known as leptons (the charged leptons also feel the electromagnetic interaction). All the known members of this class are spin-$\frac{1}{2}$ particles. Three charged leptons - the electron (e), muon (μ) and the tauon (τ) are firmly established; the electron and μ by direct observations and the τ through its decay products. Of the neutral leptons the electron neutrino (ν_e) and the muon neutrino (ν_μ) are well-known and there is experimental evidence of a distinct τ neutrino (ν_τ) [Fel-82]. The leptons fall into doublets called 'families' or 'generations' :

$$\begin{pmatrix} \nu_e \\ e \end{pmatrix}, \begin{pmatrix} \nu_\mu \\ \mu \end{pmatrix}, \begin{pmatrix} \nu_\tau \\ \tau \end{pmatrix}.$$

Some properties of the known leptons are summarized in Table 2.1.1.

A quark is defined as a fermion that carries the colour charge thus experiencing the strong force. The theory of the colour force is called Quantum Chromodynamics (QCD). So far there are known to be six kinds of quarks (called six quark flavours). The quarks are called up, down, strange, charmed, bottom and top and fall into three families analogously to the lepton families

$$\begin{pmatrix} u \\ d \end{pmatrix}, \begin{pmatrix} c \\ s \end{pmatrix}, \begin{pmatrix} t \\ b \end{pmatrix}.$$

Table 2.1.1 : Properties of the Leptons

Lepton	Symbol	Charge	Mass (MeV)	Lifetime (s)
Electron Neutrino	$\nu_e, \overline{\nu}_e$	0	< 0.017	$\sim \infty$
Muon Neutrino	$\nu_\mu, \overline{\nu}_\mu$	0	< 0.270	$\sim \infty$
Tauon Neutrino	$\nu_\tau, \overline{\nu}_\tau$	0	< 35.0	$\sim \infty$
Electron	$e^{\pm}$	$\pm e$	0.511	$\sim \infty$
Muon	$\mu^{\pm}$	$\pm e$	105.66	2.19×10^{-6}
Tauon	$\tau^{\pm}$	$\pm e$	1776.0	2.95×10^{-13}

Table 2.1.2 : Properties of the Quarks

Quark	Symbol	Charge	Constituent Mass (MeV)
Up	u	$\frac{2}{3}e$	~ 330
Down	d	$-\frac{1}{3}e$	~ 330
Charm	c	$\frac{2}{3}e$	~ 1300
Strange	s	$-\frac{1}{3}e$	~ 500
Top	t	$\frac{2}{3}e$	??
Bottom	b	$-\frac{1}{3}e$	~ 5000

The top row has electric charge $q = \frac{2}{3}e$ and the bottom row has $q = -\frac{1}{3}e$ where e is the magnitude of the electron's electric charge. Five of the quarks have been experimentally observed. The sixth quark, the top, must exist, (see Section 2.5), but it has not yet been observed.

Hadrons are strongly interacting particles built from two types of quark combinations :

$$\text{Baryon} = qqq \text{ (three quarks)},$$

$$\text{Meson} = q\bar{q} \text{ (quark} - \text{antiquark pair)}.$$

Since quarks have half-integral spin it follows that the baryons are characterized by half-integral spin and the mesons by integral spin.

Any coloured particle, according to what is currently believed but not yet rigorously proved to be a consequence of QCD, is permanently bound inside a colourless hadron. As a result there are either 'free' or 'constituent' quark masses. The properties of the quarks are summarized in Table 2.1.2.

Finally, each particle has its antiparticle. The antiparticles have opposite values of electric charge, colour charge and flavour from their particle counterparts but the same mass and spin.

The quarks and leptons are the basic particles of matter. In addition, there are the particles which transmit the forces. They are all bosons, i.e. of integral spin. Table 2.1.3 summarizes the forces, what they act on, and the bosons that transmit them. The gluons were predicted to exist and were observed at the PETRA e^+e- Collider in 1979 [TAS-79, MAR-79, PLU-79, JAD-80]. The W and Z bosons were first observed at the CERN $p\bar{p}$ Collider in 1983 [UA1-83, UA2-83a, UA2-83b]. Gravitons interact too weakly to be detected singly ; their existence and properties are inferred from the structure of the theory.

In the 1960's Weinberg, Salam and Glashow described how it might be possible to treat the electromagnetic and weak interactions as different aspects of a single electroweak interaction [Gla-61, Wei-67, Sal-68]. The symmetry between the electromagnetic and weak interactions is observed at only very large momentum transfers ($q^2 > 10^4$ GeV^2) while at lower energies the symmetry is broken. Presently there are attempts to carry out unification by including the strong and gravitational interactions, however, the ideas are still speculative and have very little experimental support.

The electroweak model in conjunction with QCD has come to be called the Standard Model. In spite of its great success (the prediction and discovery

	Gravitational	Weak	Electromagnetic	Strong
Range	∞	$\ll 10^{-14}$cm	∞	$10^{-13} - 10^{-14}$cm
Strength	5.9×10^{-39}	1.02×10^{-5}	$\alpha_{em} = \frac{1}{137}$	$\alpha_{strong} \approx 0.1$
Particles acted upon	All	Hadrons and Leptons	Charged particles	Hadrons
Particles exchanged	Gravitons(?)	Intermediate vector bosons	Photons	Gluons
Mass of exchanged particle	0	80 – 100 GeV	0	0
Spin of exchanged particle	2	1	1	1

Table 2.1.3 : The four fundamental forces.

of the gluons and W and Z bosons, for example), the theory is considered incomplete. Among its principal shortcomings is that it makes no prediction regarding the number of fermion generations, the quantization of charge or the value of the fermion masses.

In addition to the above particles of matter and forces one more class of particles is needed to make a consistent theory of particle masses and interactions - the spin-zero or scalar boson(s) called the Higgs boson(s). The Standard Model requires one electrically neutral Higgs boson but more could exist in extensions of the Standard Model. However, such boson(s) have yet not been observed nor does the model make any predictions regarding their mass. In this thesis the case where the Standard Model is minimally extended to have five Higgs bosons is studied.

For a review of the Standard Model refer to, for example, Ref. [Qui-83, Hal-84, Bar-87, Ait-89].

2.2 The Universality of Lepton Couplings to the Intermediate Vector Bosons

2.2.1 Theoretical Overview

The component of the SU(2)xU(1) Lagrangian describing the lepton and quark interactions with the W boson (see Figure 2.2.1) is used to identify into which final states the W boson is allowed to decay to. The possibilities are :

$$W^+ \rightarrow e^+\nu_e,\ \mu^+\nu_\mu,\ \tau^+\nu_\tau,\ q\bar{q}'$$

and their charge conjugates. Of the hadronic modes the decays into $u\bar{d}$, $c\bar{s}$, and $t\bar{b}$ provide the dominant contributions since the Kobayashi-Maskawa (KM) matrix elements are dominant :

$$|V_{ud}| \approx |V_{cs}| \approx |V_{tb}| \approx 1$$

and all other KM matrix elements are small in comparison. The decay of the W could be in any of the three quark colours so that each quark channel contributes three times as much to the W decay width as each leptonic channel. (The factor 3 for quarks is a slight overestimate because of the reduced phase-space factor for heavy quarks such as $t\bar{b}$ (see Section 2.5)).

$$\mathcal{L} = -\tfrac{1}{4}\mathbf{W}_{\mu\nu}\cdot\mathbf{W}^{\mu\nu} - \tfrac{1}{4}B_{\mu\nu}B^{\mu\nu}$$

{ $W^{\pm}$, Z, γ kinetic energies and self-interactions }

$$+\bar{L}\gamma^{\mu}\left(i\partial_{\mu} - g\frac{1}{2}\tau\cdot\mathbf{W}_{\mu} - g'\frac{Y}{2}B_{\mu}\right)L$$
$$+\bar{R}\gamma^{\mu}\left(i\partial_{\mu} - g'\frac{Y}{2}B_{\mu}\right)R$$

{ lepton and quark kinetic energies and their interactions with $W^{\pm}$, Z, γ }

$$+\left|\left(i\partial_{\mu} - g\frac{1}{2}\tau\cdot\mathbf{W}_{\mu} - g'\frac{Y}{2}B_{\mu}\right)\phi\right|^{2} - V(\phi)$$

{ $W^{\pm}$, Z, γ, and Higgs masses and couplings }

$$-(G_1\bar{L}\phi R + G_2\bar{L}\phi_c R + \text{hermitian conjugate}).$$

{ lepton and quark masses and coupling to Higgs }

L denotes a left-handed fermion (lepton or quark) doublet, and R denotes a right-handed fermion singlet.

Figure 2.2.1 : The SU(2) x U(1) Lagrangian.

To calculate the W boson width, Γ_W, it is necessary to calculate the matrix element absolute squared, summed and averaged over spins, and evaluate the angular integral. The decay rate or width $\Gamma_W^{l\nu_l}$ for $W \rightarrow l\nu_l$ is given by :

$$\frac{d\Gamma_W^{l\nu_l}}{d\Omega} = \frac{1}{(2\pi)^2}\frac{1}{(2E_W)}\frac{(p^*)^2 dp}{dE_f}\frac{m_l m_{\nu_l}}{E_l E_{\nu_l}}\left|\mathcal{M}\mathcal{M}^\dagger\right|$$

where p^* refers to the numerical value of the equal and opposite 3 - momenta of the lepton l and neutrino decay products. In the W boson rest-frame $E_W = M_W$ and so $p^* = \frac{M_W}{2}$ (neglecting the lepton masses relative to the W mass) where E_W and M_W is the energy and rest-mass, respectively, of the W boson.

The W boson has spin 1 and its state of polarization can be described in a relativistically invariant form by a 4-vector ϵ_μ with space coordinates e_1, e_2, e_3 and time component e_4. The W polarization states are given by

$$e_R = \left(\frac{1}{\sqrt{2}}, \frac{i}{\sqrt{2}}, 0, 0\right)$$

which describes right-handed circularly-polarized W bosons with spin component $J_z = +1$ along the z-axis. Similarly,

$$e_L = \left(\frac{1}{\sqrt{2}}, \frac{-i}{\sqrt{2}}, 0, 0\right)$$

and

$$e_z = (0, 0, 1, 0)$$

which describe left-handed ($J_z = -1$) and unpolarized ($J_z = 0$) W bosons, respectively. For example, a right-handed W state has

$$\left|\mathcal{M}\mathcal{M}^\dagger\right| = \frac{2g_l^W)^2(p^*)^2}{m_l m_{\nu_l}}(1 - \cos\theta)^2$$

where

$$g_W^2 = \frac{G_F M_W^2}{\sqrt{2}}$$

denotes the coupling of the W boson to the lepton pair and θ is the lepton emission angle with respect to the W. (G_F is the Fermi coupling constant of weak interactions).

Making this substitution and integrating over the solid angle gives,

$$\Gamma(W \rightarrow l\nu_l) = \frac{(g_l^W)^2 M_W}{6\pi} \qquad (2.2.1)$$

where l is any leptonic final state. The corresponding partial decay width for W bosons to decay into massless quarks is

$$\Gamma(W \rightarrow u_i\bar{d}_i) = \frac{g_W^2 M_W}{6\pi} |V_{ij}|^2$$

where V_{ij} represents the KM matrix elements.

The branching ratio of the W to any leptonic final state l is defined as

$$Br(W \rightarrow l\nu_l) \equiv \frac{\Gamma_W^{l\nu_l}}{\Gamma_W^{tot}}$$

where Γ_W^{tot} is the total width of the W summing up all the leptonic and hadronic possible final states. Therefore, from Equation (2.2.1)

$$R_W \equiv \frac{Br(W \rightarrow \tau\nu_\tau)}{Br(W \rightarrow e\nu_e)} = \frac{\frac{(g_\tau^W)^2 M_W}{6\pi}}{\frac{(g_e^W)^2 M_W}{6\pi}}$$

so that

$$R_W = \frac{(g_\tau^W)^2}{(g_e^W)^2}.$$

The leptons couple to the W with a universal coupling constant g_l^W so that

$$g_e^W = g_\mu^W = g_\tau^W.$$

The universality of lepton couplings to the vector bosons is a direct consequence of SU(2) gauge invariance in the Standard Model [Gla-61, Wei-67, Sal-68]. In this thesis a measurement of R_W is reported on and it is shown to be consistent with unity thus providing direct experimental evidence for the universality of the electron and τ couplings to the W boson.

The Z^0 has only flavour-diagonal interactions :

$$Z^0 \rightarrow e^+e^-,\ \nu_e\bar{\nu}_e,\ u\bar{u},\ d\bar{d}$$

for the first family and similarly for the other families. Again, the masses in the final state can be ignored except for $b\bar{b}$ and $t\bar{t}$. As for the W case, the hadronic channels have about three times the partial width than for the leptonic channels because of the colour factor. The partial width of the Z^0 to decay into massless fermions $f_1\bar{f}_2$ is

$$\Gamma(Z^0 \to f_1\bar{f}_2) = C(2\sqrt{2}g^Z_{f_1\bar{f}_2})^2 \frac{g_V^2 + g_A^2}{2} M_Z$$

where

$$g^Z_{f_1\bar{f}_2} = \frac{G_F M_Z^2}{\sqrt{2}}$$

is the coupling of the Z^0 to the fermion pair. The Standard Model weak and axial couplings are

$$g_V = T_3^f - 2\,Q^f \sin^2\theta_W$$
$$g_A = T_3^f$$

with T_3^f being the weak isospin of fermion f and Q^f is the charge of fermion f in units of electron charge , e. For leptons C = 1 while for quarks

$$C = 3\,(1 + \frac{\alpha_s(M_Z)}{\pi})$$

where the factor 3 is due to colour and the factor in parenthesis is from a QCD vertex correction to leading order.

The branching ratio of the Z^0 to $l\bar{l}$ is

$$Br(Z^0 \to l\bar{l}) \equiv \frac{\Gamma_Z^{l\bar{l}}}{\Gamma_Z^{tot}}$$

where Γ_Z^{tot} is the total width of the Z^0 summing up all the leptonic and quark possible final states. Therefore, for the electron and τ channels

$$R_Z \equiv \frac{Br(Z^0 \to \tau^+\tau^-)}{Br(Z^0 \to e^+e^-)} = \left(\frac{g^Z_\tau}{g^Z_e}\right)^2$$

assuming the lepton masses are small relative to the Z^0 mass. Again, from SU(2) gauge invariance the fermions couple to the Z^0 with a universal coupling constant g_f^Z.

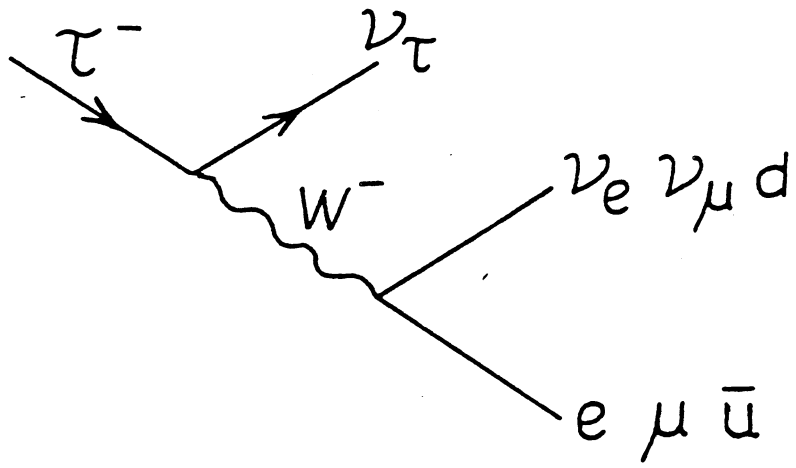

Figure 2.2.2 : The decay $\tau \rightarrow e\nu\overline{\nu}$.

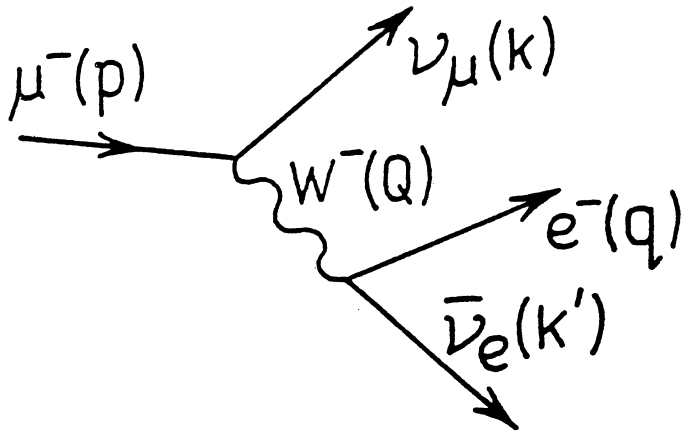

Figure 2.2.3 : The decay $\mu \rightarrow e\nu\overline{\nu}$.

Tests of the electron - τ universality to the W can also be studied in the decays of the τ and μ . The partial width for the decay $\tau^+ \rightarrow e^+\nu_e\overline{\nu}_\tau$ is

$$\Gamma(\tau^+ \rightarrow e^+\nu_e\overline{\nu}_\tau) = \frac{2\,(g_\tau^W)^2\,(g_e^W)^2\,m_\tau^5}{192\pi^3 M_W^4} = \frac{Br(\tau^+ \rightarrow e^+\nu_e\overline{\nu}_\tau)}{\tau_\tau} \qquad (2.2.2)$$

where g_τ^W and g_e^W represent the couplings of the τ and electron, respectively, to the W (see Figure 2.2.2) and τ_τ is the τ 's lifetime. For the decay $\mu^+ \rightarrow e^+\nu_e\overline{\nu}_\mu$ the corresponding expression is

$$\Gamma(\mu^+ \rightarrow e^+\nu_e\overline{\nu}_\mu) = \frac{2\,(g_\mu^W)^2\,(g_e^W)^2\,m_\mu^5}{192\pi^3 M_W^4} = \frac{1}{\tau_\mu} \qquad (2.2.3)$$

where g_μ^W and g_e^W represent the couplings of the μ and electron, respectively, to the W (see Figure 2.2.3) and τ_μ is the muon's lifetime. Therefore, from Equations (2.2.2) and (2.2.3) the ratio of coupling constants of the τ and electron to the W is (assuming at least electron - μ universality)

$$\left(\frac{g_\tau^W}{g_e^W}\right)^2 = \left(\frac{m_\mu}{m_\tau}\right)^5 \cdot \frac{\tau_\mu}{\tau_\tau} \cdot Br(\tau^+ \rightarrow e^+\nu_e\overline{\nu}_\tau) \qquad (2.2.4).$$

Test of universality derived from the τ lifetime, however, include an uncertainty related to the τ branching ratios from which the measurement discussed in this thesis is free from.

For an extended discussion on the universality of fermion couplings to the IVB refer to , for example, Ref. [Qui-83, Hal-84, Bar-87].

2.2.2 Experimental Measurements of the Lepton Coupling Universality to the Intermediate Vector Bosons

The universality of lepton couplings to the W has recently been measured in $p\overline{p}$ collisions at a centre-of-mass energy of $\sqrt{s} = 1.8$ TeV by the CDF Collaboration [CDF-91b]. The measurement is from 4.02 pb^{-1} of data taken during the 1989 run at the Fermilab Tevatron.

The measurement has been performed by observing more than 100 events of the type $W \rightarrow \tau\nu_\tau$ where the τ 's decay hadronically and by calculating the cross-section times branching ratio for $p\overline{p} \rightarrow W \rightarrow \tau\nu_\tau$. Comparing this

to $p\bar{p} \rightarrow W \rightarrow e\nu_e$ gives a direct measure of the ratio of the weak coupling constants. The measurement provides

$$\sigma \cdot \mathrm{Br}(W \rightarrow \tau\nu_\tau) = 2.04 \pm 0.22\ (\mathrm{stat}) \pm 0.18\ (\mathrm{syst})\ \mathrm{nb}$$

for data collected with an E_T^{miss} trigger and

$$\sigma \cdot \mathrm{Br}(W \rightarrow \tau\nu_\tau) = 2.08 \pm 0.40\ (\mathrm{stat}) \pm 0.26\ (\mathrm{syst})\ \mathrm{nb}$$

from data collected with a dedicated τ trigger. Combining the two samples yields

$$\sigma \cdot \mathrm{Br}(W \rightarrow \tau\nu_\tau) = 2.05 \pm 0.27\ \mathrm{nb}$$

and when compared to the CDF measurement [CDF-91cb] of

$$\sigma \cdot \mathrm{Br}(W \rightarrow e\nu_e) = 2.19 \pm 0.04\ (\mathrm{stat}) \pm 0.11\ (\mathrm{syst})\ \mathrm{nb}$$

results in the ratio of couplings

$$\frac{g_\tau^W}{g_e^W} = 0.97 \pm 0.07.$$

In addition, using recent data from the ARGUS Collaboration [Mor-92a], it is possible to make a prediction of the electron - τ universality of couplings to the W from Equation (2.2.4). Given

$m_\tau = 1776.3 \pm 2.4 \pm 1.4$

$$m_\tau = 1776.0 \pm 3.2 \pm 1.2\ \mathrm{MeV}$$

and

$$\mathrm{Br}(\tau^+ \rightarrow e^+\nu_e\bar{\nu}_\tau) = (18.3 \pm 0.3)\%,$$

Equation (2.2.4) yields

$$\frac{g_\tau^W}{g_e^W} = 0.988 \pm 0.010$$

where the remaining parameters in Equation (2.2.4) are world averages taken from Ref. [PDG-90]. This value is in agreement to within ~ 1.2 standard deviations from the prediction of lepton universality. Earlier measurements [Apu-92] of the ratio of couplings gave 0.968 ± 0.011 which shows a ~ 3 standard deviation discrepancy to the prediction of lepton universality. The

Table 2.2.1 : Partial Widths of the Z from LEP

Experiment	Γ^Z_{ee} (MeV)	$\Gamma^Z_{\mu\mu}$ (MeV)	$\Gamma^Z_{\tau\tau}$ (MeV)
ALEPH	84.25 ± 0.64	83.7 ± 1.0	84.5 ± 1.2
DELPHI	84.20 ± 0.87	82.0 ± 1.2	81.2 ± 1.8
L3	82.80 ± 0.70	84.5 ± 1.3	85.3 ± 1.5
OPAL	82.70 ± 0.70	84.6 ± 1.1	82.6 ± 1.5
$< 1990 >$	83.20 ± 0.55	83.35 ± 0.86	82.76 ± 1.5
$< 1991 >$	83.46 ± 0.40	83.71 ± 0.59	83.71 ± 0.75

current improvement is due mostly to the newly measured value of m_τ by the ARGUS Collaboration which is used instead of the former world average of $1784.1\ ^{+2.7}_{-3.6}$ [PDG-90].

The UA1 Collaboration has also reported on a measurement of electron - τ universality to the W boson based on a a large p_T^{miss} sample corresponding to 715 nb^{-1} of data [UA1-87]. The measurement provided the first observation of high - p_T τ 's from W decay. UA1 deduces

$$\frac{g^W_\tau}{g^W_e} = 1.01 \pm 0.09 \pm 0.05$$

and

$$\frac{g^W_\mu}{g^W_e} = 1.05 \pm 0.07 \pm 0.08.$$

The data provide direct experimental verification of the e - μ - τ universality of the weak charged coupling at $Q^2 = M^2_W$.

Recently, the leptonic partial widths of the Z^0 have been accurately measured at LEP [Mor-92b] and provide a test of the universality of the leptonic couplings to the Z^0 . The LEP results are consistent with lepton universality which requires that

$$\Gamma^Z_{ee} = \Gamma^Z_{\mu\mu} = \Gamma^Z_{\tau\tau}$$

(see Table 2.2.1).

Finally, the decay rate $Z^0 \rightarrow \tau^+\tau^-$ has been observed by the UA2 Collaboration [UA2-91a] and is found to be consistent with electron - τ universality to the Z^0 . The analysis has been performed on 7.4 ± 0.4 pb^{-1} of data

recorded in the 1988-1989 running periods. The measurement

$$\sigma \cdot \mathrm{Br}(Z^0 \rightarrow \tau\tau) = 121\ ^{+69}_{-43}\ (\mathrm{stat}) \pm 10\ (\mathrm{syst})\ \mathrm{pb}$$

and from the cross-section for the process $Z^0 \rightarrow e^+e^-$ measured also by the UA2 Collaboration [UA2-91b] to be

$$\sigma \cdot \mathrm{Br}(Z^0 \rightarrow e^+e^-) = 65.6 \pm 4.0\ (\mathrm{stat}) \pm 3.8\ (\mathrm{syst})\ \mathrm{pb}$$

it is found that

$$R_Z \equiv \frac{\mathrm{Br}(Z^0 \rightarrow \tau^+\tau^-)}{\mathrm{Br}(Z^0 \rightarrow e^+e^-)} = 1.8\ ^{+1.0}_{-0.6} \pm 0.2.$$

which is consistent with electron - τ universality within the relatively large uncertainties.

2.3 Mass and the Higgs Mechanism

2.3.1 Introduction

The first three terms of the Lagrangian in Equation (2.2.1) make no mention of mass terms implying that all fermions and bosons are massless while observation shows otherwise. If mass terms are added explicitly, the associated terms break the SU(2) and gauge invariances. For example, the expected mass terms for the gauge bosons, $M^2W_\mu W^\mu$, are not invariant under the gauge transformation

$$W^\mu \rightarrow W^{\mu'} = W^\mu - \frac{\partial^\mu \chi}{g}.$$

The only direct way to preserve gauge invariance and SU(2) gauge invariance of the Lagrangian is to set the mass to zero for all quarks, leptons, and gauge bosons. If masses are put in explicitly the resulting quantum field theory has non-renormalizable divergences which make the theory meaningless. However, it is possible to introduce mass without breaking gauge invariance.

In this section spontaneous broken symmetries are discussed and the consequences of spontaneous symmetry breakdown are presented along with the

mechanism developed to construct a meaningful gauge theory which includes the possibility that particles have mass.

For a further discussion on the Higgs sector in the Standard Model refer to Ref. [Vel-77, Lee-77a, Lee-77b, Sus-79, Wei-79].

It will be shown that if the Standard Model Lagrangian is invariant under an exact continuous symmetry that is not a symmetry of the physical vacuum, (i.e. the lowest energy state), at least one massless spin-zero particle, known as a Goldstone boson, must exist. Such symmetries are known as 'spontaneously broken symmetries' [Gol-61, Gol-62, Blu-63, Gil-64, Str-65, Kas-66]. At first sight this doubles the problem : gauge theories lead to unwanted massless vector bosons and the spontaneous breakdown of a continuous symmetry implies the existence of unwanted spinless particles. However, if the spontaneously broken symmetry is a local gauge symmetry an interplay between the would-be Goldstone boson and the normally massless gauge bosons gives the gauge bosons mass and removes the Goldstone boson from the spectrum. This interplay is known as the Higgs mechanism [Hig-64a, Hig-64b, Hig-66, Eng-64, Gur-64, Kib-67].

2.3.2 Spontaneous Symmetry Breaking

First, consider the Lagrangian for a self-interacting real scalar field ϕ which may be written in the form

$$\mathcal{L} = \mathrm{T} - \mathrm{V} = \frac{1}{2}\partial_\mu\phi\partial^\mu\phi - (\frac{1}{2}\mu^2\phi^2 + \frac{1}{4}\lambda\phi^4) \qquad (2.3.1)$$

with $\lambda > 0$ in order that the potential be bounded from below as $\phi \rightarrow \infty$. It is required that $\mathcal{L}$ be invariant under the symmetry operation $\phi \rightarrow -\phi$ implying that $\mathrm{V}(\phi) = \mathrm{V}(-\phi)$. The quadratic term in the potential represents the mass term and the ϕ^4 term represents an interaction of strength λ. Higher powers than the fourth are omitted so that the theory is renormalizable.

To find the particle spectrum it is necessary to find the minimum of the potential, which is the ground state of the system, and expand the fields around their value at the minimum to determine the excitations - i.e. the particles.

There exist two possible forms of the potential as is shown in Figure 2.3.1. The vacuum state is one for which the value of the field ϕ is constant, denoted by $< \phi >_0$. It corresponds to the absolute minimum or minima of the

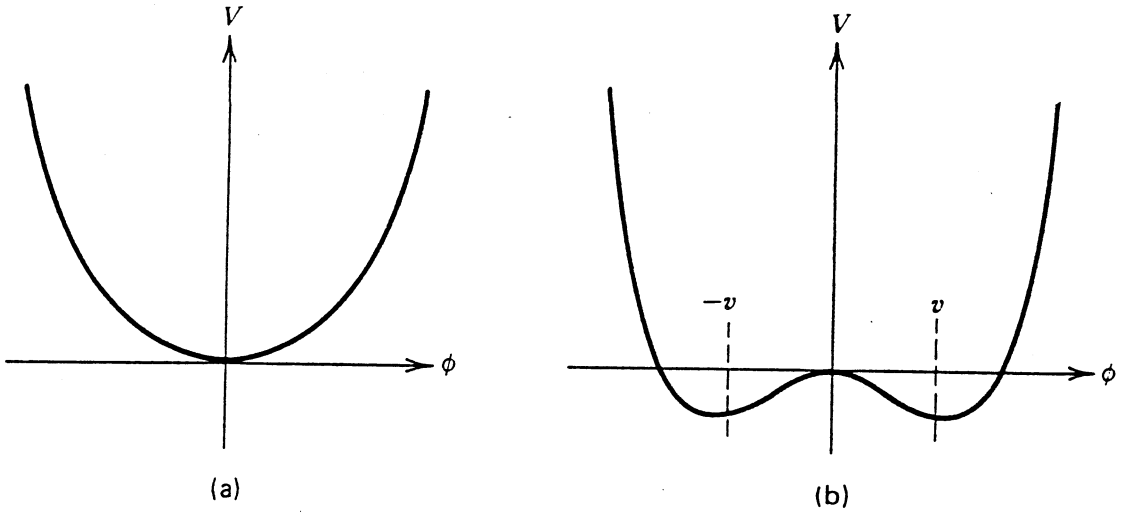

Figure 2.3.1 : The potential $V(\phi) = \frac{1}{2}\mu^2\phi^2 + \frac{1}{4}\lambda\phi^4$ for (a) $\mu^2 > 0$ and (b) $\mu^2 < 0$, and $\lambda > 0$.

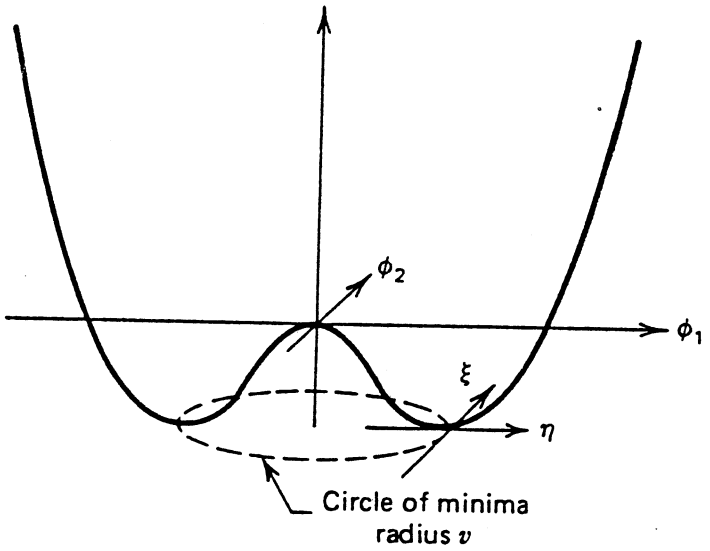

Figure 2.3.2 : The potential $V(\phi)$ for a complex scalar field for the case $\mu^2 < 0$ and $\lambda > 0$.

potential V(ϕ). The quantity $< \phi >_0$ is referred to as the vacuum expectation of the field ϕ.

If $\mu^2 > 0$ the minimum of the potential is at $< \phi >_0 = 0$. The approximate form of the Lagrangian for small oscillations around $< \phi >_0$ is

$$\mathcal{L} = \frac{1}{2}\left[(\partial_\mu \phi)(\partial^\mu \phi) - \mu^2 \phi^2\right]$$

which is that of a free particle of mass = μ .

However, there is no physical reason to require $\mu^2 > 0$. If $\mu^2 < 0$ the potential has two minima which satisfy

$$\frac{\partial V}{\partial \phi} = \phi(\mu^2 + \lambda\phi^2) = 0$$

and are therefore at

$$\phi = \pm\nu$$

where

$$\nu = \sqrt{\frac{-\mu^2}{\lambda}}$$

and which correspond to two degenerate lowest-energy states either of which may be chosen to be the vacuum. Whatever is the choice, however, the symmetry of the theory is spontaneously broken ; the parity transformation $\phi \rightarrow -\phi$ is then an invariance of the Lagrangian but not of the vacuum state.

Perturbative calculations are performed around the classical minimum $\phi = \nu$ or $\phi = -\nu$. For example,

$$\phi(x) = \nu + \eta(x) \qquad (2.3.2)$$

where $\eta(x)$ represents the quantum fluctuations about the minimum. Substituting Equation (2.3.2) into Equation (2.3.1) gives

$$\mathcal{L}' = \frac{1}{2}(\partial_\mu \eta \partial^\mu \eta) - (\lambda\nu^2\eta^2 + \lambda\nu\eta^3 + \frac{1}{4}\lambda\eta^4) + \text{const.} \qquad (2.3.3).$$

The field η can be interpreted as a mass term as η^2 has the correct sign. Therefore, the Lagrangian describes a particle with mass

$$m_\eta^2 = 2\lambda\nu^2 = -2\mu^2$$

with two self-interactions : a cubic one of strength $\lambda\nu$ and a quartic one of strength $\frac{\lambda}{4}$. Since the parameter λ is an unknown free parameter the strengths are also unknown. The constant can be ignored since the zero level of the potential can be redefined.

The Lagrangians $\mathcal{L}$ and $\mathcal{L}'$ are expected to be completely equivalent as a transformation of the type in Equation (2.3.2) cannot change the physics. However, by using $\mathcal{L}$ the perturbation series does not converge because the expansion is around the unstable point $\phi = 0$. The correct way to proceed is to use $\mathcal{L}'$ and expand in η around the stable vacuum $\phi = \pm\nu$. In perturbation theory, the scalar particle as predicted from $\mathcal{L}'$ does have a mass.

The same procedure can be applied for a complex scalar field

$$\phi = \frac{\phi_1 + i\phi_2}{\sqrt{2}}$$

described by the Lagrangian

$$\mathcal{L} = (\partial_\mu\phi)^*(\partial^\mu\phi) - \mu^2\phi^*\phi - \lambda(\phi^*\phi)^2.$$

This is invariant under a global gauge transformation

$$\phi \rightarrow \phi' = e^{ix}\phi$$

so that the symmetry of $\mathcal{L}$ is now a global U(1) continuous symmetry instead of a reflection as above. As before, the case for $\lambda > 0$ and $\mu^2 < 0$ is considered. The terms of the real components are

$$\mathcal{L} = \frac{1}{2}(\partial_\mu\phi_1)^2 + \frac{1}{2}(\partial_\mu\phi_2)^2 - \frac{1}{2}\mu^2(\phi_1^2 + \phi_2^2) - \frac{\lambda}{4}(\phi_1^2 + \phi_2^2)^2 \qquad (2.3.4).$$

There is now a circle of minima of the potential $V(\phi)$ in the (ϕ_1, ϕ_2) plane of radius ν such that

$$\phi_1^2 + \phi_2^2 = \nu^2$$

with

$$\nu^2 = \frac{-\mu^2}{\lambda}$$

as shown in Figure 2.3.2. Again, the field ϕ is translated to a minimum energy position, which without loss of generality is taken to be $\phi_1 = \nu$ and $\phi_2 = 0$. Expanding $\mathcal{L}$ about the vacuum in terms of the fields η, ξ by substituting

$$\phi(x) = \frac{\nu + \eta(x) + i\rho(x)}{\sqrt{2}}$$

into Equation (2.3.4) gives

$$\mathcal{L}' = \frac{1}{2}(\partial_\mu \rho)^2 + \frac{1}{2}(\partial_\mu \eta)^2 + \mu^2\eta^2 - \lambda\nu(\eta\rho^2 + \eta^3) -$$

$$\frac{\lambda}{2}\eta^2\rho^2 - \frac{\lambda}{4}\eta^4 - \frac{\lambda}{4}\rho^4 + \text{const.}$$

The first two terms are the kinetic energy terms. The term $\mu^2\ \eta^2$ is the mass term for the η - field ($m_\eta^2 = 2 \mid \mu^2 \mid$). There is no corresponding mass term for the ρ - field. That is, the theory also contains a massless scalar which is known as a Goldstone boson. There is a theorem, the Goldstone theorem [Gol-61, Gol-62], stating that whenever a continuous global symmetry such as U(1) is spontaneously broken, the spectrum will contain a massless, spin-zero boson. Therefore, a problem is encountered because in attempting to generate massive gauge bosons the spontaneously broken gauge theory introduces its own massless scalar.

2.3.3 The Higgs Mechanism

Previously, only global gauge invariance was considered. To describe the Higgs mechanism, spontaneous breaking of a local gauge symmetry is needed. Invariance under a local gauge transformation requires the introduction of a massless vector field A_μ and $\mathcal{L}$ as given in Equation (2.3.4) for a U(1) gauge symmetry should be written in terms of the covariant derivative

$$\partial_\mu \rightarrow D_\mu = \partial_\mu - igA_\mu$$

where the gauge field transforms as

$$A_\mu \rightarrow A'_\mu = A_\mu - \frac{1}{g}\partial_\mu \chi(x)$$

and ϕ is invariant under

$$\phi(x) \rightarrow \phi'(x) = e^{ix(x)}\phi(x).$$

The gauge invariant Lagrangian is thus

$$\mathcal{L} = (D_\mu\phi)^*(D^\mu\phi) - \mu^2\phi^*\phi - \lambda(\phi^*\phi)^2 - \frac{1}{4}F_{\mu\nu}F^{\mu\nu} \qquad (2.3.5).$$

This Lagrangian contains four independent fields or degrees of freedom - the two real scalar fields ϕ_1 and ϕ_2 and the two transverse polarization states of the massless vector boson.

For $\mu^2 > 0$ this describes the interaction of a charged scalar particle (with g = e) of mass μ with the electromagnetic field, for example. There is no mass term for A_μ.

The situation where $\mu^2 < 0$ is that of a spontaneously broken symmetry. The field ϕ can be written in the form

$$\phi(x) = \eta(x)e^{-i\rho(x)}$$

where η and ρ are real so that $\phi(x)$ can be written in the form

$$\phi(x) = \frac{\nu + h(x)}{\sqrt{2}} \qquad (2.3.6)$$

with h being real and where the transformation

$$\phi \rightarrow e^{ix(x)}\phi$$

has been used. Expanding $\mathcal{L}$ about the vacuum in terms of the field η and ρ by substituting Equation (2.3.6) into Equation (2.3.5) gives

$$\mathcal{L}' = \frac{1}{2}(\partial_\mu h)(\partial^\mu h) + \frac{1}{2}g^2\nu^2 A_\mu A^\mu - \lambda\nu^2 h^2 - \lambda\nu h^3 - \frac{\lambda}{4}h^4 +$$

$$g^2\nu h A^\mu A_\mu + \frac{1}{2}g^2 h^2 A_\mu A^\mu - \frac{1}{4}F_{\mu\nu}F^{\mu\nu}.$$

The particle spectrum of $\mathcal{L}'$ is a massive scalar η ($m_\eta = \sqrt{2\lambda\nu^2}$) and a massive vector A_μ ($m_{A_\mu} = g\nu$). There is also a single real Higgs boson, h, with mass $2\lambda\nu^2$, which has self-interactions and also cubic and quartic interactions with the gauge field A_μ. The mass of the gauge boson is fixed if g and ν are known, but the mass of the Higgs boson depends on the unknown parameter λ.

There is no Goldstone boson left over. The Goldstone boson has become the longitudinal polarization state of the gauge boson and the gauge vector boson has acquired mass. It may be said that the massless photon 'ate' the massless Goldstone boson to become a massive vector boson. This phenomenon is referred to as the Higgs mechanism.

The same procedure studied above for the spontaneous symmetry breaking of a U(1) symmetry can be repeated for a SU(2) gauge symmetry. The Lagrangian is

$$\mathcal{L} = (\partial_\mu \phi)^\dagger (\partial^\mu \phi) - \mu^2 \phi^\dagger \phi - \lambda (\phi^\dagger \phi)^2$$

where ϕ is an SU(2) doublet of complex scalar fields :

$$\phi = \begin{pmatrix} \phi^\dagger \\ \phi^0 \end{pmatrix}$$

which can be written as

$$\phi = \sqrt{\frac{1}{2}} \begin{pmatrix} \phi_1 + i\phi_2 \\ \phi_3 + i\phi_4 \end{pmatrix} \qquad (2.3.7)$$

The potential $V(\phi)$ is invariant under

$$\phi(x) \rightarrow \phi'(x) = e^{-\alpha_a(x) \cdot \frac{\tau_a}{2}} \phi(x) \qquad (2.3.8)$$

where τ_a are the Pauli matrices and α_a are multiplicative parameters and a = 1,2,3. To achieve local, i.e. $\alpha_a(x)$, SU(2) invariance of the Lagrangian, ∂_μ is replaced by the covariant derivative D_μ

$$D_\mu = \partial_\mu + ig\frac{\tau_a}{2} W_\mu^a.$$

Under the infinitesimal gauge transformation given in Equation (2.3.8) the three gauge fields transform as

$$W_\mu \rightarrow W_\mu - \frac{1}{g}\partial_\mu \alpha - \alpha W_\mu$$

so that the gauge invariant Lagrangian is then

$$\mathcal{L}' = (\partial_\mu \phi + ig\frac{1}{2}\tau_i \cdot W_{\mu,i}\, \phi)^\dagger (\partial^\mu \phi + ig\frac{1}{2}\tau_i \cdot W_i^\mu\, \phi)$$

$$- V(\phi) - \frac{1}{4} W_{\mu\nu} \cdot W^{\mu\nu} \qquad (2.3.9)$$

where i = 1,2,3.

For $\mu^2 < 0$ and $\lambda > 0$, $V(\phi)$ has its minimum at a finite value of $|\phi|$ where

$$\phi^\dagger\phi = \frac{1}{2}(\phi_1^2 + \phi_2^2 + \phi_3^2 + \phi_4^2) = \frac{-\mu^2}{2\lambda}.$$

A particular direction in SU(2) space is chosen and expanded around the minimum. To preserve the U(1) symmetry so that the photon remains massless, the choice is

$$\phi_1 = \phi_2 = \phi_4 = 0$$

$$\phi_3^2 = \frac{-\mu^2}{\lambda} \equiv \nu^2$$

so that the vacuum ϕ_0 is

$$<\phi>_0 = \frac{1}{\sqrt{2}}\begin{pmatrix} 0 \\ \nu \end{pmatrix} \qquad (2.3.10).$$

As before the spectrum is studied by expanding around the vacuum so that

$$\phi(x) = \frac{1}{\sqrt{2}}\begin{pmatrix} 0 \\ \nu + H(x) \end{pmatrix} \qquad (2.3.11).$$

To determine the masses generated for the gauge bosons, W_μ^a, it is sufficient to substitute the $<\phi>_0$ of Equation (2.3.10) into the Lagrangian. The relevant term of Equation (2.3.9) is then

$$|\, ig\frac{1}{2} \cdot W_\mu\phi\,|^2 = \frac{g^2\nu^2}{8}\left[(W_\mu^1)^2 + (W_\mu^2)^2 + (W_\mu^3)^2\right].$$

Therefore, the Lagrangian describes three massive gauge fields and one massive scalar h. In summary, the gauge fields have 'eaten up' the Goldstone bosons and become massive.

2.3.4 Gauge Boson Masses in the Standard Model

In this section, the formulation of the Higgs mechanism is presented so that the $W^\pm$ and Z^0 become massive and the photon remains massless.

The SU(2) x U(1) gauge invariant Lagrangian for the scalar fields is

$$\mathcal{L} = |\,(i\partial_\mu - g\frac{1}{2}\tau_i \cdot W_{\mu i} - g'\frac{Y}{2}B_\mu)\phi\,|^2 - V(\phi) \qquad (2.3.12).$$

To keep $\mathcal{L}$ gauge invariant, the ϕ_i must belong to SU(2) x U(1) multiplets. The most economical choice is to arrange four fields in an isospin doublet with weak hypercharge Y = 1 as in Equation (2.3.7).

To generate the gauge boson masses the Higgs potential

$$V(\phi) = \mu^2\phi^\dagger\phi + \lambda(\phi^\dagger\phi)^2$$

is used with $\mu^2 < 0$ and $\lambda > 0$. A vacuum expectation value as in Equation (2.3.10) is chosen. As before the gauge boson masses are identified by substituting $< \phi >_0$ for $\phi(x)$ in the Lagrangian. The relevant term in Equation (2.3.12) is given in Figure 2.3.3. The gauge boson masses then follow :

$$M_W = \frac{1}{2}\nu g$$

since the mass term expected for a charged boson is $M_W^2 W^+W^-$,

$$M_Z = \frac{1}{2}\nu\sqrt{g^2 + g'^2}$$

since

$$Z_\mu = \frac{g'Y_L B_\mu + gW_\mu^3}{\sqrt{g^2 + g'^2 Y_L^2}}$$

taking Y_L = -1, and

$$M_A = 0$$

since no $A^\mu A_\mu$ term appears.

From

$$e = g\sin\theta_W = g'\cos\theta_W$$

one gets

$$\frac{M_W}{M_Z} = \cos\theta_W.$$

This prediction is in excellent agreement with experimental observations of

$$M_W = 80.14 \pm 0.27,$$

[UA2-91c, CDF-90a, CDF-91d]

$$M_Z = 91.175 \pm 0.021,$$

$$\left|\left(-ig\frac{\tau}{2}\cdot\mathbf{W}_\mu - i\frac{g'}{2}B_\mu\right)\phi\right|^2$$

$$= \frac{1}{8}\left|\begin{pmatrix} gW_\mu^3 + g'B_\mu & g\left(W_\mu^1 - iW_\mu^2\right) \\ g\left(W_\mu^1 + iW_\mu^2\right) & -gW_\mu^3 + g'B_\mu \end{pmatrix}\begin{pmatrix} 0 \\ v \end{pmatrix}\right|^2$$

$$= \tfrac{1}{8}v^2g^2\left[\left(W_\mu^1\right)^2 + \left(W_\mu^2\right)^2\right] + \tfrac{1}{8}v^2\left(g'B_\mu - gW_\mu^3\right)\left(g'B^\mu - gW^{3\mu}\right)$$

$$= \left(\tfrac{1}{2}vg\right)^2 W_\mu^+ W^{-\mu} + \tfrac{1}{8}v^2\left(W_\mu^3,\, B_\mu\right)\begin{pmatrix} g^2 & -gg' \\ -gg' & g'^2 \end{pmatrix}\begin{pmatrix} W^{3\mu} \\ B^\mu \end{pmatrix},$$

Figure 2.3.3 : The term in the SU(2) x U(1) gauge invariant Lagrangian after spontaneous symmetry breaking which gives mass to the gauge bosons (see text).

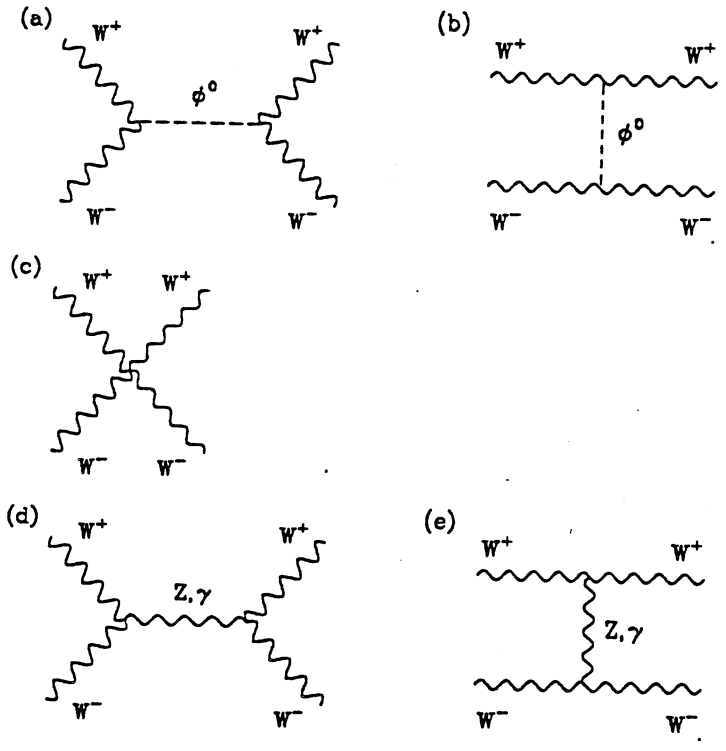

Figure 2.3.4 : The complete set of gauge invariant diagrams for WW scattering in the unitary gauge at the tree-level.

[Mor-92b]

$$\sin^2\theta_W(M_Z) \;=\; 0.2309 \pm 0.0009.$$

This result for $\frac{M_W}{M_Z}$ is a prediction of the Standard Model including a Higgs doublet. In the Standard Model, therefore, the Higgs doublet fixes

$$\rho \;\equiv\; \frac{M_W^2}{M_Z^2 \cos^2\theta_W} = 1$$

and it is also true that if additional doublets (or singlets) of Higgs fields are present, it is guaranteed that $\rho \approx 1$ at the tree level (see Section 2.6.1). Any deviation from $\rho \approx 1$ would be an indication of new physics.

2.3.5 The Fermion Masses

The same Higgs doublet which generates the $W^{\pm}$ and Z^0 masses is also sufficient to give mass to the leptons and quarks. The interaction term for leptons in the Lagrangian is

$$\mathcal{L} \;=\; g_e \left[(\overline{\nu}_e, \overline{e})_L \begin{pmatrix} \phi^+ \\ \phi^0 \end{pmatrix} e_R \;+\; \overline{e}_R \left(\phi^-, \overline{\phi}^0\right) \begin{pmatrix} \nu_e \\ e \end{pmatrix}_L \right] \qquad (2.3.13).$$

The symmetry is spontaneously broken and

$$\phi(x) \;=\; \frac{1}{\sqrt{2}} \begin{pmatrix} 0 \\ \nu + H(x) \end{pmatrix}$$

is substituted into Equation (2.3.13) to give

$$\mathcal{L}' \;=\; \frac{g_e \nu}{\sqrt{2}} \left(\overline{e_L^-} e_R^- \;+\; \overline{e_R^-} e_L^- \right) + \frac{g_e}{\sqrt{2}} \left(\overline{e_L^-} e_R^- \;+\; \overline{e_R^-} e_L^- \right) H \qquad (2.3.14).$$

The first term gives the electron mass

$$m_e \;=\; \frac{g_e \nu}{\sqrt{2}}$$

so that the Standard Model accomodates a non-zero electron mass. (The same applies for the other lepton families). The second term in Equation (2.3.14) suggests that the electron - Higgs vertex is of strength

$$\frac{g_e}{\sqrt{2}} \;=\; \frac{m_e}{\nu}.$$

For quarks the interaction Lagrangian is

$$\mathcal{L} = m_d \bar{d}d + m_u \bar{u}u + \frac{m_d}{\nu}\bar{d}dH + \frac{m_u}{\nu}\bar{u}uH.$$

Therefore, since the Higgs interacts with a strength proportional to the fermion mass, it couples most strongly to the heaviest fermions. The Higgs is difficult to discover precisely because of its characteristic property of coupling to fermions in proportion to their mass. The most readily experimentally accessible particles are light fermions (electrons, and u and d quarks in protons and neutrons) but they couple to the Higgs particle weakly. The heavier fermions, (τ , c, b, t), couple more readily to Higgs but are difficult to produce or as in the case of the top quark, have not yet been observed.

2.3.6 The Higgs Mass

One of the key unknown parameters in the Standard Model is the mass of the Higgs boson. It was shown above that the Higgs mass depends on the coefficient λ of the Higgs self-interaction in the Higgs potential. Since there is no understanding of the physical origin of λ, its numerical value is not known. Nor does any other observable depend on λ in a way that allows λ to be extracted.

In addition to generating the mass of the weak bosons, a second motivation for the introduction of a scalar Higgs particle into the Electroweak Theory is to guarantee its renormalizability [Bel-73, Lle-73, Cor-73, Cor-74]. Consider the scattering of W bosons at the tree-level as shown in Figure 2.3.4. Initially, suppose that the scattering amplitude for

$$W_L^+ W_L^- \rightarrow W_L^+ W_L^-$$

is calculated using the Standard Model Feynman rules without introducing the diagrams involving the Higgs boson. (Longitudinally polarized W bosons are studied because of their bad high energy behaviour since in the large energy limit the polarization vector of longitudinally polarized W bosons is

$$\epsilon_L^\mu(p) \approx \frac{p^\mu}{M_W}).$$

It can be shown that each individual diagram diverges as $\frac{s^2}{M_W^4}$ whereas the divergence of the sum of the diagrams goes like

$$-i\mathcal{M}\left(W_L^+W_L^- \rightarrow W_L^+W_L^-\right) \sim \frac{s}{M_W^2}$$

as $s \rightarrow \infty$ where s is the centre-of-mass energy squared for the process. Even after introducing similar diagrams incorporating the Z^0 , the sum of all diagrams still diverges as $\frac{s}{M_W^2}$. (The introduction of heavy leptons is not favoured since there is no experimental evidence for their existence).

By introducing the diagrams involving the Higgs particle, the amplitude for

$$W_L^+W_L^- \rightarrow W_L^+W_L^-$$

in the limit s, $m_{H^0}^2 \gg M_W^2$, M_Z^2 becomes :

$$\mathcal{A}(W_L^+W_L^- \rightarrow W_L^+W_L^-) = -\sqrt{2}G_F m_{H^0}^2\left[\frac{s}{s-m_{H^0}^2} + \frac{t}{t-m_{H^0}^2}\right].$$

As $m_{H^0} \rightarrow \infty$ the above amplitude grows linearly in s thus violating unitarity. However, for some finite range in m_{H^0} , the introduction of the diagrams involving the Higgs boson cancel the residual divergences in

$$W_L^+W_L^- \rightarrow W_L^+W_L^-.$$

By computing the J = 0 partial-wave amplitude matrix for the normalized states $W_L^+W_L^-$, $\sqrt{\frac{1}{2}}Z_LZ_L$, Z_LH^0, and $\sqrt{\frac{1}{2}}\,H^0H^0$ the most restrictive bound on m_{H^0} is derived from the largest eigenvalue of the amplitude matrix :

$$m_{H^0}^2 \leq \frac{4\pi\sqrt{2}}{3G_F} \approx (700\ \text{GeV})^2 \qquad (2.3.15).$$

Therefore, the tree-level amplitude violates unitarity (at sufficiently large energies) if m_{H^0} is above 700 GeV. This mass bound is interpreted as the largest Higgs mass for which perturbation theory is reliable for all s.

However, it could happen that the scalar interaction is not due to a single fundamental boson, but is generated by the non-perturbative behaviour of the theory, examples of which are bound states of $t\bar{t}$ [Nam-89a, Nam-89b]. Whatever is the case, however, some spin-zero interaction must occur to guarantee renormalizability of the Electroweak Theory.

Table 2.4.1 : Published LEP Lower Mass Limits for H^0 at 95% C.L.

Experiment	m_{H^0} Lower Mass Limits (GeV)
ALEPH	48.0
DELPHI	38.0
L3	41.8
OPAL	44.0

2.4 Experimental Limits on the Mass of the H^0

Direct searches for the Standard Model Higgs boson, H^0 , have been carried out at LEP. With more than 500 000 Z^0 events collected in e^+e^- collisions until the end of 1990, each of the four experiments at LEP has performed a search for H^0 in the mass range from zero to about 50 GeV.

The dominant H^0 production mode at LEP is the Bjorken Bremsstrahlung process [Bjo-76] as is shown in Figure 2.4.1. The H^0 is produced in association with an off-mass-shell Z^0 which decays into a fermion-antifermion pair with branching ratios which are :

$$\mathrm{Br}(Z^* \rightarrow \nu\overline{\nu}) \sim 20\%,$$

$$\mathrm{Br}(Z^* \rightarrow l^+l^-) \sim 10\%,$$

$$\mathrm{Br}(Z^* \rightarrow q\overline{q}) \sim 70\%.$$

The most background-free signature for this process is when the virtual Z^0 decays into charged leptons or neutrinos. The cross-section for this process decreases exponentially with increasing m_{H^0} and is the main limiting factor for H^0 searches in the high mass range. The LEP experiments exclude at the 95% confidence level (C.L.) the presence of the H^0 with a mass ranging from zero to a lower limit given in Table 2.4.1 [EPS-91a]. Combining the results of the four LEP experiments gives $m_{H^0} > 57$ GeV at the 95% C.L.

Recently, preliminary results on m_{H^0} have been presented by the four LEP experiments for the total 1989 to 1991 data samples [Mor-92c]. The preliminary LEP mass limits on H^0 at the 95% C.L. are given in Table 2.4.2.

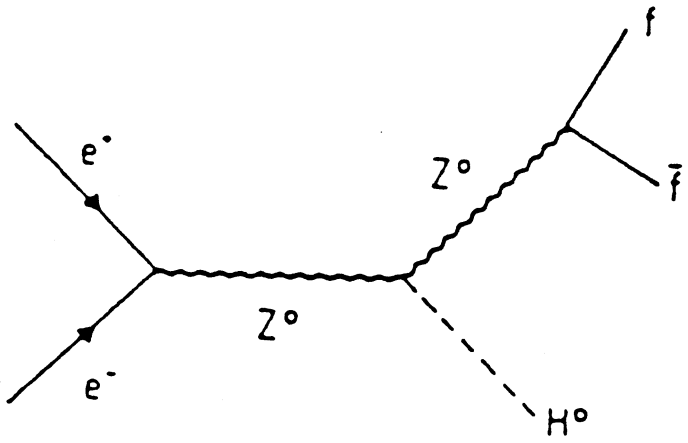

Figure 2.4.1 : The Bjorken Bremsstrahlung process for H^0 production at electron-positron colliders.

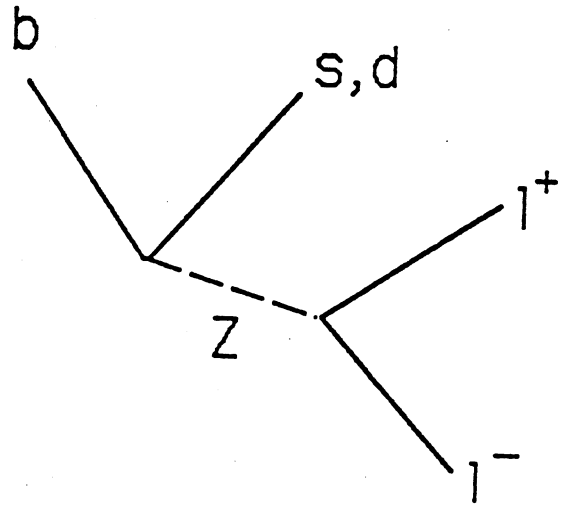

Figure 2.5.1 : Flavour - changing neutral current interaction $B \rightarrow l^+l^-X$.

Table 2.4.2 : Preliminary LEP Lower Mass Limits for H^0 at 95% C.L.

Experiment	m_{H^0} Lower Mass Limits (GeV)
ALEPH	53.0
DELPHI	47.0
L3	52.3
OPAL	51.0

The combined LEP preliminary lower mass limit is $m_{H^0} > 59.2$ GeV at the 95% C.L.

Indirect limits on m_{H^0} have been placed from a global analysis of electroweak data from LEP (including m_{Z^0}, Γ_{Z^0}, σ^0_h, $\Gamma_{b\bar{b}}$, $\Gamma_{c\bar{c}}$, A^l_{FB}, A^b_{FB}, A^τ_{pol}), and other electroweak precision data from UA2 and CDF on m_W and from low energy $\nu - q$, $\nu - e$, and e - q scattering data and $\sin^2\theta_W$ from CHARM II. (The data set has been taken from presentations at the Lepton-Photon and EPS High Energy Conference in 1991 [EPS-91b]). A global fit to the data for a top mass of 150 GeV minimizes the global χ^2 when $m_{H^0} = 10$ GeV and also yields

$$1.4 \text{ GeV} < m_{H^0} < 160 \text{ GeV at 68\% C.L. or}$$

$$0.5 \text{ GeV} < m_{H^0} < 1500 \text{ GeV at 90\% C.L.}$$

if the top mass is left unconstrained.

2.5 The Top Quark

2.5.1 Why the Top Quark Must Exist

In this section indirect evidence for the top quark is presented. Firstly, if there is no top quark such that the b-quark is in a singlet then $T^b_3 = 0$ whereas if the b-quark is in a doublet with another quark then $T^3_b = -\frac{1}{2}$. The experimental data suggest that the b-quark exists in a doublet with another quark. By definition the other quark is the top quark.

Consider the process

$$e^+e^- \rightarrow b\bar{b}$$

at electron-positron machines such as LEP. Interference of the vector and axial-vector currents can result in a cross-section for this process which is asymmetric with respect to the cosine of the angle between the electron and b-quark directions. The ratio of vector to axial-vector coupling constants can be written as

$$\frac{g_{V_b}}{g_{A_b}} = 1 \pm \frac{2Q^b}{T_3^b}\sin^2\theta_W$$

for the coupling of a b-quark to the Z^0 (see Section 2.2). A value of $\sin^2\theta_W$ can be extracted from measurements of the forward-backward asymmetry, A_{FB}^b, in the above process since the forward-backward asymmetry is given in terms of the couplings by :

$$A_{FB}^q = \frac{3}{4}\mathcal{A}_e\mathcal{A}_q$$

where

$$\mathcal{A}_f = 2\,\frac{g_{V_f}\,g_{A_f}}{g_{V_f}^2 + g_{A_f}^2}$$

and

$$Q^b = -\frac{1}{3}.$$

The LEP measurement of $\sin^2\theta_W$ from A_{FB}^b is [Mor-92b]

$$\sin^2\theta_W = 0.2325 \pm 0.0025$$

assuming that $T_b^3 = -\frac{1}{2}$. This compares favourably to the value of $\sin^2\theta_W$ using other methods at LEP (τ polarization, the Z^0 lineshape, jet charge asymmetries, and A_{FB}^l) which is [Mor-92b]

$$\sin^2\theta_W = 0.2319 \pm 0.0009.$$

Therefore, $T_3^b = -\frac{1}{2}$ and the b-quark resides in a doublet.

In addition, the absence of flavour-changing neutral currents, (FCNCs), suggests that the b-quark occurs in a doublet. Suppose the b-quark is in a singlet. Then as Kane and Peskin have indicated [Kan-82] there would exist substantial FCNC interactions such as that depicted in Figure 2.5.1. These authors predict that

$$Br(b \rightarrow l^+l^-X) > 1.3 \times 10^{-2}.$$

However, from the decay of the Y(4S) resonance to $\mu^+\mu^-X$ and e^+e^-X final states measured by the CLEO Collaboration [CLE-87],

$$Br(b \rightarrow l^+l^-X) \; < \; 3.1 \times 10^{-3}$$

thus ruling out a five-quark model.

The requirement of renormalizability of the electroweak theory adds a further constraint to the number of fermions present in the theory. Figure 2.5.2 shows a diagram in which two vector and one axial current are coupled to a fermion loop. This diagram is linearly divergent leading to an anomaly in the theory. Cancellation of the lowest order triangle diagram is sufficient to ensure that the theory is free from anomalies at all orders. The diagram must be summed over all possible fermion loops and is proportional to [Gro-72, Geo-72, Bou-72]

$$A \; = \; Tr\left[G_R^a\{G_R^b, G_R^c\}\right] \; - \; Tr\left[G_L^a\{G_L^b, G_L^c\}\right]$$

where G_R and G_L are the matrices coupling the currents to the fermion loop at each of the three corners of the traingle for right and left handed fermions, respectively. Substituting all possible combinations of G_R and G_L two of the resulting traces are zero for each fermion :

$$Tr\; T^a\{T^b, T^c\} \; = \; 0$$

$$Tr\; T^a\{Y_L, Y_L\} \; = \; 0$$

where Y is the hypercharge defined by

$$Q^f \; = \; T_3^f \; + \; \frac{Y}{2}$$

while the other traces only vanish for a complete family :

$$Tr\; \left(Y_R^3, Y_L^3\right) \; = \; 0$$

$$Tr\; Y^L\{T^a, T^b\} \; = \; 0.$$

This leads to the conclusion that complete doublets are needed if the Standard Model is to be renormalizable.

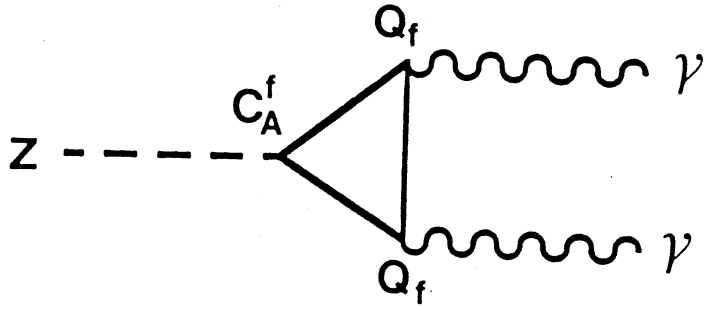

Figure 2.5.2 : Triangle diagram which may lead to an anomaly.

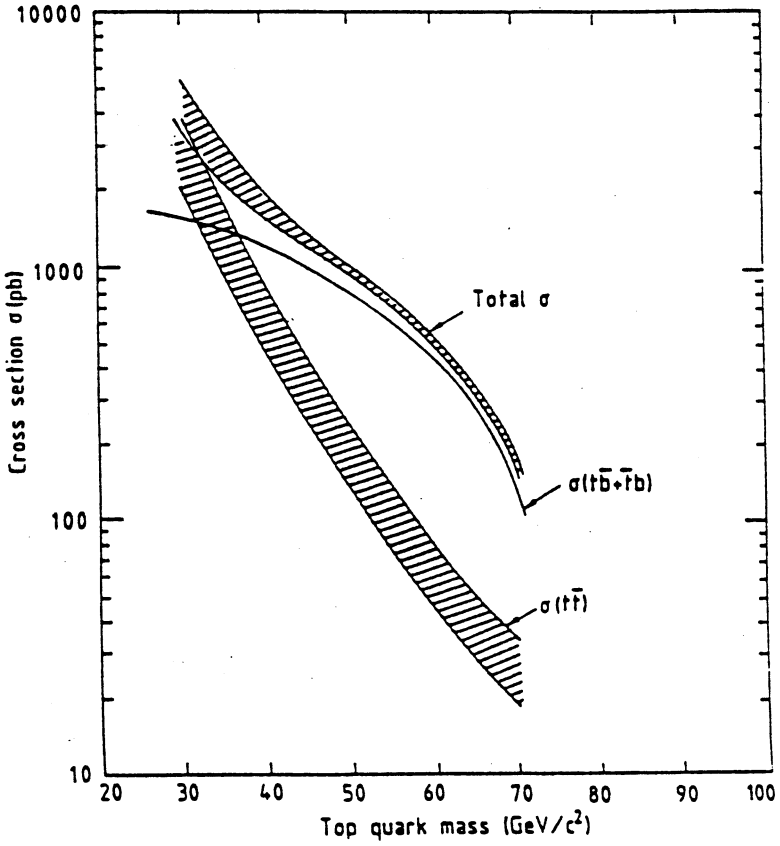

Figure 2.5.3 : The electroweak, strong and total cross-sections for top quark production at $\sqrt{s} = 630$ GeV.

2.5.2 Top Quark Production in $p\bar{p}$ Collisions

Top quarks satisfying $m_t < M_W + m_b$ could be produced at the CERN $p\bar{p}$ Collider from two dominant processes either mediated by the weak interaction $(t\bar{b})$:

$$p\bar{p} \rightarrow W + X \; ; \; W \rightarrow t\bar{b} \text{ or } \bar{t}b \qquad (2.5.1)$$

or by the strong interaction $(t\bar{t})$:

$$p\bar{p} \rightarrow t\bar{t} \; + \; X \qquad (2.5.2).$$

Figure 2.5.3 shows the expected rates of top quark production by each mechanism as a function of the top quark mass at the CERN Collider. It is seen that for m_t less than about 70 GeV the electroweak process is dominant at $\sqrt{s} = 630$ GeV.

Electroweak Production Process

A schematic of the top quark production process through the electroweak process is shown in Figure 2.5.4. The Feynman diagrams for the production of a W through the electroweak interaction to $O(\alpha_s)$ are shown in Figure 2.5.5 and the corresponding diagrams for $W \rightarrow tb$ in Figure 2.5.6. The cross-section for top quark production from process (2.5.1) can be computed from

$$\sigma_{t\bar{b}} \equiv \sigma(p\bar{p} \rightarrow W + X \rightarrow t\bar{b} + X)$$

which is

$$\sigma_{t\bar{b}} = \sigma(W \rightarrow e\nu_e) \; x \; \frac{BR(W \rightarrow t\bar{b})}{BR(W \rightarrow e\nu_e)}$$

and can be written as

$$\sigma_{t\bar{b}} = \sigma(W \rightarrow e\nu_e) \; \Phi(m_t) \; C_F \; F_{QCD}.$$

Here, $\Phi(m_t)$ is a phase space factor, taking into account that the W is decaying into massive quarks rather than light leptons, C_F accounts for the possible colour final states and F_{QCD} is a correction for higher order QCD processes. The colour and phase-space factors are

$$C_F = 3$$

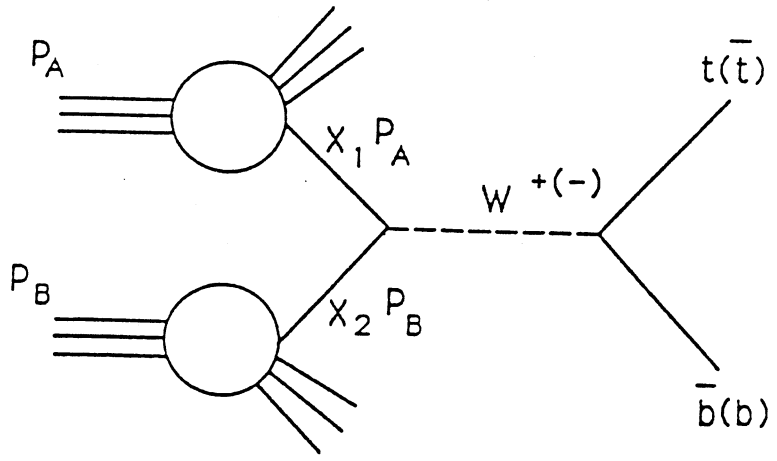

Figure 2.5.4 : A schematic diagram for W boson production through the electroweak Drell-Yan process.

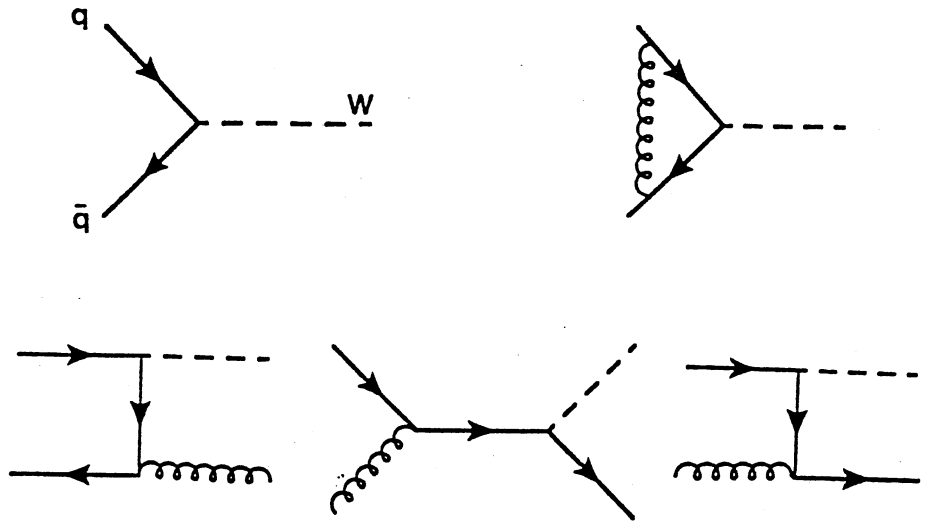

Figure 2.5.5 : The Feynman diagrams for the production of a W boson through the electroweak interaction to $O(\alpha_s)$.

Table 2.5.1 : Top Quark Production Cross-sections

m_t (GeV)	$\sigma_{t\bar{b}}$ (pb)	$\sigma_{t\bar{b}}$ xBR	$\sigma_{t\bar{t}}$ (pb)	$\sigma_{t\bar{t}}$ xBR
50	845 ± 25	530 ± 16	188 ± 56	164 ± 47
55	654 ± 25	406 ± 15	127 ± 54	111 ± 39
60	459 ± 23	282 ± 14	67 ± 20	58 ± 17
65	283 ± 20	172 ± 12	41 ± 12	36 ± 10
70	136 ± 14	82 ± 8	27 ± 8	24 ± 7

$$\Phi(\beta,\tau) = \frac{1}{2}\left[(1-\beta-\tau)^2 - 4\beta\tau\right]^{\frac{1}{2}} \cdot \left[(2-\beta-\tau) - (\beta-\tau)^2\right]$$

where

$$\beta = \frac{m_b^2}{\hat{s}} \text{ and } \tau = \frac{m_t^2}{\hat{s}}$$

with

$$s = E_{cm}^2$$

and $\hat{s} = x_1 x_2 s$ is the centre-of mass energy of the two partons involved in the hard-scattering and x_i (i=1,2) is the momentum fraction of the hadron's total momentum carried by the parton of type i as the hard interaction occurs. The QCD correction factor, F_{QCD}, becomes important if the top quark mass is close to that of the W boson. For example, for $M_W = 80.2$ GeV and $m_t = 65$ GeV, $F_{QCD} = 1.5$ [Rei-85, Alv-88]. Since this correction is determined from an incomplete theoretical calculation, it is set to the conservative value of 1.0 in this analysis and only the well-understood lowest order calculation is used to estimate the rate of top quark production.

For the 1988-1990 UA2 data, the cross-section for W production times the branching ratio for $W \rightarrow e\nu_e$ is [UA2-91b]

$$\sigma(p\bar{p} \rightarrow W + X) \text{ x } BR(W \rightarrow e\nu_e) = 682 \pm 12 \text{ (stat)} \pm 40 \text{ (syst) pb.}$$

The cross-sections for electroweak top production are given in Table 2.5.1 for $\sqrt{s} = 630$ GeV.

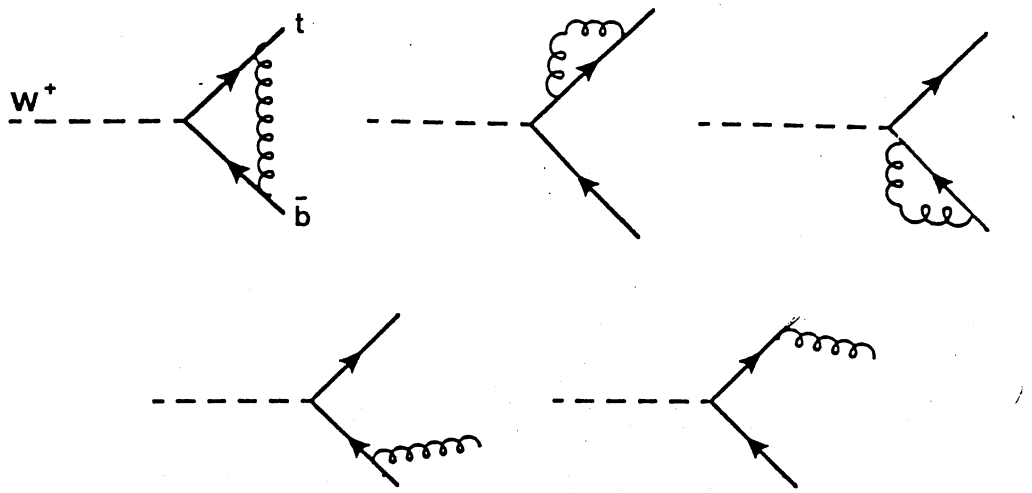

Figure 2.5.6 : The Feynman diagrams for the decay W $\rightarrow$ tb + X to O(α_s).

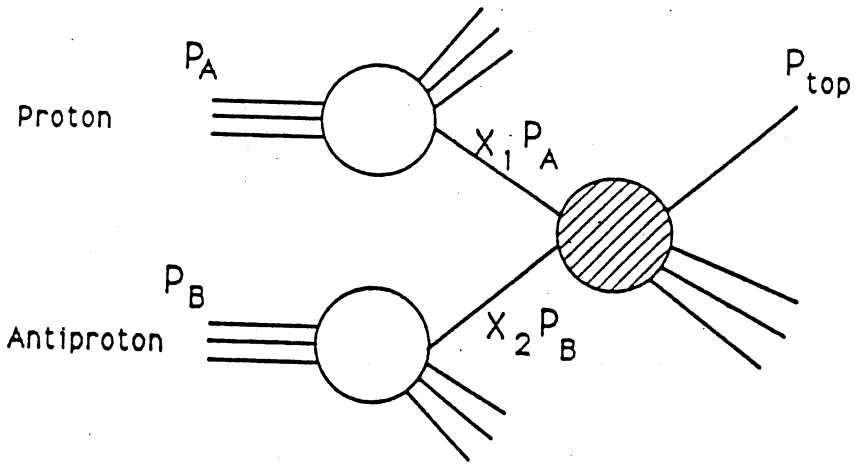

Figure 2.5.7 : Schematic diagram for top quark production through the strong interaction.

Strong Interaction Production Process

The invariant cross-section in the QCD parton model for the production of a heavy quark, Q, (such as the top quark), with momentum p and energy E in the collison of two hadrons, A and B, by the reaction

$$A(P_1) + B(P_2) \rightarrow Q(p) + X$$

is [Nas-87] (see Figure 2.5.7)

$$\frac{E\, d^3\sigma}{d^3p} = \sum_{ij} \int dx_1 dx_2 \left[\frac{E d^3\hat{\sigma}_{ij}(x_1P_1, x_2P_2, p, m_Q, \mu)}{d^3p}\right] \cdot$$

$$F_i^A(x_1, \mu)\, F_j^B(x_2, \mu) \quad (2.5.3).$$

Here, $F_i^H(x_1, \mu)$ is the number density of partons of type i carrying a momentum fraction between x and x + dx of the hadron's total momentum as the hard interaction occurs. The sum is over the light partons, i.e. the gluons and light quarks and antiquarks in the incident hadrons and $\hat{\sigma}$ is the short distance cross-section which may be expressed as a perturbation series in $\alpha_s(\mu)$ where μ is the renormalization scale (μ is taken to be of the order m_Q).

The lowest order contributions to $\hat{\sigma}$ have no mass singularities so that the short distance cross-section as defined above is equivalent to the perturbatively calculated cross-section. These first terms in the perturbation series are $O(\alpha_s^2)$ arising from quark-antiquark annihilation

$$q\bar{q} \rightarrow t\bar{t}$$

and gluon-gluon fusion

$$gg \rightarrow t\bar{t}.$$

Figure 2.5.8 shows the Feynman diagrams for the two processes at lowest order. In proton-antiproton collisions at $\sqrt{s} = 630$ GeV these two components contribute equally for $m_t = 40$ GeV while at higher masses the annihilation process dominates. At $\sqrt{s} = 1.8$ TeV for the Tevatron Collider, the gluon densities are much larger and the gluon fusion process dominates. In general the heavy quark transverse momentum, p_T^Q, is of the order m_Q, the rate of production falls rapidly for $p_T^Q > m_Q$ and the rapidity difference between the produced quark and antiquark is of order unity.

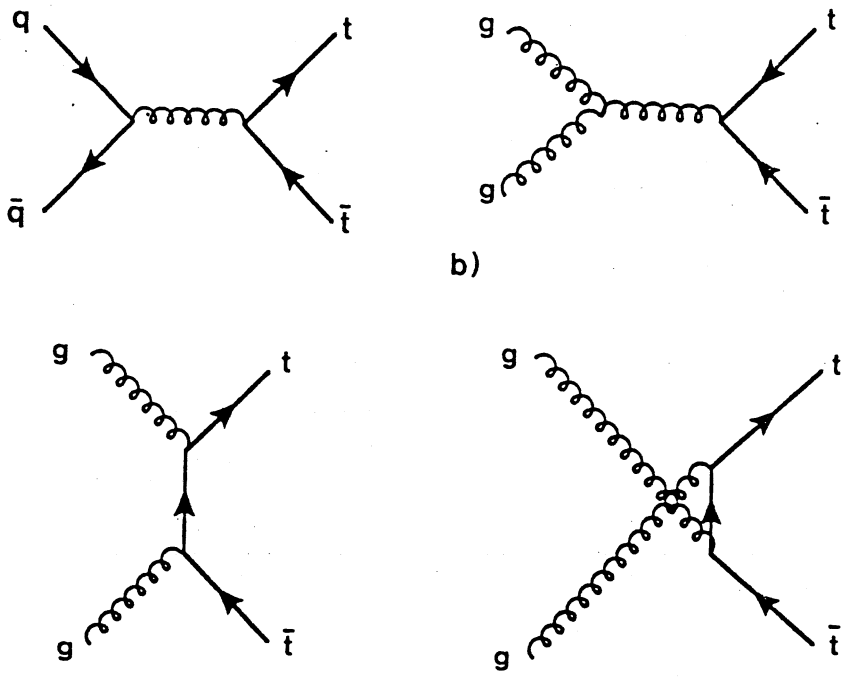

Figure 2.5.8 : Feynman diagram for top quark production to $O(\alpha_s^2)$ through the strong interaction.

The cross-sections for top quark production from the strong interaction to $O(\alpha_s^2)$ are [Com-79, Ali-87]

$$\sigma(q\bar{q} \rightarrow t\bar{t}) = \frac{\pi\alpha_s^2}{27\hat{s}^2}\left[\hat{s} + m_t^2\right]\chi$$

$$\sigma(gg \rightarrow t\bar{t}) = \frac{\pi\alpha_s^2}{3\hat{s}}\left[-\frac{1}{4}(7 + 31\frac{m_t^2}{\hat{s}})\chi + (1 + \frac{4m_t^2}{\hat{s}} + \frac{m_t^4}{\hat{s}^2})\ln\frac{1+\chi}{1-\chi}\right]$$

where

$$\chi = \sqrt{1 - \frac{4m_t^2}{\hat{s}}}.$$

The higher order corrections for heavy quark production are significant because at lowest order the rate for gluon scattering, $gg \rightarrow gg$, is at least 100 times greater than the rate for gluon fusion to a light quark-antiquark pair, $gg \rightarrow q\bar{q}$. Therefore, the $O(\alpha_s^3)$ process $g \rightarrow gg$ where one of the final state gluons splits into $Q\overline{Q}$ can be numerically as large as the $O(\alpha_s^2)$ contributions. Although a gluon jet will only fragment to a heavy $Q\overline{Q}$ pair a fraction

$$\frac{\alpha_s(m_Q^2)}{2\pi}$$

of the time, the high rate of gluon production means that this process is still significant.

Integrating the differential cross-section of Equation (2.5.3) gives

$$\sigma(s) = \sum_{ij}\int dx_1 dx_2 \hat{\sigma}_{ij}(x_1 x_2 s,\ m_Q^2,\ \mu^2) F_i^A(x_1,\mu) F_j^B(x_2,\mu).$$

The $\hat{\sigma}_{ij}$ may be written as

$$\hat{\sigma}_{ij}(\hat{s},\ m_Q^2,\ \mu^2) = \frac{\alpha_s^2(\mu^2)}{m_Q^2} f_{ij}(\rho, \frac{\mu^2}{m_Q^2})$$

where

$$\rho = \frac{4m_Q^2}{\hat{s}}$$

and μ is the renormalization scale. The complete functions f_{ij} are given in Ref. [Nas-87].

The running coupling constant, $\alpha_s(\mu)$, is described by the following renormalization group equation to two loop accuracy :

$$\mu^2 \frac{d}{d\mu^2}\alpha_s(\mu) = -b_f \alpha_s^2(1 + b_f'\alpha_s + ...) \quad (2.5.4)$$

where

$$b_f = \frac{33 - 2N_f}{12\pi}$$

and

$$b_f' = \frac{153 - 19N_f}{2\pi(33 - 2N_f)}$$

with N_f being the number of quark flavours. The α_s is related to the QCD parameter Λ by solving Equation (2.5.4) :

$$\alpha_s(\mu, N_f) = \frac{1}{b_f \ln\left(\frac{\mu^2}{\Lambda_N^2}\right)}\left[1 - \frac{b_f' \ln\left(\frac{\mu^2}{\Lambda_N^2}\right)}{b_f \ln\left(\frac{\mu^2}{\Lambda_N^2}\right)}\right].$$

It is clear that Λ depends on both the number of active flavours, N_f, and on the exact renormalization scheme used. The $\overline{MS}$ scheme is used here. The value of Λ used is [Alt-88a]

$$\Lambda^{\overline{MS}} = 170 \pm 80 \text{ MeV} \quad (2.5.5).$$

The renormalization scale is set to be m_Q and the error due to the scale uncertainties is obtained by letting μ vary in the range

$$\frac{m_Q}{2} < \mu < 2m_Q.$$

Table 2.5.1 gives the results for the $\sigma_{t\bar{t}}$ production cross-sections at the CERN Collider. The central values quoted are for $\mu = m_t$ and the DFLM structure function set [Die-88]. The uncertainties are calculated by allowing the scale μ to vary in the range given above and the structure functions have been explicitly evolved for a range of values of Λ in order to calculate the error in the cross-section corresponding to the error in Λ given in Equation (2.5.5).

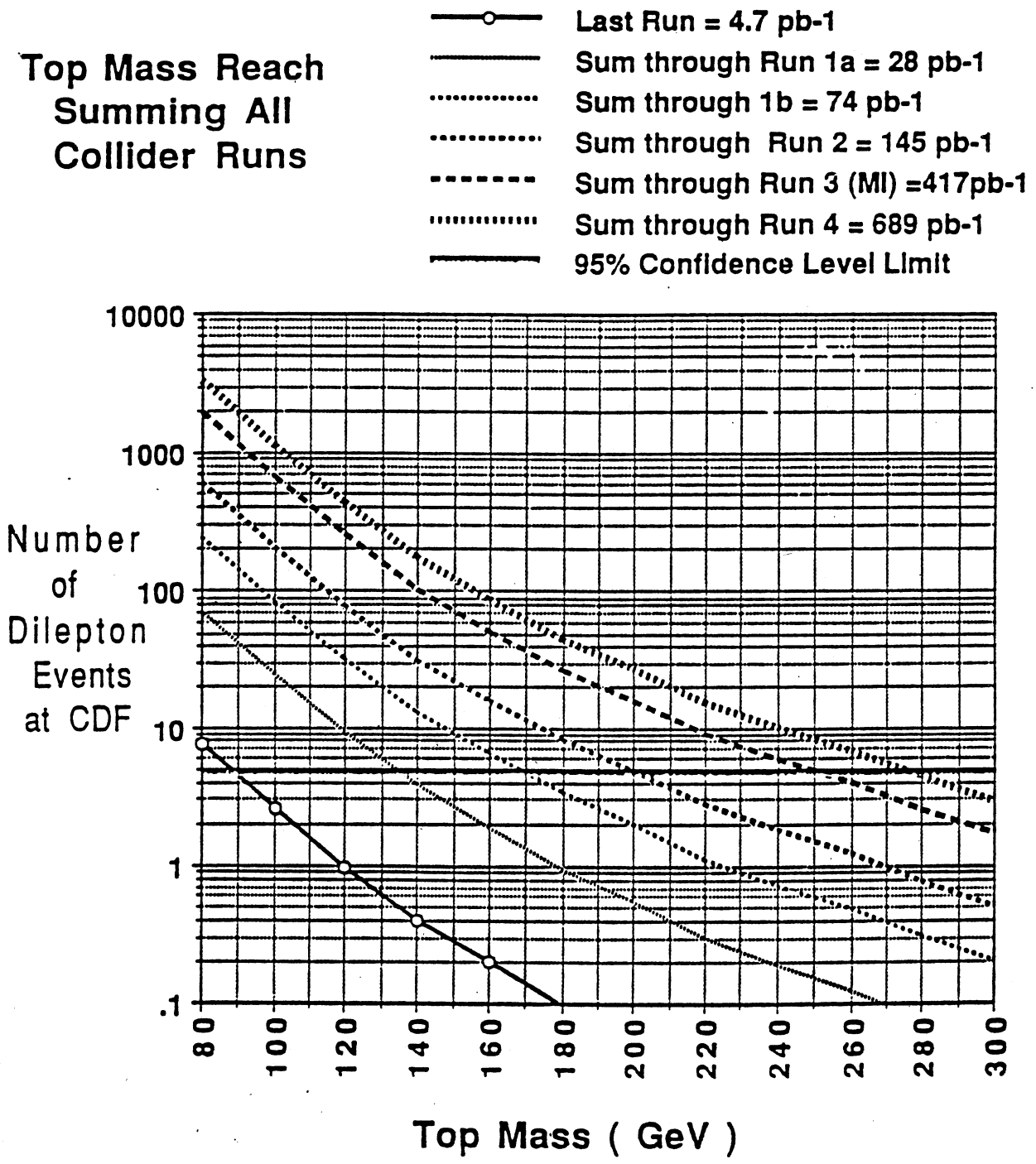

Figure 2.5.9 : Projected top quark mass sensitivity at the Fermilab Tevatron.

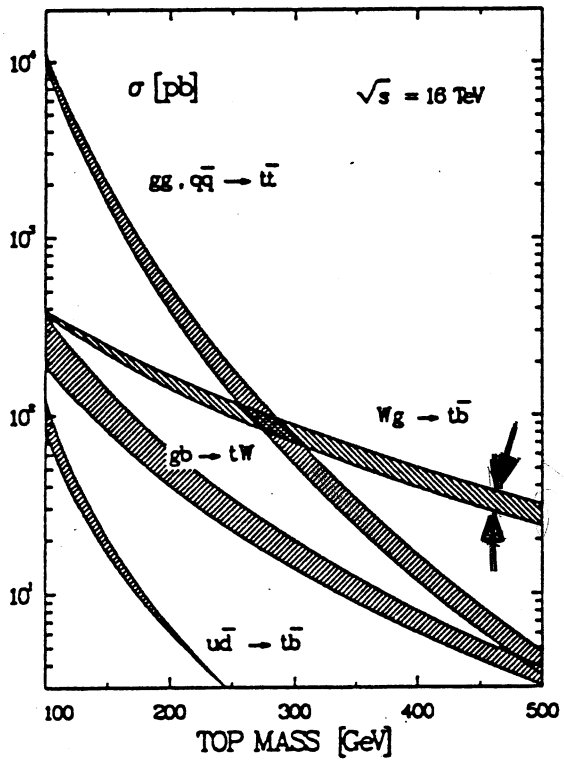

Figure 2.5.10 : Cross-sections for various mechanisms for top quark production at $\sqrt{s} = 16$ TeV.

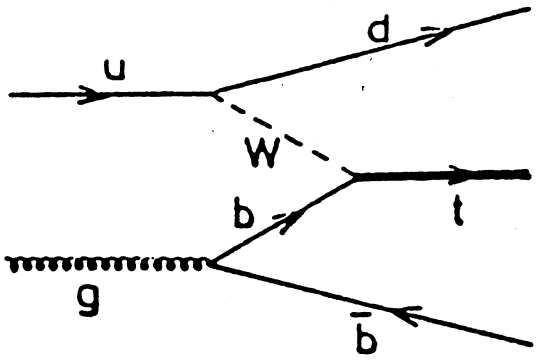

Figure 2.5.11 : Feynman diagram for Wg fusion into $t\bar{b}$.

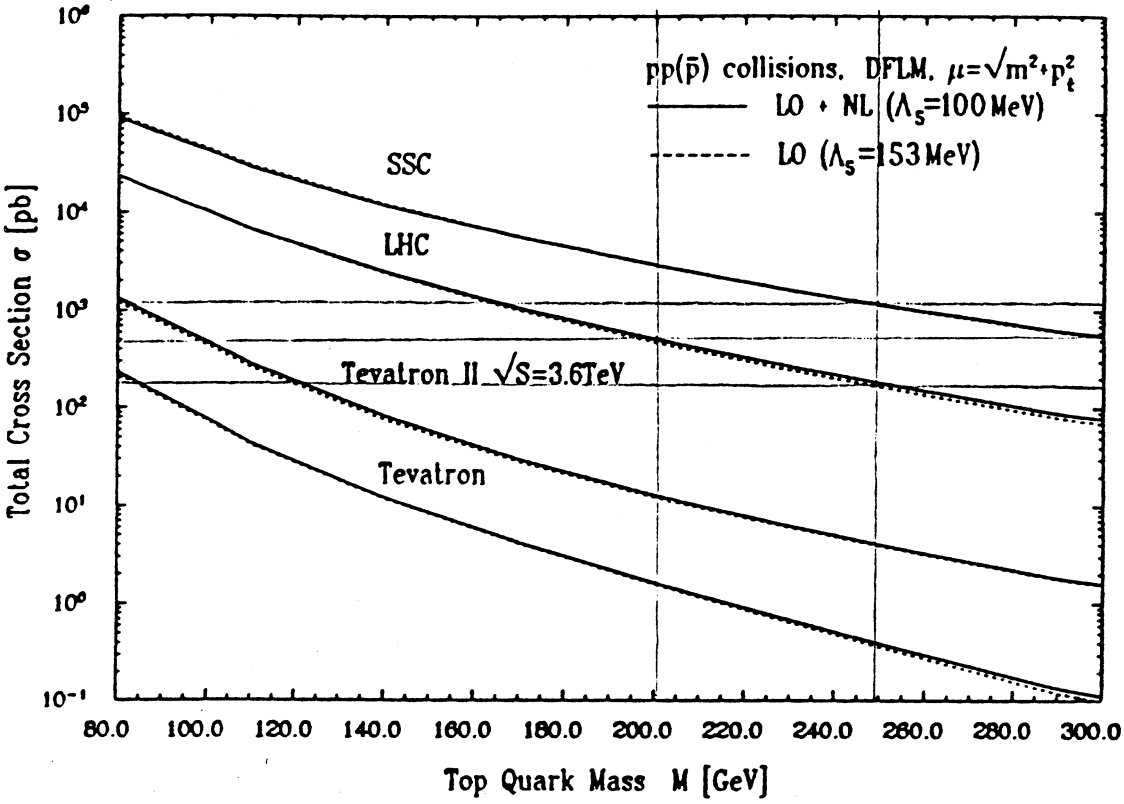

Figure 2.5.12 : Production cross-sections for $t\bar{t}$ in pp and $p\bar{p}$ colliders : Tevatron (1.8 TeV), Tevatron II (3.6 TeV), LHC (16 TeV), SSC (40 TeV).

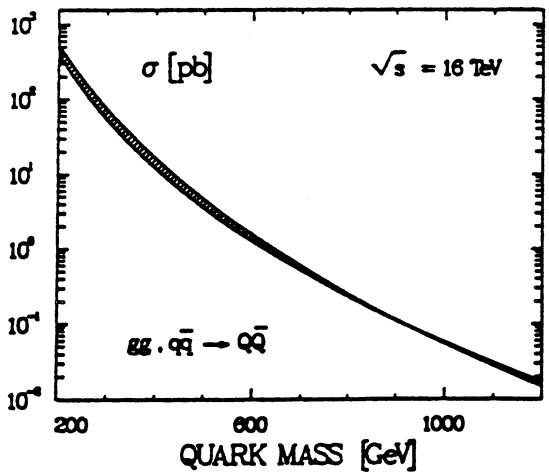

Figure 2.5.13 : Cross-section for heavy quark production in gg fusion and $q\bar{q}$ annihilation.

Top Quark Production at $\sqrt{s} = 16$ TeV

Estimates of the top quark mass based on precision measurements of the electroweak parameters (see Section 2.5.3) indicate a large value for m_t. Part of this range or eventually even the entire range can be covered at the Fermilab Tevatron by the end of the century (see Figure 2.5.9). However, if the mass were close to 200 GeV or beyond, it may need the LHC or SSC machines to discover it.

At $\sqrt{s} = 16$ TeV [Rey-90], the main production mechanisms from top quarks in proton-proton collisions are gluon-gluon fusion and quark-antiquark annihilation for top masses up to ≈ 250 GeV as shown in Figure 2.5.10. Only if the top quarks are still heavier, W-gluon fusion (see Figure 2.5.11)

$$Wg \rightarrow t\bar{b}$$

would become the dominant production process. Because the dominant part of the cross-section for the process in Figure 2.5.11 is due to b-quark exchange, the W-gluon process can be approximated by

$$u + b \rightarrow W \rightarrow d + t$$

with the b-quark distribution generated perturbatively by gluon splitting employing massless evolution equations.

$$\sigma(ub \rightarrow W \rightarrow dt) = \frac{G_F^2 M_W^2}{2\pi} \frac{(\hat{s} - m_t^2)^2}{\hat{s}(\hat{s} + M_W^2 - m_t^2)}$$

$$\sigma(d\bar{b} \rightarrow W \rightarrow d\bar{t}) = \frac{G_F^2 M_W^2}{2\pi} [1 + \frac{\hat{s}(2M_W^2 - m_t^2) - 2M_W^2 m_t^2}{\hat{s}^2} - \frac{(2\hat{s} + 2M_W^2 - m_t^2)m_t^2}{\hat{s}^2} \ln\frac{\hat{s} + M_W^2 - m_t^2}{M_W^2}].$$

These cross-sections are shown in Figure 2.5.12 for two parametrizations and models of the parton densities - the DFLM and LO GRV sets [Die-88, Glü-90].

Depending on the mass, about 10^6 to 10^8 top quarks can be produced with a total integrated luminosity of 10^4 pb^{-1}. As demonstrated in Figure 2.5.13 the discovery limit (defined by the observation of 1000 events) for any sort of heavy quark in gluon-gluon fusion of quark- antiquark annihilation reaches $m_Q \approx 1$ TeV for an integrated luminosity of 10^4 pb^{-1}.

2.5.3 Bounds on the Top Mass

The CDF Experiment

Evidence for top quark production has been sought in $p\bar{p}$ collisions at a centre-of-mass energy of $\sqrt{s} = 1.8$ TeV using the CDF detector at Fermilab [CDF-91e, CDF-91c]. The data sample was collected during 1988-1989 and corresponds to an integrated luminosity of 4.1 pb^{-1}. At such centre-of-mass energies, top quark production mediated by the QCD interactions dominate and no contribution from the electroweak top production was considered.

Previous searches by CDF [CDF-90b] consisted of electron μ final states in the decay

$$t\bar{t} \rightarrow e\nu_e b,\ \mu\nu_\mu \bar{b}$$

and [CDF-90c]

$$t\bar{t} \rightarrow e + \text{jets}$$

and these has been extended to include the ee and μ μ channels. In addition, the data sample includes events with a high- p_T lepton accompanied by hadron jets to identify a low- p_T μ as a tag of a bottom quark in

$$t\bar{t} \rightarrow l\nu_l b,\ q\bar{q}\bar{b}.$$

The electrons are identified inside the rapidity region -1.0 < η < 1.0 (central calorimeter) and 1.26 <| η |< 2.2 (plug calorimeter). Muons are identified in the region -1.2 < η < 1.2 but can trigger the apparatus only in the region -0.6 < η < 0.6. For events in the signal region each lepton is required to have $p_T > 15$ GeV and that each event has been triggered by at least one of the central electron or μ triggers. In addition, a back-to-back cut of $\Delta\phi_{ll} < 160°$ where $\Delta\phi_{ll}$ is the dilepton azimuthal angle is required and ee and μ μ events with

$$75 < M_{ll} \text{ (dilepton invariant mass)} < 105 \text{ GeV}$$

or with a $E_T^{miss} < 20$ GeV are removed.

In the b-tagging analysis events with a high- p_T electron or μ from W decay plus a low- p_T μ from direct or sequential b decays

$$t\bar{t} \rightarrow l\nu_l b,\ q\bar{q}\bar{b} \text{ with } b \rightarrow \mu \text{ or } b \rightarrow c \rightarrow \mu$$

are searched for. For each event the isolated electron and μ are required to have $p_T > 20$ GeV, $E_T^{miss} > 20$ GeV and at least two jets with $E_T > 10$ GeV in $-2.0 < \eta < 2.0$. For this analysis the electrons are required to be in $-1.0 < \eta < 1.0$ and the μ 's in $-0.6 < \eta < 0.6$. The low- p_T μ is required to have $2.0 < p_T < 15$ GeV.

At the 95% C.L. CDF finds m_t is greater than 85 GeV for the high- p_T dilepton analysis. From a combination of the high- p_T dilepton analysis with the b-tagging analysis

$$m_t > 95 \text{ GeV} \quad \text{at 90\% C.L.}$$

and

$$m_t > 91 \text{ GeV} \quad \text{at 95\% C.L.}$$

These CDF results represent the current most stringent lower limits on m_t assuming the Standard Model top decay modes.

The UA1 and UA2 Experiments

The UA1 Collaboration [UA1-90] has searched for the top quark in the $\mu + 2$ jets channel based on an integrated luminosity of 4.6 pb^{-1} at $\sqrt{s} = 630$ GeV. The lower mass limit for the top quark obtained from this analysis is

$$m_t > 60 \text{ GeV} \quad \text{at 95\% C.L.}$$

In addition, the UA2 Collaboration [UA2-90] has also searched for the production and decay of the top quark in a data sample corresponding to a total integrated luminosity of 7.5 pb^{-1}. The search is based on a sample consisting of an electron plus at least one jet. Using the rates for top quark production and decay from the Standard Model, the lower mass limit for the top quark obtained from this analysis is

$$m_t > 71 \text{ GeV} \quad \text{at 90\% C.L.}$$

and

$$m_t > 69 \text{ GeV} \quad \text{at 95\% C.L..}$$

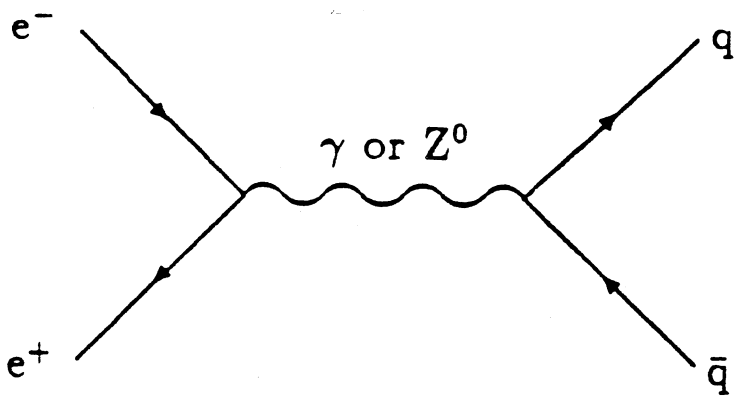

Figure 2.5.14 : Lowest order diagram for the process $e^+e^- \rightarrow q\bar{q}$ where q could be the top quark.

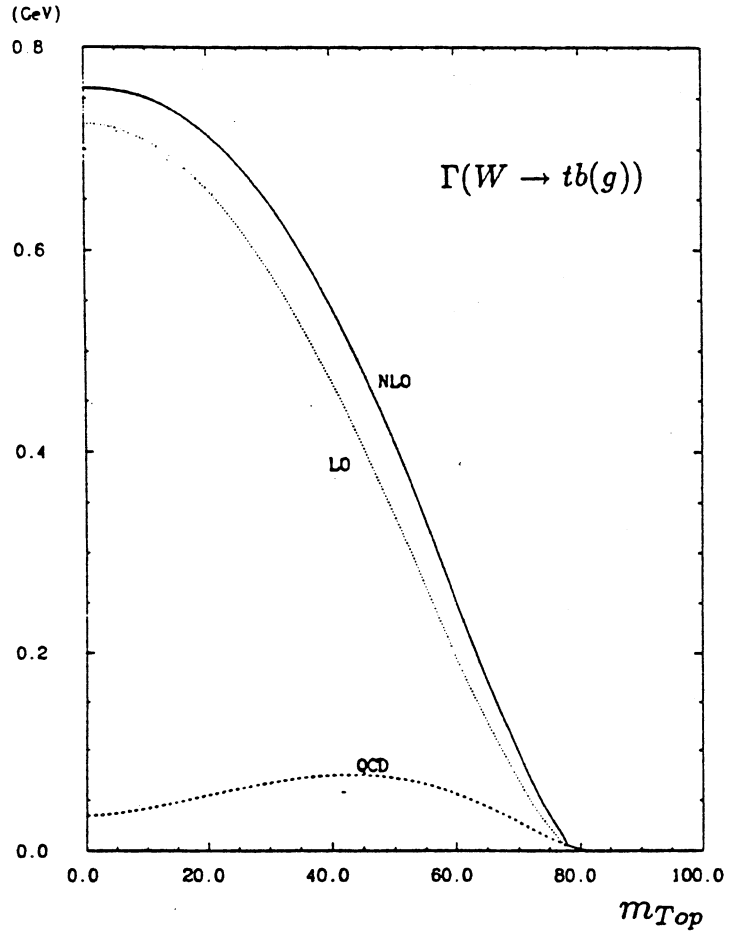

Figure 2.5.15 : The width W → tb(g) to leading order (LO) and to next-to-leading order (NLO) of $O(\alpha_s^2)$ is shown.

Table 2.5.2 : Lower Limits (95% C.L.) on the Top Quark Mass

Experiment	Top Quark Mass Limit (GeV)
ALEPH	45.8
DELPHI	44.0
L3	46.0
OPAL	45.1
MARK II	40.7

The LEP Experiments

The Z^0 decay into a pair of top quarks (see Figure 2.5.14) provides the least controversial bound on the mass of the top quark because the direct limit is obtained by comparing the cross-sections for the production of hadrons and μ 's, expressed by the ratio

$$R = \frac{\sigma(e^+e^- \rightarrow \text{hadrons})}{\sigma(e^+e^- \rightarrow \mu^+\mu^-)}.$$

The measurement of this ratio is independent of the top decay modes and may be to either $H^\pm$ or $W^\pm$. The ratio increases as the total centre-of-mass energy increases and thresholds for the production of successively heavier quarks are passed.

Table 2.5.2 [ALE-90a, DEL-90a, L3-90a, OPA-90a, MAR-89] lists the lower mass limits at 95% C.L. obtained from LEP and the SLC at Stanford. The search is in both cases limited by the respective beam energies.

From the W Width

The total width of the W boson, Γ_W^{tot}, is sensitive to any decay modes of the W whether they are experimentally detected or not. In particular, the presence of the top quark lighter than the W would result in a larger value of Γ_W^{tot} because

$$\Gamma_W^{tot} = \Gamma(W \rightarrow l\nu_l) + \Gamma(W \rightarrow q\bar{q}').$$

Therefore, Γ_W^{tot} can be used to set a lower limit on m_t . The width for the mode of interest $W \rightarrow t\bar{b}$ is shown in Figure 2.5.15. In particular, it

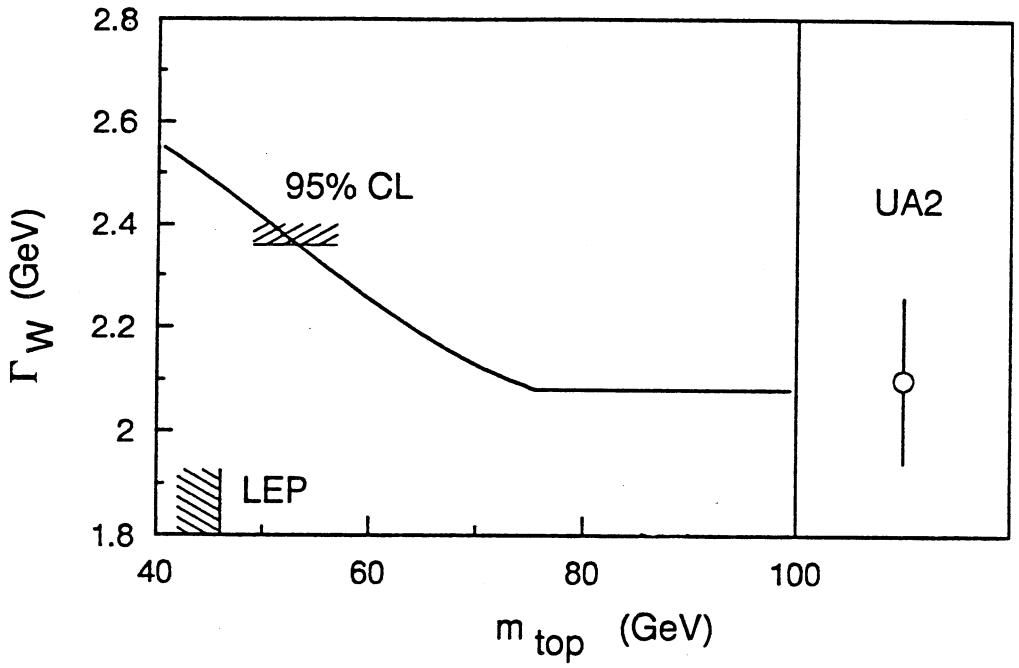

Figure 2.5.16 : The UA2 result for Γ_W compared to the Standard Model prediction as a function of the top quark mass.

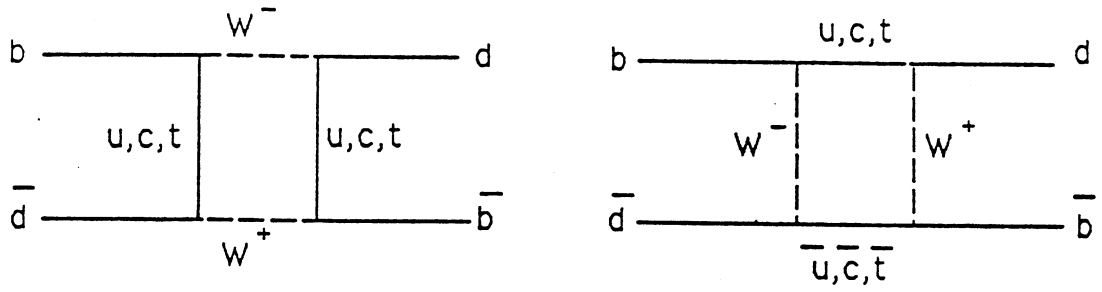

Figure 2.5.17 : Box diagrams for $B_d^0 - \overline{B}_d^0$ mixing.

is expected in the Standard Model that Γ_W^{tot} will decrease from about 2.8 GeV to about 2.1 GeV as m_t is increased from zero to the mass of the W. The dependence of Γ_W^{tot} on m_t is shown in Figure 2.5.16 including the mass dependent QCD corrections [Alv-88].

From the UA2 measurement of the width alone [UA2-91b]

$$\Gamma_W^{tot}\ (UA2) \ = \ 2.10 \ \pm \ 0.16\ GeV$$

one obtains a limit of $m_t > 53$ GeV at the 95% C.L.. The combination of UA2, CDF [CDF-91d], and UA1 [UA1-91b] data gives

$$\Gamma_W^{tot}\ (UA2) \ = \ 2.15 \ \pm \ 0.11\ GeV$$

which corresponds to $m_t > 53$ GeV at the 95% C.L..

From $B^0\overline{B}^0$ Mixing

A non-vanishing amount of $B^0\overline{B}^0$ mixing has been measured by the ARGUS Collaboration at the DORIS storage ring at DESY [ARG-87]. Defining

$$r_d \ = \ \frac{P(B_d^0 \rightarrow \overline{B}_d^0)}{P(B_d^0 \rightarrow B_d^0)}$$

which coincides with

$$\bar{r}_d \ = \ \frac{P(\overline{B}_d^0 \rightarrow B_d^0)}{P(\overline{B}_d^0 \rightarrow \overline{B}_d^0)}$$

the ARGUS Collaboration finds consistent signals of mixing which lead to the combined result

$$r_d \ = \ 0.21 \ \pm \ 0.08.$$

(An earlier report on $B^0\overline{B}^0$ mixing has been reported by the UA1 Collaboration [UA1-87]).

The ARGUS result contradicts the Standard Model predictions with three generations and a light top quark (m_t less than 40 GeV) which give $r_d \ \leq \ 0.005$. The simplest interpretation of the ARGUS result in this context is that the top quark is heavier than it was previously assumed.

The $\Delta b = 2$ flavour non-conservation in the transition from B_d^0 to $\overline{B}_d^0$ involves two charged current as is shown in Figure 2.5.17. If diagrams with

the exchange of a heavy quark Q such as the top quark dominate, then external momenta of the order of the B meson mass, $m_B \ll m_Q$, m_W, can be neglected in the calculation. QCD corrections to the box diagram can then be estimated and the matrix element of this effective four-fermion interaction between the external meson states can be evaluated. The box-diagram is proportional $m_Q^2 \mid V_{Qb}V_{Qd}^* \mid^2$ where m_Q is the mass of the heavy quarks exchanged and the $V_{qq'}$ are elements of the KM quark mixing matrix. As $\mid V_{tb}V_{td}^* \mid^2$ and $\mid V_{cb}V_{cd}^* \mid^2$ are of approximately the same magnitude, the assumption that the dominant contribution comes from top quark exchange used in the calculation is valid.

Choosing a reasonable set of extreme values for all the necessary constants to evaluate the rate of mixing [Alt-88b], the experimental observations imply that $m_t > 45$ GeV whereas central values of the parameters give $m_t > 90$ GeV.

From Precision Electroweak Data

Indirect limits on m_t [Mor-92e] have been placed from a global analysis of electroweak data (including M_Z, Γ_Z, Γ_h, Γ_l, A_{FB}^l, A_{pol}^τ and A_{FB}^b,) from LEP [Mor-92b] and from other precision electroweak data from UA2 and CDF on the mass of the W boson [UA2-91c, CDF-90a, CDF-91d] and from low energy $\nu - q$, $e - q$ and $\nu - e$ scattering data.

Comparing the Standard Model predictions for the measured observables with the corresponding LEP data [Mor-92b], the value of the top quark is

$$m_t = 155 \pm 30 \text{ GeV}.$$

The central value of m_t is smaller, $m_t = 135$ GeV for light Higgs mass (m_{H^0} = 50 - 100 GeV) while it is larger, $m_t = 175$ GeV for heavy Higgs (m_{H^0} = 0.5 - 1 TeV).

2.6 Non-minimal Higgs Sectors

2.6.1 General Two Higgs Doublet Models

The Standard Model uses one scalar doublet to spontaneously break the SU(2) x U(1) symmetry. However, there is no physical reason which prevents

the Higgs sector from having a richer structure. In particular there is no physical reason which forbids more than one scalar doublet [Gun-90a]. This thesis treats the Two Higgs Doublet (THD) model, which is the simplest extension of the minimal one-doublet Standard Model scenario.

There are two main experimental constraints on the Higgs sector. Firstly, the parameter ρ defined as

$$\rho \equiv \frac{M_W^2}{M_Z^2 \cos^2\theta_W}$$

must have a value very close to unity at the tree level [Ama-87, Cos-88]. The ρ parameter is determined by the Higgs structure of the theory. The general formula for ρ is [Lee-72]

$$\rho = \frac{\sum_{i=1}^{N} (T_i(T_i+1) - T_{i3}^2)\nu_i^2}{2\sum_{i=1}^{N} T_{i3}^2 \nu_i^2} \qquad (2.6.1)$$

factor of 2 at denom. missing

where T_i is the isospin of the i^{th} multiplet, T_{i3} is the eigenvalue of the third component of the isospin operator and ν_i is the vacuum expectation value of the multiplet. Equation (2.6.1) is satisfied by an infinite number of multiplet combinations. The simplest class of solutions are those based upon doublets and singlets while possibilities beyond such multiplets are usually discarded since the representations are too complicated.

There are also other ways to satisfy the $\rho \approx 1$ requirement at the tree level. For example, one can always choose arbitrary Higgs representations and 'fine-tune' the parameters of the Higgs potential so as to arrange $\rho \approx 1$. However, such methods are considered 'unnatural' and are usually discarded.

The second major theoretical constraint on the Higgs sector comes from the limits on the existence of flavour-changing neutral currents (FCNC's). Whereas in the minimal Higgs sector tree-level FCNC are automatically absent, this is generally not the case in the non-minimal Higgs models. In models with more than one Higgs doublet, FCNC's are elegantly avoided by invoking a postulate of Glashow and Weinberg [Gla-77, Pas-77, Kan-76] which states that tree-level FCNC's mediated by Higgs bosons are absent if all fermions of a given electric charge couple to no more than one Higgs doublet.

Moreover, THD models offer the possibility of explaining the fermion mass hierarchy, $m_c >> m_s$, $m_t >> m_b$ and $m_\tau >> m_\mu$, $m_\mu >> m_e$ if $\tan\beta$ is

much greater than unity so that $\nu_2 >> \nu_1$. This is quite possible given the constraints on tanβ from perturbation theory.

THD models consist of two $SU(2)_L$ Higgs doublets :

$$\phi_1 = \begin{pmatrix} \phi_1^0 \\ \phi_1^- \end{pmatrix}, \ \phi_2 = \begin{pmatrix} \phi_2^+ \\ \phi_2^0 \end{pmatrix}.$$

Here, the ϕ_1 doublet with hypercharge Y = -1 gives mass to the $T_3^L = -\frac{1}{2}$ quarks and charged leptons while the ϕ_2 doublet with hypercharge Y = +1 gives mass to the $T_3^L = +\frac{1}{2}$ quarks.

The Higgs potential which spontaneously breaks $SU(2)_L$ x $U(1)_Y$ symmetry down to $U(1)_{EM}$ in the THD model is [Geo-78]

$$V(\phi_1, \phi_2) = \lambda_1(\phi_1^\dagger\phi_1 - \nu_1^2)^2 + \lambda_2(\phi_2^\dagger\phi_2 - \nu_2^2)^2$$
$$+ \lambda_3[(\phi_1^\dagger\phi_1 - \nu_1^2) + (\phi_2^\dagger\phi_2 - \nu_2^2)]^2 + \lambda_4[(\phi_1^\dagger\phi_1)(\phi_2^\dagger\phi_2) - (\phi_1^\dagger\phi_2)(\phi_2^\dagger\phi_1)]$$
$$+ \lambda_5[\mathrm{Re}(\phi_1^\dagger\phi_2^\dagger) - \nu_1\nu_2\cos\xi]^2 + \lambda_6[\mathrm{Im}(\phi_1^\dagger\phi_2^\dagger) - \nu_1\nu_2\sin\xi]^2$$

where λ_i are all real parameters. If all the λ_i are non-negative then the minimum of the potential is

$$< \phi_1^0 > = \frac{1}{\sqrt{2}} \begin{pmatrix} 0 \\ \nu_1 \end{pmatrix},$$

$$< \phi_2^0 > = \frac{1}{\sqrt{2}} \begin{pmatrix} 0 \\ \nu_2 \end{pmatrix}$$

which breaks the $SU(2)_L x U(1)_Y$ down to $U(1)_{EM}$ as desired.

A key parameter of the model is the ratio of the vacuum expectation values

$$\tan\beta = \frac{\nu_2}{\nu_1}.$$

The quantities ν_1 and ν_2 are not individually predicted but they are related to the parameters of the Standard Model by

$$(\nu_1^2 + \nu_2^2)^{\frac{1}{2}} = \frac{2M_W}{g}$$

which in the low-energy limit of the electroweak theory is

$$\frac{2M_W}{g} = (\sqrt{2}G_F)^{-\frac{1}{2}} = 246 \text{ GeV}.$$

As in the minimal Standard Model, the Goldstone bosons are removed leading to physical Higgs states. The number of physical Higgs states expected is calculated by requiring that the number of independent states is consistent. Initially, there are two scalar complex fields, ϕ_1 and ϕ_2, each having four real fields since they are complex. There are three massless gauge bosons, $W^{\pm}$ and the Z^0 , with two polarization states each, so that the total number of independent fields is 14. After spontaneous symmetry breaking there are three massive gauge bosons, each with three polarization states, (J_z = -1,0,1), with 9 degrees of freedom so there are 5 physical Higgs bosons appearing as real particles.

In the charged sector, the charged Goldstone boson is

$$G^{\pm} = \phi_1^{\pm}\cos\beta + \phi_2^{\pm}\sin\beta$$

and the physical charged Higgs state is orthogonal to $G^{\pm}$

$$H^{\pm} = -\phi_1^{\pm}\sin\beta + \phi_2^{\pm}\cos\beta$$

with tree-level mass of

$$m_{H^{\pm}}^2 = \lambda_4(\nu_1^2 + \nu_2^2).$$

In the imaginary (CP-odd) sector, the neutral Goldstone boson is

$$G^0 = \sqrt{2}(\mathrm{Im}\phi_1^0\cos\beta + \mathrm{Im}\phi_2^0\sin\beta)$$

and the orthogonal neutral physical state is

$$A^0 = \sqrt{2}(-\mathrm{Im}\phi_1^0\sin\beta + \mathrm{Im}\phi_2^0\cos\beta)$$

with tree-level mass

$$m_{A^0} = \lambda_6(\nu_1^2 + \nu_2^2).$$

The real (CP-even) sector contains two physical Higgs scalars which mix through the following mass-squared matrix

$$M = \begin{pmatrix} 4\nu_1^2(\lambda_1+\lambda_3) + \nu_2^2\lambda_5 & (4\lambda_3+\lambda_5) + \nu_1\nu_2 \\ (4\lambda_3+\lambda_5) + \nu_1\nu_2 & 4\nu_2^2(\lambda_2+\lambda_3) + \nu_1^2\lambda_5 \end{pmatrix}.$$

The physical mass eigenstates are

$$H^0 = \sqrt{2}\left[(\mathrm{Re}\phi_1^0 - \nu_1)\cos\alpha + (\mathrm{Re}\phi_2^0 - \nu_2)\sin\alpha\right]$$

$$h^0 = \sqrt{2}\left[-(\mathrm{Re}\phi_1^0 - \nu_1)\sin\alpha + (\mathrm{Re}\phi_2^0 - \nu_2)\cos\alpha\right]$$

with tree-level masses

$$m^2_{H^0,h^0} = \frac{1}{2}\left[M_{11} + M_{22} \pm \sqrt{(M_{11} - M_{22})^2 + 4M_{12}^2}\right]$$

and the mixing angles are

$$\sin 2\alpha = \frac{2M_{12}}{\sqrt{(M_{11} - M_{22})^2 + 4M_{12}^2}}$$

$$\cos 2\alpha = \frac{M_{11} - M_{22}}{\sqrt{(M_{11} - M_{22})^2 + 4M_{12}^2}}$$

According to the above $m_{H^0} > m_{h^0}$.

In the THD model the Yukawa couplings of the physical $H^\pm$ to fermions are given by

$$\begin{aligned}\mathcal{L} =& \frac{g}{\sqrt{2}M_W} H^+[\cot\beta\, V_{ij}\, m_{ui}\, \bar{u}_i\, d_{jL} \\ &+ \tan\beta\, V_{ij}\, m_{dj}\, \bar{u}_i\, d_{jR} \\ &+ \tan\beta\, m_{lj}\, \bar{\nu}_j\, l_{jR}] + \text{h.c.} \qquad (2.6.2)\end{aligned}$$

where V_{ij} are KM matrix elements.

There exist theoretical constraints on the value of $\tan\beta$. An upper bound on the $H^\pm$ - fermion Yukawa coupling of Equation (2.6.2) can be derived from perturbation theory. Specifically, by requiring that the coupling in Equation (2.6.2) proportional to m_f is bounded from above by the strong coupling constant $4\pi\alpha_s$ (≈ 1.5) gives a lower bound on $\tan\beta$ [Bar-90a, Bur-90, Gun-90b]

$$\tan\beta > \frac{m_{top}\,(\mathrm{GeV})}{600\ \mathrm{GeV}} \quad (\approx \frac{1}{4}).$$

The perturbative limit on the tbH^+ coupling proportional to m_b gives the upper bound on $\tan\beta$ [Bar-90a, Bur-90, Gun-90b]

$$\tan\beta < \frac{600\ \mathrm{GeV}}{m_b\,(\mathrm{GeV})} \quad (\approx 120).$$

2.6.2 Minimal Supersymmetric Models

There exist many theoretical reasons why the Standard Model may be part of a larger structure. Such indications come from problems with the Higgs sector and are referred to as 'fine-tuning', 'naturalness', and 'hierarchy'. If the Standard Model is part of a more fundamental structure characterized by a much larger energy scale, (e.g. the Plank scale which appears in any theory incorporating gravity), the Higgs boson acquires a mass of order the large scale from radiative corrections. Only by adjusting, i.e. fine-tuning, the parameters of the Higgs potential unnaturally can one ensure a large hierarchy between the Planck scale and the electroweak symmetry breaking [Hoo-80, Sus-84, Hab-85]. The large Higgs mass cannot be controlled by the structure of the theory. However, if supersymmetry is invoked, the quadratic divergences in the Higgs mass are naturally cancelled by related graphs involving the supersymmetric partners of the Standard Model particles. The result is that the tree-level mass squared of the Higgs boson receives corrections which are limited by the extent of supersymmetry breaking. In order that the naturalness and hierarchy problems are resolved, it is necessary that the scale of the supersymmetry breaking not exceed O(1 TeV). Supersymmetric theories are especially interesting in that they provide the only theoretical framework in which the problems of naturalness and hierarchy are resolved while retaining the Higgs bosons as truly elementary scalar particles.

In the minimal supersymmetric extension of the Standard Model (MSSM), each Standard Model particle has an associated supersymmetric partner. For a review of the MSSM see, for example, Ref. [Hoo-80, Sus-84]. The MSSM is a particular case of a THD model of opposite hypercharge, the Y=-1 (Y=1) doublet coupling only to down-type (up-type) quarks and leptons.

In MSSM $\tan\beta$ and $m_{H^\pm}$ are typically chosen as the two independent parameters. Once these quantities are specified all the Higgs sector masses at the tree-level can be computed according to [Gun-90a]

$$m_{H^\pm} = m^2_{A^0} + M^2_{W^\pm}$$

$$m^2_{H^0,h^0} = \frac{1}{2}\left[m^2_{A^0} + M^2_{Z^0} \pm \sqrt{(m^2_{A^0} + M^2_{Z^0})^2 - 4M^2_{Z^0} m^2_{A^0} \cos^2 2\beta}\right]$$

and

$$m^2_{h^0} + m^2_{H^0} = m^2_{A^0} + M^2_{Z^0}$$

while the mixing angle is

$$\tan 2\alpha \;=\; \tan 2\beta \left(\frac{m_{A^0}^2 \;+\; M_{Z^0}^2}{m_{A^0}^2 \;-\; M_{Z^0}^2} \right).$$

There are several predictions evolving from the above equations :

$$m_{H^\pm} \;>\; M_W,$$

$$m_{H^0} \;\geq\; M_Z,$$

and

$$m_{h^0}^2 \;\leq\; \cos^2 2\beta \; M_{Z^0}^2.$$

It has recently been reported [Bri-91, Bri-92] that the mass of the Higgs bosons in MSSM are subject to large radiative corrections from (t, b, $\tilde{t}$, and $\tilde{b}$), loop contributions. The radiative corrections are particularly important for the H^0 and the h^0 because in the limit $M_W^2 \ll m_t^2$ and fixed $\frac{m_t}{m_{\tilde{q}}}$ the corrections are proportional to

$$\frac{\alpha}{\pi} \left(\frac{m_t^4}{M_W^2} \right).$$

The mass of the h^0 can be increased by tens of GeV, so that it can be heavier than the Z^0 . The radiative corrections to the A^0 have only a quadratic dependence on m_t . From such corrections it is now possible to have $m_{h^0} > m_{A^0}$ in contrast to the tree-level mass inequality $m_{h^0} < m_{A^0}$.

The radiative corrections to the $H^\pm$ have also been calculated [Mor-92d]. The mass of the $H^\pm$ is then

$$m_{H^\pm}^2 \;=\; M_W^2 \;+\; m_{A^0}^2 \;+\; \Delta^2$$

where Δ^2 is given in Figure 2.6.1. These results indicate that

$$m_{H^\pm} \;<\; M_W^2 \;+\; m_{A^0}^2$$

is possible even though it is highly model dependent. In addition, it it even possible that $m_{H^\pm} < M_W$ although this can only occur for small values of m_{A^0} and $(M_W - m_{H^\pm})$ and is typically not larger than a few GeV. Figure 2.6.2 shows a portion of the (m_{A^0}, m_{h^0}) plane for a particular choice in the parameter values.

Finally, there exist identical $H^\pm$ couplings to fermions in E_6 superstring-inspired models. However, such models give less restrictive mass bounds ($M_{H^\pm} > 53$ GeV) than in the MSSM [Hew-89].

$$\Delta^2 = \sum_{a=1}^{4} \frac{3H_a\tilde{m}_a^2}{8\pi^2 \sin 2\beta(m_t^2 - m_b^2)} \left(m_t^2 \log \frac{\tilde{m}_a^2}{m_t^2} - m_b^2 \log \frac{\tilde{m}_a^2}{m_b^2} \right)$$
$$- \frac{3g^2}{64\pi^2} \left(\frac{m_t^2}{\sin^2\beta} + \frac{m_b^2}{\cos^2\beta} - m_W^2 \right) \left[\frac{f(m_t^2) - f(m_b^2)}{m_t^2 - m_b^2} \right],$$

$$f(m^2) = 2m^2 \left(\log \frac{m^2}{Q^2} - 1 \right),$$

$$m_W^2 = \frac{g^2}{2}(v_1^2 + v_2^2),$$

$$H_{1,2} = \left[\frac{\partial^2 \tilde{m}_{1,2}^2}{\partial H_1^+ \partial H_2^-} \pm \frac{g^2}{2\sin^2\beta} \frac{m_t^2}{m_W^2} \frac{A_t \mu}{\tilde{m}_1^2 - \tilde{m}_2^2} \right]_{v_1, v_2},$$
$$H_{3,4} = \left[\frac{\partial^2 \tilde{m}_{3,4}^2}{\partial H_1^+ \partial H_2^-} \pm \frac{g^2}{2\cos^2\beta} \frac{m_b^2}{m_W^2} \frac{A_b \mu}{\tilde{m}_3^2 - \tilde{m}_4^2} \right]_{v_1, v_2}.$$

Figure 2.6.1 : The radiative correction to the mass of the $H^{\pm}$ in the MSSM (see text).

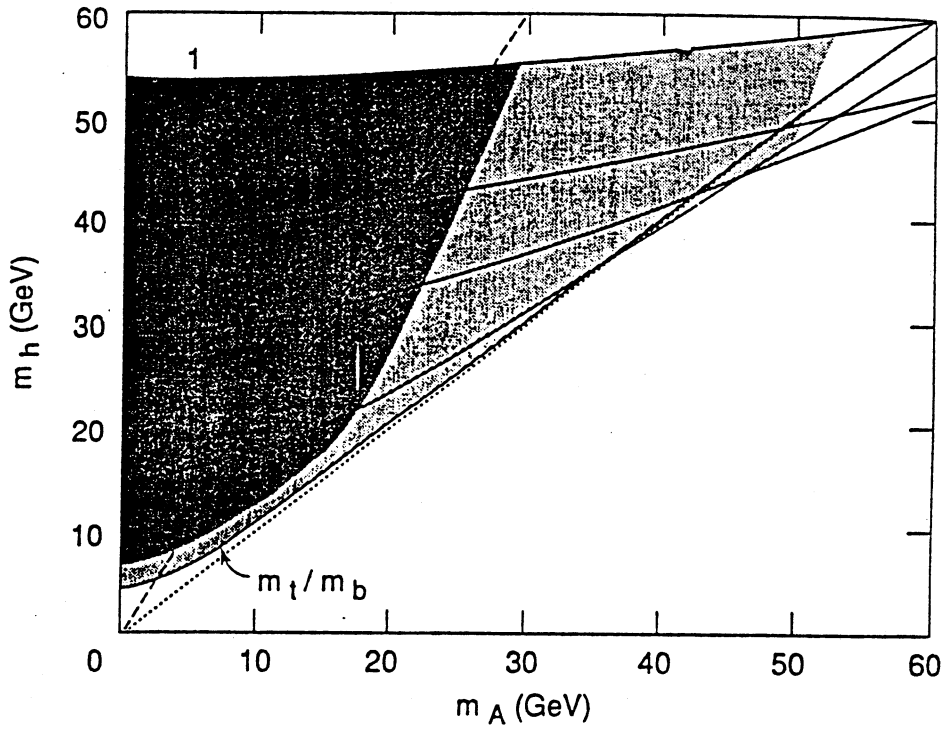

Figure 2.6.2 : Lines of constant $\tan\beta = 1$, $\sqrt{2}$, 2, 4 and $\frac{m_t}{m_b}$ in the region of the (m_{A^0}, m_{h^0}) accessible to LEP I searches. The dotted lines correspond to $m_{h^0} = m_{A^0}$ and the dashed one to $m_{h^0} = 2m_{A^0}$. The dark areas correspond to $m_{H^\pm} < M_W$ and the shaded ones to $m_{H^\pm} < M_Z$. For example, the parameter choice $m_t = 160$ GeV, $m_{\tilde{q}} = 1$ TeV

2.7 Phenomenology of Charged Higgs Bosons

2.7.1 Production and Decay of $H^{\pm}$

In this section the production of $H^{\pm}$ bosons from top quark decay is discussed.

All the top searches at hadron colliders discussed in Section 2.5 assume the Standard Model semileptonic branching ratios of the top quark

$$BR(t \rightarrow bW^{+} \rightarrow l^{+}\nu_l b) \approx \frac{1}{9}.$$

However, Glashow and Jenkins [Gla-87] have suggested that the failure to observe the Standard Model top quark at hadron colliders may be because of the existence of an alternative mechanism in which semileptonic top quark decays involving electrons and μ 's are suppressed relative to the τ 's. Such a mechanism is possible if $H^{\pm}$ exist as they are predicted in THD models.

The size of the $H^{\pm}$ signal versus the W boson background in top quark decay depends on the relative decay widths $t \rightarrow bH^{+}$ and $t \rightarrow bW^{+}$. In the approximation of a diagonal KM matrix :

$$\Gamma_{t\rightarrow bW+} = \frac{g^2}{64\pi M_W^2 m_t} \lambda^{\frac{1}{2}} \left(1, \frac{m_b^2}{m_t^2}, \frac{m_W^2}{m_t^2}\right) \cdot$$

$$[M_W^2(m_t^2 + m_b^2) + (m_t^2 - m_b^2)^2 - 2M_W^4]$$

where λ is the phase-space function

$$\lambda(a,b,c) = a^2 + b^2 + c^2 - 2ab - 2ac - 2bc$$

and

$$\Gamma_{t\rightarrow bH+} = \frac{g^2}{64\pi M_W^2 m_t} \lambda^{\frac{1}{2}} \left(1, \frac{m_b^2}{m_t^2}, \frac{m_{H\pm}^2}{m_t^2}\right) \cdot$$

$$[(m_t^2 \cot^2\beta + m_b^2 \tan^2\beta)(m_t^2 + m_b^2 - m_{H\pm}) + 4m_t^2 m_b^2]$$

from where one gets

$$Br(t \rightarrow bH^{+}) = \frac{\Gamma_{bH+}}{(\Gamma_{t\rightarrow bH+} + \Gamma_{t\rightarrow bW+})}.$$

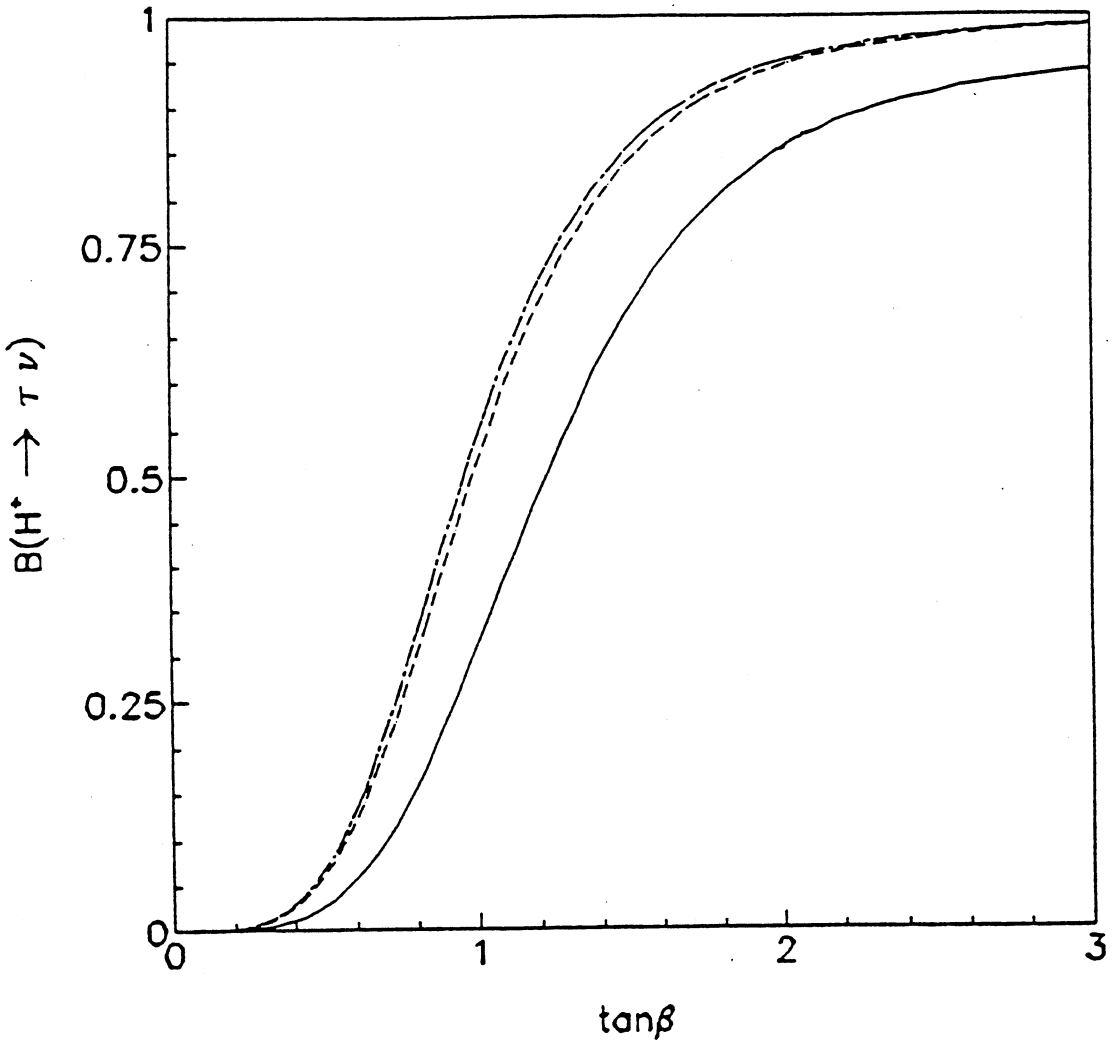

Figure 2.7.1 : BR($H^{\pm} \rightarrow \tau\nu_{\tau}$) versus tan$\beta$ at the tree-level (solid line) and with the QCD correction (see text) for top quark mass of 40 GeV (dashed line) and 70 GeV (dash-dotted line).

From Equation (2.6.2) the two significant decay modes to fermions of the $H^{\pm}$ can be calculated to be :

$$\Gamma_{H^+ \to \tau^+ \nu_\tau} = \frac{g^2 m_{H^\pm}}{32\pi M_W^2} m_\tau^2 \tan^2\beta \qquad (2.7.1)$$

and

$$\Gamma_{H^+ \to c\bar{s}} = \frac{3g^2 m_{H^\pm}}{32\pi M_W^2} (m_c^2 \cot^2\beta + m_s^2 \tan^2\beta) \qquad (2.7.2)$$

and the branching fraction to τ 's is

$$Br(H^+ \to \tau^+ \nu_\tau) = \frac{m_\tau^2 \tan^2\beta}{3\,(m_c^2 \cot^2\beta + m_s^2 \tan^2\beta) + m_\tau^2 \tan^2\beta.}$$

The corresponding branching fractions for W decay are given by the universality of the W coupling to leptons and quarks (see Section 2.2).

Recently, a calculation [Dre-91] incorporating the leading-log QCD correction to the Higgs mass results in a decrease in the $\Gamma_{H^+ \to c\bar{s}}$ value with a corresponding increase in the $\Gamma_{H^+ \to \tau^+ \nu_\tau}$ value. The QCD correction is taken into account by substituting the running quark mass

$$\tilde{m}_q(m_{H^\pm}) = m_q \left(\frac{\ln(\frac{4m_q^2}{\Lambda^2})}{\ln(\frac{m_{H^\pm}^2}{\Lambda^2})} \right)^{\frac{12}{33-2N_f}}$$

where the initial condition is

$$\tilde{m}_q(2m_q) = m_q$$

in Equation (2.7.2). The resulting QCD correction reduces the hadronic decay width of the $H^{\pm}$, especially for large $H^{\pm}$ masses. Figure 2.7.1 shows the $BR(H^+ \to \tau^+ \nu_\tau)$ versus $\tan\beta$ at both the tree-level and with the leading-log QCD correction. It is seen that with the inclusion of the QCD correction the decay $H^+ \to \tau^+ \nu_\tau$ is enhanced adding to the signal probed for in this thesis.

Figure 2.7.2 shows the $t \to bW^+$, branching ratio , where the W is either virtual or on the mass shell, versus $m_{H^\pm}$ for various values of m_t and $\tan\beta$ [Bar-90b]. The conventional $t \to bW^+$ signals are only suppressed for the case

$$m_{H^\pm} < m_t - m_b.$$

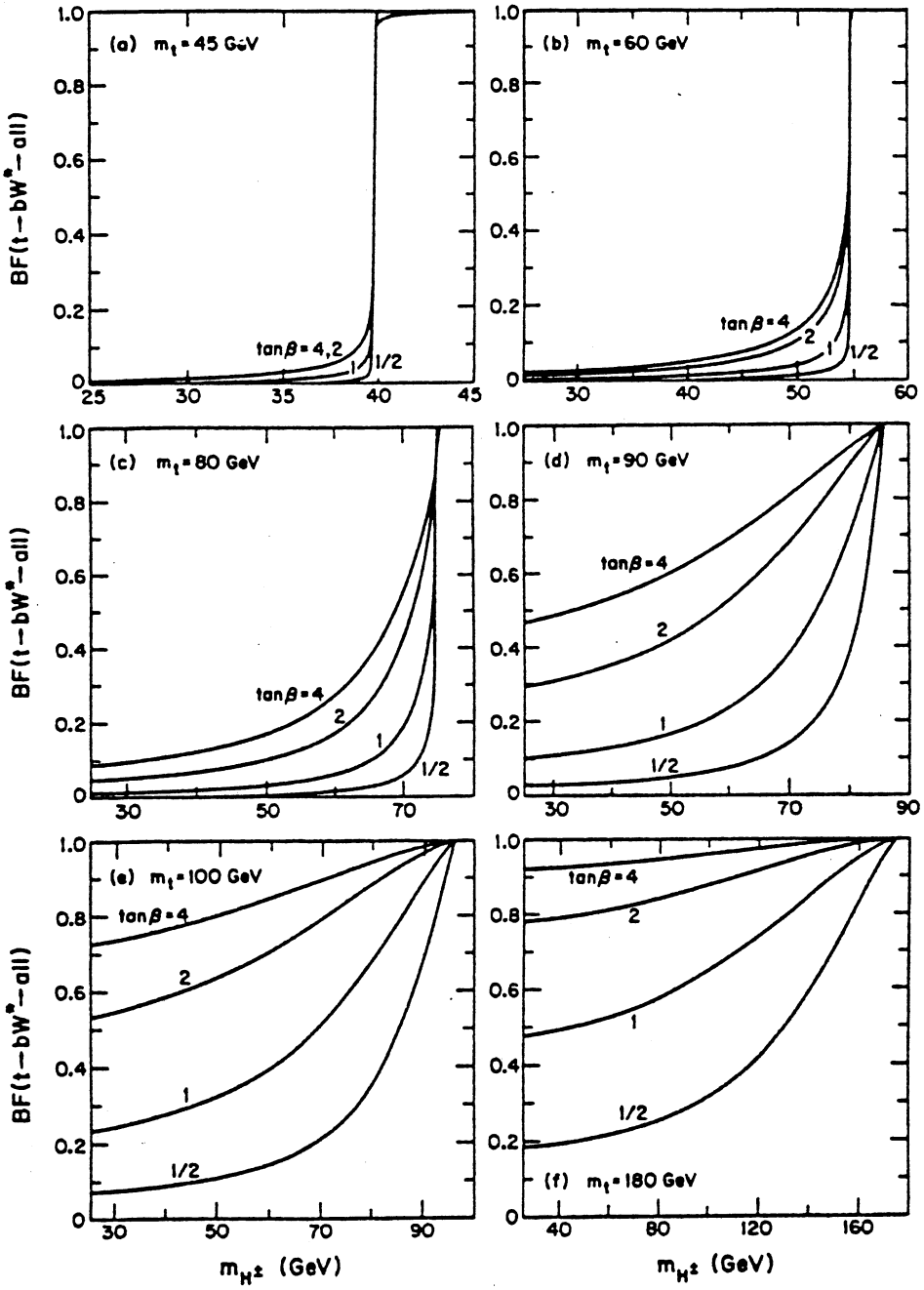

Figure 2.7.2 : The branching fraction for W-mediated top quark decays.

There is a strong suppression of $t \rightarrow bW^+$ for m_t between about 45 and 60 GeV essentially regardless of the $\tan\beta$ value. For

$$m_{H^\pm} > m_t - m_b,$$

however, the $t \rightarrow bH^+$ channel is essentially never competitive.

Because of the above restrictions, in Chapter 6 it is assumed that

$$m_t < M_W - m_b$$

and

$$m_{H^\pm} < m_t - m_b$$

so that the largest sensitivity to a $H^\pm$ from top quark decay is searched for.

Note that the usual signatures in searches for the top quark at hadron colliders, $t \rightarrow b\mu^+\nu_\mu$ and $t \rightarrow be^+\nu_e$ are , respectively, 10^2 and 10^7 times smaller in THD models than in models with no $H^\pm$. It is therefore not surprising that the top quark decay modes have yet to be experimentally observed in the case that a $H^\pm$ exists.

The τ decay topologies are different according to whether they originate from a parent $H^\pm$ or $W^\pm$ [Roy-91a, Bul-91]. For example, the τ^- leptons from

$$H^- \rightarrow \tau^- \overline{\nu}_\tau$$

are almost purely right-handed whereas those from W^- decay are predominantly left-handed. This is true in all models containing only left-handed neutrinos (and right-handed antineutrinos).

Figure 2.7.3 shows the energy distribution of the charged particles arising from various τ^- decay modes. The relevant formula is in the collinear limit (i.e. $\frac{E_\tau}{m_\tau} \gg 1$)

$$\frac{1}{\Gamma_\tau}\frac{d\Gamma}{dz}(\tau^- \rightarrow A^-\nu's) = BR(\tau^- \rightarrow A^-\nu's)H_A(z)$$

where $z = \frac{E_A}{E_\tau}$ with $A = e, \pi, \rho, a_1$, $BR(\tau^- \rightarrow A^-\nu's)$ are the corresponding branching ratios, while the functions $H_A(z)$ are given in Ref. [Hag-90]. This difference in the distribution between left-handed and right-handed τ 's can be exploited to differentiate between a $H^\pm$ and $W^\pm$. For example, the π^-

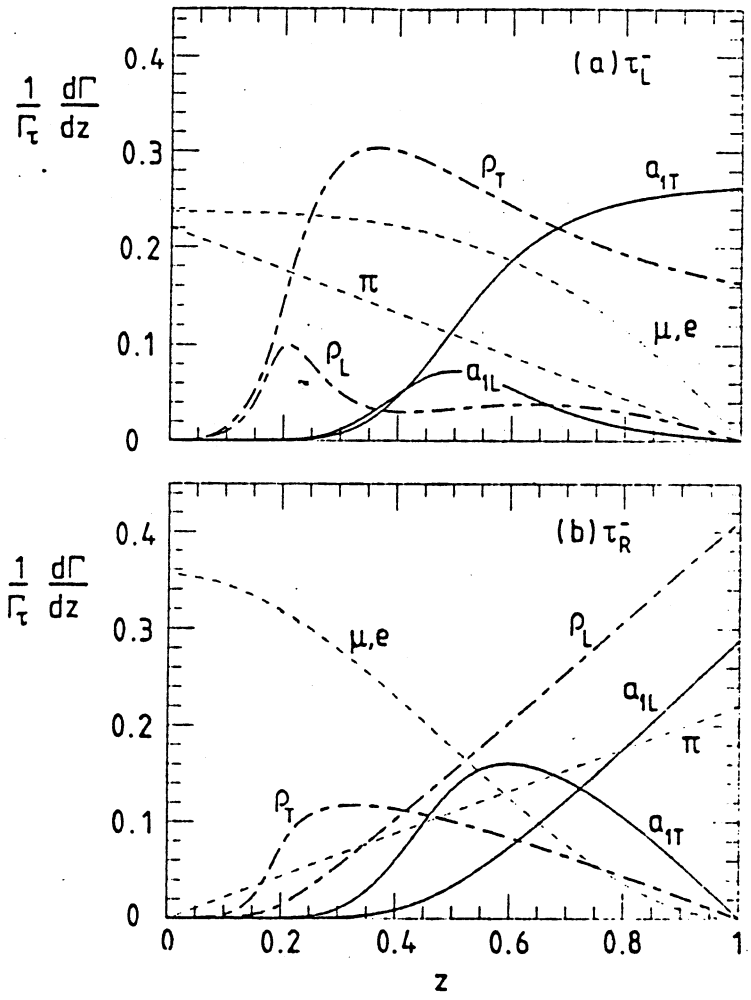

Figure 2.7.3 : The fractional energy distributions for particle A^- arising from (a) left-handed and (b) right-handed τ^- decays.

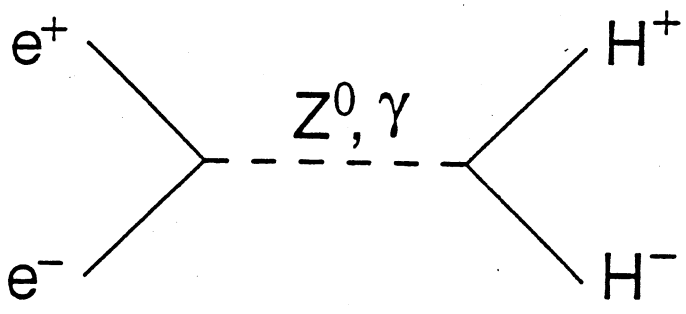

Figure 2.7.4 : Pair production of $H^\pm$ bosons at LEP.

originating from the $H^{\pm}$ and W bosons peak at z = 1 and z = 0, respectively and it is expected that

$$< z_{\pi^-} >_{H^{\pm}} \approx 2 < z_{\pi^-} >_{W^{\pm}} = \frac{2}{3}.$$

After convolution with the τ momentum, one gets for $m_{H^{\pm}} \approx m_{W^{\pm}}$

$$< p_T^{\pi^-} >_{H^{\pm}} \approx 2 < p_T^{\pi^-} >_{W^{\pm}}$$

so that a significantly harder π^- spectrum is obtained from the $H^{\pm}$ with respect to the W boson background.

2.7.2 Experimental Bounds on $M_{H^{\pm}}$.

From the LEP Experiments

Charged Higgs bosons at LEP can be pair-produced by coupling to both the intermediate state γ and Z^0 . The Feynman diagram for this process is shown in Figure 2.7.4. To lowest order the cross-section for pair-production of $H^{\pm}$ is [Gun-90a]:

$$\sigma_{H^+H^-} = \beta^3 \frac{\pi\alpha^2}{3s} \cdot \left[1 - \frac{s(s-M_Z^2)\ 2C_V C'_V}{(s-M_Z^2)^2 + M_Z^2\Gamma_Z^2} + \frac{s^2(C_V^2+C_A^2)C'^2_V}{(s-M_Z^2)^2 + M_Z^2\Gamma_Z^2}\right] \quad (2.7.3)$$

where

$$C_V = \frac{1 - 4\sin^2\theta_W}{4\sin\theta_W\cos\theta_W}$$

$$C'_V = \frac{-2 + 4\sin^2\theta_W}{4\sin\theta_W\cos\theta_W}$$

$$C_A = \frac{-1}{4\sin\theta_W\cos\theta_W}$$

and

$$\beta = \sqrt{1 - 4\frac{m^2}{s}}.$$

At LEP centre-of-mass energies ($\sqrt{s} = M_{Z^0}$) the third term in the brackets of Equation (2.7.3) is dominant so that

$$\sigma_{H^+H^-} \approx \beta^3 \frac{\pi\alpha^2}{3} \cdot \left[\frac{(C_V^2 + C_A^2)C_V'^2}{\Gamma_Z^2}\right] \quad (2.7.4).$$

The ALEPH Collaboration [ALE-90b] has performed a search for pair-produced $H^\pm$ at LEP in the decay channels

$$H^+H^- \rightarrow \tau^+\nu_\tau\ \tau^-\overline{\nu}_\tau,$$

$$H^+H^- \rightarrow \tau\nu\ cs,$$

$$H^+H^- \rightarrow c\bar{s}\ \bar{c}s,$$

and for the channels in which cs is replaced by cb. With a total integrated luminosity of 1.17 pb^{-1}, corresponding to about 25 000 hadronic decays of the Z^0 , the $H^\pm$ has been excluded at 95% C.L. in the mass range 7.6 to 43.0 GeV for

$$BR(H^\pm \rightarrow \tau\nu_\tau) = 100\%,$$

and from 8.3 to 40.6 GeV for

$$BR(H^\pm \rightarrow cs) = 50\%.$$

With cs replaced by cb, the $H^\pm$ has been excluded at 95% C.L. in the mass range 12.0 to 40.7 GeV for

$$BR(H^\pm \rightarrow cs) = 50\%,$$

and between 16.2 and 35.7 GeV for

$$BR(H^\pm \rightarrow \tau\nu_\tau) = 100\%.$$

The ALEPH exclusion regions at 95% C.L. are shown in Figure 2.7.5.

The DELPHI Collaboration [DEL-90b] used a sample of 12 000 hadronic Z^0 events to search for the production of $H^\pm$. The decay channels sought are similar to those for ALEPH but DELPHI did not probe the cb channels. Figure 2.7.6 summarises the DELPHI limits at 95% C.L. obtained from the above channels. For

$$BR(H^\pm \rightarrow \tau\nu_\tau) > 0.3,$$

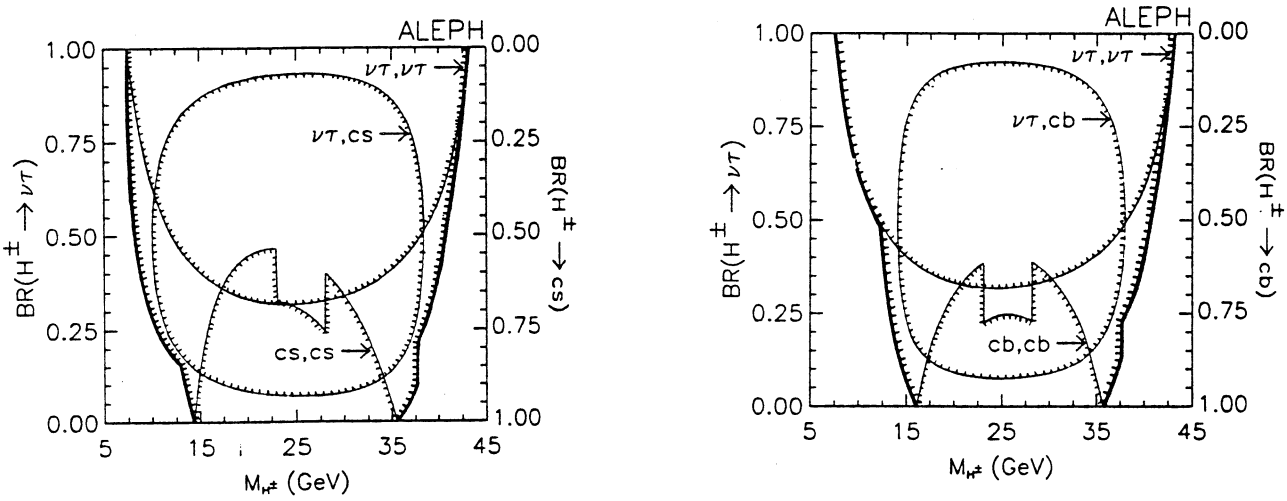

Figure 2.7.5 : The ALEPH exclusion regions for $m_{H\pm}$ at the 95 % C.L.

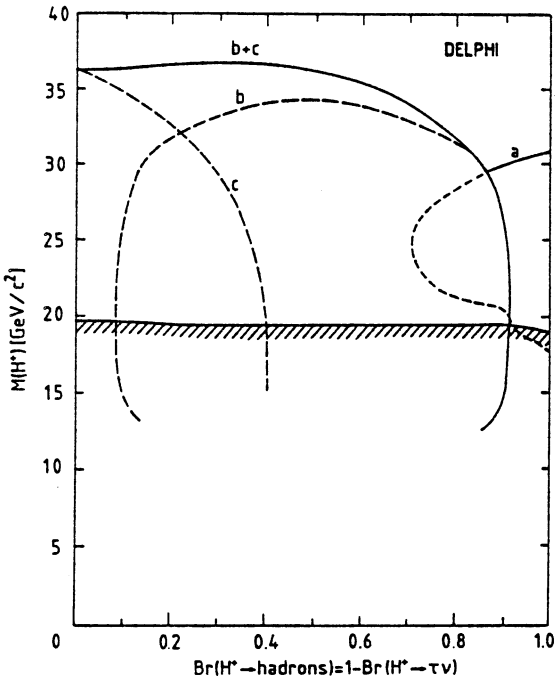

Figure 2.7.6 : The DELPHI exclusion regions for $m_{H\pm}$ at the 95 % C.L.

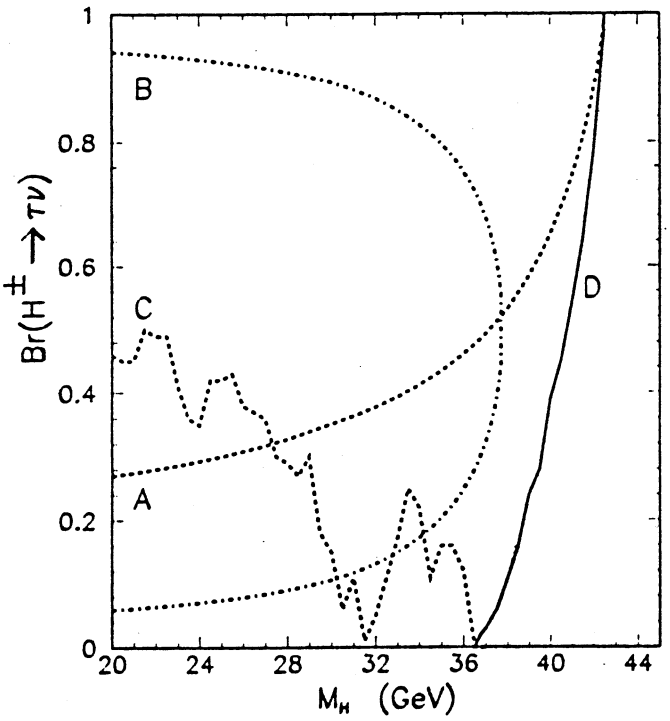

Figure 2.7.7 : The L3 exclusion regions for $m_{H\pm}$ at the 95 % C.L.

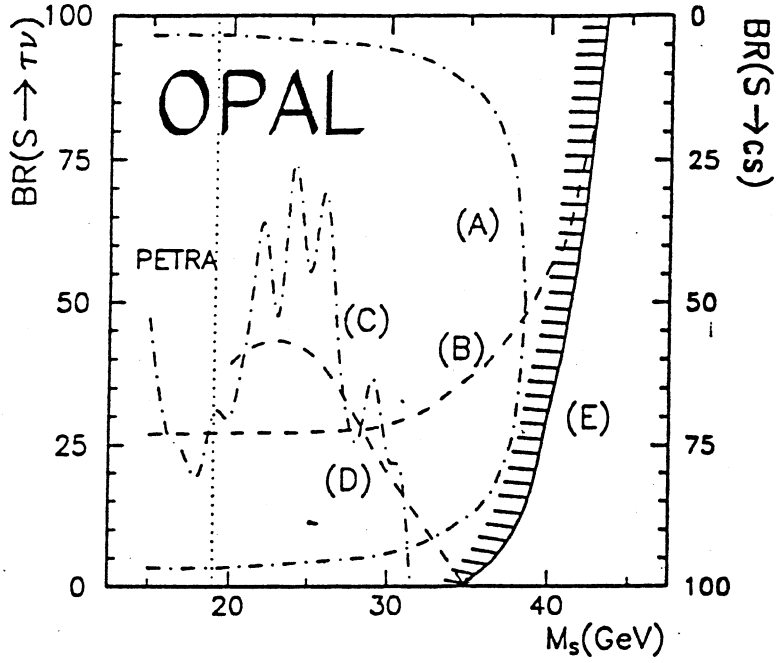

Figure 2.7.8 : The OPAL exclusion regions for $m_{H\pm}$ at the 95 % C.L.

Table 2.7.1 : Lower Limits (95% C.L.) on the $H^{\pm}$ from LEP

Experiment	$H^{\pm}$ Mass Limit (GeV) $BR(H^{\pm} \rightarrow \tau\nu_{\tau}) = 1$	$H^{\pm}$ Mass Limit (GeV) $BR(H^{\pm} \rightarrow \tau\nu_{\tau})$ Indpt.
ALEPH	45.3	41.7
DELPHI	40.0	-
L3	44.0	40.0
OPAL	43.3	35.0

a $H^{\pm}$ mass up to about 34 - 36 GeV is excluded.

The L3 Collaboration [L3-90b] has probed for pair-produced $H^{\pm}$ particles in Z^0 events in the same decay channels as DELPHI using a data sample of about 50 000 hadronic Z^0 decays. A lower limit of 36.5 GeV is obtained at the 95% C.L. for the mass of the $H^{\pm}$ independent of its decay branching ratio. Figure 2.7.7 shows the excluded regions of the $H^{\pm}$ mass as a function of $BR(H^{\pm} \rightarrow \tau\nu_{\tau})$.

The OPAL Collaboration [OPA-90b] has also performed a search for pair-produced $H^{\pm}$ using the same channels as DELPHI and L3. A lower limit of 35 GeV at 95% C.L. is obtained for the mass of the $H^{\pm}$ independent of the branching ratio $BR(H^{\pm} \rightarrow \tau\nu_{\tau})$. Figure 2.7.8 shows the 95% C.L. limits on the branching ratio

$$\frac{\Gamma(H^{\pm} \rightarrow \tau\nu_{\tau})}{\Gamma(H^{\pm} \rightarrow \text{all})}$$

as a function of the $H^{\pm}$ mass.

Recently, preliminary results from the four LEP experiments for the combined 1989 to 1991 data sample of hadronic Z^0 decays have been presented [Mor-92c]. Table 2.7.1 summarizes the latest LEP lower bounds on the mass of the $H^{\pm}$.

From the UA1 Experiment

A search for the decay

$$t \rightarrow H^{+}b \rightarrow \tau^{+}\nu_{\tau}b$$

and for its charge conjugate has been performed in $p\bar{p}$ collisions at $\sqrt{s} =$ 630 GeV using the UA1 detector at CERN [UA1-91a]. The data sample

corresponds to a total integrated luminosity of 4.7 pb^{-1} collected during the 1988 and 1989 Collider runs. The UA1 analysis seeks final states with one or more μ 's coming from the τ and b decays and accompanied by at least one jet plus p_T^{miss} from the neutrinos. Single and dimuon triggers were therefore used.

The data sample from the single muon channel is defined by the following cuts :

1. $p_T^{\mu} > 8$ GeV,
2. ≥ 2 jets with $E_T^{jet} > 7$ GeV,
3. $E_T^{jet\ 1} > 13$ GeV, $E_T^{jet\ 2} > 7$ GeV,
4. the two leading jets to lie in -2.0 $< \eta <$ 2.0 with at least one in -1.5 $< \eta <$ 1.5,
5. $\Delta R_{\mu-R} > 1$, where $\Delta R_{\mu-R}$ is the distance in $\eta - \phi$ space between the muon direction and the jet axis,
6. $M_T^{\mu\nu} < 60$ GeV, and
7. I_{μ} ($\equiv \left[\sum(\frac{1}{3}E_T^{\mu})^2 + \sum(\frac{1}{2}p_T^{\mu})^2\right]^{\frac{1}{2}}$) < 2 in a cone of $\Delta R < 0.7$ around the μ direction.

To improve the sensitivity to a possible $H^{\pm}$ signal, a likelihood function is defined using variables which exploit the differences between signal and background. The likelihood function is defined as

$$L_1 = \prod_i \frac{P^t(x_i)}{P^b(x_i)}$$

where $P^t(x_i)$ is the probability density function of the variable x_i for the top quark signal events and $P^b(x_i)$ is the probability density function of the background consisting of $b\bar{b}$ and $c\bar{c}$ events. The variables used in the single muon channel are p_T^{μ}, p_T^{miss}, and $|\cos\theta_{j2}^*|$ where θ_{j2}^* is the angle between the second-highest E_T jet and the beam axis in the rest-frame of the four-body system μ - jet_1- jet_2- p_T^{miss}. Figure 2.7.9 shows the distribution of $\ln(L_1)$ where the search region is defined as $\ln(L_1) > 1$.

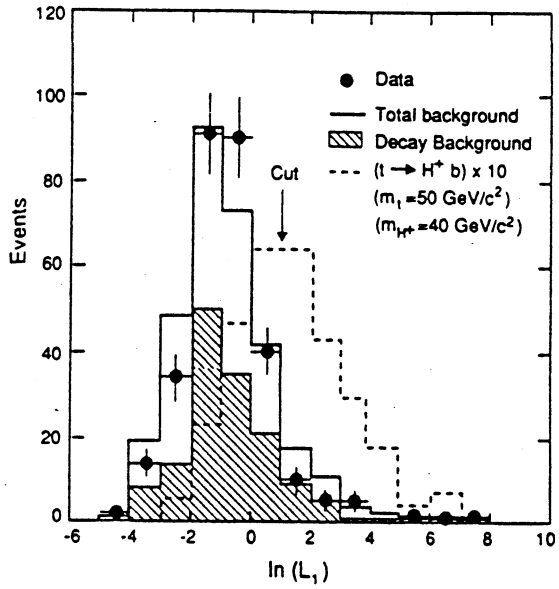

Figure 2.7.9 : Distribution in $\ln(L_1)$ for single muon events from UA1. The data are compared to a simulation of the known physics processes and the simulation of the decay $t \rightarrow H^+b$ for $m_t = 50$ GeV and $m_{H^\pm} = 40$ GeV and $BR(H^+ \rightarrow \tau^+\nu_\tau) = 95$ %.

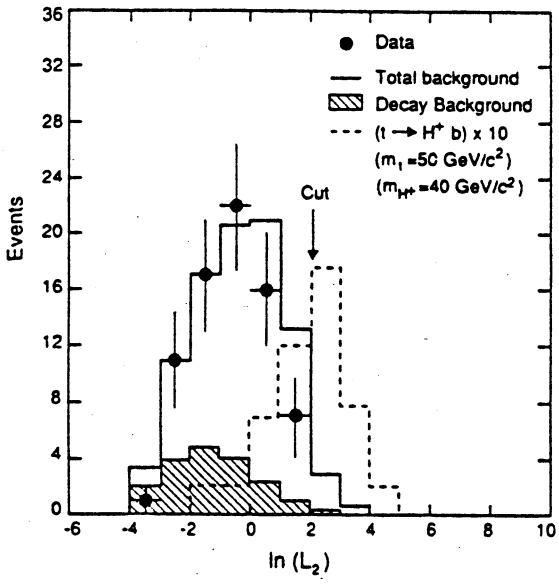

Figure 2.7.10 : Distribution in $\ln(L_2)$ for dimuon events from UA1. The data are compared to a simulation of the known physics processes and the simulation of the decay $t \rightarrow H^+b$ for $m_t = 50$ GeV and $m_{H^\pm} = 40$ GeV and $BR(H^+ \rightarrow \tau^+\nu_\tau) = 95$ %.

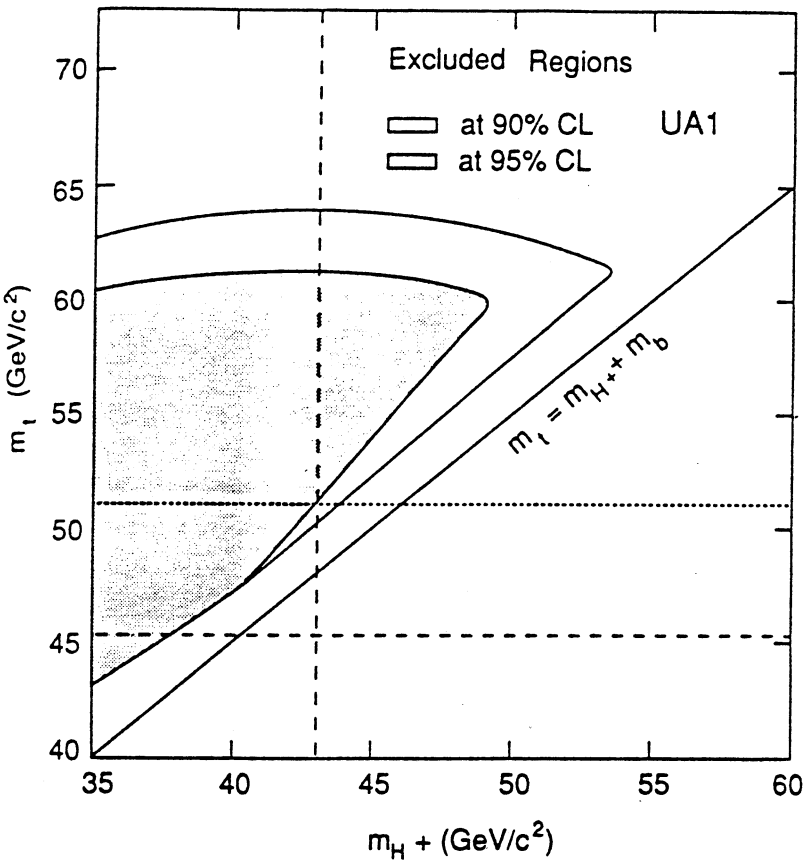

Figure 2.7.11 : Regions of the (m_t, $m_{H\pm}$) plane excluded at 90 % and 95 % C.L.

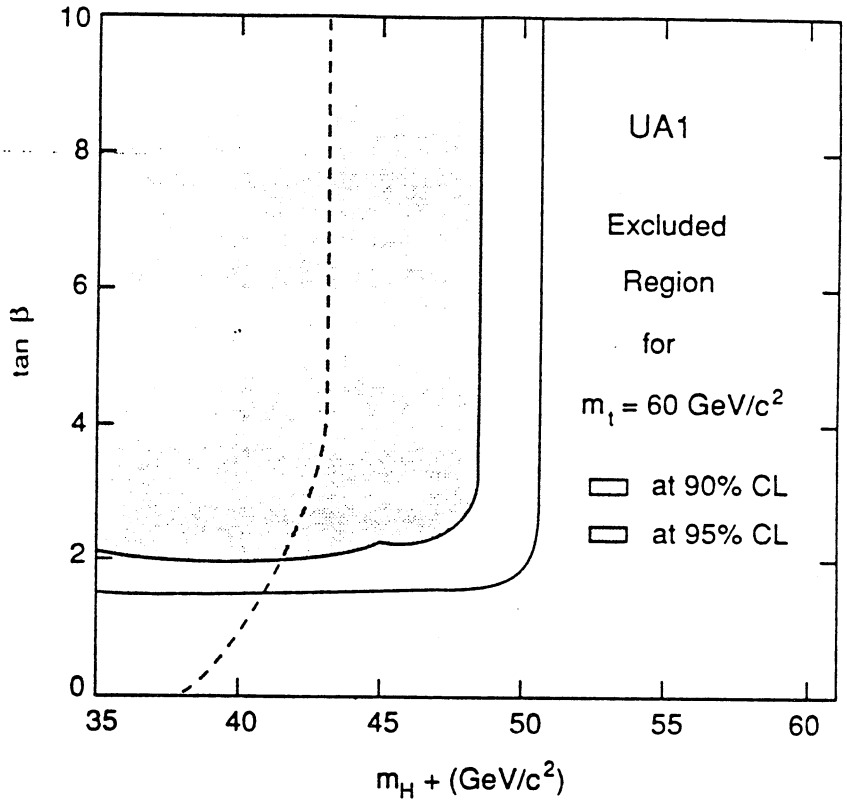

Figure 2.7.12 : Regions of the (tanβ, $m_{H\pm}$) plane excluded at 90 % and 95 % C.L.

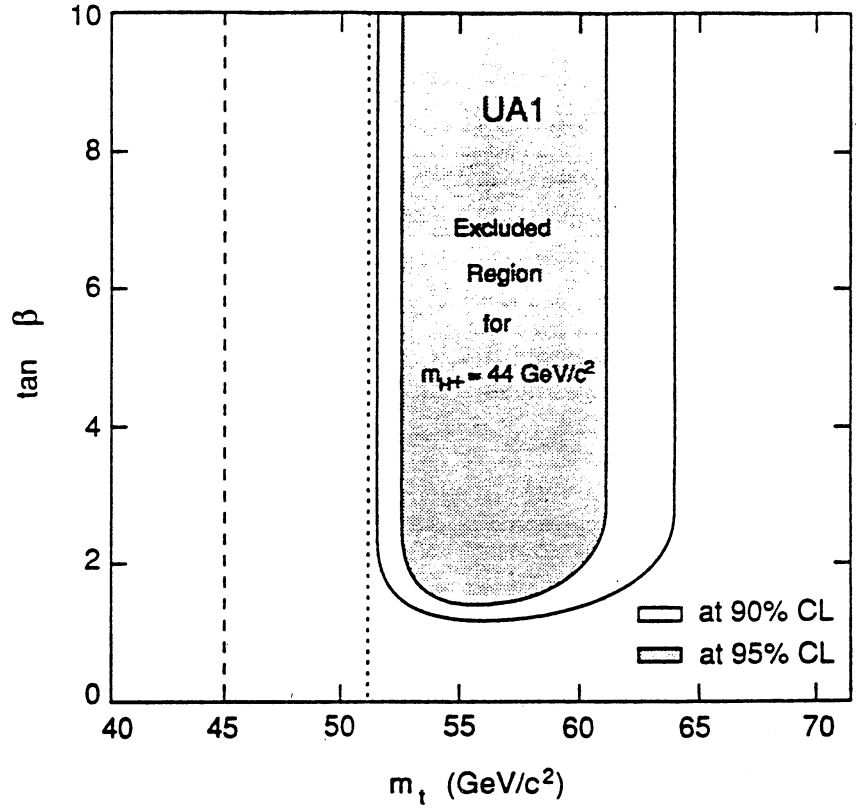

Figure 2.7.13 : Regions of the (tanβ, m_t) plane excluded at 90 % and 95 % C.L.

The data sample for the dimuon channel is defined with the following cuts :

1. $p_T^{\mu\ 1} > 6$ GeV in -1.6 $< \eta <$ 1.6,
2. $p_T^{\mu\ 2} > 3$ GeV ,
3. $\geq$ 1 jet with $E_T^{jet} > 10$ GeV in -1.5 $< \eta <$ 1.5,
4. $E_T^{jet\ 1} > 13$ GeV, $E_T^{jet\ 2} > 7$ GeV,
5. $M_T^{\mu\mu} < 50$ GeV, and
6. $I_{\mu\ 1} < 6$,
7. $I_{\mu\ 2} > 2$,
8. $30° < \Delta\phi_{\mu\ 1-j} < 160°$, and
9. $|\cos\theta_j^*|$ where θ_j^* is the angle between the jet and the beam axis in the rest-frame of the four-body system jet- μ_1- μ_2- p_T^{miss}.

A likelihood function, L_2 is defined based on $p_T^{\mu\ 1}$ and I_{μ_1}. Figure 2.7.10 shows the distribution for L_2 for both the signal and background. The search region is defined as $\ln(L_2) > 2$ in which no events are found.

The agreement between the measured distributions and those of the known physics background processes such as b- and c- quark decays, W and Z^0 , J/ψ, Y, Drell-Yan and K and π decays, shows that there is no evidence in the UA1 data for the decay $t \rightarrow H^+b$ decay. The results from the single μ and dimuon samples are combined. Figure 2.7.11 shows the regions of the (m_t ,$m_{H\pm}$) plane excluded at the 95 % and 90 % C.L. Figure 2.7.12 and 2.7.13 show, respectively, the excluded regions in the ($\tan\beta$,$m_{H\pm}$) and ($\tan\beta$,m_t) planes at the 95 % and 90 % C.L.

2.8 Prospects for $H^{\pm}$ Search in Top Quark Decay at Future Hadron Colliders

2.8.1 The Fermilab Tevatron Collider

Assuming $m_t = 150$ GeV and a $H^{\pm}$ - fermion coupling scheme suggested by MSSM or by E_6 string-inspired models, a $H^{\pm}$ via top quark decay signal is observable up to $m_{H^{\pm}} \approx 100$ GeV throughout the allowed range of the coupling parameter $0.5 \leq \tan\beta \leq 100$ [God-91, Roy-91b]. The assumption made in this analysis is of an integrated luminosity of 100 pb^{-1} at a centre-of-mass energy $\sqrt{s} = 1.8$ TeV.

The primary top production process at the Tevatron is $t\bar{t}$ production through gluon-gluon and quark-antiquark fusion. This is followed by the decay into $H^{\pm}$ or W channels, i.e.,

$$gg(q\bar{q}) \rightarrow t\bar{t}$$

$$t \rightarrow bH^{+}(W^{+})$$

$$\bar{t} \rightarrow \bar{b}H^{-}(W^{-}).$$

This is the lowest order QCD process for $t\bar{t}$ production and is the dominant production process for $m_t = 150$ GeV. In a given channel of $t\bar{t}$ decay the $W^{\pm}$ background corresponds to the WW contribution whereas the $H^{\pm}$ signal corresponds to the $(H^{\pm}H^{\pm} + W^{\pm}W^{\pm})$ contribution.

To avoid background from QCD processes such as dijet and multi-jet production at least one of the two charged bosons is required to decay into a τ channel, i.e.

$$H^{+}(W^{+}) \rightarrow \tau^{+}\nu_{\tau}$$

$$H^{-}(W^{-}) \rightarrow \bar{q}q'$$

or vice versa. Finally, the τ is observed in its hadronic or muonic decay channels, normally via

$$\tau \rightarrow \nu_{\tau}\bar{q}q' \quad (\sim 64\%)$$

$$\tau \rightarrow \nu_{\tau}\nu_{\mu}\mu \quad (\sim 18\%)$$

as a narrow jet (τ jet) or a soft muon accompanied by a large p_T^{miss}. The WW background to any of these final states can be viewed in terms of the hard dilepton channel

$$t\bar{t} \rightarrow b\bar{b}W^+W^- \rightarrow b\bar{b}l^+l^-\nu_l\bar{\nu}_l$$

where l is either an electron or μ and

$$p_T^l > 15 \text{ GeV}.$$

This provides an unambiguous normalization to the W background because of the negligible $H^\pm$ couplings to electrons and μ 's. An excess over the WW background may be evidence for $H^\pm$ production.

Figures 2.8.1 and 2.8.2 show the expected signal and background for the two most promising channels - single and double τ jet channels corresponding to the τ decay of one or both of the charged bosons. In the former channel the cuts used are

$$p_T^{\tau\ jet} > 10 \text{ GeV}, \quad p_T^{miss} > 20 \text{ GeV}$$

$$p_T^{jet\ 1} > 40 \text{ GeV}, \quad p_T^{jet\ 2} > 30 \text{ GeV}$$

where the second charged boson decays via

$$H^\pm(W^\pm) \rightarrow \bar{q}q'.$$

In the double τ jet channel the cuts used are

$$p_T^{\tau\ jet} > 10 \text{ GeV}, \quad p_T^{miss} > 20 \text{ GeV}.$$

This channel has also the advantage of being free from the W + QCD jets background.

2.8.2 The Superconducting Supercollider (SSC)

In the previous section it was shown that for $m_t = 150$ GeV a systematic comparison of the top signal in different decay channels provides an effective $H^\pm$ signature up to a $H^\pm$ mass of about 100 GeV at the Tevatron Collider. However, the reach in $H^\pm$ mass is not large enough considering that in models such as MSSM $m_{H^\pm} > m_W$. Because of this it is necessary to extend the $H^\pm$ probe beyond 100 GeV with no unresolved gaps in the parameter space.

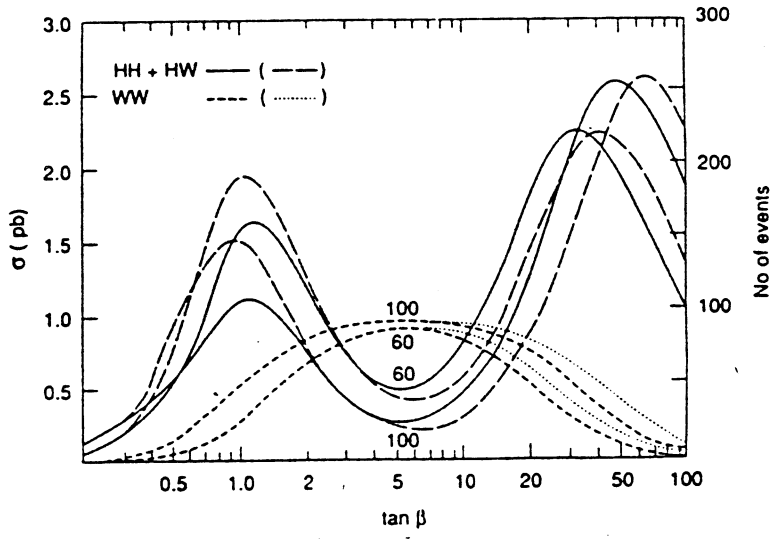

Figure 2.8.1 : Charged Higgs signal versus WW background in the single τ - jet channel. The effect of the QCD corrections are shown in parenthesis (see Section 2.7.1).

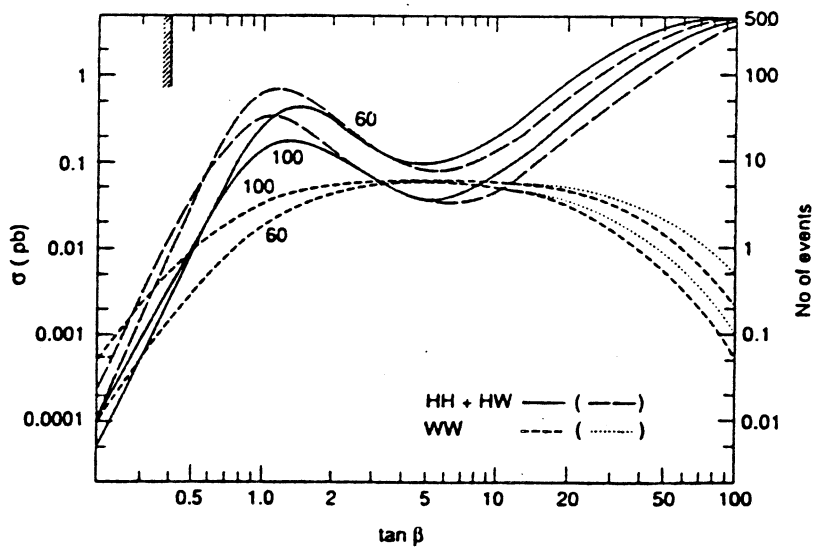

Figure 2.8.2 : Charged Higgs signal versus WW background in the double τ - jet channel. The effect of the QCD corrections are shown in parenthesis (see Section 2.7.1).

This can be achieved by an increase in the total integrated luminosity of the Tevatron. However, a larger signal size at both the LHC and SSC is expected due to the larger $t\bar{t}$ production cross-section and luminosity. For $m_{H^\pm}$ greater than 100 GeV, the increasing gap between the $H^\pm$ and W boson masses offers the possibility to enhance the signal-to- background ratio by using kinematic cuts.

In this section prospects for the discovery of $H^\pm$ from top quark decay at the SSC are discussed while the possibilities for the LHC are presented in Chapter 7.

The operating assumptions of the SSC are a centre-of-mass energy of the proton-proton collisions of $\sqrt{s} = 40$ GeV and a canonical luminosity of 10^{33} $cm^{-2}s^{-1}$ yielding 10^4 pb^{-1} per year. The jet resolution is that assumed by the Solenoidal Detector Collaboration (SDC) [SDC-90] :

$$\frac{\sigma_{jet}}{E} = \frac{50\%}{\sqrt{E}} + 4\%$$

and an electromagnetic resolution of

$$\frac{\sigma_{EM}}{E} = \frac{20\%}{\sqrt{E}} + 2\%.$$

Two methods [Bar-90c] have been studied for $H^\pm$ detection in $t\bar{t}$ events for the case $m_t = 250$ GeV and $m_{H^\pm} = 150$ GeV. Method 1 involves a search for an excess of τ events whilst Method 2 involves the recontruction of the hadronic decays $H^+ \rightarrow c\bar{s}$. The process of interest is of $t\bar{t}$ production through gluon-gluon fusion or quark-antiquark annihilation followed by their decay into $H^\pm$ or W boson channels, i.e.

$$gg \text{ or } q\bar{q} \rightarrow b\bar{b}\ (H^+H^-, H^+W^-, H^-W^+, W^+W^-)$$

where the first three terms in the parenthesis represent the $H^\pm$ signal while the fourth one the W background.

In each method the events are selected by requiring one top quark to decay via $t \rightarrow bW \rightarrow bl\nu_l$ giving an isolated electron or μ (l) with $p_T > 40$ GeV in $-2.5 < \eta < 2.5$. Further selection criteria include requiring two tagged b-jets (from the decay of the t and $\bar{t}$) with $p_T > 30$ GeV within $-2.0 < \eta < 2.0$. The non $- t\bar{t}$ background is negligible after these cuts.

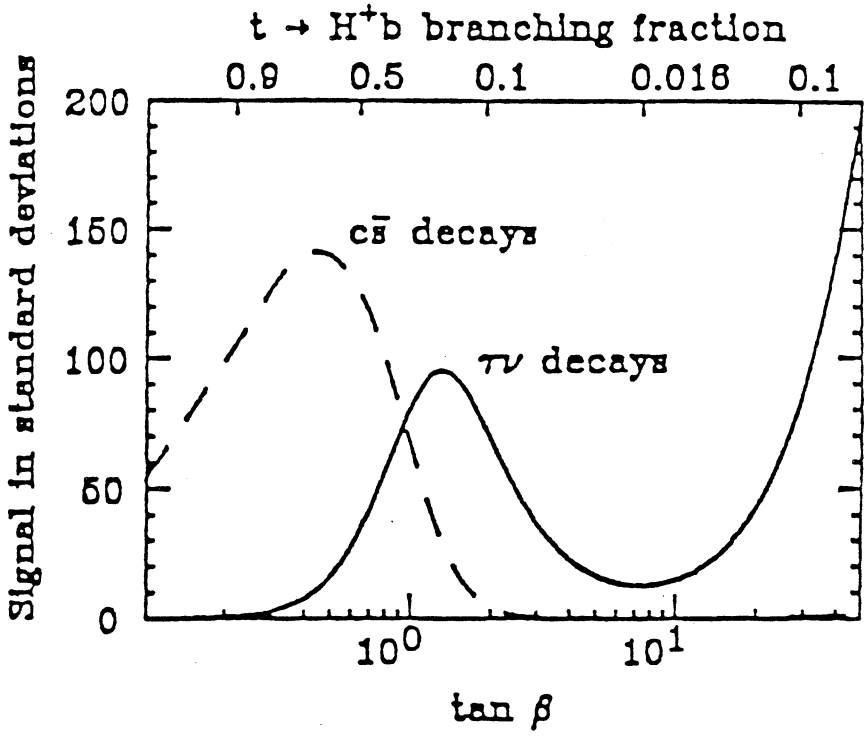

Figure 2.8.3 : The statistical significance for Method 1 (solid curve) and for Method 2 (dashed curve) in identifying a charged Higgs boson over the W background at the SSC (see text).

In Method 1 l - τ events given by :

$$t \rightarrow bW^+ \rightarrow bl^+\nu_l \text{ and}$$

$$\bar{t} \rightarrow \bar{b}H^- \text{ or } \bar{b}W^- \rightarrow \bar{b}\tau^-\bar{\nu}_\tau$$

are searched for in τ decays to a single $\pi^\pm$ (or $K^\pm$) with $p_T > 40$ GeV (or 100 GeV). In Method 2 the top quark decays to H^+ or W^+ with the charged bosons decaying to $c\bar{s}$.

The statistical significance of the excess in the observed number of isolated pions over the prediction from universality from Method 1 is given in Figure 2.8.3. To quantify the statistical significance of the $H^\pm$ mass peak from Method 2, the number of standard deviations above the background is plotted in Figure 2.8.3 as a function of $\tan\beta$. Therefore, requiring a 5 standard deviation effect, the detection of the $H^\pm$ boson over the entire mass and $\tan\beta$ range using either $H^+ \rightarrow \tau^+\nu_\tau$ or $H^+ \rightarrow c\bar{s}$ decays or both is feasible.

Chapter 3

The UA2 Experiment

3.1 Introduction

The UA2 experiment first took data at the CERN proton-antiproton ($p\overline{p}$) Collider during the years 1982-1985. During this time UA2 investigated topics in W and Z physics [UA2-83a, UA2-83b, UA2-86a, UA2-87a, UA2-87b, UA2-88a], QCD jets [UA2-85a, UA2-85b, UA2-86b, UA2-87c], direct photon production [UA2-88b], exotics [UA2-87d] and jet physics [UA2-82, UA2-83c]. With the introduction of the Antiproton Collector Ring (ACOL), the UA2 detector was upgraded and a new three-level triggering scheme was implemented to improve its physics capabilities.

The upgrade of the UA2 detector consisted primarily of extending the calorimeter coverage and enhancing the particle identification and track reconstruction using information supplied by the central detector. A cross-section through the upgraded UA2 detector can be seen in Figures 3.1.1 and 3.1.2. Two higher level on-line software triggers were also introduced alongside the existing first level hardware trigger to handle the expected increase in the machine luminosity.

The increased calorimeter acceptance is intended to improve the measurement of the total momentum of an event and also to increase the QCD jet acceptance. A neutrino, or any other weakly interacting particle such as that from supersymmetric particles of normal matter, are inferred from an imbalance in the total detected momentum of an event. Because of the loss of particles produced at small angles to the beam outside the calorimeter accep-

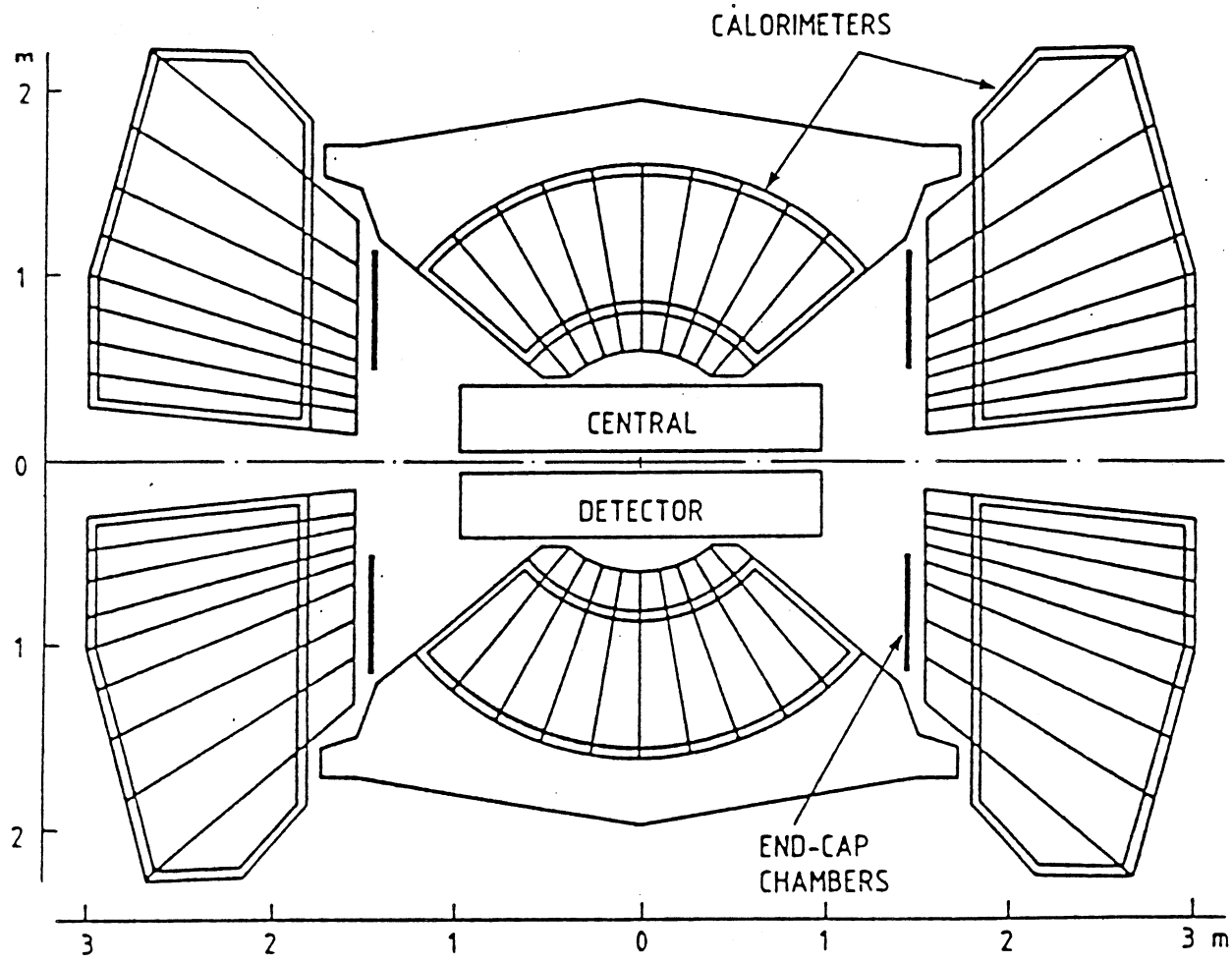

Figure 3.1.1 : Cross-section view of the UA2 detector.

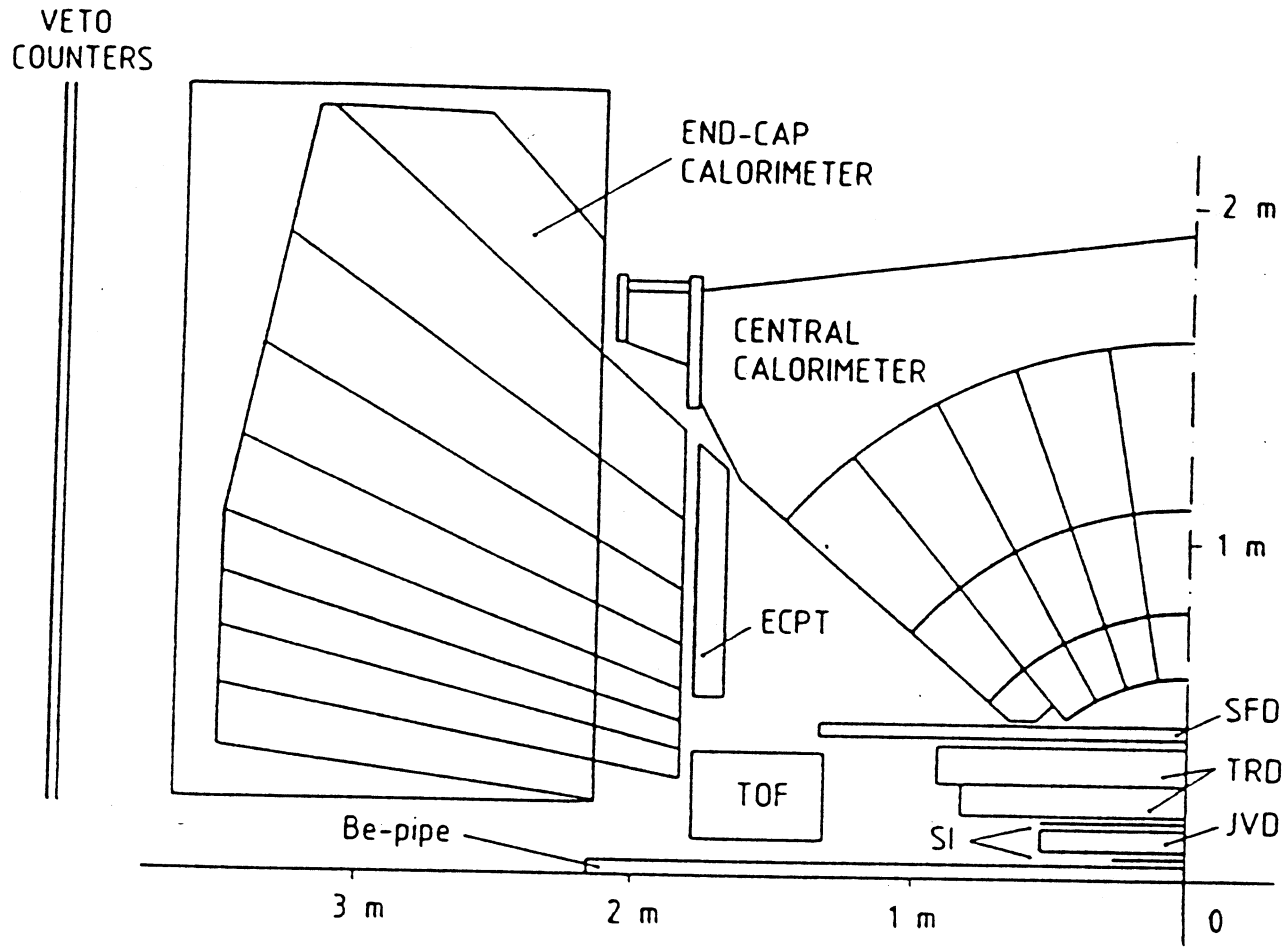

Figure 3.1.2 : Cross-section through a quadrant of the UA2 detector.

tance, the momentum component along the beam cannot be measured so that the quantities of physical interest are the transverse momentum and missing transverse momentum, p_T^{miss}, coming from the momentum imbalance of the event. In addition, the combination of the central detector and calorimeter information with characteristic signals from the subdetectors provide a good means for electron identification.

Because UA2 has no central magnetic field and no muon detection capabilities the following should be noted :

1. All tracks are straight and only a momentum measurement comes from the calorimeters.
2. There is no distinction between an electron and a positron.
3. The e^+e^- pair from a γ or π^0 does not separate.
4. The only leptonic states studied in UA2 are electrons and τ's.

The UA2 coordinate system is a conventional right-handed Cartesian system having x=y=z=0 at the centre of the detector with z increasing in the proton beam direction.

In this chapter a description of the experimental facilities used for the analysis presented in Chapter 5 and 6 is discussed. Section 3.2 overviews the CERN $p\overline{p}$ Collider. In Section 3.3 the UA2 detector is described and its trigger and data acquisition systems are presented in Section 3.4. Finally, Section 3.5 discusses the dedicated τ trigger implemented in 1990.

3.2 The CERN Proton - Antiproton Collider

The backbone of the CERN $p\overline{p}$ Collider is the Proton Synchroton (PS), the Super Proton Synchroton (SPS), and the Antiproton Collector (ACOL) [Eva-87, Jon-86, Wil-83]. The latter was commissioned in 1987 and is comprised of the antiproton production source (AP), the antiproton collector ring (AC), and the already existing antiproton accumulator (AA) around which the AC is built. The layout of the Collider complex, including all the experimental

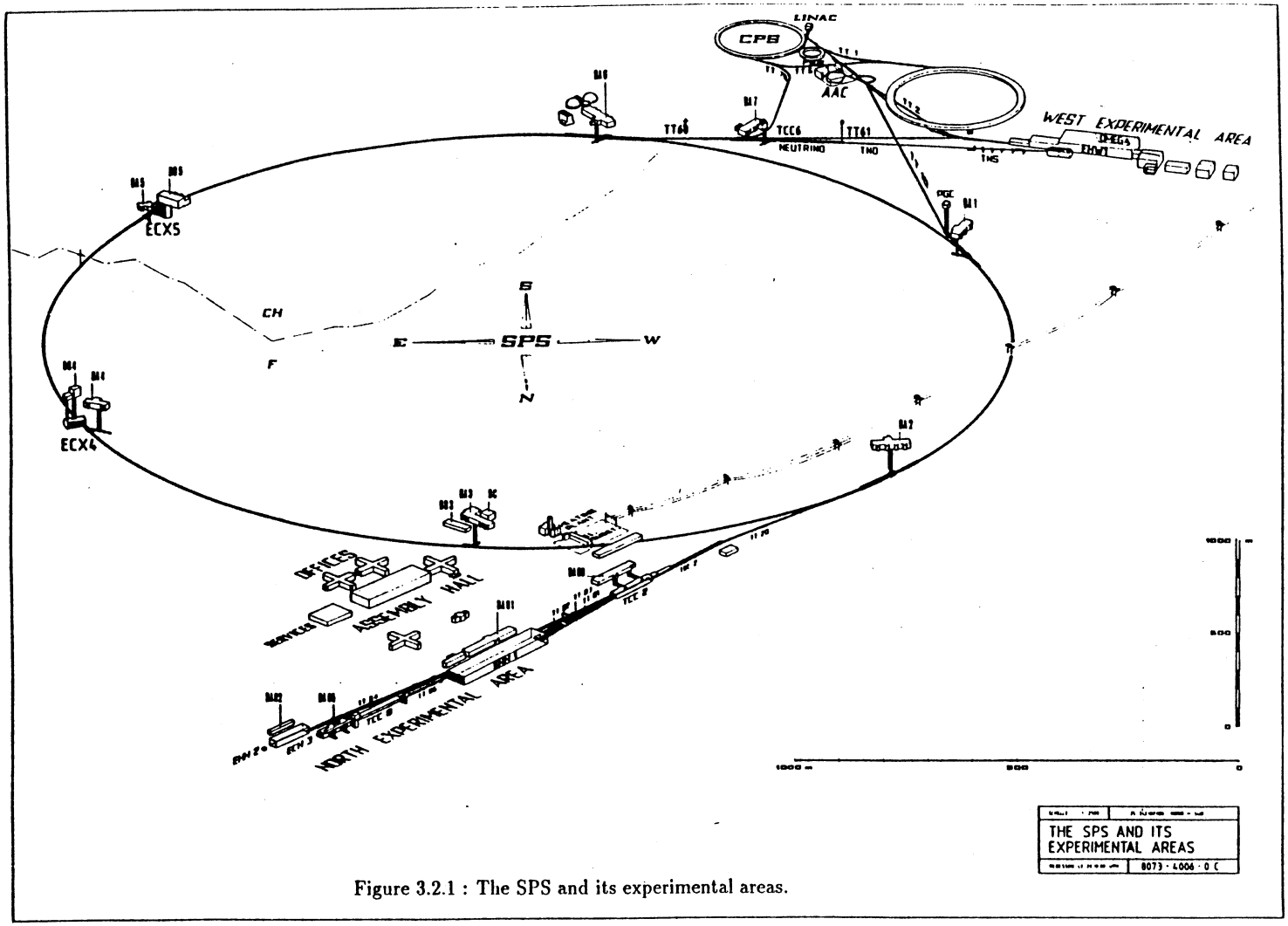

Figure 3.2.1 : The SPS and its experimental areas.

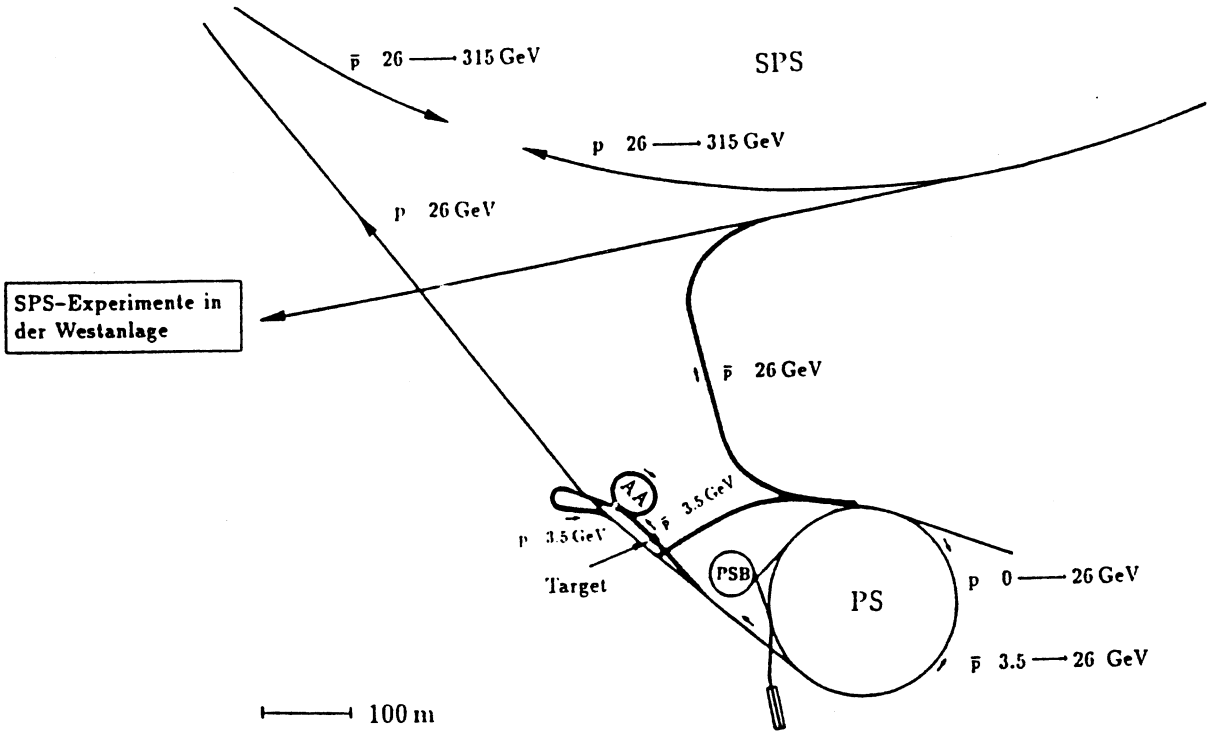

Figure 3.2.2 : The CERN proton-antiproton accelerator complex.

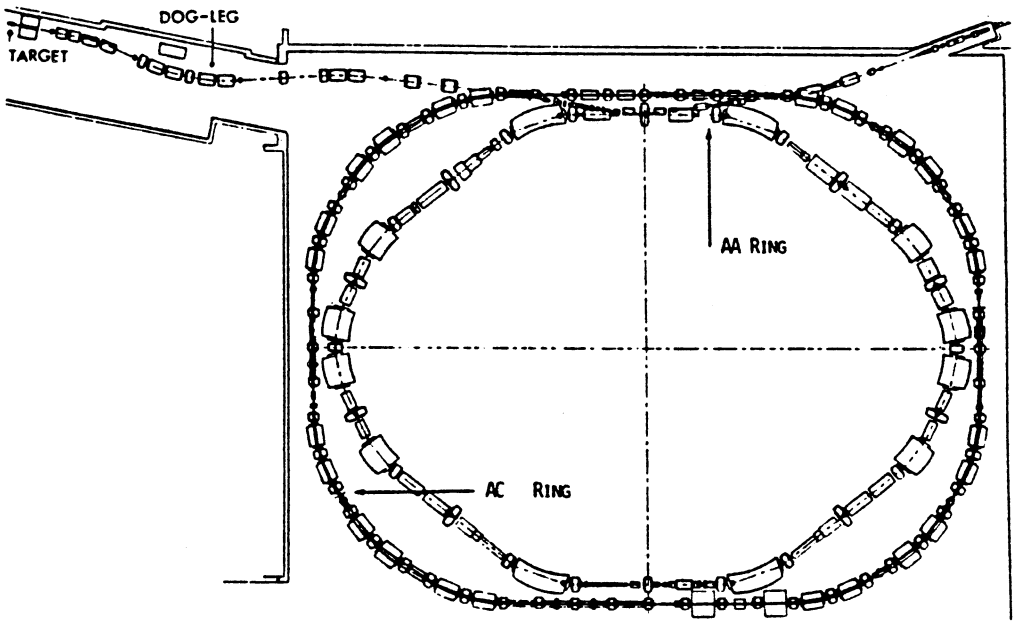

Figure 3.2.3 : The Antiproton Collector and Accumulator.

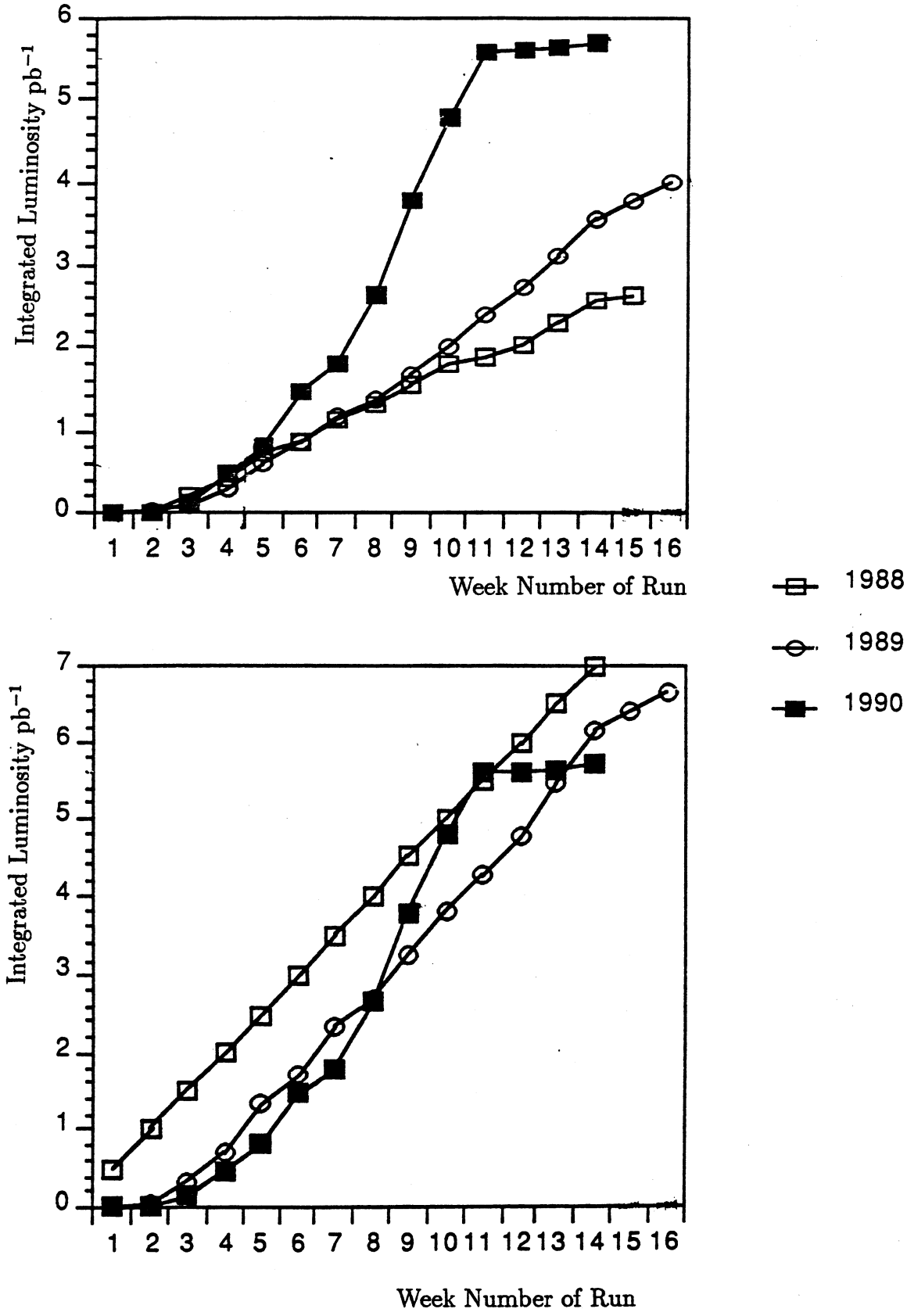

Figure 3.2.4 : Comparison between total integrated luminosity for the three Collider runs from 1988 to 1990.

areas, is shown in Figure 3.2.1. The UA2 detector surrounds the interaction region ECX4. Figure 3.2.2 shows the different components of the Collider in more detail.

The first $p\bar{p}$ collisions in the SPS were observed in July 1981. In autumn 1982, the first physics run took place with 28 nb^{-1} of luminosity produced for the two experiments UA1 and UA2 in which evidence for the existence of the W boson was found [UA1-83, UA2-83]. In 1983, the integrated luminosity was increased to 153 nb^{-1} and the Z^0 particle was seen [UA1-83, UA1-83].

Antiprotons are produced by accelerating protons to 26 GeV in the PS and colliding them with an iridium target of dimensions 3.5 x 55 mm^2. This creates a burst of particles from which antiprotons of mean energy 3.5 $\pm$ 0.1 GeV are selected. The antiprotons pass through a lithium rod at the same time of passage as 420 kA of pulsed current. The current produces a magnetic field of constant gradient and is thus a linear focusing lens for the traversing antiprotons. This lithium lens gives the antiprotons a momentum and angular spread of 6% and 100 mrad , respectively.

The AC consists of a debuncher and a stochastic pre - cooling ring. Antiprotons are injected into the AC ring with a 5 bunch structure and are captured into 5 of the 6 9.55 MHz RF buckets. After full debunching the momentum bite has decreased to 1.6% . Transverse stochastic cooling is then performed in both the horizontal and vertical planes together for about 1 s. This reduces the emittance in both planes from 250π to 25π mm rad. Finally, the momentum spread is reduced further to 0.2% in a further second. After cooling 300 ms remain before the next PS cycle is due to arrive on the target. During this time the antiproton beam is rebunched with a 2 MHz RF cavity and then ejected and transferred to the AA for accumulation and final cooling.

On the AA injection orbits further vertical and momentum cooling is still necessary before the newly injected beam joins the stack. This is achieved by a 1 - 2 GHz RF system that decreases the vertical emittance to 15π mm rad and the momentum spread to 1 $-$ 1.5%. The AC and AA complex is shown in Figure 3.2.3.

After stacking antiprotons for about 12 hrs, the PS and SPS prepare for a fill. First, 6 proton bunches are sent to the SPS at 2.4 s intervals and stored at 26 GeV. These 6 bunches are placed equidistant from one another around the SPS circumference. They have been specially 'shaped' in the PS by a 100 and 200 MHz RF system until each fits into a single 5 ns long

SPS bucket. Then a single antiproton bunch is unstacked from the AA and injected into the SPS in a trajectory opposite to the protons for a collision in UA2 to an accuracy of less than 1 ns. This is followed at 2.4 s intervals by five more antiproton bunches. The SPS then accelerates both the proton and antiproton beams to the storage energy of 315 GeV, squeezes them at the low $-\beta$ quadrupole insertions in less than 1 s and keeps the two beams in storage for about 12 hrs while the next batch of antiprotons is being prepared in the AA.

For the 1990 SPS Collider run additional low $-\beta$ quadrupoles at a distance of 7.5 m. from the bunch crossing point were installed in order to reduce the beam size at $z = 0$, thus increasing the luminosity [Dil-89]. The luminosity is given by

$$L = \frac{M\, N_p\, N_{\bar{p}}\, f}{\sqrt{[(\sigma_H^p)^2 + (\sigma_H^{\bar{p}})^2]\,[(\sigma_V^p)^2 + (\sigma_V^{\bar{p}})^2]}}$$

where M is the number of bunches, f is the revolution frequency and N_p, ($N_{\bar{p}}$) is the number of protons (antiprotons) per bunch. The σ_H and σ_V are the beam sizes given by their rms deviation from the central orbit (assuming a Gaussian shape), in the x - z horizontal and y - z vertical planes, respectively.

In each plane a beam particle at any z is described by its distance from the central orbit (x or y) and its angular divergence (x' or y'). All particles occupy an elliptical region in the (x,x') or (y,y') planes with areas ϵ_H and ϵ_V, respectively, where ϵ is the beam emittance. At a given energy these areas are constant due to Liouville's theorem. Therefore, to increase the luminosity one needs minimal transverse dimensions at the bunch crossing point implying maximal angular divergences. Because of this increased angular deviation it is important to verify that the beams still fit into the UA2 vacuum pipe which has a length of $\pm$2250 mm. with repect to z=0.

Tables 3.2.1 and 3.2.2 compare beam parameters for the 1988-1989 and 1990 runs, respectively. To check whether the beam fits in the vacuum chamber the ratio R/σ is calculated, where R is the vacuum chamber radius. The parameters in the tables are given for $z = 2250$ mm. where the beam size is maximum inside the vacuum chamber. The beam also fits into the vacuum chamber since they are $\geq 13.5\sigma$ away from the chamber wall at injection and $\geq 19.9\sigma$ away from the chamber during storage at 315 GeV energies. However, during storage the beam sizes double everywhere giving a clearance of

Parameters for the 1988-89 run

	β^*_H	β_H (z=2.25)	σ_H mm	R/σ_H	β^*_V	β_V (z=2.25)	σ_V mm	R/σ_V
Injection $\varepsilon = 2.27$	7 m	7.72 m	2.09	11.9	3.5 m	4.95 m	1.68	14.9
315 GeV $\varepsilon = 0.187$	1.0 m	6.06 m	0.53	47.0	0.5 m	10.63 m	0.70	35.5

Table 3.2.1 : Beam parameters for the 1988 and 1989 Collider runs.

Parameters for the 1990 run

	β^*_H	β_H (z=2.25)	σ_H mm	R/σ_H	β^*_V	β_V (z=2.25)	σ_V mm	R/σ_V
Injection $\varepsilon = 2.27$	4 m	5.27 m	1.73	14.5	1.0 m	6.06 m	1.85	13.5
315 GeV $\varepsilon = 0.187$	0.6 m	8.3 m	0.65	38.5	0.15 m	33.9 m	1.26	19.9

Table 3.2.2 : Beam parameters for the 1990 Collider run.

only $\sim 10\sigma$. This corresponds to a background increase near the end of a store which is averted by cutting the beam tails.

Figure 3.2.4 shows the increase in the total integrated luminosity over previous runs due primarily to the inclusion of the new quadrupoles.

3.3 The UA2 Detector

3.3.1 The UA2 Calorimeter

The Central Calorimeter

The UA2 Central Calorimeter (CC) [Bee-84] covers the pseudorapidity range $-1 <\mid \eta \mid < 1$ and is segmented into 240 cells subtending 10° in polar angle θ. The cells are segmented radially into one electromagnetic compartment followed by two hadronic compartments, thus giving a tower structure as shown in Figure 3.3.1. The azimuthal coverage is divided into $\Delta\phi = 15°$ slices, called 'orange slices', which are sub-divided into 10 cells. The orange slices are mechanically self-supporting and contain the light-guides, photomultipliers, and calibration devices in addition to the absorber, scintillator plates and wavelength shifter. The electromagnetic compartment of each cell is attached to the front hadronic absorber plate with the light-guides passing along the sides of the hadronic compartments. Since the design has a spherical geometry, each cell points toward the interaction region with the front face approximately 600 mm radially away from this point.

The electromagnetic compartment consists of 26 3.5 mm thick lead plates and 27 4 mm thick NE104 scintillator plates, giving a total thickness of 17 r.l. The hadronic calorimeter consists of 40 15 mm thick iron plates interspersed with 5 mm POLIVAR scintillator plates. Together the three compartments have a depth of 4.5 absorption lengths.

The End – Cap Calorimeters

The need to detect hadron jets down to as small an angle as possible and to make an improved measurement of the p_T^{miss} in an event necessitated the construction of calorimeters in the forward and backward directions. The End-Cap Calorimeters (EC) [Boo-86] cover the pseudorapidity region $1 <\mid \eta \mid < 3$ over the full azimuthal range. Each EC consists of 12

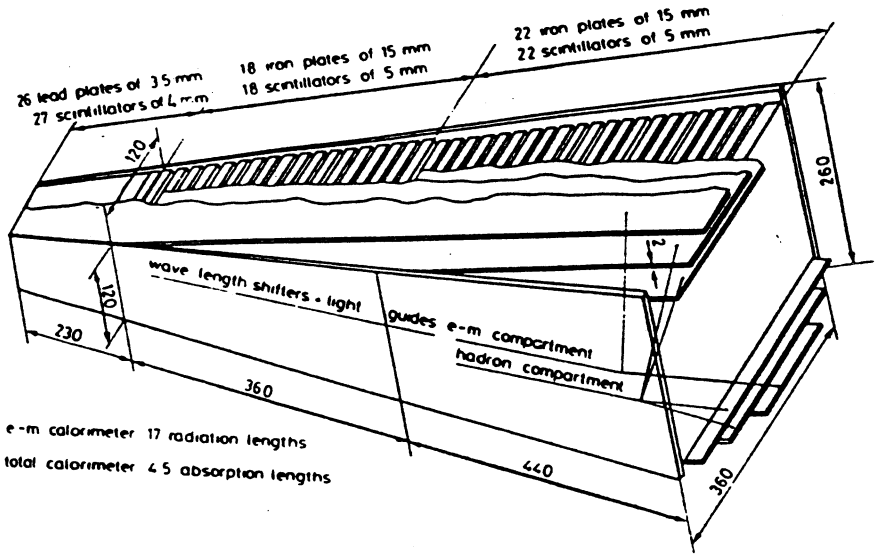

Figure 3.3.1 : Perspective view of a Central Calorimeter cell.

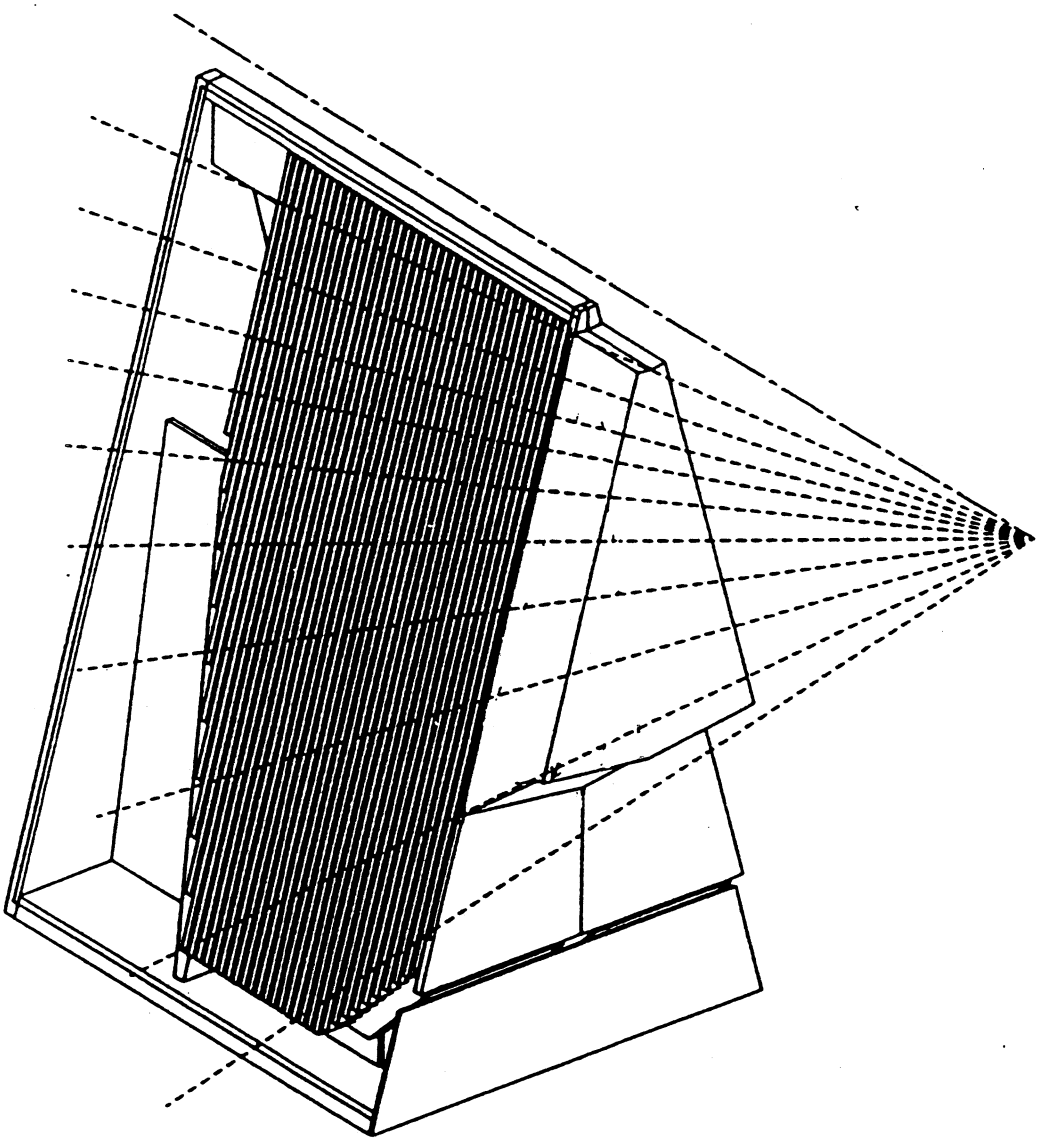

Figure 3.3.2 : Perspective view of an End-Cap Calorimeter module.

modules and each module is segmented into 16 cells. In a given module the two cells closest to the beam axis $2.5 <| \eta |< 3.0$ and $2.2 <| \eta |< 2.5$ cover 30° in azimuth. The cells have a constant segmentation of $\Delta\phi = 15°$ and $\Delta\eta = 0.2$. All the cells in the pseudorapidity interval $1.0 <| \eta |< 2.5$ have one electromagnetic and one hadronic compartment. The electromagnetic compartment is a multi-layer sandwich of lead and scintillator, with a total thickness varying from 17.1 to 24.4 r.l. depending on the polar angle. The hadronic compartment is a multi-layer sandwich of iron and scintillator corresponding to about 6.5 absorption lengths, including the electromagnetic compartment. Extra cells, with a hadronic compartment only, overlap the coverage of the CC in the region $0.9 <| \eta |< 1.0$ to ensure hermiticity in the region between the CC and EC.

As for the CC, a modular design has been adopted which incorporates the scintillator, wavelength shifter, and calibration systems for each 30° sector into the one unit. A pointing geometry has been adopted together with a novel modification to prevent particles traversing the inter-sector cracks, i.e. a 50 mrad rotation of each module around the symmetry axis of the first hadronic absorber plate. A perspective view of an EC module is shown in Figure 3.3.2.

The thirteen electromagnetic cells per end-cap are arranged as shown in Figure 3.3.3a with two $\Delta\phi = 15°$ sectors of 6 cells followed by the seventh cell spanning across both sectors. With the calorimeter segmented into equal pseudorapidity intervals, the energy clustering algorithm amongst neighbouring cells is independent of the cluster angle. Cells 1 and 6 have a segmentation of $\Delta\eta = 0.2$ while cell 7 has $\Delta\eta = 0.3$. The hadronic cells are arranged as shown in Figure 3.3.3b.

The absorber and scintillator plates are mounted perpendicular to the beamline and so their thickness varies as a function of the polar angle. While the absorber plates are continuous, the scintillators are laser cut to define the cell boundaries. After extensive tests POLIVAR scintillator was selected because of its relatively long attenuation length and low cost. As detailed in Figure 3.3.4. the cell thickness is considerably larger than in the CC in order to reduce the hadronic leakage for 40 GeV electrons. A 17 r.l. depth as in the CC is insufficient for 98% shower containement but instead requires 20 r.l.

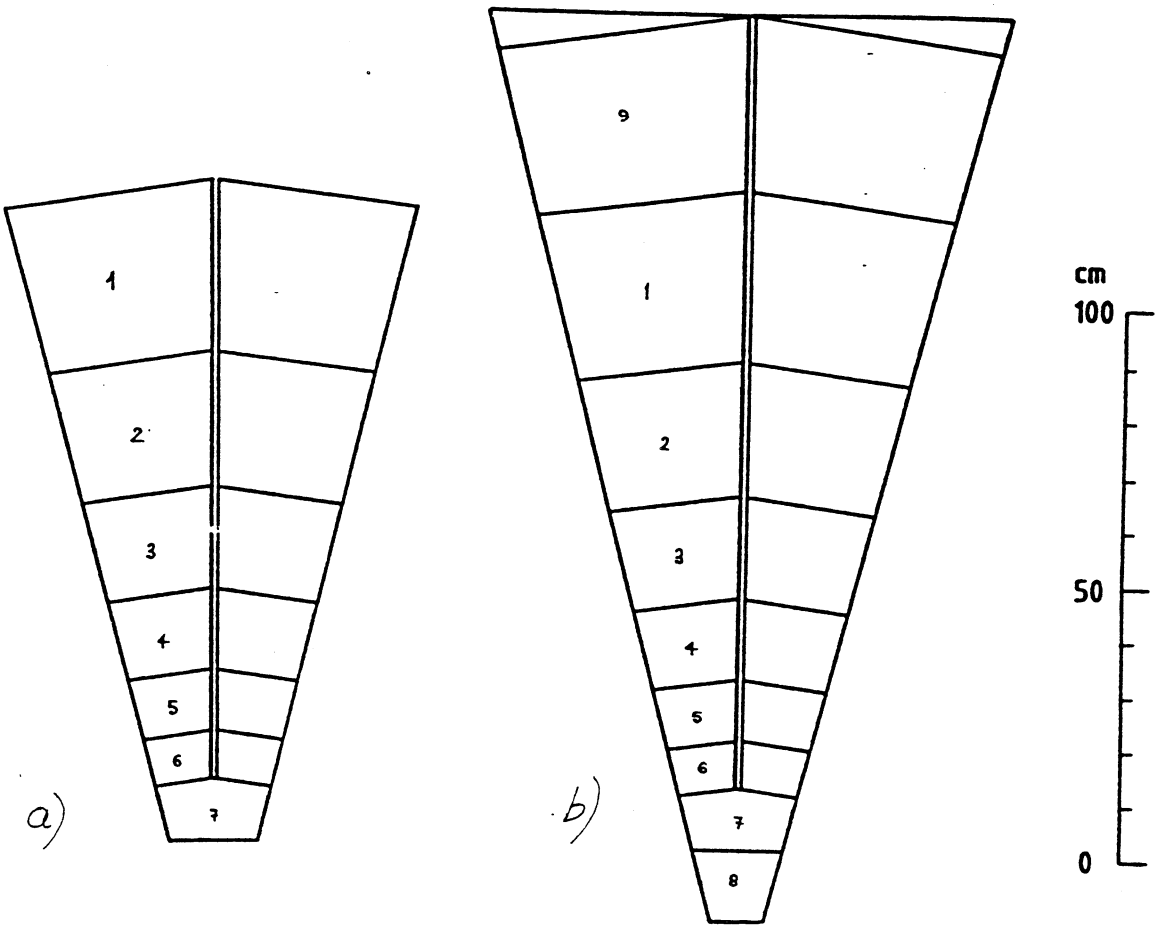

Figure 3.3.3 : Arrangement of the End-Cap Calorimeter cells for the (a) electromagnetic and (b) hadronic compartments.

Electromagnetic calorimeter

technique	Pb-scintillator sandwich K-27 wavelength shifter read out
material	32 Pb plates, 3 mm thick 33 scintillator plates, 4 mm thick
sampling	0.54 to 0.70 X_0
total thickness	17.1 to 24.4 X_0

Hadronic calorimeter

technique	Fe-scintillator sandwich K-27 wavelenght shifter read out
material	Fe plates, 25 mm thick scintillator plates, 4 mm thick $5^\circ < \theta < 20^\circ$: 38 plates $20^\circ < \theta < 40^\circ$: decreasing from 38 to 29 plates
sampling	0.15 to 0.19 λ_0
total thickness	5.6 to 6.2 λ_0 (0.6 to 0.8 λ_0 in addition from the electromagnetic calorimeter)

Segmentation

structure	towers pointing to the centre of the detector
cell size	$1.0 < \lvert\eta\rvert < 2.2$: $\Delta\phi \times \Delta\eta = 15^\circ \times 0.2$ $2.2 < \lvert\eta\rvert < 2.5$: $\Delta\phi \times \Delta\eta = 30^\circ \times 0.3$ $2.5 < \lvert\eta\rvert < 3.0$: $\Delta\phi \times \Delta\eta = 30^\circ \times 0.5$ (only hadronic)
depth segmentation	one electromagnetic and one hadronic compartment
sector	30° in azimuth, 24 sectors in total rotation angle 50 mrad (see text)
number of cells	electromagnetic 312 hadronic 384
number of channels	2 PM's per cell, 1392 total

Approximate weight

	120t for each end cap

The thicknesses in radiation length (X_0) and absorption length (λ_0) vary as a function of the polar angle θ between 5° and 40° with respect to the beam axis.

Figure 3.3.4 : The parameters of the End-Cap Calorimeter.

Calorimeter Read – out

Light produced in the scintillation plates of both calorimeters is collected by BBQ K-27 wavelength shifters (WLS) and guided to photomultipliers (PM) at the rear of each module. The WLS performs a number of tasks including shifting the light signal to larger wavelengths where the photon attenuation length is larger, re-directing the light signal towards the rear of the calorimeter and also acting as a light-guide to the PM.

All the photomultipliers used throughout the calorimeters have been subject to extensive stability and linearity tests. The tests involve a 38 hour ageing period at high voltage followed by a 12 hour stability test at constant voltage. Then follows exposure to varying light sources as a check on the response linearity. The PMs are of two types : Phillips XP2008 and XP2012 and because of the better stability of the latter they are used in the electromagnetic compartment.

The high voltage supply to the PMs are adjusted so that each PM's gain is proportional to the transverse energy rather than the energy. Since the physics phenomena of interest depend on transverse energy and the calorimeter cells subtend approximately the same azimuthal and pseudorapidity interval, the PM signals can be used directly for transverse energy triggers. This simplifies the trigger electronics as well as reducing the time needed for trigger decisions. The high voltage settings are established in test beams where each PM is individually calibrated.

The scintillation light is emitted in the UV region at a number of different wavelengths. The attenuation length of these wavelengths is small (about 200 mm.) and strongly dependent on the wavelength. Shorter wavelengths have shorter attenuation lengths and this dependence leads to a non-exponential light attenuation curve through the scintillator. A fraction of the scintillation light entering the WLS is absorbed and re-radiated isotropically at larger wavelengths. At these larger wavelengths the photon attenuation length is of the order of 2-3 m. The BBQ absorbs wavelengths in the range 375-398 nm and emits them at 432 nm.

Calorimeter Electronics

In both the CC and EC the PM signals are used in two ways. Firstly, they are processed to ADCs for the energy deposition measurement, and secondly they are used to make various sums for trigger decisions. These tasks are

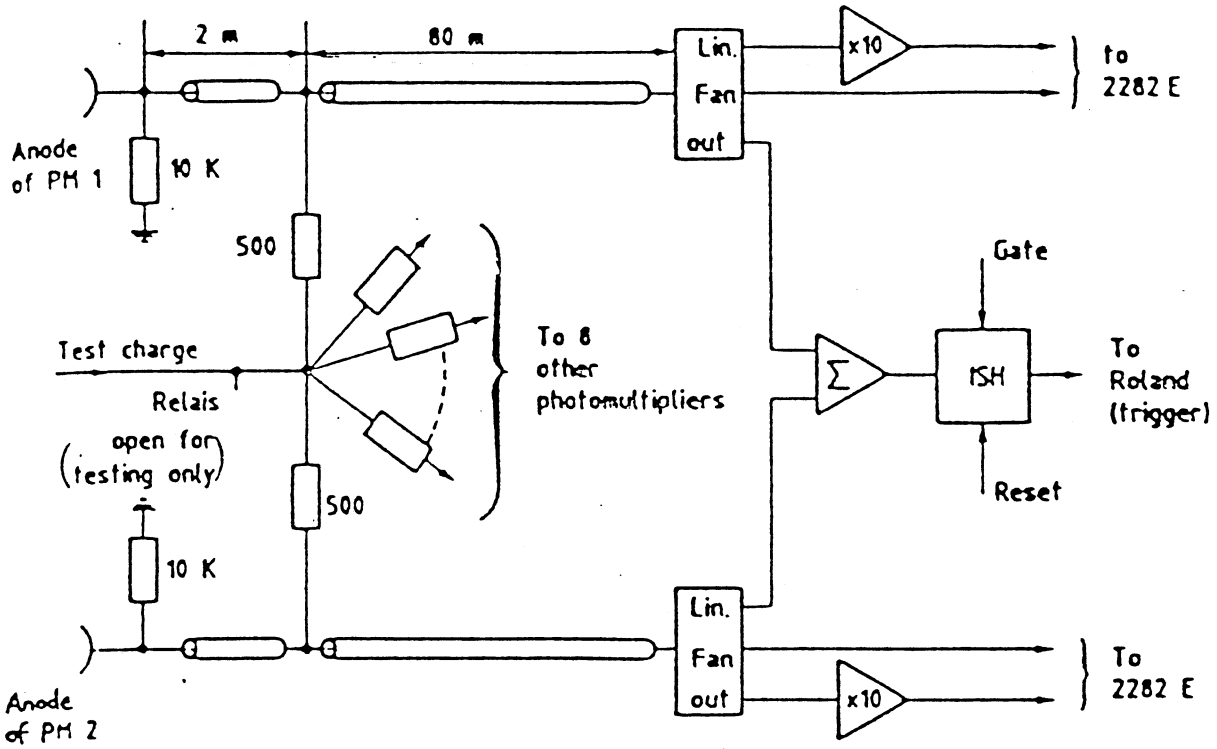

Figure 3.3.5 : The electronics of a single electromagnetic cell.

realized through separate fanouts to the calorimeter electronics and trigger electronics.

A schematic diagram of the calorimeter electronics is shown in Figure 3.3.5. The PM signal is a current pulse with the integrated charge over 400 ns being proportional to the energy deposition. In the counting room, 80 m away, the signal enters an OLIFAN module which is capable of accepting 20 inputs and is thus suitable for one compartment of a central 'orange' slice or for cells 1 to 5 for both sectors of the EC. The OLIFAN has the following outputs :

1. Via a multi-coaxial ribbon cable to the 2280 ADCs.
2. Via a multi-coaxial cable to a second set of 2280 ADCs for the accurate measurement of the low energy deposition (for the electromagnetic compartment only).
3. Via an integrating sample and hold circuit (ISH) and flat ribbon cable to a ROLAND module. The ISH performs an analogue integration of the input pulse, arithmetically sums the result with the other PM for that cell and then provides an output voltage level for the time duration of the first level electron triggers ($\sim$ 800ns.)
4. A fast analog sum of the 20 input signals used for the first level missing transverse momentum and jet trigger electronics.
5. To an output used to monitor the individual signals.

Two signals, the gate and clear, are required to operate the OLIFAN. The 400 ns gate is generated from electrodes about 50 m upstream from the detector and signal the arriving proton bunch thus allowing the bunch crossing time in the detector to be determined. For an event rejected at the first level the OLIFAN clear signal to reset the ISHs arrives 3 μs after the bunch crossing allowing 1 μs for clearing. The same gate and clear signals are used for the 2280 ADCs, which are readout by CAMAC.

Calorimeter Calibration

It is of extreme importance to have an accurate and stable calorimeter. Therefore, a variety of different calibration systems have been devised [Bag-89, Jak-89a, Jak-89b]. Each calorimeter cell is exposed to a test beam of

	Resolution, with E in GeV
$\Delta E/E$ for centre of cell	$15\%/\sqrt{E}$
$\Delta E/E$ for all cell	$16\%/\sqrt{E}$
Constant term	1.3 %
Energy scale uncertainty	1 %
Cell to cell variation	1 %

Table 3.3.1 : Central electromagnetic calorimeter energy resolution.

	Resolution, with E in GeV		
Average resolution $\Delta E/E$	$32\%E^{-1/4}$		
Energy scale uncertainty	2%		
Cell to cell variation	CCH1	CCH2	ECH
	5%	2.5%	3%

Table 3.3.2 : Central hadronic calorimeter energy resolution.

	λ_{EM}	λ_{H1}	λ_{H2}
EM shower	1.00	1.00	1.00
pion	1.27	1.00	1.09
jet	1.18	1.00	1.06

Table 3.3.3 : Energy weights applied in the Central Calorimeter.

	λ_{ECEM}	λ_{ECH}	λ_{CATCH}
EM shower	1.00	1.00	1.00
jet	1.20	1.00	1.75

Table 3.3.4 : Energy weights applied to the End-Cap Calorimeter.

known energy so that the PM voltage can be adjusted until a predetermined response is obtained. By choosing a calibration constant of 0.08 GeV per pC of charge and with the ADC design of -0.25 pC per count, the 12 bit ADCs can measure up to 80 GeV transverse energy per compartment before saturation. This implies that for a 40 GeV electron at a polar angle of 90° the PMs are adjusted to produce -512 pC or 2048 ADC counts. The response of the other cells is then given by :

$$\overline{Q}[\mathrm{pC}] \;=\; 12.5 \cdot \mathrm{E[GeV]} \cdot \sin\theta$$

where $\overline{Q}$ is the mean charge measured in the ADC, E is the beam energy and θ is the polar angle of the centre cell. This technique was used for the electromagnetic calorimeters using a 40 GeV electron beam.

The EC hadronic calorimeter is calibrated using a 40 GeV pion beam in which a weighted sum of the energy deposited in the electromagnetic and hadronic compartments is used to determine the mean response. Because the CC hadronic calorimeter consists of two compartments, a 40 GeV pion beam only deposits a small amount of energy in the second compartment. Therefore, muons are used in this calibration which penetrate the entire depth of the calorimeter.

Table 3.3.1. shows the estimated resolution of the central electromagnetic calorimeter. The resolution contains an energy dependent part and a constant part which must be combined in quadrature. Also listed are the overall cell energy scale uncertainty and cell-to-cell rms fluctuations. Table 3.3.2. lists the resolution of the central hadronic calorimeter. The linearity of the electromagnetic compartment of the CC is shown in Figure 3.3.6. The corresponding plot for the EC is shown in Figure 3.3.7 along with the energy resolution of the EC.

Calorimeter Weights

The UA2 calorimeter is non-compensating, i.e. it does not give the same signal in response to an electron and to a charged hadron of the same energy. To account for this difference, the signals are multiplied by weights according to what particle is believed to have passed through. The procedure to establish these weights involves the use of test beams of muons, electrons, and charged pions of known energy.

By adjusting the applied voltages, the photomultiplier response to muons for the left and right read-out of each cell is equalized. The relative responses

for the electromagnetic and hadronic compartments are adjusted in the ratio of the lengths of scintillator to give an output proportional to the transverse energy.

The response to electrons and charged pions is then measured to establish the conversion factors from ADC counts to GeV and the appropriate weights for electrons and hadrons. The weights for the CC are given in Table 3.3.3. Those applied to jets take into account the typical mixture of particle types and energies present. The weights for the EC, including the hadronic only cell covering the crack region between the CC and EC, λ_{catch}, is given in Table 3.3.4. These weights have been chosen to provide the minimum hadronic resolution.

Calorimeter Monitoring

After each PM of the calorimeter is calibrated initially it is then imperative to monitor the calibration throughout the calorimeter's operational life. As well as the deteoration of the scintillator due to normal ageing and radiation damage, failure or variations of the PMs or electronics requires a variety of methods to be able to correct for these changes. The methods include a movable ^{60}Co radioactive source of intensity 4 mCi and a light flash system for the scintillator and WLS, a precision pulse generator system (PPG), a pedestal program for the electronics and an analysis of the energy flow throughout the calorimeter for minimum bias events. Below is listed the general strategy for accounting for these corrections. The corrections can be expressed as

$$\text{E[GeV]} = \text{C}[\frac{\text{GeV}}{\text{pC}}] \cdot \text{Q[pC]} \cdot \frac{\text{I}_0}{\text{I}_1} \cdot \text{M}$$

where C is the calibration constant from test beam and Q is the PPG and pedestal corrected charge. Linear interpolations between the ^{60}Co measurements are sufficient to provide a calibration stability of $< 3\%$. The observed ageing of the calorimeter is a few percent per year while the error in a particular ^{60}Co measurement to fix the rate of ageing is $\sim 0.3\%$. The electronics gain is found to be stable to $< 0.3\%$ between running periods and the HV drift is found to be $< 0.2\%$. The corrections made for differences from channel to channel in the photomultipliers obtained from minimum bias events are $\pm 1\%$ and $\pm 2\%$ for the electromagnetic and hadronic compartments, respectively. An energy scale error for a cell changes the number of events observed in a given energy range.

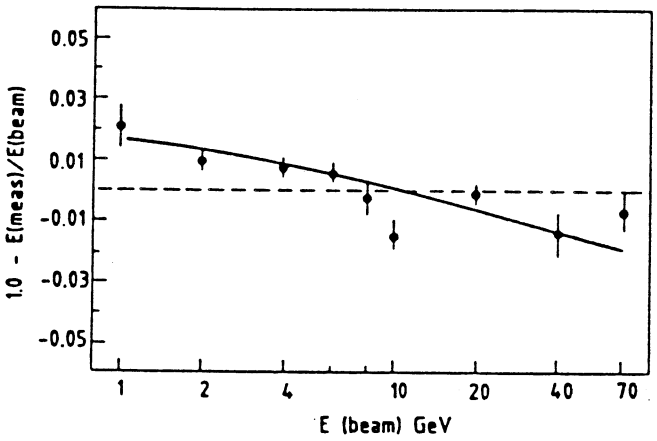

Figure 3.3.6 : Linearity of the central electromagnetic calorimeter.

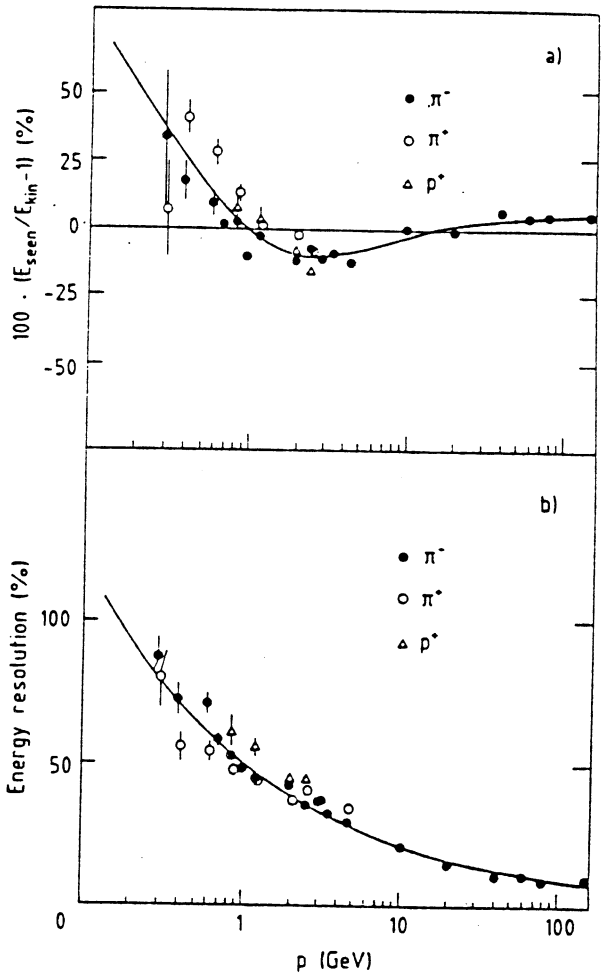

Figure 3.3.7 : (a) Linearity of the End-Cap Calorimeter, and (b) the energy resolution of the End-Cap Calorimeter.

3.3.2 The Central Detector

The Beam Pipe

The UA2 beam pipe [Boo-86] is cylindrical and made from beryllium of outer diameter 63 mm. and thickness just 0.9 mm. corresponding to 0.25% r.l. Because traversing particles see such a small number of radiation lengths of material, the rate of photon conversions and delta-ray production is reduced thus improving the primary electron identification.

The UA2 Silicon Hodoscopes

Semiconductor detectors are solid-state ionization chambers. A charged particle creates electron-hole pairs on its way through a crystal. The crystal is situated between two electrodes generating an electric field. During the ionization process electrons from the valence band are excited by the passing particle and are transferred to the conduction band, leaving behind a hole in the valence band. After the passage of the incident particle there remains a tube around the track with high concentrations of electrons and holes 10^{15} to 10^{17}per cm^3. The electrons must then be collected on the anode before they recombine with the holes.

A characteristic property of a monocrystalline semiconducting material is the small separation between the electron conduction band and the valence band. The photoelectric effect, in which a photon excites an electron to the conduction band, provides a measurement of the band gap which in silicon is 1.12 eV. For energetic particles, however, the process is more complicated due to energy loss fluctuations and it is found that on average 3.62 eV is deposited in the silicon for each generated electron-hole pair [Dea-66, Ber-68,]. In contrast, for gases ionization energies between 20 and 40 eV are needed while in scintillation counters as much as 400 to 1000 eV are required in order to detect via the scintillation light falling onto a photocathode one photoelectron. Thus, the amount of ionization produced for a given incident particle energy is an order of magnitude greater for silicon, resulting in an increased energy resolution.

Electrons of typical energy 40 GeV detected by the UA2 silicon hodoscopes are minimum ionizing particles (mips) named so because they undergo the minimum energy deposition in the silicon. Beyond this minimum only a very small increase occurs. The average minimum energy deposition in

silicon is ~ 0.35 MeV mm^{-1}. The term mip is also used as a unit of energy deposition by normalizing the value of the energy deposited by a charged particle to that of a minimum ionizing particle.

Energetic particles lose energy through successive interactions with close or distant electrons in the silicon. This is a statistical process so that the actual energy loss and energy deposition for a particle traversing a layer of silicon is described by a probability distribution - the Landau distribution [Lan-44]. A small number particles undergo a large energy loss (represented by the tail of the distribution). Most particles lose an energy around 0.28 keV μm^{-1}. The signal generated by a mip consists of about 80 000 charges (1.28 pC) per mm of silicon so that for the 300 μm thick UA2 silicon hodoscopes the signal consists of about 24 000 charges.

The Outer Silicon Detector

The Outer Silicon detector (OSI) [Bor-87, Bor-88, Bor-89, Boo-86] was constructed to measure both the ionization charge deposited by the traversing charged particles and to provide a space point in the longitudinal z direction for track recognition with a resolution of 9 mm. Because of the absence of a central magnetic field in UA2, e^+e^- pairs produced are unresolved in space. Such pairs are produced in Dalitz decays

$$\pi^\circ \rightarrow \gamma e^+e^-$$

and in photon conversions

$$\gamma X \rightarrow e^+e^- X$$

in the Collider vacuum pipe and in the OSI itself and can fake single electrons and positrons. The OSI assists in the identification of such e^+e^- pairs by providing a measure of the ionization energy deposited. As seen in Figure 3.3.8 the energy deposited in the OSI by an e^+e^- pair from photon conversions, for example, is most probably twice what is deposited by a single electron or positron.

The OSI hodoscope consists of 432 silicon counters subdivided into 7 pads of 8.7x40 mm^2 each, separated by 100μm -wide oxide strips and having a total active area of 61x40 mm^2. The silicon thickness is 300μm. The total sensitive area of the hodoscope is ~ 1m^2 and is arranged as a cylinder of 1 m in length at a radius of 147.5 mm from the beam pipe. The geometry is

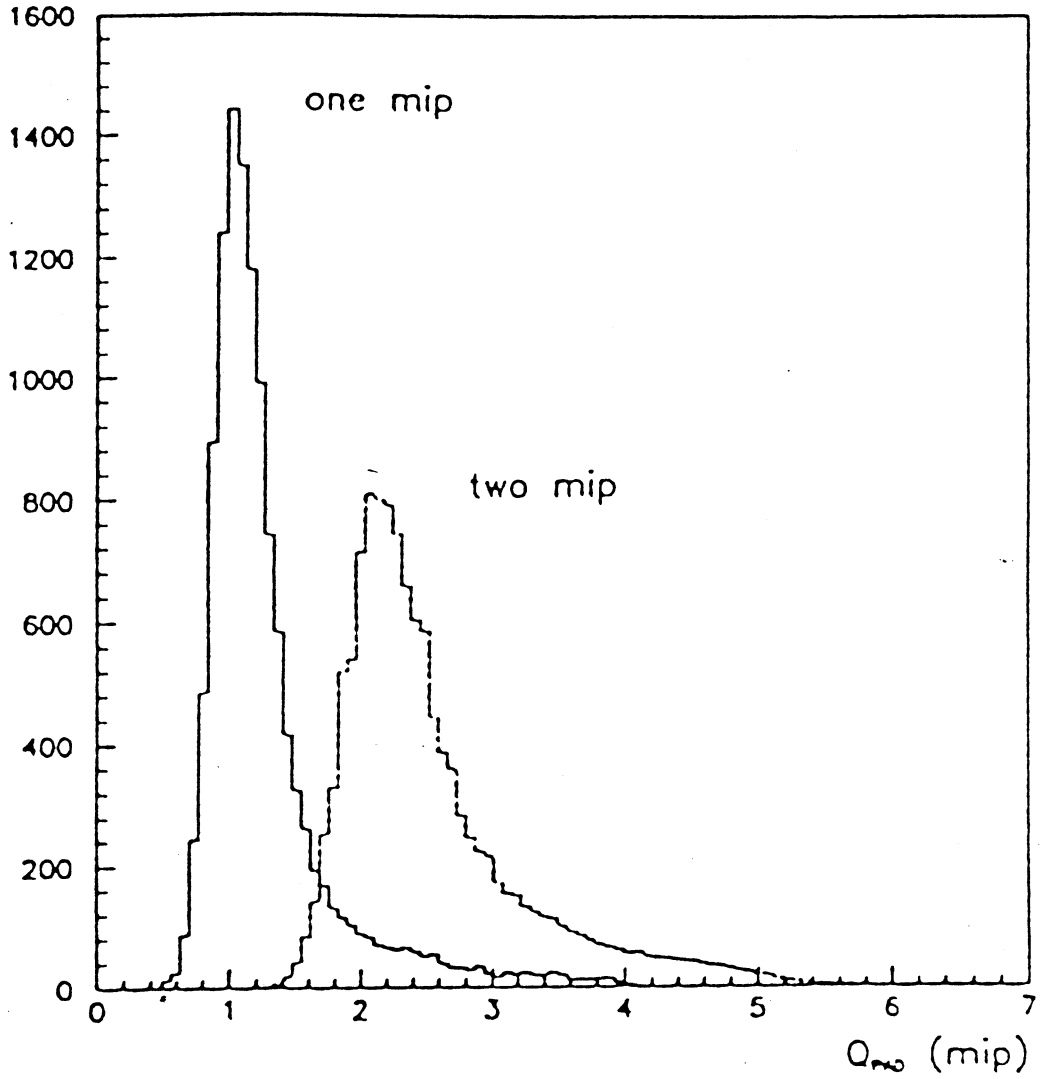

Figure 3.3.8 : Signal distribution in an OSI pad for single electrons (1 mip) and electron-positron pairs (2 mips).

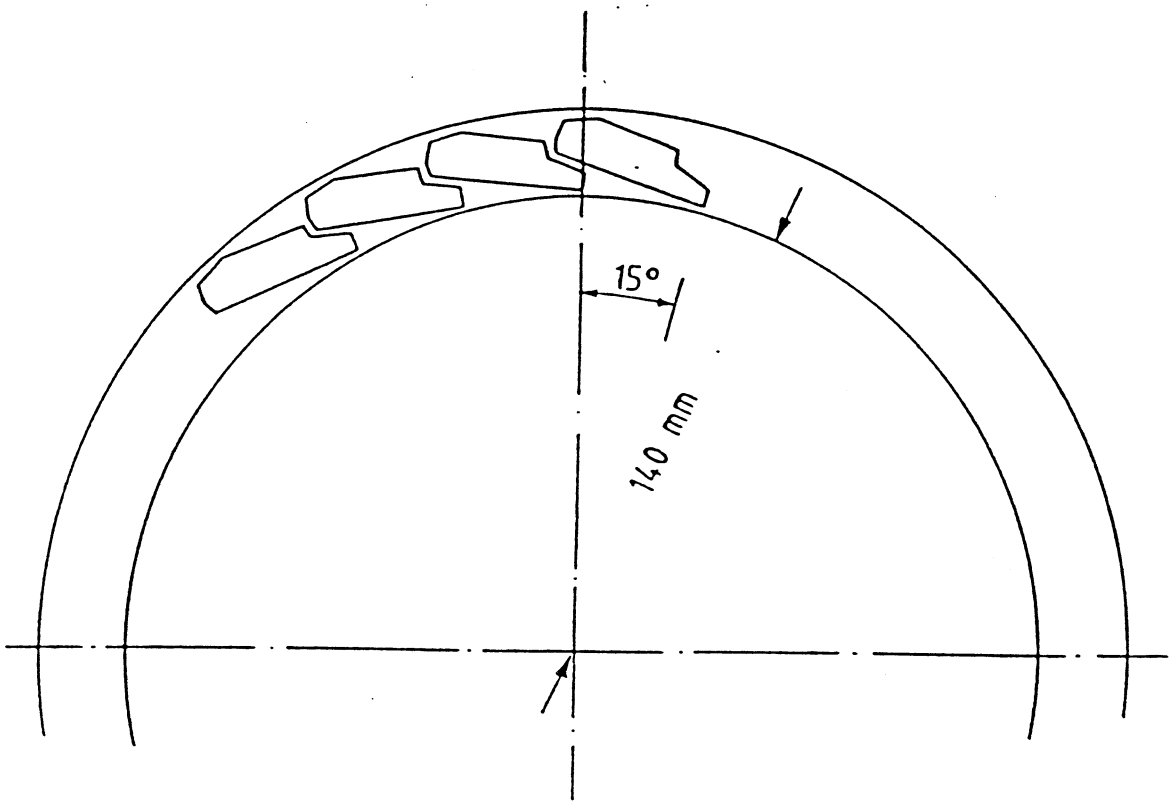

Figure 3.3.9 : Transverse view of the OSI showing the positioning of the motherboards. The motherboards are staggerd so as to avoid insensitive areas.

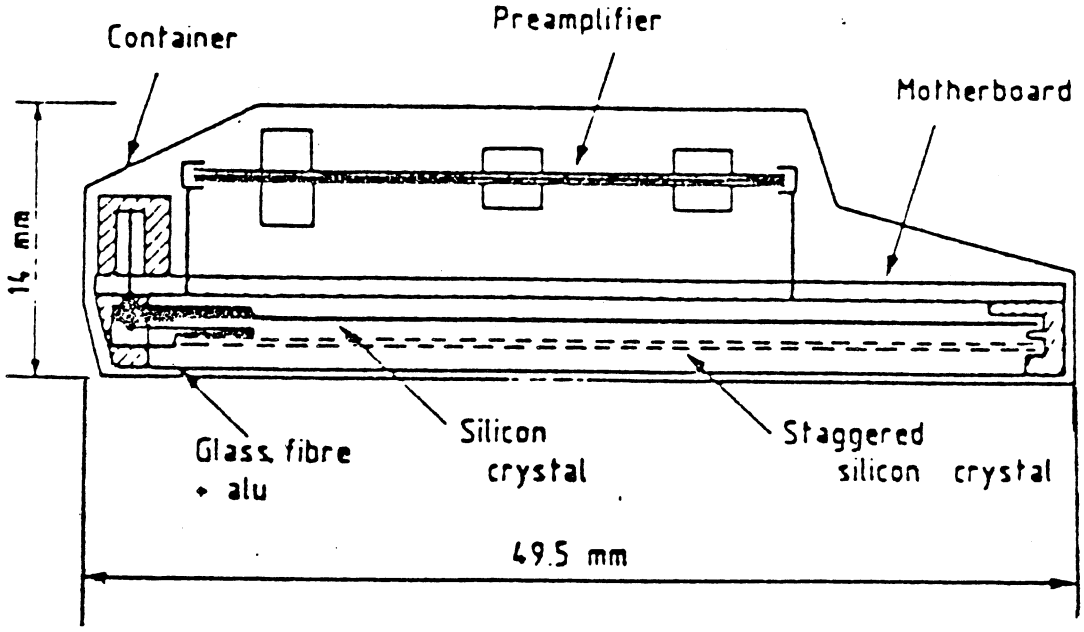

Figure 3.3.10 : Cross-section view of an OSI motherboard.

optimized to cover the complete solid angle used for electron identification ($25° < \theta < 155°$) so that $|\eta| < 1.9$ and with full azimuthal coverage. Figure 3.3.9 shows a cross-section through the OSI.

The individual silicon counters are arranged in groups of 9 on 48 modules. The counters of each module are mounted on a motherboard of dimensions 50x582 mm^2 consisting of a six-layer printed circuit board of 0.7 mm total thickness. Figure 3.3.10 shows a cross-section through an OSI motherboard. The side opposite the counters is equipped with the corresponding amplifiers (see below). Each module is staggered in height by 1 mm to avoid dead spaces and covers 15° in azimuth. The nine counters are covered by a common 0.1 mm thick fibreglass sheet and are enclosed in aluminium foil to provide electrical shielding. The volume surrounding the silicon counters is flushed with nitrogen and the preamplifiers are cooled with flowing air at 20 °C. Each module is slid into a polygonal container of 0.2 mm thick fibreglass. The support structure for the module consists of two concentric carbon fibre cylinders each 0.6 mm thick.

The silicon counters are commercially manufactured on 3 in. $< 111 >$ silicon wafers with n-type resistivity $2 - 15$ kΩ cm. The typical capacitance of each junction is 120-130 pF at the full depletion voltage (see below). The active area of the counters consists of 7 ion-implanted pn junctions (pads) and are surrounded by a common guard ring of 100 μm width. Each counter is glued along one side on a 7x55 mm^2 printed circuit board of 1 mm thickness. The pads are wire-bonded to this board and the latter is attached mechanically and electrically via contact pins to the motherboard.

For particles at normal incidence emerging from the interaction vertex the OSI has an average thickness of 3% r.l. which includes 0.45% preceding the silicon counters, (from the carbon fibre support cylinder, fibreglass and aluminium), 2.22% after the counters, (from the motherboard, preamplifiers and shielding), and 0.32% from the silicon itself.

The complete electronics chain for the OSI consists of low noise charge sensitive preamplifiers, shaping amplifiers, and analog multiplexing circuits. A schematic diagram is shown in Figure 3.3.11. The shaping amplifiers, track-and-hold and multiplexing are located in an electronics box at the end of the module, and the preamplifier signals are transmitted there via the multilayer motherboard. The preamplifiers, LABEN type 5315, are 7 channel hybrid circuits with J-FET input stage, input decoupling capacitors and individual bias voltage filters for each pad. The compact size 30x51 mm^2 of

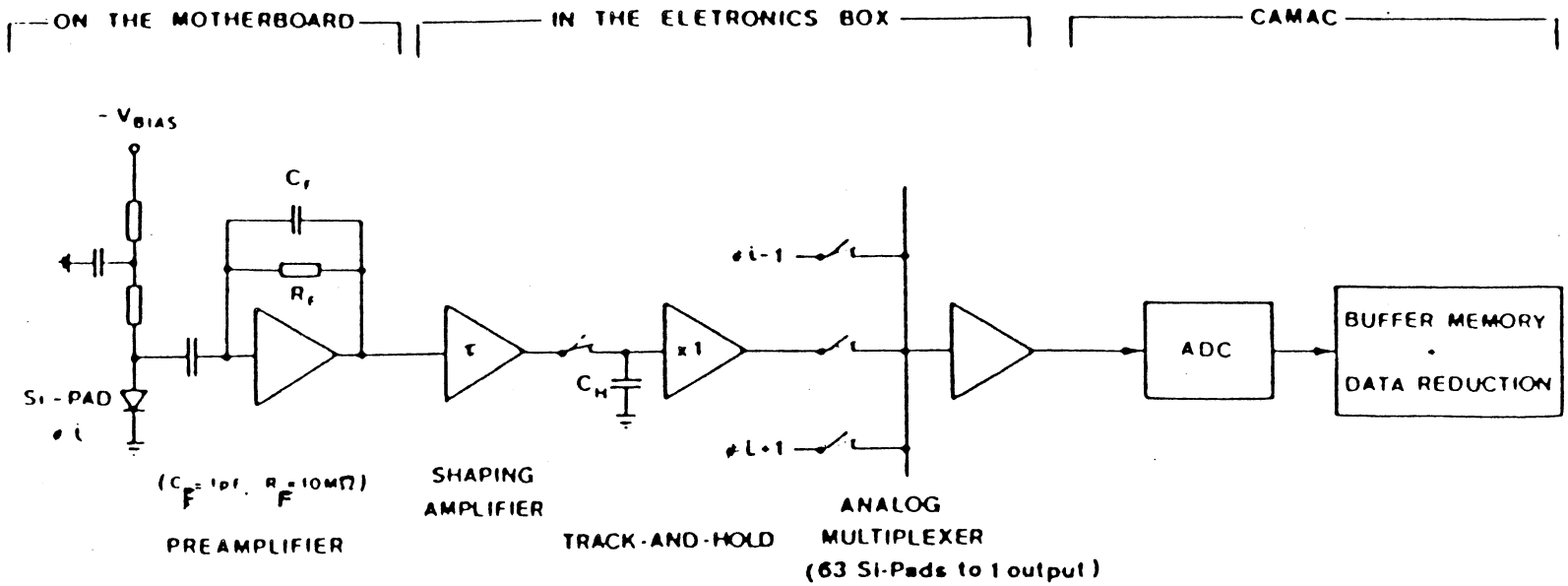

Figure 3.3.11 : Schematic diagram of the OSI electronics chain and read-out.

the preamplifier circuit allows it to be placed opposite to the silicon counters on the multilayer motherboards.

The preamplifiers offer a good compromise between noise performance and power consumption. Using an external load capacitance of 150 pF at the input and the shaping amplifier described below, the noise is typically 0.6 fC FWHM (1600 electrons rms) at 27 mW/channel. The preamplifier gain is about 0.7 mV/fC.

The shaping amplifiers are hybrid circuits with a double differentiating and double integrating shaping stage ($\tau_{\text{diff}} = \tau_{\text{int}} = 0.73\mu s$) followed by a track-and-hold circuit. In the track mode the width of the shaped signal is $2\mu s$ at half maximum and $4\mu s$ at the base. This is compatible with the $4\mu s$ beam crossing time of the Collider. The output amplitude is 25 mV/fC.

After the beam crossing, the signal is held until a first level trigger decision has been made $\sim 1.5\mu s$ after the event occurred. After a valid first level trigger the voltage levels at the track-and-hold amplifier outputs are digitized sequentially otherwise the circuits are switched back to the track mode. The hold phase needed for the multiplexed readout is 1 ms long.

The signals of the 63 pads of each module are digitized successively by a single FERA-ADC. Only 3 16-channel ADC modules of 11-bit resolution and 48 channel lines are needed for the whole detector. The scanning of the 63 signals per module is performed using four analog CMOS multiplexers of level 63:1.

The static electrical characteristics of each OSI counter were measured on a test bench prior to allocation onto the modules [Gos-86]. Measurements are made of the reverse (leakage current) for each pad in the range 0 - 5 000 nA with a resolution of 2.5 nA and the junction capacitance in the range 0 - 500 pF with a resolution of 0.5 pF as a function of the reverse bias voltage.

A typical value for the leakage current is 50 nA per pad at full depletion, namely about 14 nA/cm^2. The criterion for the acceptance of a counter in UA2 is that the leakage current is less than 250 nA for each pad of the counter when operated at 19 °C and at full depletion voltage. This is the value of the leakage current for which the typical shot noise contribution (about 1450 electrons rms) approximates the intrinsic preamplifier noise. Figure 3.3.12 shows the leakage current dependence on the bias voltage of all 7 pads of a counter not satisfying the above criterion. While pads 2 and 4 show a typical leakage current, pads 5 and 6 have a high leakage current. Pads 1 and 7 show defective pads with a breakdown of the diode junction at low

depletion voltage. To verify the long term counter behaviour the leakage current is monitored at regular intervals during 24-48 hours of operation at full depletion.

The counter capacitance versus bias voltage of each pad is measured to determine the full depletion voltage, approximately the optimum operating voltage. The results for one counter are shown in Figure 3.3.13. The counters are grouped together according to the full depletion voltage for allocation on the motherboards. The great majority of counters fully deplete at between 10 and 50 V.

The calibration of the full OSI array to measure the gain of each pad and its associated electronics channel was performed at the CERN SPS H2 test-beam employing 10 and 40 GeV pion beams in 1987. The pedestal position and width of each pad was measured every 5 hours. A typical pedestal width σ_{ped} was $\sim 9\%$ of the response of a mip. The pedestal was subtracted online and the resulting ADC count value for each pad with more than 50 ADC counts (about 0.3 mips equalling $3\sigma_{\text{ped}}$) was written to tape. The signal-to-noise ratio for a mip, defined as the ratio between the most probable energy deposited and the pedestal width was found to be typically about 12:1. The response of the individual electronic channels was monitored daily by injecting a known charge at the input of the preamplifier using a pulse generator. The variation of the gain of each channel was negligible.

The ADC count distribution (after pedestal subtraction) of each pad was fitted with a Landau distribution convoluted with a Gaussian distribution of mean and width given by the pedestal measurement for that pad. The maximum of the resulting fitted function fixed the correspondence between the mip equivalent scale and the ADC count scale. Figure 3.3.14 shows a typical pulse height distribution of a left width half maximum $\sim 16\%$ of a mip from the passage of a mip at normal incidence with a fit superimposed as discussed above. The figure shows a clear separation of the signal from the pedestal.

In the course of the calibration the rejection power against photon conversions was estimated to be 20:1 with a 90% electron efficiency. Figure 3.3.14 shows the effect of a contamination of photon conversions in the electron beam.

Since data for this thesis is collected over the 3 running periods 1988 to 1990, it is necessary to verify the stability of the OSI for this time. The signal-to-noise ratio has deviated negligibly over this period from 12:1. In

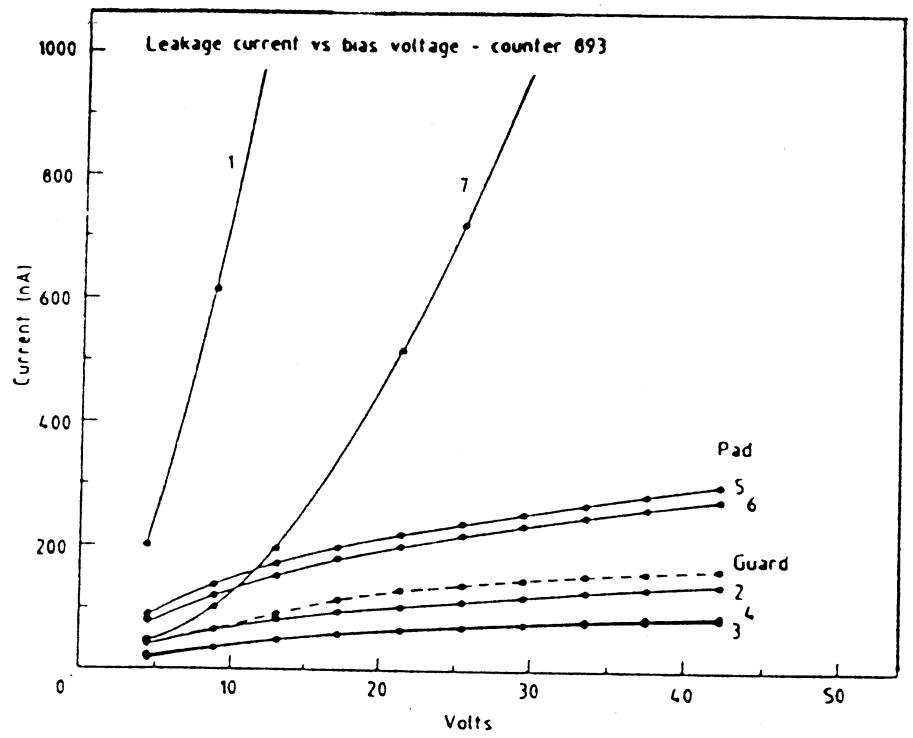

Figure 3.3.12 : Reverse leakage current versus bias voltage for one OSI counter.

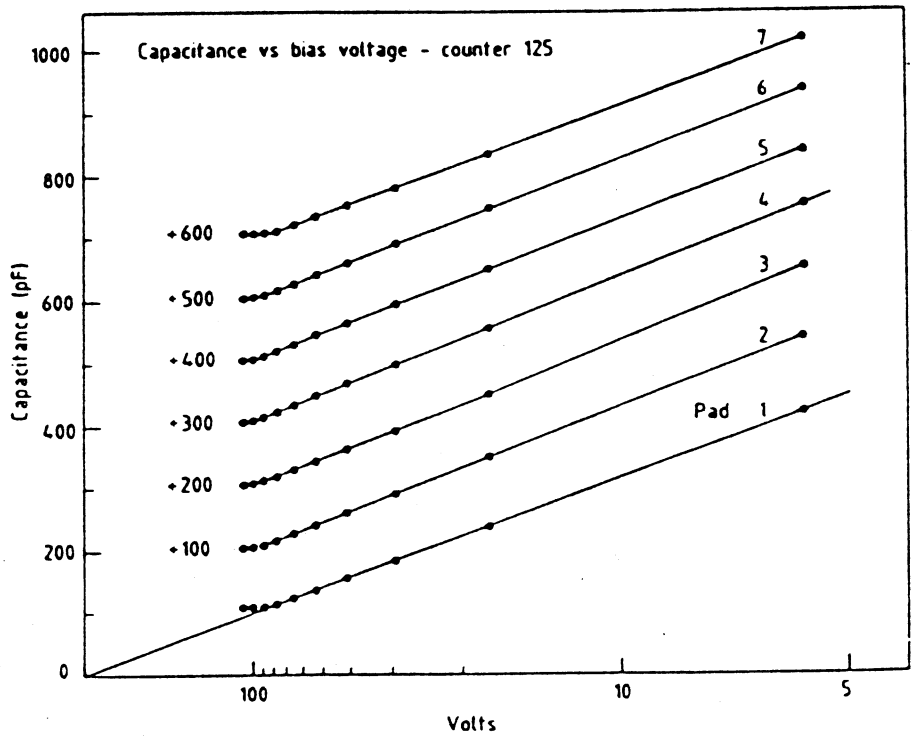

Figure 3.3.13 : Capacitance versus bias voltage for one OSI counter.

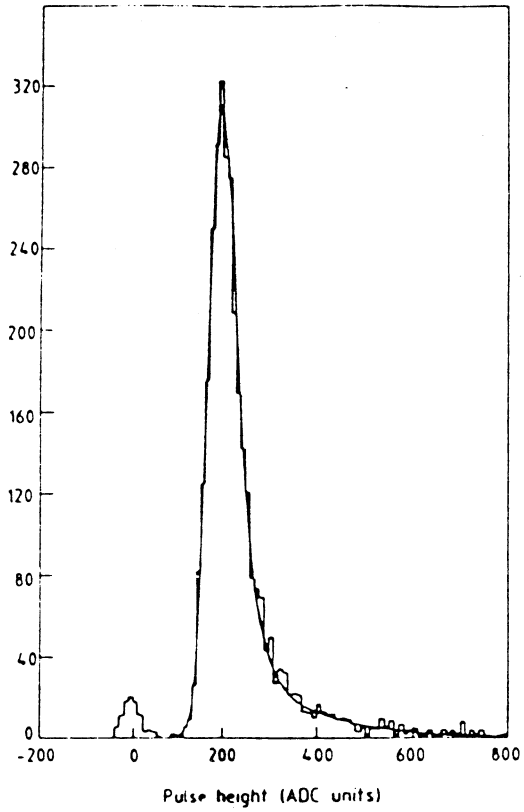

Figure 3.3.14 : The OSI pulse height distribution measured using a 150 GeV muon beam. The solid line is a fit of a Landau distribution convoluted with a Gaussian resolution function obtained from the pedestal.

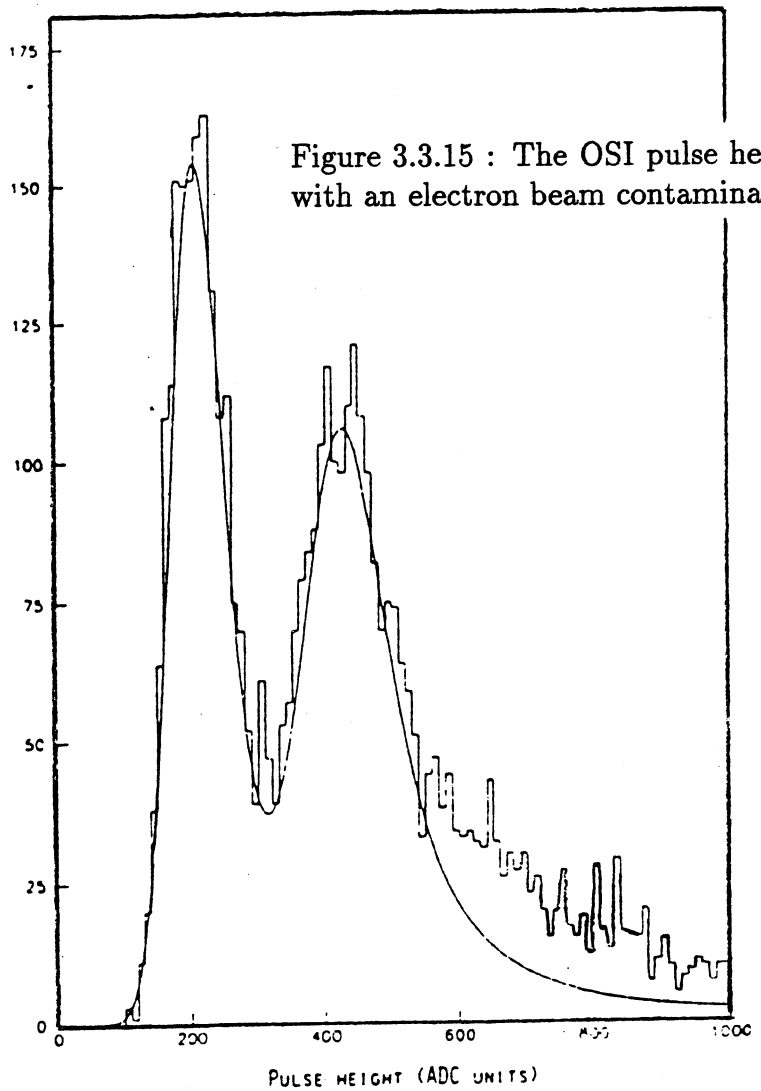

Figure 3.3.15 : The OSI pulse height histogram obtained from a test be with an electron beam contaminated with photons.

addition, the number of dead channels for the three running periods was $< 1\%$ and the average online pedestal and pulser values for each board over this period has varied by $< 5\%$.

The Inner Silicon Detector

The main motivation for the insertion of the second silicon hodoscope, the Inner Silicon Detector (ISI) [Bor-87, Bor-88, Bor-89, Boo-86] at a radial distance of 30 mm. from the beam was that of offering, in conjunction with the OSI, a tracking device capable of providing a fast measurement of the event vertex which at the Collider has an approximately Gaussian longitudinal distribution of rms width about 110 mm. along the beam direction. In addition, as for the OSI, the ISI measures the ionization charge deposited by the charged particles and provides a space point for track recognition.

Before the insertion of the ISI, tracking was based on the Jet Vertex Detector (JVD) and Scintillating Fibre Detector (SFD). However, the complete analysis of the full data sample from the JVD and SFD is time-consuming and can only be performed offline. This is particularly true of high multiplicity events from multivertex collisions. At luminosities of $\sim 10^{30}\text{cm}^{-2}\text{sec}^{-1}$ the rate of single and double event interactions are 0.35 and 0.15 per bunch crossing, respectively. In contrast, the two silicon arrays provide space point information online quickly albeit with limited accuracy. The pattern recognition requires only 0.2% of the total computer time required for a full event pattern recognition with the JVD and SFD.

Using just the two silicon layers the Gaussian resolution for a single track at the interaction point is about 1.2 mm resulting in a vertex accuracy of $1.2/\sqrt{\text{N}}$ mm where N is the number of tracks participating in the event. A two-vertex separation of about 1 cm is achieved.

Figure 3.3.16 shows a histogram of the distribution of the interaction points along the beam axis for a W candidate event using only the OSI and ISI layers. Figure 3.3.17 shows the difference of the vertex positions from the silicon arrays and from the full event reconstruction for 192 W candidate events.

The ISI consists of 192 silicon counters arranged in 12 rows of 16 crystals each. The dimensions of the crystals are 17.3x33.5 mm^2 with 16 pads of 2 mm pitch separated by 200μm oxide. The thickness of the crystal is 300μm and the total number of pads is 3072. Each pad is a diode produced by

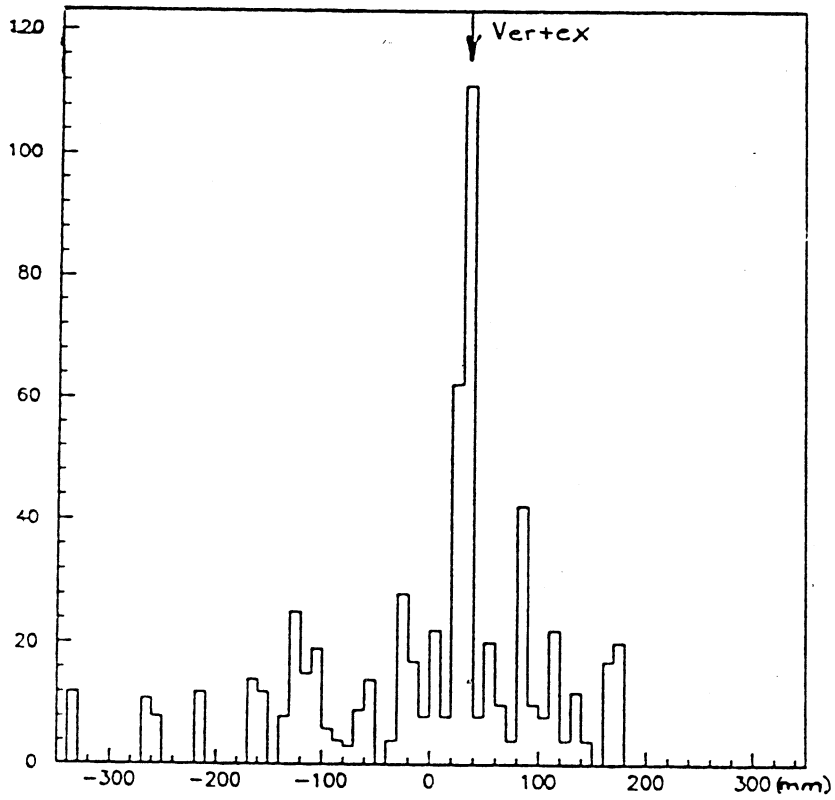

Figure 3.3.16 : Interaction vertex for W candidate events using only information from the ISI and OSI.

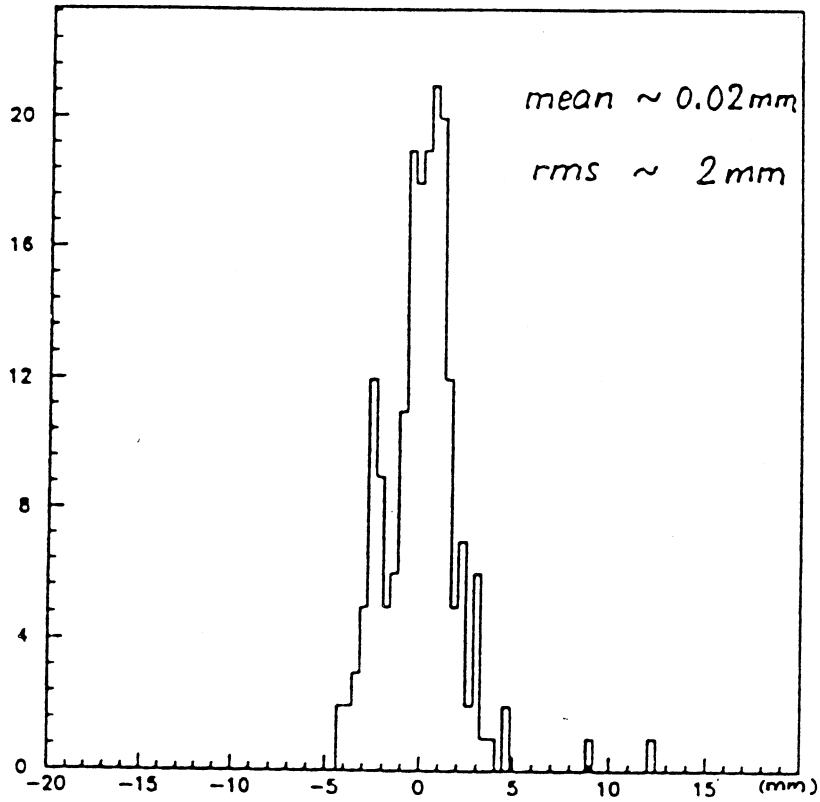

Figure 3.3.17 : Difference in the interaction vertex as provided only by the silicon detectors and from full event reconstruction.

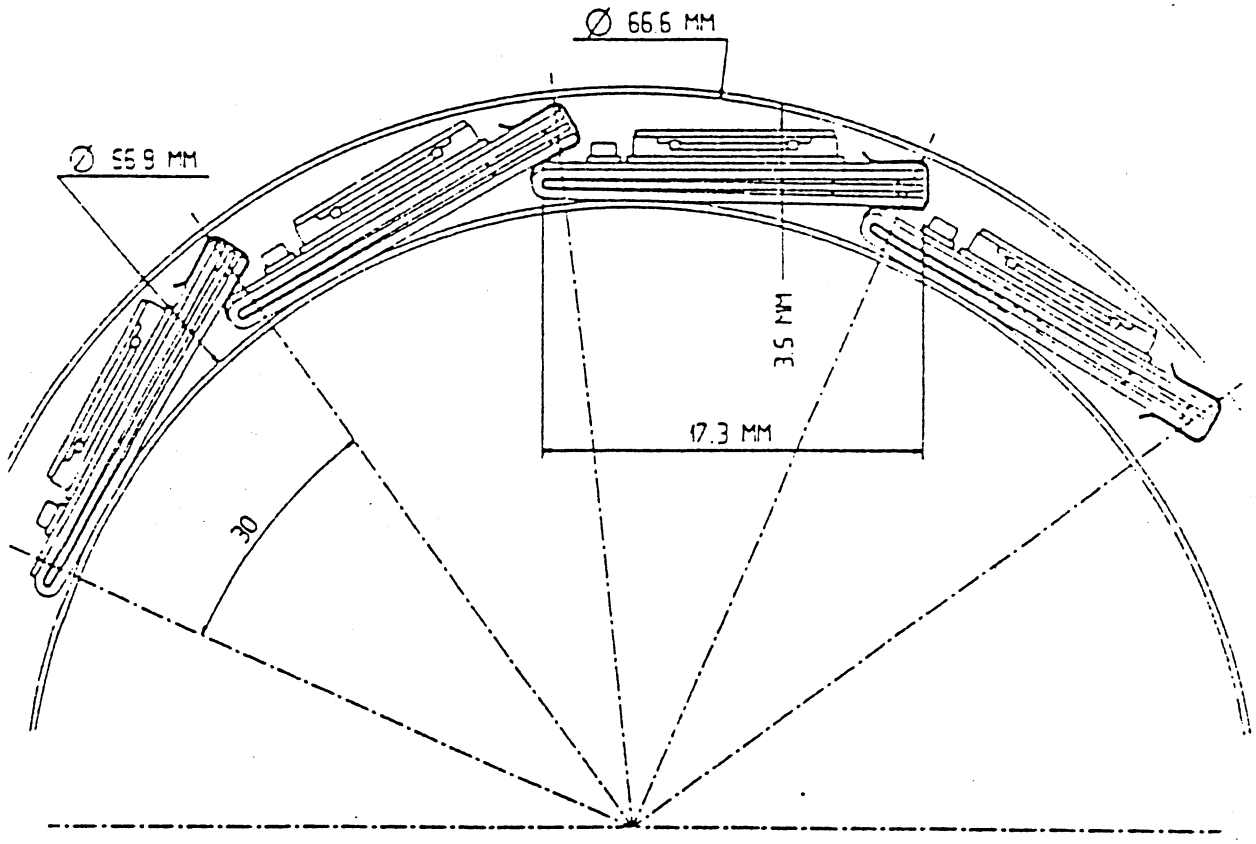

Figure 3.3.18 : Transverse view of the ISI assembly.

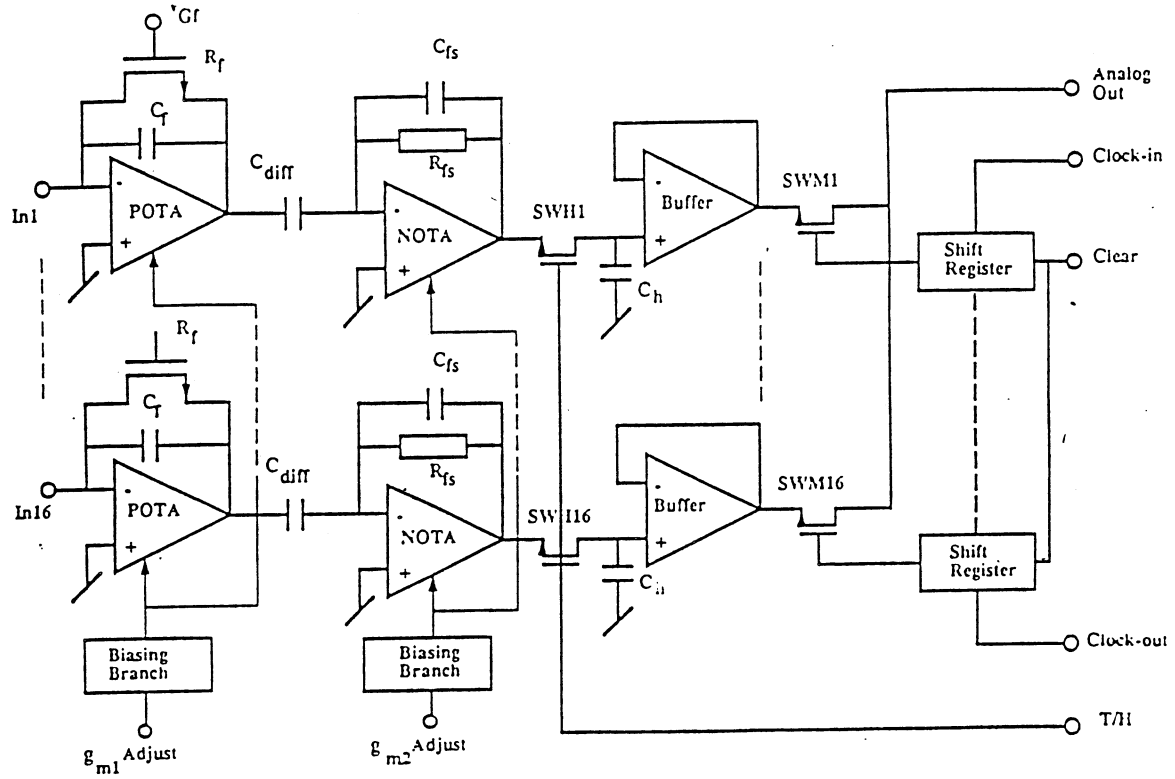

a)

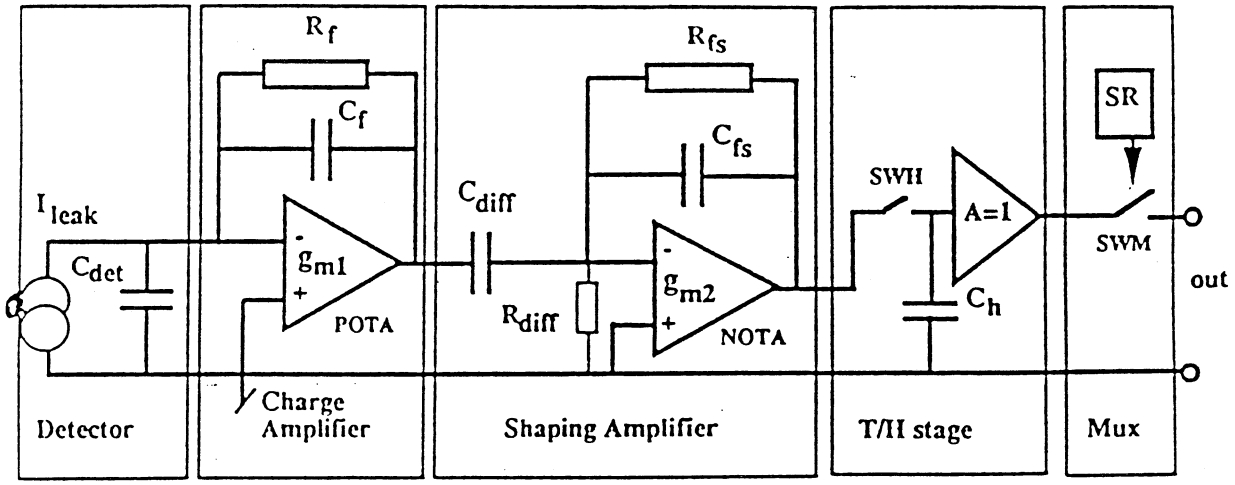

b)

Figure 3.3.19 : (a) Schematic diagram of the AMPLEX electronics. (b) Schematic diagram of the ISI electronics chain and read-out.

ion-implantation onto an n-type silicon crystal. Each pad is fully depleted throughout the junction region by a reverse bias voltage (see below). The modules are fixed to a carbon fibre support cylinder of 0.3 mm thickness around the beam pipe. Each row subtends 30° in azimuth and has an azimuthal width of 16.4 mm. The total ISI hodoscope is ~ 0.1 mm^2 and is a cylinder of length 55 cm along the beam. Figure 3.3.18 shows the ISI geometrical configuration.

The 16 counters in each row are mounted on a multilayer flex-rigid printed circuit board made of fibreglass and kapton layers. This also supports the 16 Application Specific Integrated Circuits (ASICs) each one containing 16 channels of front end electronics for one crystal as will be described below. The connection of the detector to the printed circuit board is obtained using a conducting rubber ribbon thus allowing the crystals to be easily replaced if necessary.

The total thickness of the detector is less than 3.5 mm and on average 2% r.l. for a particle traversing normally. The amount of material before the silicon wafers totals 0.35% (from the carbon fibre support cylinder, the kapton, the conducting rubber and the shielding). The material behind the silicon wafers is 1.1% of a radiation length (from the conducting rubber, AMPLEX and support profiles). Finally the silicon crystal is 0.39% r.l. The only additional material preceding the ISI is the beryllium beam pipe of 0.3% r.l.

In view of the small volume available to insert the ISI, the associated electronics have been designed in the form of an ASIC chip called AMPLEX [Bor-88, Ans-89, Bea-89]. The chip contains 16 dc-coupled MOSFET charge sensitive preamplifiers followed by shaping, track-and-hold and multiplex stages. It uses a 3 μm n-well CMOS process and the chip has dimensions of approximately 4x4 mm^2. A block diagram of the processor is shown in Figure 3.3.19(a) and a schematic diagram of the full ISI electronics chain and readout is shown in Figure 3.3.19(b).

There were two specifications for the AMPLEX to be considered before it was applied in the ISI. The first is power consumption, which is limited to 1 mW per channel, (3 W for the entire ISI), because cooling the detector system around the beam pipe is difficult in the Collider environment. The second is the signal shaping time which is between 600 and 800 ns. to be compatible with Collider cycling time. For a total input impedance of 20 pF an equivalent noise charge referred to the input of the charge amplifier is

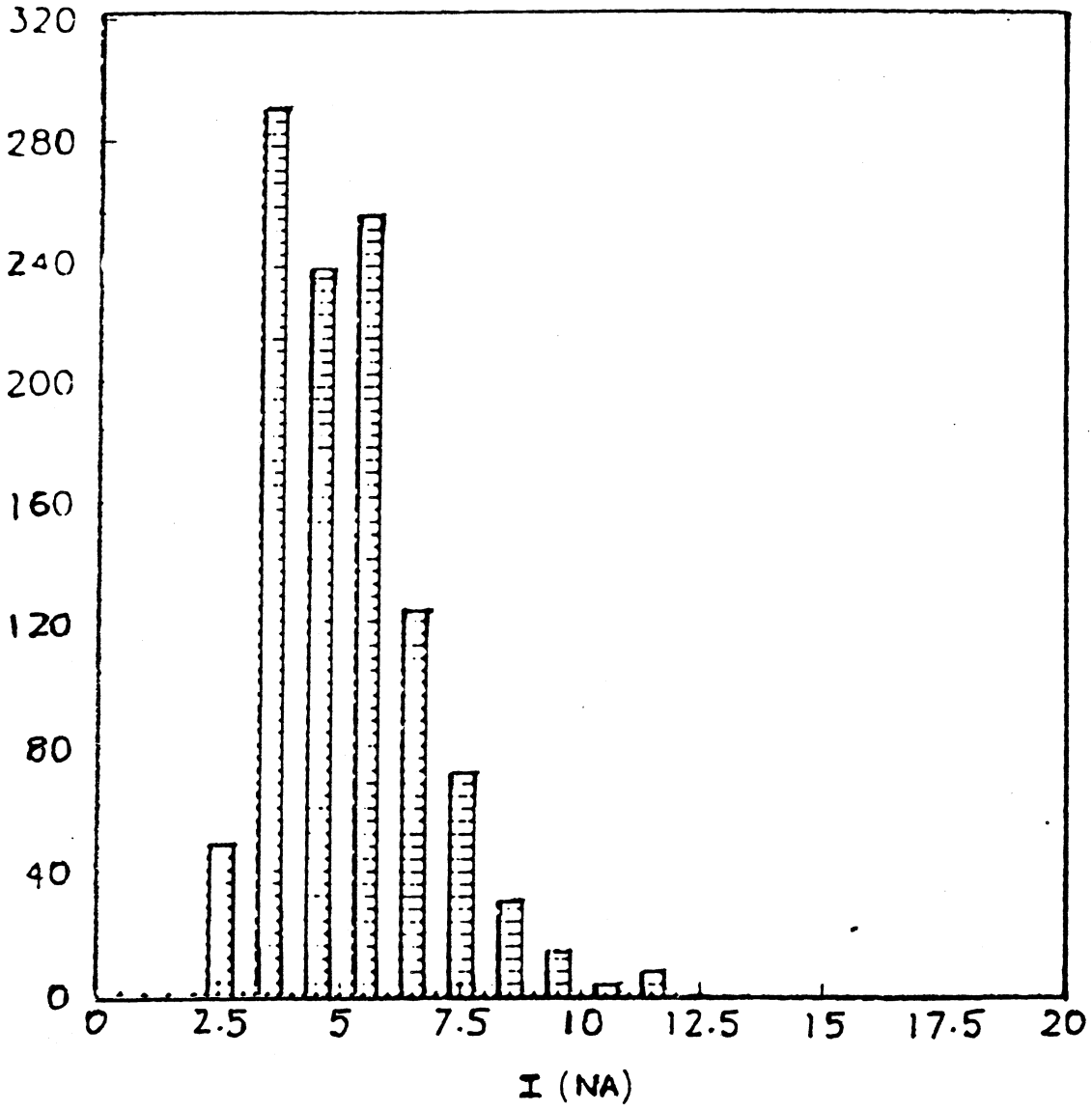

Figure 3.3.20 : Leakage current distribution for a fraction of the ISI counters.

about 1 000 electrons rms.

The analog circuit design of the charge amplifier and the shaping amplifier is based on the continuous time filtering technique. The building block of the charge amplifier stage is a folded cascade operational transconductance amplifier (POTA). The shaper amplifier is constructed around a second transconductance amplifier (NOTA). The track-and-hold section of the AMPLEX stores the amplitude of the output pulse at a time defined by an external trigger. The track-and-hold charge injection is about 3 mV and the droop rate is $< 20\mu$V/ms. In a multilevel trigger system the switches SWH enable the return from the hold mode into the track mode without executing the readout sequence, thus making the system sensitive to a new event within $\sim 1\mu$s. after a negative trigger decision.

Digitization is done by FERA-ADCs. One FERA-ADC channel digitizes the signals of 8 AMPLEX chips, namely the multiplexing level is 128, and 24 ADC-channels (2 ADC modules) are required. The hold-time for the AMPLEX chip, namely the time needed to digitize all the pad signals is about 0.9 ms. for 9-bit resolution or 1.2 ms. for 10-bit resolution.

The static characteristics of the ISI counters are measured on three test benches at CERN, Cambridge and Perugia [Gos-88]. The leakage current distribution for a fraction of the ISI counters upon installation is shown in Figure 3.3.20. The acceptance limit was 11 nA/pad at full depletion voltage at 21 °C. The full depletion voltage measured for each pad ranges from 30 to 40 V. The calibration of the full ISI array was performed in 1990 using pion beams at the CERN SPS H2 testbeam and details are presented in Appendix A.

The Jet Vertex Detector

Occupying the radial space between 35 and 135 mm from the beam line is the Jet Vertex Detector (JVD) [Bos-89]. It is a cylindrical drift chamber used to measure tracks close to the production vertex with particular ability to give the track's azimuthal position. The JVD consists of 16 azimuthal sectors as shown in Figure 3.3.21, staggered so as to minimize the ambiguity between tracks passing either side. There are 13 sense wires, surrounded by field shaping wires of length 1000 mm in the z-direction per sector and are equipped with 100 MHz FERA-ADCs to provide charge and time measurements. Charged particles passing through the chamber deposit ionization in

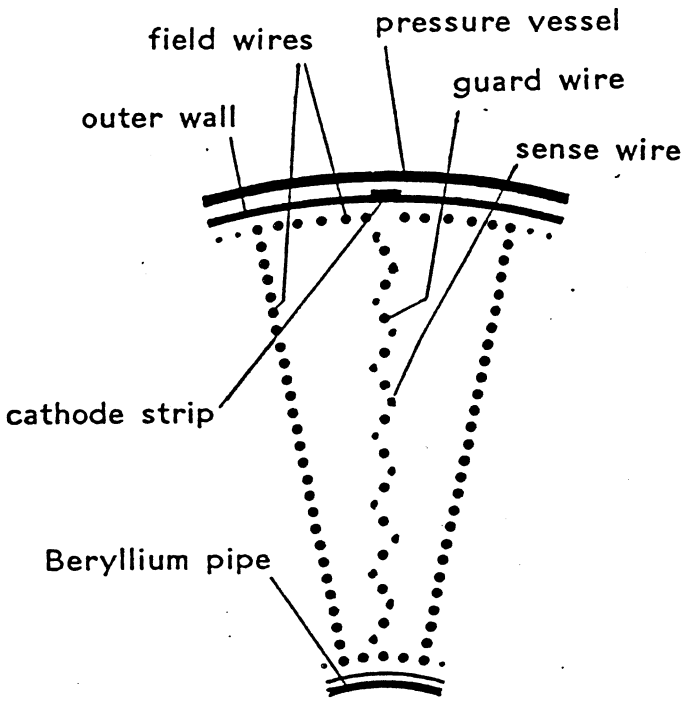

Figure 3.3.21 : Cross-section through a sector of the JVD.

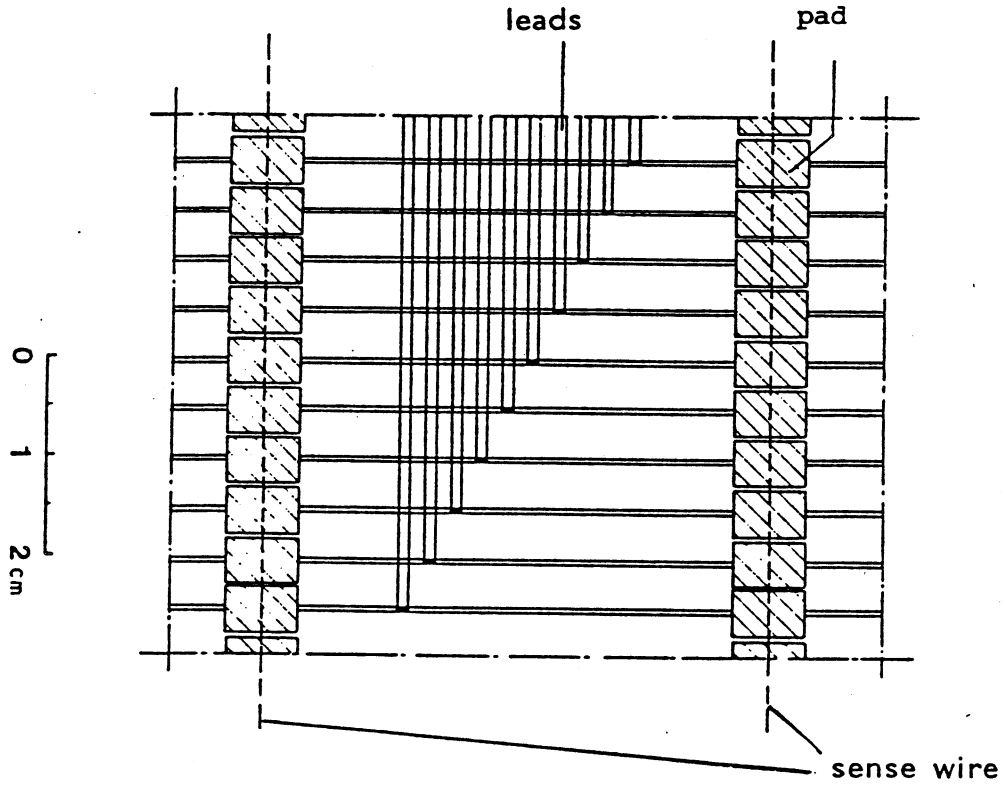

Figure 3.3.22 : The JVD cathode-strip read-out.

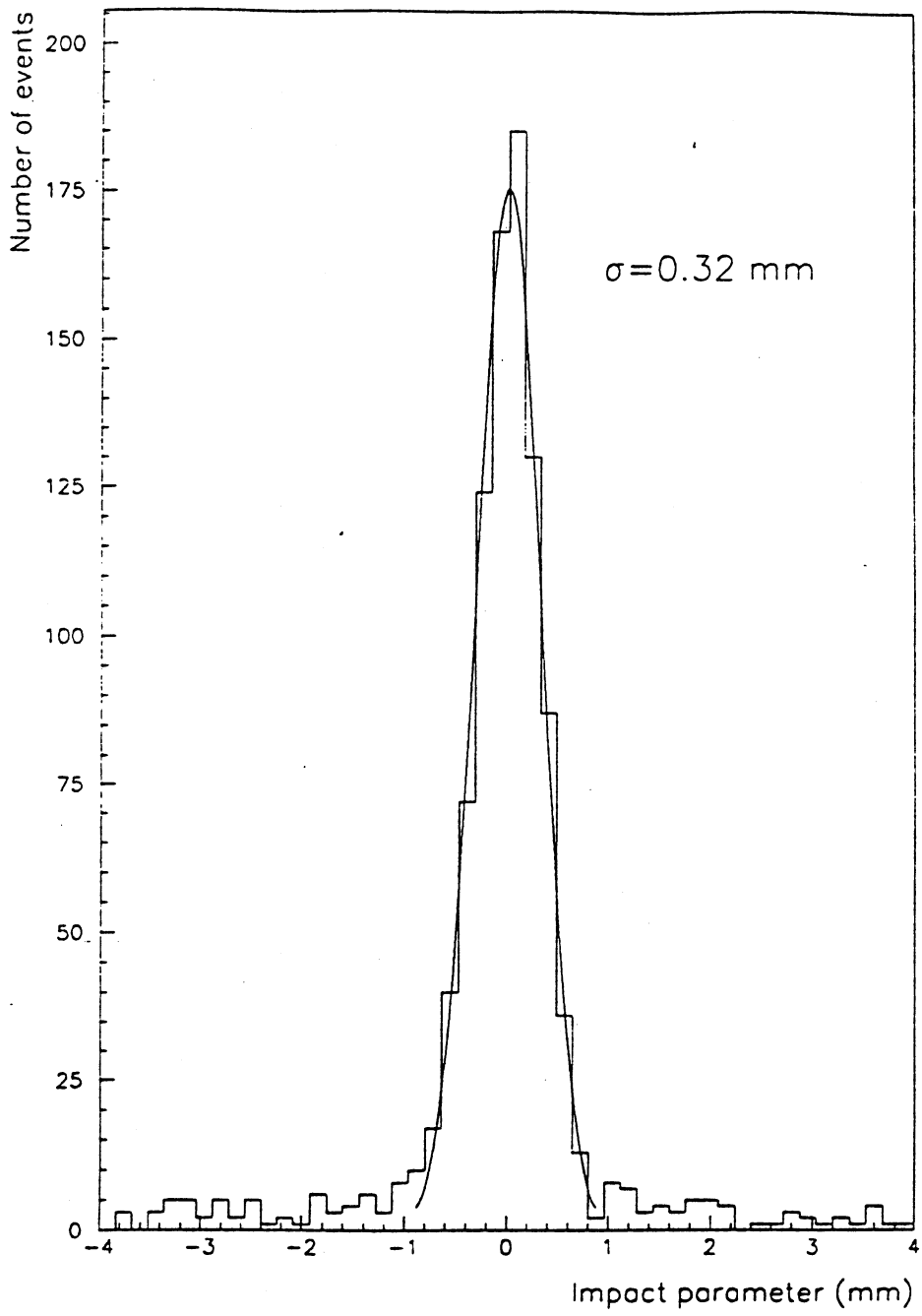

Figure 3.3.23 : The transverse distance from the centre of gravity of a JVD track segment to a global track with a fitted Gaussian curve superimposed.

the gas which drifts towards the sense-wires. The time of arrival to these wires is proportional to the azimuthal distance away and is a measure of the r x ϕ coordinate. Ionization charge is produced in a gas mixture of 60% Ar and 40% ethane operated at 1 atm pressure.

Two methods are used to measure the longitudinal coordinate z. On the outer wall of the detector, 160 cathode strips are mounted perpendicular to the beam as shown in Figure 3.3.22 and measure the z-coordinate of the avalanches on the outermost sense-wires. In addition, since both ends of each sense-wire are equipped with FERA-ADCs, charge division gives an independent measurement of the z-coordinate.

The JVD measures 13 space points per charged track with < 300 μm. resolution as shown in Figure 3.3.23 for a sample of electron candidate tracks. The detector also provides a two track resolution of < 1000 μm and gives the longitudinal coordinate with a resolution of 2.5 cm. for isolated tracks. The quality of the latter information is poor compared to that given by the silicon detectors and is thus rarely used (see section above).

In order to minimize photon conversions, the detector is made as transparent as possible. Since photon conversions are serious for a clean electron identification, the mechanical support for the tension of the wires is borne by the outer cylindrical wall. The amount of material between the vertex and the sensitive volume of the JVD is < 2.5 % r.l. at normal incidence and includes the material of the beam-pipe and ISI.

The Transition Radiation Detector

The Transition Radiation Detector (TRD) [Ans-88a, Boo-86] consumes the majority of the volume of the central detector and is the principle detector used to differentiate electrons from charged pions. A charged particle emits transition radiation when it crosses an interface between media of different refractive index. The rate of emission is proportional to the Lorentz factor γ of the particle. At high energy transition radiation is primarily emitted as X-rays. The total energy emitted upon crossing a single surface is

$$E = 2\alpha\omega_p\gamma/3$$

where α is the fine structure constant and ω_p is the plasma frequency of the medium,

$$\omega_p = \sqrt{\frac{4\pi\alpha Z N_A \rho}{Am}}$$

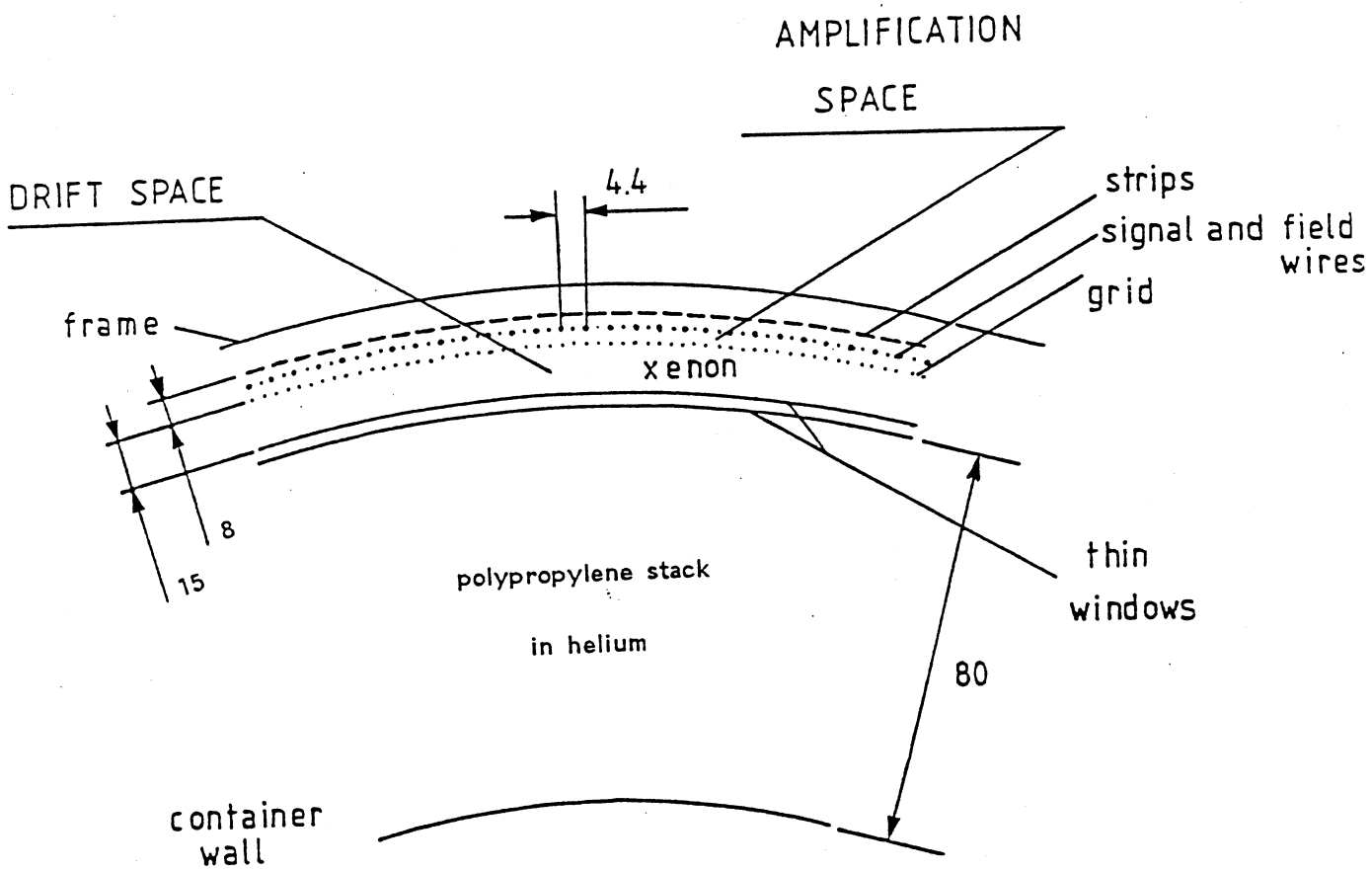

Figure 3.3.24 : Cross-section through one TRD module.

where A,Z and ρ is the atomic mass, atomic number and density of the medium and m is the incident particle's mass. The mean number of X-rays emitted per surface is

$$< N > \sim 0.5 \cdot \alpha$$

and are emitted strongly forward into a cone at an angle θ ($\sim 1/\gamma$) with the particle's direction.

The UA2 TRD consists of two concentric cylindrical detectors (C1 and C2). Each consists of layers of polypropylene radiator in helium gas chosen because of its low cross-section for the absorption of X-rays between 4 and 20 keV emitted by a 40 GeV electron passing through the stack. Each radiator is made of 400 20 μm. thick foils spaced 200 μm. apart. This is followed by an amplification region filled with Xe gas because of its good X-ray conversion and contains field and grid wires as shown in Figure 3.3.24.

The chambers have an asymmetric construction. Between the window, which is maintained at -1 000 V, and the grid, which is at 0 V, is a long drift space. This is followed by the amplification space which has a high field gradient between the grid and field wires which are at +1 500 V. Signal wires at +50 V between the field wires detect the charge. These are connected to preamplifiers which are read out by FERA ADCs.

A traversing 40 GeV $\pi^{\pm}$ of $\gamma \sim 300$ will produce relatively uniform ionization across the chamber, whereas a 40 GeV $e^{\pm}$ of $\gamma \sim 80000$ will on average produce 2 or 3 detected photons of mean energy 6 keV per chamber in addition to ionization. In both cases, the ionization charge produced in the amplification region drifts to the sense wires producing an early signal. However, for electrons some of the X-rays produced in the polypropylene-helium stack will convert in the Xe gas, depositing their charge as a late signal. The rejection factor of electrons over charged pions is greater than 15 for 80% electron efficiency. Figure 3.3.25 shows the raw FERA ADC values for a typical electron event. The first pulse arises from ionization charge, while the other two are X-rays absorbed in the Xe and are characteristic of an energetic electron.

The outer cathode of the chamber is made of helical strips connected to preamplifiers and FERA ADCs which detect an induced charge opposite the avalanche on the struck sense wires. The strips measure the longitudinal coordinate of both the ionization and avalanche charge, further assisting in the identification of electrons. Various algorithms have been tested for the

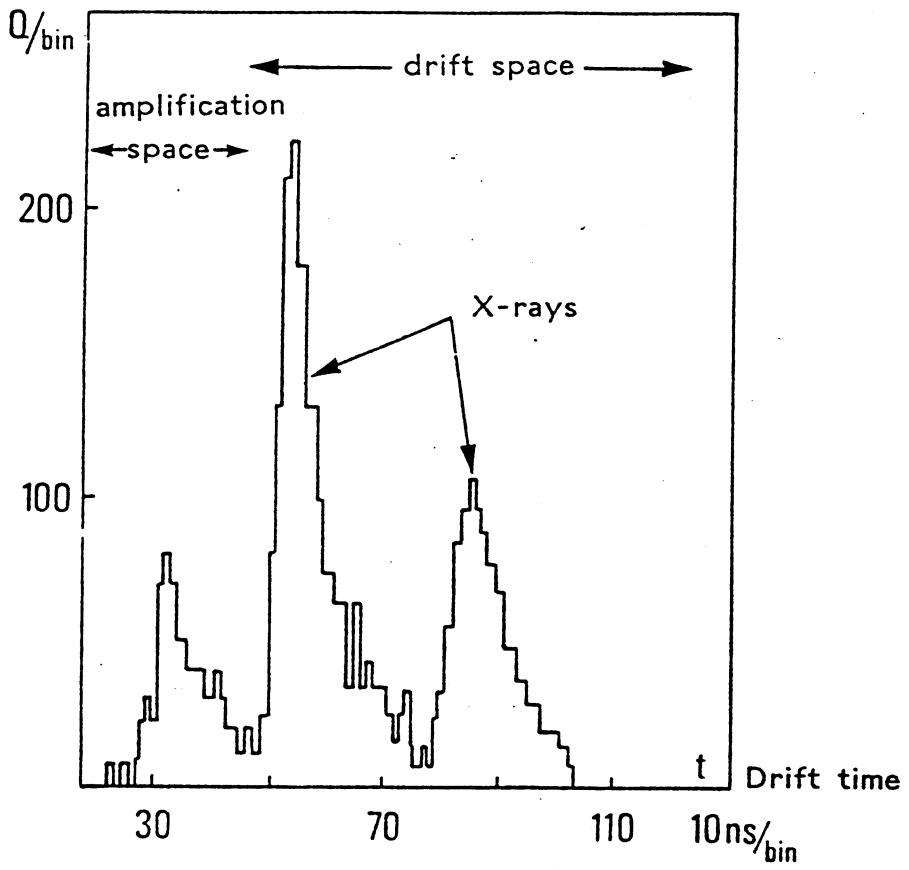

Figure 3.3.25 : TRD raw FERA ADC values for an electron event from W decay.

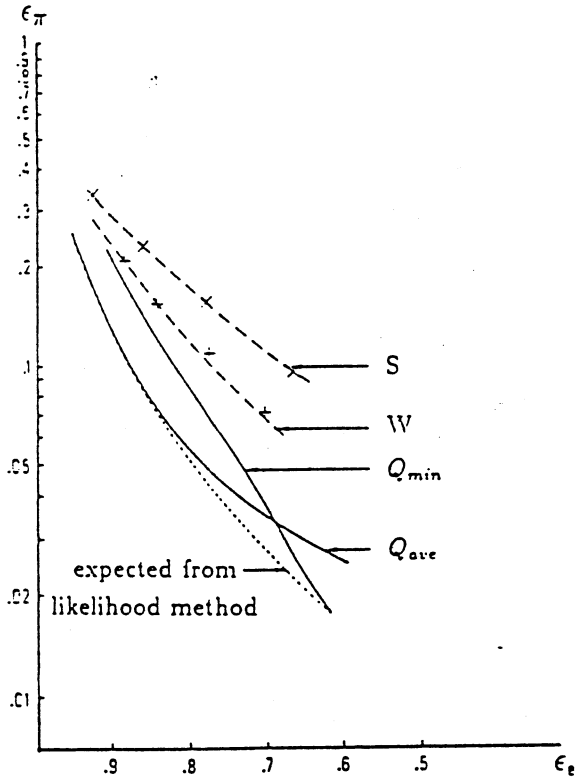

Figure 3.3.26 : TRD electron and pion efficiencies with respect to cuts on W, S, Q_{min} and Q_{ave}.

discrimination of charged pions from electrons. These include a cut on the total charge, a cut on the number of charge clusters above a threshold or a likelihood method where each cluster is weighted according to the charge alone or charge and time.

Figure 3.3.26 shows various curves from different algorithms. Curves W and S correspond to a cut on the total charge on the wires and strips in the two chambers where

$$W = Q^{C1}_{wires} + Q^{C2}_{wires}$$

$$S = Q^{C1}_{strips} + Q^{C2}_{strips}.$$

The charge on a wire or strip is the charge sum deposited by all the nearby tracks and the rejection against charged pions is improved if only isolated tracks are considered. Other variables used are

$$Q_{min} = \min(Q^{C1}_{wires}, Q^{C1}_{strips}, Q^{C2}_{wires}, Q^{C2}_{strips})$$

$$Q_{ave} = 0.5(\min(Q^{C1}_{wires}, Q^{C1}_{strips}) + \min(Q^{C2}_{wires}, Q^{C2}_{strip}))$$

The Scintillating Fibre Detector

The Scintillating Fibre Detector (SFD) [Ans-88b, Ali-88, Ali-89] , as shown in Figure 3.3.27 is a 2.1 m. long cylindrical detector consisting of 24 layers of 1 mm diameter scintillating plastic fibres (about 60 000 in total). Its inner radius is 388 mm and it extends close to the central calorimeter to a radius of 440 mm. It covers the polar angle range from 20° to 160°. The layers are arranged in 8 stereo triplets. The inner 6 triplets are used as a tracking detector and are followed by a 1.5 % r.l. lead converter in the region of the central calorimeter so that the last two triplets are used as a preshower detector. In each stereo triplet the angle the fibres make with respect to the cylinder axis are $-\alpha$, 0, and $+\alpha$ with $\alpha = 15.75°$ for the tracking part and 21° for the preshower component. The stereo angles were chosen after Monte Carlo studies as a compromise between the resolution in the z-direction which is enhanced with a larger stereo angle and the occurrence of accidental overlaps of hits due to different particles.

The scintillating fibres have a polystyrene core of refractive index 1.59 and are doped with butyl-D and POPOP which produce scintillation light wavelength-shifted to about 440 mm. The scintillators have a 15 μm. thick

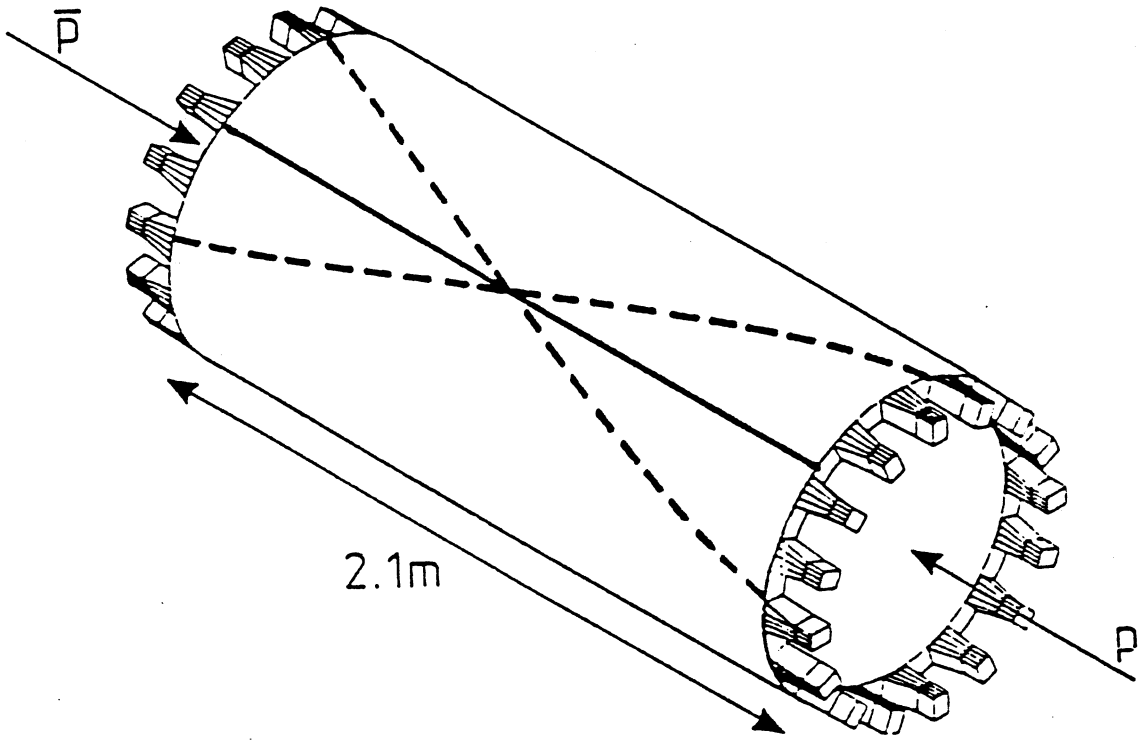

Figure 3.3.27 : Perspective view of the SFD.

cladding of refractive index 1.46 to preserve the optical quality of the scintillator surface and to ensure total internal reflection for the 10 % of light which is within cones of half-angle 24° about the fibre axis. To prevent cross-talk between adjacent fibres, due in part to non wavelength-shifted primary photons, the fibres are aluminized by sputtering. This has no negative effect on the optical properties and it also improves the resistance to physical damage. The attenuation length for 1 mm diameter fibres is 2.2 m and the light yield at a distance of 1 m for a particle passing normally through this diameter is 26 photons.

Because of the low light yield and because only a small fraction of the 60 000 fibres are hit in any one event, the signal is weak. This implies a need for amplification, multiplexing and data compaction and is performed, respectively, by image intensifiers (IIs), charged-couple devices (CCDs), and purpose-built FASTBUS digitizers. Each fibre is read out at only one end and the other end is equipped with a reflector and about 6 % of them can be illuminated to act as fiducial fibres. Thirty-two independent read-out chains are used, 16 at each end of the cylinder, each processing the signals from about 2000 fibres. Fibres from an 11° sector of the detector are grouped in a rectangular array and held rigidly in position at the input of the II chain by a perforated plate.

Because it is necessary to transmit the signal from 20 000 fibres (200 cm^2) to a CCD of area $\sim$ 0.25 cm^2, a demagnifying image intensification is needed. This is done in 3 stages as shown in Figure 3.3.28. The first II reduces the image from a diameter of 80 mm. to 18 mm. with a photon gain of about 10, while the last II reduces it from 18 to 7 mm. and provides a gain of about 6. The second II is a high-gain microchannel plate (MCP) intensifier which does not change the image size. The overall gain is about 50 000.

In II_1 and II_3 photons strike a S20 photocathode and liberate photoelectrons. These are accelerated and focussed by an applied electric field of 15 to 20 kV to reach a phosphor screen where each energetic electron liberates a number of photons. The II_2 provides a gain of about 1 000 by using an MCP. Photons produce photoelectrons at a S20 photocathode, and these electrons are accelerated by a 200 V potential to the MCP input. This consists of many closely-packed conductive hollow tubes of 6 μm. diameter with a potential gradient of about 800 V along the tubes. The electrons are accelerated down the tubes striking the tubes and producing many secondary showers. The electrons emerging from the MCP are accelerated by 6 kV across a short gap

to hit a phosphor and produce light.

Both the detection and multiplexing of the signal coming from the II chain is performed by a CCD having 144 lines of 208 pixels in total about 30 000 pixels each 30 μm^2. A CCD is an array of potential wells in a photosensitive semiconductor layer. The potential wells exist in an electrode structure forming a set of shift registers. Image read-out consists of shifts in perpendicular shift registers. First, the whole image region is shifted 'vertically' by one line, moving the first line in the output register. This register is then clocked out 'horizontally', transferring each pixel in turn to the output port. After this the second line is shifted 'up' and 'out'. Therefore, the output consists of a train of pixel pulses, line by line, with a clock frequency of 8 MHz. The CCD is cleared just before every bunch crossing time. If an external trigger has been received, the CCD clears are suppressed and the II signal is integrated. Before the next bunch crossing, the II chain is gated off, to prevent subsequent events from being detected and the CCD readout is started. The integration time of the CCD is ~ 2 μs. Once the image has been transferred to the storage zone of the CCD the II gate is opened again.

The CCD signal of 30 000 pulses from one read-out chain is sampled with a track-and-hold, preamplified locally and transmitted to a digitizer in the counting room. In the digitizers, which employ a pipeline design, the signal is amplified and sampled with a 8-bit FERA ADC to give digitized pixel contents from which a pedestal is then subtracted. Resulting values which are below a threshold are suppressed. Pixels are then assigned to fibres according to a map which is constructed using the fiducial fibres. Therefore, the data from the 30 000 pixels is reduced to words containing the number of each hit fibre and the pulse height in the fibre. There are on average 12 pixels per fibre and typically about 40 fibres will be hit per read-out. In the same crate an ALEPH event builder, using a 68020-based microprocessor buffers data from the 32 digitizers for read-out and performs calibration and monitoring tasks.

The optical resolution of the whole system has been measured. The image of a single fibre has a $\sigma \sim 0.4$ mm in real space as shown in Figure 3.3.29 implying that 80% of the light will fall in the region 1.3x1.3 mm^2. The resolution of the rϕ and z-coordinates has been measured with electrons from W events and is $\sigma_{r\phi} = 0.4$ mm. and $\sigma_z = 1.1$ mm. This is shown in Figure 3.3.30. For the preshower component, requiring the signal to be greater then 2 mips gives for a 40 (10) GeV electron a 98.4(96.3)% efficiency while accepting only 7.3%

	II_1	II_2	II_3
input diameter	80 mm	18 mm	18 mm
output diameter	18 mm	81 mm	7 mm
photon gain	~10	~1 000	~7
cathode-anode potential	20 kV	7 kV	15 kV
photocathode	S20	S20	S20
phosphor	P47	P47	P46

Figure 3.3.28 : Image intensifier parameters.

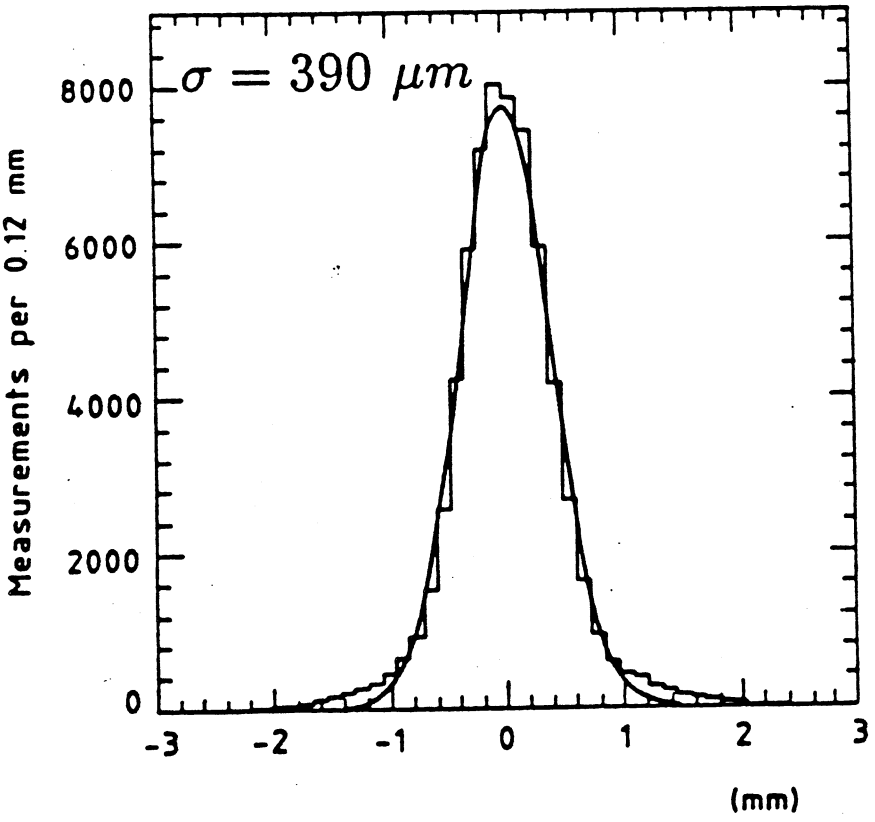

Figure 3.3.29 : Image resolution of a single fibre in real space.

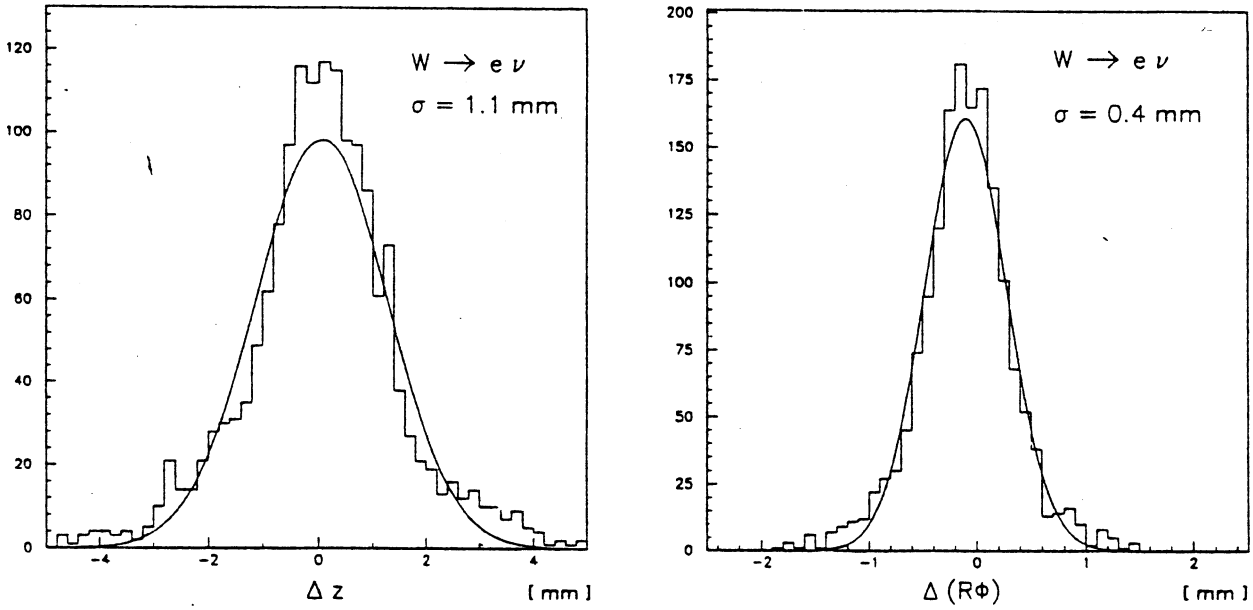

Figure 3.3.30 : Resolution of the rϕ and z - coordinates measured using electrons from W decay.

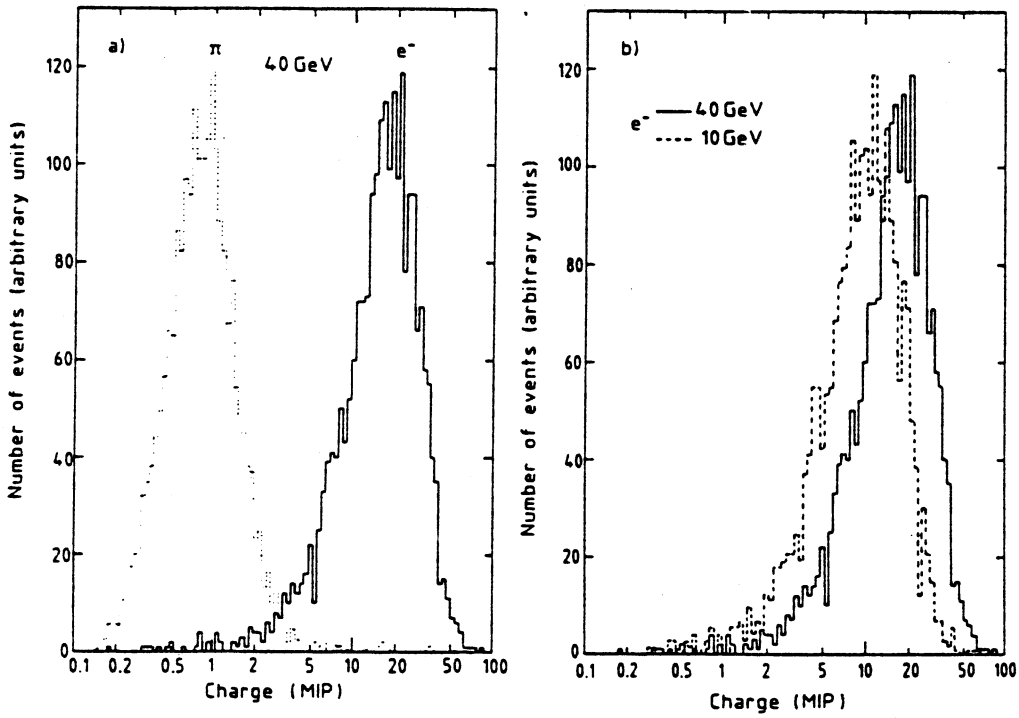

Figure 3.3.31 : The SFD preshower charge for (a) testbeam electrons and (b) isolated electrons from W events, compared to testbeam charged pions.

of 40 GeV charged pions. This is shown in Figure 3.3.31.

3.3.3 The Forward Detectors

The End – Cap Proportional Tubes

With the addition of the EC down to a polar angle of 5°, it was necessary to extend the particle tracking and identification beyond the central region. Because the cylindrical shape of the central detector is unsuited to further angular extension, an additional detector is placed in front of the EC. The End-Cap Proportional Tubes (ECPT) [Boo-86] provide tracking information and localize the start of electromagnetic showers produced by electrons and photons in the forward/backward regions. A view of the ECPT is shown in Figure 3.3.32.

Each of the two ECPT detectors is divided into 8 45° azimuthal sectors covering the polar angle range $22.5° < \theta < 37.5°$. The active planes of each sector are made from 9 mm square extruded aluminium tubes of 1 mm wall thickness covering 30 μm wires and operate with a 80% Ar and 20% CO_2 gas mixture in proportional mode. In the front section of each sector, tracking is performed with six planes forming two stereo triplets at stereo angles $\pm 67.5°$. These are followed by a 2 r.l converter made of lead and iron and a third stereo triplet which acts as a preshower detector.

Individual planes have an efficiency of 99.2%. For electrons, the spatial resolution has a $\sigma = 3$ mm in the tracking region and a $\sigma = 2.3$ mm in the preshower region. Cutting on the pulseheight in the preshower planes, electrons can be efficiently separated from hadrons. For 60 GeV electrons, an efficiency of 98% can be obtained with a rejection factor of 13 against charged pions.

The Veto Counters

The Veto Counters (VC) [Boo-86] are used to remove beam halo events produced by particles which have escaped from the beam but travel along at about the same speed to enter the side of the detector depositing most of their energy in the calorimeters. Beam-halo is characterized by particles entering the calorimeters from behind, as shown in Figure 3.3.33, after passing through the VC planes at a mean time of -18 ns. relative to the nominal bunch

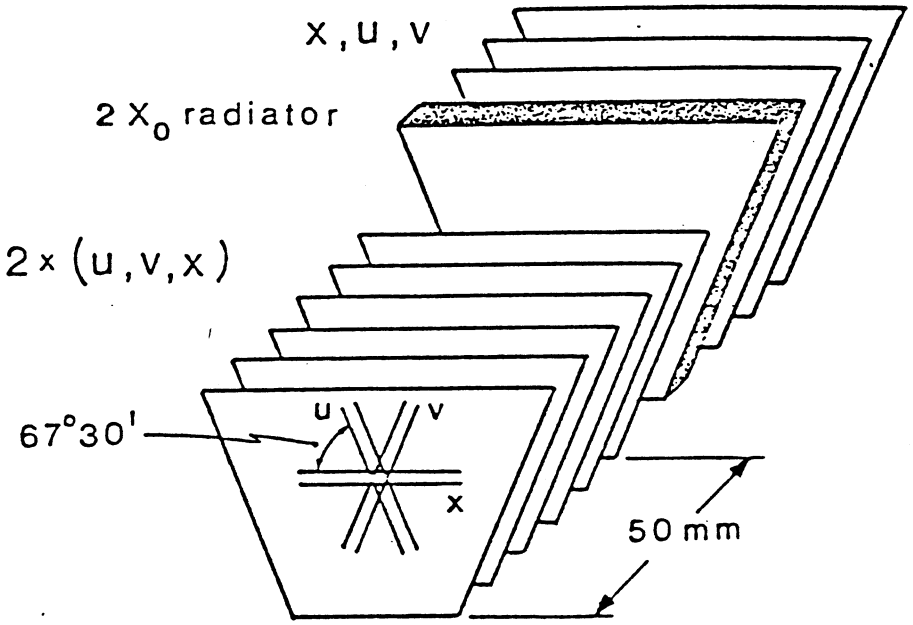

Figure 3.3.32 : Perspective view of the ECPT chamber.

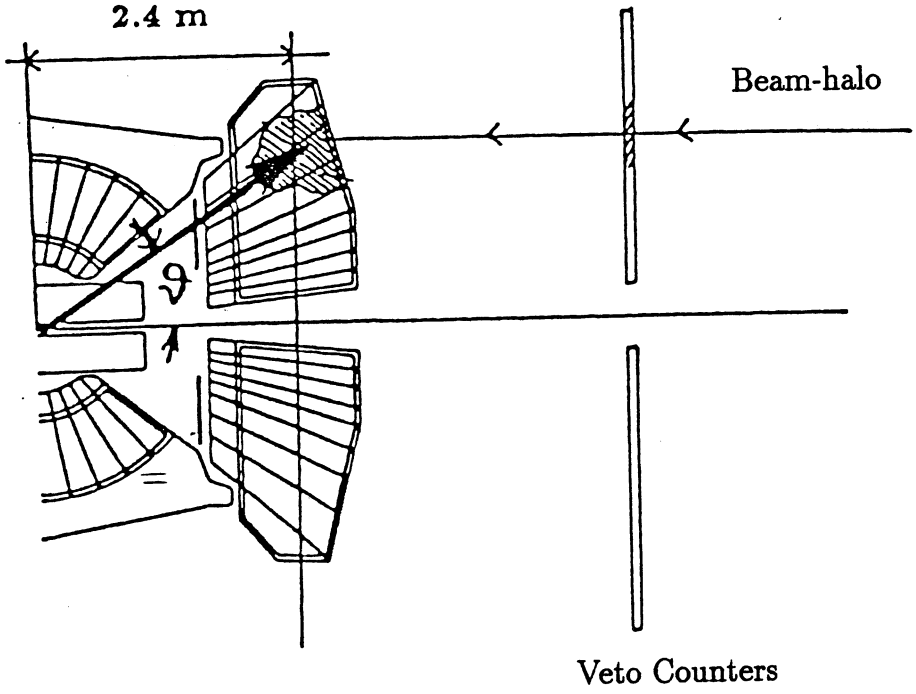

Figure 3.3.33 : Beam-halo topology

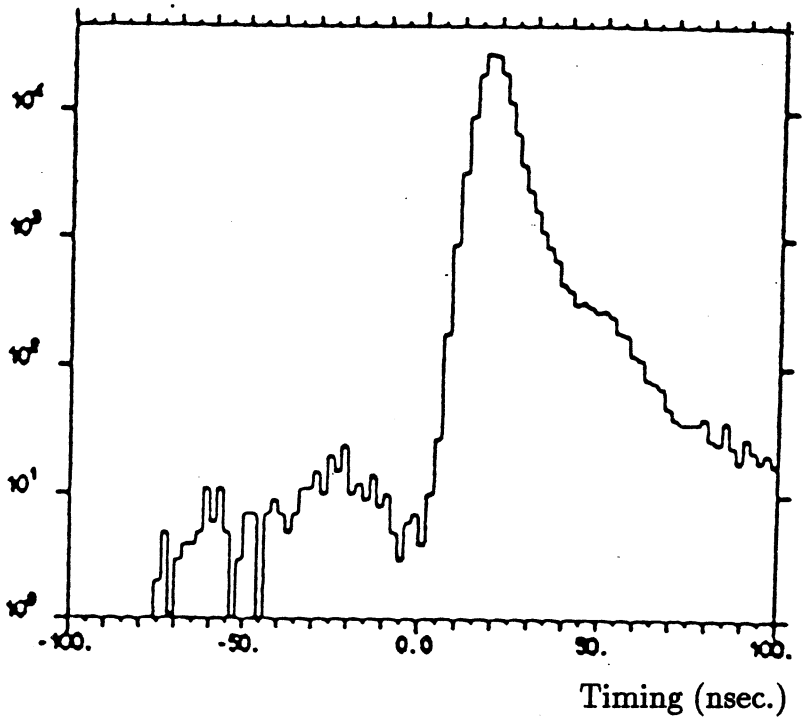

Figure 3.3.34 : Beam-halo timing with respect to the nominal bunch crossing time (at t=0).

crossing time (see Figure 3.3.34). Though less frequent, beam-gas events produced by the interaction of residual gas molecules in the beam pipe with beam particles can also be removed with the VC. Such fake events tend to contaminate the missing momentum trigger stream in particular (see Section 3.4).

The counters are made from 34 rectangular scintillation counters and are positioned ±5410 mm away from the interaction region in two planes perpendicular to the beam axis. The counters on the first and second planes are mounted horizontally and vertically, respectively. Each counter is read out by a photomultiplier tube whose signal is digitized by ADCs.

The VC allow the detection of the passage of charged particles by providing an estimate of both the space and time coincidence coordinates of its impact points with the two counter planes. Delays due to the travel of light in the counters are taken into account. In the case of a $p\bar{p}$ collision in the centre of the detector, the charged particles hitting the VC produce a signal at a time $t > t_0$ (late hits), where t_0 is the bunch crossing time, whilst beam halo particles hits have $t < t_0$ (early hits) and can be discarded. Signals from the VC counters are timed to a few nanoseconds.

The Luminosity Counters

The luminosity monitor [Dil-87a, Dil-87b] consists of 4 rectangular scintillation counters, 100x200 mm^2, in each of 4 planes. The counters are positioned at $z = \pm 9989$ mm and $z = \pm 8151$ mm, and cover the pseudorapidity range $4.0 < |\eta| < 4.8$. Signals from a pair of counters in the same azimuthal position and on the same side of the detector are sent to coincidence units with a resolution of 5 ns. The timing requirement of the coincidence is such that any particles going away from the interaction region produce a signal. A similar but independent set of coincidences is sensitive to particles in time with the incident beams and is used to monitor the beam-gas background.

The luminosity monitor is sensitive to the total inelastic cross section except the single diffractive part. The UA4 [UA4-84, UA4-87a, UA4-87b] measurements of the total cross section, σ_{tot}, the ratio of the elastic to total cross sections, σ_{el}/σ_{tot}, and the single diffractive cross section, σ_{sd}, are measured and are used to calculate the visible cross section

$$\sigma_{vis} = \sigma_{tot} \cdot (1 - \sigma_{el}/\sigma_{tot}) - \sigma_{sd} = 38.7 \pm 1.8 \text{ mb}.$$

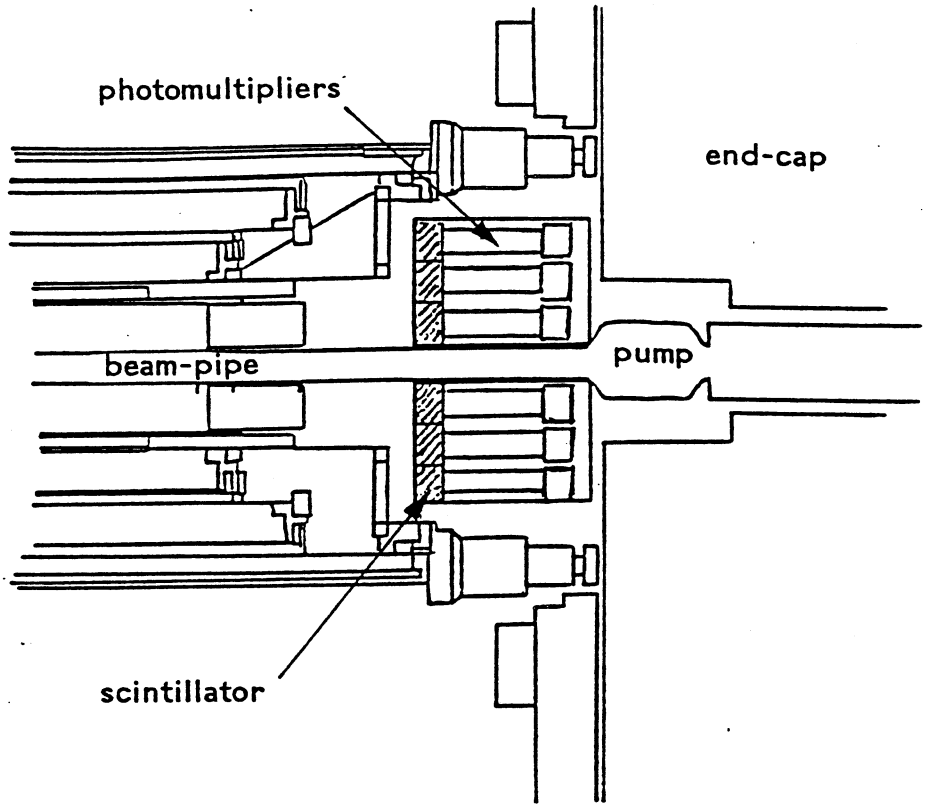

View of Scintillators

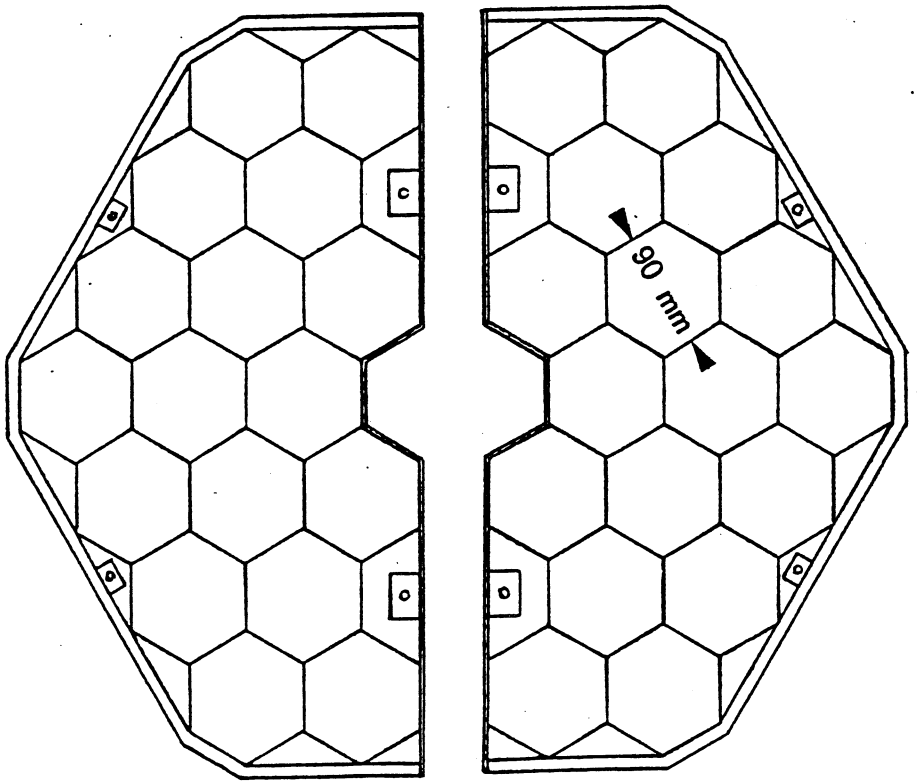

Figure 3.3.35 : The TOF hodoscope.

For low luminosities the mean rate of coincidence between beam-beam signal from each side is

$$N_{LR} = \int \mathcal{L}dt \cdot \sigma_{vis} \cdot \epsilon_{lum}$$

where ϵ_{lum} is the efficiency including the geometrical acceptance of the luminosity counter and $\mathcal{L}$ is the luminosity sought. This equation is valid to better than 1.5% for $\mathcal{L} < 5x10^{29}$ $cm^{-2}s^{-1}$ since more than one interaction per bunch crossing is rare. The algorithm used to find the total integrated luminosity includes a correction for the possibility of more than one interaction per bunch crossing at luminosities greater than $\sim 5x10^{29}$ $cm^{-2}s^{-1}$.

The Time of Flight Counters

The TOF [Boo-86] hodoscopes are installed in the forward/backward regions of UA2, outside the central detector but within the EC, to principally provide a minimum bias trigger for non-diffractive scattering. A plane of 6 scintillation counters, 80 mm thick, are mounted perpendicular to the beam axis at 1.2 m of each side of the interaction region. Each counter has an hexagonal shape and allows the timing to less than 0.5 ns of the passage of charged particles in the pseudorapidity range $2.9 <| \eta |< 4.2$. The scintillators are connected directly to photomultipliers whose signal is then digitized. Figure 3.3.35 shows a cross-section through the TOF.

Due to the close proximity to the interaction point, good timing resolution is needed to distinguish the signal from a $p\bar{p}$ collision from background sources such as beam halo. The time resolution of the TOF is less than 100 ps (smaller than 30 mm).

The time separation between consecutive RF buckets in the SPS is 5 ns compared to the 8 ns time separation between the TOF counter planes. Allowing for events vertex spread, a narrow time window of ± 2.4 ns for the combined signal from each TOF counter plane is therefore required to define a good beam-beam interaction. This requirement forms the minimum bias trigger. A scatter plot of the timings in the forward and backward regions is shown in Figure 3.3.36.

In addition, the signal arrival times at opposite sides enables the determination of the interaction vertex along the beam with a resolution of $\sigma = 20$ mm. This is useful for fast track reconstruction. The correlation between the vertex provided from the TOF and that obtained from the central

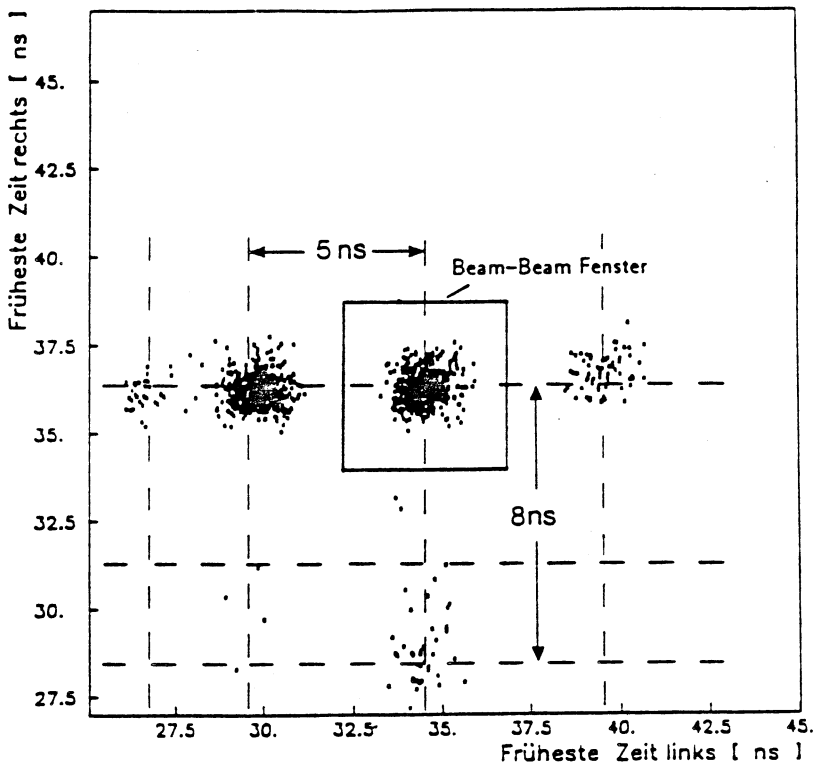

Figure 3.3.36 : Scatter plot of the timings in the forward and backward regions of the TOF.

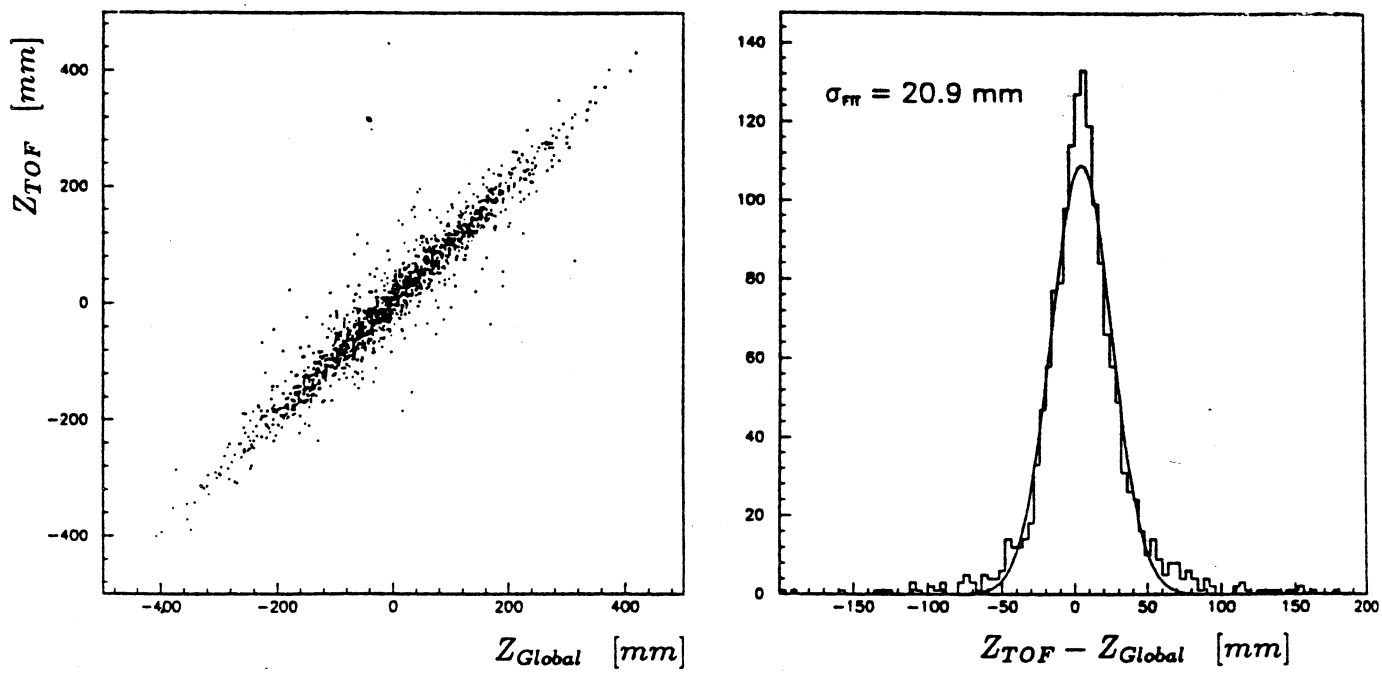

Figure 3.3.37 : Correlation between vertex provided from the TOF and that obtained from the central detectors.

detectors is shown in Figure 3.3.37. The TOF counters can also give information when more than one interaction occurs in the same bunch crossing and a veto against beam-halo and beam-gas interactions from the different arrival times in the two detectors. However, with a time resolution of less then 100 ps., this is not possible for most double interactions.

3.4 The UA2 Trigger and Data Acquisition

At the CERN proton-antiproton Collider the events involving physics processes of interest make up a small fraction of the total number of collisions. For example, the cross-section for W-boson production is $\sim 10^{-32}$ cm^2 while the machine luminosity is of the order of 10^{30} cm^{-2}s^{-1} with a bunch crossing time of 3.8μs. Thus, with the number of interesting events being

$$N = \sigma \int \mathcal{L}\, dt$$

$$\sim 10^{-32}[cm^2] \cdot 10^{30}[cm^{-2}s^{-1}] \cdot t$$

the observation of one event takes 100 sec. ($\sim$ 2.5x10^7 bunch crossings). It is therefore imperative to have a means of filtering out only those events of interest to minimize the detector deadtime caused by reading out an event as well as to collect a reasonable amount of data to process. This is the essential task of a trigger.

The UA2 trigger [Bac-88, Bla-88, Boo-86] is a multi-level system consisting of first level hardware and second and third level software components. Because the bunch-crossing time is less than the time taken to read out and digitize the information from some of the detectors, the first level uses information only from the calorimeters and TOF counters. Figure 3.4.1 is a schematic of the UA2 trigger system and is described below.

The First Level Trigger

The first level (LVL1) decision is based on the analogue sums of the electromagnetic compartments of the calorimeters within $|\eta| < 2.0$ and is made within 1.3μs. In the case of a rejected event a general clear can be performed before the next beam crossing. The clearing time of the UA2 readout electronics is 2.5 μs.

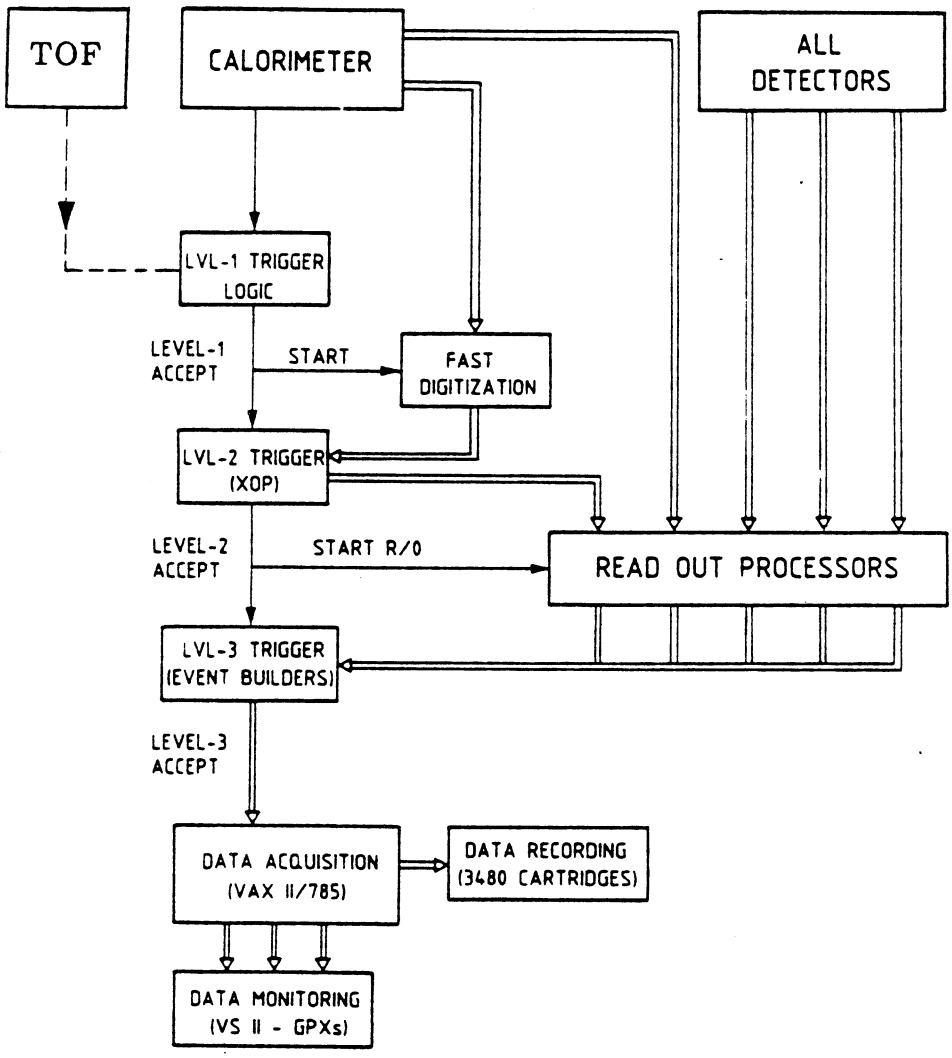

Figure 3.4.1 : A schematic diagram of the three UA2 trigger levels and data acquisition system.

The Missing Momentum Trigger

A signature of neutrinos or any other undetected particle produced in an interaction is the presence of a large missing transverse momentum p_T^{miss}. An effective way of measuring the p_T^{miss} is to surround the interaction region with a hermetic calorimeter and measure

$$p_T^{miss} \sim \mid \sum E_T^i \cdot \overline{u}_i \mid$$

where E_T^i is the transverse energy deposited in calorimeter cell i, $\overline{u}_i$ is the unit vector pointing from the interaction vertex to the centre of the cell and the sum i is over all the calorimeter cells. The missing transverse energy is measured instead of the missing energy because the longitudinal component cannot be measured at hadron colliders since many particles escape down the beam pipe.

The requirements placed on a calorimeter for an accurate measurement of p_T^{miss} are :

1. Good hermiticity to minimize the particles escaping through cracks thus going undetected and a coverage over a large polar angle range as possible.

2. High segmentation in both the azimuthal and polar angles coupled with a good energy resolution.

A major effort has been performed in UA2 to provide these calorimeter requirements as described in Section 3.3.1

Events appearing in the p_T^{miss} trigger stream are predominantly found to be either beam-halo or dijet events with a large E_T imbalance [Inc-88]. Beam halo enters the p_T^{miss} stream because such events are characterized by particles entering primarily either the forward or backward EC from behind after passing through the VETO counter planes at a mean time of -18 ns. relative to the nominal bunch crossing time. Little or no energy is observed on the opposite end-cap thus incurring a momentum imbalance. Dijet events enter the p_T^{miss} stream since a momentum imbalance can occur if one of the jets is outside the calorimeter acceptance or from jet energy fluctuations in the calorimeter.

Studies of events in the p_T^{miss} stream show that of the original sample of events passing a 15 GeV P_T cut at $|\eta| < 2.2$, $\sim 80\%$ have no early VETO counter hit and $\sim 20\%$ do. Of those with an early VETO counter hit, $\sim 88\%$ are beam halo and of those events without early VETO counter hits $\sim 80\%$ are neutral beam halo or dijet events. Therefore, only $\sim 16\%$ of all triggers in the p_T^{miss} stream have no *a priori* reason for being rejected.

The p_T^{miss} trigger logic uses the basic building blocks of the jet triggers as input (see below). These consist of 12 pulses, each of which is the weighted sum of the photomultiplier signals from all calorimeter cells making up a wedge extending over 30° in azimuth and over the pseudorapidity range $|\eta| < 2.0$. The integral of each pulse is proportional to the transverse energy deposition in the corresponding wedge.

The p_T^{miss} trigger logic performs the following operations :

1. Integrates the 12 input pulses.
2. Builds the vector sum of the 12 signals in order to obtain p_x and p_y in digital form, where p_x and p_y are the two orthogonal components of p_T^{miss}.
3. Calculates $p_T^2 = p_x^2 + p_y^2$.
4. Applies a threshold on p_T^2.

The integration is performed by the 12 ISH circuits which are also extensively used in configuring the other UA2 triggers. They provide an input voltage of 3V which is stable to a few mV over a time period of several microseconds. The integration time, which depends on the width of the photomultiplier signals, is ~ 350 ns.

The vector sum is calculated using a special CAMAC module. The 12 input signals are digitized by 50 MHz, 8-bit FERA ADCs weighted by the sines and cosines of the azimuthal angles of the 12 wedges using two 4 Kbyte, 10-bit look-up tables and the results are summed using fast Arithmetic Logic Unit (ALU) chips. The look-up tables are separately accessible through CAMAC in read/write mode for loading and checking the calibration constants. The results are presented on 2 10-bit busses in the MBNIM standard. This retains homogeneity with the rest of the LVL1 triggers which are also implemented in MBNIM.

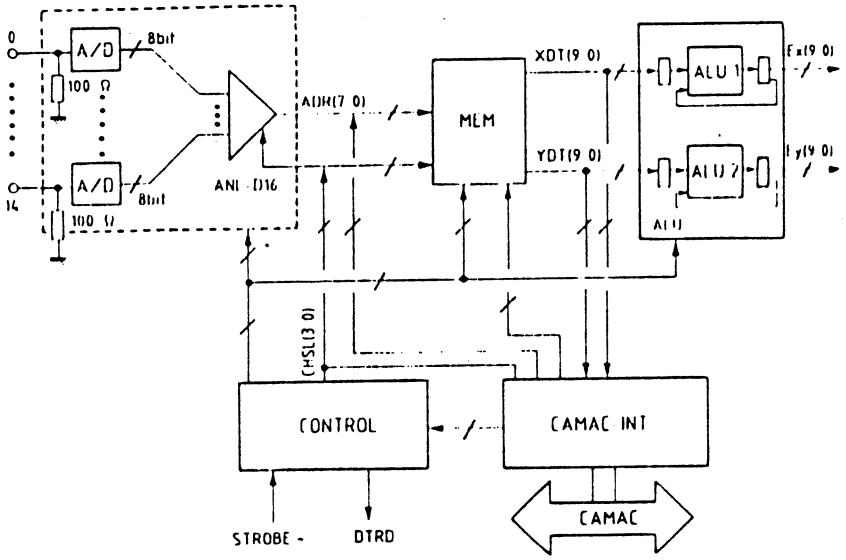

Figure 3.4.2 : A block diagram of the MISSPET module electronics.

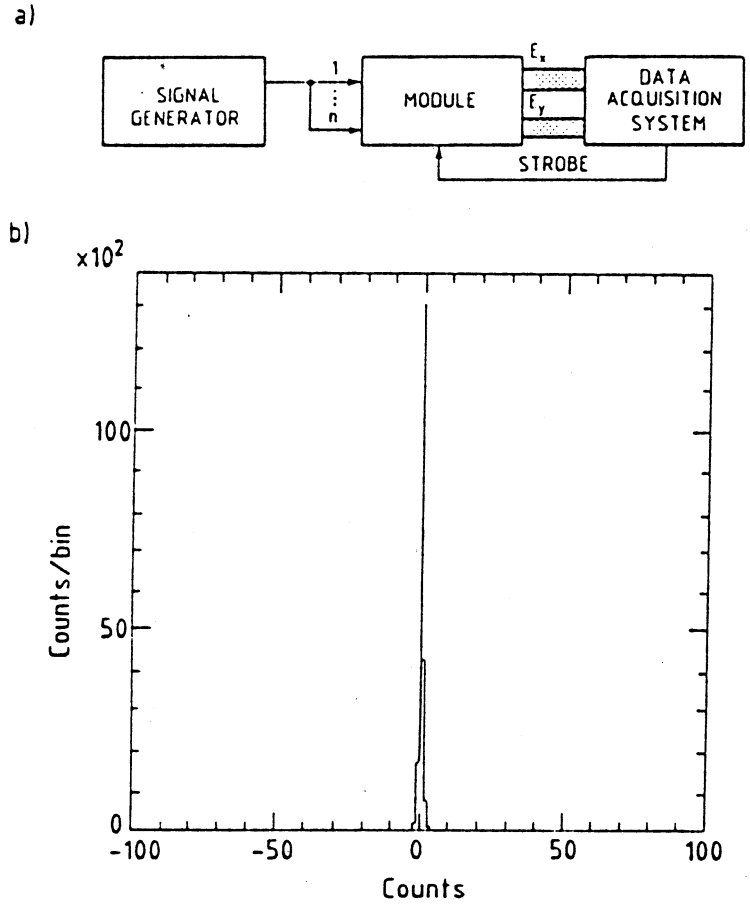

Figure 3.4.3 : Performance of the MISSPET module.

The last two steps are performed with standard electronics modules in the MBNIM standard. These modules perform such operations within about 100 ns., which is well within the required speed.

A special purpose CAMAC module called MISSPET [Mor-90] is used to calculate p_x and p_y. It accepts input signals with levels from 0 to -3V and has an input impedance of 100 Ω. A block diagram is shown in Figure 3.4.2. At the input each signal is split into x- and y- components depending on the azimuthal angle for that input. The components are then separately summed and transmitted on an MBNIM bus to separate Random Access High Speed Memory (RAHM) MBNIM modules. The input word to the RAHM is used as the address of a memory location which is pre-programmed to contain the square of their address. The output of these two memories is then summed together to give the p_T^2 for the event. A further RAHM module is used as a look-up-table with its output on a single MBNIM bus line being raised when the input exceeds the value corresponding to a threshold.

The p_T^{miss} electronics are calibrated before each data-taking period with a PPG system. Various charges are injected isotropically throughout the calorimeter electronics so to produce $p_T^{miss} = 0$. The good performance of the MISSPET module is shown in Figure 3.4.3, where a low output impedance signal generator drives all the inputs in parallel and the module is randomly triggered. The output values on the MBNIM busses are expected to be always zero within a few counts. For a full scale sine wave at the input, the output has a $\sigma \sim 0.7$ counts with a full width at the base of 6 counts.

Minimum bias or ΣE_T triggers include only a small fraction of events in which the production of an energetic neutrino or other particle which does not interact with the calorimeter, leads to an apparent momentum imbalance. For such triggers, the p_T^{miss} is due mostly to fluctuations in the energy measurement and the loss of particles outside the calorimeter acceptance. Each component of the total transverse momentum has a Gaussian distribution, as shown in Figure 3.4.4a and b and whose width increases with ΣE_T. The number of events therefore decreases exponentially with $(p_T^{miss})^2$ (see Figure 3.4.4c). Writing

$$\frac{dN}{d(p_T^{miss})^2} = \frac{N}{\Delta^2} \cdot e^{\frac{p_T^{miss\,2}}{\Delta^2}}$$

the p_T^{miss} resolution is derived by parametrizing the variation of Δ with ΣE_T

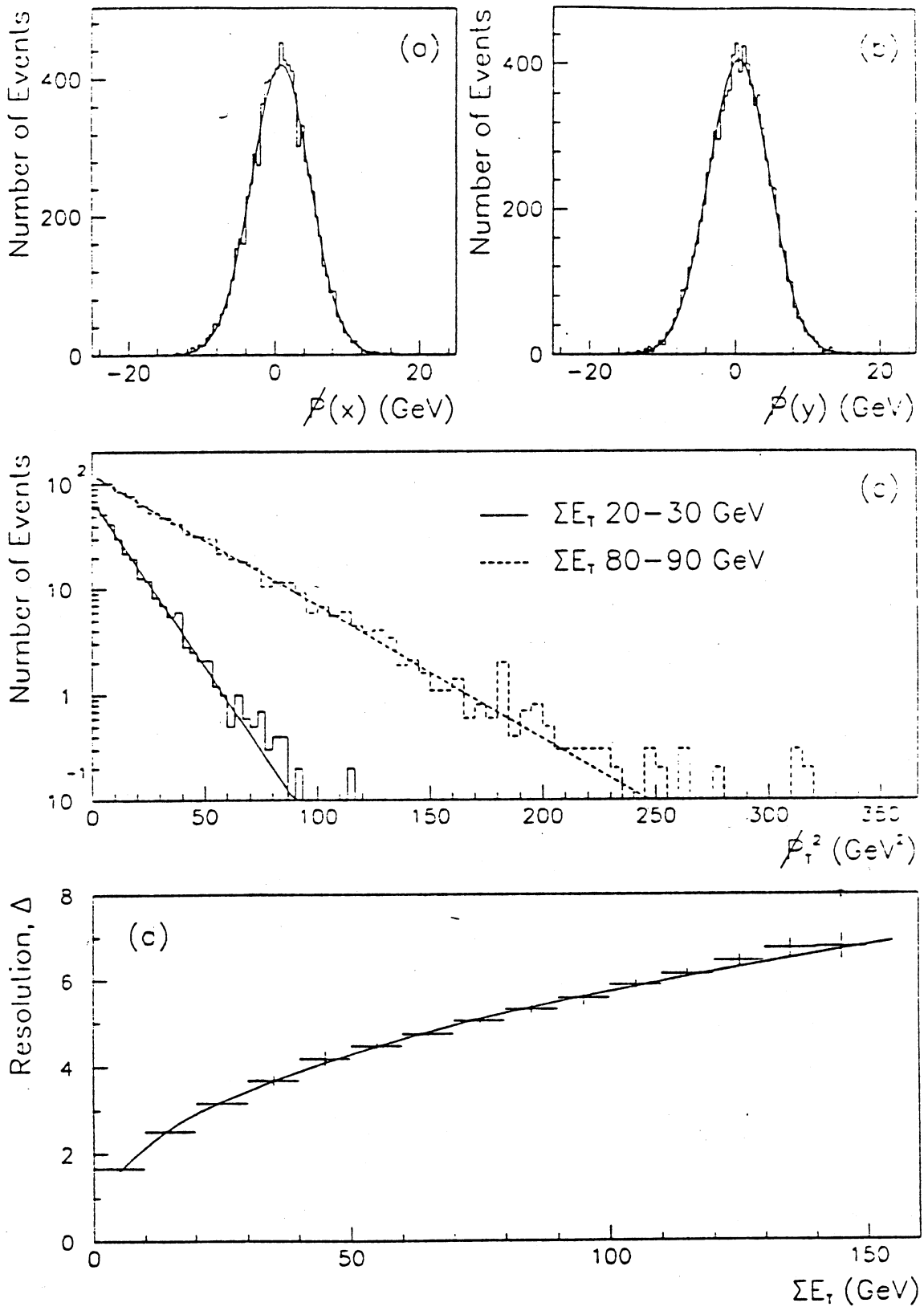

Figure 3.4.4 : Distributions of (a) the x- and (b) y-components of the p_T^{miss} for events with $90 < \Sigma E_T < 100$ GeV, (c) the distribution of p_T^{miss2} for events with (i) $30 < \Sigma E_T < 40$ GeV and (ii) $90 < \Sigma E_T < 100$ GeV. (d) The parametrization of Δ as a function of E_T

as shown in Figure 3.4.4d by

$$\Delta = \alpha(\Sigma E_T)^{\beta}$$

where $\alpha = 0.82 \pm 0.02$ and $\beta = 0.43 \pm 0.01$.

The Jet Triggers

The LVL1 jet triggers include the two jet high (2JH) trigger which functions by digitizing the analogue sum of the signals from all the photomultipliers in each of the 12 60° wedges centred at $\phi = 0°, 30°, ..., 330°$ over the pseudorapidity range $| \eta | \leq 2.0$. The wedge sums are then compared to a threshold and a 'MISTER BIT' is set when it is exceeded. The pattern of MISTER BITS is then checked to see if any pair of azimuthally opposite wedges are both above threshold in which case the trigger fires.

The jet trigger electronics are implemented in NIM, MBNIM, and CAMAC modules. The trigger requires MBNIM ALU to test the event topology for opposite wedges exceeding the relevant threshold. The monitoring electronics includes LeCroy 2249 ADCs for each wedge formed so that E_T thresholds can be inspected online. The electronics was calibrated at the beginning of each data-taking period with a PPG system.

The calorimeter information is available via an OLIFAN fanout as an .OR. of the 20 PMs. The OLIFAN integrates the sum of the current pulses for each pair of PMs per cell resulting in 10 output voltage levels. The ISH circuits receive the same gate as the ADCs (400 ns) as well as the general clear after the final trigger decision is made. The ISH voltage levels are accepted by ROLAND modules in which cell clustering and trigger threshold comparisons are made. The ROLAND module is shown in Figure 3.4.5. While the electromagnetic calorimeter cells fully contain high energy (40 GeV) electrons incident at the cell centre, it is generally necessary to sum at least a couple of cells for off-centre cell showers. The maximum trigger efficiency is achieved by summing adjacent cells in 2 by 2 clusters.

Other UA2 LVL1 Triggers

Following is a list of some other specimen UA2 LVL1 triggers that were active during the years noted.

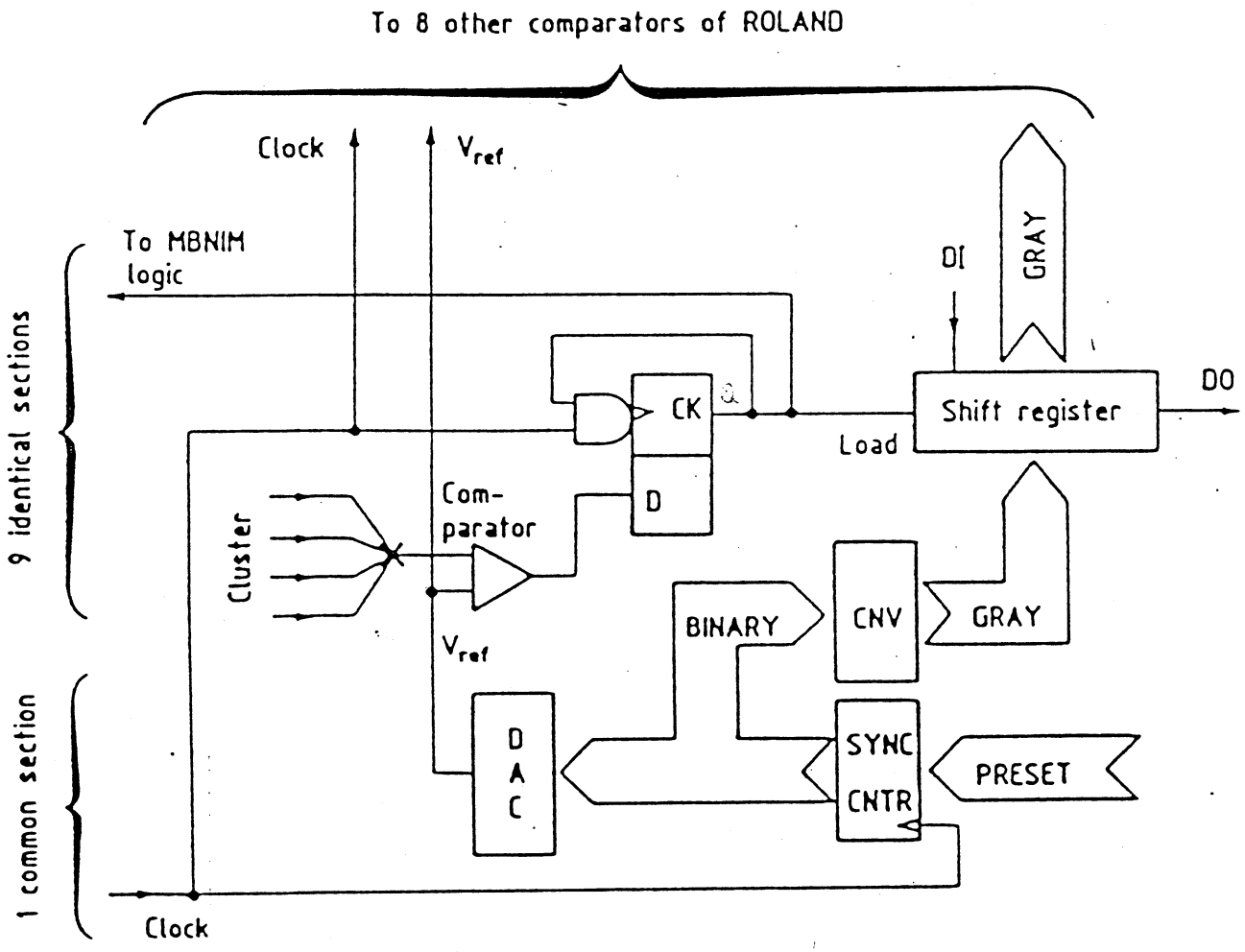

Figure 3.4.5 : Schematic of the ROLAND module electronics.

- Single Jet Trigger : the total transverse energy in a 60° azimuthal wedge of the calorimeter is greater than a threshold of about 20 GeV, (1988,1989).

- E_T Trigger : consists of two scalar sums of the transverse energy ΣE_T^{tot} for $| \eta | < 2.0$ and ΣE_T^{cen} for $| \eta | < 1.0$. These are formed by the summation of the $\Delta\phi = 30°$ wedges. The respective LVL1 thresholds were 90 and 70 GeV, (1988, 1989, 1990).

- Z Trigger : at least two electromagnetic clusters with $E_T^{EM} > 4.5$ GeV separated by $\geq 60°$ in the azimuthal plane and having an invariant mass $M^{EM-EM} = 9$ GeV, (1988, 1989, 1990).

- W Trigger : at least one electromagnetic cluster with $E_T^{EM} > 11.5$ GeV (1988, 1989, 1990).

- Photon Trigger : a photon candidate event requires an electromagnetic cluster with centroid in $| \eta | < 0.76$ and $P_T > 15$ GeV.

- Minimum Bias : the rate of minimum bias triggers as provided by the TOF is used to calculate the delivered luminosity. Only a preset small fraction of the triggers are read out and only the TOF and veto counter information is recorded. There exist occassional dedicated runs of several thousand minimum bias triggers for which the whole detector is read out for special studies.

The Second Level Trigger

A deficiency of the LVL1 trigger is the broad energy range over which the trigger efficiency increases from 0 % to 100 %. This yields a threshold cut which is not sharp. For example, for the LVL1 2JH trigger, the energy resolution is approximately 10 GeV, i.e. there is a 20 GeV interval from 0 % to 100 %. This is caused by fluctuations in the energy deposition pattern, such as low E_T clusters associated with a 'hot' minimum bias event or vice versa and to drifts in the electronics. The role of the LVL2 trigger is to sharpen the energy thresholds so that only a minimal amount of data below 100 % trigger efficiency is accepted. The sharper energy measurement is due

to the use of the calibration constants of the calorimeter which are available in digital form at LVL2.

The LVL2 trigger has been designed to reduce the LVL1 trigger rate from about 50 Hz to approximately 10 Hz and to make the decision in 1 ms. so that the dead-time is $< 20\%$. During the period of the LVL2 trigger decision the full detector read-out is preceeding in case of an accepted event. For a rejected event at LVL2 a general clear is issued to all detectors enabling them to be ready for the next bunch crossing in $\sim 10\mu$s. If the event is accepted the digitization and read-out continues for another 7 ms. with the event pieces being collected from the detector electronics into Read Only Processes (ROP) located in FASTBUS crates. The event components from the CAMAC-based detectors, (the calorimeters, the ECPT and the silicon arrays), are collected into one ROP while the SFD, JVD, and TRD are written to a separate ROP. The SFD takes up the most time for the complete event read-out because the digitization and clustering of the CCD pixel information takes about 8 ms. The event pieces from each ROP are collected by a master FASTBUS module containing an M68020 processor and called the ALEPH Event Builder (AEB).

The AEB consists of two FASTBUS cards, one containing a 20 MHz 68020/68881 processor while the second contains 0.5 MByte of dual-port RAM in Data Space and 2 KByte of dual-port RAM in CSR space. This module plays the role of Read-out Processor, Master Event Builder and third trigger level processor.

The LVL2 trigger is implemented in a special purpose trigger processor called the eXtended Online Processor (XOP). The XOP is a micro-programmable 16-bit integer arithmetic processor. The basic instruction execution time is 100 ns. but because of parallelism and pipelining the overall performance is better than this. Certain instructions can be performed in vector mode at a rate of 20 MIPS. The data memory bandwidth is 40 MBytes/s. The pipeline block transfer allows a data transfer rate of upto 32 MBytes/s.

The LVL1 trigger will start a fast digitization of the calorimeter information. The compartment energies are multiplied through a FERA ADC system to the XOP ECLine interface. The transfer speed is limited by the FERA driver to 105 ns./word. The data coming in over the ECLine is gain corrected and pedestal subtracted before being stored in the XOP memory. It takes 165 μs. including the ADC conversion time to transfer the 1200 10-bit

words into the XOP memory.

Following an initialization routine, the calorimeter cells are collected into clusters. It takes 100 ns. to reject a cell below threshold. Therefore, the processing time for an event with 10 clusters and 10 cells per cluster is 250 μs. which is more than 20 times faster than a VAX 780. The next step is to calculate the centre of gravity and radius of the cluster. This is done in cell units in the θ and ϕ projections. Also, the leakage of the cluster, which is the ratio of the cluster energy deposited in the hadronic calorimeter over the total deposited energy, is calculated. At this point one can identify electron candidates using the transverse cluster energy, the cluster leakage which is compared to an energy dependent leakage cut and the cluster radius or to calculate the invariant masses of cluster calculations.

The precision of the calculations is limited by the precision in the energy measurement (using the analogue sum of the two PMs through a 10-bit ADC in the trigger, while for the full read-out, the two PM signals are digitized by two separate 12-bit ADCs), and by the 16-bit integer constraint.

The LVL2 p_T^{miss} trigger is essentially identical to the LVL1 because the same pseudorapidity interval is used. The only difference comes from the ADC conversion in the p_T^{miss} module instead of the FERA ADCs. The LVL2 2JH trigger implements a transverse energy cut on the clusters about 6 GeV higher than at LVL1. The resolution of this cut is 4 GeV and is optimal for eliminating events below 100% trigger efficiency and thus maximizing the data acquisition live-time.

At LVL2 new triggers may be formed with information from LVL1. For example, the LVL1 ΣE_T triggers are used as input into the LVL2 multijet triggers where at least 3 clusters exceeding 8 GeV are required. The LVL2 multijet trigger decision is made by utilizing the LVL1 Single Jet and 2JH triggers.

The Third Level Trigger

The third level trigger (LVL3) algorithm takes about 300 ms. to execute and reduces the accepted event rate from 10 Hz. at LVL2 to approximately 3 Hz. Since the master AEB has the capability of buffering events, i.e. it is capable of digitizing a new event even though the previous event has not been safely transferred, until a slave AEB is free, there is no dead-time introduced at LVL3. However, the rejected events at LVL3, which apart from time lost

in changing between cassette drives, is the only source of dead-time in the data acquisition system. Events accepted at LVL3 are written to cassette via the main VAX 11/785 computer.

In the LVL3 AEB all the data is available and a more sophisticated trigger algorithm is executed. A repetition of the LVL2 algorithm with floating-point calculations, improved energy measurements and full digitization give a factor of 2 to 3 rejection. Since the event processing does not interfere with the read-out of the new events, several processes can thus work in parallel.

Data Recording

The interface between FASTBUS and the VAX is provided by the CERN FASTBUS Interface (CFI), which is capable of autonomously executing lists of operations. The elements in a list can either be FASTBUS operations or references to user subroutines which are then executed on a 68000 processor in the module.

When the buffer is full, the CFI is notified using a FASTBUS Service Request. The CFI transfers the accepted event buffer to the VAX, where it is unpacked, recorded on tape and then made available for online monitoring. This monitoring may take place on the main VAX 11/785 or after distribution over DECNet to one of the additional micro-VAX PX-II workstations which also provide graphics support for the online displays.

While most of the digitization electronics are constructed in FASTBUS, a large amount is imbedded in REMUS, thus requiring the integration of these two systems. The interface between the two is provided by a device that looks like a standard Read/Write Branch Driver (RWBD) on the REMUS side. On the FASTBUS side, the configuration depends on whether the REMUS operation is a read or a write. For a REMUS read, an autonomous scan is initiated from either the front panel or via FASTBUS, and the resulting data is transferred into an 8K 16-bit word buffer. For a REMUS read, a FASTBUS data cycle is mapped into a corresponding REMUS write cycle.

3.5 The Tau Trigger

The data in this analysis were obtained in the three major collider runs in 1988, 1989, and 1990 corresponding to a total integrated luminosity of

13.0 ± 0.7 pb^{-1}. The data from the 1988 and 1989 running periods were collected with the p_T^{miss} trigger whilst that for the 1990 run a dedicated τ trigger [Inc-91a] was implemented.

The decay chain

$$t \rightarrow H^+b,\ H^+ \rightarrow \tau^+\nu_\tau,\ \tau \rightarrow \text{hadrons} + \overline{\nu}_\tau \qquad (3.5.1)$$

yields a final state which is very similar to that of

$$W^+ \rightarrow \tau^+\nu_\tau,\ \tau^+ \rightarrow \text{hadrons} + \overline{\nu}_\tau \qquad (3.5.2)$$

but with the addition of jets from the b-quarks and a lower p_T^{miss} because of $m_{H^\pm} < m_W$ (see Figure 3.5.1).

The lower p_T^{miss} expected from $H^\pm \rightarrow \tau\nu_\tau$ necessitates a decrease from the 16 GeV p_T^{miss} threshold used for the 1988 and 1989 running periods to increase the τ acceptance. However, because of the anticipated increase by a factor of about 2 to 3 in the peak accelerator luminosity in 1990, the p_T^{miss} threshold needed to be increased from 16 GeV so as to minimize the deadtime caused by the detector read-out and the amount of data written to tape. Since the p_T^{miss} trigger was previously used as the basis for the study of τ 's in UA2, an increase in the threshold means a reduction in the τ acceptance which as is seen in Figure 3.5.1 is already relatively low even for $W \rightarrow \tau\nu_\tau$ events. It was therefore mandatory to find a method to compensate for the increased luminosity so that the p_T^{miss} threshold would not have to be increased and could even be lowered.

Because events appearing in the p_T^{miss} trigger stream are predominantly found to be either beam-halo or dijet events with a large E_T imbalance, some fraction of these events are eliminated by adjoining a dijet veto and a veto on events with early VETO counter hits to the LVL1 p_T^{miss} and minimum bias triggers. This results in the τ trigger logic

$$p_T^{miss}\ (|\eta| < 2) \cdot \overline{2JH} \cdot \text{VETO} \cdot \text{MB}.$$

The VETO counter veto rejects beam halo. The hardware modification to the VETO counters consists of feeding the numerous discriminator outputs from the photomultiplier signals at each end of the counters into logic units to form an OR of all such signals in a time window of approximately 1 μs ending at the nominal bunch crossing time. The logic units are gated in time so that only early hits contribute to the OR logic.

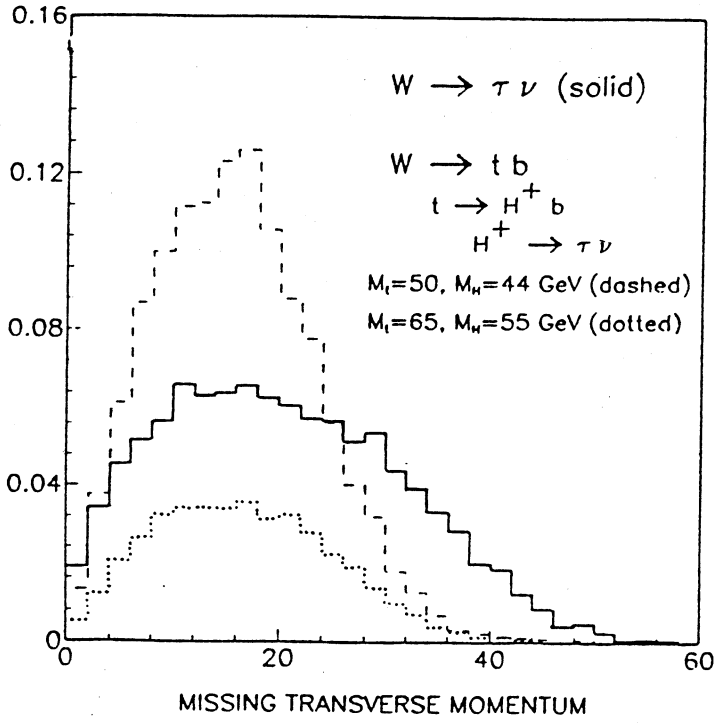

Figure 3.5.1 : The missing transverse momentum distributions for $W \rightarrow t\bar{b}$ and $W \rightarrow \tau\nu_\tau$ events as in Equations 3.5.1 and 3.5.2, respectively. The curves are normalized to the total integrated luminosity.

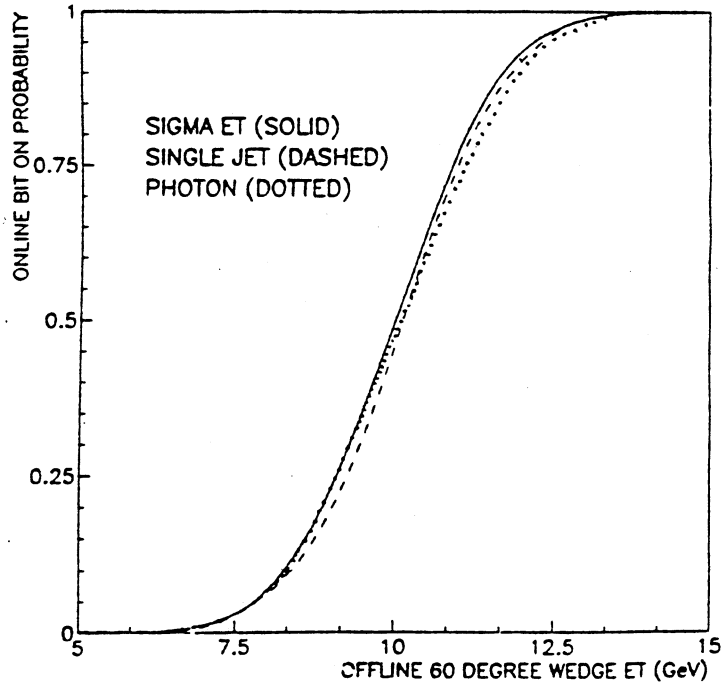

Figure 3.5.2 : For the ΣE_T, Single Jet and Photon triggers, the probability that the online MISTER BIT is set as a function of the online 60° wedge E_T. The nominal dijet wedge threshold is 13.6 GeV.

Table 3.5.1 : The level 1 1990 τ trigger parameters.

$\not{p}_T$ threshold [GeV]	di-jet threshold [GeV]	run range	$\int L\,dt$ [%]
12.7	13.6	[9100,9348]	21.2
13.4	17.7	[9349,9447]	6.9
14.3	23.1	[9448,9935]	71.9

Table 3.5.2 : The level 1 1990 τ trigger rates at a luminosity of $1x10^{30}$ cm^{-2} s^{-1}

$\not{p}_T$ threshold [GeV]	di-jet threshold [GeV]	Rate [Hz]
12.7	17.7	15.3
12.7	13.6	11.8
13.4	17.7	10.7
13.4	16.3	9.6
14.3	23.1	8.0

This veto reduced the LVL1 τ trigger rate by $\sim$ 10% for the case of a 14 GeV p_T^{miss} threshold. Even though this represents a small fraction at LVL1 these events would not otherwise have been rejected at LVL2 and LVL3 where they would represent larger fractions of events as well as detector deadtime and an enhanced number of events written to tape. After extensive tests it was found that the VETO counter veto reduced the number of events written to tape by a factor of about 2.

In the τ trigger, the 2JH trigger was used to veto the p_T^{miss} trigger. Initially, the di-jet threshold was set to 13.6 GeV which corresponds to the value at which full acceptance of dijets is obtained when treating the trigger in the manner for which it was originally intended and not as a veto. However, when used as a veto this threshold corresponds to being fully efficient for accepting events with opposite wedges below about 7 GeV as shown in Figure 3.5.2. Since the wedge E_T is generally larger than that of any cluster centred inside the wedge, the trigger is thus not fully efficient for clusters opposite the τ candidate at the desired opposite E_T threshold. The dijet veto was therefore raised. As a result of this and the increased peak accelerator luminosity obtained in the middle of the run, the p_T^{miss} and $\overline{2JH}$ thresholds were altered twice in the course of the 1990 run. Table 3.5.1 lists the different threshold settings and their corresponding run ranges and fractions of the total integrated luminosity. The final p_T^{miss} threshold at LVL1 is 14.3 GeV which is about 2 GeV lower than in the 1988 and 1989 runs.

The final thresholds at run number 9448 are chosen to give a deadtime for the τ trigger below that of the W/Z triggers. At a luminosity of $\sim 3.0 \times 10^{30}$ $cm^{-2}s^{-1}$ the deadtime of the τ trigger is 2.8% compared to 3.5% for the W/Z triggers. The overall livetime of the online system at this luminosity was $\sim$ 90%.

In Table 3.5.2 the LVL1 trigger rates for various settings of the p_T^{miss} and dijet veto thresholds at a luminosity of 1.8×10^{30} $cm^{-2}s^{-1}$ are given. The trigger rate varies linearly with luminosity for a given set of thresholds. The rate increases by a factor of about 2 per GeV decrease in the p_T^{miss} threshold.

The addition of the dijet and VETO counter vetoes result in a significant reduction of the trigger rate relative to the 1988 and 1989 rates. At a luminosity of 1.8×10^{30} $cm^{-2}s^{-1}$ the LVL1 p_T^{miss} trigger rate in 1989 was 5 Hz for a threshold of 16 GeV (so that the rate would have been about 17 Hz for a threshold of 14.3 GeV), whereas the 1990 rate at this luminosity is 8 Hz indicating a reduction by a factor of about 2 in the rate that would have

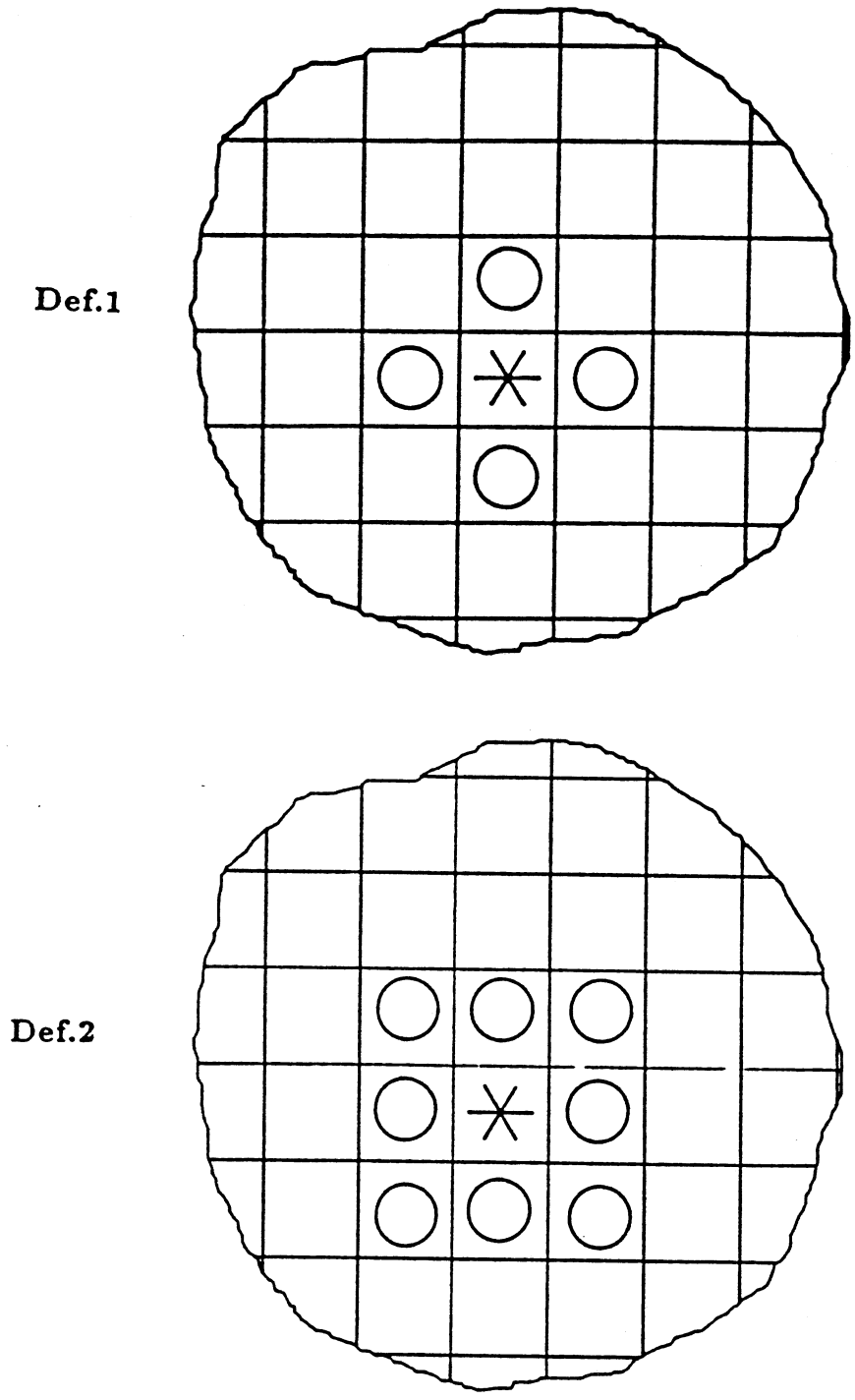

Figure 3.5.3 : The two definitions of the calorimeter cluster profile ρ.

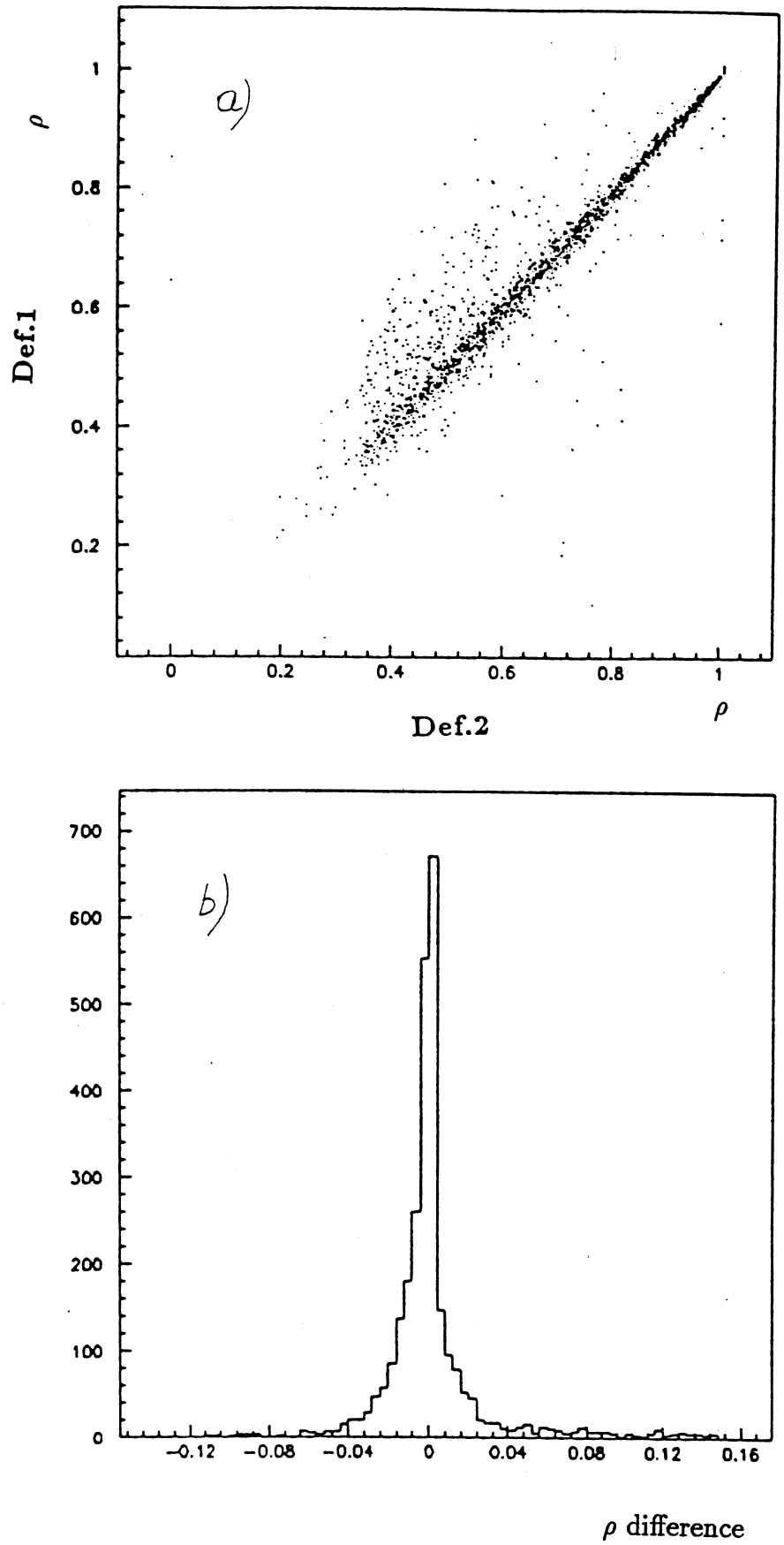

Figure 3.5.4 : (a) Correlation between the two definitions of ρ and (b) the distribution of the difference between the two ρ definitions. The plots are produced from the 1990 τ data sample.

occurred in the absence of the vetoes. Note that the absolute trigger rate in 1990 was significantly higher than in 1988-1989 because of the increased accelerator luminosity.

At LVL2 and LVL3 the selection of τ candidate events with p_T^{miss} is initiated while the rejection of the dijet and beam halo background is continued. At these levels the p_T^{miss} is calculated using the calibrated cell E_T in $| \eta | < 3$ with a threshold of 14 GeV and $E_T^1 > 10$ GeV in $| \eta | < 3$ where E_T^1 is the transverse energy of the leading cluster in the event.

The τ candidates are sought on the basis of the profile ρ and hadronicity ξ of the leading cluster, defined as :

$$\rho = \frac{E_1 + E_2}{E_{TOT}}$$

$$\xi = \frac{E_{HAD}}{E_{TOT}}$$

where E_{HAD} is the energy of the cluster contained in the hadronic calorimeter compartments, E_{TOT} is the total cluster energy, E_1 is the energy of the leading cell in the cluster and E_2 is the energy of the highest energy cell neighbouring the leading cell in the cluster.

Figure 3.5.3 indicates with a '*' the leading calorimeter cell in the cluster which defines E_1 and the 'o' indicate the neighbouring cells which are candidates for E_2. The two sketches show the two different methods studied to identify the cell with E_2. The method shown in (a) is finally chosen because it covers a smaller number of cells than method (b) and is thus expected to better discriminate the narrower τ jets from the QCD background. Figure 3.5.4 shows the difference between the two ρ definitions for τ candidates from the 1990 τ trigger.

The ρ is a measure of the narrowness of a cluster and values for τ jets are in general larger than for QCD jets because of their relative narrowness. The radius R $\left(= \sqrt{(\Delta\eta)^2 + (\Delta\phi)^2} \right)$, in the pseudorapidity - azimuthal space, of a cone around the cluster axis that contains 95% of the cluster energy is found to be approximately 0.2 for a τ jet and about 0.7 for a QCD jet. Distributions of ρ for MC τ 's and jets from dijet data are shown in Figure 3.5.5. It is seen that $\sim 87\%$ of all τ's have $\rho > 0.75$ while the region $\rho < 0.60$ has only $\sim 2\%$ of τ's and is made up predominantly by QCD jets. At the trigger level $\rho > 0.35$ is required so that enough QCD jets remain so

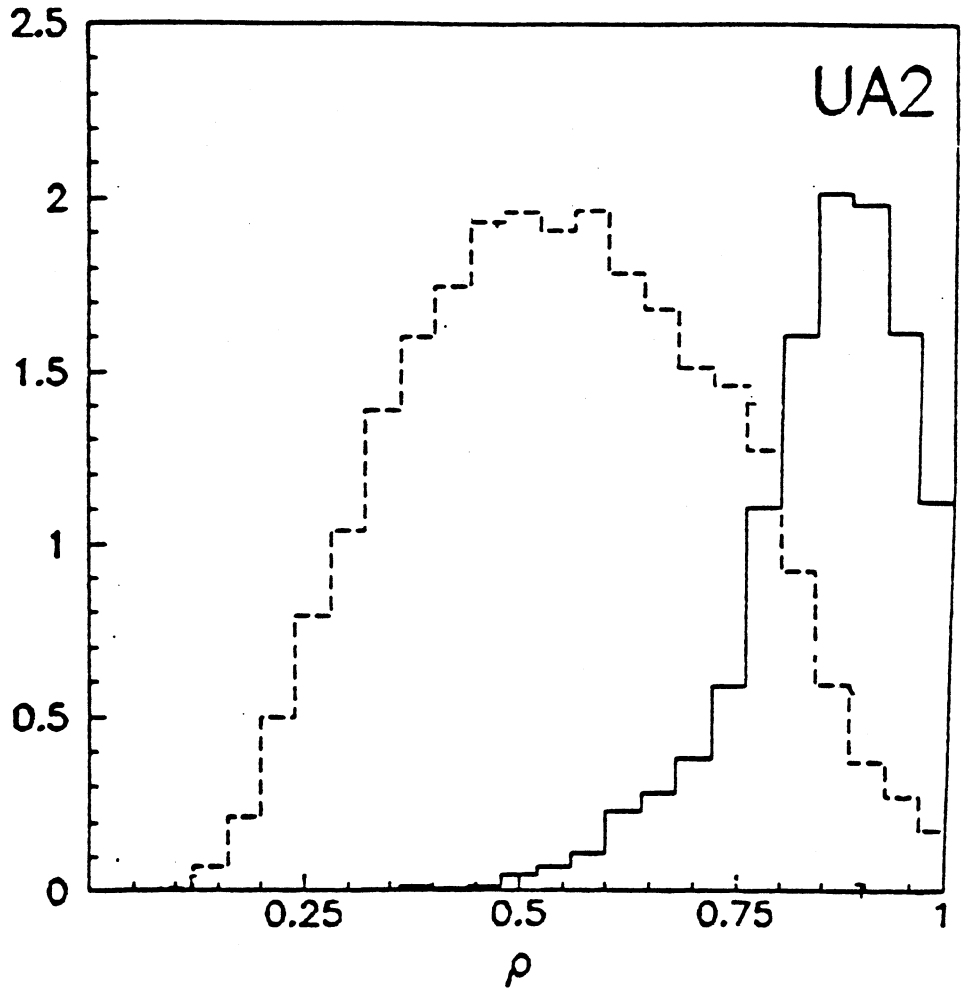

Figure 3.5.5 : Profile distribution for hadronic τ decays (solid line) obtained from an EKS MC of $W \rightarrow \tau\nu_\tau$ and for dijets from UA2 data (dashed line).

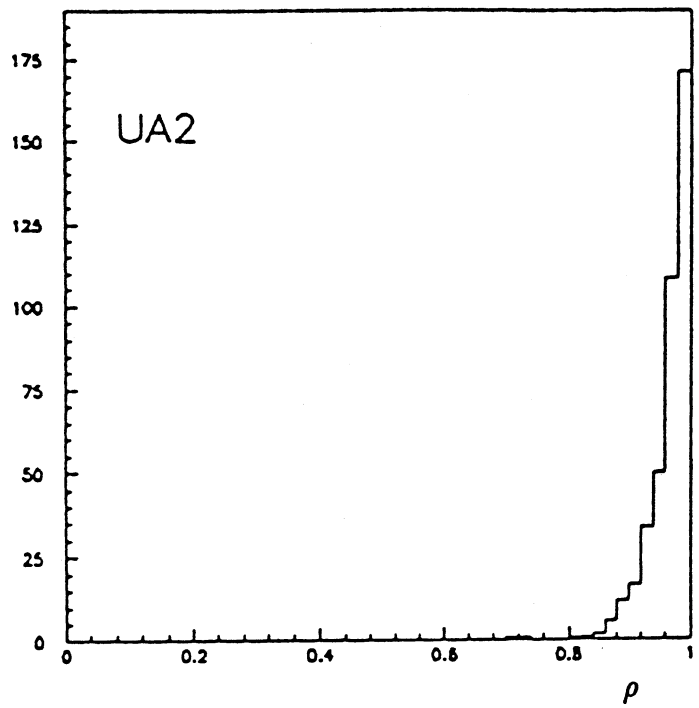

Figure 3.5.6 : Profile distribution for electrons from UA2 data.

as to subtract statistically the QCD background (see Chapter 5). Electrons produce very narrow calorimeter clusters thus yielding high ρ values as is shown in Figure 3.5.6.

The ξ is used to reject beam halo. Figures 3.5.7 to 3.5.10 show the ξ distributions for various event types where it is seen that beam halo events are characterized by large ξ values because they predominantly enter the calorimeters from behind and deposit most of their energy in the hadronic calorimeter compartments. Therefore, to reject the beam-halo, ξ is required to be less than 0.95 (LVL3 only). Electrons are predominantly contained in the electromagnetic compartments and are thus characterized by low ξ values. Hadronic τ decays are expected to yield a ξ distribution which is relatively flat while non-τ jets are expected to yield broad ξ distributions.

In addition, the centre of the leading cluster centroid is required to be in the pseudorapidity interval $\mid \eta \mid < 1.5$ and the τ candidate is required to have no opposite cluster at $140° < \Delta\phi < 220°$ with $E_T > 8$ at any η to further reduce QCD dijets.

In summary, the LVL1 and LVL2 modifications result in a reduction in the detector deadtime which allows the p_T^{miss} threshold to be set slightly below the 1988 and 1989 values. Also, the combination of the VETO counter veto at LVL1 and the LVL3 trigger algorithm keep the volume of triggers written to tape at tolerable levels. The number of p_T^{miss} triggers written to tape in 1989 is 68 Kbytes per pb^{-1} while the 1990 τ trigger results in 64 Kbytes per pb^{-1} written.

The 1988-1989 p_T^{miss} trigger is fully efficient above an off-line threshold of 23 GeV and are $\geq 96\%$ efficient for thresholds with $20 < p_T^{miss} < 23$ GeV. Also, as is shown Figure 3.5.11, the 1990 p_T^{miss} component of the τ trigger is fully efficient above a threshold of 20 GeV so this value is taken as a preliminary selection criterion in all subsequent studies defining the final event sample.

To quantify the effect of the LVL1 2JH veto the probability that a MISTER BIT is set for a 60° wedge as a function of the offline wedge E_T is parametrized using data from several different data streams. Figure 3.5.2 shows the distributions obtained with the ΣE_T, Single Jet and Photon triggers when the dijet threshold is 13.6 GeV. Figure 3.5.12 shows the probability distributions for all three dijet thresholds as obtained with the ΣE_T data.

Starting from the distributions in Figure 3.5.12 a simulation routine was developed to determine the effect of the dijet veto on the signal acceptance.

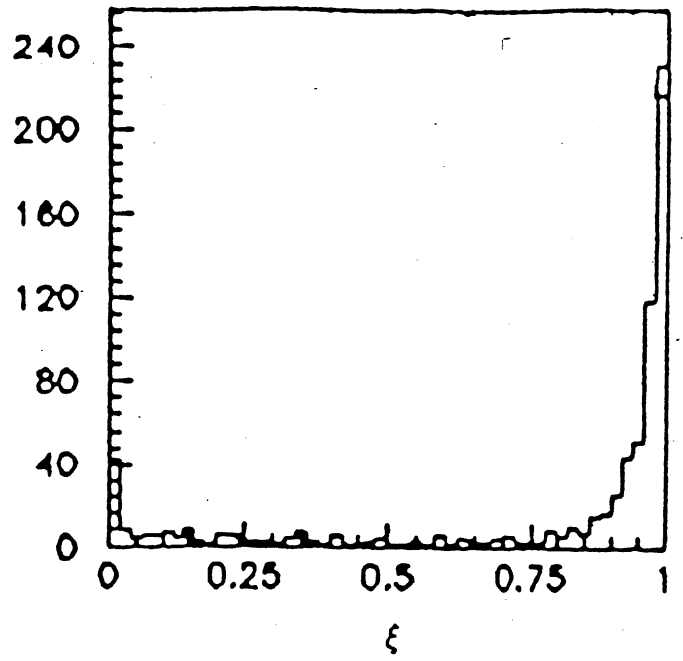

Figure 3.5.7 : The hadronicity distribution for beam-halo events.

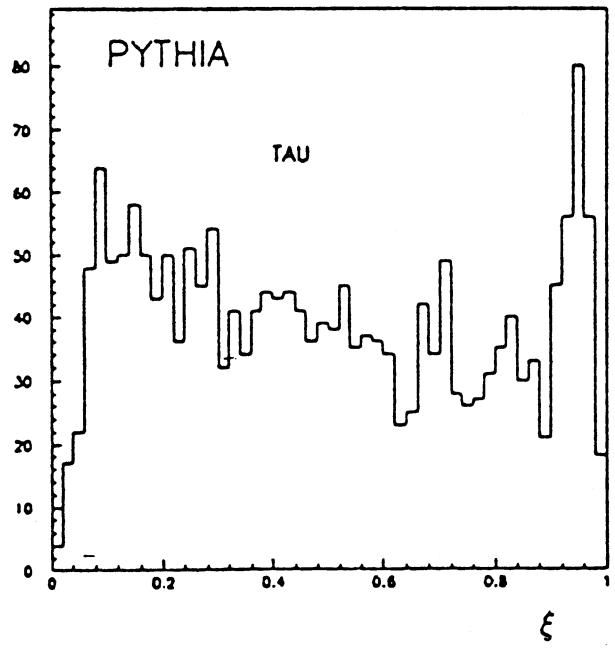

Figure 3.5.8 : The hadronicity distribution for hadronic τ decays from a $W \rightarrow \tau\nu_\tau$ EKS MC.

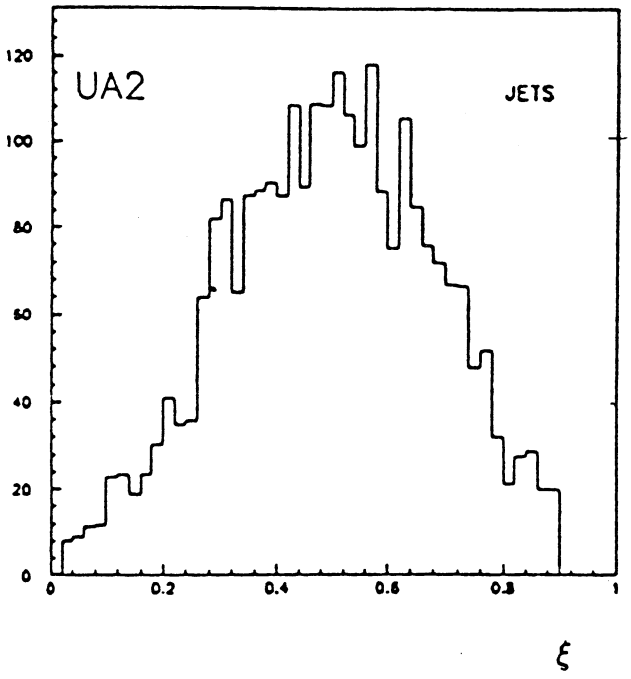

Figure 3.5.9 : The hadronicity distribution for non-τ jets from UA2 data. The cut $0.01 < \xi < 0.90$ has already been applied.

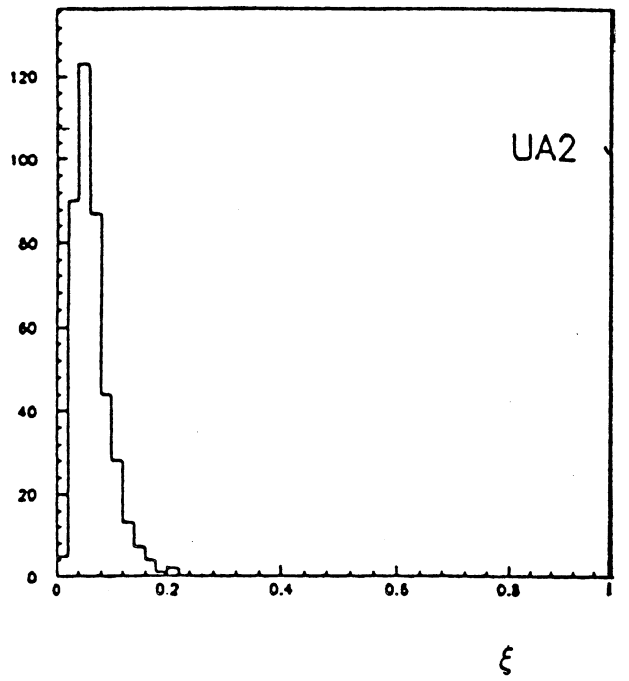

Figure 3.5.10 : The hadronicity distribution for electrons from UA2 data.

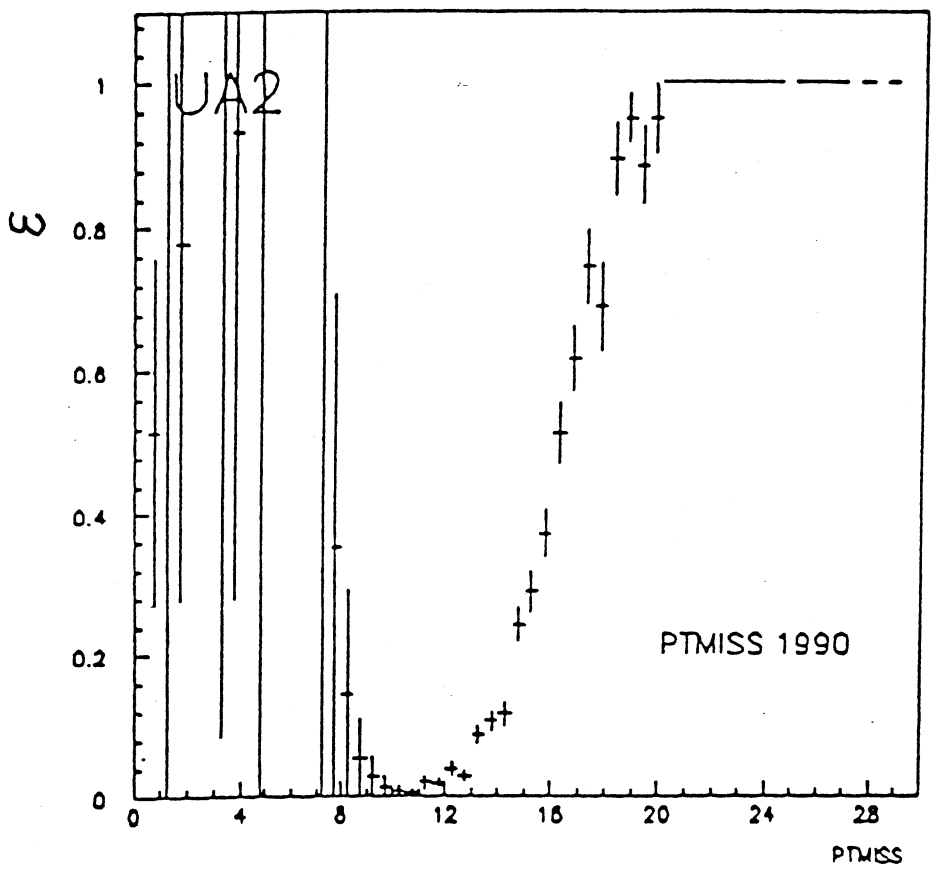

Figure 3.5.11 : The distribution of the p_T^{miss} efficiency versus the p_T^{miss} for the 1990 τ trigger.

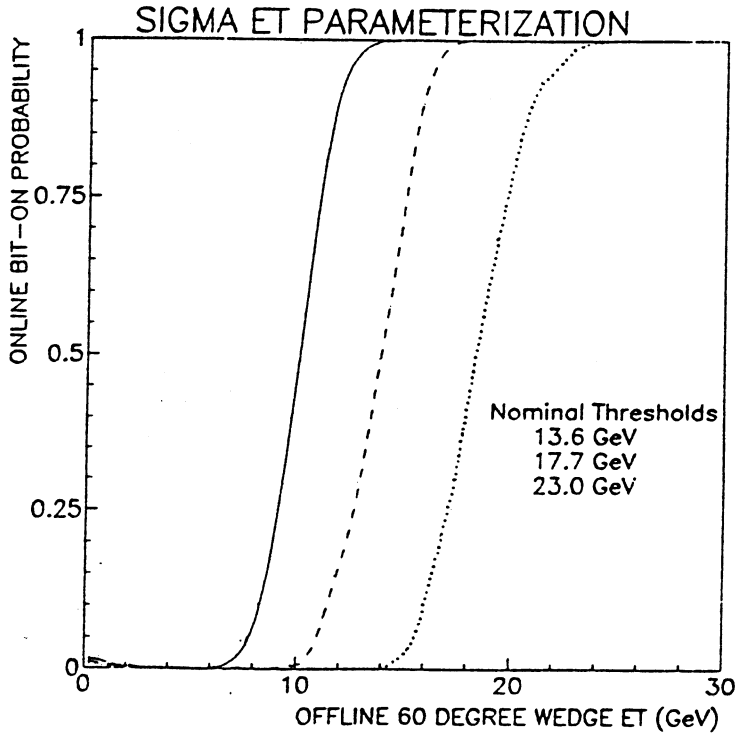

Figure 3.5.12 : Using $\sum E_T$, the online bit-on probabilities are shown for the three thresholds used in 1990.

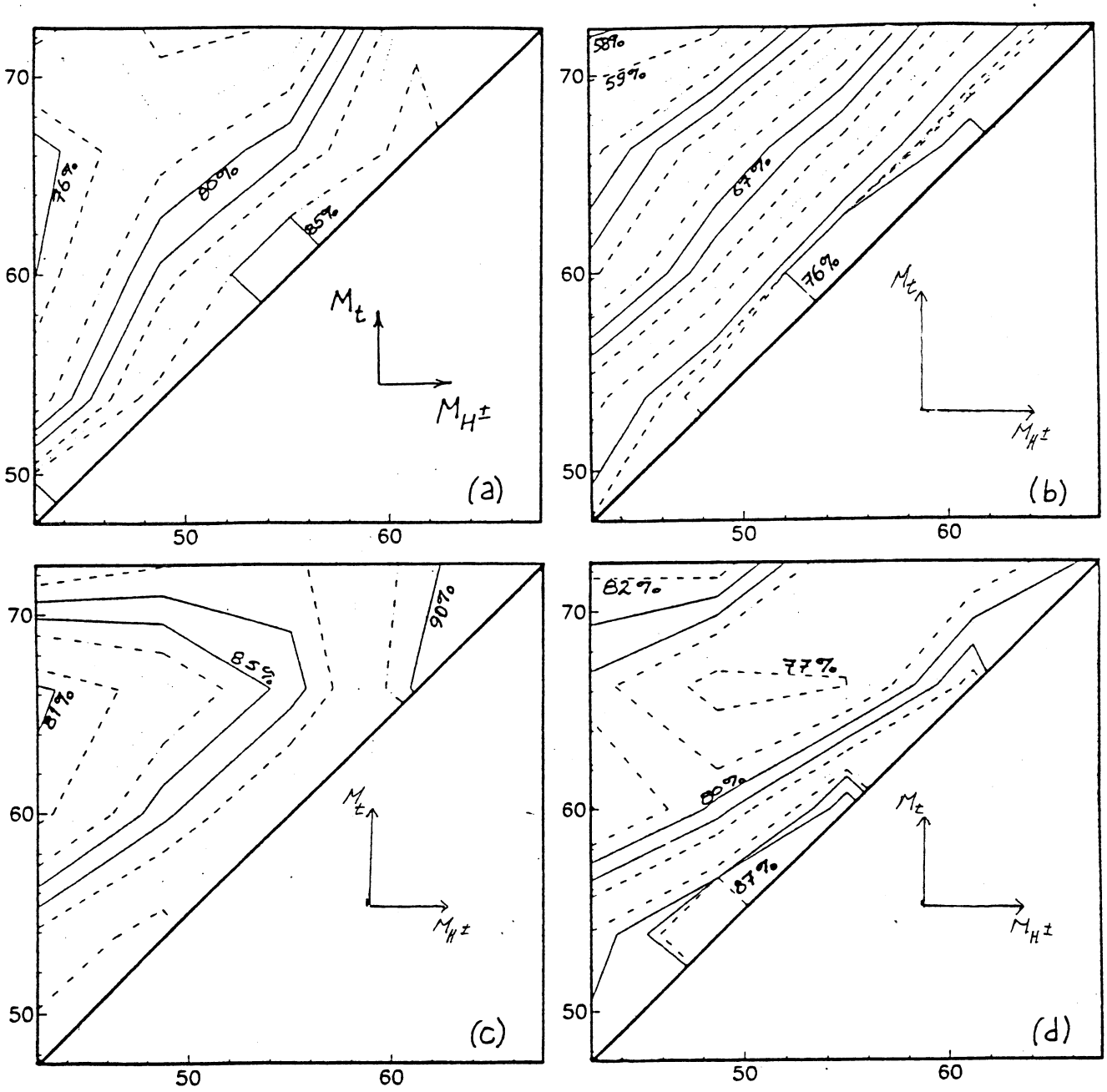

Figure 3.5.13 : Contours of the trigger acceptance after the analysis cuts. $p\bar{p} \rightarrow t\bar{t}$ events subdivided into (a) τ + 0jets and (b) τ + jets samples and $W \rightarrow t\bar{b}$ events subdivided into (c) τ + 0jets and (d) τ +jets samples. The τ +0jets and τ +jets are defined offline according to whether an additional cluster with $E_T > 10$ GeV appears in the event or not.

The simulation is done by calculating the twelve 60° wedge E'_Ts. For a given threshold choice the corresponding parametrization in Figure 3.5.12 is used to obtain the probability that the MISTER BIT would have been set online for each of the wedge E'_Ts. The wedge is then said to have its MISTER BIT set if a random number from a uniform distribution in the range [0,1] does not exceed the calculated probability for the wedge E_T. The dijet veto is said to have fired whenever the MISTER BIT pattern indicates that two opposite wedges have their bits set.

To determine the acceptances over the whole 1990 run, the acceptance for each threshold α_i is calculated and the overall acceptance α is obtained as the weighted sum

$$\alpha = \sum_{i=1}^{3} = f_i \cdot \alpha_i$$

where f_i is the fraction of the total integrated luminosity at threshold i.

To test whether the above procedure accurately reproduces the online dijet veto it is run on UA2 $W \rightarrow e\nu_e$ data collected during the 1990 run and the decisions of the simulator are compared to the online decision. Using these data it is found that the online dijet veto is not active for 1399 of 1488 events whereas the simulator estimates that it should not be active for 1392 events, thus giving an agreement within $\pm 0.5\%$.

The simulation program is then used to determine if the τ trigger introduces any signal loss beyond that incurred from the analysis cuts. This is done by first applying all the analysis cuts to signal events obtained from Monte Carlo (see Chapter 4 for a discussion on the Monte Carlo set-up) and then applying the trigger simulation to see if there are any additional events lost. After all the analysis cuts it is indeed found that the trigger incurs some losses in the signal acceptance. Figure 3.5.13 shows contours representing the factor by which the signal acceptance is diminished by the trigger after all analysis cuts. The losses tend to increase for increasing mass difference $\Delta M = m_t - m_{H^\pm}$. In most cases the net acceptance of the trigger exceeds $\sim 70\%$.

Chapter 4

The Monte Carlo Simulation

4.1 Monte Carlo Simulation of Charged Higgs Production

In the search for $H^{\pm}$ from top quark decay in UA2, the observed number of τ decays is compared to that expected from electron - τ universality together with a hypothetical excess from the process considered. The τ excess depends on the production and decay mechanism of both the $H^{\pm}$ and top quark and on the unknown parameters of the theoretical model, $m_{H^{\pm}}$ and $\tan\beta$. (See Chapter 2 for a discussion of the theoretical assumptions). The τ excess also depends on the event kinematics and on how each event manifests itself in the UA2 detector.

The generation of the top quark to $H^{\pm}$ signal events has been performed with the PYTHIA Monte Carlo (MC) [Ben-84, Ben-87, Sjo-88] as it contains the correct matrix elements for the necessary tree level diagrams. In addition, there are capabilities for treating the event component not coming from the hard scattering process such as initial and final state QCD and QED radiation, parton fragmentation and decay, and spectator parton interactions. Finally, the simulation of the UA2 detector can be performed on these generated events as well as the superposition of minimum bias (MB) events taken from UA2 data.

It is necessary in the MC to correctly reproduce global variables such as $\sum E_T$ and $\sum Q$ where Q is the charge measured in the Outer Silicon detector (OSI). Taking $W \rightarrow e\,\nu_e + X$ from MC and UA2 data, the parameters of

the former have been tuned together with the superposition of UA2 MB events so that the above global variables are in agreement with the data.

In the search, events are divided into two classes called 'τ +0jet' and 'τ +jets' depending on whether they do or do not contain an additional cluster above 10 GeV which is opposite in azimuth ($140° < \Delta\phi < 220°$) to the leading cluster. Because the number of events in each class is checked individually for a τ excess it is imperative that the MC reproduces the correct cluster population by adequately reproducing the cluster multiplicities and cluster angular distributions . The ratio

$$R_{01} = \frac{W \rightarrow e\nu_e \ + \ 1 \text{ jet } (E_T \ > \ 10 \text{ GeV})}{W \rightarrow e\nu_e \ + \ 0 \text{ jet } (E_T \ > \ 10 \text{ GeV})}$$

is used to monitor this aspect of the MC. The event component other than that from the hard scattering is expected to significantly contribute to the production of clusters. Therefore, it is crucial that the MC reproduces this event component adequately. The b-quarks in the signal also contribute to the cluster multiplicity but it is assumed that they are well simulated by the MC. An uncertainty associated with the fragmentation of the b quarks is seperately assessed.

4.1.1 The PYTHIA Event Generator

At the centre of the PYTHIA MC generator are the matrix elements for $2 \rightarrow 1$ and $2 \rightarrow 2$ tree level hard scattering subprocesses. The cross sections $\sigma(s, t, u)$ for the hard scatterings are convoluted with the structure functions which incorporate the leading-log scaling violations to form the total cross section σ_{tot} for the subprocess.

The cross sections for the hard scattering subprocesses are calculated from lowest order perturbation theory and do not include higher order QCD corrections. The QCD corrections are included using a parton shower cascade approach where the initial and final state parton showers are evolved on an iterative use of the branchings $q \rightarrow qg$, $g \rightarrow gg$, $g \rightarrow q\bar{q}$ as given by the Altarelli-Parisi evolution equations [Alt-77].

Parton fragmentation is performed using the Lund string fragmentation model from the JETSET MC [Ben-84, Ben-87, Sjo-88]. This model is based on the observation that QCD is linearly confining at large distances and that the simplest Lorentz covariant implementation of a linear potential is

provided by a massless relativistic string. This mathematical string has no transverse extent but can be considered to parametrize the position of the axis of a cylindrically symmetric colour-flux tube between a quark-antiquark or diquark-antidiquark pair. Gluons correspond to energy- and momentum-carrying kinks on the string. As these particles move apart the potential energy stored in the intermediate string increases until the string breaks producing a new quark-antiquark pair so that the system splits into two colour singlet subsystems $q\bar{q}'$ and $q'\bar{q}$. If the invariant mass of either of these subsystems is large enough further breaks may occur until ordinary hadrons remain.

The fragmentation of light quarks (u,d,s) has been performed using the symmetric Lund fragmentation function

$$f(z) = 1/z \cdot (1-z)^a \cdot \exp(-bm_T^2/2)$$

where m_T is the transverse mass of the hadron and the default PYTHIA values of $a = 0.5$ GeV^{-2} and $b = 0.9$ GeV^{-2} have been used. This function gives the fraction z of the remaining energy plus momentum taken by the hadron and is symmetric in that it generates left-right symmetrical jets since quarks and antiquarks are expected to fragment in similar ways.

For heavy quark (c,b,t) fragmentation the SLAC heavy flavour fragmentation function [Pet-83] given by

$$f(z) = \frac{1}{[z \cdot (1 - 1/z - c/(1-z))^2]}$$

where $c = m_q/m_{top}$ has been used. The reason for choosing such a function is that the fragmentation of heavy quarks into heavy hadrons has hard distributions characterized by large z-values because a heavy quark is expected to lose a small fraction of its momentum so the hadron formed carries most of the quark's momentum.

The divergences which arise when only tree level diagrams at a given order are included without the virtual diagrams are controlled by a cut on the transverse momentum of the light quark with respect to the parton from which it is radiated. A cut of 2 GeV is used as the default.

4.1.2 Monte Carlo Generation of $H^{\pm}$ Signal

The PYTHIA MC has been used to produce about 8000 events (see Table 4.1.1) per $(m_t, m_{H^{\pm}})$ mass pair for the signal chain

$$t \rightarrow H^+b,\ H^+ \rightarrow \tau^+\nu_\tau,\ \tau^+ \rightarrow \text{hadrons} + \overline{\nu}_\tau$$

and its charge conjugate in the range

$$50.0 < m_t < 71.5 \text{ GeV}$$

and

$$44.0 < m_{H^{\pm}} < 66.0 \text{ GeV}.$$

Sixteen mass pairs, approximately equally spaced, for each of the strong and electroweak top quark production modes have been generated in the pseudorapidity interval -3.5 $< \eta <$ 3.5.

The generation for the electroweak production of the top quark has been done using the $2 \rightarrow 2$ tree level processes

$$f_i\,\bar{f}_j \rightarrow gW$$

$$f_i g \rightarrow f_k W$$

where $f_i(\bar{f}_i)$ represent quarks(antiquarks) of flavour i. The production of the top quark from the strong interaction has been performed using the $2 \rightarrow 2$ tree level massive final quark matrix elements

$$f_i\bar{f}_i \rightarrow t\bar{t}$$

$$gg \rightarrow t\bar{t}.$$

The top quark has been fragmented into either a top meson or top baryon and only one of the τ 's in the decay chain is forced to decay hadronically.

In both cases above the structure function used is that of Eichten *et.al.* set 1 [EHL-84, EHL-86] with Λ_{QCD} = 200 MeV, α_s is taken to be the first order running coupling constant and $Q^2 = \frac{1}{2(m^2_{T_1}+m^2_{T_2})}$ and the W mass is 80.5 GeV.

Table 4.1.1 : $H^{\pm}$ MC Events

m_t (GeV)	$m_{H^{\pm}}$ (GeV)	Events
50	44	7747
55	45	7686
55	49	7729
60	45	7752
60	50	7713
60	54	7774
65	45	7727
65	50	7718
65	55	7650
65	59	7729
70	45	7553
70	50	7718
70	55	7710
70	60	7739
70	64	7702
71.5	66	7736

4.1.3 The UA2 Detector Simulation

It is possible to simulate the response of every detector of the UA2 apparatus to the particles of the generated event. However, only the calorimeter and OSI are simulated. This is because of the larger amount of computer time needed by some of the tracking detectors to be simulated and because the measured tracking efficiencies for electrons can be taken from UA2 data as given in Section 5.2.3.

The UA2 calorimeter simulation uses the results from extensive electron, pion, and muon test beam studies over the energy range 0.3 GeV to 150 GeV. Electron and pion beams were used for the high energy studies (E > 10 GeV) and were carried out at the CERN SPS. Because the particle showers contain many low energy particles, it is of particular importance to study the calorimeter response to such particles. Therefore, beams of electrons and pions in the energy range 0.3 < E < 4.6 GeV from the CERN PS have been used.

The energy of each showering particle is first corrected for energy smearing according to the measured energy resolution given in Section 3.3.1. Then, a correction depending on the energy is applied to account for the calorimeter's non-linear response. The particle is then allowed to penetrate the calorimeter before interacting to a depth parametrized by an exponential distribution. The energy deposited in each calorimeter compartment is parametrized from test beam results of the longitudinal shower development. The compartment energy is finally shared with adjacent cells in a 3x3 matrix according to the lateral shower development observed in test beam data.

The longitudinal shower development of pions is shown in Figure 4.1.1 where the following parametrizations have been adopted

$$\begin{aligned} < E >_{EM} &= \alpha \cdot P^{\beta} + \gamma \cdot P & \alpha = 0.34, \beta = 0.63, \gamma = 0.15 \\ < E >_{HAD} &= \alpha \cdot P^{\beta} + \gamma \cdot P & \alpha = -0.48, \beta = 0.74, \gamma = 0.97 \\ < E >_{TOT} &= \alpha \cdot P^{\beta} & \alpha = 0.97, \beta = 1.01. \end{aligned}$$

The longitudinal shower development for electrons is shown in Figure 4.1.2 where it is seen that most of the energy is deposited in the electromagnetic compartment as expected. The following parametrizations have been adopted

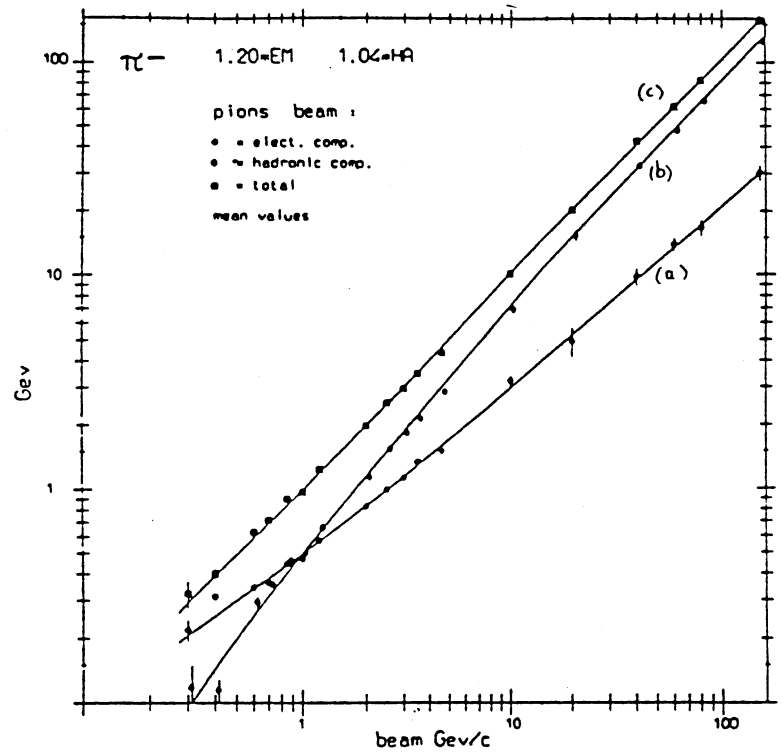

Figure 4.1.1 : The longitudinal shower development as a function of the incident pion momentum for (a) the electromagnetic compartment, (b) the hadronic compartment, and (c) the total measured energy.

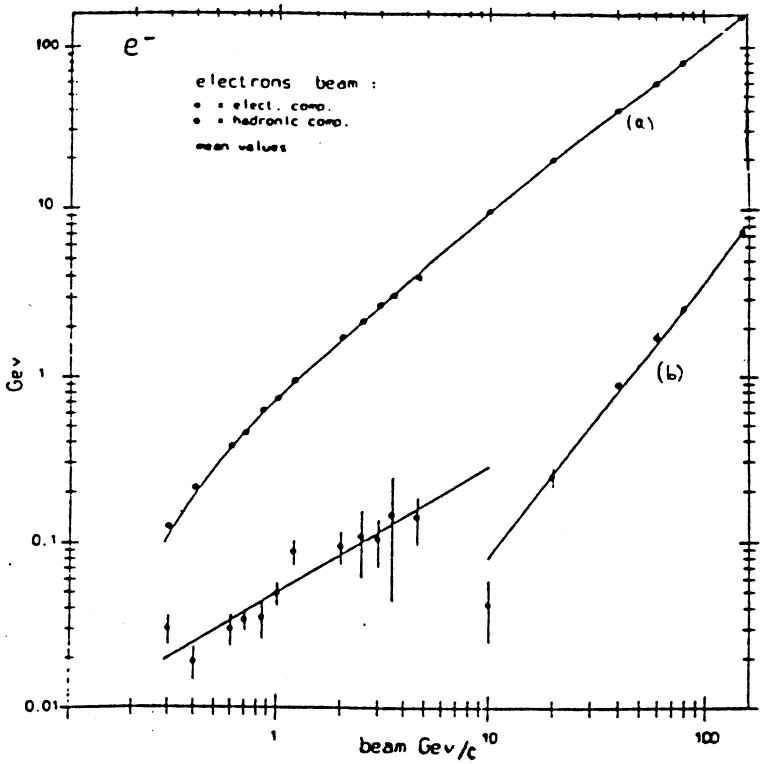

Figure 4.1.2 : The longitudinal shower development as a function of the incident electron momentum for (a) the electromagnetic compartment, and (b) the hadronic compartment.

$$< E >_{EM} = \alpha \cdot P^{\beta} + \gamma \cdot P \qquad \alpha = -0.30, \beta = -0.33, \gamma = 1.04$$

$$< E >_{HAD} = \alpha \cdot P^{\beta} \qquad \alpha = 0.05, \beta = 0.76, (P < 10\text{GeV})$$

$$< E >_{HAD} = \alpha \cdot P^{\beta} \qquad \alpha = 0.0017, \beta = 1.67, (P \geq 10\text{GeV}).$$

The compartment energies are then shared with the surrounding 8 cells according to parametrizations determined from scans of electron and pion beams across the face of the central cell in a cell nonet. Finally, local response corrections are made to the cell energies depending on the particle impact point to take into account the variation of the energy response as a function of the distance from the cell centre.

The response of the calorimeter to hadrons from τ decay has been simulated using the parametrization of the transverse energy for single pions from test beam.

In addition, the OSI response to charged particles is simulated. Firstly, the most probable energy loss of a traversing particle in the OSI is derived from

$$\epsilon_{prob} = \frac{At}{\beta^2}[B + 1.06 + 2\ln(\frac{p}{m_i c}) + \ln(\frac{At}{\beta^2}) - \beta^2 - \delta] \quad (GeV)$$

where A = 0.0766 and B = 16.66 for silicon, t is the silicon thickness in g/cm^2, δ is the density effect correction and p is the incident particle momentum [Ste-61]. The Landau energy scale is given by

$$\xi = \frac{At}{\beta^2}.$$

To include Landau fluctuations, a variable A_L is drawn randomly from a Landau distribution with the relevant energy scale ξ. The actual energy loss is then

$$\epsilon_{loss} = (A_L + 0.225) \cdot \xi + \epsilon_{prob} \quad (GeV)$$

which is subsequently converted into mips. Having the pulse height for each track in the OSI, a sum is made to obtain the total pulse height in each pad.

The detector noise is included by convoluting the pulse height with the pedestal for the given pad obtained from a randomly chosen experimental run.

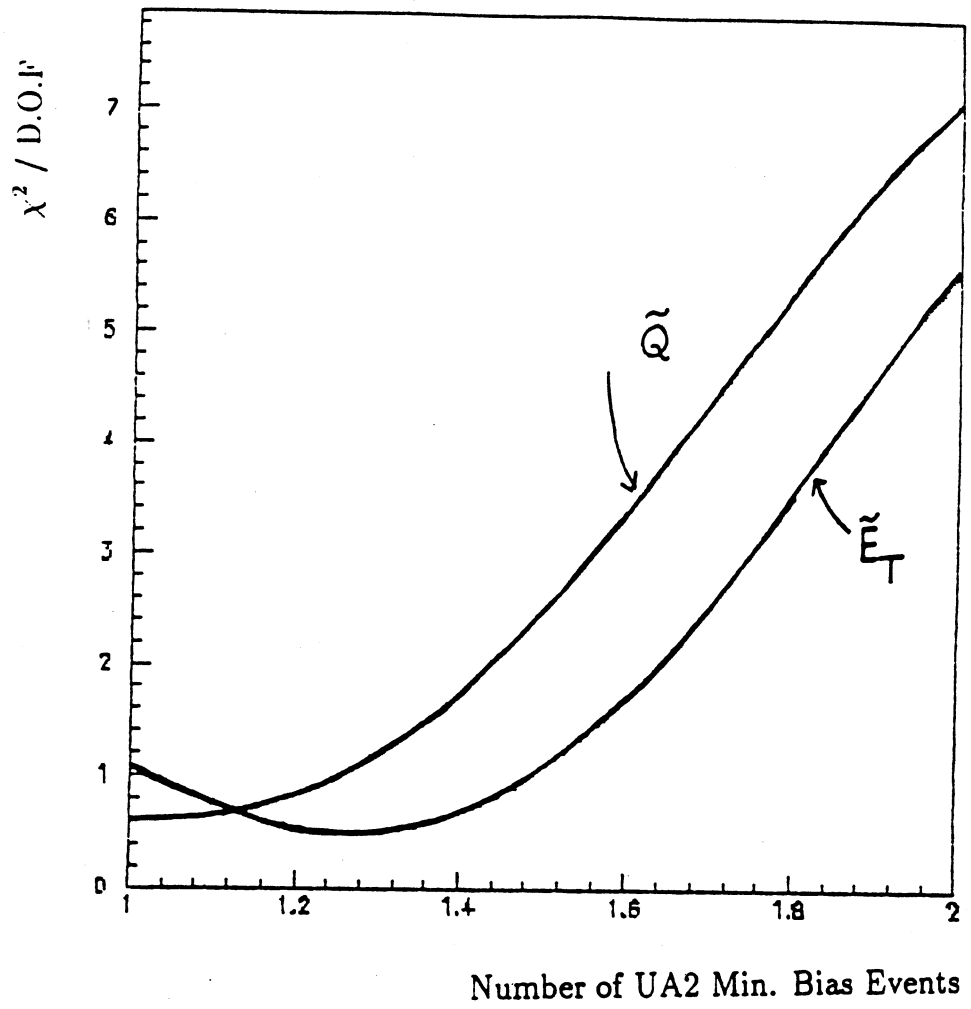

Figure 4.1.3 : Variation in agreement between $W \rightarrow e\nu_e + X$ events from a PYTHIA Monte Carlo simulation and UA2 data with the number of minimum bias events superimposed.

An additional feature which has been developed for this analysis is the ability to simulate the response of the OSI to superimposed UA2 MB events (see below). The same choice of MB events is superimposed on both the calorimeter and OSI.

4.1.4 Comparison Between Monte Carlo and UA2 Data

To tune the PYTHIA MC parameters a study has been undertaken to compare certain variables from $W \rightarrow e\nu_e + X$ events from UA2 data to a PYTHIA simulation. Firstly, $\tilde{E}_T$ is investigated where

$$\tilde{E}_T = \left(\sum_{\text{cells}} E_T^{\text{cell}} \right) - E_T^{\text{ele}}$$

and is a measure of the energy remaining in events with no hadronic jet of $E_T > 5$ GeV (coming mostly from QCD bremsstrahlung processes) after subtracting the electron energy. Therefore, $\tilde{E}_T$ is a measure of the underlying event component coming from such processes as spectator parton interactions. The underlying event component has been simulated by superimposing randomly chosen UA2 MB events onto the MC events. (The underlying event from the PYTHIA generator itself is inadequate because both the energy and charge flow are underestimated). The number of MB events so superimposed per generated event has been varied between 1 and 2 by merging samples of 1 and 2 MB events until adequate agreement between data and MC is achieved. Figure 4.1.3 plots the level of agreement expressed as a χ^2. From this diagram, it is sufficient to superimpose 1 UA2 MB event per generated event to correctly describe the average underlying event energy distribution.

In addition, with the above settings the $\sum E_T$ between data and MC is in good agreement as shown in Figure 4.1.4 and the ratio R_{01} is

$$R_{01}^{\text{data}} = 0.11 \pm 0.01$$

for UA2 data and

$$R_{01}^{\text{MC}} = 0.12 \pm 0.01$$

for MC data so that the correct population of jet clusters is observed.

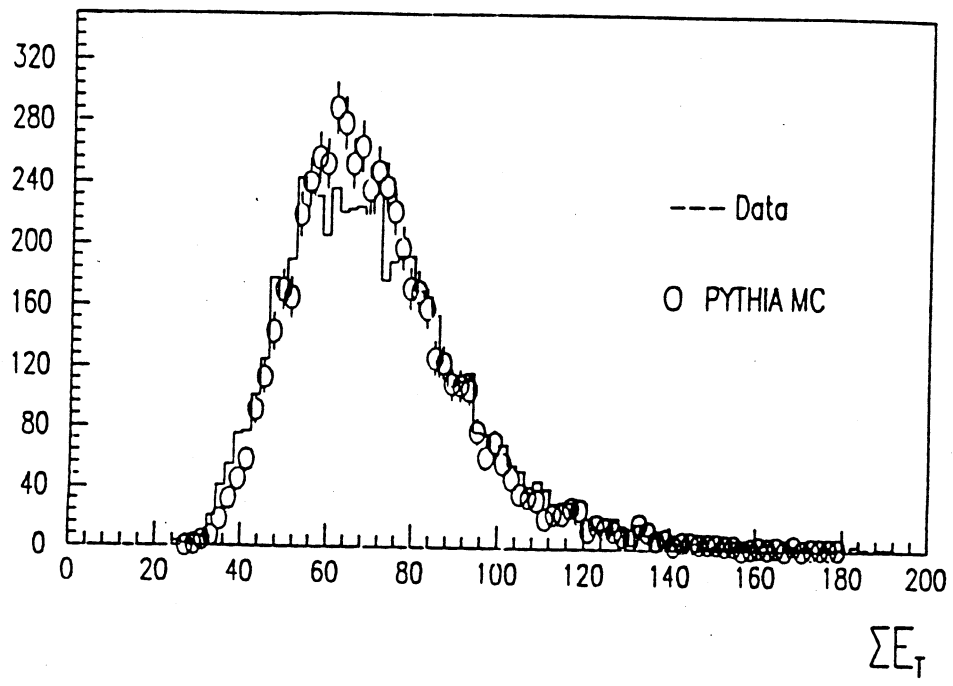

Figure 4.1.4 : $\sum E_T$ for $W \rightarrow e\nu_e$ + X events from a PYTHIA Monte Carlo simulation and from UA2 data.

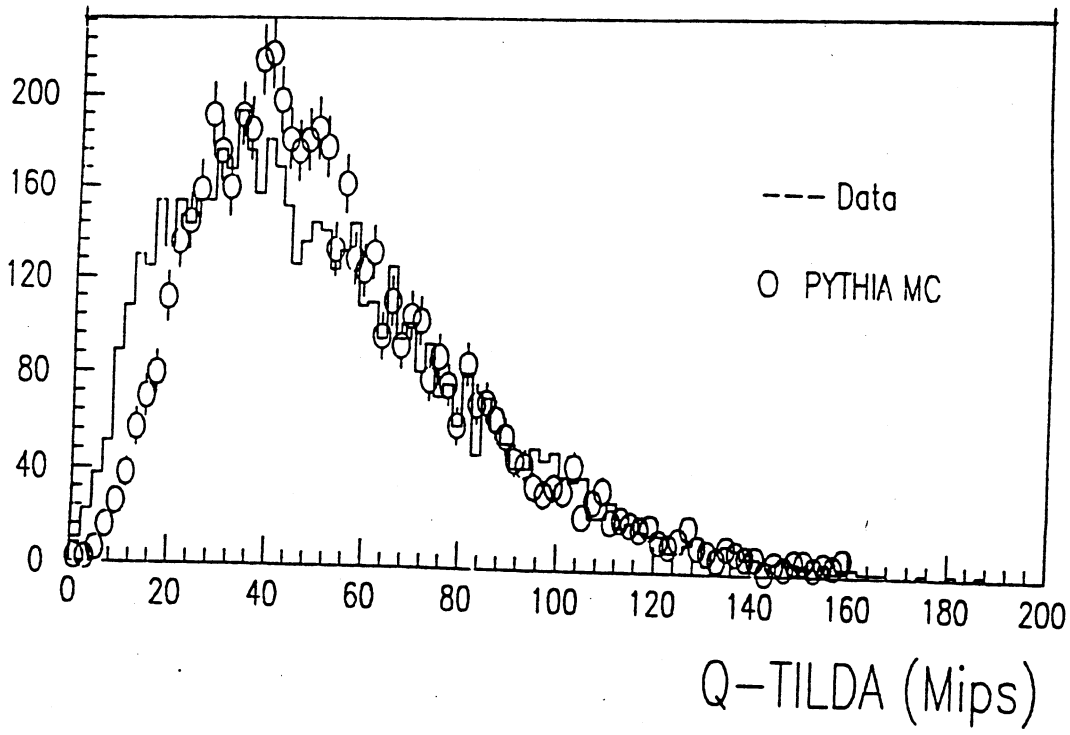

Figure 4.1.5 : $\tilde{Q}$ for $W \rightarrow e\nu_e$ + X events from a PYTHIA Monte Carlo simulation and from UA2 data.

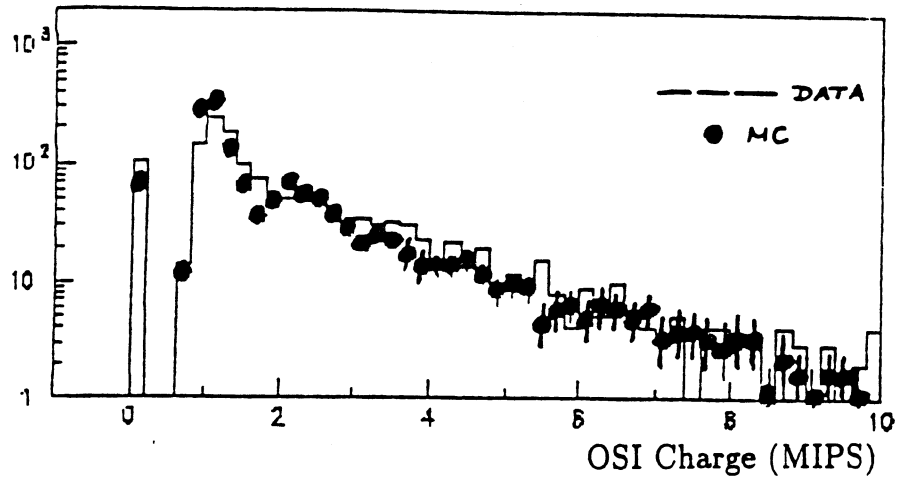

Figure 4.1.6 : The charge in a cone of radius R=0.4 for W $\rightarrow e\nu_e$ + X events from a PYTHIA Monte Carlo simulation with the superposition of 1 UA2 minimum bias event and from UA2 data.

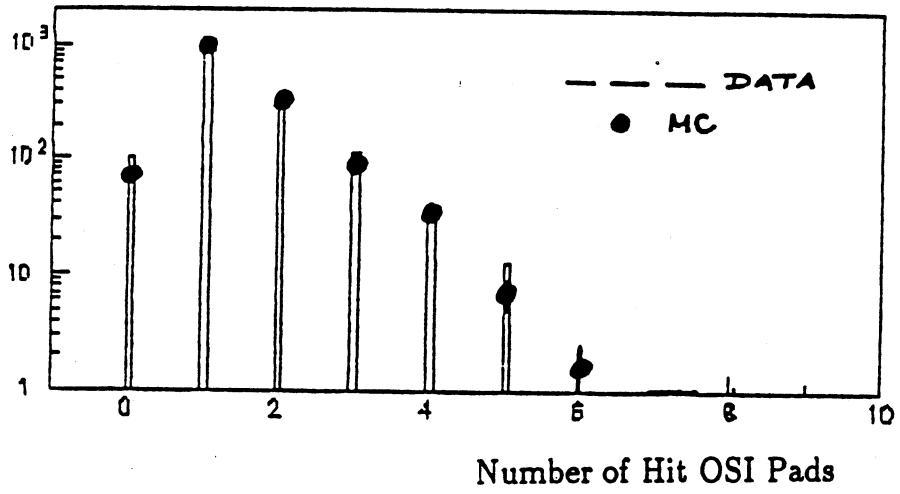

Figure 4.1.7 : The number of hit OSI pads in a cone of radius R=0.4 for W $\rightarrow e\nu_e$ + X events from a PYTHIA Monte Carlo simulation with the superposition of 1 UA2 minimum bias event and from UA2 data.

In additon, OSI charge information is used to compare $W \rightarrow e\nu_e + X$ events from data and MC. The variable $\tilde{Q}$ is defined as

$$\tilde{Q} = \left(\sum_{\text{pads}} Q^{\text{pad}} \right) - Q^{\text{ele}} \quad \text{(mips)}$$

(which is the charge equivalent to $\tilde{E}_T$) is used to study the number of MB events required to adequately describe the average charge flow in the OSI.

The same procedure as for $\tilde{E}_T$ is used to identify the number of MB events required and as for the $\tilde{E}_T$ measurement one MB event is needed to correctly reproduce the average charge flow as shown in Figure 4.1.3. Figure 4.1.5 compares the $\tilde{Q}$ distribution for $W \rightarrow e\nu_e + X$ events from MC and data where it is seen that a good agreement exists.

Further comparison between MC and UA2 data is performed by adding up the charge and number of hit OSI channels within a cone. The cone axis is defined as being along the candidate electron track and its radius is given by

$$R = \sqrt{(\Delta\eta)^2 + (\Delta\phi)^2}$$

where η is the pseudorapidity and ϕ is the angle in the azimuthal plane. Figure 4.1.6 and Figure 4.1.7 show the charge and number of hit channels for MC and data for R=0.4. The radius R has been varied between 0.1 and 0.6 and such agreement persists.

4.2 The EKS Monte Carlo Simulation

The calculation of the MC acceptances for $W \rightarrow l\nu_l + X$ where l is either an electron or τ has been performed by using events produced by the QCD MC of Ellis *et.al.*, called the EKS MC [Ell-85, Ber-89a, Ber-89b], and passing the generated events through the UA2 detector simulation as described in Section 4.1.3. To leading order the production of an IVB is described by the Drell-Yan mechanism [Dre-70, Dre-71], however, the strong interaction accounts for corrections, such as initial and final state radiation, resulting in hadronic jets produced in association with the IVB. The ratio of W + 1jet to W + 0jet events is measured to be 0.1403 ± 0.0104 for jets with $E_T > 10$ GeV [Jak-90].

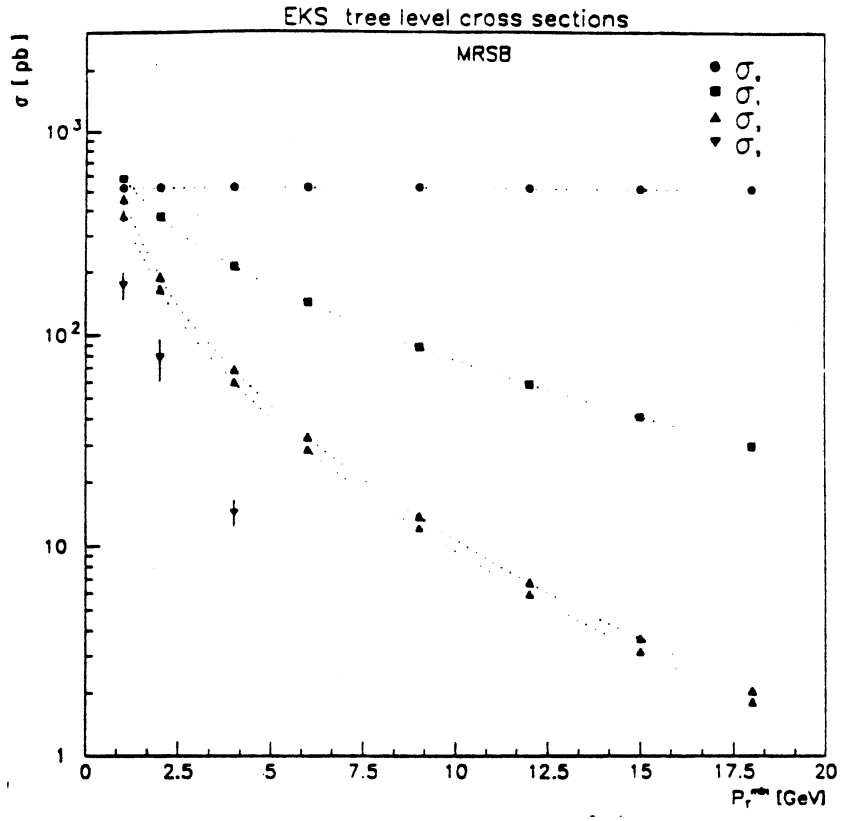

Figure 4.2.1 : The EKS tree-level cross-sections as a function of the cut-offs p_T^{min} and ω_{min}. The ω_{min} dependence is indicated by the band for σ_2 and corresponds to a variation of ω_{min} between 10° and 20°.

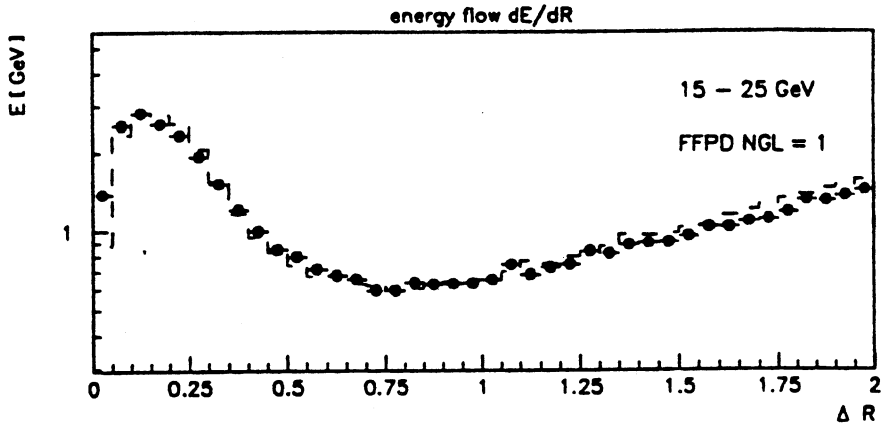

Figure 4.2.2 : The energy flow, dE/dΔR, for UA2 data and EKS MC for jet energies in the range 15 to 25 GeV.

The matrix elements for all tree level diagrams up to order α_s^3 have been calculated and are implemented into the EKS MC. Since only tree level diagrams are considered, the infrared and collinear divergences, which show up in higher order tree-level diagrams are regularized by imposing the following parton-level cuts in the MC simulation :

- Require the p_T of each outgoing parton (quark or gluon) to be greater than some minimum p_T^{min}, (p_T^{min} = 12 GeV).
- Require the opening angle between each pair of outgoing partons (quarks or gluons) to be greater than some minimum ω_{min} (only relevant to configurations with at least two final state jets, $\omega_{min} = 20°$).

The angular cut controls the collinearity associated with final state radiation configurations while the minimum p_T requirement prevents the emission of partons which are arbitrarily soft and collinear with the incoming partons. Therefore, the initial and final state partons are separated in phase space and perturbative cross-sections are finite. The dependence of the cross-section on the cut-off parameters is shown in Figure 4.2.1. As expected, there is a strong dependence of the cross-section σ_i ($i \geq 1$ jet) on p_T^{min} as well as a divergent behaviour in the region of small p_T^{min} values. The dependence on ω_{min} is found to be smaller and is characterized by the band for σ_2 which corresponds to a variation of ω_{min} from 10° to 20°.

Since the simulation is performed in the $\overline{MS}$ renormalization scheme, only structure function parametrizations extracted in this scheme are used in order to work in a consistent framework. The Martin *et.al.* (MRSB) [MRS-88, MRS-89] structure function set 1 is chosen with Λ_{QCD} = 200 MeV. The Q^2 scale is set equal to the W mass which is taken to be 80.5 GeV.

In the EKS MC only the exact matrix element calculation and the decay of the W into lepton and neutrino is performed. The conversion of the outgoing quarks and gluons from the hard-scattering process into hadrons is performed according to the independent fragmentation model of Field and Feynman [Fie-78], in which each outgoing parton hadronizes independently from the others and from the rest of the event.

The Field-Feynman fragmentation model can be tuned to correctly reproduce the experimental energy flow distributions observed for W + jet events in the UA2 experiment. To do so gluon bremsstrahlung has been added to

the Field-Feynman model [Dar-83, Jak-90]. In this modification a gluon is radiated with an energy in the interval

$$\frac{1}{c} E_0 < E_{gluon} < \frac{1}{2} E_0$$

where E_0 is the parton energy. The energy spectrum is generated according to the 1/E bremsstrahlung spectrum and the gluon is radiated with an angle between α_{min} and α_{max}. In addition to the parameters c, α_{min} and α_{max}, the number of gluons radiated, NGL, is a parameter of the model. After the splitting, the outgoing partons are fragmented independently by using the Field-Feynman prescription with an average hadron p_T of 0.4 GeV with respect to the jet axis. The parameter values which describe adequately and simultaneously

- the cluster radius distribution,
- the ratio between the cone and cluster energy, and
- the energy flow around the jet axis, $dE/d\Delta\phi$ and $dE/d\Delta R$, where $\Delta\phi$ is the azimuthal and $\Delta R = \sqrt{(\Delta\phi)^2 + (\Delta\phi)^2}$ the radial distance to the jet axis

are $\alpha_{min} = 5°$, $\alpha_{max} = 30°$, NGL = 1 and the parameter c is chosen so that the minimum energy of the radiated gluon is 7 GeV. Figure 4.2.2 shows the energy flow $dE/d\Delta R$ for UA2 data and EKS MC generated events for a jet energy in the range 15 to 25 GeV while Figure 4.2.3 shows the corresponding cluster radius distribution for jets in the energy range 25 to 35 GeV. In both cases satisfactory agreement between MC and data is observed.

In addition, the underlying event is not generated by the EKS MC but is simulated by adding real UA2 MB events to the generated hard-scattering process. The underlying event is well-simulated by superimposing two independent UA2 MB events per generated event. The superposition of two events accounts for the fact that the underlying event activity in W events is found to be higher than in MB events [Dar-86, Dar-87, Kur-89]. The number of MB events superimposed onto the EKS MC is higher than in the case of the PYTHIA MC above because in the latter case there is also an inherent underlying event produced by the generator which is not produced in the EKS MC. Figure 4.2.4 shows the underlying event contribution to the

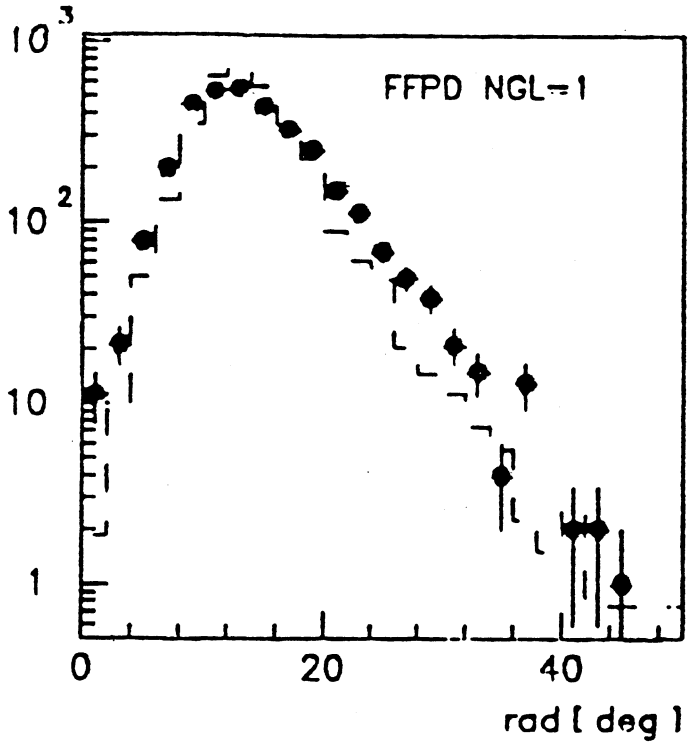

Figure 4.2.3 : The cluster radius distribution for UA2 data and EKS MC for jets in the energy range 25 to 35 GeV.

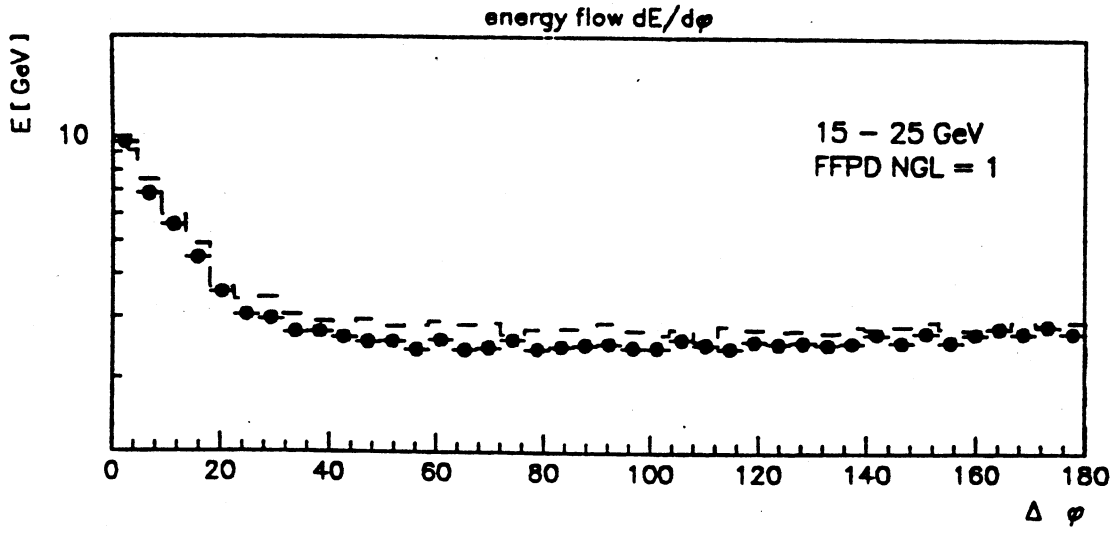

Figure 4.2.4 : The underlying event contribution to the energy flow, $dE/d\phi$, for jets in the energy range 15 to 25 GeV. The energy from the EKS MC is given by the dashed curve while that from UA2 data is represented by the points.

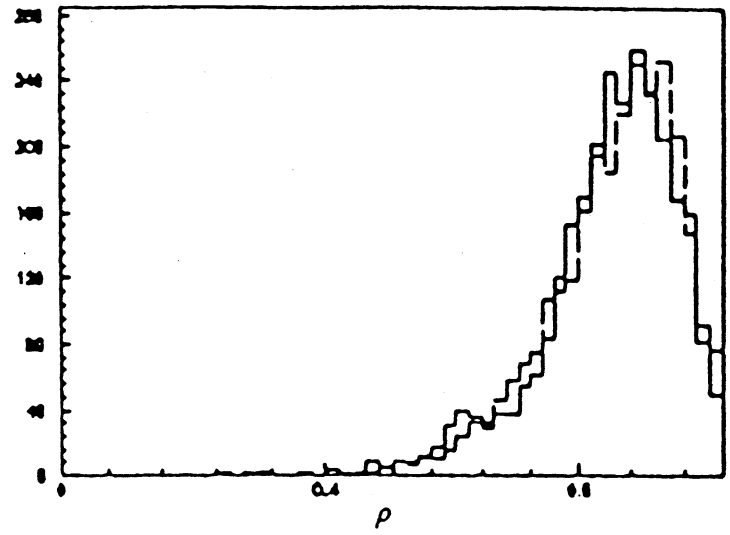

Figure 4.2.5 : Comparison of the τ profile distribution from $W \rightarrow \tau\nu_\tau$ simulated events from PYTHIA (dashed line) and EKS (full line).

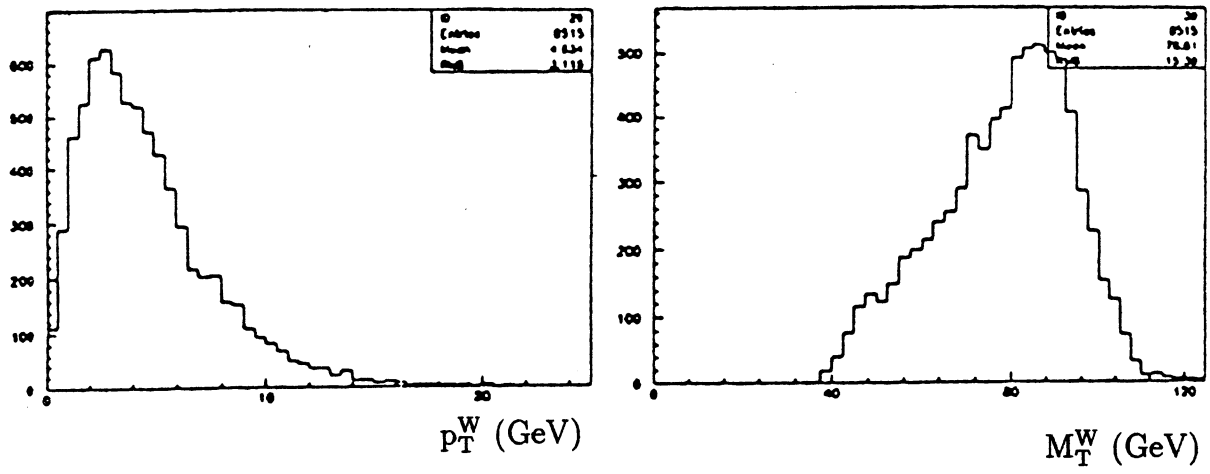

Figure 4.2.6 : The PYTHIA MC p_T^W (right) and M_T^W (left) distributions.

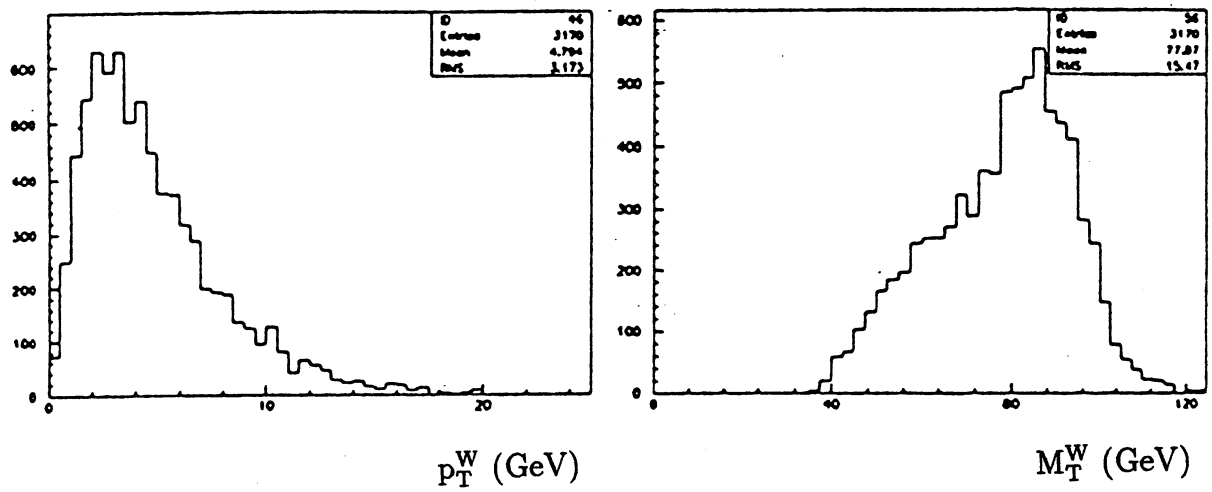

Figure 4.2.7 : The EKS MC p_T^W (right) and M_T^W (left) distributions.

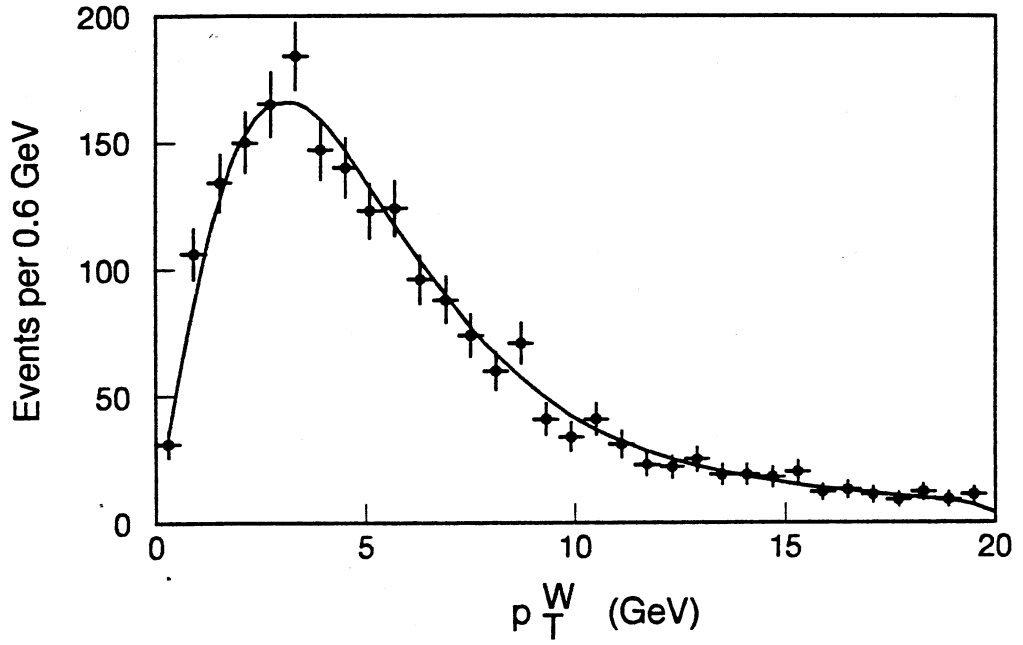

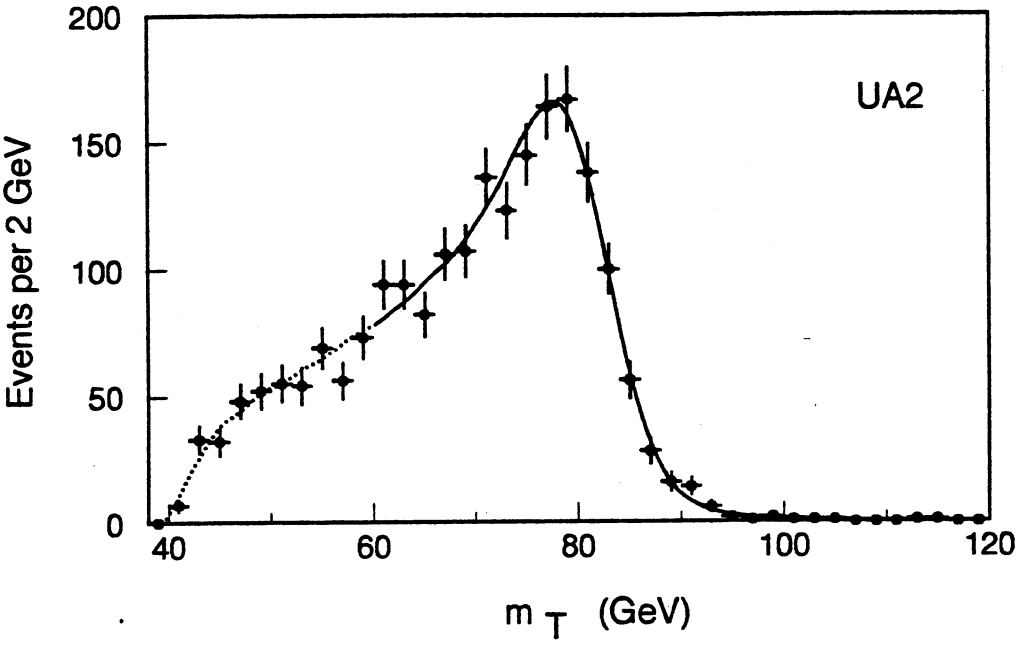

Figure 4.2.8 : The p_T^W (top) and M_T^W (bottom) distributions from UA2 data.

energy flow $dE/d\Delta\phi$ for the simulated event (hard scattering + 2 UA2 MB events + UA2 detector simulation) and for UA2 data.

The EKS simulation, however, represents only a partial calculation of the IVB total cross-section because loop diagrams and tree-level diagrams not satisfying the p_T^{min} and ω_{min} requirements are not accounted for. Also, diagrams of higher order than α_s^3 are not included. The size of these missing contributions is given by multiplicative correction factors called K-factors [Ell-85].

The total cross section to α_s^2 is

$$\sigma^{[2]} = \sigma_0 K_0 + \sigma_1 K_1 + \sigma_2 K_2$$

where σ_i are the tree level cross sections for the production of an IVB accompanied by i partons and K_i are the K-factors defined as

$$K_i = \frac{\tilde{\sigma}_i}{\sigma_i} = 1 + \sum_{k=i+1} \frac{(\alpha_s)^k a_{ik}}{\sigma_i}$$

where $\tilde{\sigma}_i$ is the generic topological cross section for production of an IVB accompanied by i partons and the a_{ik} are defined in the perturbative expansion

$$\tilde{\sigma}_i = \sigma_i + \sum_{k=i+1} (\alpha_s)^k a_{ik}.$$

The K-factors used are $K_2 \equiv 1.0$, $K_1 = 1.27$ and $K_0 = 1.15$.

Finally, the simulation of $W \rightarrow \tau\nu_\tau$ events by EKS and PYTHIA are shown to be in agreement. Using the respective schemes as described in Section 4.1 for PYTHIA and in this section for EKS, Figure 4.2.5 depicts the ρ distribution for the τ from the two different MC's. In addition, Figures 4.2.6 and 4.2.7 show the transverse momentum, p_T^W, and the transverse mass, M_T^W, of the W calculated from $W \rightarrow e\nu_e$ simulated events with PYTHIA and EKS. Table 4.2.1 compares certain parameters from the distributions from where good agreement is seen to exist between PYTHIA and EKS. Figure 4.2.8 shows the corresponding distributions for UA2 data.

Table 4.2.1 : EKS and PYTHIA MC Parameters

	EKS	PYTHIA
$< p_T^W >$ (GeV)	4.634 ± 0.053	4.794 ± 0.056
σ_T^W (GeV)	3.118	3.173
$< M_T^W >$ (GeV)	78.61 ± 0.27	77.67 ± 0.26

Chapter 5

Measurement of the Electron - Tau Universality

5.1 Introduction

In this chapter a measurement of the ratio of branching fractions

$$R_W = \frac{Br(W \rightarrow \tau\nu_\tau)}{Br(W \rightarrow e\nu_e)} \quad (5.1)$$

is presented [UA2-91a, UA2-92, Cav-90, Cav-91a, Cav-91b, APS-91, EPS-91c, SSS-91, Mor-92f]. Neglecting lepton masses relative to the W mass, this quantity is the ratio of the squares of the charged current couplings of the τ and electron to W bosons so that

$$R_W = \frac{(g_\tau^W)^2}{(g_e^W)^2}$$

(see Section 2.2). The measurement of R_W thus provides a direct test of the equality of these couplings.

In terms of quantities which are measured from data or obtained by Monte Carlo (MC), the cross-section times branching fraction for the process $W \rightarrow \tau\nu_\tau$ is written as

$$\sigma_W \text{ x } Br(W \rightarrow \tau\nu_\tau) = \frac{N_\tau}{(1+f_\tau)\epsilon_\tau\eta_\tau Br(\tau \rightarrow h\nu_\tau)L} \quad (5.2)$$

where f_τ represents the fraction of τ events coming from other sources (e.g. $Z \rightarrow \tau^+\tau^-$), ϵ_τ and η_τ are the $W \rightarrow \tau\nu_\tau$ event acceptances of the analysis cuts measured from the data and MC, respectively, $Br(\tau \rightarrow h\nu_\tau)$ is the branching ratio of the τ's decaying to any hadronic state h, and L is the total integrated luminosity. The estimated number of events in the sample having final state τ 's with $\rho > 0.75$ after all analysis cuts and after subtracting events in which the leading cluster is electromagnetic is given by

$$N_\tau = N_0 - N_{BKD} \qquad (5.3)$$

where N_0 is the total number of events remaining after the cuts and subtraction and N_{BKD} is the estimated remaining number of background events which do not contain τ's from $W \rightarrow \tau\nu_\tau$. The background event contribution comes from various sources and can be expressed as

$$N_{BKD} = N_{HALO} + N_{RES} + N_{IVB} + N_{JJ} \qquad (5.4)$$

where N_{HALO} is the number of beam-halo events, N_{RES} is the number of residual events with identified final state electrons, N_{IVB} is the number of events from IVB decay accompanied by jets, and N_{JJ} is the number of multijet events, comprised mostly of dijets, which pass the selection cuts and enter into the sample. The τ acceptance ϵ_τ is decomposed as

$$\epsilon_\tau = \epsilon_o \kappa_\tau \qquad (5.5)$$

where κ_τ is the τ selection efficiency of the requirement that at least one charged particle track be in a 10° cone around the cluster axis defined as the line from the vertex to the energy-weighted barycentre of the calorimeter cluster and where

$$\epsilon_o = \epsilon_{VTX}\epsilon_{VETO}\epsilon_{MB}\epsilon_{TOF} \qquad (5.6)$$

where each efficiency corresponds, respectively, to the vertex, VETO detector, minimum bias (MB), and TOF detector requirements (see Section 5.3).

For the process $W \rightarrow e\nu_e$ the analogous formula is

$$\sigma_W \times Br(W \rightarrow e\nu_e) = \frac{N_e}{(1+f_e)\epsilon_e\eta_e L} \qquad (5.7)$$

where f_e is the fraction of events with final state electrons coming from other sources (e.g. $W \rightarrow \tau\nu_\tau, \tau \rightarrow e\nu\overline{\nu}$), ϵ_e and η_e are defined analogously to ϵ_τ and η_τ and N_e is the estimated number of $W \rightarrow e\nu_e$ events in the sample. The efficiency ϵ_e can be written as

$$\epsilon_e = \epsilon_o \kappa_e \tilde{\epsilon}_e \qquad (5.8)$$

where κ_e is the electron tracking efficiency of requiring at least one charged particle track in a 10° cone around the cluster axis and

$$\tilde{\epsilon}_e = \epsilon_{EM}\epsilon_{PS}\epsilon_{\chi^2} \qquad (5.9)$$

where ϵ_{EM} is the electron detection efficiency of the calorimeter, ϵ_{χ^2} is the efficiency of a cut on the electron quality variable, $P(\chi^2)$, and ϵ_{PS} is the preshower efficiency. The selection criteria are discussed in the text below.

From Equations (5.2) and (5.7) the ratio of branching fractions in Equation (5.1) can be written as

$$R_W = \frac{1}{\Omega}\frac{\tilde{N}_\tau}{\tilde{N}_e} \qquad (5.10)$$

where

$$\Omega \doteq \frac{\eta_\tau Br(\tau \rightarrow h\nu_\tau)}{\eta_e}\frac{\kappa_\tau}{\kappa_e} \qquad (5.11)$$

$$\tilde{N}_\tau = \frac{N_\tau}{1+f_\tau} \qquad (5.12)$$

and

$$\tilde{N}_e = \frac{N_e}{(1+f_e)\tilde{\epsilon}_e} \qquad (5.13).$$

5.2 Particle Identification

5.2.1 Calorimeter Clusters

Clusters of deposited energy are formed in the calorimeter by joining all cells with an energy greater than 400 MeV and sharing a common edge. The

energy-weighted barycentre of the cluster in the polar coordinate θ and in the azimuthal coordinate ϕ is given by

$$\theta_{\rm clus} = \frac{\sum_i E_i \theta_i}{\sum_i E_i}$$

and

$$\phi_{\rm clus} = \frac{\sum_i E_i \phi_i}{\sum_i E_i},$$

respectively, where the sum is over all calorimeter cells defining the cluster.

Clusters with a small lateral size and leakage into the hadronic compartments consistent with a shower from a single isolated electron as measured in test beams are marked as electromagnetic and are characteristic of electron and photon showers. Clusters not marked as electromagnetic are assigned to jets from the fragmentation of quarks and gluons. Hadronic τ decays are also marked as non-electromagnetic.

The condition that the cluster has a small lateral size is applied by calculating the cluster radii R_θ and R_ϕ defined as

$$R_\theta^2 = \frac{\sum_i (\theta_i - \theta_{\rm clus}) E_i}{\sum_i E_i}$$

$$R_\phi^2 = \frac{\sum_i (\phi_i - \phi_{\rm clus}) E_i}{\sum_i E_i}$$

and represent the energy-weighted rms deviations of the θ and ϕ values of the cell centres for all cells in the cluster. In terms of cell units the average cluster radius in the central calorimeter is

$$\overline{R}_\theta = \frac{R_\theta}{10^\circ}$$

and

$$\overline{R}_\phi = \frac{R_\phi}{15^\circ}.$$

The condition applied, $R_\theta,\ R_\phi < 0.6$, is fully efficient for isolated electrons as deduced from testbeam.

The hadronic leakage requirement, defined as

$$\xi' = 1 - \frac{E^{\rm EM}}{E^{\rm EM+HAD}}$$

depends to a large extent on the energy fraction carried by photons. The leakage must satisfy the parametrization

$$\xi' < f \cdot (0.023 + 0.034 \ln E^{EM+HAD})$$

where f = 1.5 for cells 1 to 9 of the central calorimeter and f = 3.0 for cells 1 and 10.

To exclude calorimeter clusters with impact points near the edges of the central calorimeter where the showers are not well-contained and away from the shortened edge cells of the central calorimeter, only calorimeter clusters whose axis is in the pseudorapidity interval $|\eta| < 0.76$ are accepted.

5.2.2 Electron Identification

In measuring the electron-τ universality an accurate particle identification is necessary to distinguish the signal from any background. As a first step that means identifying electrons and non- τ jets. Figure 5.2.1 shows the characteristic response of the UA2 detector to the passage of various particles. Such differences in response are exploited to identify particles.

An electron is characterized by a single charged track in the central detector giving rise to a pulse height in both silicon layers characteristic of a minimum ionizing particle (mip). Figure 5.2.2 shows the OSI pulse height for electrons from W-decay. The electron gives rise to a mostly electromagnetic shower in the calorimeter where both the lateral and longitudinal spreads are small. A large signal is also expected in the preshower component of the SFD. Figure 5.2.3 shows a transverse view of the SFD depicting the hit fibres in the tracking and preshower layers for electrons from W candidates. The corresponding pulse heights in the preshower layers is illustrated in Figure 5.2.4.

A single charged hadron (e.g. $\pi^{\pm}$) also gives rise to a single 1 mip track in each silicon layer but the SFD preshower signal is small as a shower is not initiated in the lead. Also, the calorimeter shower is expected to be predominantly hadronic.

Another background is conversions which refers to a converted photon γ, or neutral pion π°. If the conversion occurs in the layer of lead before the SFD preshower, as it does in Figure 5.2.1, the signal consists of a large preshower pulse height plus a shower in the calorimeter characteristic of electrons and

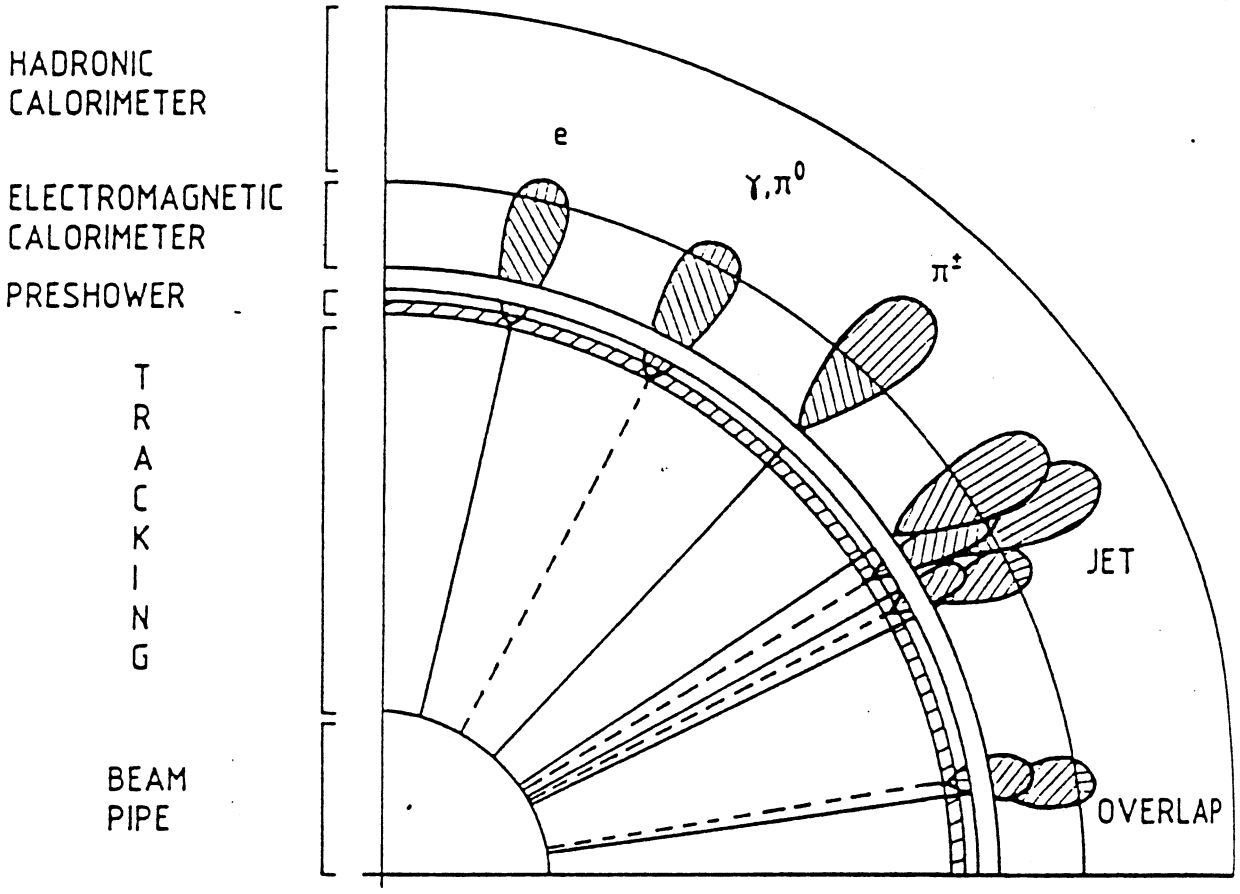

Figure 5.2.1 : Response of the UA2 subdetectors to the passage of different particles. A solid line in the tracking region represents the track from a charged particle while a broken line the undetected trajectory of a neutral particle.

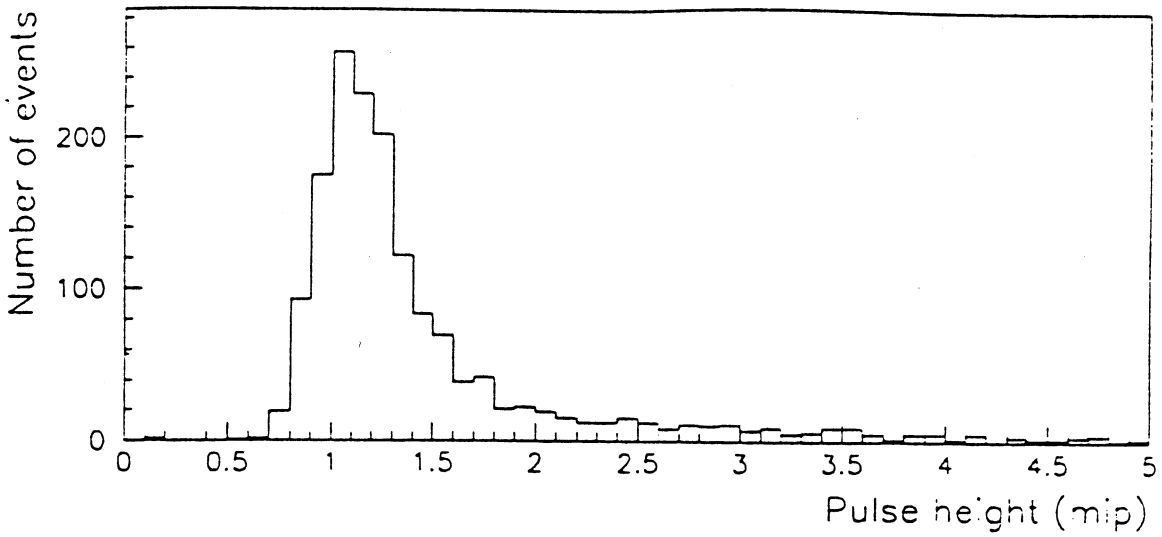

Figure 5.2.2 : The OSI pulse height for W electrons.

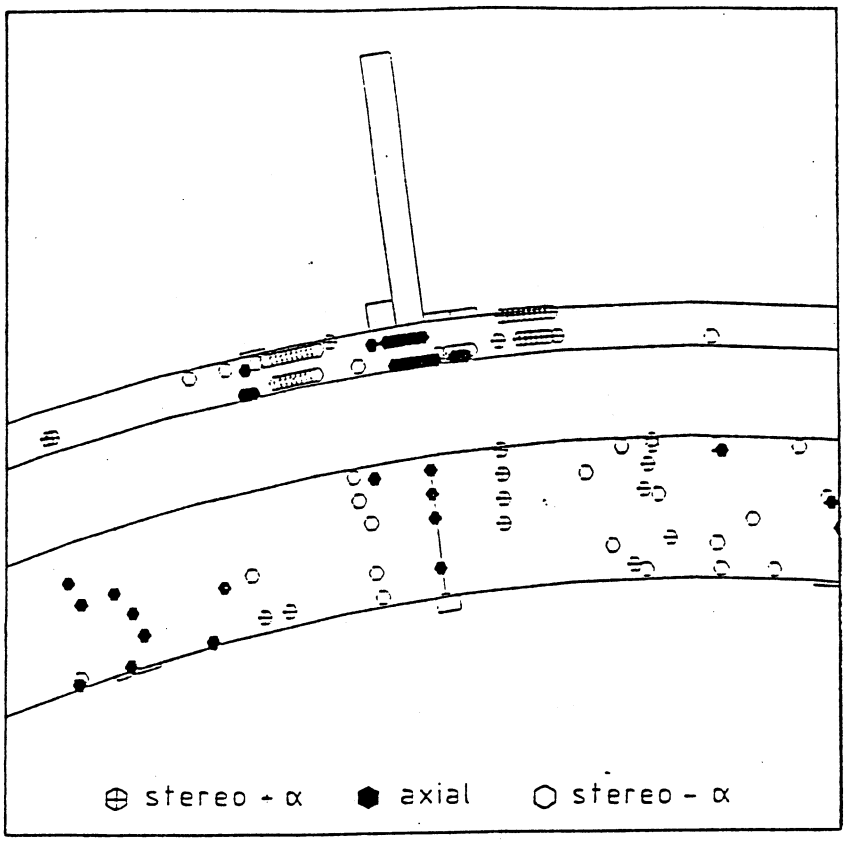

Figure 5.2.3 : A transverse view of the SFD showing hit fibres in the tracking and preshower layers for electrons from W candidates.

is not preceeded by a track. Such a combination rejects this conversion background. However, if the conversion takes place in an earlier part of the detector the pattern recognition cannot distinguish the two closely-separated tracks because of the absence of a magnetic field in UA2. The extrapolated track then points to a preshower and calorimeter response characteristic of electrons. The silicon layers, however, are used to reject such background as either a zero or two mip signal is expected (depending on the radius at which the conversions occur), and so a cut on the pulse height from the silicon layers rejects such background.

In addition, there exists a background source consisting of an overlap of a γ or π^0 with a low energy charged hadron. The hadron gives a single charged track while not depositing enough energy in the calorimeter to spoil the electromagnetic shower. The conversion of the γ or π^0 in the layer of lead leads to a large preshower signal. However, a cut on the match between the extrapolated track and preshower signal allows a high rejection against this background.

Below is a list of cuts in the central detector used for electron identification in this analysis after the initial selection of electron candidates using the calorimeter cluster information.

- Track – Preshower : The tracking and preshower sections of the SFD are used to match candidate electron tracks with the position of electromagnetic preshowers with resolution $\sigma_{r\phi} = 0.4$ mm in the rϕ plane and $\sigma_z = 1.1$ mm along the beam direction. The quality of the track-preshower match is defined by $d_\sigma^2 = (\frac{\Delta_{r\phi}}{\sigma_{r\phi}})^2 + (\frac{\Delta_z}{\sigma_z})^2$ where $\Delta_{r\phi}$ and Δ_z are the measured displacements between the track and preshower positions. Accidental overlaps in space between photon showers and charged tracks give large values of d_σ^2 while electron candidates are required to have $d_\sigma^2 < 25$. Figure 5.2.5 shows the distribution of the track-preshower variable d_σ^2 for electrons from W candidates. In addition, for electron candidates it is required that each fibre layer in the preshower cluster have a charge in excess of twice that expected from a minimum ionizing particle.

- Quality : The longitudinal and lateral profiles of the electromagnetic showers, given the impact point and direction of the track , are required to be consistent with those expected for a single isolated electron inci-

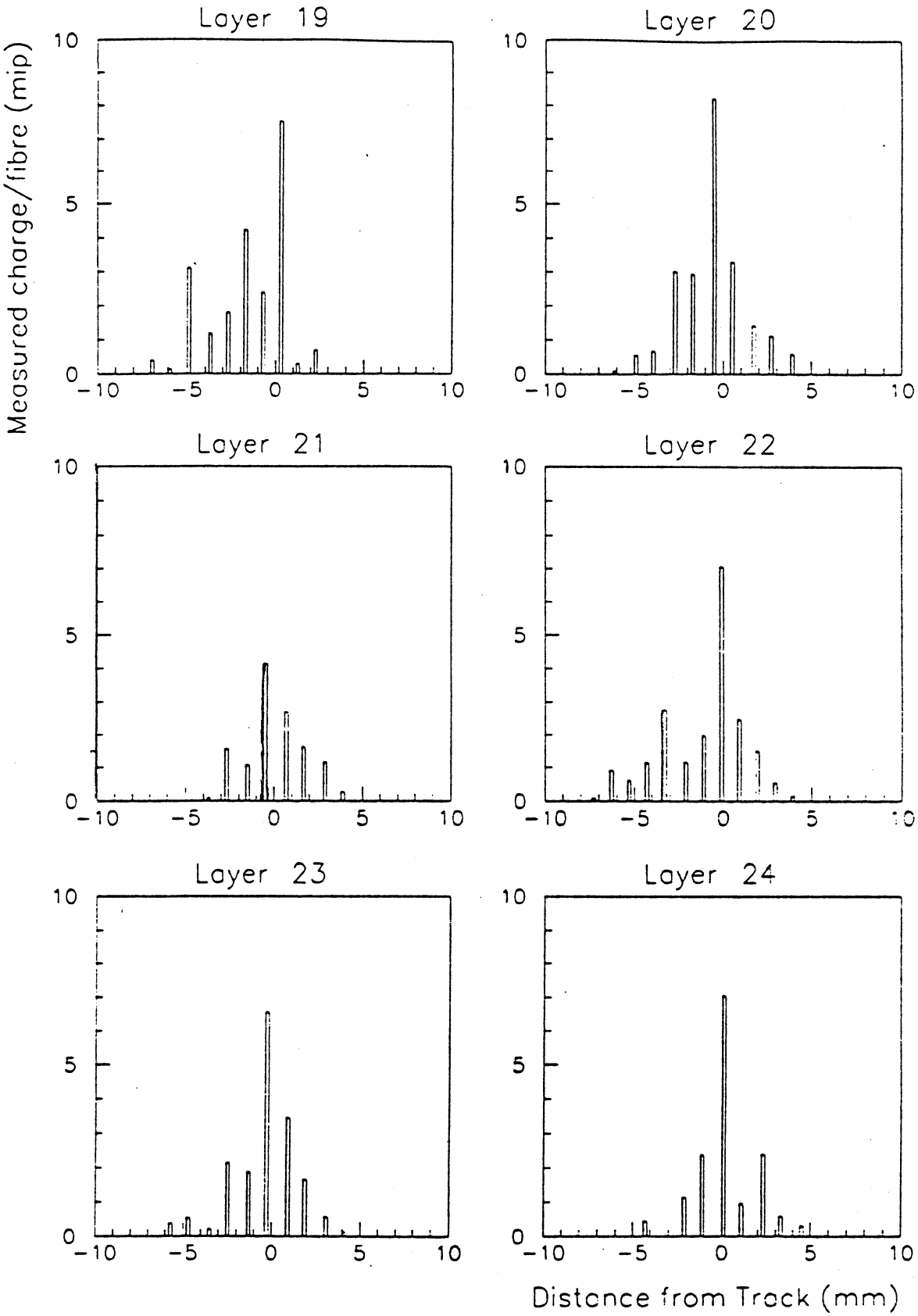

Figure 5.2.4 : The SFD preshower pulse heights for a W electron.

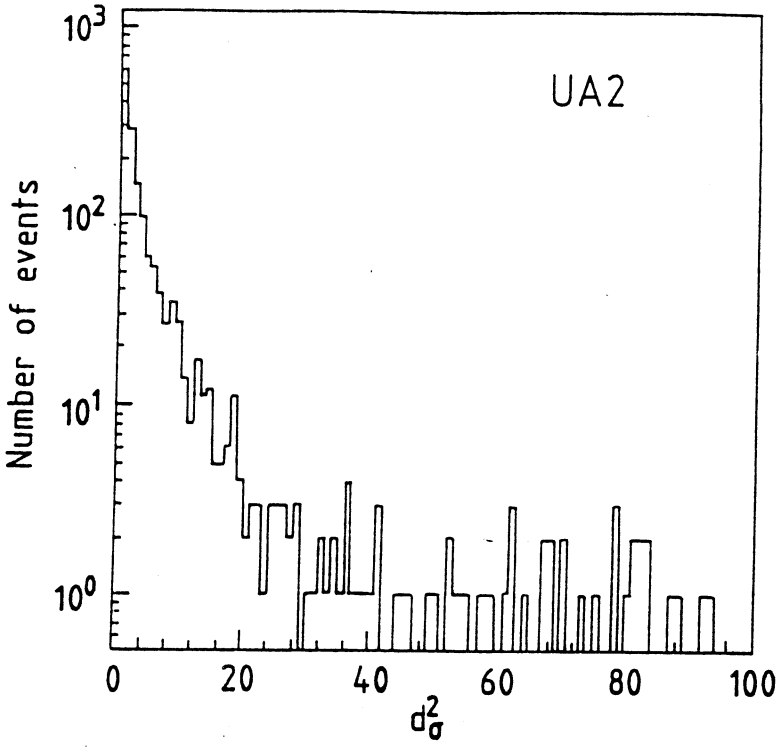

Figure 5.2.5 : Distribution of the track-preshower match variable d_σ^2 for a sample of electrons from W candidates.

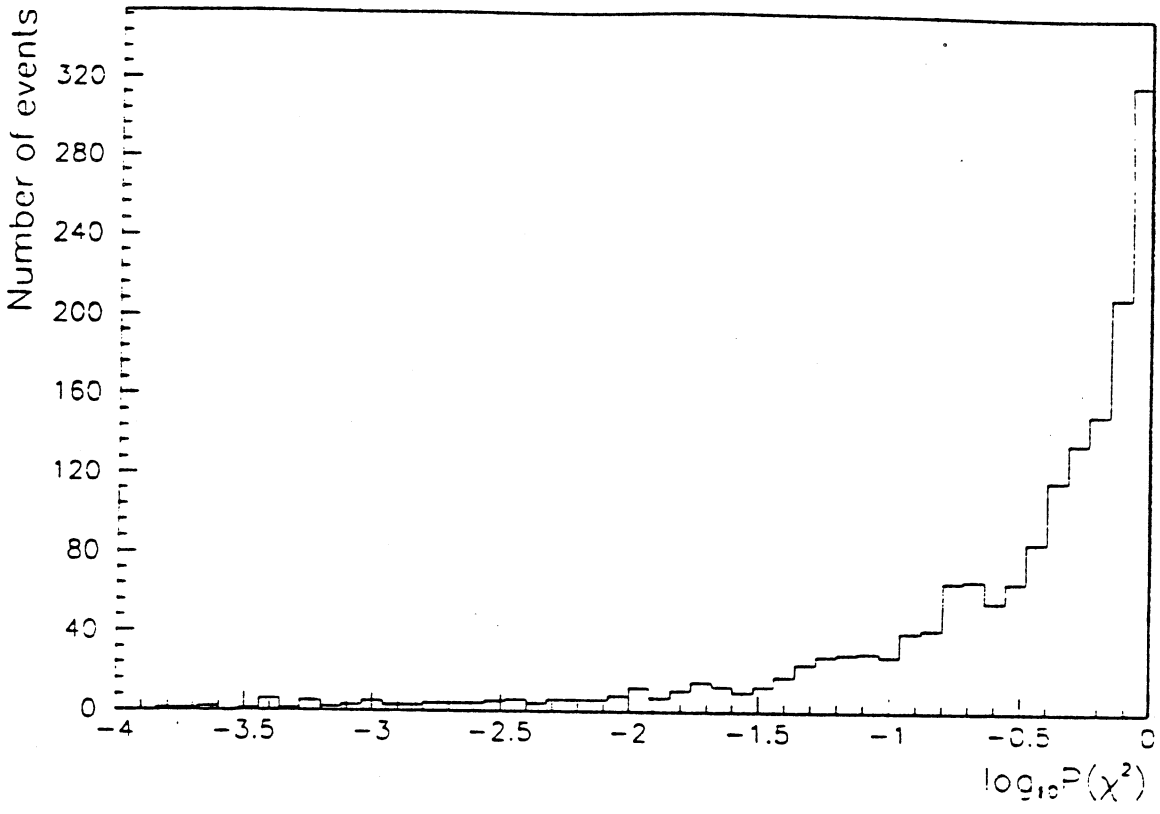

Figure 5.2.6 : Distribution of the electron quality variable $P(\chi^2)$ for a sample of electrons from W candidates.

dent along the track direction as determined in the test beam. From the observed and expected quantities a χ^2 test for the electron hypothesis $P(\chi^2)$ is defined. $P(\chi^2)$ is not a true χ^2 probability because the experimental distributions have significant non-Gaussian tails. The distribution of $P(\chi^2)$ for electrons from W decay is shown in Figure 5.2.6. A cut $P(\chi^2) > 10^{-4}$ is made.

The main loss in efficiency is for electrons impinging on the central calorimeter near an inter-cell boundary which then produces a larger leakage into the hadronic compartment. To avoid this, electron tracks having an impact point on the calorimeter within $\Delta x \leq 5$ mm and $\Delta\phi \leq 5°$ to the cell boundary are not counted.

The electron's detected energy is summed in a small number, (typically two or three), of calorimeter cells which are assigned to the electron. Energy corrections are applied according to the precise electron direction and impact point in the calorimeter based on data obtained from testbeam electrons. The corrected energy is used together with the direction given by the tracking detectors to define the electron p_T.

5.2.3 Electron Detection Efficiencies

- Calorimeter : The efficency for finding an electromagnetic cluster from an electron in the calorimeter is measured using electron test beam data with a range of impact points and directions. The average efficiency is evaluated by weighting the efficiencies for each effective vertex position according to the vertex position distribution expected at the Collider. The average efficiency for finding an electromagnetic cluster in the central calorimeter is $\epsilon_{EM} = (96.5 \pm 1.1)$ % [Woo-91].

- Track – Preshower : The track-preshower match efficiency, including a charge cut of 2 mips per projection, is $\epsilon_{PS} = (87.9 \pm 2.0)$ % and (83.2 ± 2.0) % for 1988/89 and 1990, respectively, as calculated from electrons from W decay [Woo-91].

- Quality : The quality factor $P(\chi^2)$ cut has an efficiency of (96.9 ± 1.2) % for 1988/89 and (95.2 ± 1.5) % for 1990 [Woo-91].

The total electron efficiency $\tilde{\epsilon}_e$ is then (82.2 $\pm$ 2.3) % and (76.3 $\pm$ 2.4) % for the 1988/89 and 1990 running periods, respectively. Any change in the efficiencies between 1988/89 and 1990 data samples are due to the increased machine luminosity in 1990 and to the ageing of the detector components.

5.3 The Selection of Events

Events passing the online trigger requirements were subsequently filtered offline to produce the final data sample. The filter requires that there is only one reconstructed interaction vertex having its z-coordinate, (displacement along the beam-line from the nominal centre of the detector), satisfy $| z_{VTX} | < 300$ mm. The restriction on the position of the event vertex is to ensure that the vertex finding efficiency is well-defined. Within the stated range, a sufficiently large fraction of the tracks pass the ISI acceptance to define the event vertex. Only one vertex is required in order to avoid ambiguities in assigning the event information to the correct interaction vertex. To reduce the number of beam-gas and beam-halo events in the sample, it is required that there be no early VETO counter hits and also not more than one early or late hit in the TOF counter outside a time window of $\pm$ 3 ns for 1988 and $\pm$ 2.6 ns for 1989 around the nominal beam-crossing time, while for 1990 it is required that no such early or late hits exist in order to eliminate additional background from beam-gas interactions. Also, it is required that there are < 115 global reconstructed tracks.

At least one calorimeter cluster is required. The energy-weighted centroid of the leading E_T cluster is required to lie in the pseudorapidity interval $| \eta | < 0.76$ and not near a cell boundary as described above. These requirements restrict the leading cluster to lie within the fiducial region of the central calorimeter, away from cell boundaries and the two central calorimeter edge cells. (Because the central calorimeter has a finer granularity than the end-cap calorimeter, it has a better ability to distinguish between electron and jet-induced clusters). Therefore, the search is restricted to events with a centrally- produced leading jet because for the heavy top and $H^{\pm}$ masses considered, the τ decay products tend to be in this pseudorapidity range in constrast to the dominant background sources. As is shown in Figure 5.3.1, the pseudorapidity restriction $| \eta | < 0.76$ has very little effect on the τ data after the application of the kinematical cuts on p_T^{miss} and E_T^1 where E_T^1 is the

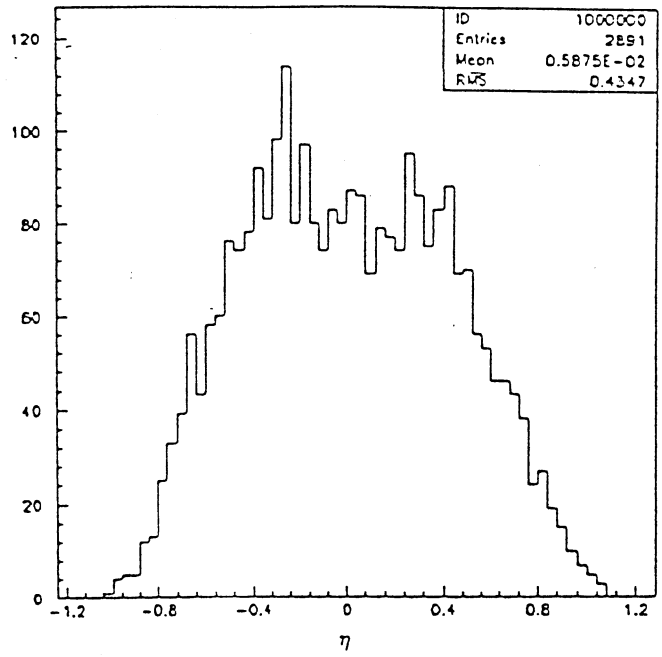

Figure 5.3.1 : The pseudorapidity distribution η of the leading E_T cluster for the 1990 data sample. Only events with $|\eta| < 1.0$ are shown.

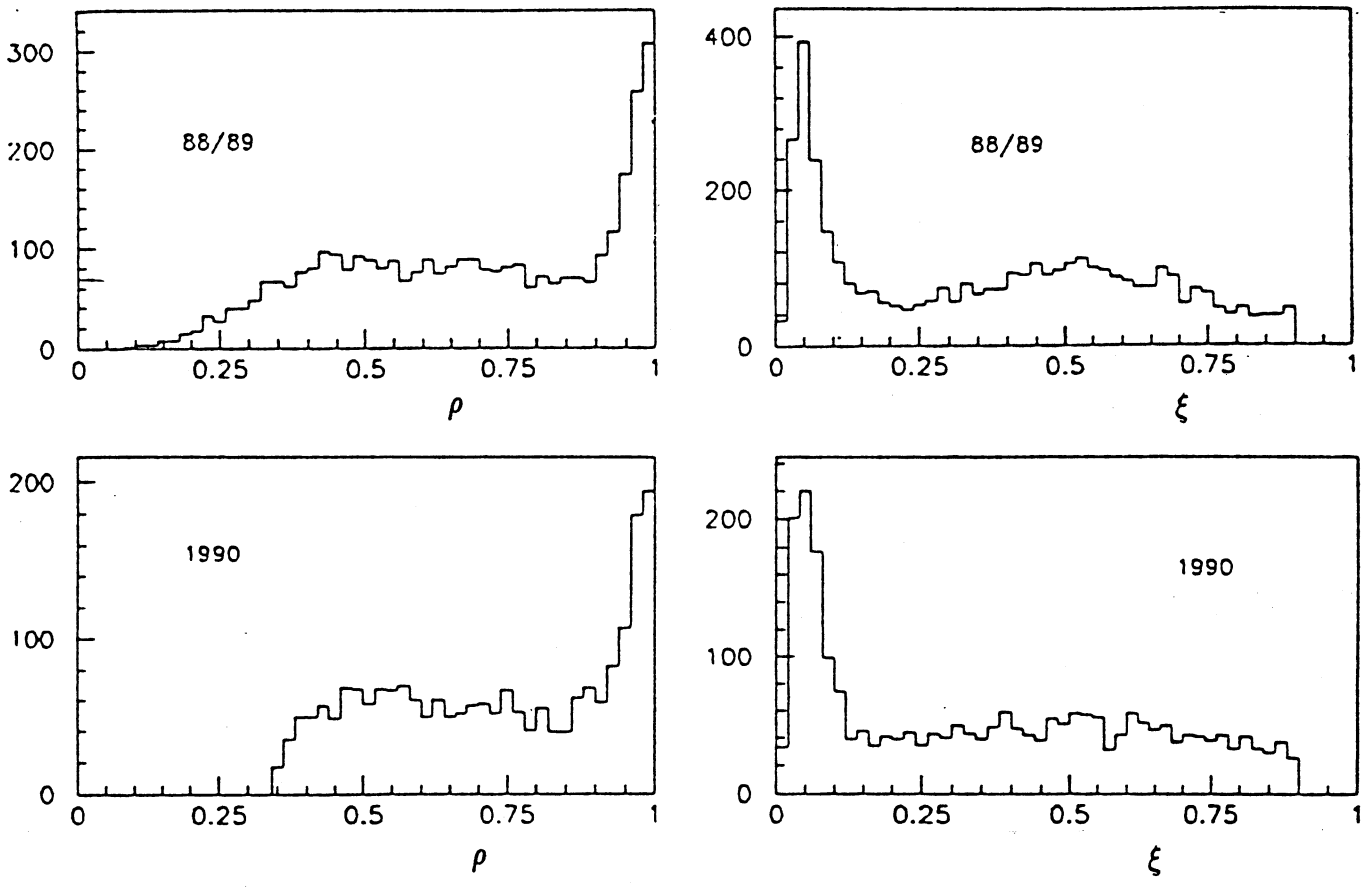

Figure 5.3.2 : The calorimeter cluster profile ρ and hadronicity ξ for the leading cluster after all analysis and trigger cuts shown here for the case $p_T^{miss} > 25$ GeV, $E_T^1 > 22$ GeV and $E_T^{opp} < 10$ GeV.

transverse energy of the leading cluster in the event (see below). Additional requirements on the leading cluster are $0.01 < \xi < 0.90$ where ξ is the cluster hadronicity and at least one charged track in a 10° cone around the cluster axis.

The number of events selected by the online trigger is 318 483 in 1988/89 using the p_T^{miss} trigger corresponding to a total integrated luminosity of (7.4 ± 0.4) pb^{-1} and 113 728 in 1990 using the τ trigger from a total integrated luminosity of (5.6 ± 0.6) pb^{-1}. Following the above filter cuts 6 801 and 6 167 events in 1988/89 and 1990, respectively, remain thus giving a total data sample of 12 968 events.

Subsequently, the kinematic cuts on p_T^{miss} and E_T^1 are applied. Two streams are produced : (a) $p_T^{miss} > 20$ GeV, $E_T^1 > 17$ GeV and (b) $p_T^{miss} > 25$ GeV, $E_T^1 > 22$ GeV. These variables are calculated offline and are corrected for the displacement of the interaction vertex.

The production of two separate streams is necessary because for a sufficiently high p_T^{miss} threshold, (e.g. 25 GeV), the contribution of τ's from $H^\pm \rightarrow \tau\nu_\tau$ is expected to be small in most cases of the $H^\pm$ mass so that $\frac{N_\tau}{N_e} \sim 1$. However, for a lower p_T^{miss} threshold (e.g. 20 GeV), $H^\pm \rightarrow \tau\nu_\tau$ is expected to yield a τ excess so that $\frac{N_\tau}{N_e} > 1$. Therefore, the sample with the lower kinematical cuts is used for the measurement of the electron-τ universality to the W which is used in Chapter 6 to set lower limits on the $H^\pm$ mass and the sample with the higher kinematical cuts is used to produce a value of universality which will be shown to have the smallest uncertainty.

To further reduce dijet backgrounds there is required to be no cluster with transverse energy, E_T^{opp}, above a certain threshold opposite to the leading cluster within the azimuthal range $140° < \Delta\phi < 220°$. The threshold has been studied by varying it between 2.5 and 10.0 GeV and will be discussed below.

The data is then divided in 'τ + 0jet' and 'τ +jets' subsamples depending on whether an additional cluster with $E_T > 10$ GeV and having an azimuthal angular separation with the leading cluster of $\Delta\phi < 140°$ does or does not appear in the event. Figure 5.3.2 shows the ρ and ξ distributions for the leading cluster of the τ + 0jet sample after all selection cuts and with $p_T^{miss} > 25$ GeV, $E_T^1 > 22$ GeV, and $E_T^{opp} < 10.0$ GeV.

Table 5.3.1 lists the efficiencies of the applied cuts. (The first four cuts are applied only to the data and could not be applied to the MC simulated

Table 5.3.1 : Cuts Applicable to UA2 Data Only

Criterion	1988/89 Efficiency	1990 Efficiency
MB	0.971 ± 0.007	0.971 ± 0.007
TOF	0.935 ± 0.008	0.799 ± 0.016
VETO	0.950 ± 0.006	0.896 ± 0.006
Vertex	0.900 ± 0.009	0.806 ± 0.010
Fid. Vol.	0.85	0.85
e track	0.91 ± 0.01	0.81 ± 0.01

events). The efficiency of the MB signal requirement is the same for all three runs. The other efficiencies are different for 1990 than for the previous runs. Except for the case of the TOF-cut efficiency, for which the requirement was changed, this is the result of the difference in beam conditions in 1990. For example, the drop in the vertex efficiency is because of the larger number of multi-vertex events in the higher-luminosity 1990 run.

5.4 The Composition of the Data Sample

Following the above selection cuts, the remaining data are made up of various types of events. These include leptonic decays of the IVBs, dijet events in which one jet has a mismeasured transverse energy giving rise to a transverse momentum imbalance, residual beam-halo and beam-gas events not removed by the VETO counter or TOF detector requirements, and events with final state electrons and τ's. To distinguish the various event types the calorimeter cluster profile ρ and ξ distributions are exploited.

5.4.1 Background from Intermediate Vector Boson Decays

In addition to $W \rightarrow e\nu_e$ and $W \rightarrow \tau\nu_\tau$ events, where the τ decays hadronically, there are further IVB decays which yield equivalent final states in UA2. To quantify the extent of this IVB background contribution the EKS MC is used as described in Section 4.2 above. The W and Z cross-sections are taken

Table 5.4.1 : Background to $W \rightarrow e\nu_e$

	τ + 0jet $p_T^{miss} > 25$ GeV $E_T^1 > 22$ GeV	τ + 0jet $p_T^{miss} > 20$ GeV $E_T^1 > 17$ GeV	τ + jets $p_T^{miss} > 20$ G $E_T^1 > 17$ Ge
$\tilde{Br}(W \rightarrow \tau\nu_\tau,\ \tau \rightarrow e\nu\overline{\nu})$	3.85×10^{-2}	5.92×10^{2}	6.38×10^{-2}
$\tilde{Br}(Z \rightarrow \tau^+\tau^-,\ \tau \rightarrow e\nu\overline{\nu},\ \tau \rightarrow \mu\nu\overline{\nu})$	0.14×10^{-2}	0.23×10^{-2}	0.23×10^{-2}
$\tilde{Br}(Z \rightarrow \tau^+\tau^-,\ h(\text{unseen})\nu,\ \tau \rightarrow e\nu\overline{\nu})$	0.0	0.80×10^{-2}	1.00×10^{-2}

Table 5.4.2 : Background to $W \rightarrow \tau\nu_\tau$

	τ + 0jet $p_T^{miss} > 25$ GeV $E_T^1 > 22$ GeV	τ + 0jet $p_T^{miss} > 20$ GeV $E_T^1 > 17$ GeV	τ + jets $p_T^{miss} > 20$ GeV $E_T^1 > 17$ GeV
$\tilde{Br}(Z \rightarrow \tau^+\tau^-,\ \tau \rightarrow h\overline{\nu},\ \tau \rightarrow \mu\nu\overline{\nu})$	3.7×10^{-2}	3.7×10^{-2}	3.7×10^{-2}
$\tilde{Br}(Z \rightarrow \tau^+\tau^-,\ h\nu,\ \tau \rightarrow e\nu\overline{\nu})$	0.6×10^{-2}	1.0×10^{-2}	0.9×10^{-2}
$\tilde{Br}(Z \rightarrow \tau^+\tau^-,\ h\nu,\ h'\overline{\nu})$	0.7×10^{-2}	1.3×10^{-2}	1.0×10^{-2}

from the UA2 measurement [UA2-91b] to be

$$\sigma_W^e = 682 \pm 12 \pm 40 \text{ pb},$$

$$\sigma_Z^e = 65.6 \pm 4.0 \pm 3.8 \text{ pb}.$$

After applying the geometric and kinematic analysis cuts, the predominant modes with final state electrons and their rate of occurrence relative to the decay $W \rightarrow e\nu_e$ (indicated by $\tilde{Br}$) are given in Table 5.4.1. Summing the individual contributions for each data sample from left to right yields

$$f_e = (3.99,\ 6.95,\ 7.61) \times 10^{-2},$$

respectively, for the quantity in Equation 5.7.

Similarly, the predominant background production of hadronic τ decays and their rate of occurrence relative to the process $W \rightarrow \tau\nu_\tau$, $\tau \rightarrow h\overline{\nu}$ are given in Table 5.4.2 where the symbols h and h′ refer to hadronic final states

of the τ. These events fake $W \rightarrow \tau\nu_\tau$, $\tau \rightarrow h\nu$ when the leading cluster results from the hadronic τ decay. Therefore,

$$f_\tau = (5.0,\ 6.0,\ 5.6)\text{x}10^{-2}$$

for the quantity appearing in Equation 5.2.

It has been assumed that the couplings of the electron and τ to the IVB are equivalent to within $\pm 10\%$ as measured previously [UA2-91a]. For the background being considered here, the uncertainty in the equality of the charged current couplings has negligible effect upon the uncertainty in the final result for the ratio R_W in Equation 5.1.

5.4.2 Beam-Halo Background

A study of the beam-halo was performed on 10% of the p_T^{miss} data. The beam-halo sample was selected by requiring at least one early hit in the VETO counters. The analysis cuts described in Section 5.3 are applied, except for the VETO counter and hadronicity cuts. Thirty-four events remain of which 31 have $\xi > 0.96$. No events are found to have $0.01 < \xi < 0.90$ so that $N_{HALO} = 0$.

The uncertainty on the number of residual beam-halo events in the partial data sample is assumed to be 1.14 events which is the mean number of events representing the 68% C.L. upper limit for zero observed events assuming Poisson statistics. Taking this to be the uncertainty on the number of beam-halo events in the partial sample and scaling up to the full statistics an uncertainty of 21 events is obtained. However, $\sim 45\%$ of all beam halo events are known to have an early VETO counter hit [Vol-90] so would not pass the VETO counter cut. Therefore, the uncertainty in the beam-halo is reduced accordingly to 9 events.

5.4.3 Electrons

The cross-section for $W \rightarrow e\nu_e$ has been measured by UA2 [UA2-91b] for data obtained from an inclusive electron trigger. However, the measurement has been re-done for data from the p_T^{miss} stream in order to assure the cancellation of systematic errors coming from the luminosity and some of the selection criteria when calculating the ratio R_W in Equation 5.1. Electrons are identified using the procedure described in Section 5.2.

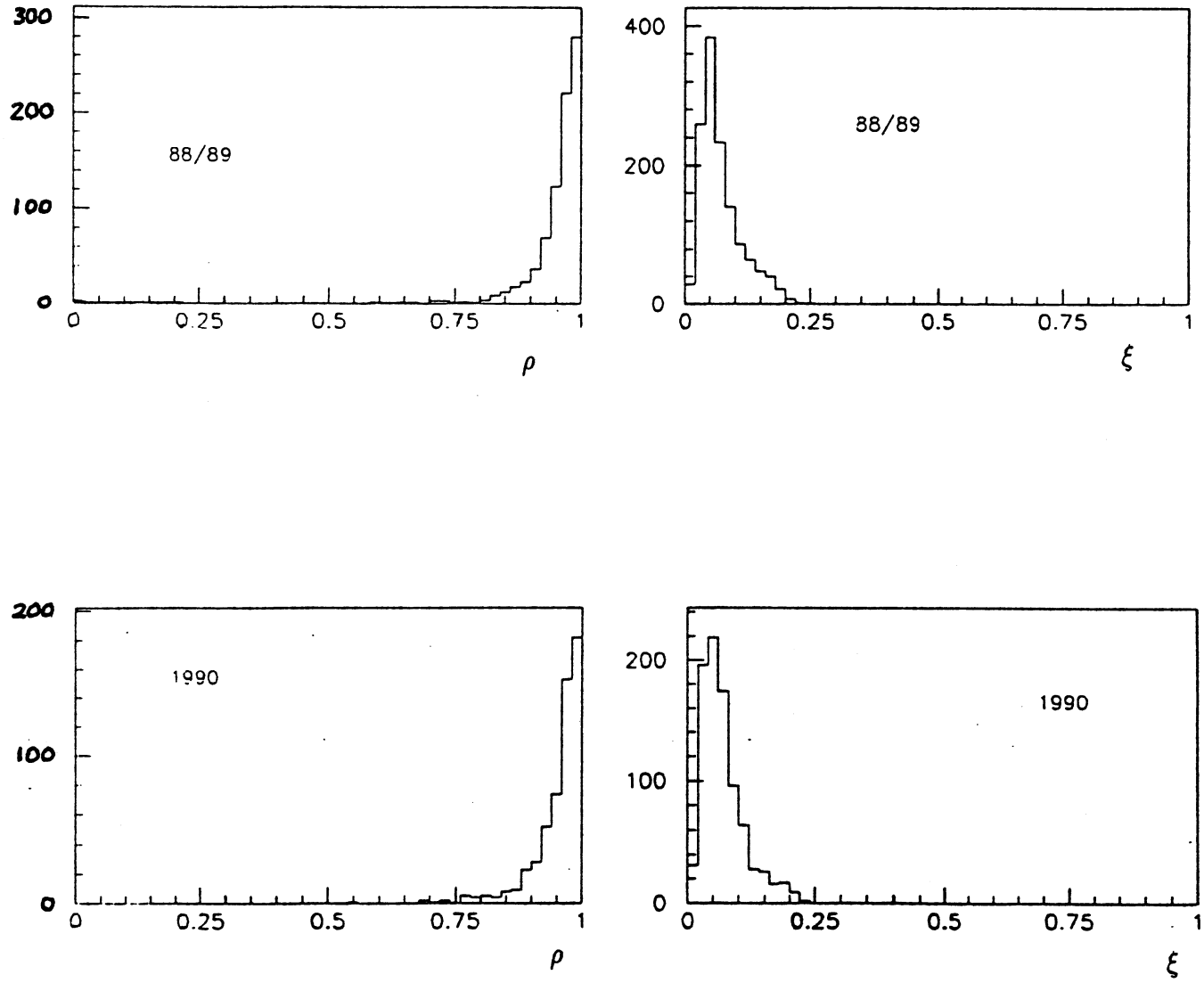

Figure 5.4.1 : The ρ and ξ distributions for electrons.

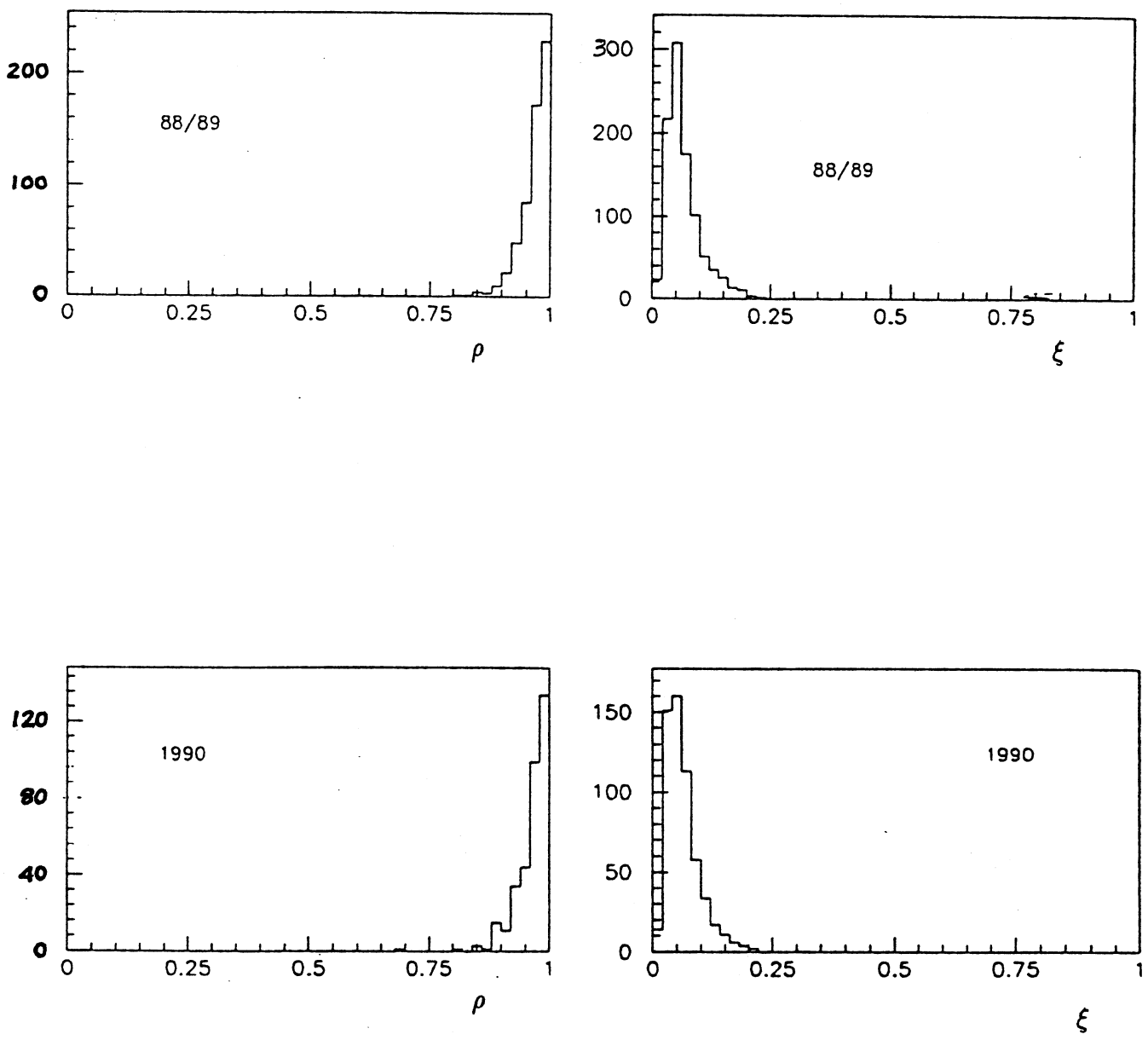

Figure 5.4.2 : The ρ and ξ distributions for electromagnetic clusters.

The number of electrons in the data sample has been verified to scale with the total integrated luminosity. The ratio of the number of electrons for the 1988/89 and 1990 runs is

$$R_e = \frac{N'_e(1990)}{N'_e(1988/89)}$$

where

$$N'_e = \frac{N_e}{(\tilde{\epsilon}_e \epsilon_{tot} \kappa_e)}$$

and where

$$\epsilon_{tot} = \epsilon_{MB}\epsilon_{VETO}\epsilon_{TOF}\epsilon_{fid.vol.}\epsilon_{VTX}.$$

R_e is measured to be 0.796 ± 0.030 for $E_T^{opp} < 2.5$ GeV, 0.828 ± 0.030 for $E_T^{opp} < 5.0$ GeV, and 0.818 ± 0.030 for $E_T^{opp} < 10.0$ GeV, and is in good agreement with the ratio of total integrated luminosities $R_{LUM} = 0.77 \pm 0.06$.

The number of identified events in the τ +0jet sample with final state electrons from $W \rightarrow e\nu_e$ is $N_e = 960 \pm 31$ and $N_e = 464 \pm 22$, respectively for 1988/89 and 1990. The kinematical cuts applied are $p_T^{miss} > 20$ GeV, $E_T^1 > 17$ GeV, and $E_T^{opp} < 10.0$ GeV. The uncertainty has been calculated by assuming Poisson statistics in the number N_e. The N_e are not corrected for the tracking efficiency κ_e since the requirement is already imposed in the selection of the data sample as described in Section 5.3.

Combining N_e with the product of efficiencies $\tilde{\epsilon}_e$ and f_e, the estimated number for $\tilde{N}_e$ appearing in Equation 5.13 is 1092 ± 40 for 1988/89 and 569 ± 34 for 1990. The uncertainty has been calculated by forming the quadratic sum :

$$\frac{\delta\tilde{N}_e}{\tilde{N}_e} = \sqrt{\left(\frac{\delta N_e}{N_e}\right)^2 + \left(\frac{\delta f_e}{1+f_e}\right)^2 + \left(\frac{\delta\tilde{\epsilon}_e}{\tilde{\epsilon}_e}\right)^2}.$$

Numbers for $\tilde{N}_e$ calculated with various different cuts on E_T^{opp} are given Table 5.4.1 and 5.4.3 for 1988/89 and 1990, respectively for the τ +0jet sample. For the τ +jets sample with $p_T^{miss} > 20$ GeV, $E_T^1 > 17$ GeV and with $E_T^{opp} < 10.0$ GeV, $N_e = 98$ for 1988/89 and 34 for 1990 from which $\tilde{N}_e = 111 \pm 12$ for 1988/89 and 41 ± 7 for 1990 (see Table 5.4.6). Figure 5.4.1 and Figure 5.4.2 illustrate the ρ and ξ distributions for electrons and for electromagnetic clusters, respectively. As expected, the corresponding distributions are similar.

Table 5.4.1 : 1988/89 τ + 0jet Universality Measurement with $p_T^{miss} > 20$ GeV and $E_T^1 > 17$ GeV

	E_T^{opp} <2.5	E_T^{opp} <5.0	E_T^{opp} <6.0	E_T^{opp} <7.0	E_T^{opp} <8.0	E_T^{opp} <10.0
Total Cand.	1946	2705	2960	3171	3376	3750
EM Clust.	1012	1215	1254	1266	1282	1308
Cand. After EM Subtrac.	934	1490	1708	1905	2094	2442
$N_{JJ} + N_{IVB}$ (total)	636	1158	1372	1554	1737	2063
N_o - Jet bkd. $\rho > 0.75$	231	255	256	271	275	294
N_{RES}	32	38	39	39	40	41
$\tilde{N}_\tau$	217 ± 21	241 ± 24	242 ± 26	255 ± 27	260 ± 28	278 ± 30
$\tilde{N}_e$	869 ± 45	1026 ± 51	1053 ± 52	1063 ± 52	1071 ± 52	1092 ± 40

To minimize the number of residual electrons in the sample, events are removed if the calorimeter information of the leading cluster is consistent with that expected from an isolated electron (i.e electromagnetic as described in Section 5.2), without requiring any additional information from the central detectors.

After subtracting the electromagnetic cluster events from the sample, the estimated residual number of events containing final state electrons is

$$N_{RES} = \frac{N_e(1 - \epsilon_{EM})}{\tilde{\epsilon}_e}$$

where ϵ_{EM} is the efficiency of the electromagnetic criteria for selecting electrons in the calorimeter. For the kinematic cuts $p_T^{miss} > 20$ GeV, $E_T^1 > 17$ GeV and $E_T^{opp} < 10.0$ GeV, N_{RES} is 41 events in 1988/89 and 21 events in 1990 for the τ +0jet sample (see Tables 5.4.1 and 5.4.3). The corresponding numbers for the τ +jets sample are 4 and 1, respectively, for 1988/89 and 1990 (see Table 5.4.5).

The majority of other events which are discarded are due to jets which have calorimeter cluster properties consistent with those expected for elec-

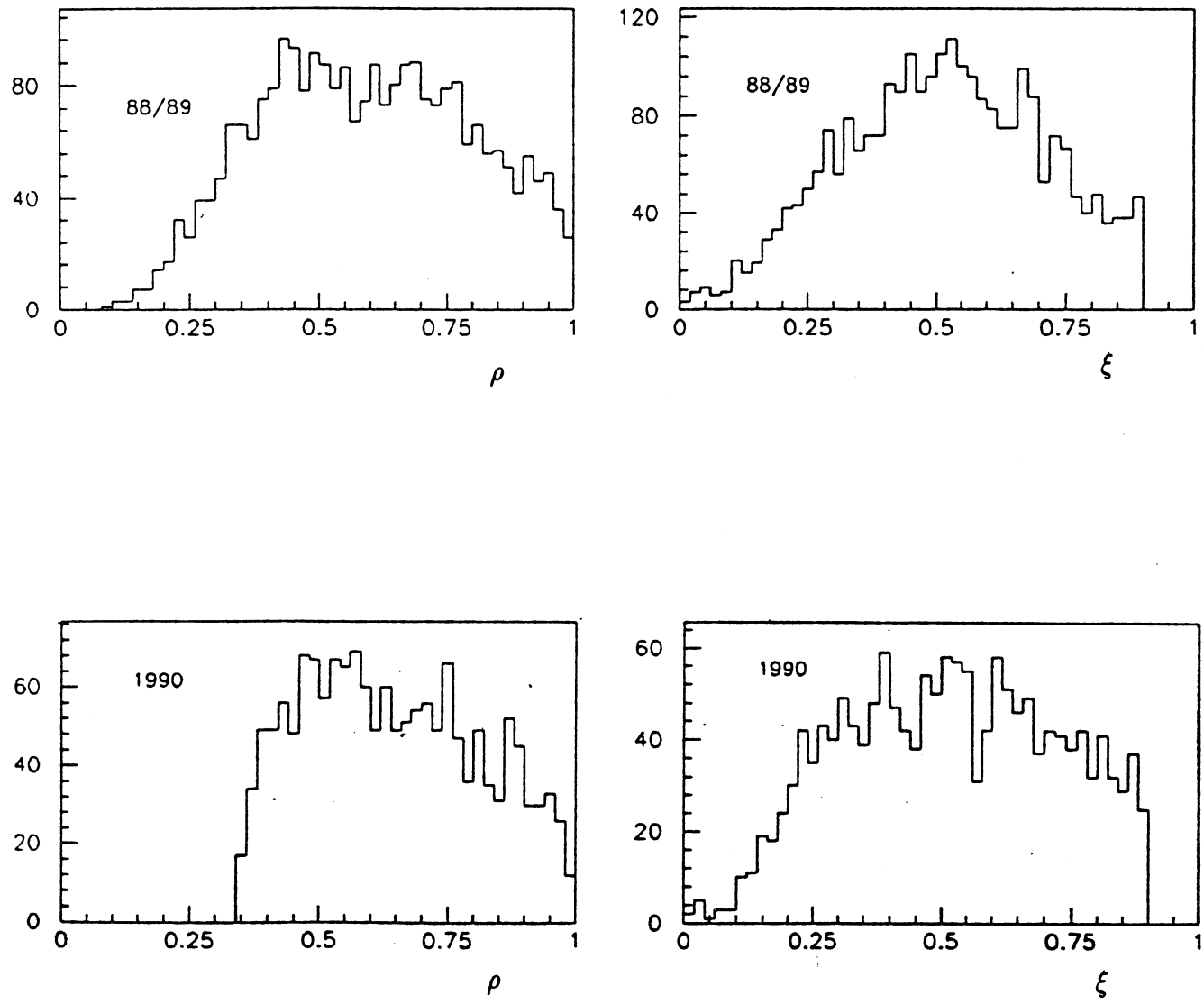

Figure 5.4.3 : The ρ and ξ distributions for the leading jet in the τ +0jet sample after subtracting the events in which the leading cluster is electromagnetic.

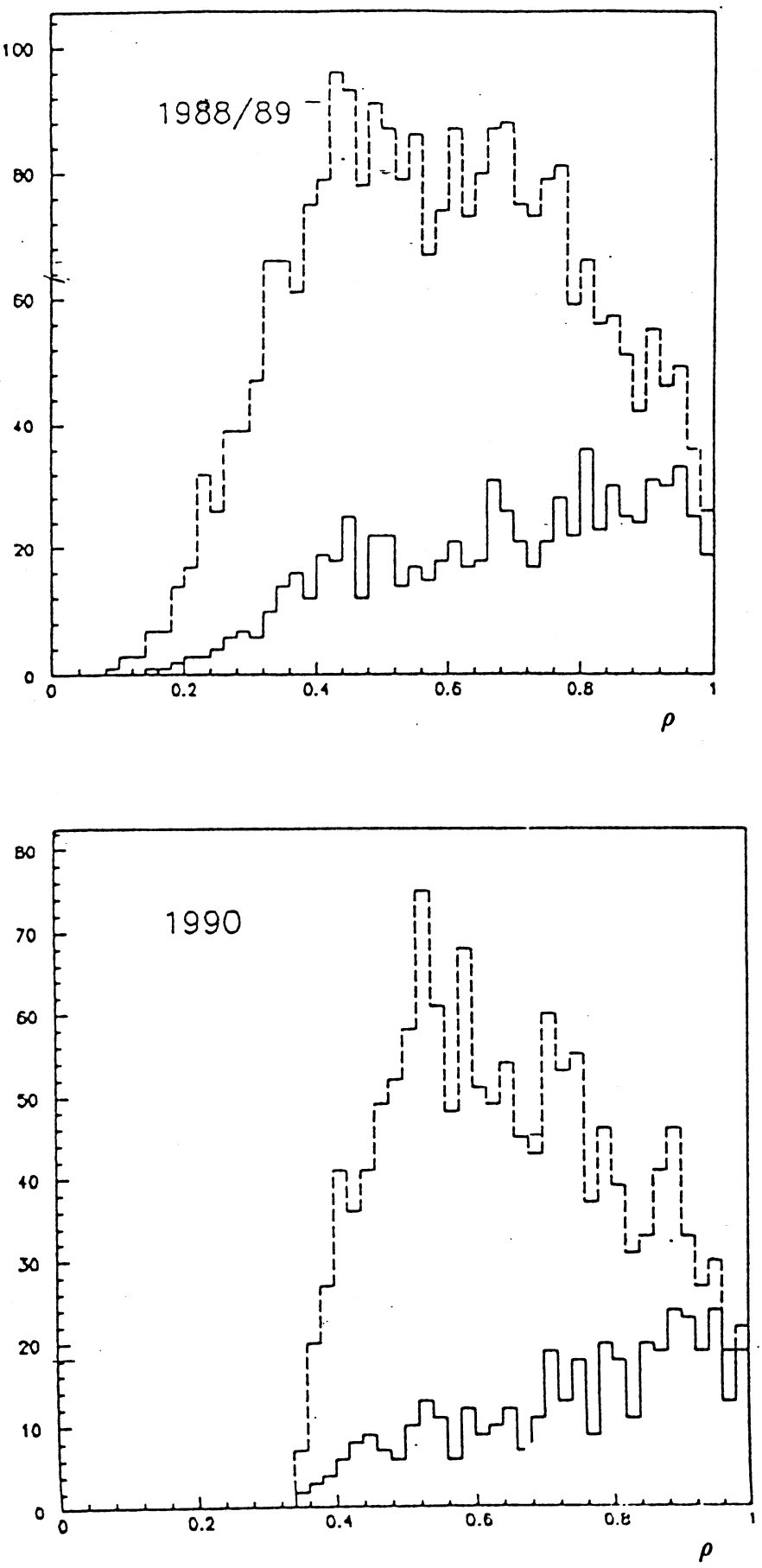

Figure 5.4.4 : The profile distribution for the leading cluster of the τ +0 jet sample after rejecting the events in which the leading cluster is electromagnetic. The dotted line corresponds to the kinematic cuts $p_T^{miss} > 20$ GeV, $E_T^1 > 17$ GeV and the full line to $p_T^{miss} > 25$ GeV, $E_T^1 > 22$ GeV.

Table 5.4.2 : 1988/89 τ + 0jet Universality Measurement with $p_T^{miss} > 20$ GeV and $E_T^l > 17$ GeV

	R_W	$\sqrt{R_W}$
E_T^{opp} <2.5	$0.966 \pm 0.109 \pm 0.082$	$0.982 \pm 0.057 \pm 0.041$
E_T^{opp} <5.0	$0.906 \pm 0.107 \pm 0.072$	$0.952 \pm 0.062 \pm 0.039$
E_T^{opp} <6.0	$0.886 \pm 0.108 \pm 0.074$	$0.941 \pm 0.065 \pm 0.040$
E_T^{opp} <7.0	$0.927 \pm 0.112 \pm 0.077$	$0.963 \pm 0.063 \pm 0.040$
E_T^{opp} <8.0	$0.935 \pm 0.114 \pm 0.077$	$0.967 \pm 0.063 \pm 0.040$
E_T^{opp} <10.0	$0.981 \pm 0.119 \pm 0.081$	$0.991 \pm 0.061 \pm 0.041$

Table 5.4.3 : 1990 τ + 0jet Universality Measurement with $p_T^{miss} > 20$ GeV and $E_T^l > 17$ GeV

	E_T^{opp} <2.5	E_T^{opp} <5.0	E_T^{opp} <6.0	E_T^{opp} <7.0	E_T^{opp} <8.0	E_T^{opp} <10.0
Total Cand.	1138	1626	1754	1861	1923	1958
EM Clust.	553	676	690	702	706	707
Cand. After EM Subtrac.	585	953	1064	1159	1217	1251
$N_{JJ} + N_{IVB}$ (total)	438	768	876	967	1020	1050
N_o - Jet bkd. $\rho > 0.75$	113	143	145	148	152	156
N_{RES}	16	20	21	21	21	21
$\tilde{N}_\tau$	106 ± 16	135 ± 20	138 ± 21	140 ± 22	144 ± 22	147 ± 23
$\tilde{N}_e$	445 ± 28	544 ± 18	557 ± 33	564 ± 33	568 ± 33	569 ± 34

Table 5.4.4 : 1990 τ + 0jet Universality Measurement with $p_T^{miss} > 20$ GeV and $E_T^1 > 17$ GeV

	R_W	$\sqrt{R_W}$
E_T^{opp} <2.5	$0.926 \pm 0.156 \pm 0.077$	$0.962 \pm 0.088 \pm 0.040$
E_T^{opp} <5.0	$0.955 \pm 0.156 \pm 0.079$	$0.977 \pm 0.083 \pm 0.040$
E_T^{opp} <6.0	$0.948 \pm 0.159 \pm 0.079$	$0.973 \pm 0.086 \pm 0.040$
E_T^{opp} <7.0	$0.956 \pm 0.162 \pm 0.079$	$0.978 \pm 0.086 \pm 0.041$
E_T^{opp} <8.0	$0.978 \pm 0.164 \pm 0.081$	$0.988 \pm 0.085 \pm 0.041$
E_T^{opp} <10.0	$0.998 \pm 0.166 \pm 0.083$	$0.999 \pm 0.083 \pm 0.041$

Table 5.4.5 : τ + jets Universality Measurement with $p_T^{miss} > 20$ GeV and $E_T > 17$ GeV

	Total Candidates	EM Clusters	Cand. after EM Subtrac.	N_o $\rho > 0.75$	$N_{JJ} + N_{IVB}$ $\rho > 0.75$	N_{RES} $\rho > 0.75$
1988/89	580	148	432	105	62	4
1990	262	61	201	46	37	1

Table 5.4.6 : τ + jets Universality Measurement with $p_T^{miss} > 20$ GeV and $E_T > 17$ GeV

	N_τ	N_e	$\tilde{N}_\tau$	$\tilde{N}_e$	R_W	$\sqrt{R_W}$
1988/89	39	98	37 ± 11	111 ± 12	$1.29 \pm 0.41 \pm 0.11$	$1.13 \pm 0.18 \pm 0.05$
1990	8	34	7 ± 8	41 ± 7	$0.66 \pm 0.76 \pm 0.06$	$0.81 \pm 0.47 \pm 0.03$

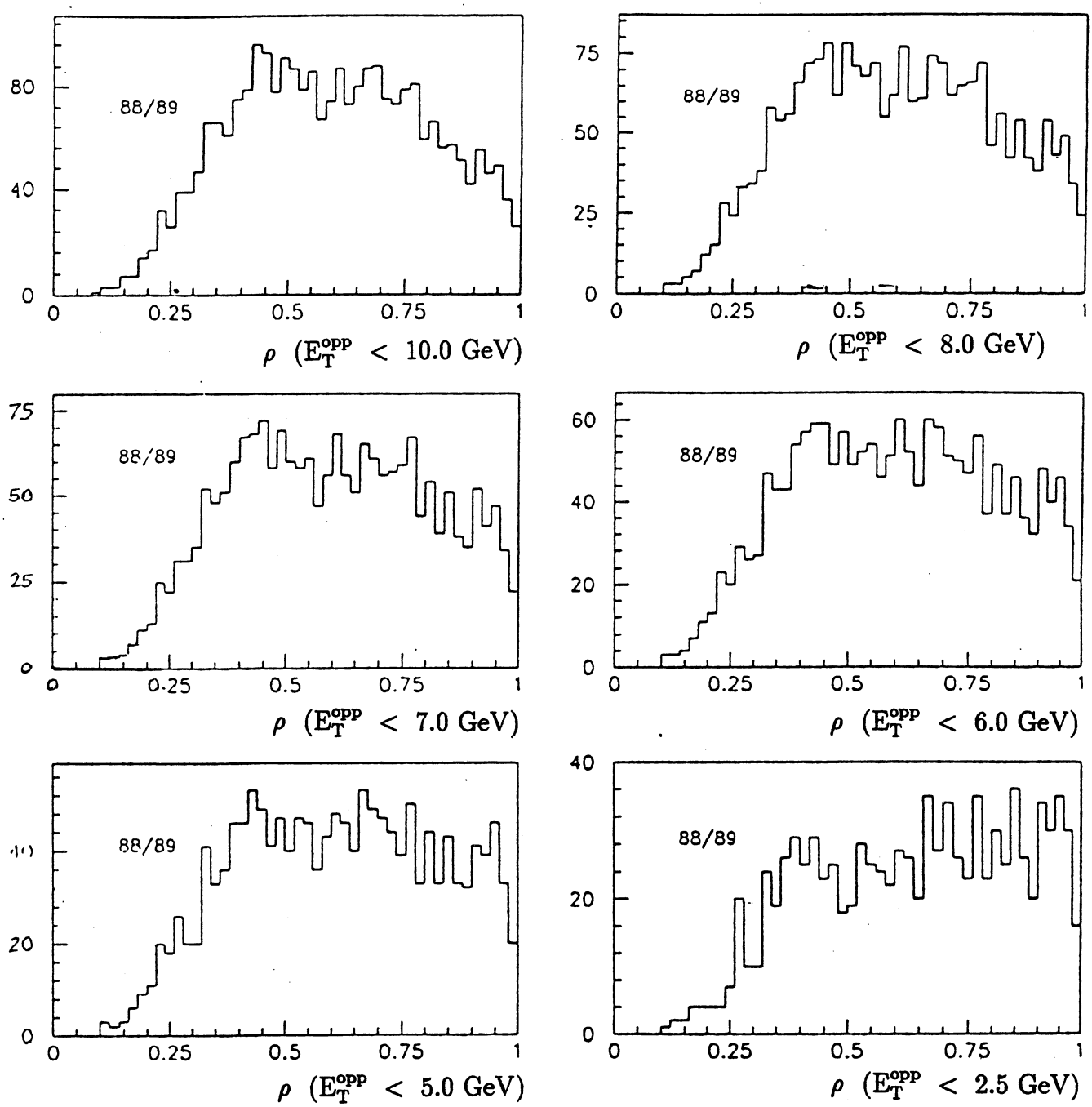

Figure 5.4.5 : The profile distribution of the τ +0jet data sample for 1988/1989 after subtracting the electrons.

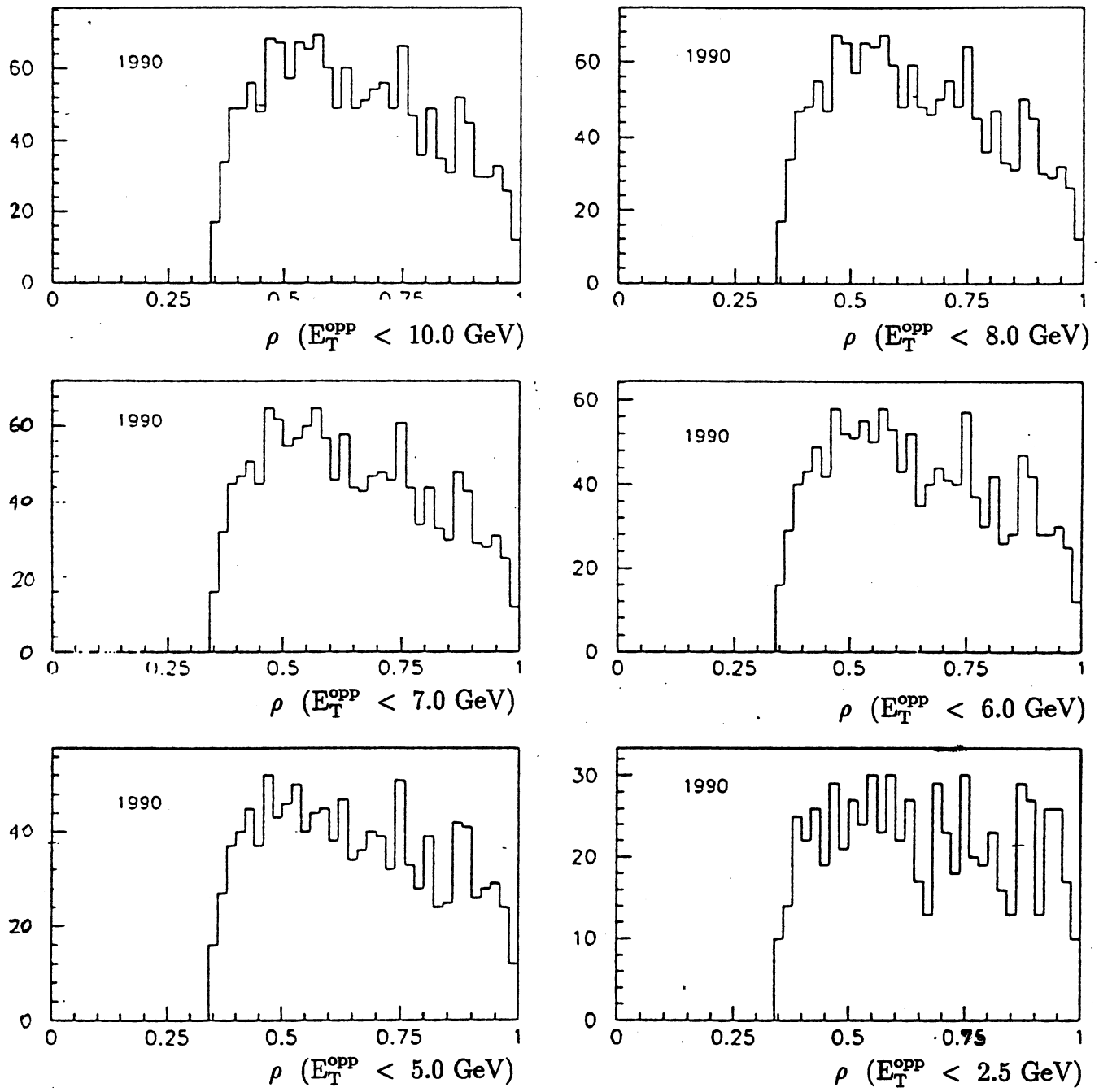

Figure 5.4.6 : The profile distribution of the τ +0jet data sample for 1990 after subtracting the electrons.

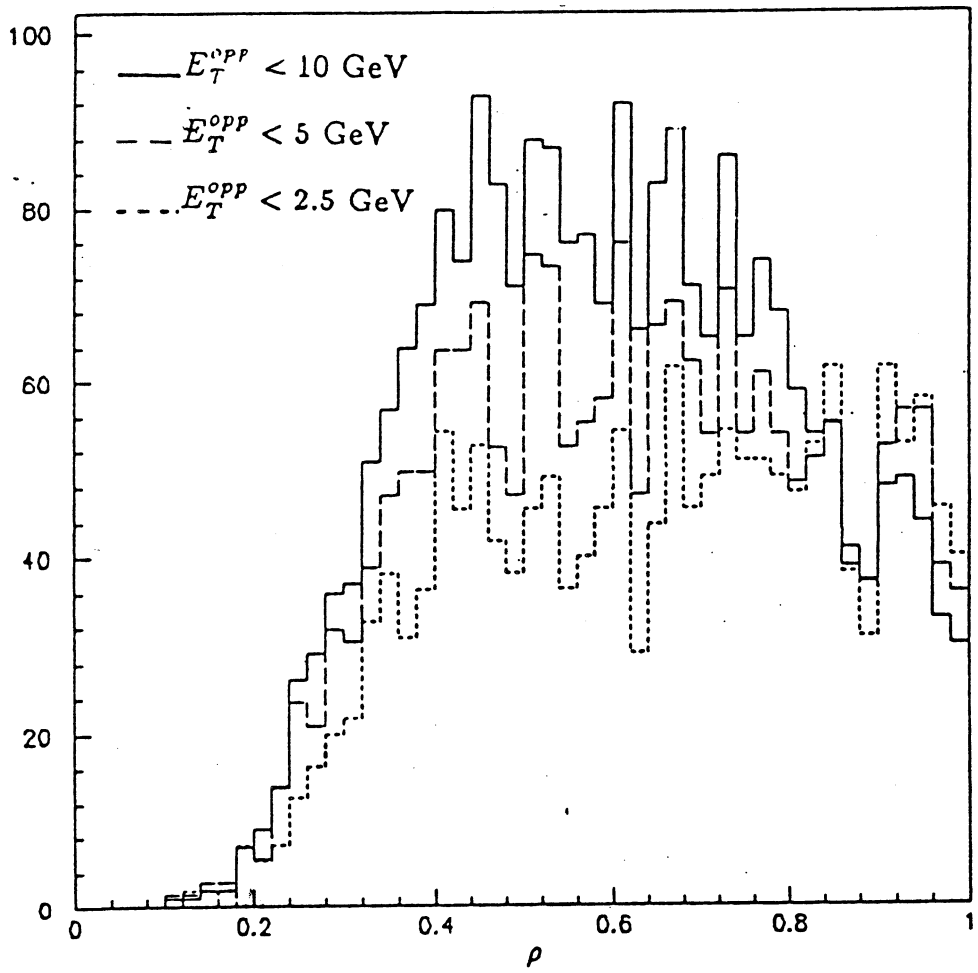

Figure 5.4.7 : Comparison of the profile distribution for the τ +0jet sample after subtracting the electrons for three different values of the E_T^{opp} cut.

trons. Less than $\sim 15\%$ of hadronic τ decay events are lost as a consequence of this subtraction.

Figure 5.4.3 shows the ρ and ξ distributions of the τ +0jet data sample after subtracting the events in which the leading cluster is electromagnetic for for $p_T^{miss} > 20$ GeV, $E_T^1 > 17$ GeV and $E_T^{opp} > 10.0$ GeV. Figure 5.4.3 shows the ρ distributions for the leading cluster of the τ +0jet sample after rejecting the events in which the leading cluster is electromagnetic for (a) $p_T^{miss} >$ 20 GeV, $E_T^1 >$ 17 GeV and (b) $p_T^{miss} > 25$ GeV, $E_T^1 >$ 22 GeV and where $E_T^{opp} < 10$ GeV. It is seen that with the introduction of the lower kinematical cuts, the jet background increases so that a cut on the Outer Silicon (OSI) charge multiplicity was developed (see below). Figures 5.4.5 and 5.4.6 show the corresponding distributions for ρ for various cuts on $E_T^{opp}$and Figure 5.4.7 superimposes three of these ρ distributions. The kinematical cuts are $p_T^{miss} >$ 20 GeV and $E_T^1 >$ 17 GeV.

5.4.4 Jets and τ's

To distinguish events in which the leading cluster is a QCD jet from those in which it is from the hadronic decay of the τ , the differences in the profile distributions of the two cases are exploited. Profile distributions for QCD jets are obtained from a sample of di-jet events from the 2JH trigger stream denoted by '2J2J' and from a sample of dijet events collected with the p_T^{miss} trigger denoted by '2JPM'. The events in both samples are selected by requiring the maximum E_T cluster to satisfy all of the selection requirements discussed in Section 5.3 and that the next-to-leading E_T cluster have $E_T > 10.0$ GeV , lie in the pseudorapidity region $| \eta | < 2.5$ and be opposite to the leading cluster in azimuth ($140° < \Delta\phi < 220°$).

Figure 5.4.8 shows the difference in the ρ distribution of the leading cluster in dijet events obtained with the p_T^{miss} (solid line) and with the 2JH trigger (dashed line) for $p_T^{miss} > 25$ GeV and $E_T^1 >$ 22 GeV. In particular, the ratio of the fraction of events with $\rho > 0.75$ to the fraction of events with $\rho < 0.6$, R_{2J}, is 0.49 ± 0.05 and 0.27 ± 0.02 for the '2JPM' and '2J2J' samples, respectively. When introducing the cut $\rho > 0.35$, as done for the 1990 data, the corresponding numbers are 0.61 ± 0.06 and 0.37 ± 0.02.

Comparing the shapes of the profile distributions using the Kolmogorov-Smirnov (KS) [Ead-71] test shows that the difference occurs predominantly at low profile values. For $\rho > 0.7$ the KS confidence level for the comparison

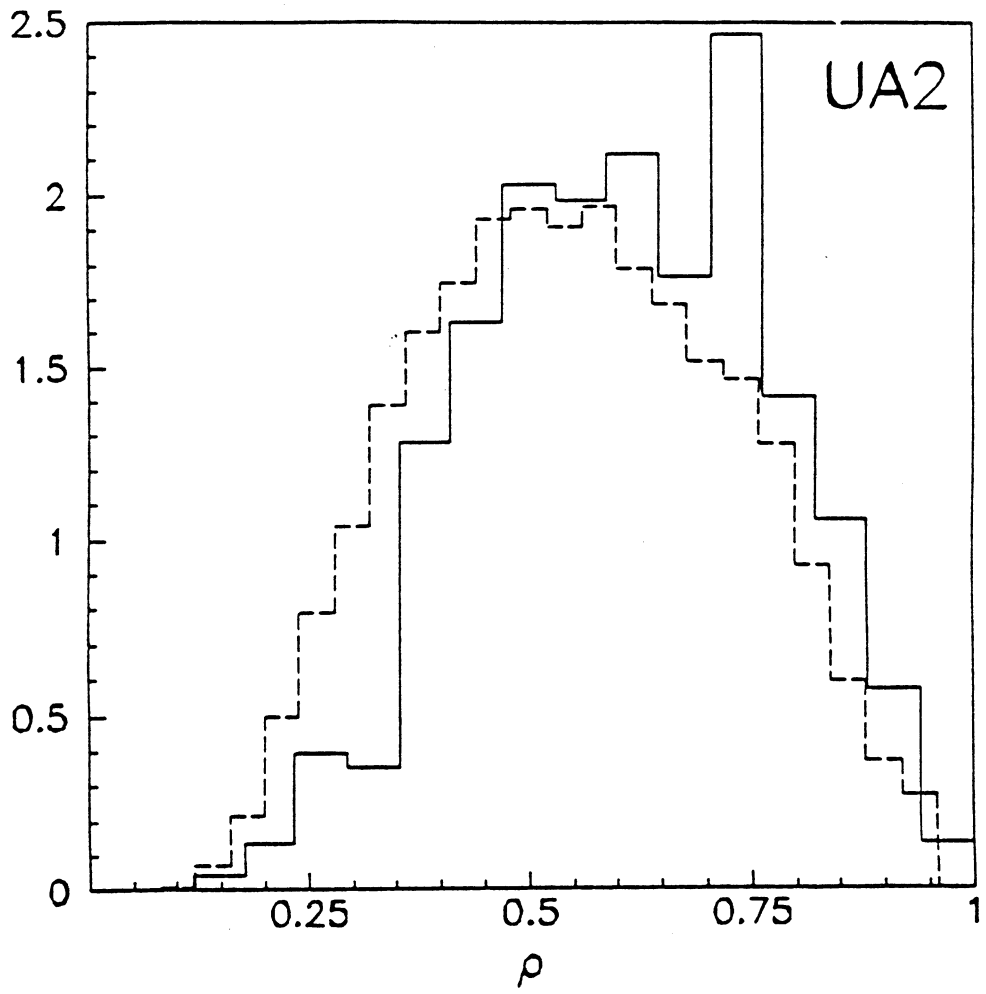

Figure 5.4.8 : Profile of the leading cluster in dijet events obtained with the p_T^{miss} trigger (solid line) and with the dijet trigger (dashed line). The area under each line is normalized to unity.

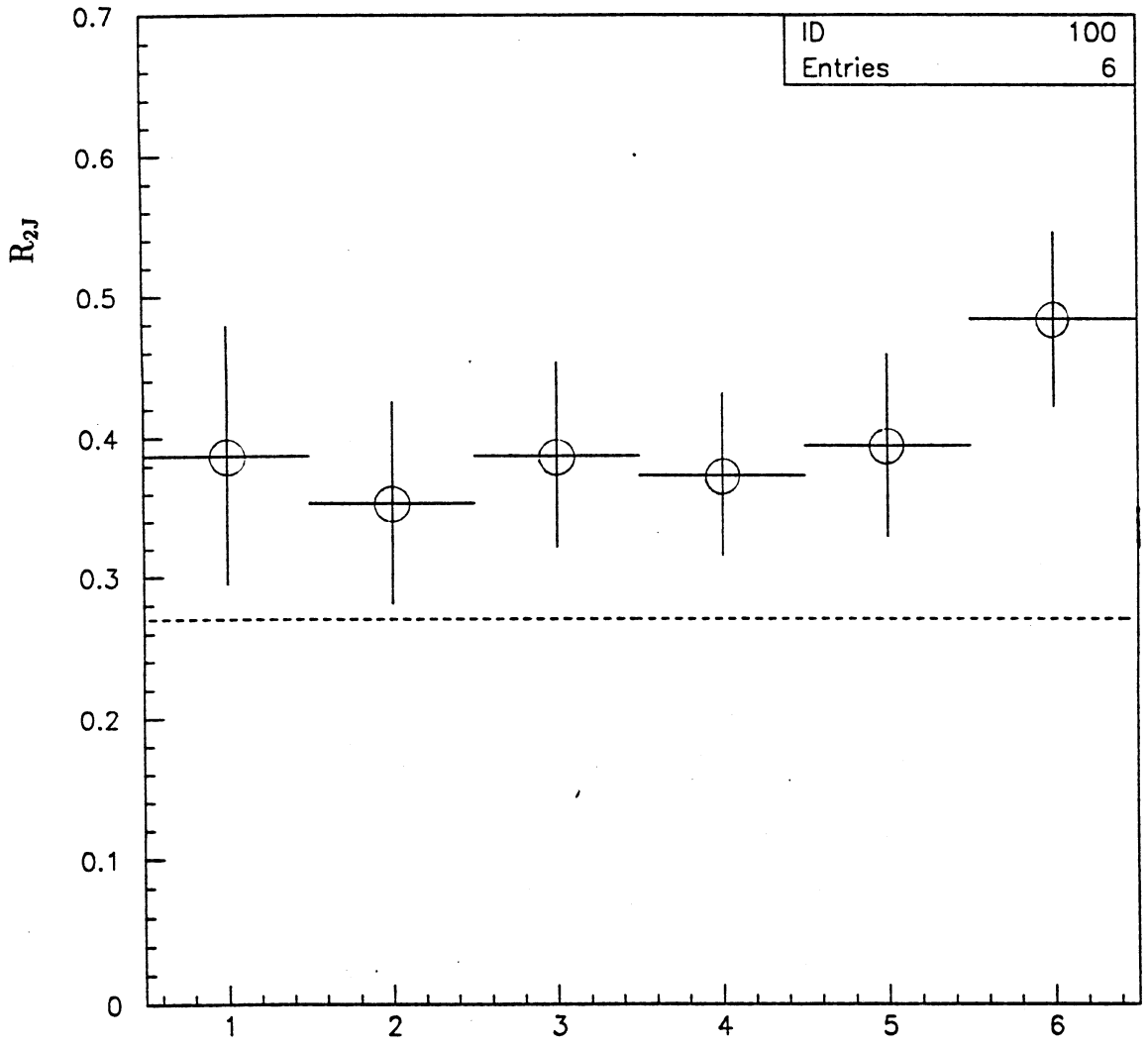

Figure 5.4.9 : Comparison of R_{2J} between data from the '2JPM' sample (open circles) to data from the '2J2J' sample given for $E_T^{opp} < 2.5$ GeV (horizontal line). The values for the '2JPM' stream correspond from left to right to an E_T^{opp} in the range [< 2.5], [2.5,5.0], [2.5,6.0], [2.5,7.0], [2.5,8.0] and [2,5,10.0] GeV. The kinematical cuts applied are $p_T^{miss} > 25$ GeV and $E_T^1 > 22$ GeV.

is $> 90\%$ whereas for $\rho < 0.5$ it is $< 1\%$. This implies that there exists a bias toward high profile values for the leading jet in dijet events with a large p_T^{miss}. Figure 5.4.9 compares R_{2J} taken from the '2JPM' and '2J2J' data samples.

An additional source of jet background comes from IVB decays decaying into final state leptons where the leptons go undetected and the accompanying jet(s) pass the E_T^1 cut. Figure 5.4.10 illustrates the IVB background for the case of an associated single jet production from gluon bremsstrahlung. The processes of interest together with their production cross-sections are given in Table 5.4.7.

In such IVB events the missing transverse momentum arises mostly from the presence of final state neutrinos rather than from detector resolution effects and fluctuations in the hadronic shower development. Thus, the jets accompanying IVB decays are in general not expected to have the bias in profile seen for jets in events selected with the p_T^{miss} trigger. Therefore, the number of IVB + jet events estimated by MC to be contained in the data sample are assumed to have the profile distribution of jets from the dijet trigger.

As Figure 5.4.11 shows, R_{2J} from the '2J2J' and '2JPM' samples are identical for the lower kinematical cuts. Therefore, the jet profile distributions for jet backgrounds coming from IVB decays and from dijet events with the lower kinematical cuts are taken from the same 2JH jet profile distribution and $R_{2J} = 0.27 \pm 0.02$ for 1988/89 and 0.37 ± 0.02 for 1990. With the higher kinematical cuts, the QCD jets in the sample are estimated from the '2JPM' sample and $R_{2J} = 0.49 \pm 0.05$ for 1988/89 and 0.61 ± 0.06 for 1990. These values have a larger uncertainty than those calculated from the '2J2J' sample because of the smaller amount of statistics in the '2JPM' data sample.

The number of jets (dijets plus IVB + jet(s)) in the data sample with $\rho > 0.75$ is

$$N_{jets}(\rho > 0.75) \;=\; R_{2J} \cdot N_{jets}(\rho < 0.60)$$

where

$$R_{2J} \;=\; \frac{N_{>0.75}}{N_{<0.60}}$$

obtained from the '2J2J' sample. The uncertainty is

$$\frac{\delta N_{jets}\,(\rho > 0.75)}{N_{jets}\,(\rho > 0.75)} \;=\; \sqrt{\left(\frac{\delta N_{jets}\,(\rho > 0.60)}{N_{jets}\,(\rho > 0.60)}\right)^2 + \left(\frac{\delta N_{>0.75}}{N_{>0.75}}\right)^2 + \left(\frac{\delta N_{<0.60}}{N_{<0.60}}\right)^2}.$$

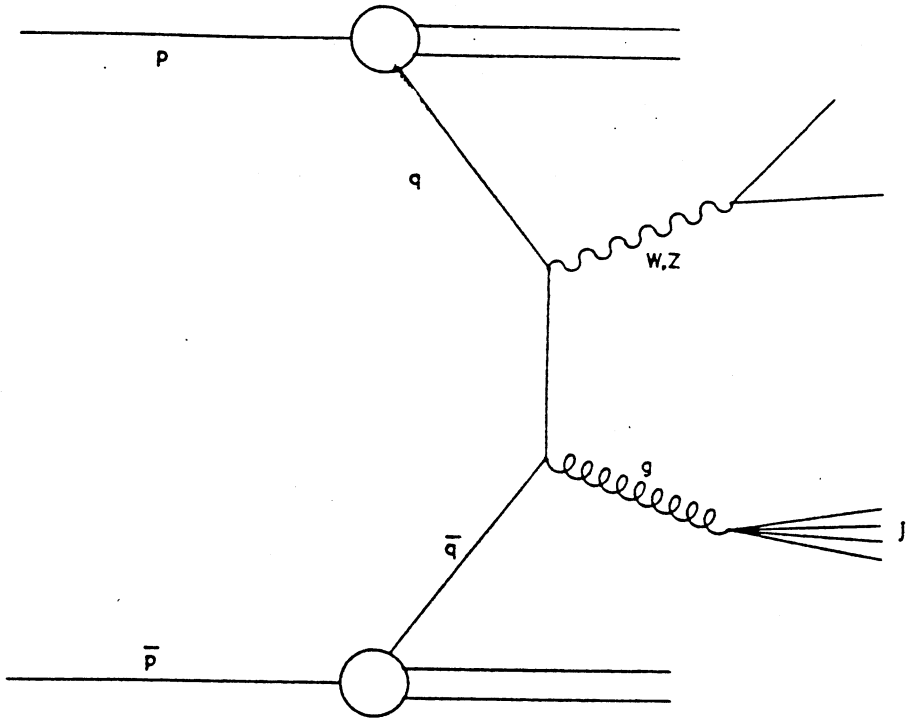

Figure 5.4.10 : W boson production with an associated jet from gluon bremsstrahlung.

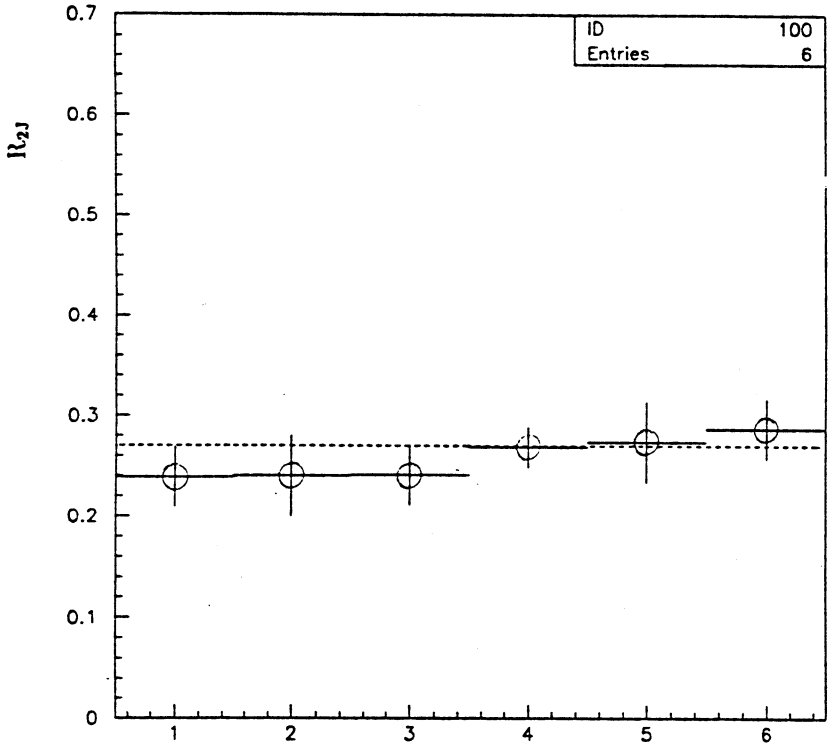

Figure 5.4.11 : Comparison of R_{2J} between data from the '2JPM' sample (open circles) to data from the '2J2J' sample given for $E_T^{opp} < 2.5$ GeV (horizontal line). The values for the '2JPM' stream correspond from left to right to an E_T^{opp} in the range [< 2.5], [2.5,5.0], [2.5,6.0], [2.5,7.0], [2.5,8.0] and [2,5,10.0] GeV. The kinematical cuts applied are $p_T^{miss} > 20$ GeV and $E_T^1 > 17$ GeV.

Table 5.4.7 IVB + jet(s) Production Cross-sections

	$\sigma_{1\text{ jet}}$ (pb)	$\sigma_{2\text{ jets}}$ (pb)
$W \rightarrow \mu\nu_\mu$ + jet(s)	152.6	24.0
$W \rightarrow \tau\nu_\tau$ + jet(s)	26.7	4.2
$Z \rightarrow \mu\bar{\mu}$ or $\nu\bar{\nu}$ + jet(s)	114.1	17.9

The total number of jet events (dijets plus IVB jet(s)) for $p_T^{miss} > 20$ GeV and $E_T^1 > 17$ GeV are given in Tables 5.4.1 and 5.4.3 for the τ +0jet sample and in Table 5.4.5 for the τ +jets sample.

The number of jets from IVB + jet events in the region $\rho < 0.60$ is subtracted from the total number in this region and it is then assumed that all of the events remaining in the region $\rho < 0.60$ are from QCD dijet events and have the profile distribution of the 2J2J sample. In this way a normalization is obtained for the profile distribution of the dijet events.

5.4.5 Monte Carlo Calculation of the Ratio of Acceptances Ω

To calculate the experimental value R_W the ratio $\frac{\tilde{N}_\tau}{\tilde{N}_e}$ must be divided by the MC ratio of acceptances Ω of Equation 5.11. The quantity Ω corrects for the effects of the kinematic, tracking, profile, and hadronicity cuts and also includes the geometric acceptance of the detector for leptons from W decay. The efficiencies for vertex, MB, TOF, VETO counters, and fiducial volume are assumed to be the same for electrons and τ's thus canceling in the ratio R_W. The total hadronic branching ratio of the τ, $Br(\tau \rightarrow h\nu)$ is 0.645 [PDG-90].

The ratio Ω is determined from an EKS MC given the following production cross-sections for the semileptonic W decays :

$$\sigma(\text{lowest order}) = 0.46 \text{ nb}$$

$$\sigma(\alpha_s) = 0.156 \text{ nb}$$

$$\sigma(\alpha_s^2) = 0.024 \text{ nb}$$

The final result is obtained by combining the results at the various orders in α_s weighted by their relative cross-sections.

The tracking efficiency ratio $\frac{\kappa_e}{\kappa_\tau}$ in a 10° cone around the cluster barycentre assumes a single charged particle tracking efficiency of 0.91 ± 0.01 for 1988/89 and 0.81 ± 0.01 for 1990 as measured for W electrons. The τ tracking efficiency includes the fact that there are both singly- and multiply - charged particle τ decays. The branching ratio for the 1-prong hadronic decays is 78% while for the 3-prong hadronic decays it is 22% [PDG-90]. (Less than 1% of τ decays are to greater than 3 final state charged particles). After imposing the analysis cuts, however, the branching ratios become 54% and 46%, respectively. The efficiency for having at least one track detected inside the cone is calculated by first determining the probabilities for having 1, 2, or 3 tracks inside the cone and then applying the single track efficiency to each track. The τ tracking efficiency is thus 0.94 ± 0.01 for 1988/89 and 0.84 ± 0.01 for 1990. The uncertainties in the tracking efficiencies cancel to a large extent in the ratio $\frac{\kappa_e}{\kappa_\tau}$.

Not all the systematic errors for electrons and τ's cancel in the ratio Ω. Because of the presence of the additional ν_τ in τ decays, such decays have a characteristically lower mean E_T than electron events. Therefore, a variation of the E_T threshold at low values results in a larger variation in the number τ's and electrons. Uncertainties in the energy scale and the W mass are equivalent to uncertainties in the E_T threshold. In addition, the different energy scale uncertainties for hadronic and electromagnetic showers leads to different uncertainties on the electron and τ acceptances. Varying the thresholds for τ's and electrons in the MC after all other selection cuts are applied, the above effects result in a $\pm 3\%$ uncertainty for η_τ and a negligible uncertainty for η_e. The final result is then computed to be

$$\Omega = 0.259 \pm 0.006.$$

5.5 Systematic Uncertainties

Below are listed the systematic uncertainties in the measurement of R_W.

- The largest single uncertainty comes from the ξ criterion $0.01 < \xi < 0.90$. A $\pm 5\%$ width for a flat uncertainty distribution is obtained for ξ by con-

sidering the difference in the hadronicity values for charged pions and electrons from test beam impinging near the calorimeter cell boundaries.

- The uncertainty in the τ efficiency from the profile cut $\rho > 0.75$ is $\pm 4\%$ derived from a Gaussian error distribution by comparing the profile distribution of 10 GeV pions from test beam to that of pions from MC.

- The kinematic cuts, (p_T^{miss} and E_T^1), have a combined uncertainty of $\pm 3.4\%$ given as the width of a flat uncertainty distribution. It has been determined by varying the thresholds in accord with the uncertainties in the electromagnetic ($\pm 1\%$) and hadronic ($\pm 2\%$) compartments of the calorimeter. It is assumed that there is no correlation between the electromagnetic and hadronic energy scales. The contribution from the electrons is negligible since the majority of the central electrons from W decay are well above the E_T^1 threshold.

- The uncertainty in the electron identification efficiency associated with the electron energy reconstruction in the calorimeter is found to be a flat distribution of width $\pm 1.0\%$.

- There is expected to be no beam-halo contribution to the data sample. The uncertainty on the number of τ's resulting from the uncertainty in the beam-halo estimate is determined to be $\pm 1\%$ and distributed normally.

- The systematic error assigned to the jet background subtraction is $\pm 3.4\%$, which is flatly distributed, and is evaluated by taking the difference between the ratio of the number of observed τ's and electrons for the case of an opposite jet transverse energy E_T^{opp} cut of 10 GeV and that obtained for a cut at 2.5 GeV.

- Using electrons from W decay the uncertainty in the tracking efficiencies for electrons and τ's is determined to be $\pm 3\%$ and assumed to be a flat distribution.

Added in quadrature the individual systematic errors on R_W yield a total systematic uncertainty of $\pm 8.6\%$.

5.6 The Ratio of Branching Fractions R_W

Finally, $\tilde{N}_\tau$ remains to be evaluated to calculate R_W. From Section 5.1

$$\tilde{N}_\tau = \frac{N_\tau}{1+f_\tau} = \frac{N_0 - N_{HALO} - N_{RES} - (N_{IVB} + N_{JJ})}{1+f_\tau} \quad (5.14).$$

For the τ +0jet sample with the cuts $p_T^{miss} > 20$ GeV, $E_T^1 > 17$ GeV and $E_T^{opp} < 10.0$ GeV, $N_\tau = 294$ for 1988/89 and 156 for 1990 so that from Equation (5.14), $\tilde{N}_\tau = 278 \pm 30$ for 1988/89 and 147 ± 23 for 1990 (see Tables 5.4.1 and 5.4.3). For the τ +jets sample $N_\tau = 39$ for 1988/89 and 8 for 1990 so that $\tilde{N}_\tau = 37 \pm 11$ and 7 ± 8, respectively for 1988/89 and 1990. The uncertainties are added in quadrature so that

$$\delta N_\tau = \sqrt{(\delta N_0)^2 + (\delta N_{RES})^2 + (\delta(N_{IVB} + N_{JJ}))^2}$$

and

$$\frac{\delta\tilde{N}_\tau}{\tilde{N}_\tau} = \sqrt{\left(\frac{\delta N_\tau}{N_\tau}\right)^2 + \left(\frac{\delta f_\tau}{1+f_\tau}\right)^2}.$$

Substituting $\tilde{N}_e$, $\tilde{N}_\tau$ and Ω into Equation (5.10), the ratio of electron and τ couplings to the W are calculated to be

$$\tau + 0\text{jets} \quad : \quad \frac{g_\tau^W}{g_e^W} = 0.99 \pm 0.06 \pm 0.04$$

$$\tau + \text{jets} \quad : \quad \frac{g_\tau^W}{g_e^W} = 1.04 \pm 0.18 \pm 0.05$$

for the combined 1988/89 and 1990 data samples given $p_T^{miss} > 20$ GeV, $E_T^1 > 17$ GeV and $E_T^{opp} < 10.0$ GeV. The results are summarized in Tables 5.4.2 and 5.4.4 for the τ +0jet sample and in Table 5.4.6 for the τ +jets sample. Figure 5.6.1 shows the good agreement between $\sqrt{R_W}$ for different cuts on E_T^{opp}. The result to be used in Chapter 6 to calculate the $H^\pm$ lower mass limit is that calculated for $E_T^{opp} < 10.0$ GeV.

The uncertainty on g_τ^W/g_e^W is calculated from

$$\delta\left(\frac{g_\tau^W}{g_e^W}\right) = \frac{\delta R_W}{2\sqrt{R_W}}.$$

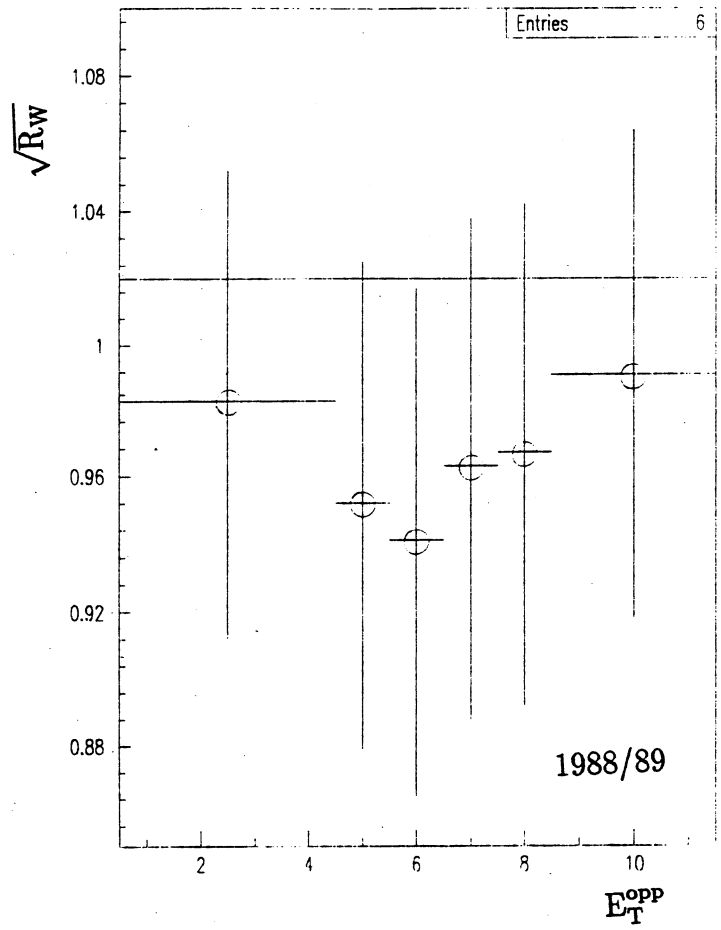

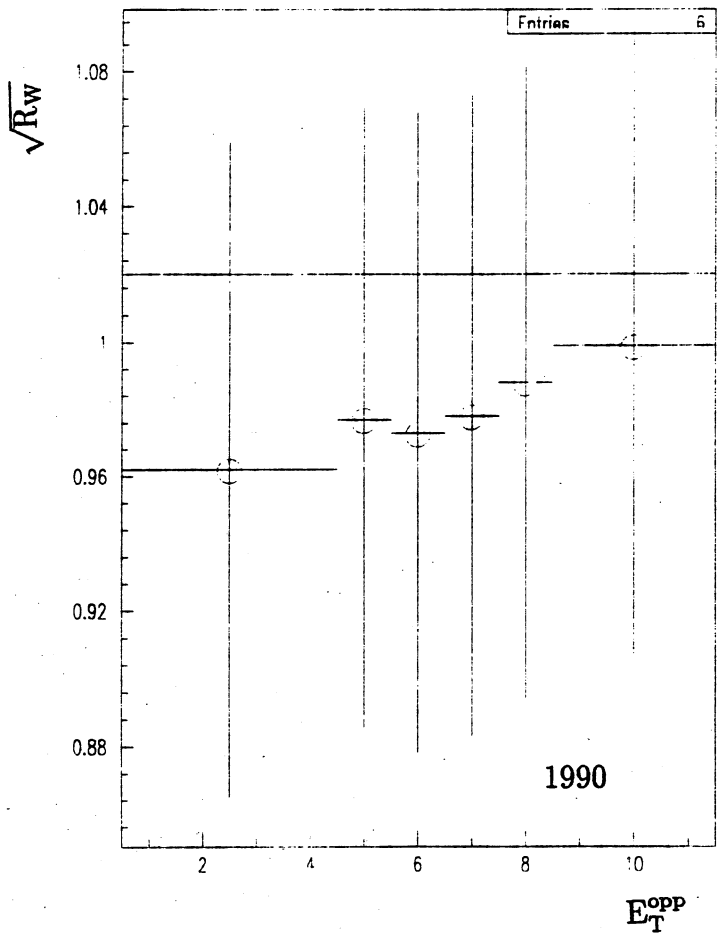

Figure 5.6.1 : The value of $\sqrt{R_W}$ for different cuts on E_T^{opp}. The horizontal line is the value for $\sqrt{R_W}$ for $p_T^{miss} > 25$ GeV, $E_T^l > 22$ GeV, and $E_T^{opp} < 2.5$ GeV which is taken to be the most precise value of the electron-τ universality

5.7 Universality Measurement with $p_T^{miss} > 25$ GeV and $E_T^l > 22$ GeV

The UA2 Collaboration has previously measured the electron-τ universality from IVB decays to be

$$\tau + 0\text{jets} \quad : \quad \frac{g_\tau^W}{g_e^W} = 0.997 \pm 0.056\ (\text{stat}) \pm 0.042\ (\text{syst})$$

using a data sample corresponding to (7.4 ± 0.4) pb^{-1} collected during 1988/89 [UA2-91a]. The analysis was performed by requiring $p_T^{miss} > 25$ GeV, $E_T^l >$ 22 GeV and $E_T^{opp} < 2.5$ GeV. The analysis presented in this section is from the full data sample over 1988-1990 and corresponds to a total integrated luminosity of (13.0 ± 0.7) pb^{-1} and having the same kinematical cuts as in Ref. [UA2-91a]. The measurement of the electron-τ universality proceeds identically to what is presented above for the lower kinematical cuts. Only the measurement for the τ +0jet sample is performed as this provides the smallest uncertainty relative to the τ +jets sample.

The number of QCD jets in the sample with $\rho > 0.75$ is

$$N_{JJ}\ (\rho > 0.75) = R_{2J} \cdot N_{JJ}\ (\rho < 0.60)$$

and is calculated from the '2JPM' sample from where $R_{2J} = 0.49 \pm 0.05$ and 0.61 ± 0.06 for the 1988/89 and 1990 samples, respectively. The number of IVB + jet events in the region $\rho < 0.60$ is subtracted from the total number of events in this region and it is then assumed that all the remaining events in the region $\rho < 0.60$ are from QCD dijet events and have the profile distribution of the '2JPM' sample. In this way a normalization is obtained for the ρ distribution of the dijet events. The number of dijet events with $\rho > 0.75$ is given in Table 5.7.1.

The number of IVB + jet events expected is calculated from the EKS MC described in Section 4.2 :

$$N_{IVB} = L \cdot (\sigma_{1\ \text{jet}}^{tot} \cdot f_1 + \sigma_{2\ \text{jets}}^{tot} \cdot f_2) \cdot \epsilon'_{tot}$$

which can be written as

$$N_{IVB} = L \cdot S \cdot \epsilon'_{tot}$$

where L is the total integrated luminosity, $\sigma^{tot}_{1\ jet}$ and $\sigma^{tot}_{2\ jets}$ are the total production cross-sections for IVB plus 1 and 2 jets, respectively, f_1 and f_2 are the corresponding MC acceptances and

$$\epsilon'_{tot} = \epsilon_{VTX}\epsilon_{VETO}\epsilon_{MB}\epsilon_{TOF}\epsilon_{tr}$$

where

$$\epsilon_{tr} = \frac{\kappa_e}{\kappa_\tau} = 0.97 \pm 0.02.$$

The uncertainty is given by

$$\frac{\delta N_{IVB}}{N_{IVB}} = \sqrt{\left(\frac{\delta L}{L}\right)^2 + \left(\frac{\delta S}{S}\right)^2 + \left(\frac{\delta \epsilon}{\epsilon}\right)^2}$$

where the luminosity error is $\approx 5\%$, the error on $\epsilon'_{tot} \leq 2\%$ and the error on S is calculated assuming Poisson statistics. Because, as discussed above, the number of IVB + jet events calculated by MC to be contained in the data sample are assumed to have the profile distribution of jets from the dijet trigger, the number of IVB + jet events with $\rho < 0.60$, N^1_{IVB}, and the number with $\rho > 0.75$, N^2_{IVB}, is given by

$$N^1_{IVB} \equiv N_{IVB}\ (\rho < 0.60) = N_{IVB} \cdot p_1$$

and

$$N^2_{IVB} \equiv N_{IVB}\ (\rho > 0.75) = N_{IVB} \cdot p_2$$

where p_1 and p_2 are the fraction of events with $\rho < 0.60$ and $\rho > 0.75$, respectively, and are calculated from the '2J2J' stream and N_{IVB} is the total number of IVB + jet(s) events. The uncertainty is given by

$$\frac{\delta N^i_{IVB}}{N^i_{IVB}} = \sqrt{\left(\frac{\delta N_{IVB}}{N_{IVB}}\right)^2 + \left(\frac{\delta p_i}{p_i}\right)^2}$$

where i = 1 or 2. Table 5.7.1 lists the number of IVB + jet events with $\rho > 0.75$.

The remaining numbers going into Equation (5.10) to calculate R_W are given in Tables 5.7.1 and 5.7.2. The value of the MC calculation of the ratio of acceptances is $\Omega = 0.209 \pm 0.005$. Therefore,

$$\frac{g^W_\tau}{g^W_e} = 0.997 \pm 0.060 \pm 0.043 \qquad (1988/89)$$

Table 5.7.1 : τ + 0jet Universality Measurement with $p_T^{miss} > 25$ GeV and $E_T^1 > 22$ GeV

	Candidates	N_{RES}	N_{IVB}	N_{JJ}
1988/89	237	30	12	11
1990	136	15	6	11

Table 5.7.2 : τ + 0jet Universality Measurement with $p_T^{miss} > 25$ GeV and $E_T^1 > 22$ GeV

	$\check{N}_\tau$	$\check{N}_e$	R_W	$\sqrt{R_W}$
1988/89	175 ± 19	843 ± 42	$0.993 \pm 0.119 \pm 0.085$	$0.997 \pm 0.060 \pm 0.043$
1990	98 ± 13	431 ± 24	$1.088 \pm 0.157 \pm 0.094$	$1.043 \pm 0.075 \pm 0.045$

and

$$\frac{g_\tau^W}{g_e^W} = 1.043 \pm 0.075 \pm 0.045 \quad (1990).$$

By reducing $E_T^{opp}$from 10.0 GeV to 2.5 GeV, the jet contribution to the data is greatly diminished while the estimated number of τ 's is not strongly affected [UA2-91a]. Below 2.5 GeV the resulting uncertainties increase as a result of larger losses in the number of τ 's. Therefore, the result with $E_T^{opp}<$ 2.5 GeV is chosen as the final result since the smaller number of jet events in this sample may render it less susceptible to the uncertainty in the jet subtraction method.

The value of $\sqrt{R_W}$ calculated with the 1990 data is consistent with Ref [UA2-91a] and with the expectation of electron-τ universality to the W. The combined value of $\sqrt{R_W}$ for 1988/89 and 1990 is

$$\sqrt{R_W} \equiv \frac{g_\tau^W}{g_e^W} = 1.016 \pm 0.043 \text{ (stat)} \pm 0.042 \text{ (syst)}$$

and represents the most precise measurement of the couplings ratio by UA2 and supersedes the value published in Ref. [UA2-91a]. It is seen, as expected, that the statistical error has decreased by a factor of ≈ 1.3 relative to Ref.

[UA2-91a] since the data sample has increased by a factor of ≈ 1.8. The systematic uncertainty remains unchanged since the same analysis method was used as Ref. [UA2-91a].

5.8 Charge Information from the Outer Silicon Detector

Information from the OSI could be effective in discriminating real hadronic τ decays from non- τ jet backgrounds by taking advantage of the charge multiplicity profile of τ decays. The variable used is $\delta = Q(0.5) - Q(0.1)$, where Q(x) is the total signal charge in units of minimum ionizing particle equivalent (mip) measured in a cone centred on the cluster axis and of radius $x = \sqrt{(\Delta\eta)^2 + (\Delta\phi)^2}$. This quantity is a measure of the jet narrowness and isolation in terms of charged particles and is clearly correlated with the calorimeter cluster profile. By requiring $\delta < 4.0$ mips, the efficiency for retaining τ's from $W \rightarrow \tau\nu_\tau$ decays is calculated from MC to be $\sim 85\%$ while $\sim 80\%$ of the QCD jets are rejected as is shown in Figures 5.8.1a and 5.8.1b. The effect of the OSI cut on the data sample is shown in Figure 5.8.1c and yields a high rejection of $\sim 70\%$ for a $\delta > 4.0$ mip cut.

Including a cut on the OSI reduces the number of events having $\rho < 0.6$ which are expected to be predominantly from QCD jets. The profile distribution of the data sample is shown in Figure 5.8.2 with and without a cut on the OSI information. Figure 5.8.3 compares the profile distributions of the data sample with MC τ's from $W \rightarrow \tau\nu_\tau$ decays after all analysis cuts. In addition, the number of jet background events in the τ signal region $\rho > 0.75$ has decreased by a factor of about 3.

The measurement of the electron- τ universality follows the same procedure as described above but with the additional cut on the OSI. The value of $\Omega = 0.241 \pm 0.006$. For 1988/89 $R_{2J} = 1.29 \pm 0.02$ while for 1990 $R_{2J} = 1.56 \pm 0.02$. The results for $p_T^{miss} > 20$ GeV and $E_T^1 > 17$ GeV are :

$$\frac{g_\tau^W}{g_e^W} = 0.98 \pm 0.05 \pm 0.04$$

for the τ + 0jet sample, and

$$\frac{g_\tau^W}{g_e^W} = 1.21 \pm 0.17 \pm 0.04$$

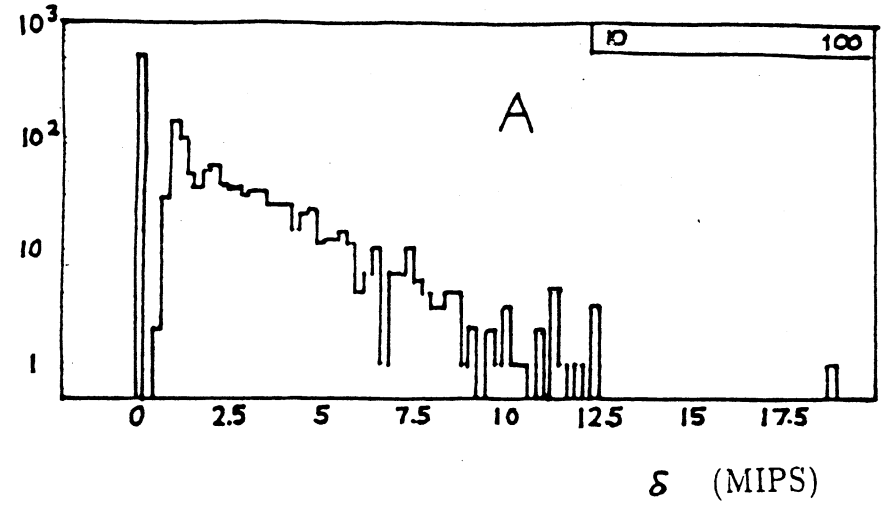

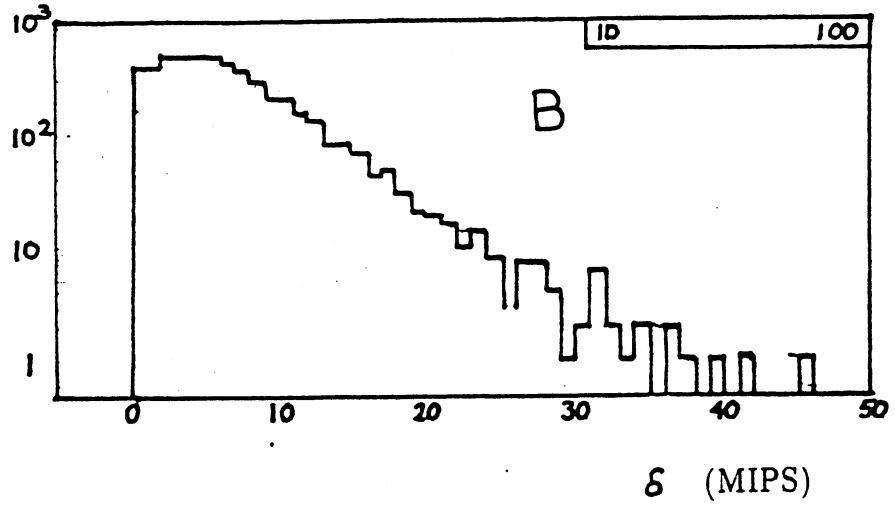

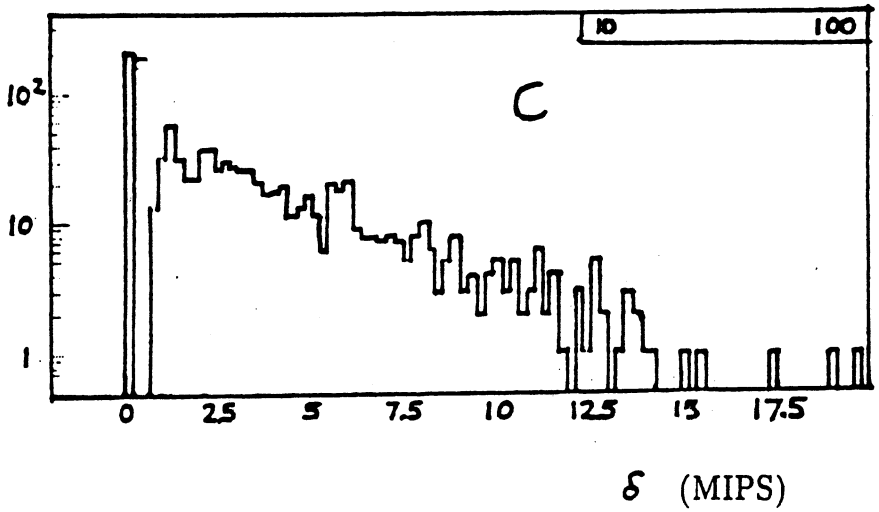

Figure 5.8.1 : OSI δ distribution for (a) τ's from a $W \rightarrow \tau\nu_\tau$ MC, (b) dijets from the 2JH stream, and (c) the 1988/89 τ +0jet data sample.

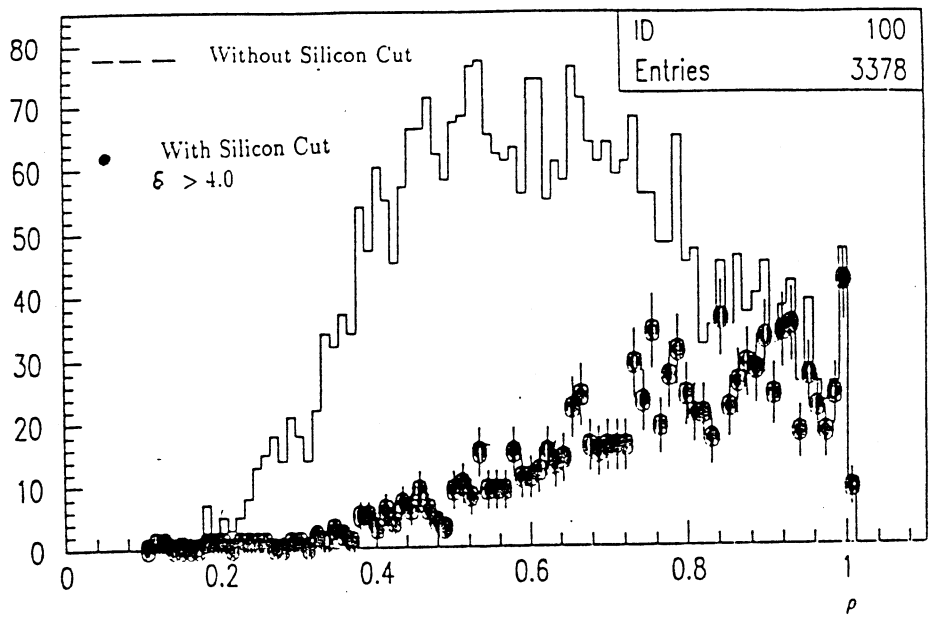

Figure 5.8.2 : The calorimeter profile distribution from the 1988/89 τ +0jet data sample with and without an OSI cut.

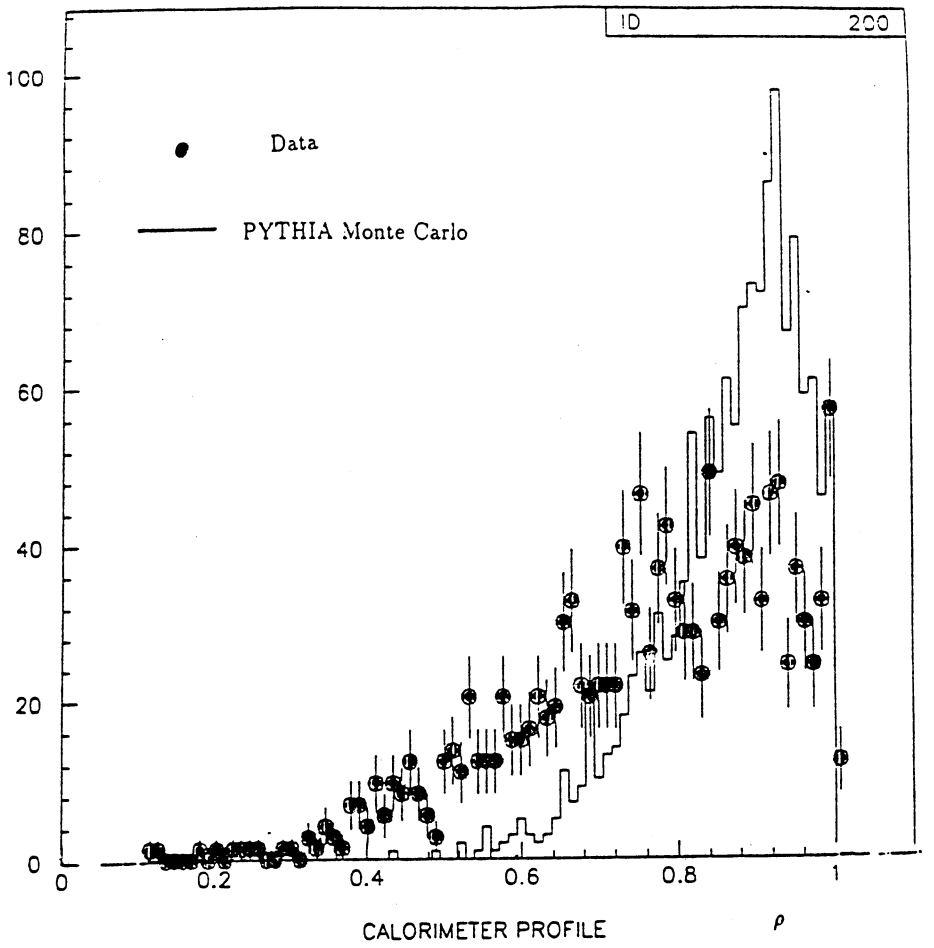

Figure 5.8.3 : Calorimeter profile distribution for τ's from a $W \rightarrow \tau\nu_\tau$ MC and from the 1988/89 τ +0jet sample after a cut at $\delta > 4.0$.

Table 5.8.1 : OSI τ + 0jet Universality Measurement with $p_T^{miss} > 20$ GeV and $E_T^1 > 17$ GeV

	Total Candidates	EM Clusters	Cand. after EM Subtrac.	N_o $\rho > 0.75$	$N_{JJ} + N_{IVB}$ $\rho > 0.75$	N_{RES} $\rho > 0.75$
1988/89	1886	1162	724	437	148	37
1990	1067	635	432	258	113	20

Table 5.8.2 : OSI τ + 0jet Universality Measurement with $p_T^{miss} > 20$ GeV and $E_T^1 > 17$ GeV

	N_τ	N_e	$\tilde{N}_\tau$	$\tilde{N}_e$	R_W	$\sqrt{R_W}$
1988/89	252	870	237 ± 26	989 ± 50	$0.994 \pm 0.123 \pm 0.086$	$0.997 \pm 0.061 \pm 0.043$
1990	126	430	118 ± 21	527 ± 32	$0.929 \pm 0.176 \pm 0.080$	$0.963 \pm 0.091 \pm 0.041$

for the τ + jets sample. The relevant numbers going into R_W are given in Tables 5.8.1 to 5.8.4.

The results including the OSI information are compatible with universality, thus confirming the results given in Section 5.7 but in the presence of a much reduced background. However, the statistical uncertainties do not decrease because the reduced number of background jets increases the uncertainty on their profile distribution. The systematic uncertainties on the jet subtraction are also not reduced because of the stronger energy dependence of the OSI multiplicity variable with respect to the calorimeter profile (see

Table 5.8.3 : OSI τ + jets Universality Measurement with $p_T^{miss} > 20$ GeV and $E_T > 17$ GeV

	Total Candidates	EM Clusters	Cand. after EM Subtrac.	N_o $\rho > 0.75$	$N_{JJ} + N_{IVB}$ $\rho > 0.75$	N_{RES} $\rho > 0.75$
1988/89	235	121	114	64	23	4
1990	120	53	67	33	17	1

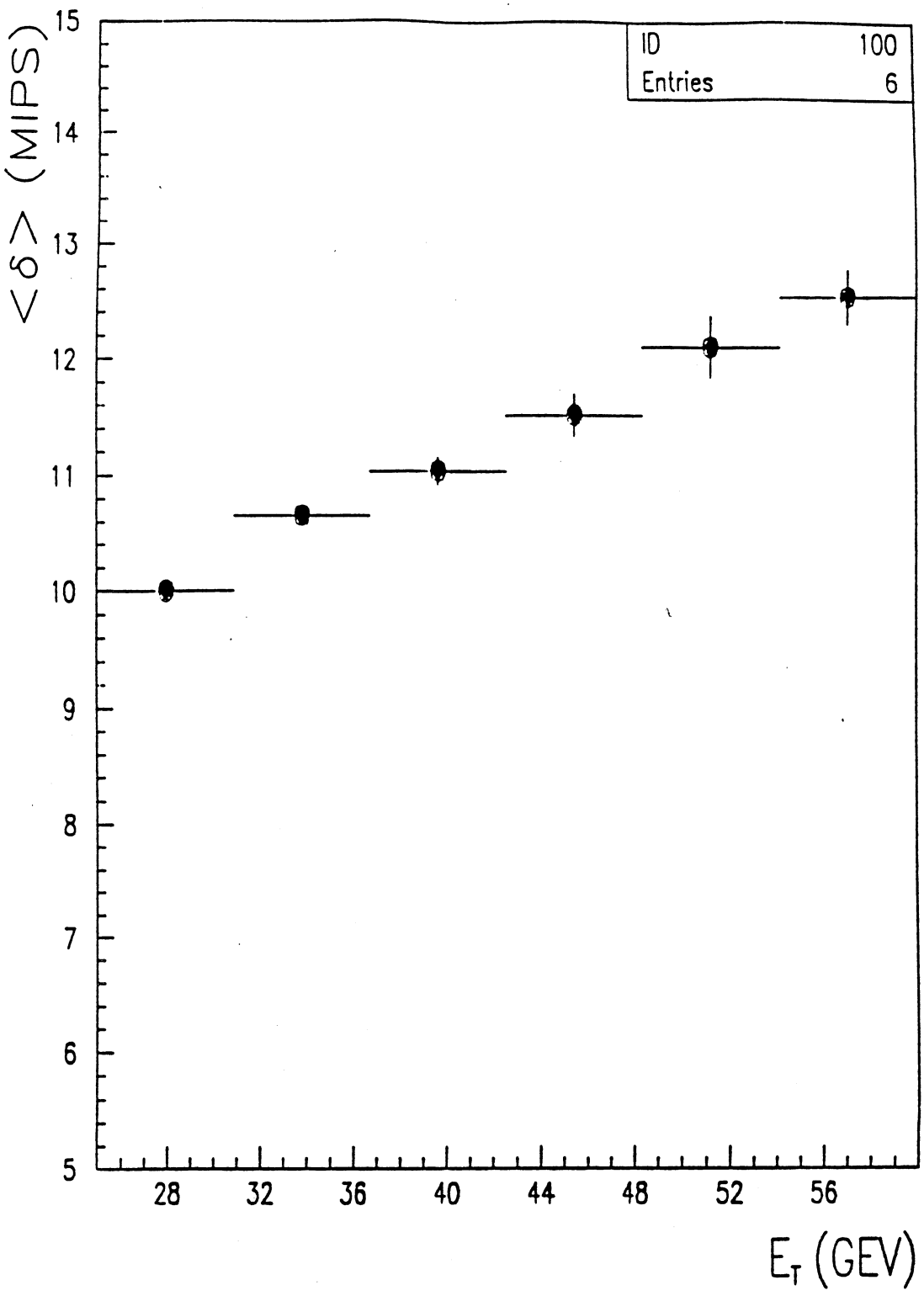

Figure 5.8.4 : Variation of the mean δ value $< \delta >$ as a function of the QCD jet E_T.

Table 5.8.4 : OSI τ + jets Universality Measurement with $p_T^{miss} > 20$ GeV and $E_T > 17$ GeV

	N_τ	N_e	$\tilde{N}_\tau$	$\tilde{N}_e$	R_W	$\sqrt{R_W}$
1988/89	37	88	35 ± 10	99 ± 11	$1.467 \pm 0.451 \pm 0.126$	$1.211 \pm 0.186 \pm 0.052$
1990	15	31	14 ± 8	38 ± 7	$1.529 \pm 0.519 \pm 0.131$	$1.236 \pm 0.371 \pm 0.053$

below). Such techniques, however, may prove useful tool for τ identification with a larger event sample as expected at future colliders.

Another way which the OSI information can be used is to drop the calorimeter profile altogether and to define a signal region based on δ. This has the advantage that the useful pseudorapidity range can be extended to include the full acceptance of the OSI ($| \eta | < 1.9$) thus increasing the number of events in the data sample by about a factor of 2.

However, whereas ρ for QCD jets is approximately independent of the p_T^{miss} and E_T, the δ increases with increasing kinematical cuts as is shown in Figure 5.8.4. This makes a jet subtraction based on the δ distribution of QCD jets alone very difficult because there is not enough data from the 2JH stream with $p_T^{miss} > 20$ GeV and not enough p_T^{miss} stream data in total to be able to satisfactorily parametrize the δ distributions over a fine enough (p_T^{miss}, E_T) grid.

The efficiency of the OSI cut selecting MC τ's from $W \rightarrow \tau\nu_\tau$ decays is $(85 \pm 4)\%$ and $(86 \pm 6)\%$ for τ's in the E_T range (17,25) GeV and (30,60) GeV, respectively. This suggests that the OSI variable is independent of the τ E_T. An explanation is that with increasing jet E_T more particles are created in dijet events thus increasing δ while the number of charged particles resulting from τ decay does not vary appreciably with the τ E_T.

Chapter 6

The Charged Higgs Lower Mass Limit

6.1 Measurement of the τ Excess

Having determined in the previous chapter that the ratio of couplings of the electron and τ to the W is consistent with unity for both the 'τ +0jets' and the 'τ +jets' samples, it can be concluded that no excess is detected in the number of τ events. This can be quantified by calculating τ excesses under the assumption that electron-τ universality is strictly valid. From the number of observed electrons and the assumption that the ratio of couplings of the electron and τ to the W is unity, estimates are obtained for the expected number of τ 's from $W \rightarrow \tau\nu_\tau$ in the 'τ +0jets' and 'τ +jets' samples which can be compared to the observed numbers in order to extract quantitative excesses [UA2-92, Cav-91a, Cav-91b, APS-91, EPS-91a, SSS-91, Mor-92f].

The absolute number of τ 's in the data sample is

$$N_\tau^{obs} = \frac{\tilde{N}_\tau}{\epsilon_{tot}\kappa_\tau}$$

where a correction is made for the efficiencies of Table 5.3.1 with

$$\epsilon_{tot} = \epsilon_{MB}\epsilon_{VETO}\epsilon_{TOF}\epsilon_{fid.vol.}\epsilon_{VTX},$$

κ_τ is the tracking efficiency for τ 's and $\tilde{N}_\tau$ is the quantity defined in Equation (5.12). Because the efficiencies on the 1988/89 and 1990 data samples are

different, the events are summed after the corrections so that

$$N_\tau^{obs} = N_\tau^{obs}(1988/89) + N_\tau^{obs}(1990).$$

For the combined 1988/89 and 1990 running periods the following estimates are obtained :

$$'\tau + 0\text{jets}' : N_\tau^{obs} = 760 \pm 31 \pm 25$$

$$'\tau + \text{jets}' : N_\tau^{obs} = 68 \pm 8 \pm 3.$$

The systematic errors coming into the calculation of N_τ^{obs} are due to the beam-halo, jet subtraction procedure, and energy threshold criteria (see Section 5.5). The errors are computed by taking the quadratic sum of the various contributions to the uncertainties giving a total systematic uncertainty of $\pm 5\%$.

To convert the observed number of electrons into a prediction of the number of τ 's from $W \rightarrow \tau\nu_\tau$, the MC ratio of acceptances for τ 's and electrons from W decay is used, ($\Omega = 0.259 \pm 0.006$). Therefore,

$$R_W \equiv 1 = \frac{1}{\Omega} \frac{\tilde{N}_\tau^U}{\tilde{N}_e}$$

which is analogous to Equation (5.10) for the particular case of measuring $\tilde{N}_\tau^U$ - the value of $\tilde{N}_\tau$ obtained assuming strict universality ($R_W = 1$). This yields

$$\tilde{N}_\tau^U = \tilde{N}_e \, \Omega$$

and correcting for the efficiencies of Table 5.3.1 gives

$$N_\tau^U = \frac{\tilde{N}_\tau^U}{\epsilon_{tot} \, \kappa_\tau}.$$

For the combined 1988/89 and 1990 running periods the following estimates for the number of τ 's from $W \rightarrow \tau\nu_\tau$ assuming strict universality are obtained

$$'\tau + 0\text{jets}' : N_\tau^U = 754 \pm 68 \pm 54$$

$$'\tau + \text{jets}' : N_\tau^U = 73 \pm 24 \pm 5$$

where again

$$N_\tau^{obs} = N_\tau^{obs}(1988/89) + N_\tau^{obs}(1990).$$

The systematic errors arise from the profile, hadronicity, and electron identification requirements giving a total systematic uncertainty of ±6.5%. Again, the errors are computed by taking the quadratic sum of the various contributions.

The τ excess is defined as

$$N_\tau^{exc} = N_\tau^{obs} - N_\tau^{U}$$

giving for the combined 1988/89 and 1990 samples

$$'\tau + 0\text{jets}' : N_\tau^{exc} = -6 \pm 75 \pm 60$$

$$'\tau + \text{ jets}' : N_\tau^{exc} = +5 \pm 25 \pm 6$$

It is seen that the excess in both samples is consistent within uncertainties to be zero. The 'τ +jets' sample is more sensitive to any deviation from universality because of the smaller uncertainties.

6.2 Signal Expected from the $H^{\pm}$ Process

The estimated number of τ 's expected for each $(m_t, m_{H^{\pm}})$ pair is determined by passing the PYTHIA MC generated events of the type

$$t \rightarrow H^+b,\ H^+ \rightarrow \tau^+\nu_\tau, \tau^+ \rightarrow \text{hadrons} + \overline{\nu}_\tau \qquad (6.2.1)$$

and its charge conjugate both through all the applicable standard analysis cuts discussed in Section 5.3 and through the trigger cuts described in Section 3.5. The application of the first four criteria in Table 5.3.1, pertaining to UA2 data only, is not performed on the MC.

In this section distributions from the PYTHIA MC for various kinematical and topological variables are shown for the signal process (6.2.1). All diagrams shown are for the τ + 0jet subsample. Figure 6.2.1 depicts the pseudorapidity η and the azimuthal angle ϕ distributions for τ 's, where it is seen that the τ 's are preferentially produced at low pseudorapidities and are uniformly distributed in ϕ. Figure 6.2.2 shows the η and ϕ distributions for the leading E_T jet. Whereas the ϕ distribution is still uniform and well-correlated to the τ ϕ, (see Figure 6.2.3), the η distribution is different than that of the τ candidate and in particular is flatter. This is one example of

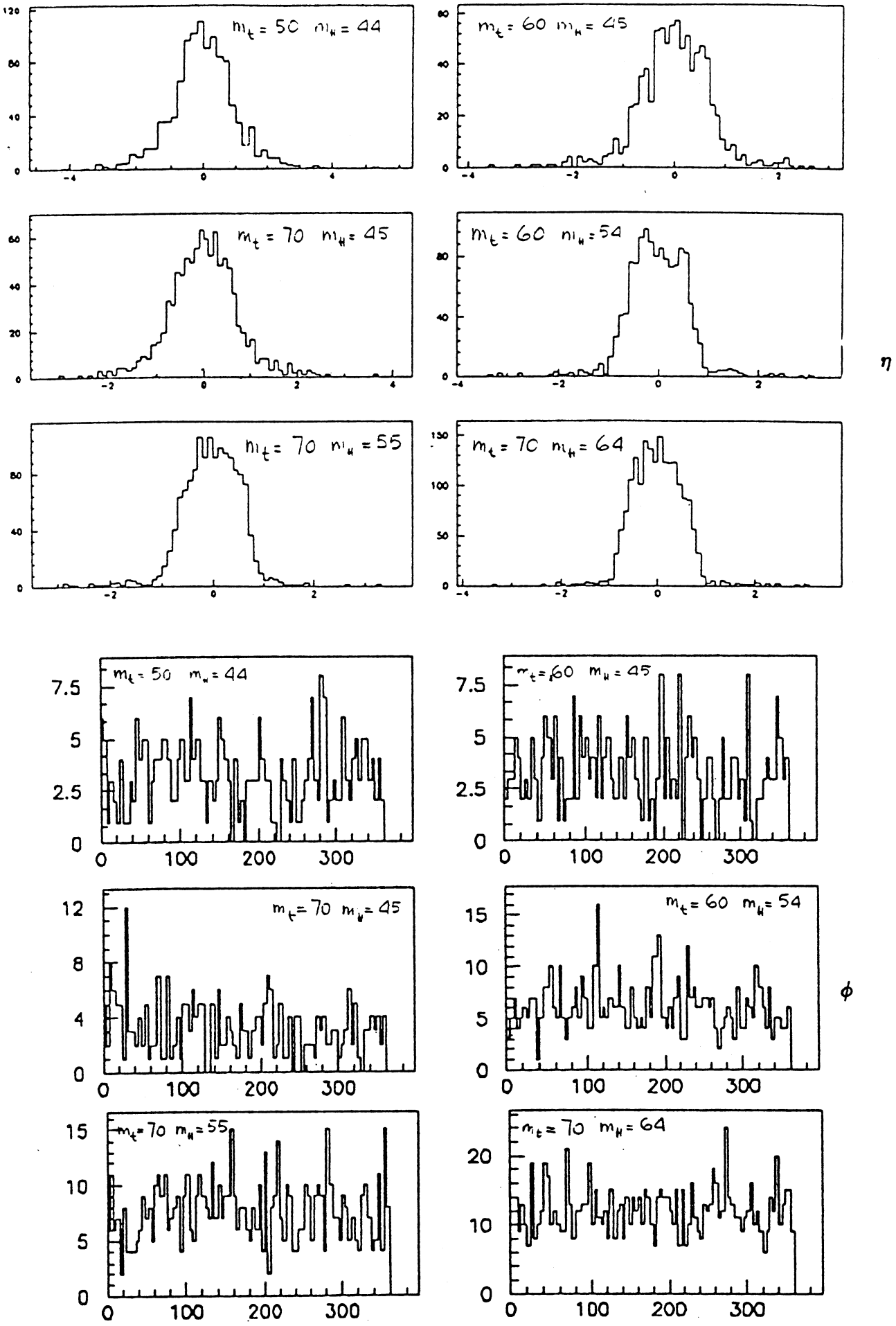

Figure 6.2.1 : The pseudorapidity η and azimuthal angle ϕ for τ 's from the τ data sample for various $(m_t, m_{H^\pm})$ pairs.

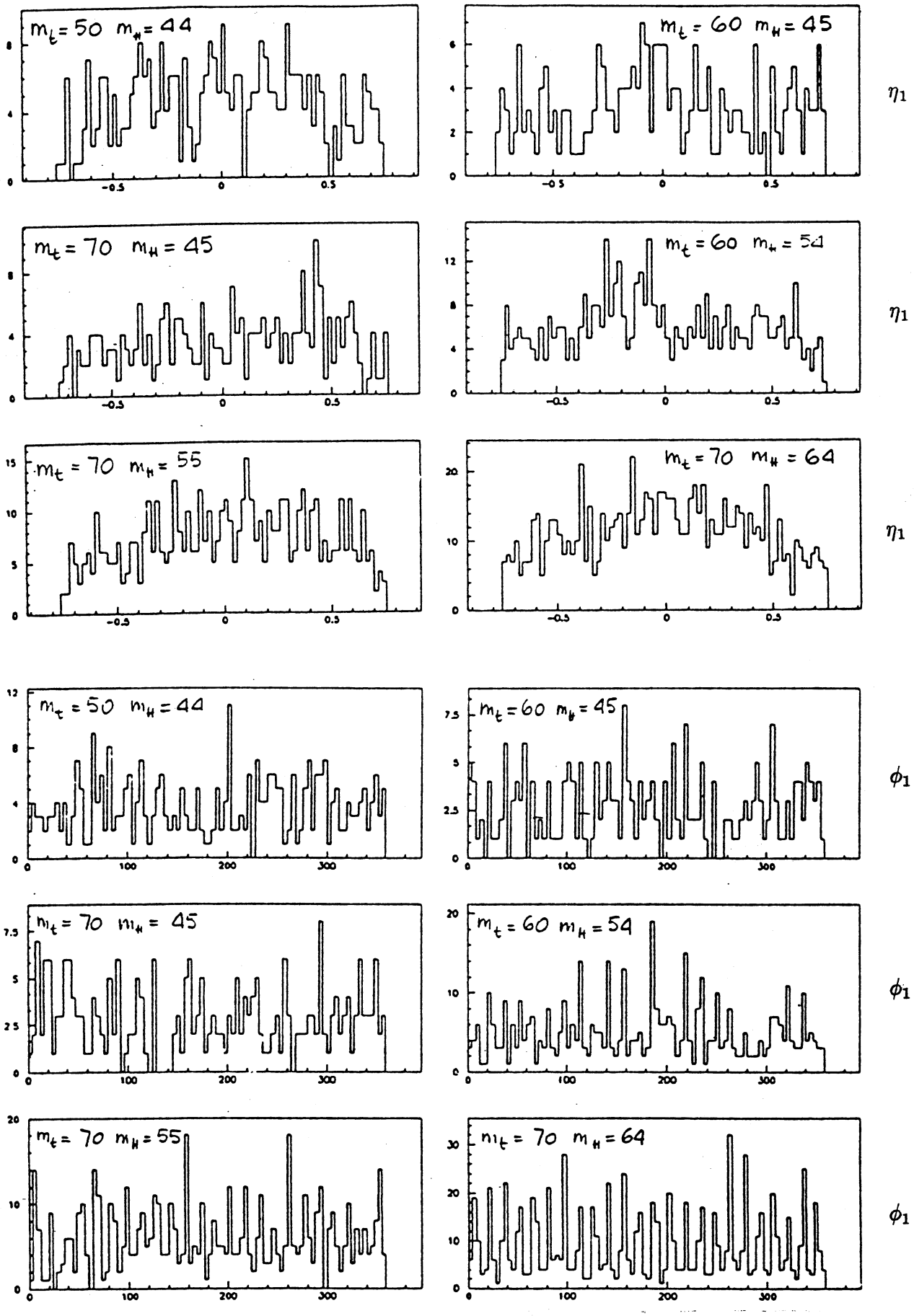

Figure 6.2.2 : The pseudorapidity η and azimuthal angle ϕ for the leading cluster from the τ data sample for various $(m_t, m_{H^\pm})$ pairs.

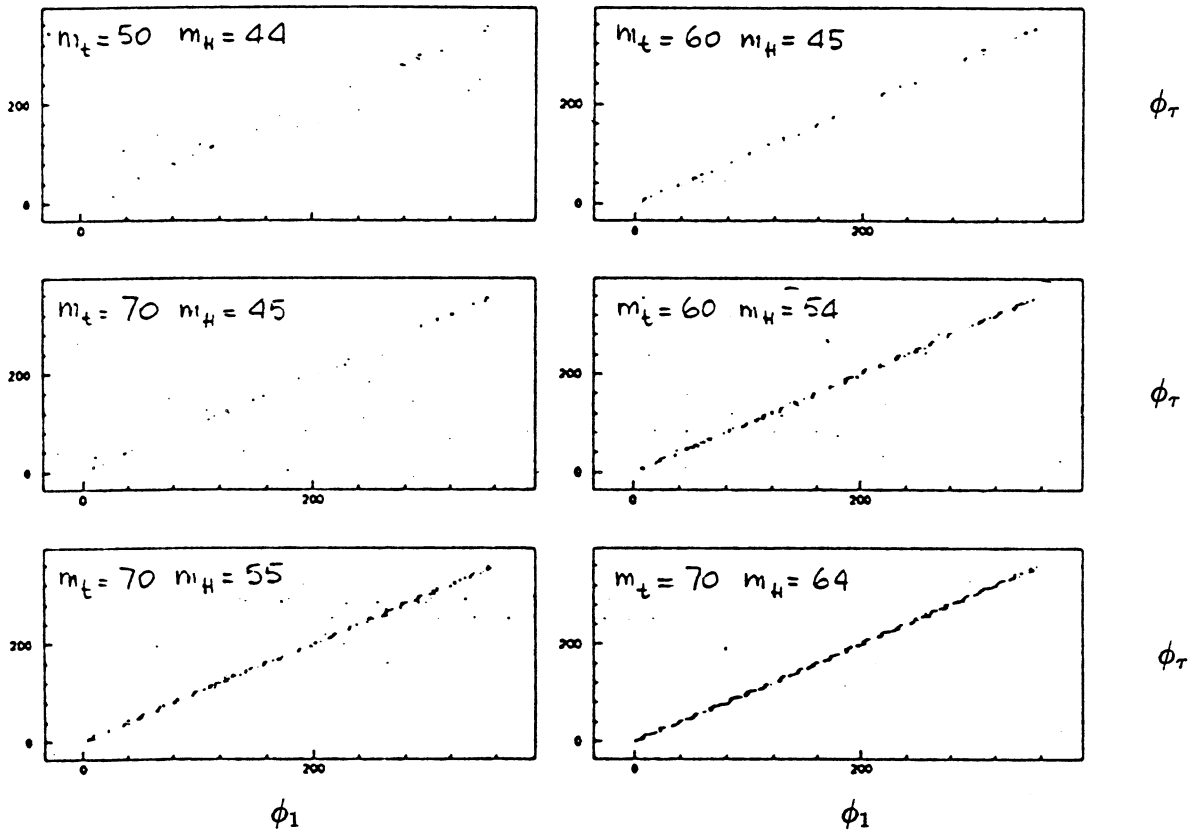

Figure 6.2.3 : Correlation in ϕ between the τ candidate and the leading jet in the event.

suggesting that the τ candidate is not always associated with the leading E_T cluster. The leading jet E_T, E_T^1, and the candidate τ E_T, E_T^τ, are shown in Figure 6.2.4. The correlation between E_T^1 and E_T^τ is shown in Figure 6.2.5 where it is seen that E_T^τ is well-correlated with E_T^1 only when the mass difference $m_t - m_{H^\pm}$ is small. The ρ distribution for the leading jet is shown in Figure 6.2.6 for two different mass pairs. It is noted that for $m_t = 70$ GeV and $m_{H^\pm} = 64$ GeV, the fraction of events having $\rho < 0.75$ is 0.22 ± 0.02 whereas for $m_t = 70$ GeV and $m_{H^\pm} = 45$ GeV, this fraction is 0.67 ± 0.06. The former value is characteristic of τ 's whereas the latter value is typical of non-τ jets which, because of their relative broadness, populate the lower ρ region. Therefore, it can be concluded that as the $(m_t, m_{H^\pm})$ mass difference increases the less likely it is for the τ to be associated with the leading cluster of the event. This is also illustrated in Figure 6.2.7 where it is shown, for example, that for $m_t = 70$ GeV and $m_{H^\pm} = 45$ GeV, it is highly likely that the candidate τ is associated with a non-leading cluster. In addition, as is shown in Figure 6.2.8, with an increasing $(m_t, m_{H^\pm})$ mass difference the number of jets in the event with $E_T > 10$ GeV increases. This suggests that it becomes less likely to correctly identify the τ candidate as the leading cluster because of the competition with non-τ jets which predominantly come from the b-quarks.

Finally, the p_T^{miss} distribution is shown in Figure 6.2.9 where it is seen that, as expected, given a m_t value, the p_T^{miss} distributions peak at larger values as the $(m_t, m_{H^\pm})$ mass difference decreases. Figure 6.2.10 shows the event topology for the strong and electroweak top production processes with the top decaying to $H^\pm$.

In the MC simulation τ 's from $H^\pm$ decay are generated with no polarization (contrary to τ 's from W decay for which polarization effects are taken into account). As pointed out in Ref. [Roy-91, Bul-91], the effect of polarization in the $H^\pm$ decay would increase the mean momentum of the decay hadrons, thus increasing the acceptance of the process (6.2.1). This effect is $\sim 5 - 10\%$ as checked for various mass pairs, corresponding to an increase of $\sim 2 - 3\%$ for the CL of the excluded region in the $(m_t, m_{H^\pm})$ mass plane (see Section 6.4).

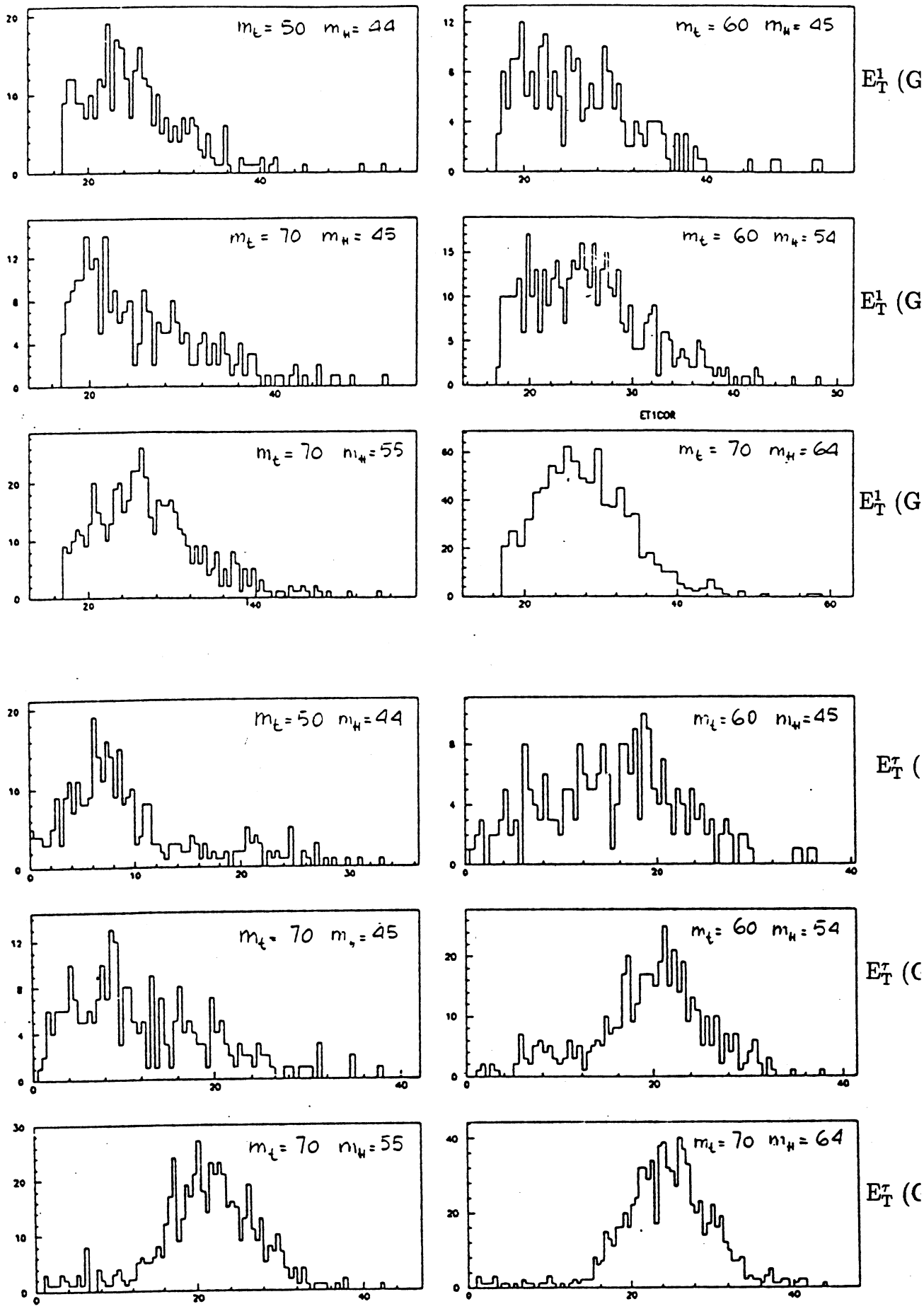

Figure 6.2.4 : The leading jet E_T, E_T^1, and the candidate τ E_T, E_T^τ.

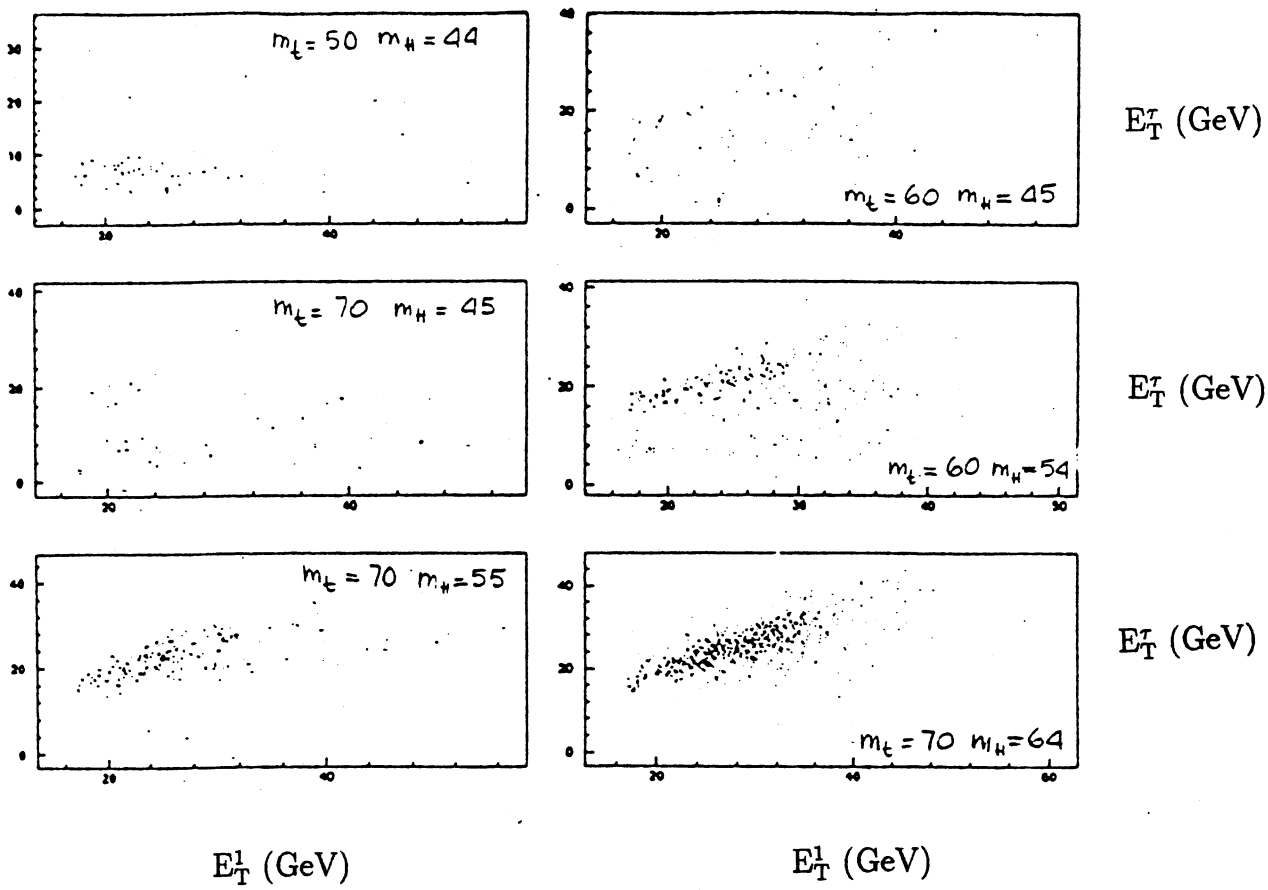

Figure 6.2.5 : The correlation between E_T^l and E_T^τ.

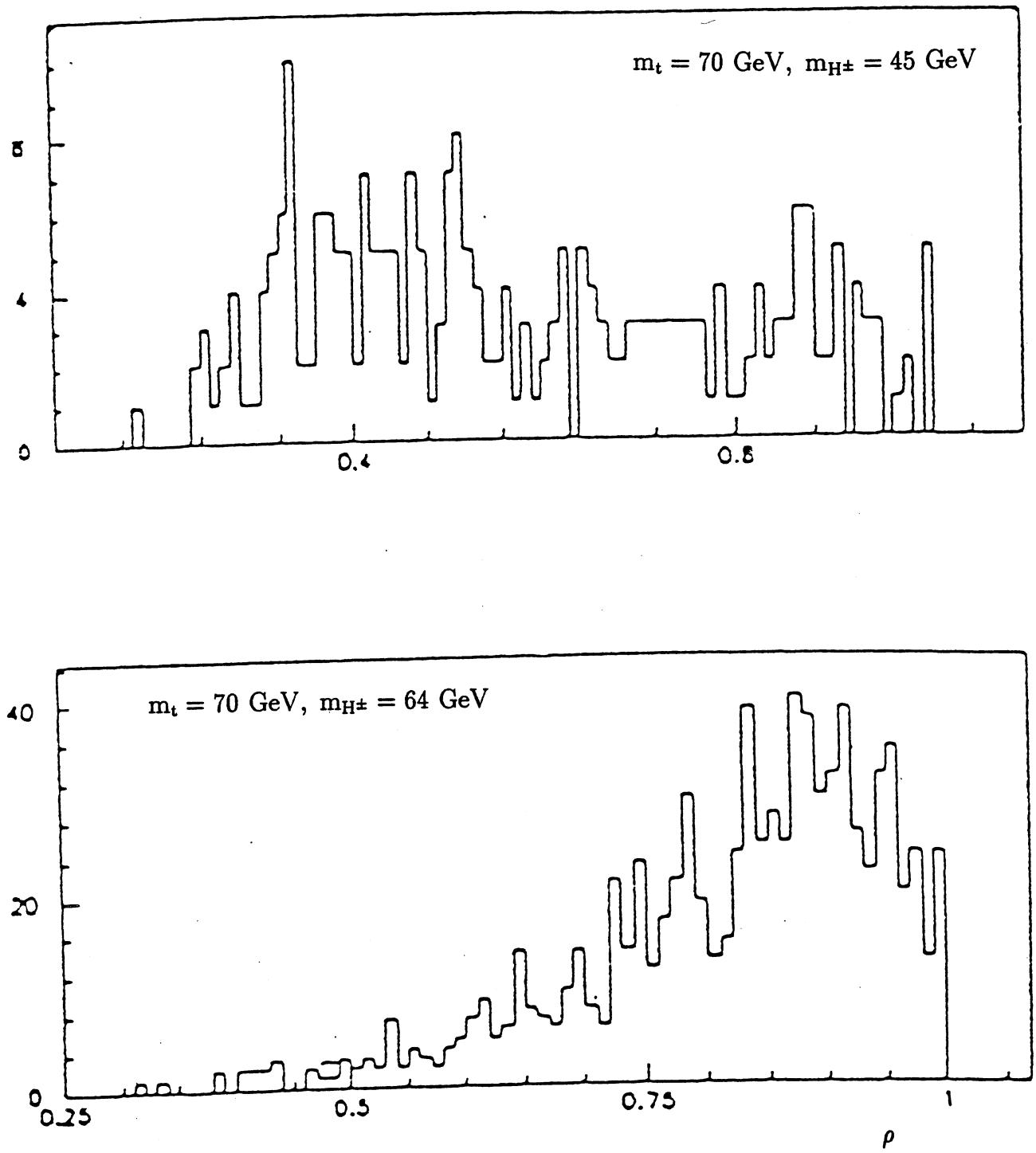

Figure 6.2.6 : The leading jet profile distribution for various $(m_t, m_{H\pm})$ mass pairs.

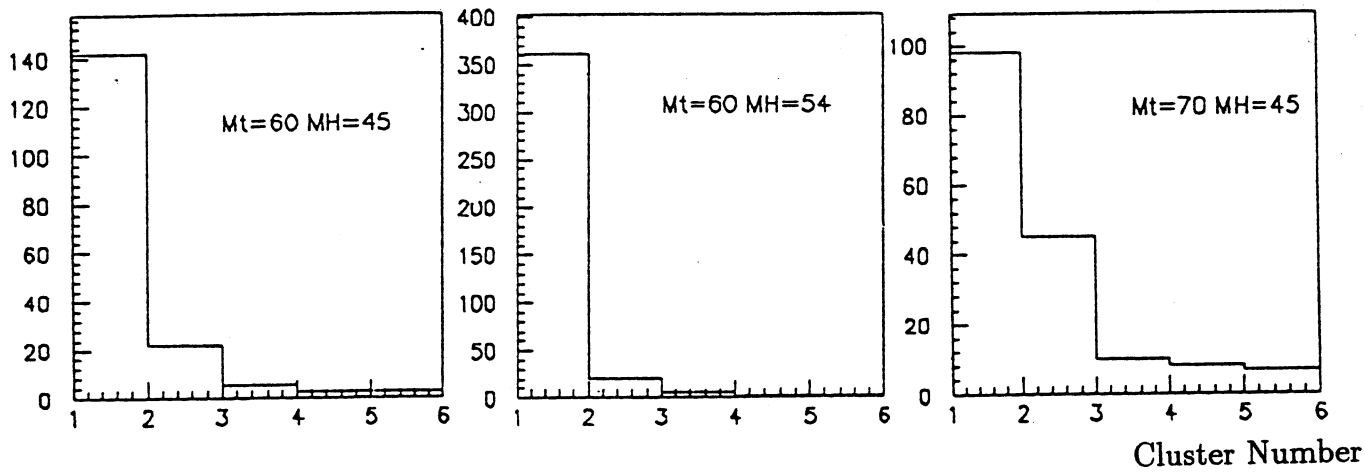

Figure 6.2.7 : The placing of the τ candidate cluster in an E_T -ordered list. A τ candidate identified as the leading cluster in the event is indicated in the first bin of the histogram.

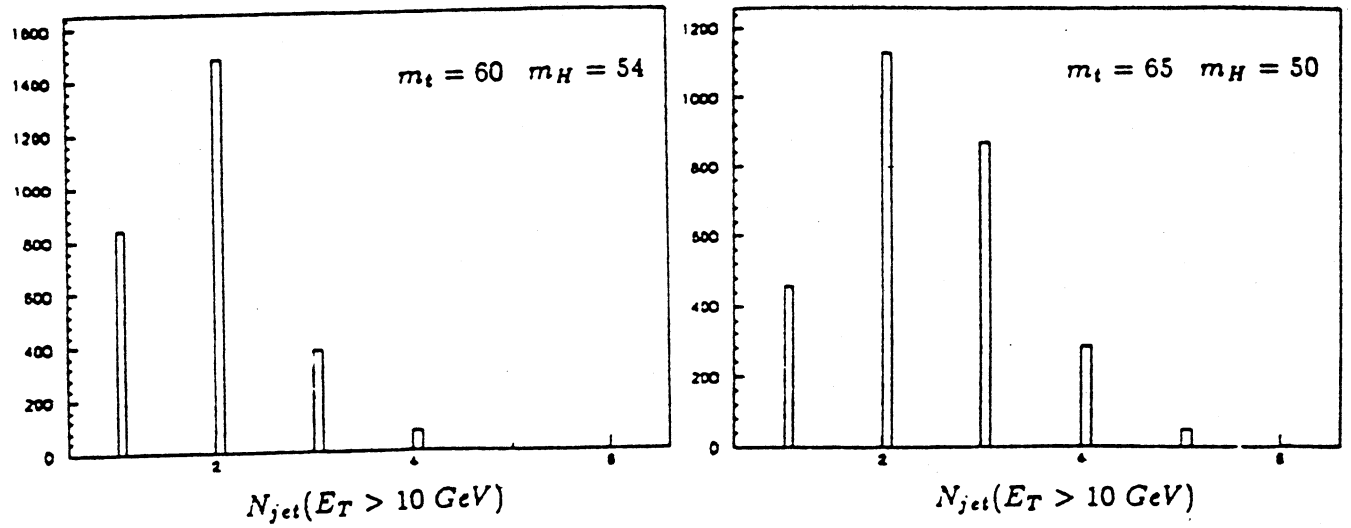

Figure 6.2.8 : The number of clusters with $E_T > 10$ GeV in an event for various $(m_t, m_{H\pm})$ mass pairs.

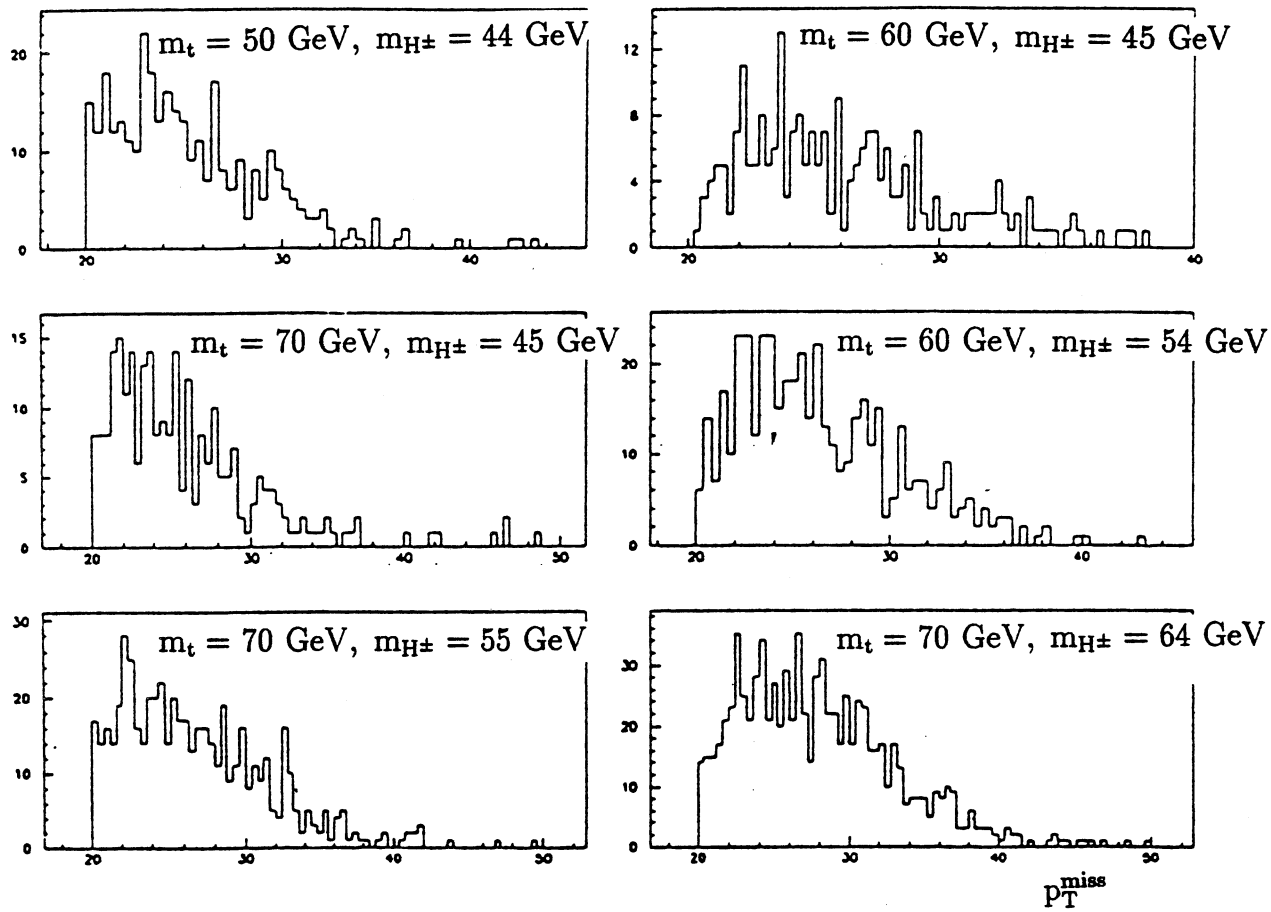

Figure 6.2.9 : The p_T^{miss} distibutions following the application of the analysis cuts for various $(m_t, m_{H^\pm})$ mass pairs.

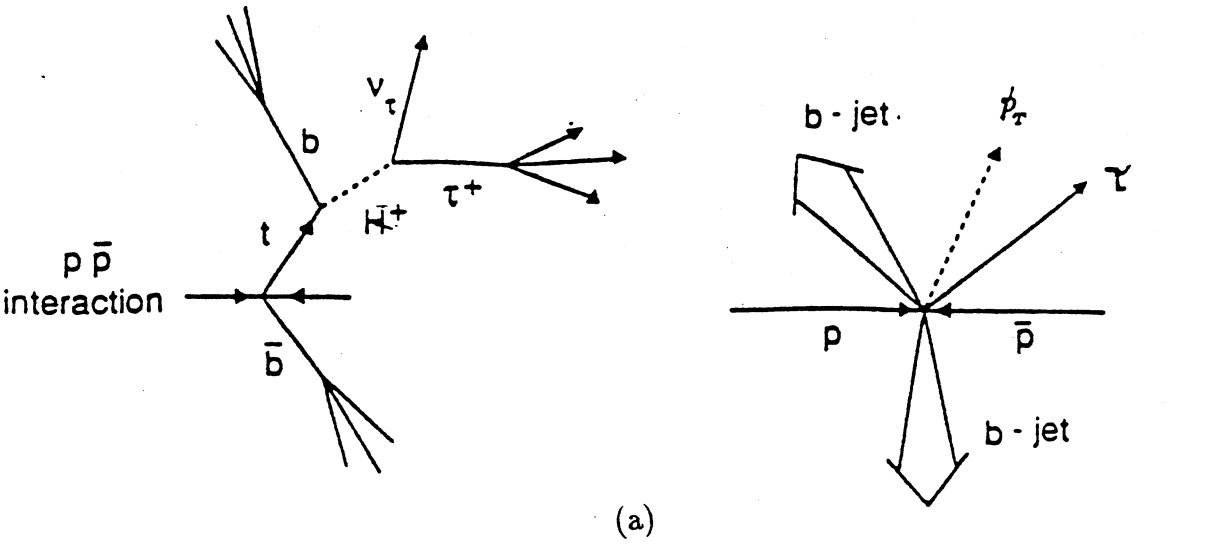

(a)

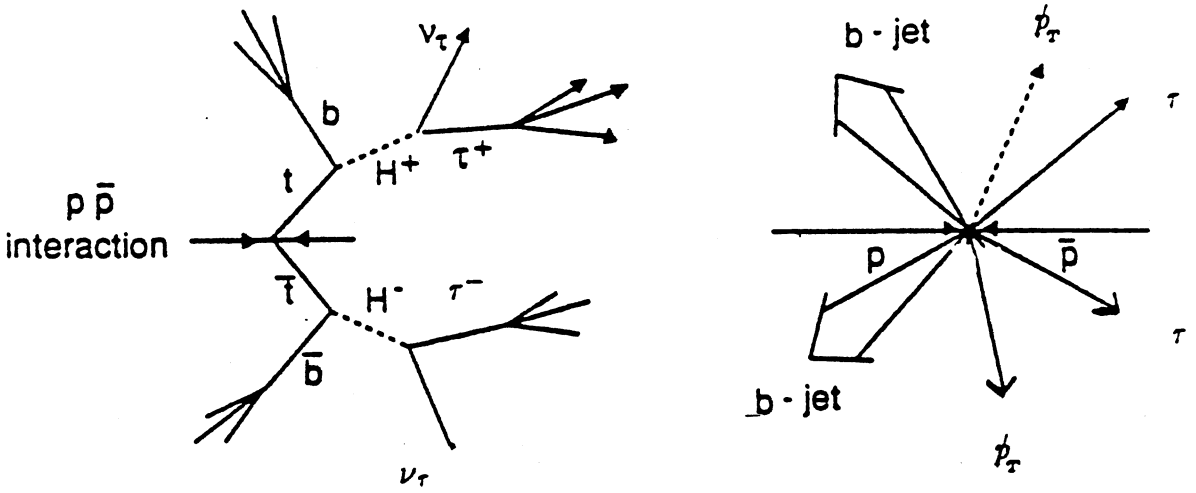

(b)

Figure 6.2.10: The top production and decay topology for the (a) $t\bar{b}$ and (b) $t\bar{t}$ channels.

6.3 Systematic Uncertainties

The systematic uncertainties in the number of τ 's expected from W decay and of τ 's observed are given in Section 5.5. Below are listed the systematic uncertainties for the expected number of τ 's coming from the channel in (6.2.1). Contributions to the uncertainties are from theoretical, MC, and experimental sources.

- The uncertainty in the total integrated luminosity is $\pm 6.0\%$ (Gaussian distribution).
- The uncertainty in the number of produced top quarks depends on the accuracy to which the production cross-section is known. A mass-dependent uncertainty of between $\pm 3\% - 10\%$ for the electroweak production process and $\leq 30\%$ for the strong production process is evaluated assuming a Gaussian distribution.
- The effect of the energy scale uncertainties is estimated by varying the energy thresholds. The shapes of the distributions of the kinematic variables near thresholds, and consequently of the τ selection efficiencies, vary with m_t and $m_{H^\pm}$ between $\pm 2\%$ and $\pm 10\%$ (widths of flat distributions).
- To estimate the effect of the uncertainties in the MC reproduction of the additional jets which enter the data sample as jets opposite or in addition to the leading jet, the ratio

$$R_{01} = \frac{W \rightarrow e\nu_e + 1 \text{ jet } (E_T > 10 \text{ GeV})}{W \rightarrow e\nu_e + 0 \text{ jets}}$$

  calculated from an EKS $W \rightarrow e\nu_e$ MC is compared to that measured from UA2 data. The former is found to have a value of $\sim 10\%$ below that of the latter. The MC ratio matches that of the data by varying the jet threshold by 500 MeV. A conservative estimate of ± 1 GeV is therefore assumed for the uncertainty in the MC additional jet energy. The effect of this on the MC $H^\pm$ data is mass-dependent but in no case exceeds a $\pm 10\%$ variation in the signal acceptance.

- The uncertainty resulting from the method of reconstructing spectator parton interactions is estimated by taking the difference in the signal efficiency obtained for two different MC configurations. In the first case, 1 UA2 MB event is superimposed on the PYTHIA generated event in which the diquark fragmentation is included. In the second case 2 UA2 MB events are superimposed on the event and diquark fragmentation is not included. This is found to be a mass-dependent effect but does not exceed $\pm 25\%$ in any of the cases considered. As a result of these tests a $\pm 25\%$ uncertainty in the signal acceptance is therefore associated with the simulation of the underlying event.

- Finally, the effect of varying the fragmentation parametrization for heavy quarks (c,b,t) in the SLAC heavy flavour fragmentation function, (see Section 4.1), to be consistent with LEP data yields a variation in the signal acceptance which does not exceed $\pm 8\%$ in any of the cases studied. The parameter $c = \frac{m_q}{m_t}$ for q = c,b,t has been changed from the default value of zero to 0.01 [Sjo-91].

In the case of mass-dependent uncertainties, the maximum uncertainties mentioned above are used.

6.4 Excluded Regions in the $m_t - m_{H^\pm}$ Plane

Given the above mass-dependent τ excesses coming from $H^\pm$ decays and their calculated uncertainties, it is possible to ascertain whether the observations are consistent with theoretical expectations from the process (6.2.1). Because the observed τ excess for both the 'τ +0jet' and 'τ +jets' data samples are consistent with zero, it is necessary to investigate if the uncertainties in these results and the size of the hypothetical excess coming from the MC are sufficient to rule out the decay mode of (6.2.1) for certain parameter values. Levels of confidence (CL) for the exclusion of process (6.2.1) for the parameters of the 16 $(m_t, m_{H^\pm})$ mass pairs used in the MC and for two choices for $Br(H^\pm \rightarrow \tau\nu_\tau)$ of 1.0 and 0.5, (corresponding to $\tan\beta \geq 2$ and $\tan\beta = 1$, respectively), are calculated.

The number of expected $H^\pm$ decays with $\rho > 0.75$ is

$$N'_{H^\pm} = L \cdot \sigma_{H^\pm} \cdot A$$

where L is the total integrated luminosity of the collected data, A is the MC acceptance for the decay chain (6.2.1) and is calculated for each $(m_t, m_{H^\pm})$ mass pair. For the electroweak top production process

$$\sigma_{H^\pm} = \sigma_{t\bar{b}}\, \mathrm{Br}(t \to H^\pm b)\, \mathrm{Br}(H^\pm \to \tau\nu_\tau)\, \mathrm{Br}(\tau \to h\overline{\nu}_\tau)$$

where $\sigma_{t\bar{b}}$ is the cross-section times branching ratio for $t\bar{b}$ production from W decay. For the strong interaction process

$$\sigma_{H^\pm} = \sigma_{t\bar{t}}\, [\mathrm{Br}(t \to H^\pm b)]^2\, [\mathrm{Br}(H^\pm \to \tau\nu_\tau)]^2\, \mathrm{Br}(\tau \to h\overline{\nu}_\tau)$$

where $\sigma_{t\bar{t}}$ is the cross-section for $t\bar{t}$ production and where only one of the τ 's is forced to decay hadronically.

In the case of the τ +0jet sample,

$$N'_{H^\pm} = N'_{H^\pm}(t\bar{b})$$

because the contribution from $t\bar{t}$ is negligible but for the τ +jets sample

$$N'_{H^\pm} = N'_{H^\pm}(t\bar{b}) + N'_{H^\pm}(t\bar{t}).$$

Table 6.4.1 gives the expected number of events together with the acceptances, A, for $\mathrm{Br}(H^\pm \to \tau\nu_\tau) = 1.0$ and for $E_T^{opp} < 10.0$ GeV.

The non-τ jets must be subtracted from the $\rho > 0.75$ region and is done as follows :

$$N_{jet}(0.75) = R_{2J} \cdot N_{H^\pm}$$

is the number of non-τ jets expected to populate the $\rho > 0.75$ region, R_{2J} is given in Section 5.4.4, and $N_{H^\pm}$ is the number of $H^\pm$ events with $\rho < 0.60$. The number of $H^\pm$ signal events in the region $\rho > 0.75$ after subtracting the non-τ background is then

$$N''_{H^\pm}(0.75) = N'_{H^\pm} - N_{jet}(0.75)$$

and the acceptance after all cuts is

$$A = \frac{N''_{H^\pm}}{N_{TOT}}$$

where N_{TOT} is the total number of generated events. The uncertainty associated with $N''_{H^\pm}$ is

$$\sigma_{N''_{H^\pm}} = \frac{1}{A} \cdot \sqrt{\frac{A \cdot (1-A)}{N_{TOT}}}$$

where it is assumed that the uncertainty on the total integrated luminosity is negligible.

For a given data sample and set of parameter values, the various uncertainties in the number of observed and expected τ 's are combined into a single uncertainty $\sigma_i(m_t, m_{H^\pm})$, (i = 0,1 corresponds to the 'τ +0jet' and 'τ +jets' samples, respectively), using an MC program which takes into account the shapes of the individual uncertainty distributions given in the last section. The MC also takes into account any known correlations between the uncertainties. The error distribution obtained from the MC programme is found to be approximately Gaussian.

For each of the two data samples, a probability distribution for the observed τ excess is defined using the hypothetical excess as the mean of the distribution and $\sigma_i(m_t, m_{H^\pm})$ as its width. The probability that the expected excess for a given sample lies at or below the observed τ excess is calculated from

$$P_i(y_i \leq x_i) = \frac{1}{\sqrt{2\pi}\sigma_i(m_t, m_{H^\pm})} \int_{-\infty}^{x_i} \exp\left(\frac{(x_i - y_i)^2}{2(\sigma_i(m_t, m_{H^\pm}))^2}\right) dx$$

where x_i is the observed τ excess and y_i is the expected τ excess for the 'τ +0jet', (i=0), and 'τ +jets', (i=1) data samples. The results of the samples are combined by taking a weighted average.

Before the CL's are calculated the quantities x_i, y_i and $\sigma_i(m_t, m_{H^\pm})$ are first scaled by $\frac{1}{y_i}$. Such scaling does not alter the value of $P(y_i \leq x_i)$ given above. Therefore, the quantity $\frac{x_i}{y_i}$ is the fraction of the expected τ 's which are actually observed. For both samples the mean value expected for this quantity is unity if the $H^\pm$ hypothesis of (6.2.1) is valid. The combined probability distribution of the two data samples has mean expectation of unity and a weighted mean observation given by

$$\alpha = \sum_{i=0}^{1} \frac{x_i y_i}{(\sigma_i(m_t, m_{H^\pm}))^2}$$

Table 6.4.1 : Acceptances and Expected Number of Events for (6.2.1)

m_t (GeV)	m_H (GeV)	$\tau + 0jet$ A for $t\bar{b}$	$\tau + 0jet$ Expected	$\tau + jets$ A for $t\bar{b}$	$\tau + jets$ A for $t\bar{t}$	$\tau + jets$ Expected
50	44	.007	25	.016	.057	118
55	45	.015	39	.019	.058	92
55	49	.027	72	.027	.073	125
60	45	.019	35	.013	.050	44
60	50	.046	85	.023	.072	70
60	54	.058	106	.040	.103	113
65	45	.015	17	.017	.046	31
65	50	.044	49	.021	.073	41
65	55	.088	98	.019	.087	42
65	59	.114	128	.024	.109	52
70	45	.010	5	.013	.044	14
70	50	.034	18	.021	.057	21
70	55	.085	45	.021	.087	25
70	60	.149	80	.021	.103	28
70	64	.169	90	.026	.120	33
71.5	66	.185	79	.025	.122	27

Table 6.4.2 : Exclusion Confidence Levels

m_t (GeV)	m_H (GeV)	$\tau + 0jet$ B = 1	$\tau + jets$ B = 1	ALL B = 1	$\tau + 0jet$ B = .5	$\tau + jets$ B = .5	ALL B =.5
50	44	60.7	99.9	99.9	55.7	92.5	92.6
55	45	65.4	99.4	99.5	58.1	88.2	88.5
55	49	76.4	99.9	99.9	64.3	92.9	93.5
60	45	64.2	91.9	92.6	57.5	72.8	73.7
60	50	79.8	98.4	98.9	66.5	83.9	85.9
60	54	85.0	99.9	99.9	70.1	92.6	93.8
65	45	57.5	83.1	83.5	54.1	64.8	65.3
65	50	69.1	90.6	92.0	60.2	71.3	73.0
65	55	83.0	91.1	95.0	68.6	71.9	77.3
65	59	89.3	95.4	98.2	73.5	77.3	83.4
70	45	52.8	63.2	63.4	51.7	52.7	52.9
70	50	57.8	72.5	73.5	54.2	57.8	58.6
70	55	68.1	77.9	81.5	59.6	61.3	64.1
70	60	78.6	80.6	87.8	65.7	63.0	69.4
70	64	81.4	84.7	91.2	67.5	66.1	72.7
71.5	66	78.7	79.3	87.2	65.8	62.2	68.9

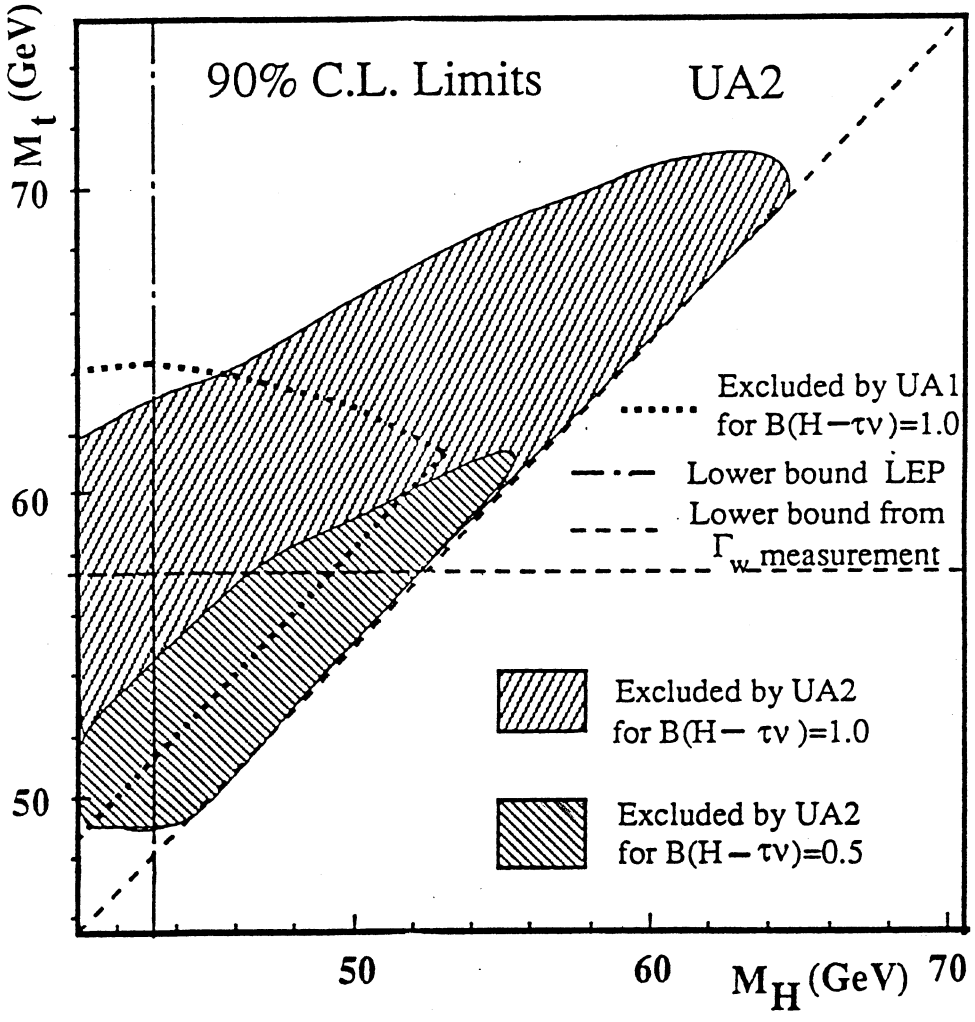

Figure 6.4.1 : Regions of the $(m_t, m_{H^\pm})$ plane excluded at 90% CL. The LEP bound is for $Br(H^+ \to \tau\nu_\tau) = 1$ at 95% CL.

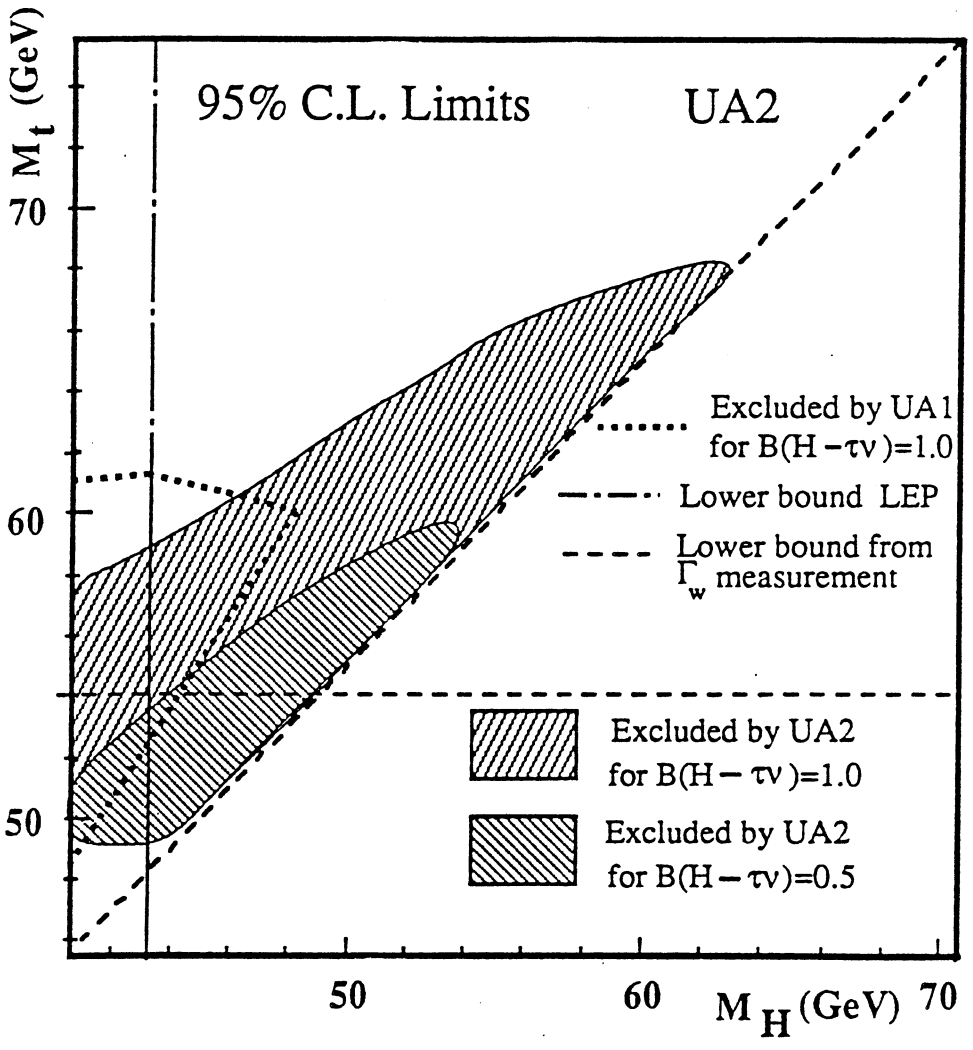

Figure 6.4.2 : Regions of the $(m_t, m_{H^\pm})$ plane excluded at 95% CL. The LEP bound is for $Br(H^+ \to \tau\nu_\tau) = 1$ at 95% CL.

and standard deviation

$$\frac{1}{\sigma_i(m_t, m_{H^\pm})} = \sqrt{\frac{1}{\sum_{i=0}^{1}(\frac{y_i}{\sigma_i(m_t, m_{H^\pm})})^2}}$$

from where the CL for the exclusion of the $H^\pm$ hypothesis is

$$CL = 100\% \ (1 - P(y_i \leq x_i)).$$

The CLs for the 16 mass pairs used in the MC generations are given in Table 6.4.2. For the 'τ +0jet' sample the error is dominated by the statistical uncertainty whereas for the 'τ +jets' sample the statistical and systematic uncertainties are of similar size. It can be seen also here that the 'τ +jets' sample has a greater sensitivity to the $H^\pm$ hypothetical signal.

By interpolating between the 16 ($m_t, m_{H^\pm}$) mass points it is possible to define regions in the ($m_t, m_{H^\pm}$) plane which are excluded at 90 and 95% CL. These are shown in Figures 6.4.1a and 6.4.2a. For comparison, the regions excluded by UA1 [UA1-91a] are also illustrated. Lower bounds, for m_t, obtained independently of the top decay mode, from hadron collider measurements of Γ_W [UA2-91b, CDF-91a, UA1-91b] and for $m_{H^\pm}$ from LEP [ALE-90b, DEL-90b, L3-90b, OPA-90b] are also shown.

Chapter 7

The Charged Higgs at the Large Hadron Collider

7.1 The Large Hadron Collider (LHC)

The Large Hadron Collider (LHC) [Aac-90, ECF-84, Mul-87, Mul-88] is a future proton-proton machine at CERN operating at a centre-of-mass energy of $\sqrt{s} \approx 16$ TeV and at a nominal luminosity of $1.7 \text{x} 10^{34}$ $\text{cm}^{-2}\text{s}^{-1}$. A high luminosity is an essential requirement at higher energies because the cross-sections typically fall as $\frac{1}{s}$ and because a high luminosity allows the detection of rare events which may otherwise be masked by backgrounds. The lower energy of the LHC relative to the Superconducting Super Collider (SSC) project in the U.S.A. ($\sqrt{s} \approx 40$ TeV), is offset by a lower SSC luminosity of 10^{33} $\text{cm}^{-2}\text{s}^{-1}$. It is the aim of the LHC to reach collision energies above 1 TeV at the constituent (quark and gluon) level.

The LHC can be accommodated in the LEP tunnel using superconducting bending magnets with fields as high as 10 T and capable of handling counterrotating proton beams of ≈ 8 TeV energy. In addition, the existing accelerator complex at CERN consisting of the 50 MeV linac, the 1 GeV Booster, the 26 GeV Proton Synchroton (PS) and the 450 GeV Super Proton Synchroton (SPS) constitute an excellent injection complex for the LHC as is shown in Figure 7.1.1. The proposed operating parameters for the machine are given in Table 7.1.1. In addition, the construction of the LHC in the LEP tunnel opens up the possibility of having electron-proton collisions

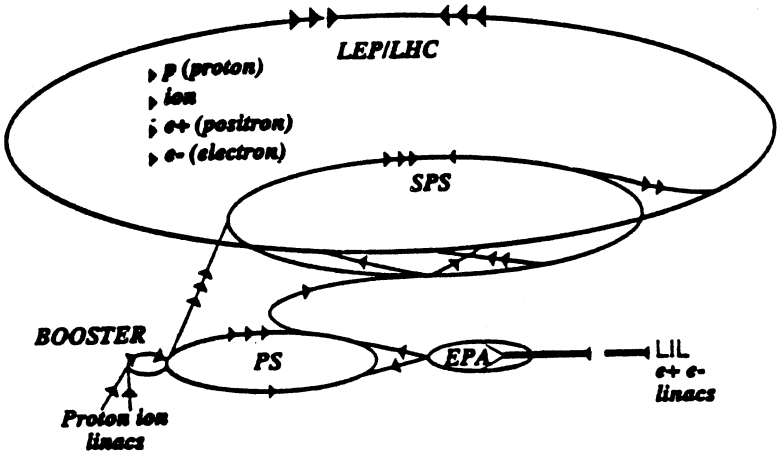

Figure 7.1.1 : The proposed LHC complex at CERN.

Circumference	26658.833 m
Revolution time	88.924 μs
Nominal bending field	10.0 T
Nominal beam energies	7.7 TeV
Injection energy	0.45 TeV
No. of interact. regions (initially)	3
Full bunch length	0.30 m
RF frequency	400.8 MHz
Min. inter-bunch spacing	15 ns
No. of proton bunches/beam	4725
No. of protons/bunch	1.10^{11}
Intensity/beam	850 mA
Stored energy/beam	583 MJ
Total synchro. rad. (two beams)	17.5 kW
Beam radius at $\beta^*= 0.5$ m	15 μm
Free space at I.R.	32 m
Luminosity at $\beta^*= 0.5$ m (for three simultaneous experiments)	1.7×10^{34} cm^{-2}s^{-1}

Table 7.1.1 : The proposed LHC operating parameters.

up to 1.7 TeV and eventually Pb-Pb collisions up to 1312 TeV energies.

A technical challenge which must be overcome is the realization of the superconducting dipole magnets. A proposed solution is shown schematically in Figure 7.1.2 in which both beams are bent by separate coils in the same device (the 'two-in-one' configuration) in order to achieve lower costs and compactness. The magnet would consist of a 50 mm. bore having two coils of NbTi operating at 1.8 K and a cold iron yoke. In addition to the bending magnets both focusing and correcting magnets are required (see Table 7.1.2).

The questions that the LHC will aim to answer include :

1. What is the mechanism for the electroweak symmetry breaking that gives rise to particle masses ? This implies a sensitivity to the Higgs boson(s) in the largest possible Higgs mass range.

2. What are the properties (e.g. mass and decay characteristics) of the top quark ?

3. Are there additional heavy bosons which indicate the presence of new, as yet undiscovered forces.

4. Do supersymmetric partners to the known particles exist ?

5. Are leptons and quarks elementary or are they composed of more fundamental particles ?

6. What is the precise nature of the gauge boson couplings ?

It is clear that the LHC should also be sensitive to unexpected new physics.

7.2 EAGLE - An Experiment for Accurate Gamma, Lepton and Energy Measurements

7.2.1 The Detector Lay-out

The EAGLE detector [Jen-91, Gos-92, EAG-92] is a proposed apparatus to exploit the full discovery potential of the LHC right from its start-up and

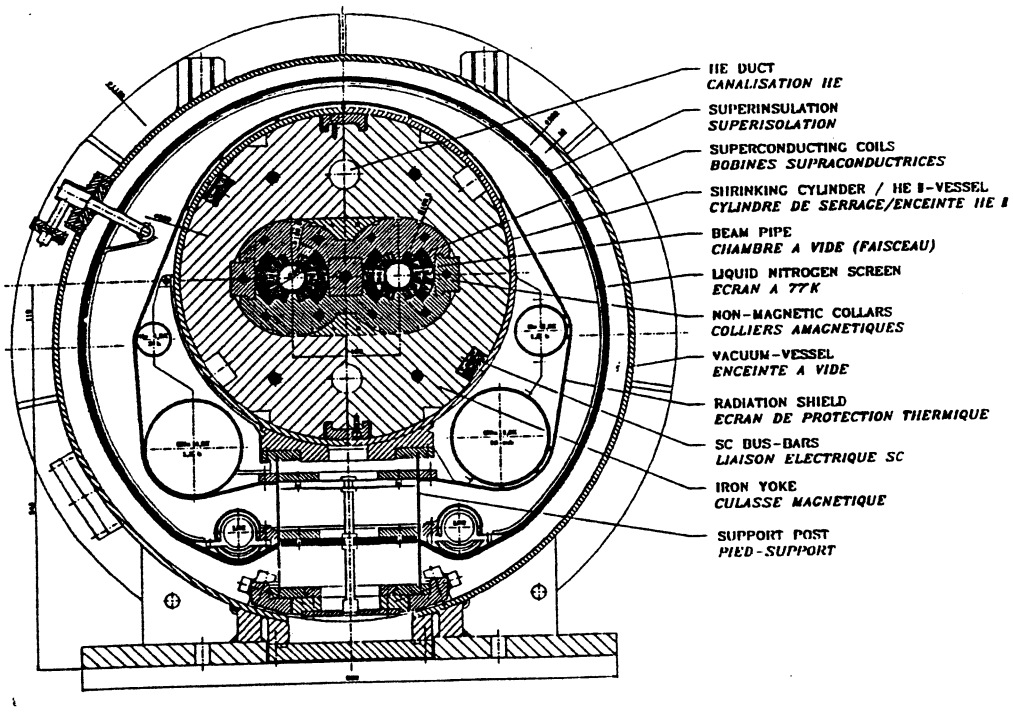

Figure 7.1.2 : Cross-section through a dipole superconducting magnet at the LHC.

		Magnetiic Length (m)	Number of magnets
Dipoles	B_0 = 10 T	9.00	2 x 1792
Quadrupoles	G = 250 T/m	3.05	2 x 642
Tun. quads,	G = 120 T/m	0.72	2 x 400
Sextupoles	B" = 4500T/m^2	1.0	2 x 800
Orbit corr. dipoles	B_0 = 1.5 T	1.0	2 x 552
Higher-order multipoles			2 x 1600

Table 7.1.2 : The proposed magnet parameters for the LHC.

to operate at the nominal high luminosity of 1.7×10^{34} $cm^{-2}s^{-1}$. The detector will have a balanced sensitivity to electron, gamma, muon, jet and missing transverse energy signatures so that different final states can be used to corroborate possible new physics signals. This balanced approach makes EAGLE able to deal with the variety of physics examples expected to be studied at the LHC and also illustrates the detector's potential for unexpected new physics.

In addition, during the expected initial low luminosity running period at 10^{33} $cm^{-2}s^{-1}$, and to a high a luminosity as possible, the apparatus would be able to detect processes involving the τ and heavy flavours. Such capabilities allow a more accurate determination of the top quark mass and searches for pseudoscalar SUSY Higgs decays to τ pairs and for $H^{\pm}$ to τ decays.

The main elements of the EAGLE detector are sketched in Figure 7.2.1 and are :

- An inner detector in a 2 T central superconducting solenoidal field to provide accurate momentum measurements over a large pseudorapidity coverage ($-2.5 < \eta < 2.5$) for isolated leptons. Figure 7.2.2b shows the momentum resolution as a function of the pseudorapidity for 1 TeV tracks (the assumed detector geometry is illustrated in Figure 7.2.2a).

  In addition, the inner detector will aid in enhancing efficiently the electron identification. Isolated and non-isolated electrons must be identified from a background of QCD jets (including direct photons, π^0 's from jet fragmentation, and conversions) that fake the signature for electron detection. To reach the level of real electrons from heavy flavour and W decays a rejection of 10^5 to 10^6 against QCD jets and of 10^2 to 10^3 against π^0 's and photons is required. Figure 7.2.3 shows the expected rates from simulation for the inclusive production of QCD jets, π^0 's, and photons as a function of the p_T threshold. Also shown are the expected inclusive electron rates from b-quark, W- and Higgs decay. The remaining backgrounds come from e^+e^- pairs from photon conversions and Dalitz decays and from hadron or hadron + photon overlaps (expected to be $\sim 10^{-6}$ smaller than real electrons from W-decay). The calorimeter selection criteria, based on a cluster radius cut of less than 1 cell unit and a cluster energy within 3σ of the nominal energy, reject jets only at the level of 10^3.

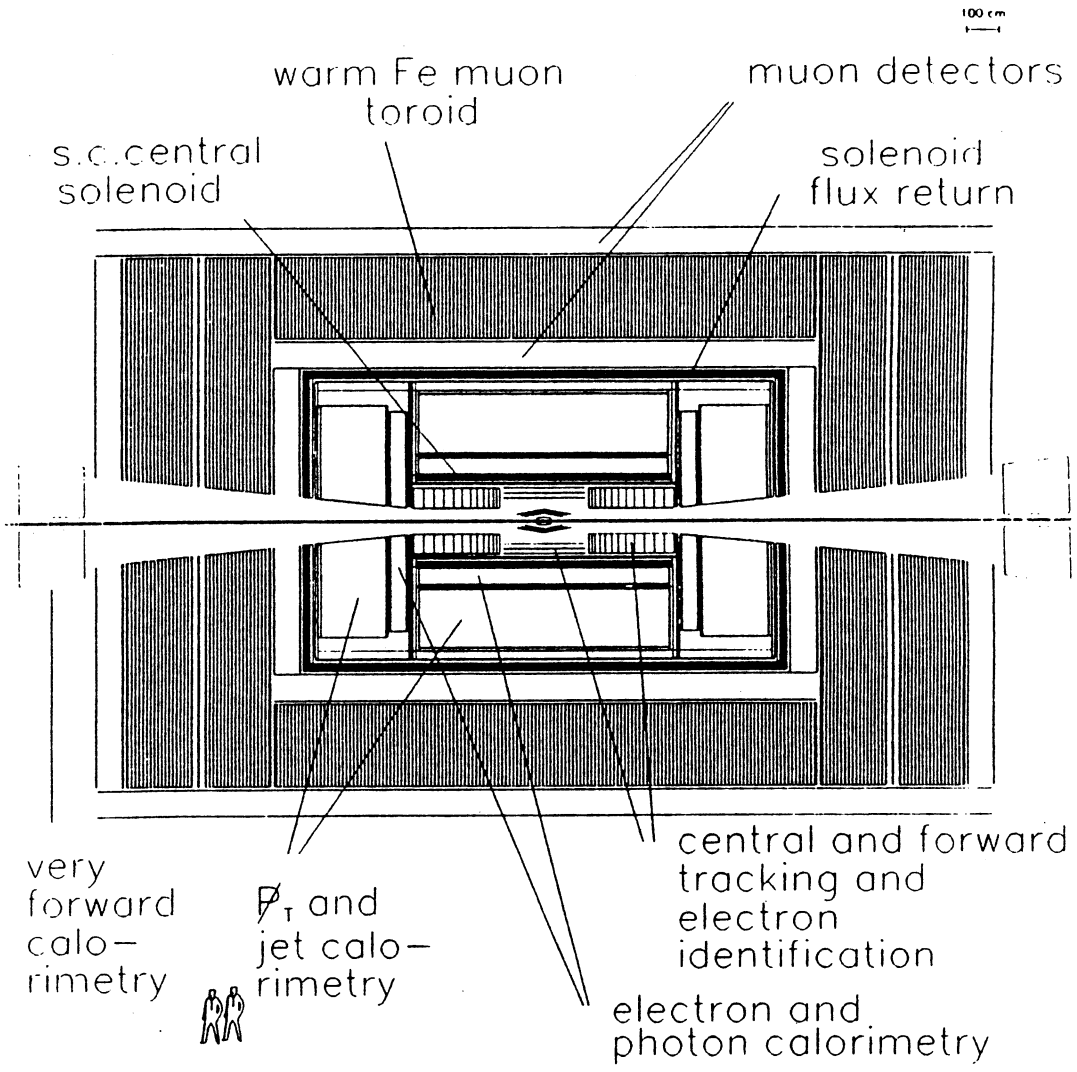

Figure 7.2.1 : Cross-section through the proposed EAGLE apparatus for the LHC.

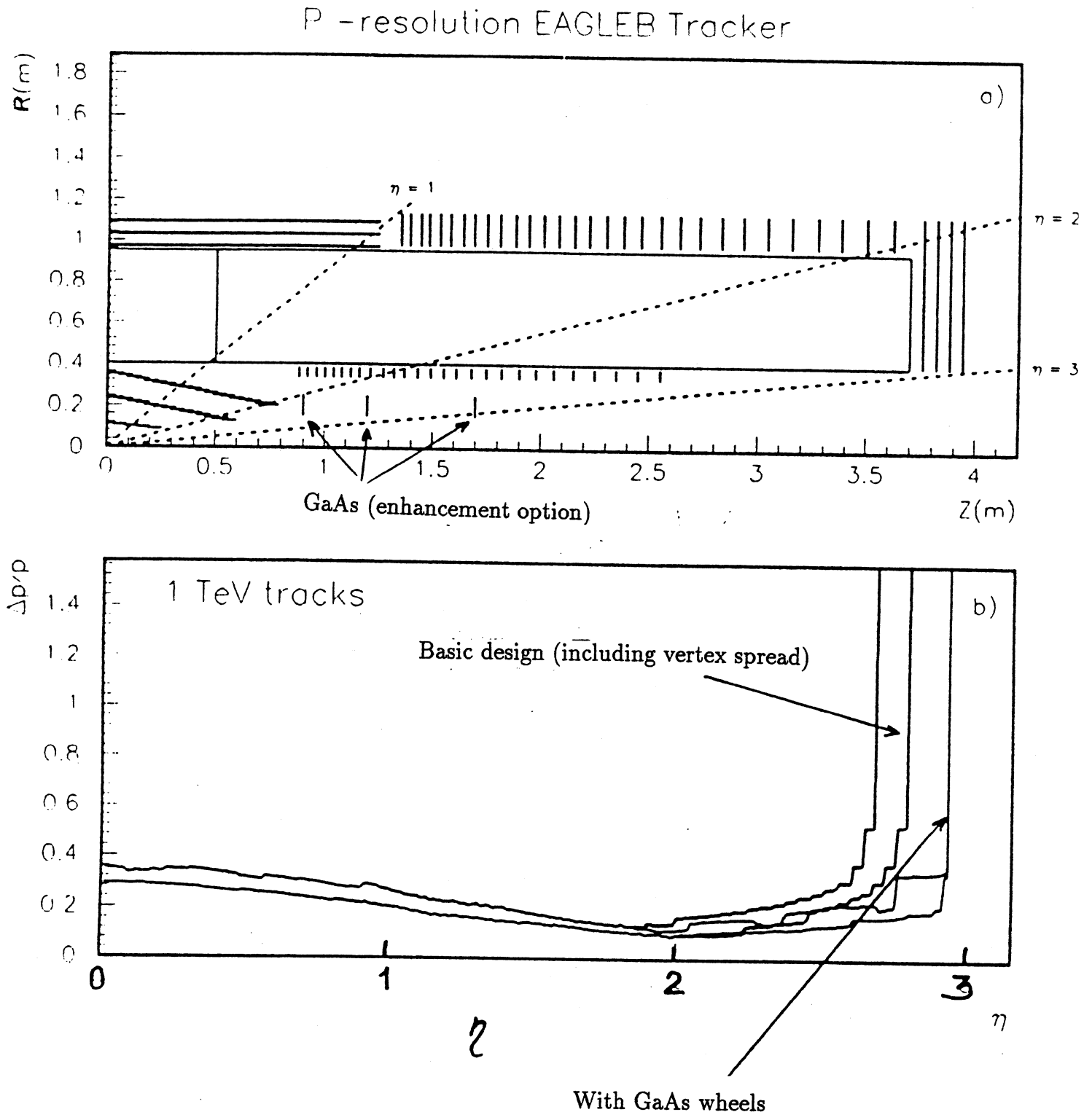

Figure 7.2.2 : The inner detector (a) geometry and (b) momentum resolution for 1 TeV tracks.

Simulations based on matching the electron energy in the calorimeter, E_{cal}, to its track momentum in the inner detector, p_{track}, lead to background estimates of $< 10\%$ of the real electron rate for $p_T > 20$ GeV electrons and $\frac{E_{cal}}{p_{track}} < 1.2$ at the nominal high luminosity.

The simulated electron tracking efficiencies are given in Table 7.2.1. They include (a) a pattern recognition based on defining roads from the calorimeter and muon detector and demanding 3 out of 4 hits in the inner tracker and 5 out of 6 hits in the outer tracker, (b) $\frac{E_{cal}}{p_{track}} < 1.2$ and (c) the above calorimeter electron selection criteria.

Options for different parts of the inner detector are combinations of silicon micro-strip and pad detectors (see Section 7.2.2), micro-strip gas counters (MSGC) and transition radiation detectors (TRD). Scintillating fibre and GaAs micro-strip detectors are also being considered. Figure 7.2.4 depicts two of the proposed configurations for the inner detector.

The MSGC detector concept is shown in Figure 7.2.5 and its operating parameters are given in Table 7.2.2.

The TRD aids in pattern recognition in -2.5 $< \eta <$ 2.5 with 40 points per track and also in the electron identification because of the low 3% occupancy at the nominal high luminosity. The apparatus consists of 300 000 straw tubes of $Xe/CF_4/CO_2$ gas mixture and polypropylene foil radiator and is of overall thickness $\sim$ 10% r.l. The performance of the prototype TRD, evaluated in testbeam and by simulations, gives a spatial resolution of 150 μm per straw leading to a momentum resolution of $\delta p_T/p_T$ of $\sim 8\%$ at 100 GeV. The rejection of hadron and e^+e^- pairs from photon conversions and Dalitz decay backgrounds to isolated electrons is 30 and 50, respectively, for an electron efficiency of 95%. Figure 7.2.6 shows the event display of the TRD for various particle types.

The GaAs micro-strip detectors offer the possibility to extend tracking and momentum measurements upto $|\eta| \approx 3$. The conceptual design consists of 3 wheels on each side of the interaction region and with two layers per wheel in the radial space between 25 and 35 cm from the beam line. The counters are to be 200 μm. thick and have a 60 μm strip pitch giving in total $\sim 10^6$ channels.

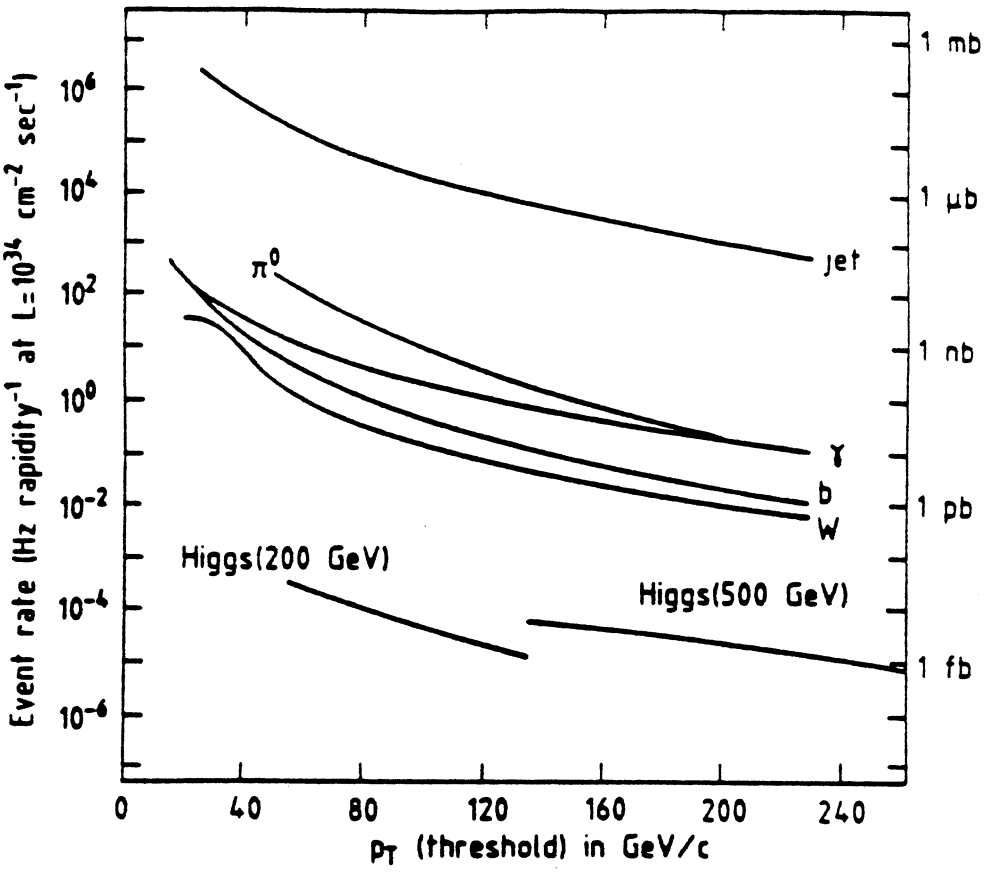

Figure 7.2.3 : Expected rates from a PYTHIA Monte Carlo simulation for the inclusive production of QCD jets, neutral pions, and photons as a function of the p_T threshold. Also shown are the expected inclusive electron rates from b-quark, W and Higgs decay.

η	configuration	10 GeV	20 GeV	40 GeV
0	no TRD, no pile-up	0.93	0.97	0.98
1.2	no TRD, no pile-up	0.87	0.94	0.97
1.2	with TRD and pile-up	0.92	0.96	0.98

note: - rejection against em jets is under study

Table 7.2.1 : Simulated electron tracking efficiencies.

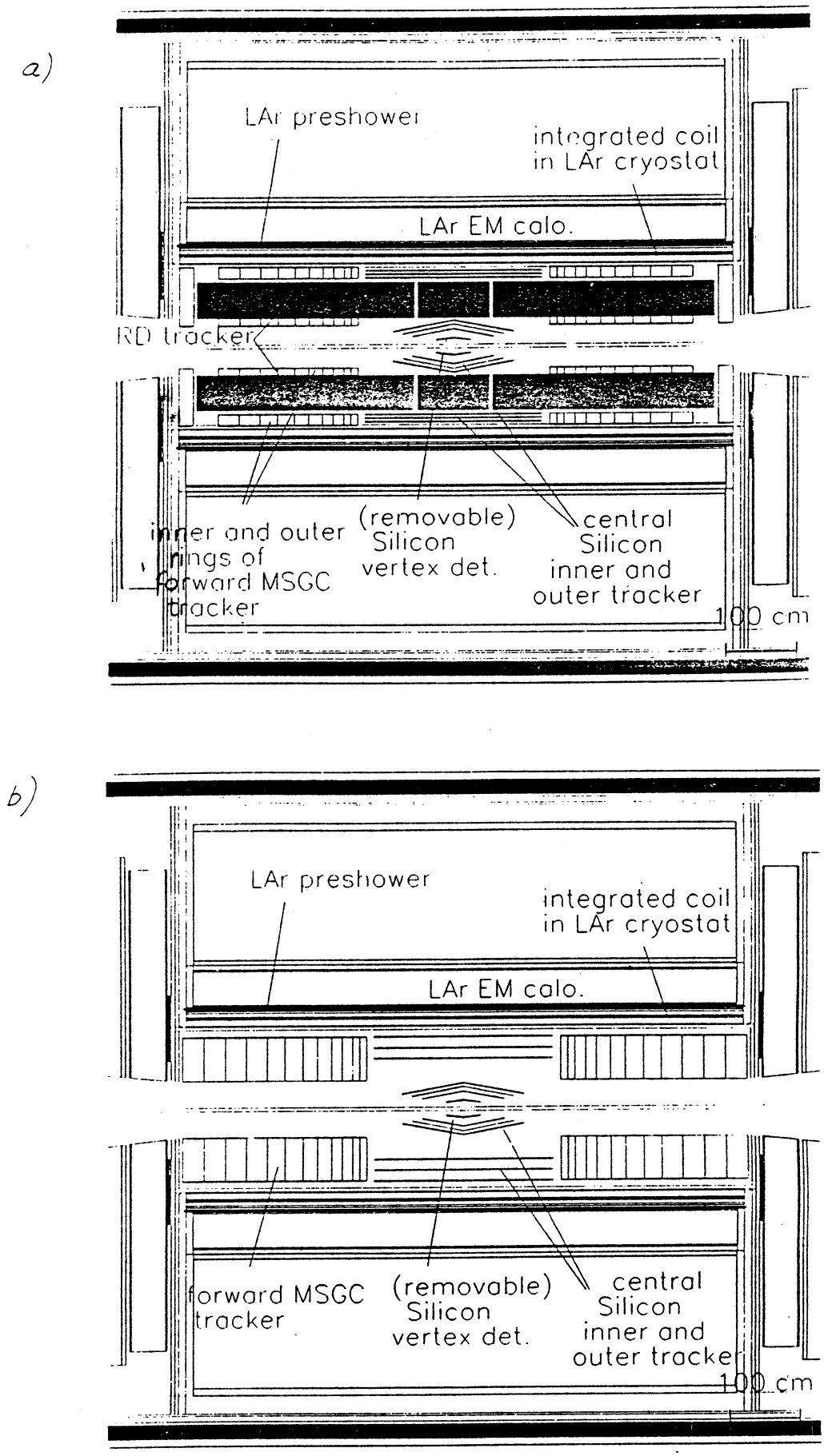

Figure 7.2.4 : Two of the proposed configurations for the inner detector : (a) the EAGLE A version, and (b) the EAGLE B version.

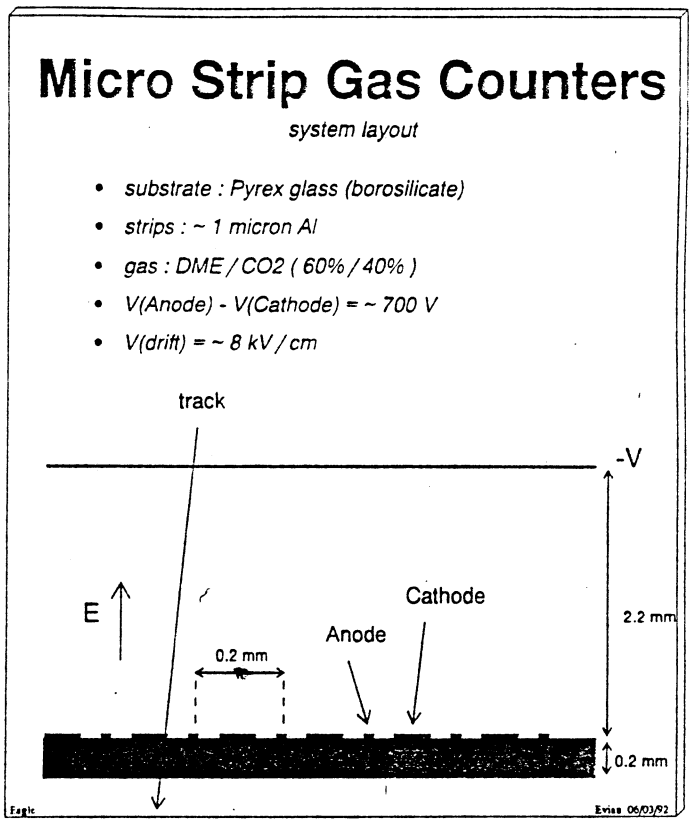

Figure 7.2.5 : The MSGC system lay-out.

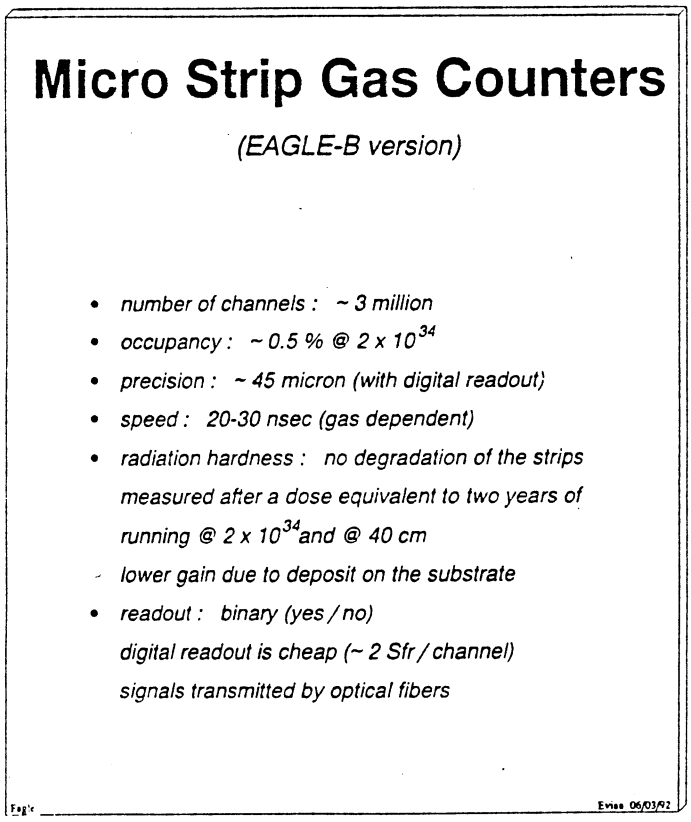

Table 7.2.2 : The MSGC operating parameters.

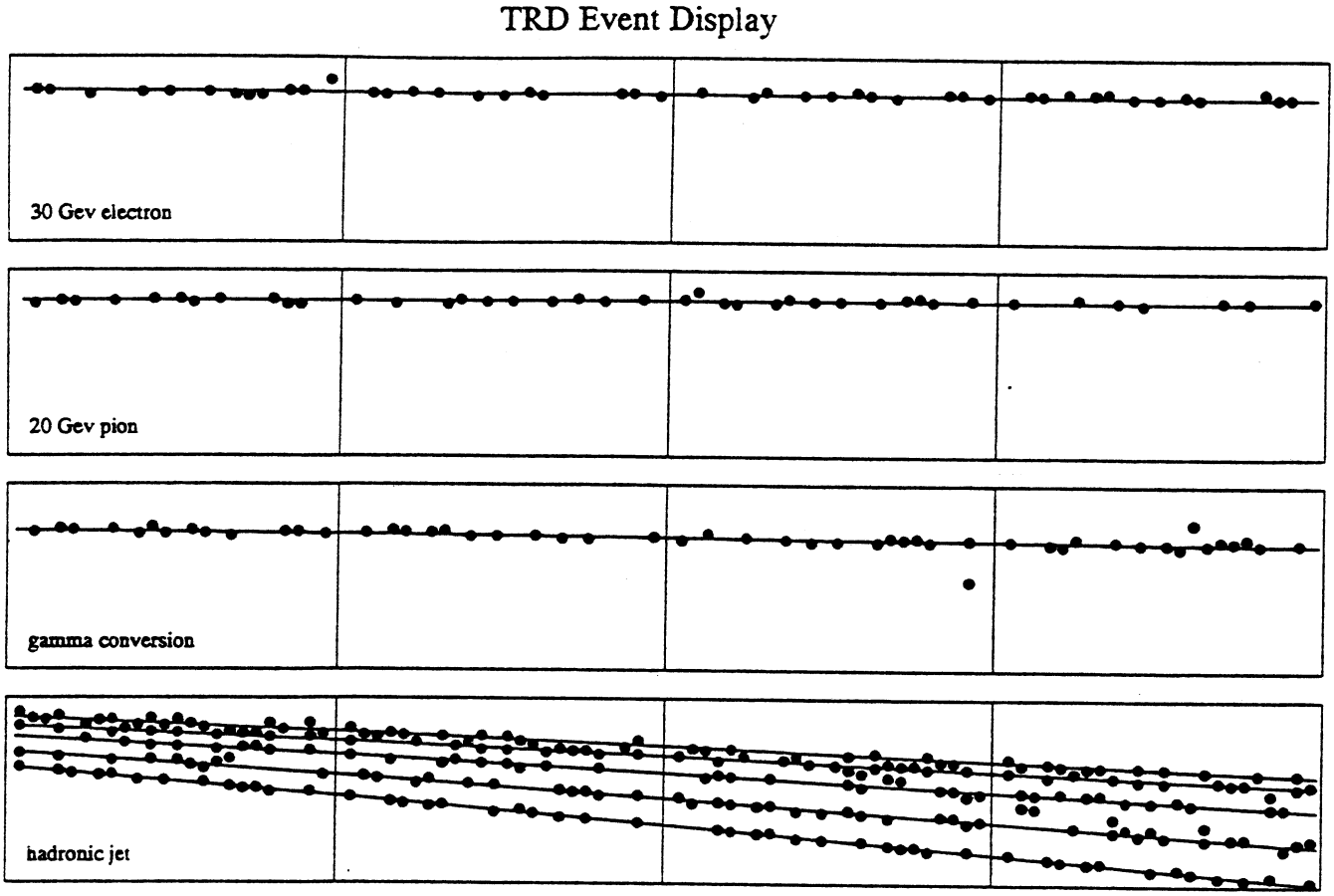

Figure 7.2.6 : TRD event dispay for different incident particles.

- An electromagnetic sampling calorimeter of depth 25 – 30 r.l. for electron and photon measurements in -3 < η < 3. Both liquid argon (LAr Accordion) and scintillating fibre (SPACAL) electromagnetic calorimetry are investigated.

  The LAr calorimeter has an Accordion structure for the absorber (1.8 mm - thick Pb clad with steel) as is shown in Figure 7.2.7. The cells are projective with $\Delta\eta$ x $\Delta\phi$ $\sim$ 0.02 x 0.02 with three longitudinal samples, giving a total of 230 000 readout channels. Resolution measurements from a testbeam prototype give

$$\frac{\sigma(\mathrm{E})}{\mathrm{E}} = \frac{10\%}{\sqrt{\mathrm{E}}} + 0.6\% + \frac{0.32}{\mathrm{E}}$$

  which includes a 3.3 r.l. preshower detector. The position resolution is

$$\sigma_{\mathrm{x}} = \frac{3.7\mathrm{mm}}{\sqrt{\mathrm{E}}}$$

  and

$$\sigma(\omega) = \frac{48}{\sqrt{\mathrm{E}}} + \frac{365}{\mathrm{E}}\ (\mathrm{mrad}).$$

  The SPACAL calorimeter (see Figure 7.2.8) consists of 1 mm. diameter fibres and has a Pb absorber to fibre ratio of 1.8:1. The structure is quasi-projective with $\Delta\eta$ x $\Delta\phi$ $\sim$ 0.02 x 0.02 (with a 6° tilt). A 4-cell prototype module with 500 μm. diameter fibres and a Pb to fibre ratio of 4:1 gives

$$\frac{\sigma(\mathrm{E})}{\mathrm{E}} = \frac{10.5\%}{\sqrt{\mathrm{E}}} + 0.5\%$$

  and

$$\sigma_{\mathrm{x}} = \frac{1.6\ \mathrm{mm}}{\sqrt{\mathrm{E}}} + 0.1.$$

  A LAr preshower detector consisting of two layers of orthogonal strips preceding the electromagnetic calorimeter is being evaluated. The granularity is $\Delta\eta$ x $\Delta\phi$ $\sim$ 0.08 x 0.002 and 0.002 x 0.08 for each layer. It consists of 300 000 channels having a dynamic range from 0.25 to less than 300 mips. A schematic of the preshower detector is given in Figure 7.2.9. It gives a rejection of a factor of 5 for $\pi^0 \rightarrow \gamma\gamma$ given a single photon efficiency of 90% (see Figure 7.2.10).

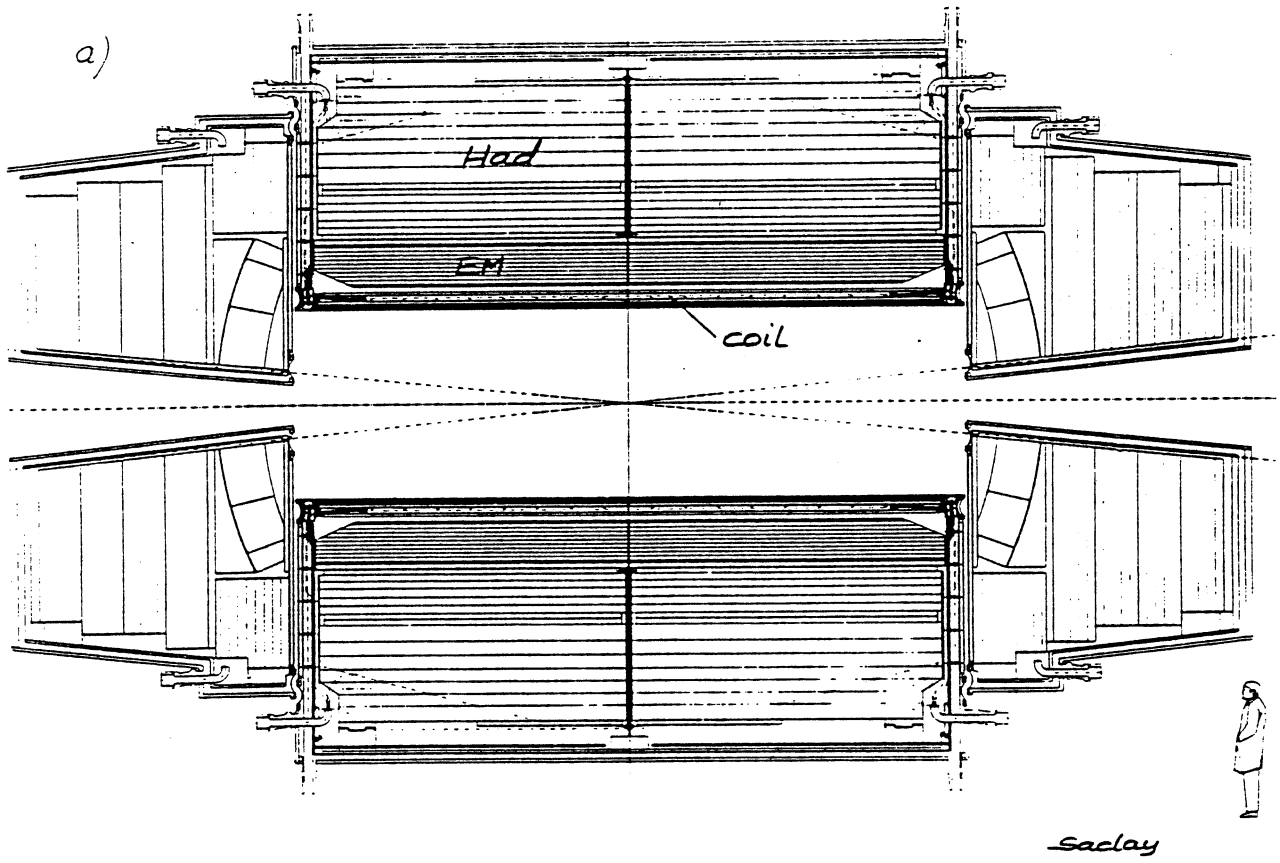

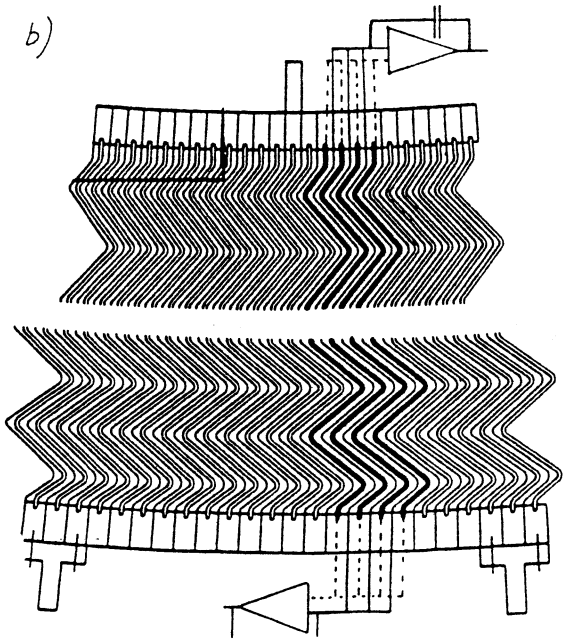

Figure 7.2.7 : (a) The LAr Accordion calorimeter system design and (b) the Accordion Pb absorber geometry.

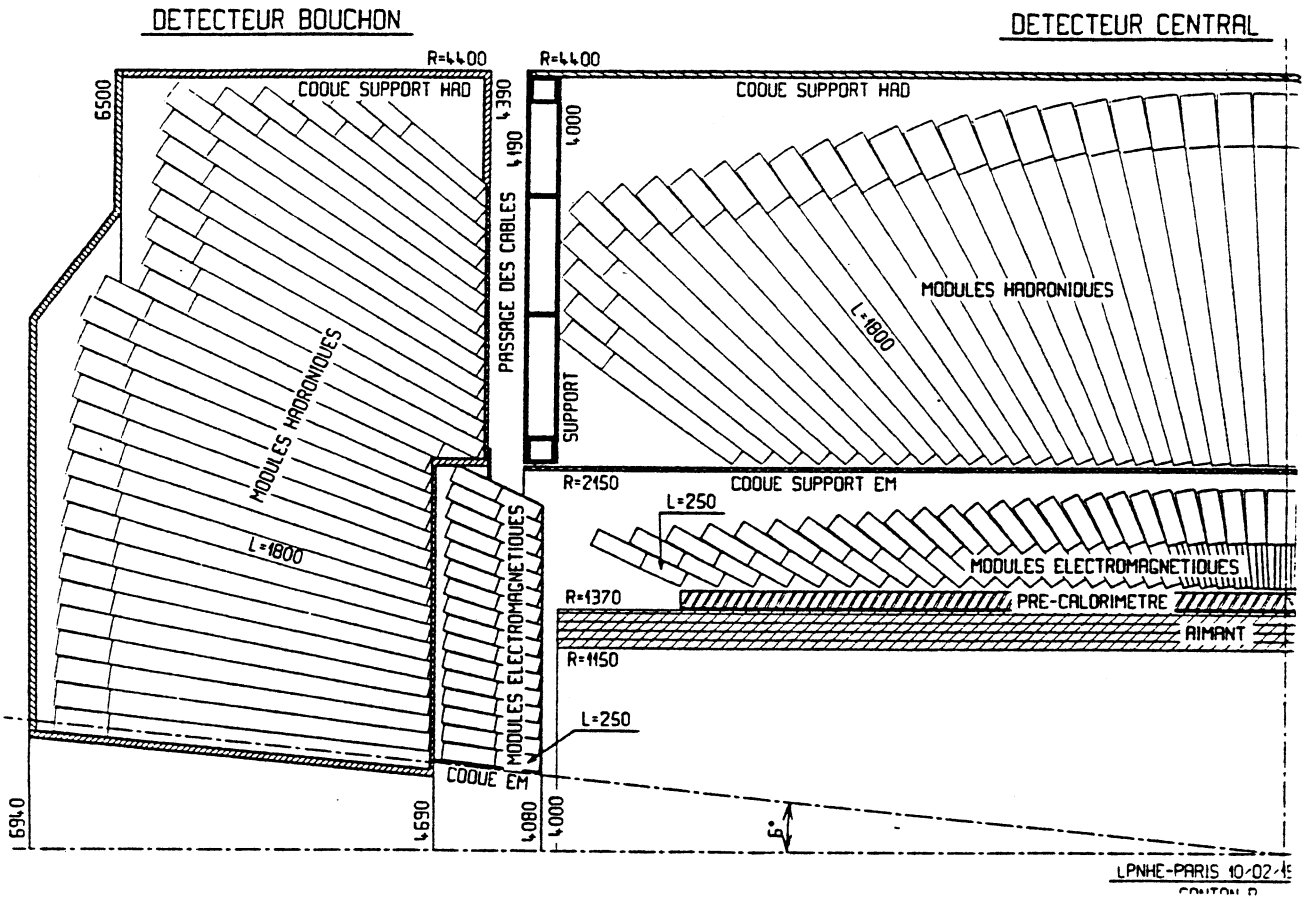

Figure 7.2.8 : The SPACAL calorimeter design.

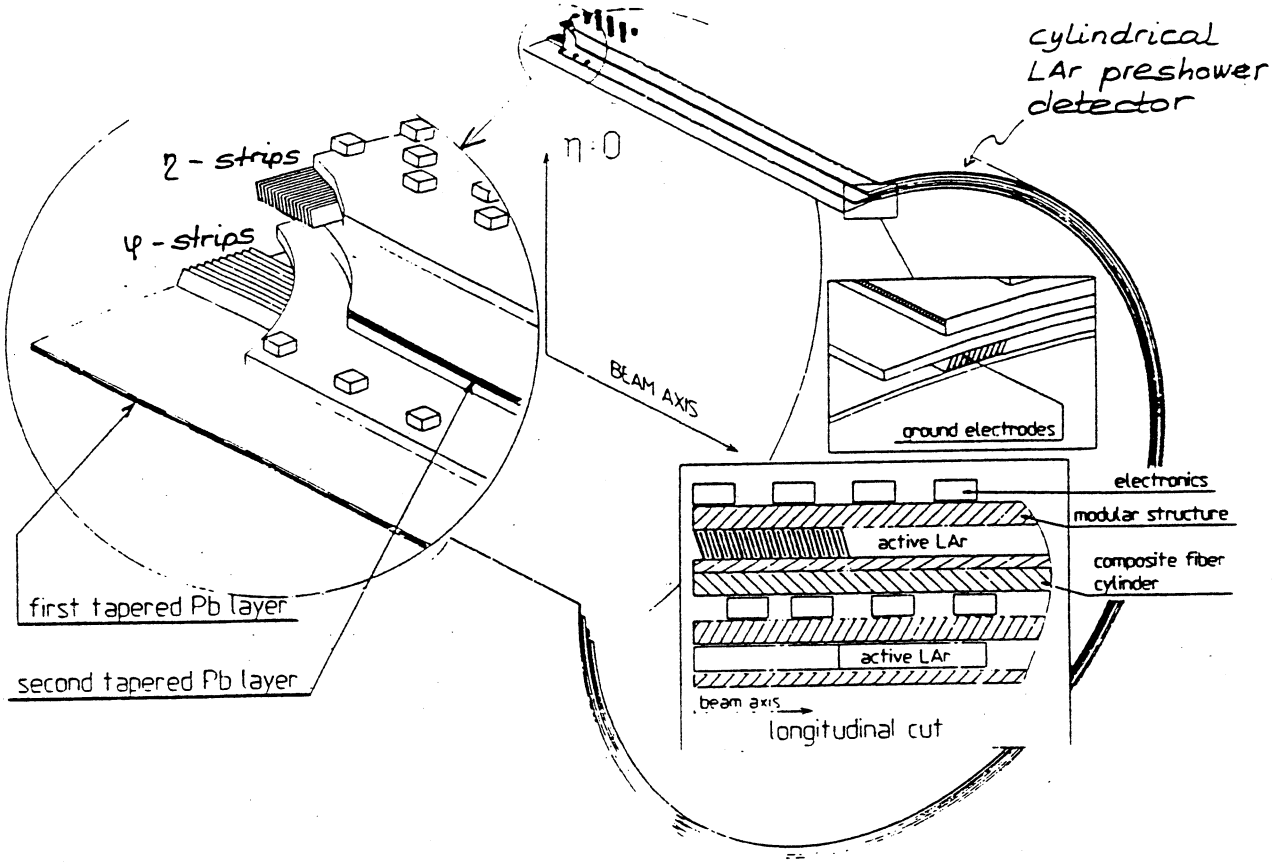

Figure 7.2.9 : The LAr preshower detector.

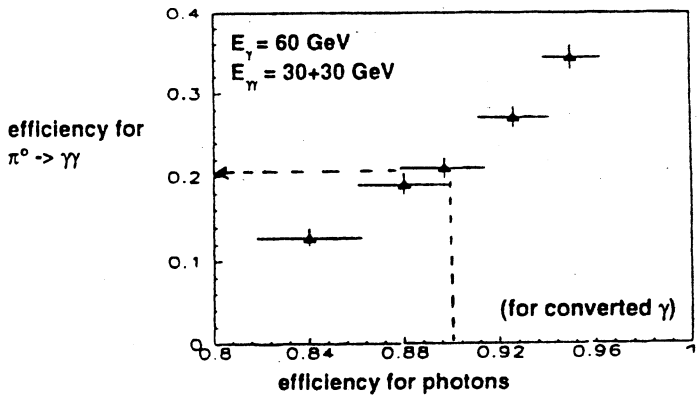

Figure 7.2.10 : The LAr preshower rejection of $\pi^0 \rightarrow \gamma\gamma$ versus the single photon efficiency.

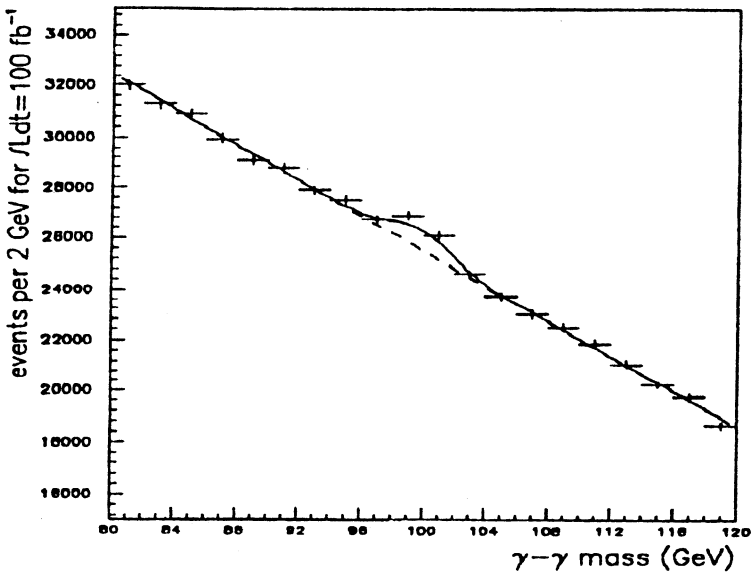

Figure 7.2.11 : A 100 GeV $H^0 \rightarrow \gamma\gamma$ simulation using the LAr preshower and electromagnetic Accordion calorimeter performances from testbeam.

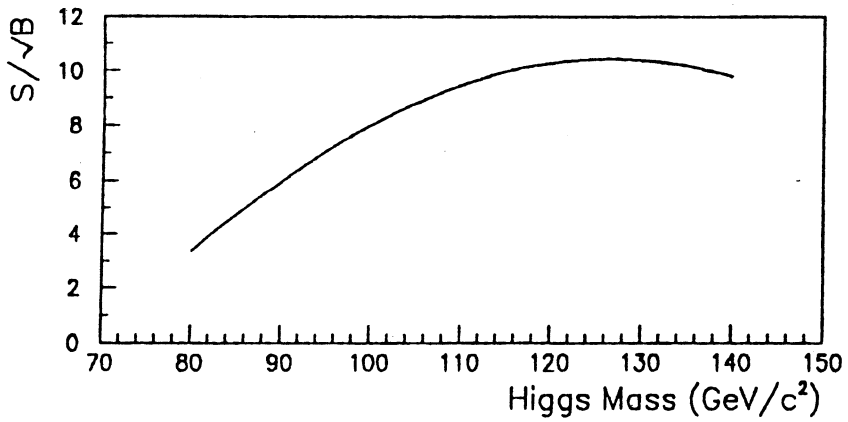

Figure 7.2.12 : $H^0 \rightarrow \gamma\gamma$ significance as a function of the Higgs mass for a luminosity of 10^5 pb^{-1}.

The electromagnetic calorimeter and preshower detector should have the capability to study the $H^\circ \rightarrow \gamma\gamma$ channel. Figure 7.2.11 shows a 100 GeV $H^\circ \rightarrow \gamma\gamma$ simulation using the LAr preshower and electromagnetic LAr Accordion calorimeter performances from testbeam (the simulation of both QCD jets and π^0 background has been included). The significance as a function of the Higgs mass for 10^5 pb^{-1} is given in Figure 7.2.12.

- A hermetic hadron calorimeter for jet and missing transverse energy measurement in -5 $< \eta <$ 5 and with a total depth including the electromagnetic calorimeter of $10 - 12$ λ. Both LAr and scintillator (fibre and tile) hadron calorimetry are being considered.

  The hadronic LAr concept consists of steel absorbers (1 to 1.5 cm thick) forming an Accordion structure. It is projective with $\Delta\eta$ x $\Delta\phi$ $\sim$ 0.05 x 0.05 and with 4 longitudinal samples giving a total of 60 000 readout channels. The expected jet resolution combined with the LAr Accordion electromagnetic calorimeter is from Monte Carlo simulations

$$\frac{\sigma(E)}{E} = \frac{60\%}{\sqrt{E}} + 3\%$$

  with no longitudinal weighting, and

$$\frac{\sigma(E)}{E} = \frac{40\%}{\sqrt{E}} + 2.2\%$$

  including longitudinal weighting.

  The scintillator fibre hadronic calorimeter consists of a Fe absorber to fibre ratio of 5-20 : 1 with 2 mm diameter fibres. The cells are projective with $\Delta\eta$ x $\Delta\phi$ $\sim$ 0.05 x 0.05 giving 14 000 cells in total. The expected jet resolution (combined with the SPACAL electromagnetic calorimeter) is from simulations

$$\frac{\sigma(E)}{E} = \frac{38\%}{\sqrt{E}} + 1\%.$$

  The scintillating tile hadronic calorimeter is shown in Figure 7.2.13. Each cell has a granularity of $\Delta\eta$ x $\Delta\phi$ $\sim$ 0.1 x 0.1. There are 4 longitudinal samples interspersed with Fe absorber giving in total 15 000

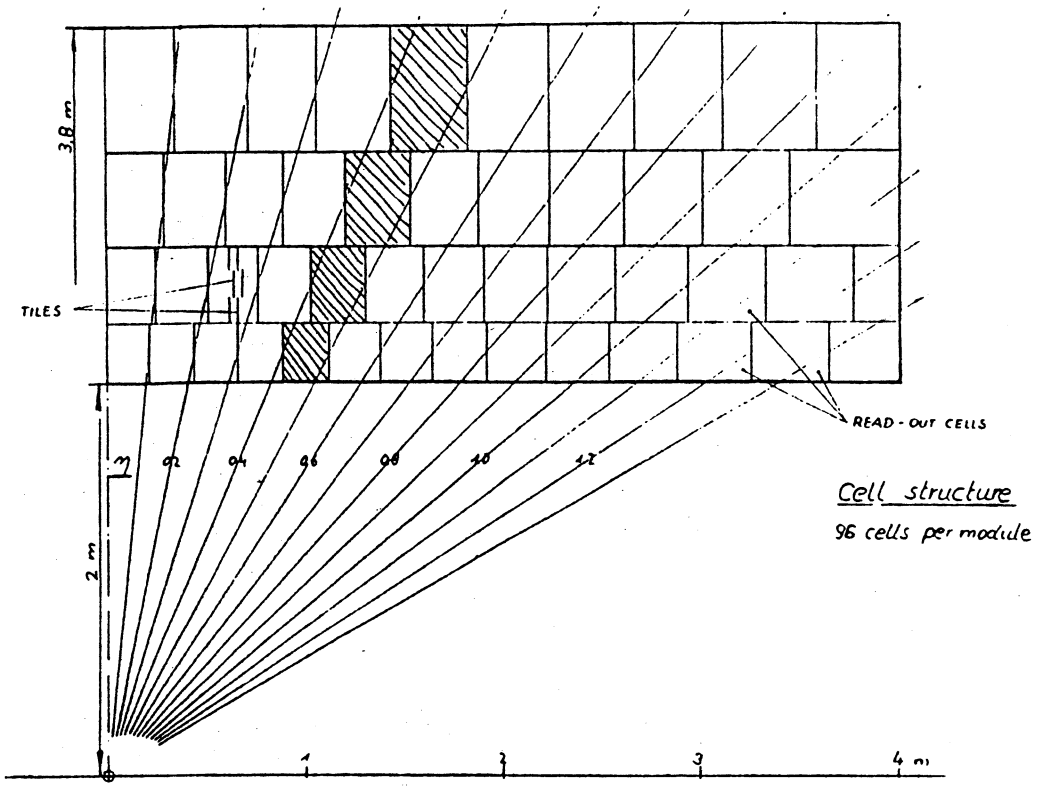

Figure 7.2.13 : The scintillator tile hadron calorimeter conceptual design.

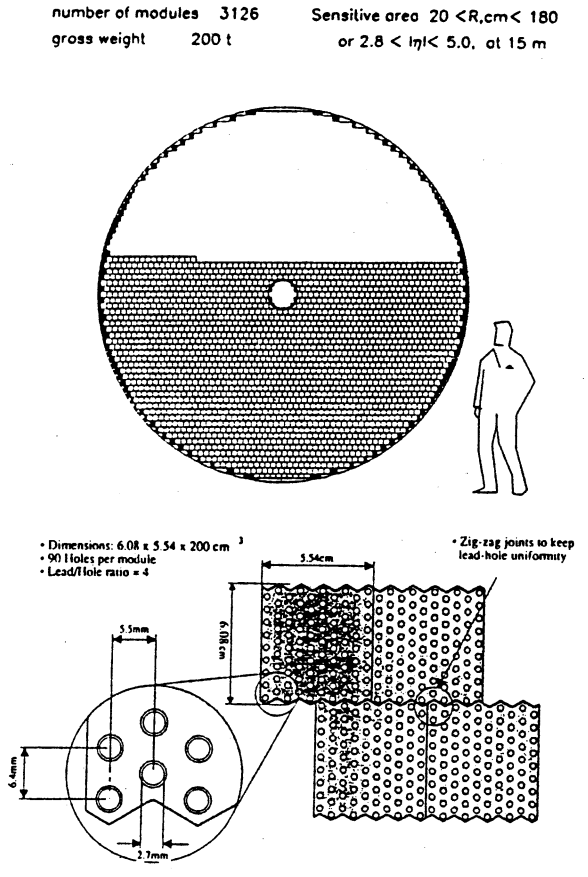

Figure 7.2.14 : The liquid scintillator for the very forward calorimeter assembly.

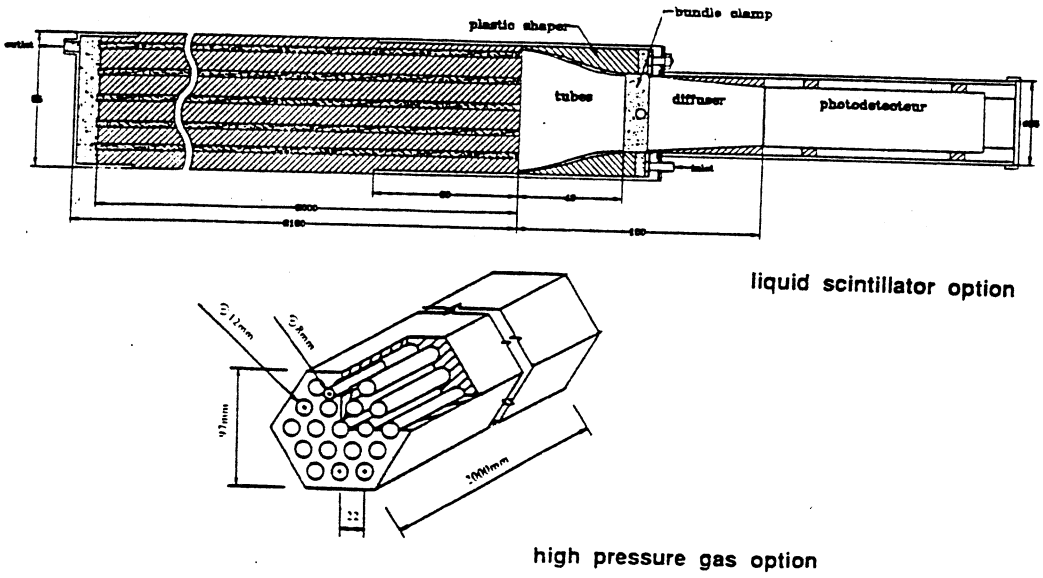

Figure 7.2.15 : The high pressure gas option for the very forward calorimeter assembly.

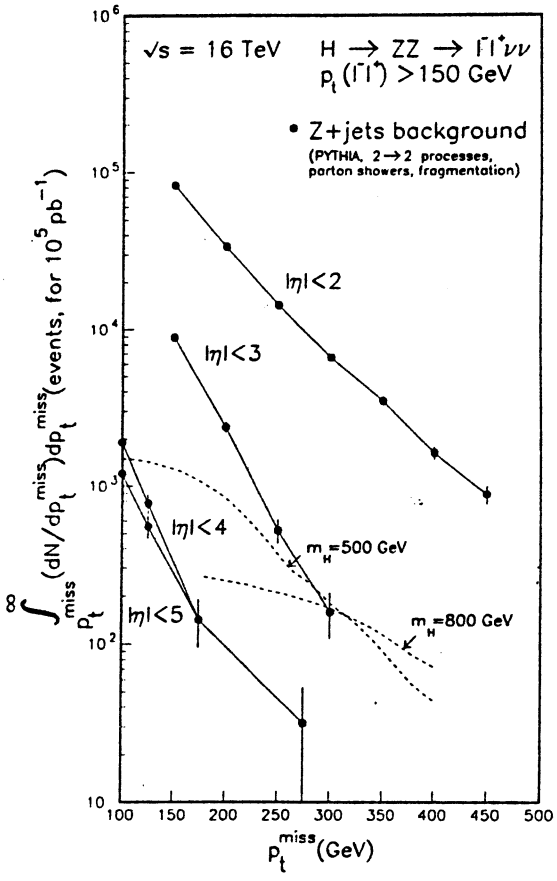

Figure 7.2.16 : The dependence of the $H^0 \rightarrow \gamma\gamma \rightarrow ZZ \rightarrow l^+l^-\nu\nu$ signal on the calorimeter coverage.

channels. The expected jet resolution from a simulation assuming a 25 r.l. Pb-LAr electromagnetic calorimeter in front is

$$\frac{\sigma(E)}{E} = \frac{41\%}{\sqrt{E}} + 2\%.$$

- Liquid scintillator (see Figure 7.2.14) and high pressure gas (see Figure 7.2.15) calorimeters are to cover the very forward regions ($3 < |\eta| < 5$) to complement the missing momentum measurements in top quark physics, SUSY searches and $H^0 \rightarrow ZZ \rightarrow l^+l^-\nu\overline{\nu}$,, (where l represents any leptonic final state), and for jet tagging in the heavy Higgs search. The conceptual design consists of a quasi-projective geometry of typical cell size 6x6 mm^2 giving 1000 to 3000 cells per side. The active media should be replaceable due to the hard radiation environment and are to consist of either liquid scintillator or gas (90% Ar + 10% CF_4 at 20 - 30 atm). The energy resolution is expected to be

$$\frac{\sigma(E)}{E} = \frac{100\%}{\sqrt{E}} + 5\%$$

and the response is to be better than 30 ns. Figure 7.2.16 shows the effect of the very forward calorimeter coverage on the $H^0 \rightarrow ZZ \rightarrow l^+l^-\nu\overline{\nu}$ signal.

- A warm iron toroid muon spectrometer in $-3 < \eta < 3$ for muon identification and stand-alone momentum measurement capability which is independent of that provided by the inner detector. The muon detection system is sketched in Figure 7.2.17. Both drift and cathode readout chambers and resistive plate chambers for triggering are evaluated. Figure 7.2.18 depicts the muon momentum resolution for a combined inner detector and muon system measurement.

- An inner silicon micro-strip tracker and vertex detector (SITV) consisting of 3 superlayers of 2 layers each (see Figure 7.2.19). The detectors will be either single or preferentially double-sided silicon strip detectors of pitch 50 to 100 μm covering in total 13 m^2 and consisting of 4 to

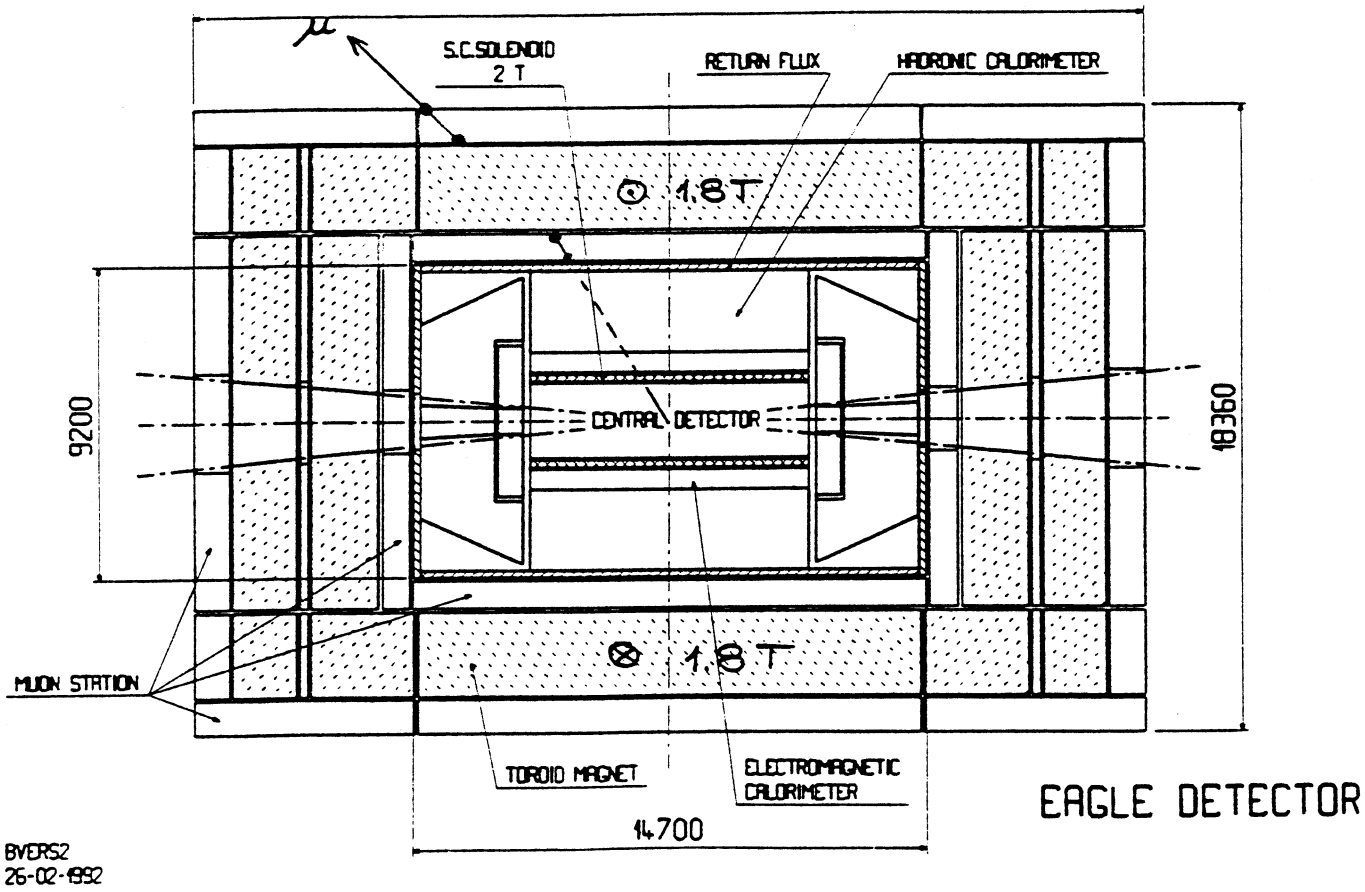

Figure 7.2.17 : The EAGLE muon detection system.

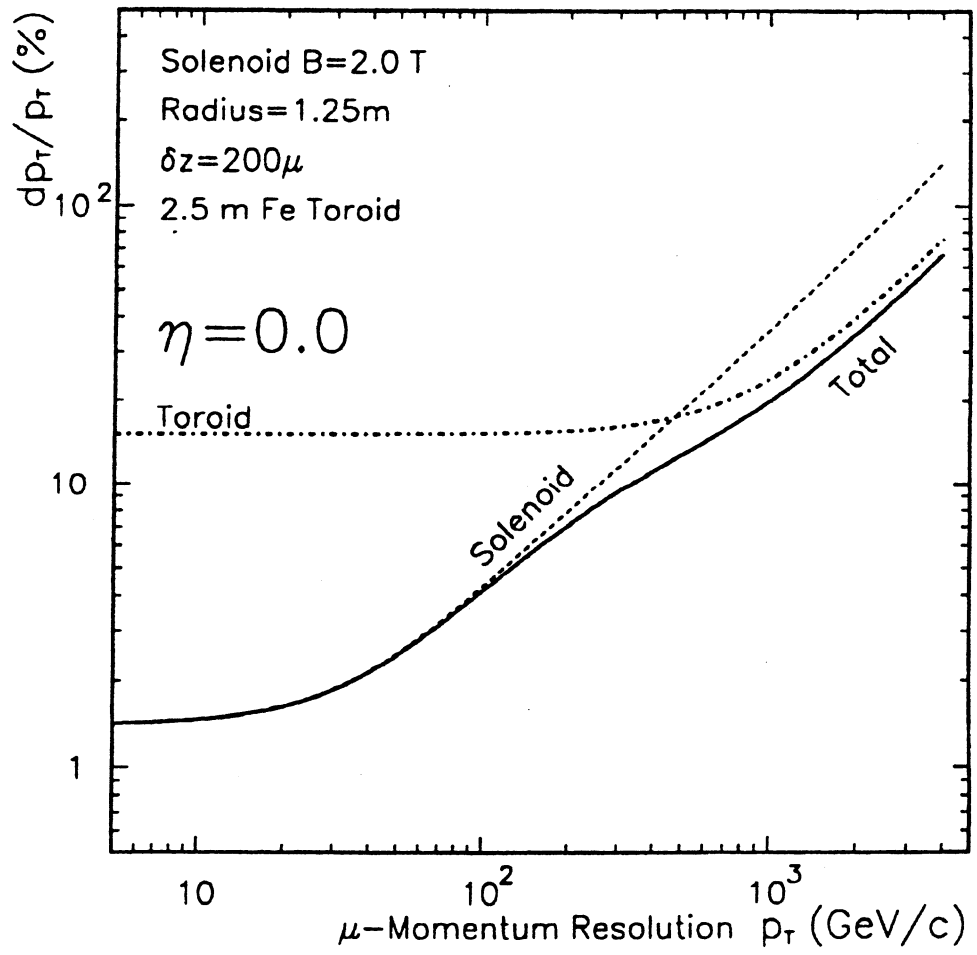

Figure 7.2.18 : Muon detection resolution for a combined inner detector and muon system measurement.

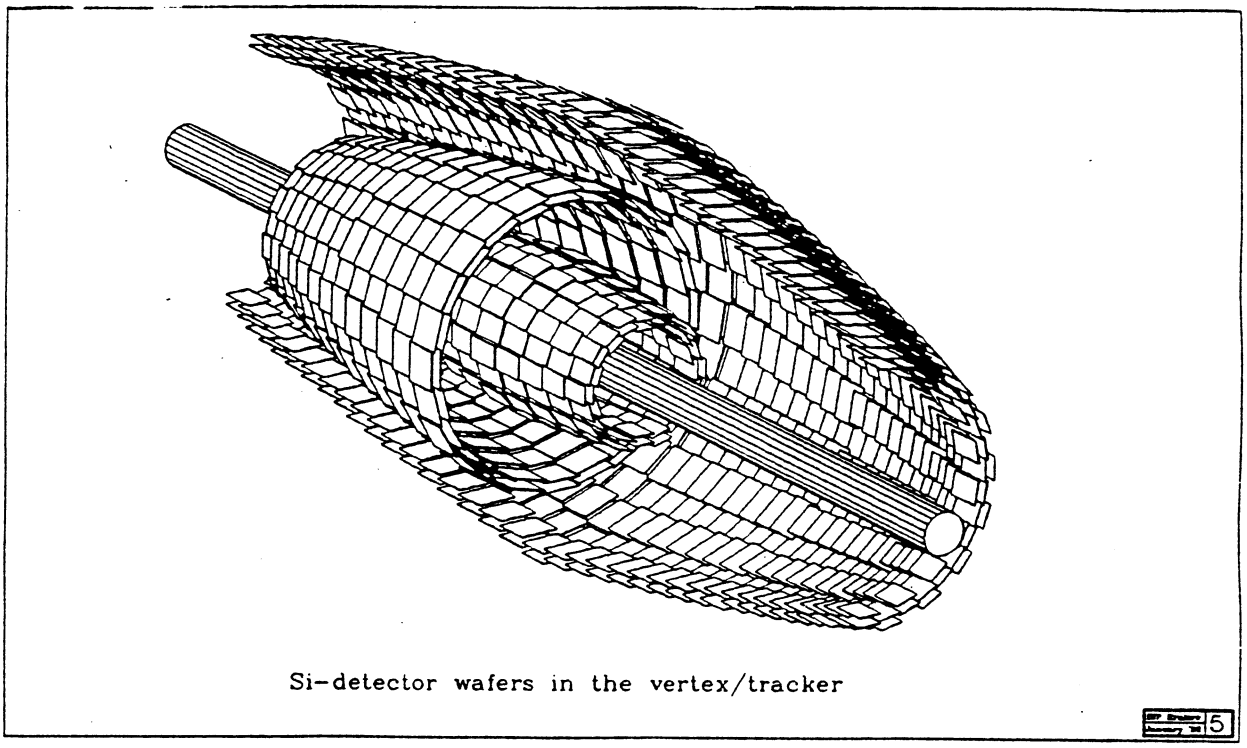

Figure 7.2.19 : The silicon wafer arrangement in the SITV geometry.

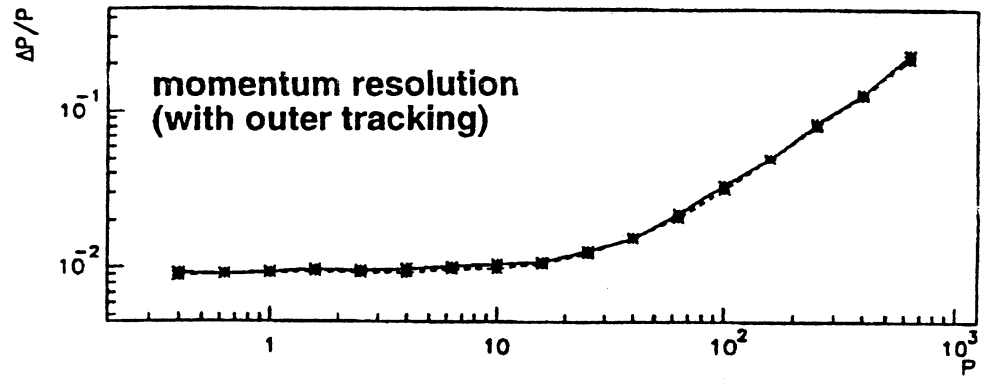

Figure 7.2.20 : Simulated SITV momentum resolution at $\eta = 0$ as a function of the track momentum (in GeV).

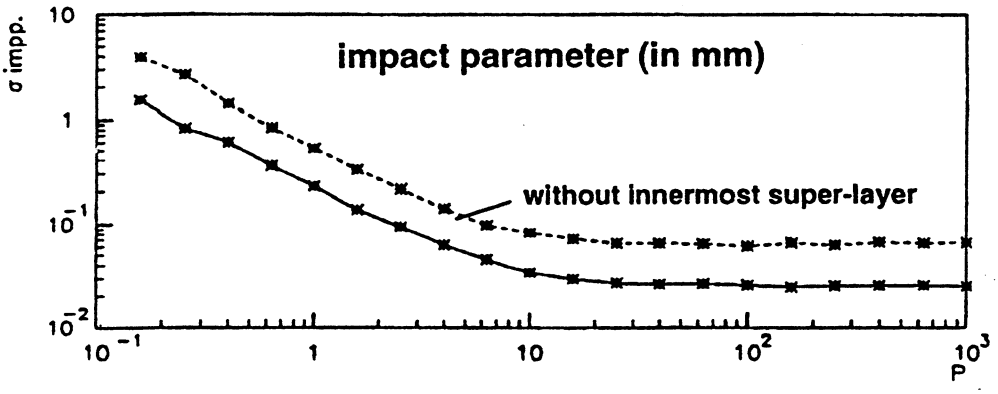

Figure 7.2.21 : Simulated SITV impact parameter resolution at $\eta = 0$ as a function of the track momentum (in GeV).

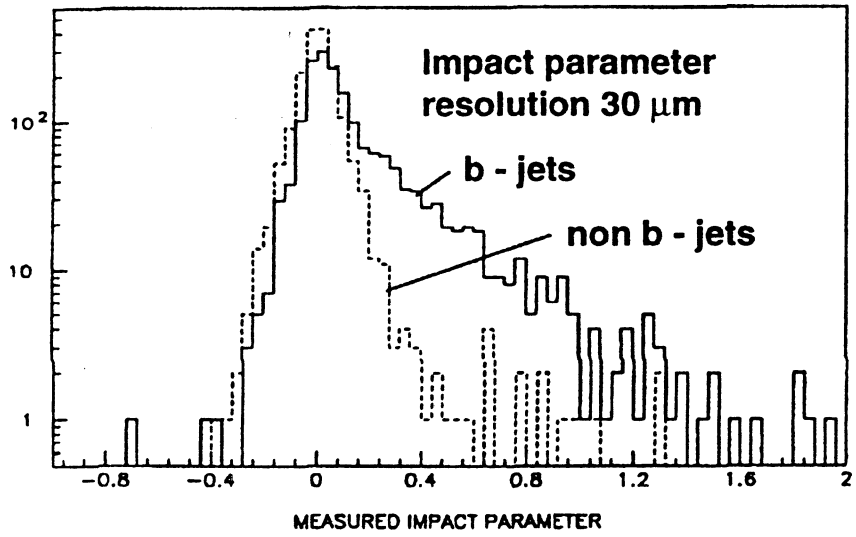

Figure 7.2.22 : Simulated SITV impact parameter measurement from $t\bar{t}$ events (see text).

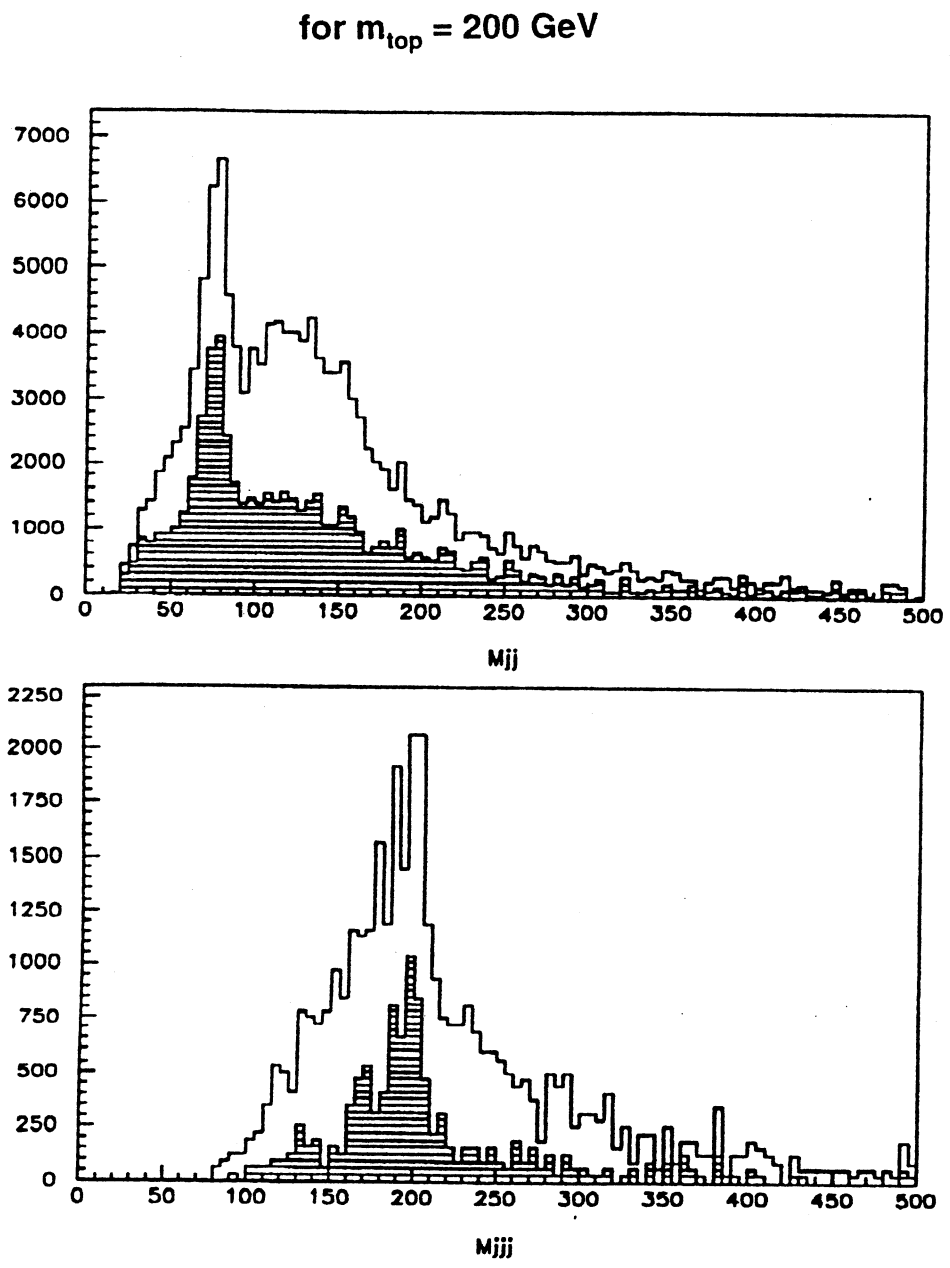

Figure 7.2.23 : 2-jet (top) and 3-jet (bottom) top quark mass reconstruction with (shaded) and without (unshaded) b-tagging information from the SITV.

5 million channels. The total radiation length of material depends on the angle and ranges from 4 to 9 % r.l..

The middle and outer superlayers are mainly for momentum measurements in -2 $< \eta <$ 2. The expected SITV momentum resolution is shown in Figure 7.2.20. The inner superlayer is mainly for vertex finding in -1.5 $< \eta <$ 1.5 and will especially aid in the secondary vertex determination for τ and heavy flavour decays. Figure 7.2.21 shows the SITV simulated impact parameter resolution as a function of the momentum.

An example of the SITV physics performance is b-tagging in $t\bar{t}$ events with $t \rightarrow Wb$ where one $W \rightarrow l\nu$ (l is either an electron or muon with $p_T > 40$ GeV) acts as a tag. Figure 7.2.22 shows the impact parameter measured by studying the jets ($p_T > 40$ GeV) and tracks ($p_T > 2$ GeV) in the opposite hemisphere to the tagged-top for b- and non-b- jets. This difference can be exploited when reconstructing the t-quark 2-jet or 3-jet mass as is shown in Figure 7.2.23 for a t-quark mass of 200 GeV.

7.2.2 The Silicon Track/Preshower Detector

Electron identification at both the trigger and analysis levels is of high priority in EAGLE. To this end a research and development project is ongoing to study the use of track and/or preshower techniques in electron identification which will lead to the development of an appropriate silicon detector (SITP) [SIT-90, SIT-92a, SIT-92b]. In addition, the tracking component of the detector can give a stand-alone momentum measurement of

$$\frac{\sigma_{p_T}}{p_T} \sim 1.5\text{x}10^{-3}\ p_T\ (\text{GeV})$$

and can also aid in τ identification an example of which will be discussed below.

The principle of identification of electrons over photons and charged pions using a track/preshower detector preceding the electromagnetic and hadronic calorimeter is shown in Figure 7.2.24. The electron can be identified by

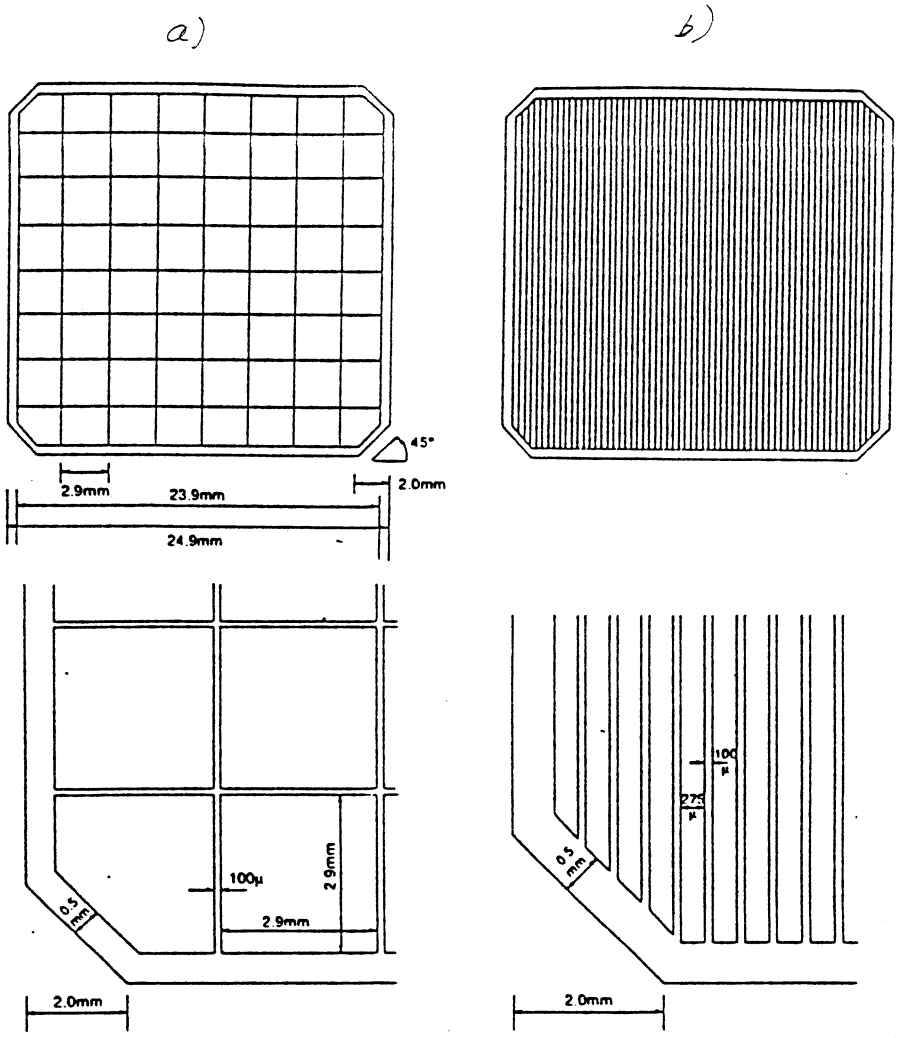

Figure 7.2.25 : The SITP geometry of (a) pad and (b) micro-strip detectors.

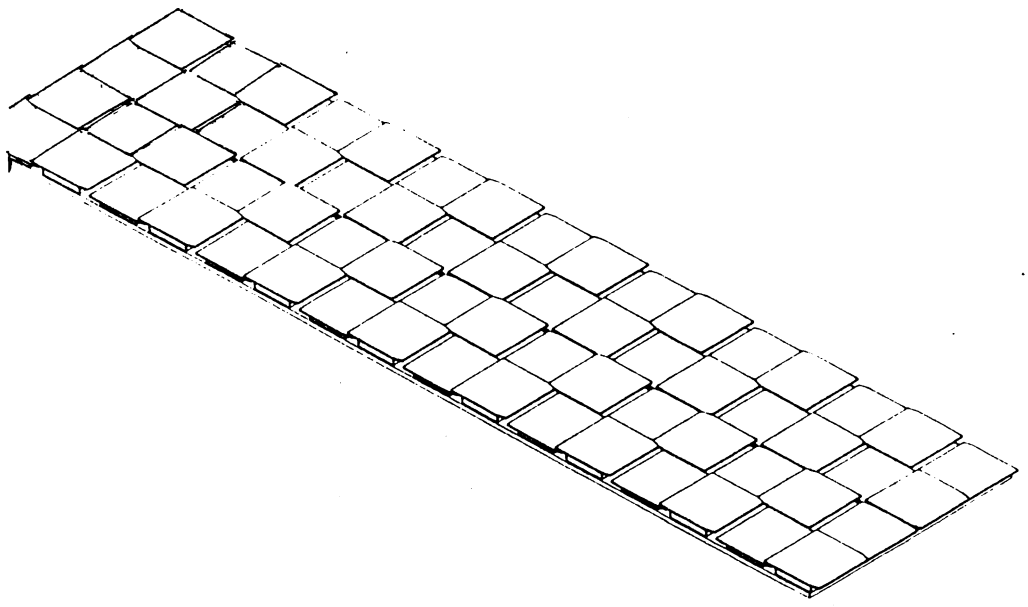

Figure 7.2.26 : SITP counter lay-out.

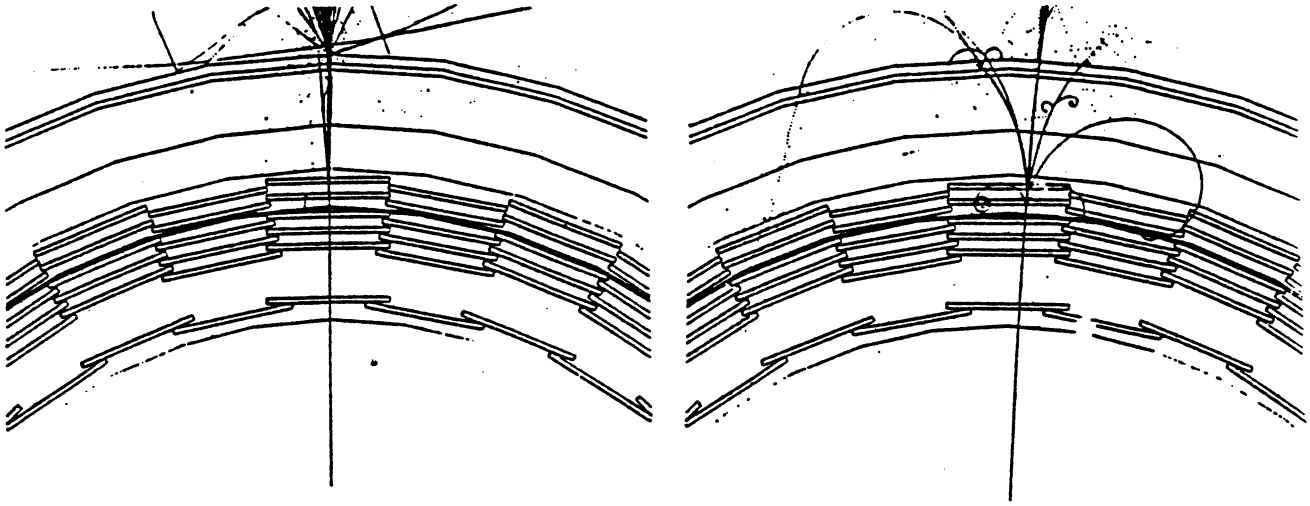

Figure 7.2.27 : A typical shower simulation of a 40 GeV electron at normal incidence. The Pb radiator is of 1.5 X_o thickness. The cases of (a) no central magnetic field, and (b) a field of 1.5 T, are shown.

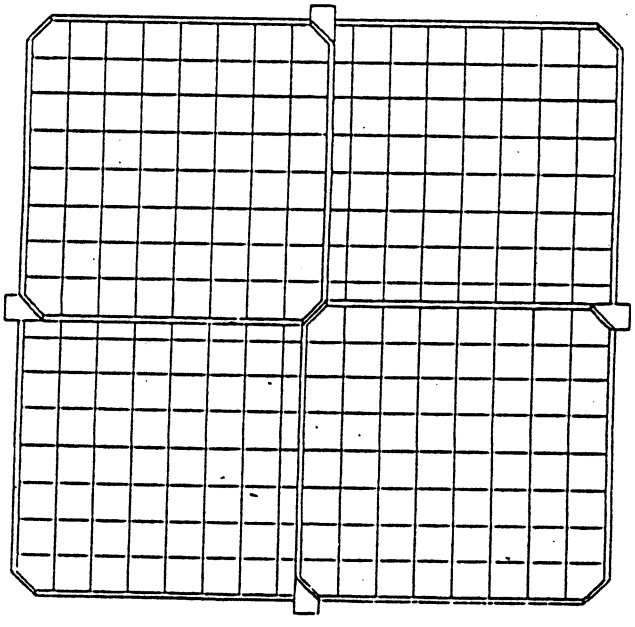

Figure 7.2.28 : A plane of pad detectors as used in the 1991 SITP testbeam.

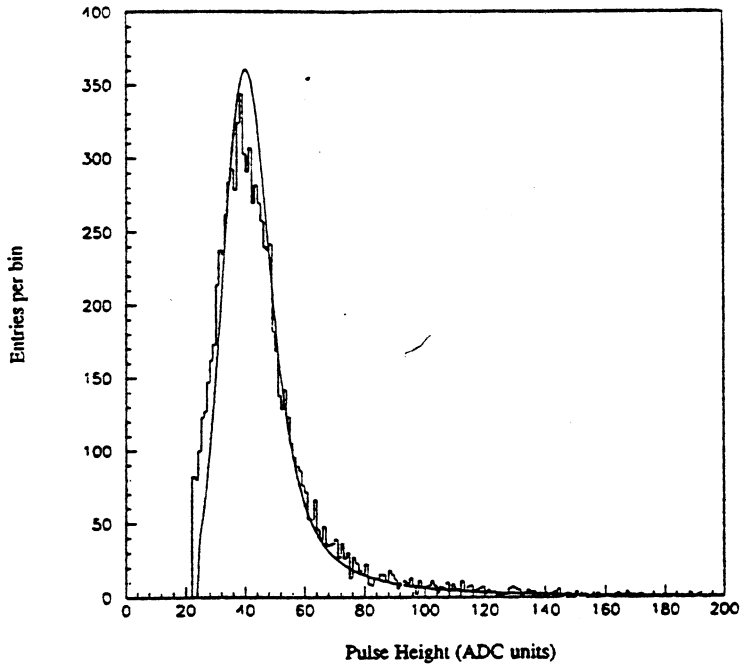

Figure 7.2.29 : Minimum ionizing particle signal in the first tracking plane from the 1991 SITP testbeam. The Landau fit includes a superimposed Gaussian signal noise.

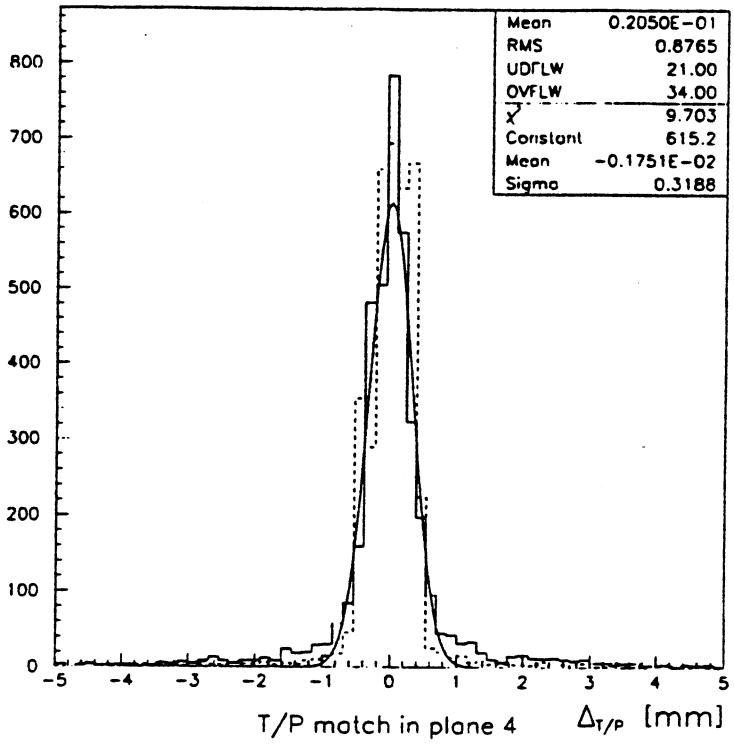

Figure 7.2.30 : Track-preshower match of 40 GeV electrons in the first plane after the converter from the 1991 SITP testbeam. Simulation results are superimposed (dashed histogram) together with a Gaussian fit to the data.

(a) a good spatial match between a minimum-ionizing reconstructed track stub, a preshower signal having a pulse height consistent with that expected for an electron and an electromagnetic energy deposition in the calorimeter, and
(b) the isolation of the electron signal from nearby charged and neutral tracks.

The SITP Collaboration has chosen as its prototype a 6-layer silicon counter design consisting of 64 pads or micro-strips. The pad dimensions are 3 mm x 3 mm (giving a 1 mm resolution along the beam direction) and the micro-strips are of dimension 24 mm x 375 μm and are to be used in a crossed configuration. The counter geometry is shown in Figure 7.2.25. Therefore, the channel number and area are identical for both counter types. The detectors are expected to have a thickness of 300 μm. The counters are laid out in a chessboard pattern (see Figure 7.2.26) giving almost complete coverage. The basic module is a slice , containing individual boards each supporting 64 detectors. The boards are overlapped within the slice along the beam direction and the slices are overlapped in the azimuthal direction giving a hermetic arrangement. The 6 layers are to fit between the radial range of $\sim$ 75 cm to $\sim$ 95 cm from the beam pipe. In total there is expected to be about 10 million channels covering $\sim$ 80 m^2. Radiators of varying thickness can be interleaved with the detector planes. Figure 7.2.27 shows a typical shower simulation of a single 40 GeV electron incident on a 1.5 r.l. radiator in a 0 T and 1.5 T solenoidal magnetic field.

To evaluate the effectiveness of the silicon detector as a track/preshower device in an LHC experiment, a series of testbeam studies are underway in the H2 beam of the SPS at CERN [Spi-92]. Data are collected using electrons of 10, 20, 30, 40, 80, and 150 GeV momentum and charged pions of 40 GeV momentum. Four planes were equipped for the 1991 testbeam each of which consisted of a 2x2 array of pad and micro-strip detectors (see Figure 7.2.28). A converter of either 1.0 or 1.5 r.l. was placed after the second silicon plane. A minimum ionizing signal in the first tracking plane is shown in Figure 7.2.29 measured for single hits above a $4\sigma_{\mathrm{ped}}$ threshold. The fitted Landau distribution , which is convoluted with a Gaussian electronic noise (σ_{ped} = 6.2 ADC counts), has a peak value of 36.5 ± 0.1 ADC counts. This leads to a signal-to-noise ratio of about 6. In addition, using tracks defined by the layers preceding the radiator and taking the shower position as that of the largest preshower digitization, Figure 7.2.30 shows the track/preshower

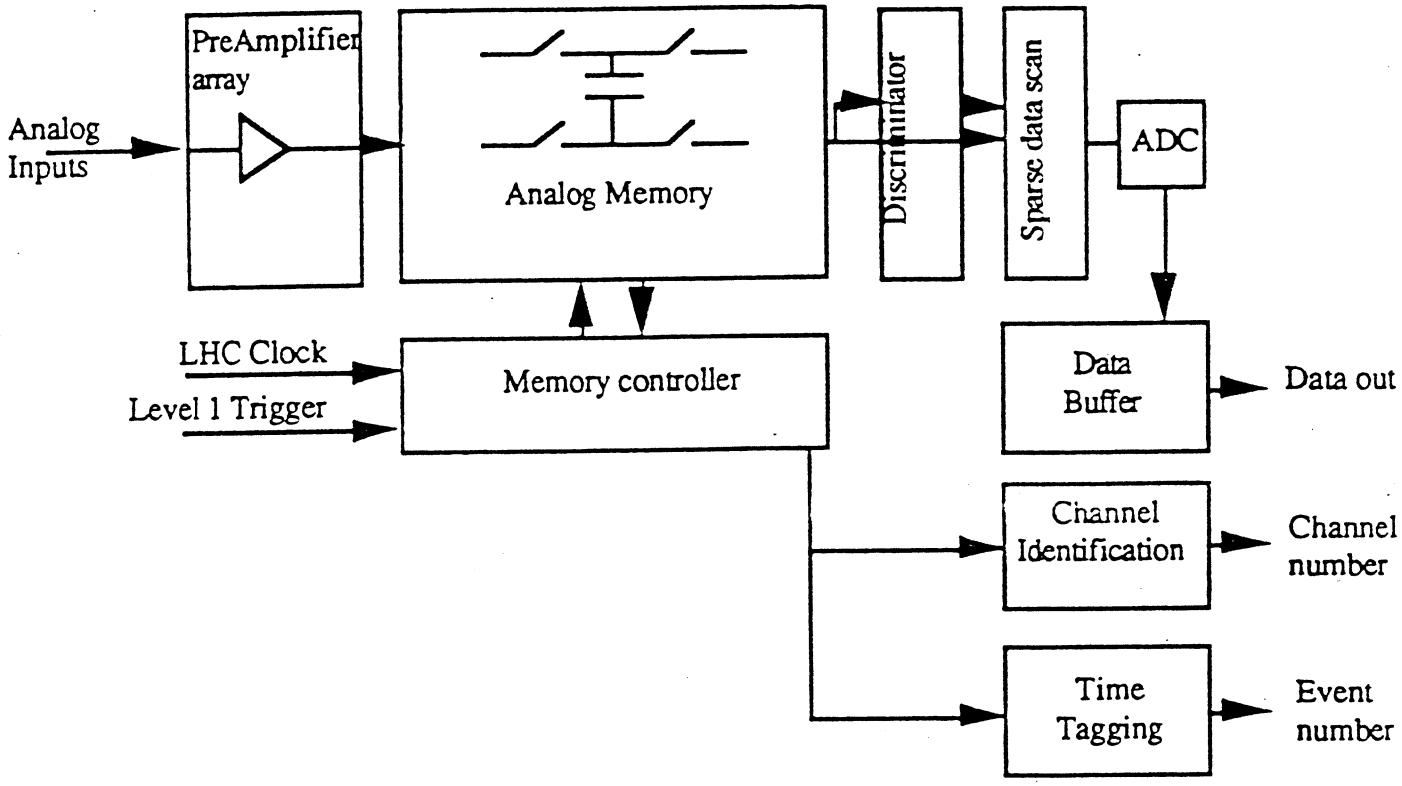

Figure 7.2.31 : The SITP front-end chip architecture.

separation at the strip detector following the radiator. In 95% of the cases a preshower signal exceeding 0.7 mip (corresponding to a 3 σ_{ped} threshold) is identified within 10 mm of the track.

The LHC collision rate of 67 MHz requires immediate front-end data processing in order to reduce the data to manageable levels. Such rates can be handled because of the high intrinsic speed of the silicon. For a 200 μm thick silicon detector biased at 80 V, the collection time is less than 1.5 ns [Jar-89]. Therefore, for a 10 mm^2 5 pF capacity detector element,the charge transfer between detector and amplifier can be very fast. The front-end architecture has an analog memory array for data storage and selection (time compaction), a sparse data readout (space compaction) and a low speed, low power ADC (see Figure 7.2.31). It is intended to make the front-end electronics from Application Specific Integrated Circuits (ASICs) and to mount the chips directly on the detectors so that there is one chip per counter.

7.3 Prospects for Charged Higgs from Top Quark Decay

7.3.1 Introduction

If there exists a $H^{\pm}$ which is lighter than $m_t - m_b$ then for a top quark mass $m_t > m_W + m_b$ the on-shell decays $t \rightarrow W^+b$ and $t \rightarrow H^{\pm}$ b are both allowed. The relative branching ratios depend on m_t and $m_{H^{\pm}}$ and as is shown in Figure 7.3.1 on tanβ [Big-86, Bar-90b]. In this analysis the decay mode of $H^{\pm}$ to $\tau\nu_\tau$ is probed. For tan$\beta \geq 2$, the Br($H^{\pm} \rightarrow \tau\nu_\tau$) is approximately constant at $\sim 95\%$ and dominates over Br($H^{\pm} \rightarrow c\bar{s}$).

For certain tanβ values the $H^{\pm}$ would preferentially decay to $\tau\nu_\tau$ so that it could induce a violation in the universality of the leptonic couplings to the W in top quark decay by enhancing the $t \rightarrow \tau\nu_\tau b$ channel over the $t \rightarrow \mu\nu_\mu b$ and $t \rightarrow e\nu_e b$ channels. The degree to which lepton universality is broken can be quantified by defining

$$R_{\tau\mu} \equiv \frac{Br(t \rightarrow \tau\nu_\tau b)}{Br(t \rightarrow \mu\nu_\mu b)}$$

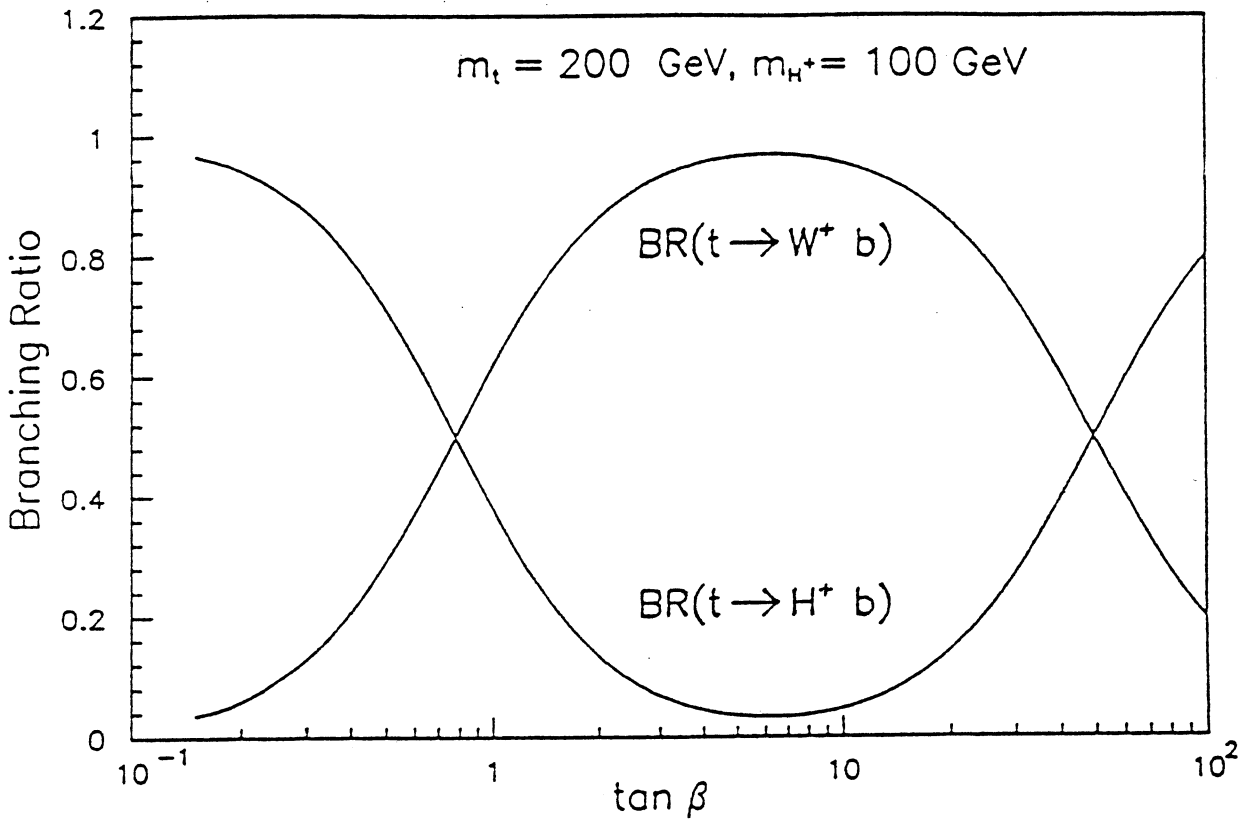

Figure 7.3.1 : Branching fractions for $t \rightarrow W^+b$ and for $t \rightarrow H^+b$ for m_t = 200 GeV and $m_{H^\pm}$ = 100 GeV as a function of tanβ.

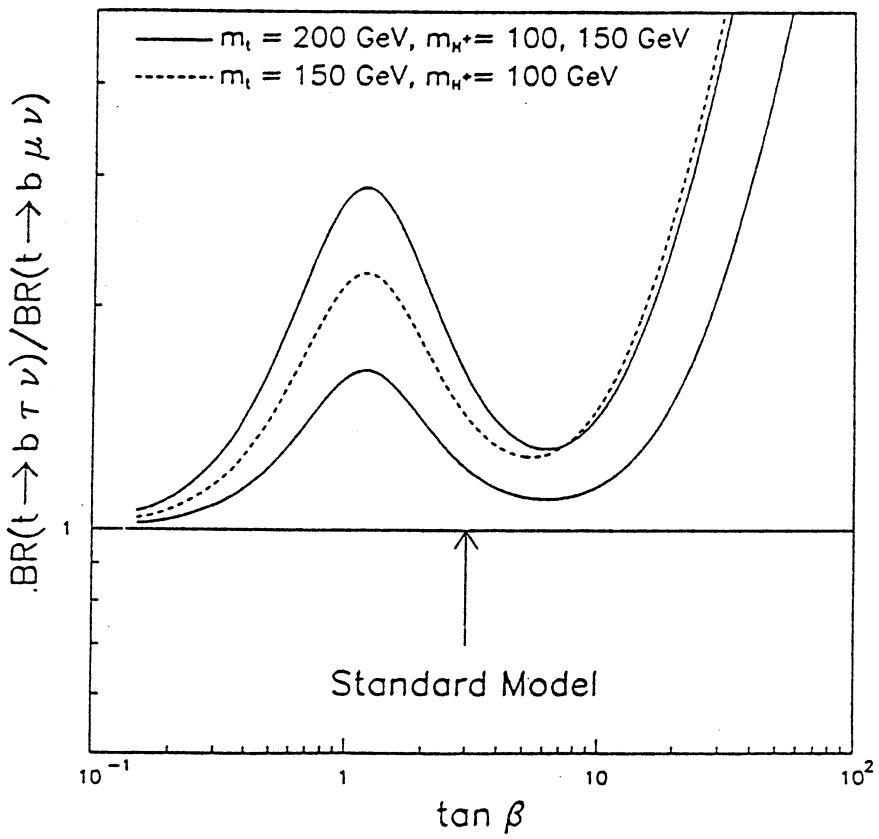

Figure 7.3.2 : The expected theoretical distribution for $R_{\tau\mu}$ as a function of tanβ for three different $(m_t, m_{H^\pm})$ mass pairs.

$$R_{\tau\mu} = 1 + \frac{Br(t \rightarrow H^+b)\ Br(H^+ \rightarrow \tau^+\nu_\tau)}{Br(t \rightarrow W^+b)\ Br(W^+ \rightarrow \tau^+\nu_\tau)}$$

so that

$$R_{\tau\mu} \equiv 1 + \delta R_{\tau\mu}$$

If there exists no $H^\pm$ so that lepton universality to the W is observed then $\delta R_{\tau\mu} = 0$. A value of $\delta R_{\tau\mu} \neq 0$ would be evidence for a $H^\pm$ in top quark decay. Figure 7.3.2 shows the expected theoretical distribution for $R_{\tau\mu}$ as a function of tanβ for three different (m_t , $m_{H^\pm}$) mass pairs.

7.3.2 The Data Sample

The event sample is selected from $t\bar{t}$ events by asking one of the top quarks to decay in the 'isolated' e - 'non- isolated' μ channel as is shown in Figure 7.3.3. Such a sample is called 'tagged-top'. The other top can decay to any of the three leptonic final states $t \rightarrow e(\mu)(\tau)\nu_{e(\mu)(\tau)}b$ via a $H^\pm$ or W. The cuts required to define the sample are [Fay-90] :

$$p_T^e > 75 \text{ GeV},$$

$$p_T^\mu > 25 \text{ GeV, and}$$

$$20^\circ < \Delta\phi(e - \mu) < 100^\circ$$

where $\Delta\phi$ is the angle between the electron and μ in the azimuthal plane. The cuts have been chosen to provide a predominantly $t\bar{t}$ sample.

The ratio of the number of 'tagged-top' events $N_{e\mu\tau}$ of the type ('isolated' e - 'non-isolated' μ) - 'isolated' τ where the second top quark decays via $t \rightarrow \tau^+\nu_\tau b$ to the number of 'tagged-top' events $N_{e\mu\mu}$ of the type ('isolated' e - 'non-isolated' μ) - 'isolated' μ where the second top quark decays via $t \rightarrow \mu^+\nu_\mu b$ is directly related to the quantity $\delta R_{\tau\mu}$:

$$\frac{N_{e\mu\tau}}{N_{e\mu\mu}} = \frac{Br(\tau \rightarrow \nu)\epsilon_{W\rightarrow\tau}}{\epsilon_{W\rightarrow\mu}} (1 + \frac{\epsilon_{H\rightarrow\tau}}{\epsilon_{W\rightarrow\tau}} \delta R_{\tau\mu}).$$

Here $\epsilon_{H\rightarrow\tau}$ and $\epsilon_{W\rightarrow\tau}$ refer to the efficiency in identifying, in the 'tagged-top' sample, the hadronic τ decays in events which the τ from the second top quark comes from the $H^\pm$ or W decay, respectively ; $\epsilon_{W\rightarrow\mu}$ is the efficiency

$p_T^e > 75$ GeV/c

$p_T^\mu > 25$ GeV/c

$20° < \Delta\varphi_{(e-\mu)} < 100°$ (to reduce the $b\bar{b}$ background)

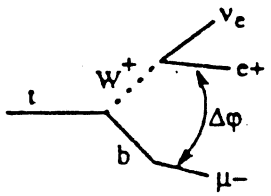

$\Delta\varphi$ is the angular separation in the transverse plane.

Figure 7.3.3 : The definition of the 'tagged-top' sample.

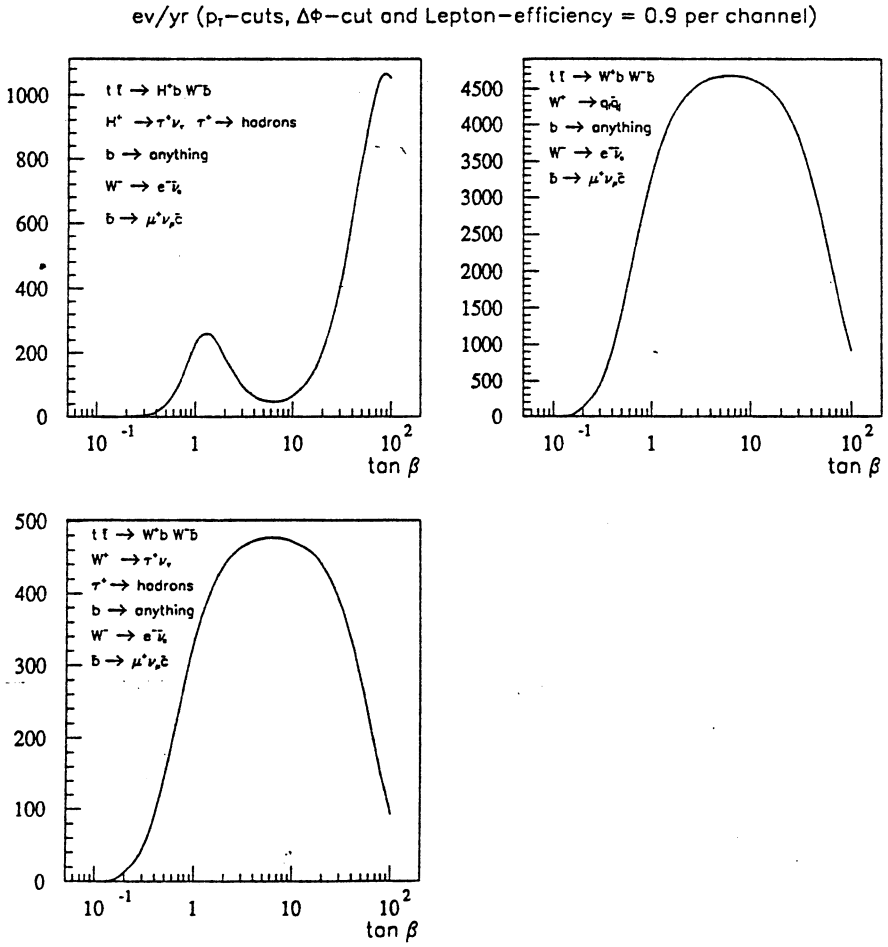

Figure 7.3.4 : The number of expected events from the signal and background 'tagged-top' events.

of identifying the $t \rightarrow \mu^+\nu_\mu b$ decay of the second top quark. If a $H^\pm$ exists in top quark decay then

$$R_{\tau\mu}^{expt} \equiv 1 + \frac{\epsilon_{H\rightarrow\tau}}{\epsilon_{W\rightarrow\tau}}\delta R_{\tau\mu}$$

will be larger than unity.

The main background to the $t \rightarrow \tau^+\nu_\tau b$ signal comes from events in which the second top quark decays via $t \rightarrow q_i\bar{q}_j b$ where one of the final state quarks (after hadronization) can fake a hadronic τ decay. The ratio of $t \rightarrow \tau^+\nu_\tau b$ events, where the τ decays hadronically, to $t \rightarrow q_i\bar{q}_j b$ events is ~ 0.1 in the Standard Model. In addition, jets from initial and final state radiation and from the underlying event can contribute to the non-τ background. To achieve a reduction in this background a series of cuts are performed to enhance the sample with $t \rightarrow \tau^+\nu_\tau b$ events (see Section 7.3.4).

The number of expected events from the signal and background 'tagged-top' events are shown in Figure 7.3.4 as a function of $\tan\beta$ for $m_t = 200$ GeV and where appropriate for $m_{H^\pm} = 150$ GeV. The numbers are based on the assumption of 1 year running at the LHC at a luminosity of 10^{33} $cm^{-2}s^{-1}$ with a fiducial region defined by $-2 < \eta < 2$. The global lepton efficiency has been taken as 90%. The Monte Carlo generation has been performed with PYTHIA [Ben-84, Ben-87, Sjo-88] including initial and final state radiation and the EHLQ set 1 structure functions with $\Lambda_{QCD} = 200$ MeV [Eic-84, Eic-86]. The $t\bar{t}$ production cross-section used here is 0.7 nb [Alt-88a, Nas-88]. Therefore, assuming no $H^\pm$ in top quark decay, there is expected to be 7021 'tagged-top' events. It should be noted that the number of $b\bar{b}$ events, where one b-quark decays to an electron and the other to a μ, is 133 after defining the 'tagged-top' sample.

7.3.3 The Detector Simulation

In this analysis the following detector capabilities are assumed :

- A calorimeter coverage in $-2 < \eta < 2$ and of granularity $\Delta\eta$ x $\Delta\phi$ = 0.02 x 0.02. The energy resolution for electromagnetic showers is

$$\frac{\sigma(E)}{E} = \frac{10\%}{\sqrt{E}} + 6\%$$

and for hadronic showers it is

$$\frac{\sigma(E)}{E} = \frac{50\%}{\sqrt{E}} + 2\%$$

Jet clusters are reconstructed in cones of radius 0.7 cell units in $\eta - \phi$ space and are accepted if their their $E_T > 10$ GeV.

- A muon identification capability in the interval $-2 < \eta < 2$ and assuming a momentum resolution of

$$\frac{\sigma(p)}{p} = A + Bp$$

where A = 15% and B = 0.015% (p is in GeV).

- An SITP detector as described in Section 7.2.2. Only a single tracking layer at radius 79.5 cm. (either pad or micro-strip) is used for a multiplicity measurement.

7.3.4 Sensitivity to $H^{\pm}$ from Top Quark Decay

To reduce the background $t \rightarrow q_i\bar{q}_j b$ to $t \rightarrow \tau^+\nu_\tau b$ events in the 'tagged-top' sample a series of cuts has been applied to each jet in the hemisphere opposite to the 'tagged-top'. (The opposite hemisphere is defined as the region in which the difference in azimuthal angle between the jet barycentre and the 'isolated' electron is $> 90°$). Firstly, the jet transverse energy, E_T^{jet}, is required to be > 30 GeV. In addition, it is required that the number of hit SITP channels within a cone of radius R = 0.8 around the jet axis, H(0.8), satisfy $1.0 \leq H(0.8) < 6.0$. Figures 7.3.5 and 7.3.6 show, respectively, the various E_T^{jet} and H(0.8) distributions for non- τ and for τ jets from $H^{\pm}$ and W decays. The distributions for H(0.8) are given for an SITP pad layer and are identical for a micro-strip layer. The difference observed between the τ and non-τ jets can be exploited to enhance the 'tagged-top' sample with τ jets.

Table 7.3.1 lists the acceptances for each applied cut for both τ and non-τ jets. It is seen that the overall acceptance for τ jets from $H^{\pm}$ and W is

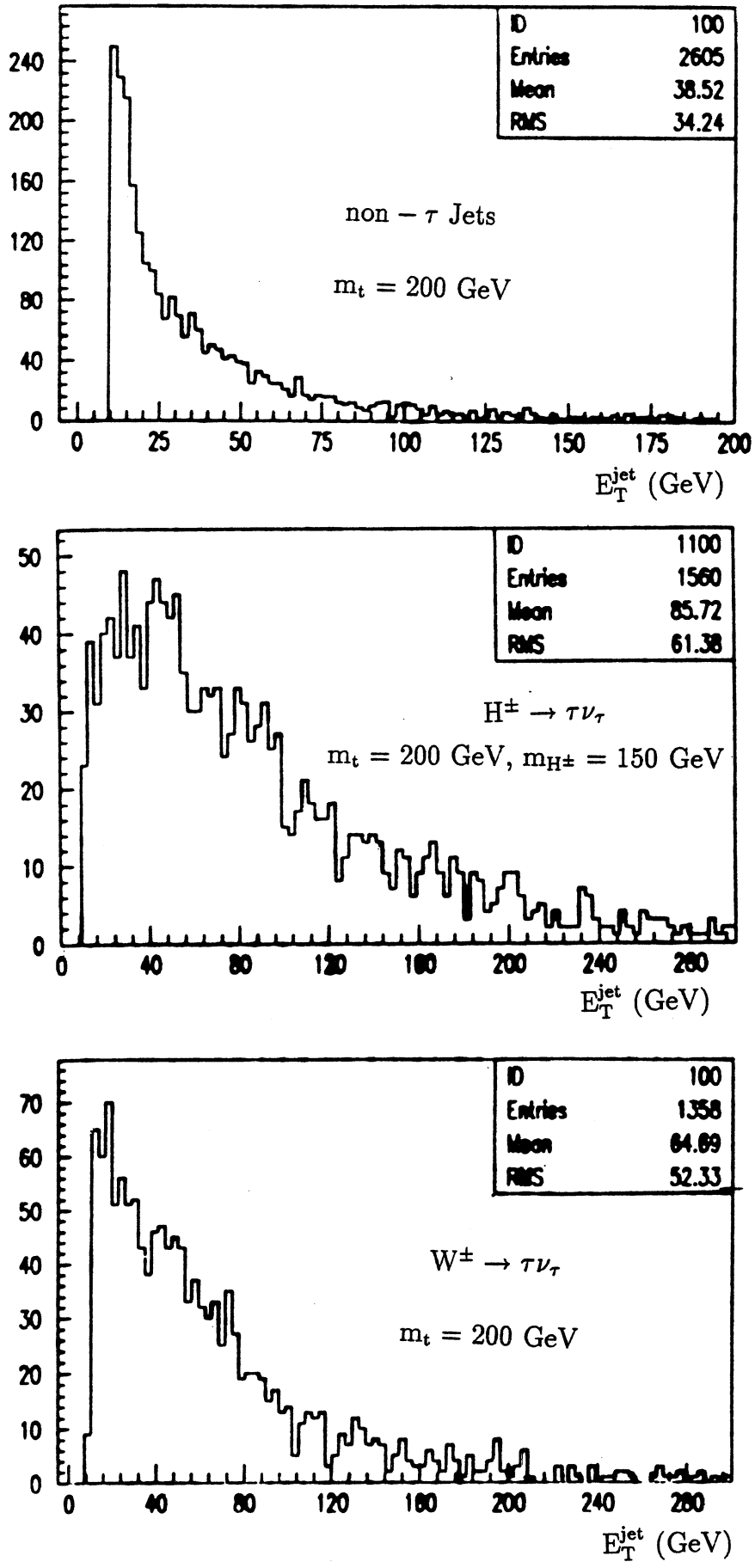

Figure 7.3.5 : The E_T^{jet} distributions for τ jets from $H^{\pm}$ and W and for non-τ jets.

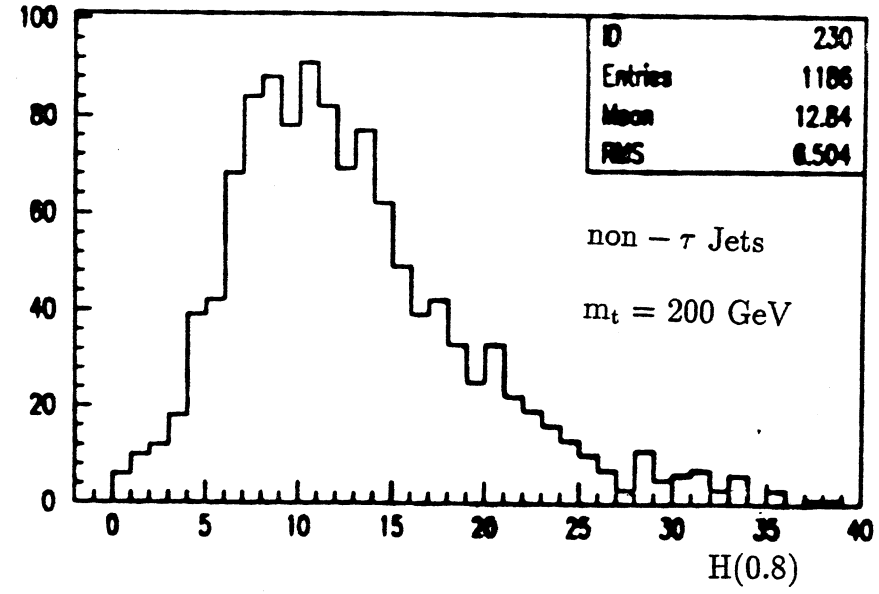

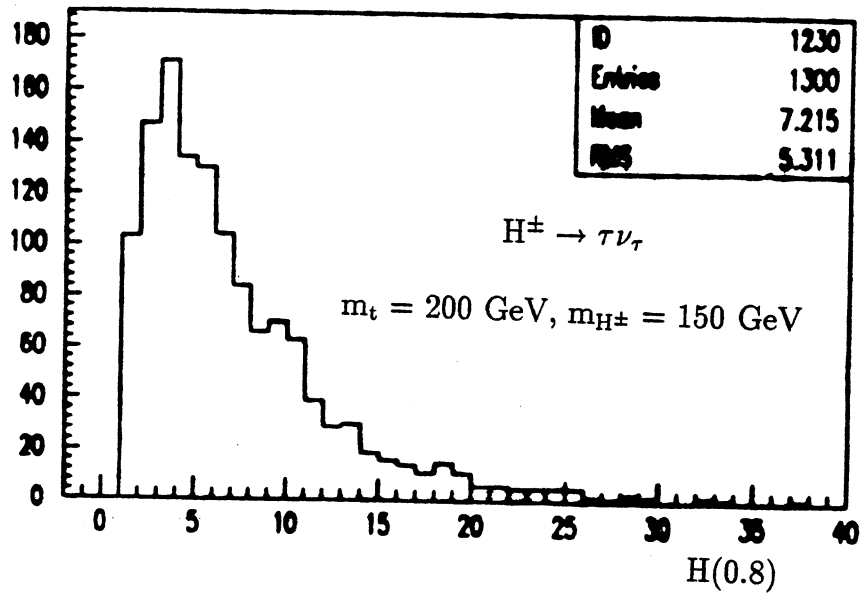

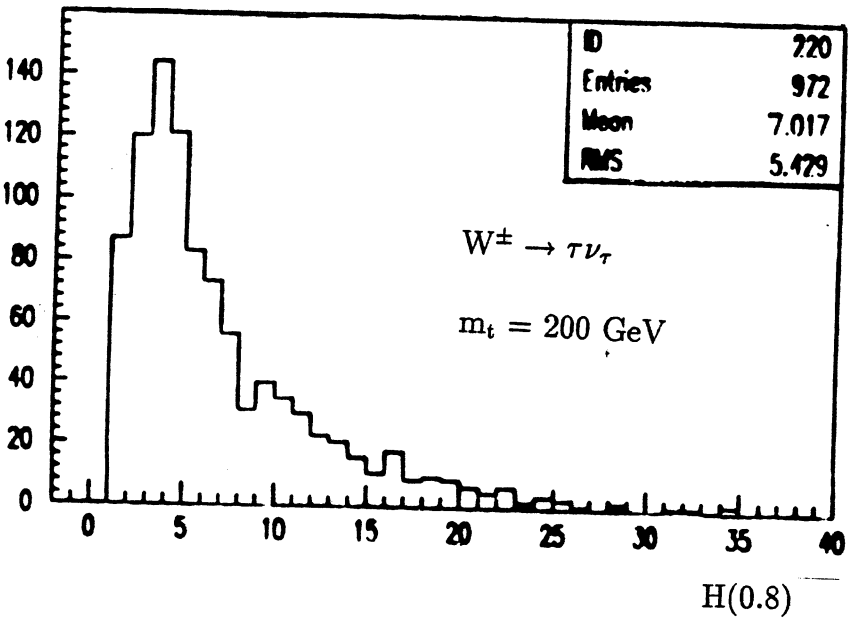

Figure 7.3.6 : The H(0.8) distributions for τ jets from $H^{\pm}$ and W and for non-τ jets.

Table 7.3.1 : Monte Carlo Acceptances

Cut	Non-τ Jet	τ Jet from W m_t = 200 GeV	τ Jet from $H^{\pm}$ m_t = 200 GeV $m_{H^{\pm}}$ = 150 GeV	τ Jet from $H^{\pm}$ m_t = 200 GeV $m_{H^{\pm}}$ = 100 GeV
E_T^{Jet}	0.46	0.72	0.83	0.79
H(0.8)	0.09	0.57	0.53	0.57
Overall	0.043	0.41	0.44	0.45

about a factor of 10 greater than that for non-τ jets. From this table $\epsilon_{H\to\tau}$ = 0.44 for m_t = 200 GeV and $m_{H^{\pm}}$ = 150 GeV, $\epsilon_{H\to\tau}$ = 0.41 for m_t = 200 GeV and $m_{H^{\pm}}$ = 150 GeV, and $\epsilon_{W\to\tau}$ = 0.41.

Therefore, starting from a 'tagged-top' sample of 7021 events and assuming no $H^{\pm}$ in top quark decay, $N_{e\mu\tau}$ = 207 events and the number of background events, N_{BKD}, is 201 events for m_t = 200 GeV. From the same 'tagged-top' sample, asking for an additional μ with $p_T^{\mu} > 20$ GeV (see Figure 7.3.7), gives $N_{e\mu\mu}$ = 703 so that $\epsilon_{W\to\mu}$ = 0.9.

The measured $R_{\tau\mu}^{expt}$ is affected by both statistical and systematic uncertainties. The statistical uncertainty is given by

$$\left(\frac{\Delta R_{\tau\mu}^{expt}}{R_{\tau\mu}^{expt}}\right)_{stat} = \frac{1}{\sqrt{N_{e\mu\mu}}}\left(1 + \sqrt{\frac{\epsilon_{W\to\mu}}{Br(\tau\to h\nu)\epsilon_{W\to\tau}}}\right)$$

and equals 11%.

The systematic uncertainties come from :

- The variation in the shower development of initial and final state radiation, by changing the default PYTHIA constant multiplying the Q^2 - scale of the hard scattering that defines the maximum parton vitruality allowed in space- and time- like showers [Sjo-92a]. The variation results in

$$\Delta N_{BKD} \leq \pm 1\%.$$

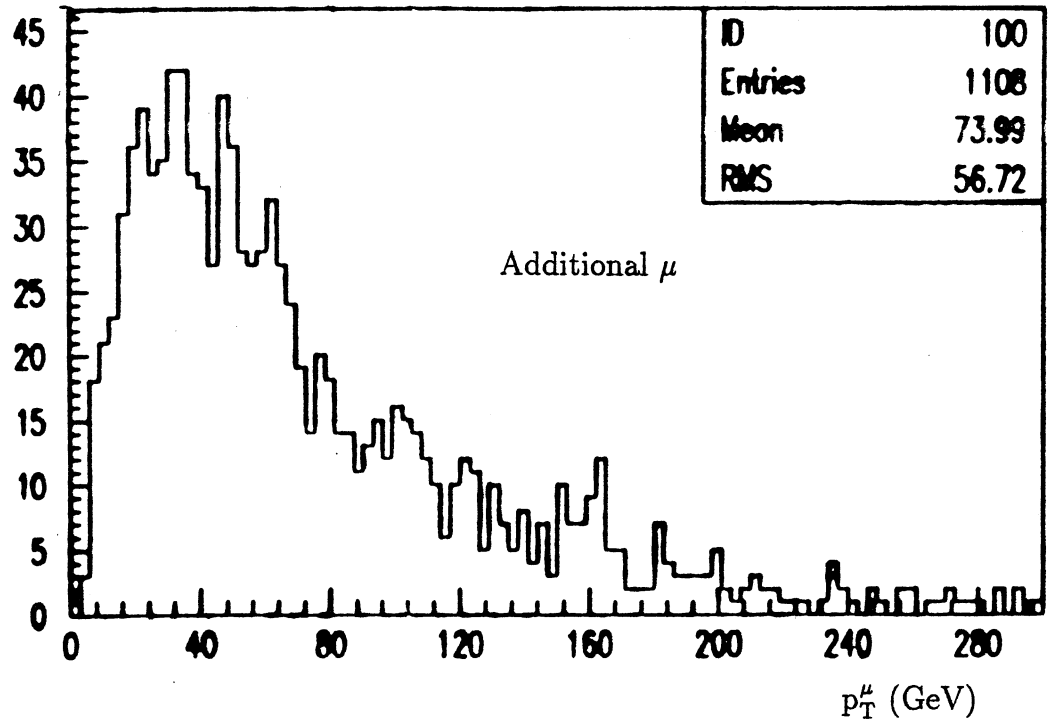

Figure 7.3.7 : The p_T distribution for the additional μ coming from the second top quark decay via $t \rightarrow \mu\nu_\mu b$.

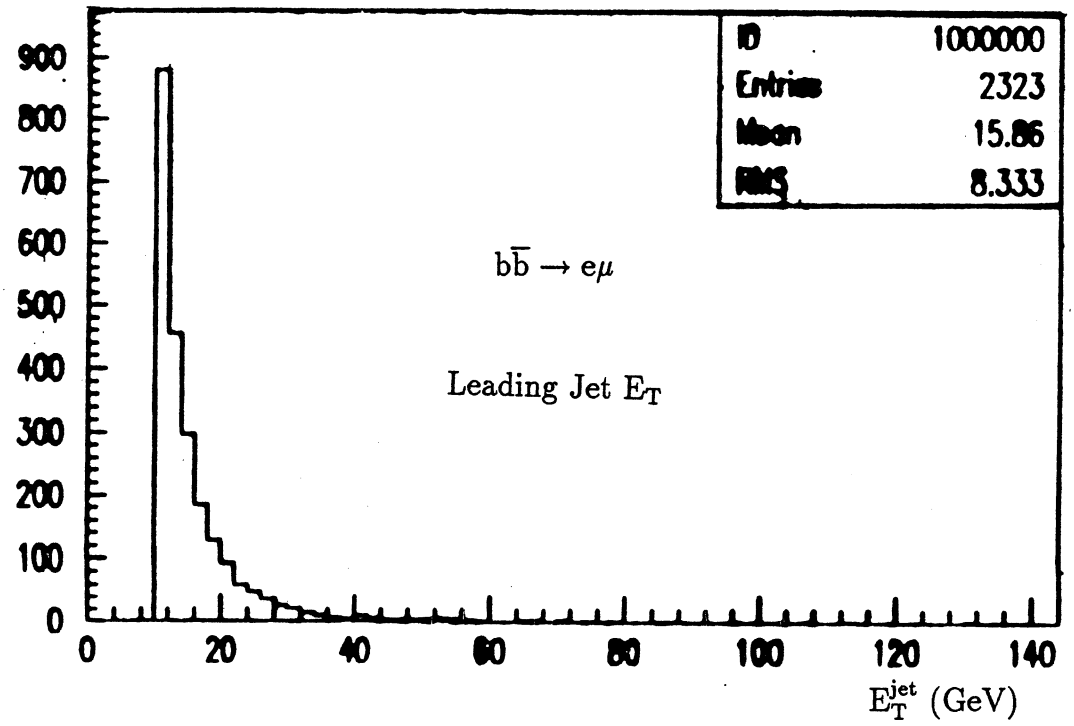

Figure 7.3.8 : The p_T distribution for the leading jet in $b\bar{b}$ events in which one of the b-quarks decays to an electron and the other to a μ.

- The cone radius used in the jet reconstruction algorithm has been varied from the default PYTHIA value which leads to a change in the jet multiplicity [Sjo-92b]. The variation results in

$$\Delta N_{BKD} \leq \pm 5\%.$$

- The cone radius used in the jet reconstruction algorithm has been varied from 0.7 to 0.4 cell units and leads to a systematic uncertainty of

$$\Delta N_{BKD} \leq \pm 5\%.$$

- A variation in the E_T^{jet} threshold according to an assumed energy scale uncertainty of 2% and 1% for electromagnetic and hadronic showers, respectively yields

$$\Delta N_{BKD} \leq \pm 3\%.$$

The uncertainty in the $t\bar{t}$ cross-section, the $Br(W \rightarrow l\nu_l)$ (where l is any leptonic final state), and the structure function set used are negligible. In addition, the uncertainty coming from the $b\bar{b}$ background is negligible because of the 133 $b\bar{b}$ events expected to contribute to the 'tagged-top' sample only a negligible number remain after applying the E_T^{jet} cut (see Figure 7.3.8).

Therefore, added in quadrature the total systematic uncertainty amounts to $\Delta N_{BKD} = \pm 8\%$. This corresponds to 8% of $N_{e\mu\tau}$. In summary, it is seen that at luminosities of 10^{33} $cm^{-2}s^{-1}$ the statistical uncertainty is dominant in this method. The total uncertainty, calculated by adding in quadrature the statistical and systematic errors, is 13.6%.

Figure 7.3.9 shows the significance in standard deviations of $R_{\tau\mu}^{expt}$ for various choices of m_t and $m_{H^\pm}$. The significance has been calculated assuming the combined statistical and systematic uncertainties). It is seen that over a large range of $\tan\beta$ values the method described here is sensitive to a potential $H^\pm$ signal. For lower m_t masses, e.g. m_t = 150 GeV and $m_{H^\pm}$ = 100 GeV, the value of the significance lies between the two curves shown in Figure 7.3.9.

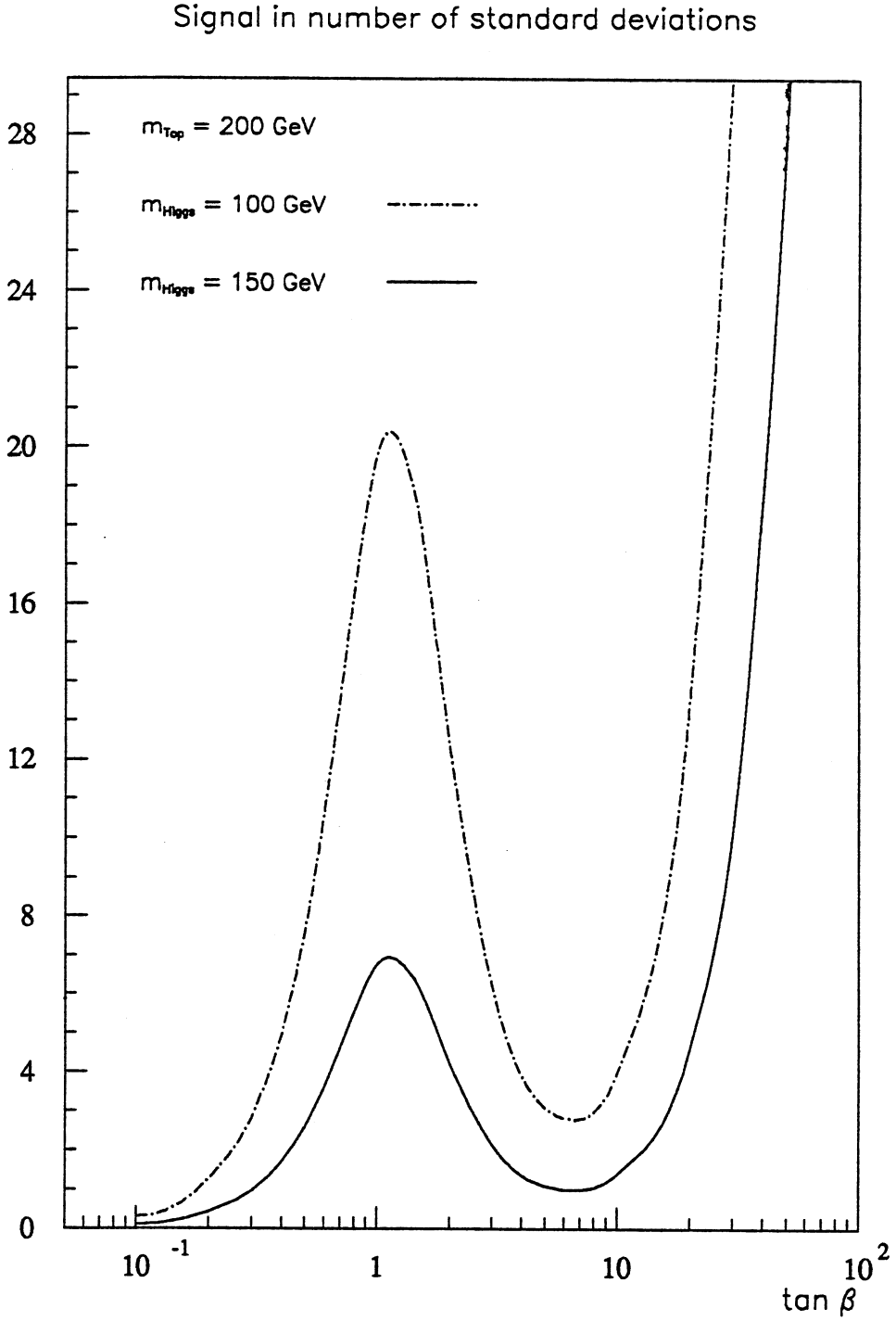

Figure 7.3.9 : The significance in standard deviations of $R_{\tau\mu}^{expt}$ for various choices of m_t and $m_{H^\pm}$.

Table 7.3.2 : Monte Carlo Acceptances with 1 Minimum Bias Event

Cut	Non-τ Jet	τ Jet from W m_t = 200 GeV	τ Jet from $H^{\pm}$ m_t = 200 GeV $m_{H^{\pm}}$ = 150 GeV
E_T^{Jet}	0.40	0.74	0.84
H(0.8)	0.06	0.38	0.30
Overall	0.026	0.28	0.26

7.3.5 Effect of Minimum Bias Superposition

At the nominal high LHC luminosity of 1.7×10^{34} $cm^{-2}s^{-1}$ it will be unavoidable to pile-up several minimum bias events in the same trigger gate, thus adding a non-negligible level of background. The mean number of interactions $< n >$ is ~ 20 which leads to pile-up effects. Such pile-up events can be simulated by adding ~ 20 minimum bias interactions which is calculated assuming σ_{inel} = 80 mb [Cia-90], an inter-bunch spacing of 15 ns and the nominal high LHC luminosity. However, for luminosities $\leq 10^{33}$ $cm^{-2}s^{-1}$, $< n > \leq 1$ which leads to a superposition of ~ 1 minimum bias event per bunch crossing thus resulting in small pile-up effects.

A similar analysis has been performed as presented in Section 7.3.4 but with the addition of 1 minimum bias event per bunch crossing. The corresponding acceptances are shown in Table 7.3.2. As expected the efficiency of identifying τ 's has decreased resulting mostly from an increased silicon multiplicity selection inefficiency. Nonetheless, the acceptance of τ and non-τ jets is still a factor of 10 larger for the former. The distributions in E_T^{jet} and H(0.8) are shown in Figures 7.3.10 and 7.3.11, respectively.

Therefore, starting from a 'tagged-top' sample of 7021 events and assuming no $H^{\pm}$ in top quark decay, $N_{e\mu\tau}$ = 139 events and the number of background events, N_{BKD}, is 123 events for m_t = 200 GeV. The value of $N_{e\mu\mu}$ remains 703 so that $\epsilon_{W \to \mu} = 0.9$.

The statistical uncertainty has increased to 12% and still dominates the total uncertainty as the systematic uncertainty has remained stable. This is as expected since only a minimal amount of pile-up has been assumed. The combined uncertainty is 14.4%. Figure 7.3.12 shows the corresponding

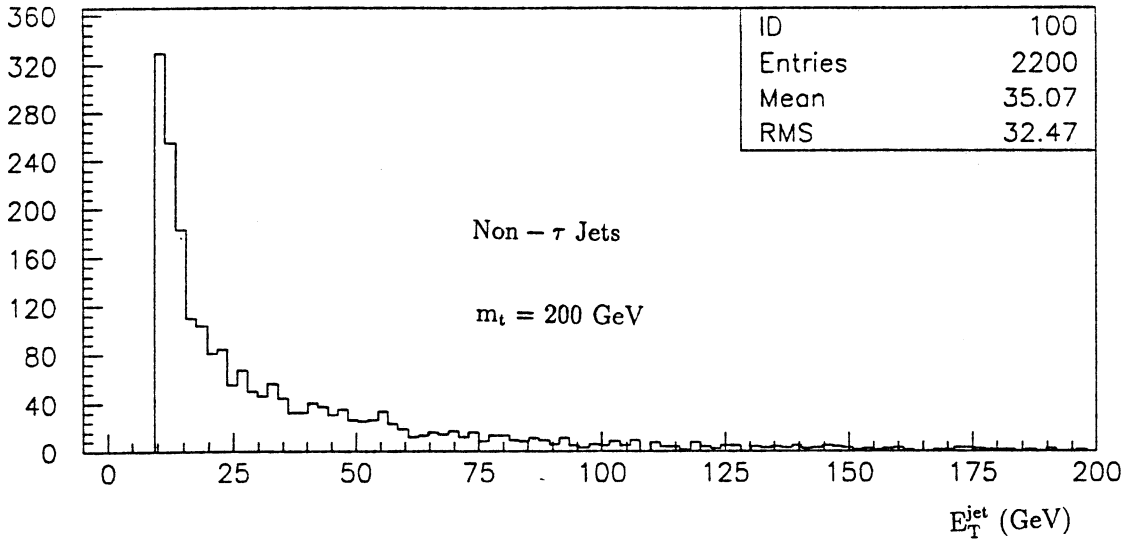

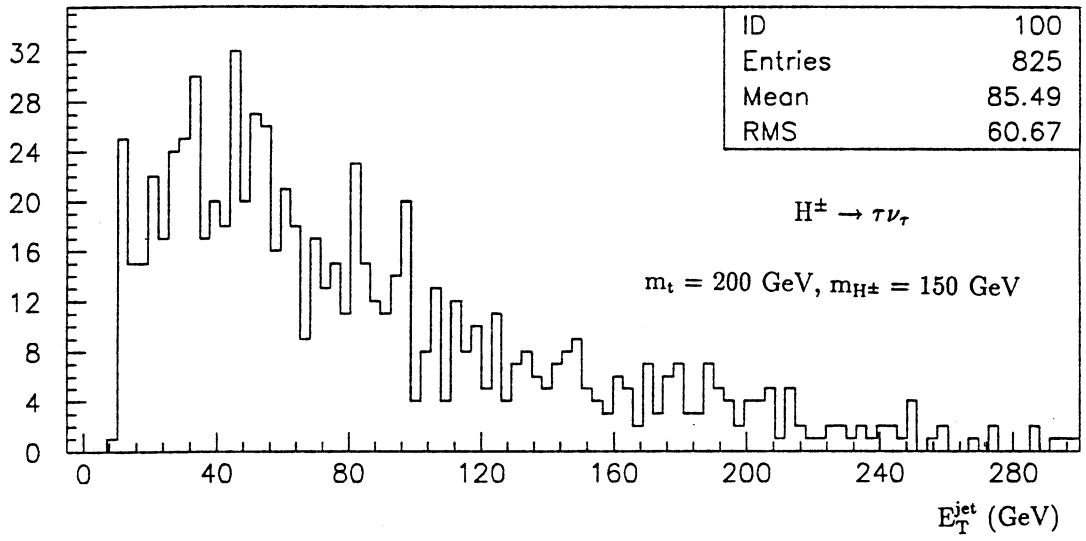

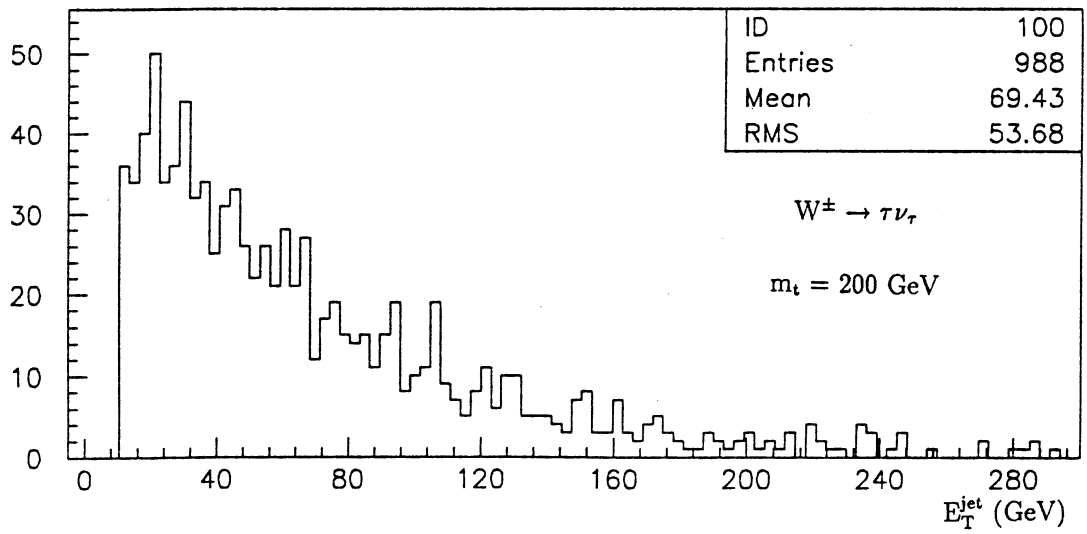

Figure 7.3.10 : The E_T^{jet} distributions for τ jets from $H^{\pm}$ and W and for non-τ jets including the superposition the 1 minimum bias event.

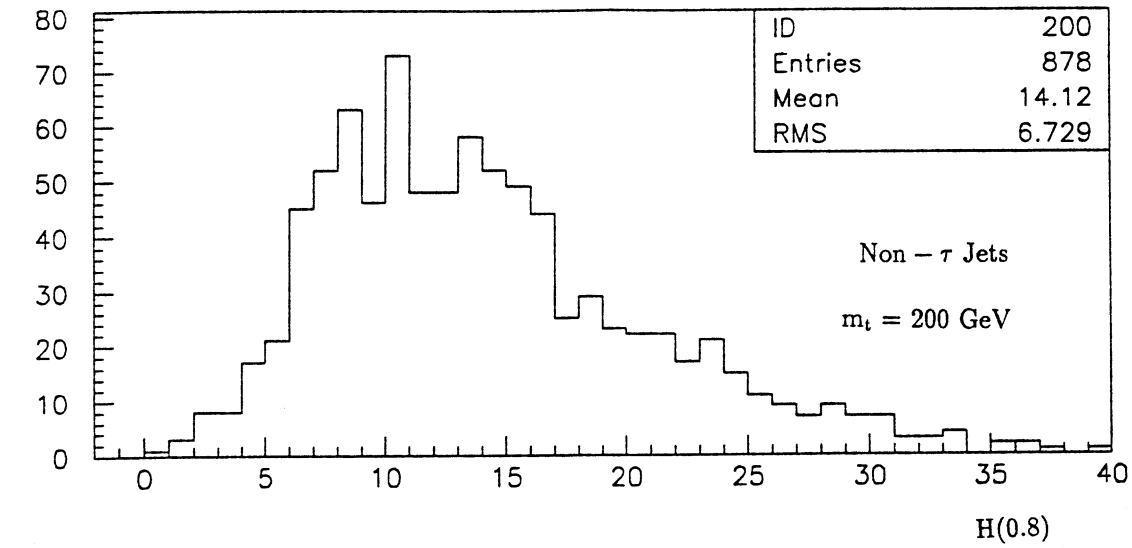

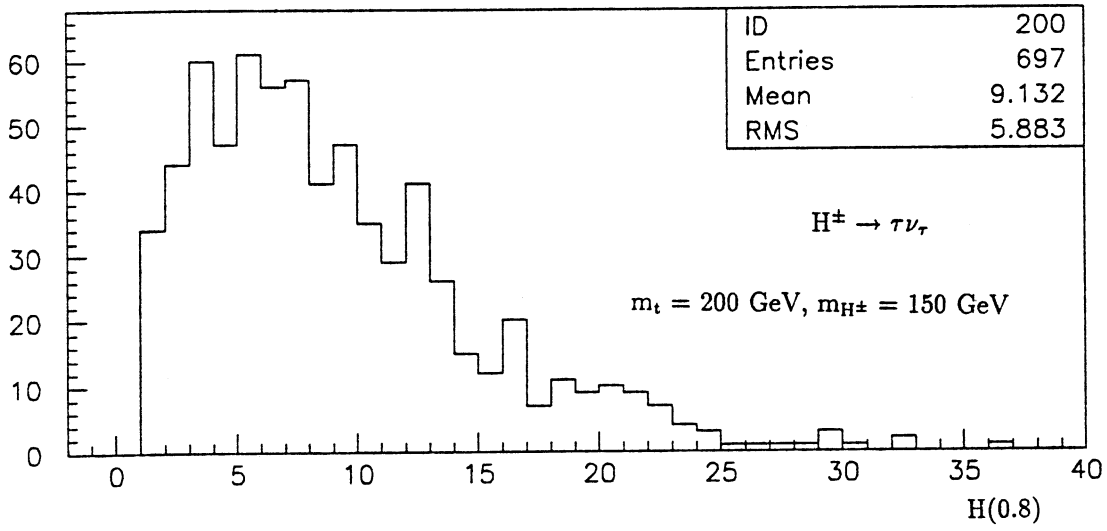

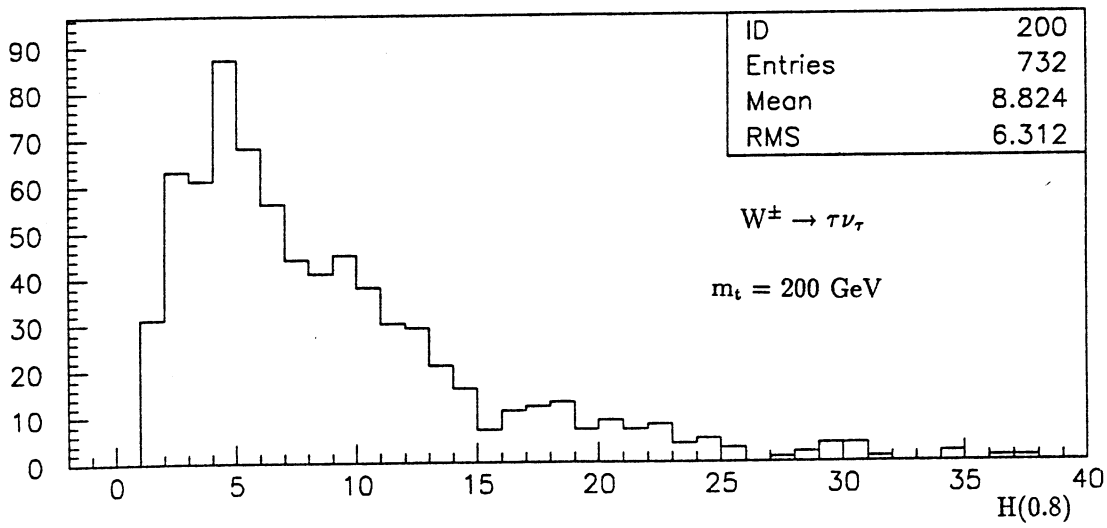

Figure 7.3.11 : The H(0.8) distributions for τ jets from $H^{\pm}$ and W and for non-τ jets including the superposition of 1 minimum bias event.

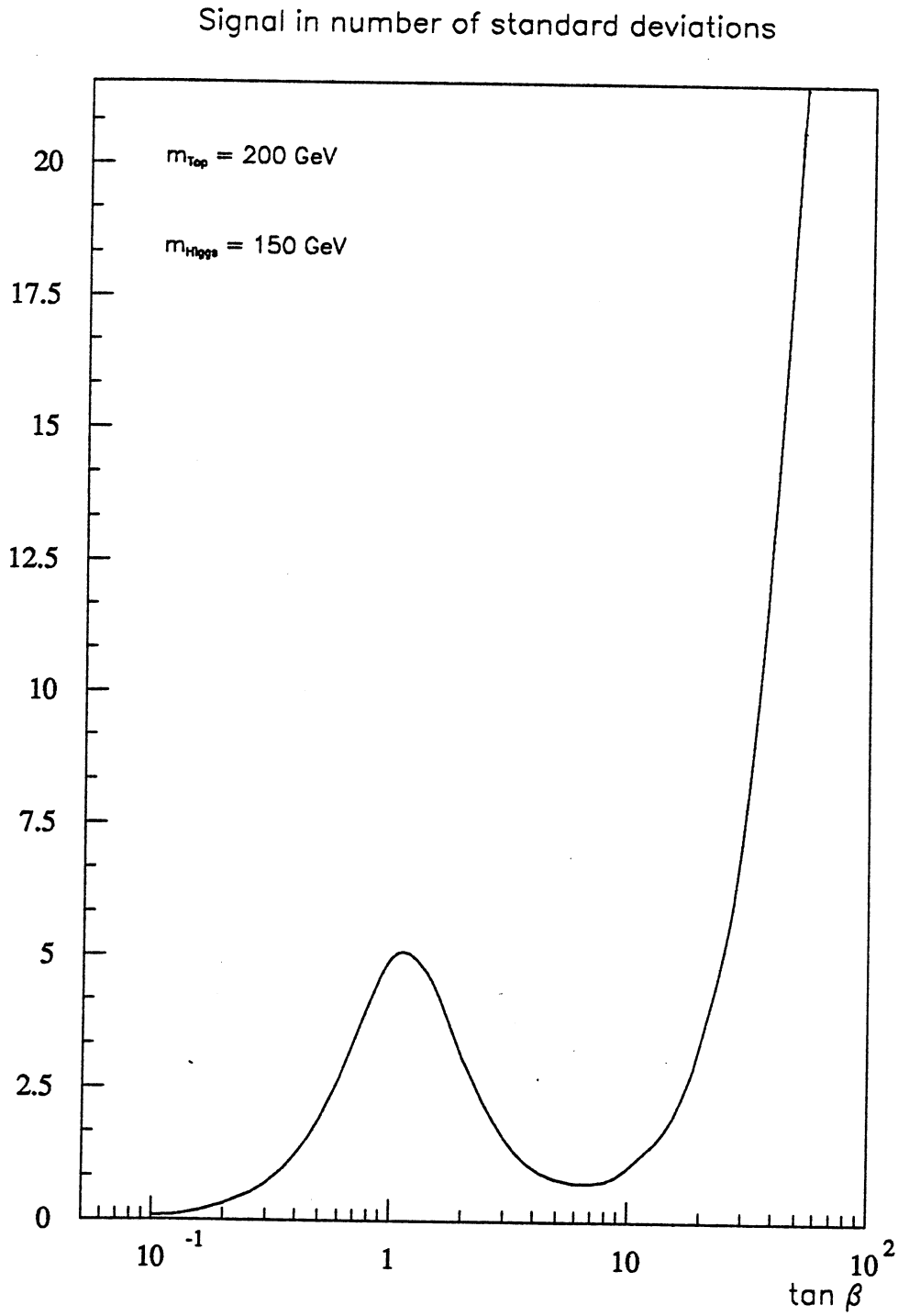

Figure 7.3.12 : The significance in standard deviations of $R_{\tau\mu}^{expt}$ for $m_t = 200$ GeV and $m_{H^{\pm}} = 150$ GeV including the superposition of 1 minimum bias event.

significance of $R_{\tau\mu}^{expt}$ for $m_t = 200$ GeV and $m_{H^\pm} = 150$ GeV. It is seen that a potential $H^\pm$ signal is still discernible after superimposing one minimum bias event.

The search method described here is only feasible at low machine operating luminosities ($\leq 10^{33}$ $cm^{-2}s^{-1}$) where there are small pile-up effects (simulated by superimposing 1 minimum bias event per bunch crossing). This results mostly because of the increasing difficulty in differentiating between τ and non-τ jets using multiplicity information like H(0.8), for example. This difficulty results in a large inefficiency in detecting τ 's as is shown when comparing the acceptances in Tables 7.3.1 and 7.3.2.

A similar sensitivity to a $H^\pm$ signal from top quark decay has been obtained independently in another study [Fel-90]. The study has investigated the possibiliy of measuring the rate of $t \rightarrow \tau^+\nu_\tau$ decays at LHC using $t\bar{t}$ events generated with the ISAJET MC program [Pai-86]. and comparing it to the ratio of $t \rightarrow \mu^+\nu_\mu$. (The simulation does not include any detector simulation and no MB events have been superimposed). One year running at the LHC energies is assumed at a luminosity of 10^{33} $cm^{-2}s^{-1}$.

The study starts by identifying a 'tagged-top' sample as defined above. To reduce the $t \rightarrow q_i\bar{q}_j b$ background the following cuts have been used : each jet in the hemisphere opposite to the tagged top is required to have a transverse energy larger than 30 GeV. In addition, the number of charged tracks, N_{ch}, in a cone $\Delta R < 0.1$ around the jet axis is required to be less than 3 and the sum of the transverse energy in the calorimeter cells (the distance between the centres of two contiguous calorimeter cells is assumed to be $\Delta R = 0.04$), with $0.1\Delta R < 0.4$ around the jet axis, to be less than 5 GeV.

Figure 7.3.13 shows the value of $R_{\tau\mu}^{expt}$ as defined above for $m_t = 200$ GeV and different values of $m_{H^\pm}$ versus $\tan\beta$. Also shown is the Standard Model prediction and the 1.64 σ_{stat} value.

Chapter 8

Conclusions

The Standard Model of particle physics continues to provide the best description of the electroweak and strong interactions. However, the existence of the top quark and of the particle responsible for spontaneous symmetry breaking, the Higgs boson, are the two main unresolved elements of the Standard Model. Direct searches for the top quark at both hadron and electron-positron machines show no evidence for its existence. In addition, little experimental information exists on the Standard Model Higgs sector. This stems mostly because the mass of the Higgs boson is not predicted by the theory and so its discovery is more challenging. The quest for the top and Higgs boson in the Standard Model will continue at future machines such as the Fermilab Tevatron, the Large Hadron Collider (LHC), the Superconducting Super Collider (SSC), and at electron-positron machines such as the Large Electron Positron Collider upgrade (LEP200).

The simplest extensions beyond the one-doublet Higgs sector are models with two doublets of complex scalar fields which predict the existence of the charged Higgs, $H^{\pm}$. In these models the decay of the top quark may be altered from

$$t \rightarrow Wb \rightarrow l\nu_l b$$

(where l is any leptonic final state), expected in the one-doublet models. This is because for $m_t > m_{H^{\pm}} + m_b$ the decay $t \rightarrow H^+b$ competes with the standard top decay $t \rightarrow W^+b$, (where the W is either virtual or on the mass shell), depending on the values of $m_{H^{\pm}}$ and $\tan\beta$. The two significant fermion decay channels of the $H^{\pm}$ are to $\tau^+\nu_\tau$ and $c\bar{s}$. To avoid the significant QCD

background only the τ channel has been considered in this thesis and the τ is assumed to decay hadronically to exploit the large branching ratio.

In this thesis hadronic τ decays and electrons have been counted in a sample of events having a large missing transverse momentum. The event sample has been collected with the UA2 detector over the period 1988 to 1990 and corresponds to an integrated luminosity of 13.0 ± 0.7 pb^{-1} at $\sqrt{s}$ = 630 GeV. No excess in the number of events containing τ 's beyond that expected from Intermediate Vector Boson decays is observed allowing the decay chain

$$t \rightarrow H^+b,\ H^+ \rightarrow \tau^+\nu_\tau,\ \tau^+ \rightarrow \text{hadrons} + \overline{\nu}_\tau \quad (8.1)$$

to be excluded in new regions of the $m_t - m_{H^\pm}$ plane for different values of BR($H^+ \rightarrow \tau^+\nu_\tau$). In addition, the ratio of couplings of the τ and electron to the W has been measured to be

$$\frac{g_\tau^W}{g_e^W} = 1.02 \pm 0.04\ (\text{stat}) \pm 0.04\ (\text{syst})$$

which is consistent with the electron - τ universality of couplings to the W.

Finally, in this thesis the prospects for $H^\pm$ from top quark decay have been studied for LHC energies. It has been shown that by extracting information from a highly-segmented calorimeter and silicon tracking detector , τ identification in top quark events is feasible but only at low luminosities of $\leq 10^{33}$ cm^{-2}s^{-1}. Simulations show that data collected in 1 year LHC running at luminosities of 10^{33} cm^{-2}s^{-1} is sensitive to a $H^\pm$ signal over a large range of the parameter space for top quark masses up to 200 GeV.

Appendix A

The Calibration of the UA2 Inner Silicon Detector

The Inner Silicon detector (ISI) in UA2 is used for both event reconstruction and in the determination of the charged particle multiplicity in an event as described in Section 3.3. To do so the response of the silicon detectors to minimum ionizing particles (mips) needs to be accurately known and so all the boards of the ISI were calibrated using 40 GeV charged pions in a testbeam at the CERN SPS H2 site [Ber-90, Spi-92]. Pions were used instead of electrons so as to enable the positioning of the boards one behind another for the simultaneous calibration of 8 boards.

A.1 Experimental Set-up

A schematic diagram of the experimental set-up is shown in Figures A.1 and A.2. The scanning table allows the selection of each channel and is computer-controlled so that 1 encoder unit (eu) on the computer corresponds to 1.044 mm on the scanning table. Therefore, to shift the boards across by one pad the table must be moved by about 3.6 eu. The charged pion beam has a Gaussian distribution in space with a $\sigma \sim 4$ mm and is normally incident on the boards. Because the beam covers on average 4 pads at one position of the scanning table, a run is taken for 2 pads and then the scanning table is moved by 7.2 mm. The boards are mounted behind one another in a storage box that shields them from light. The only material apart from the box preceding

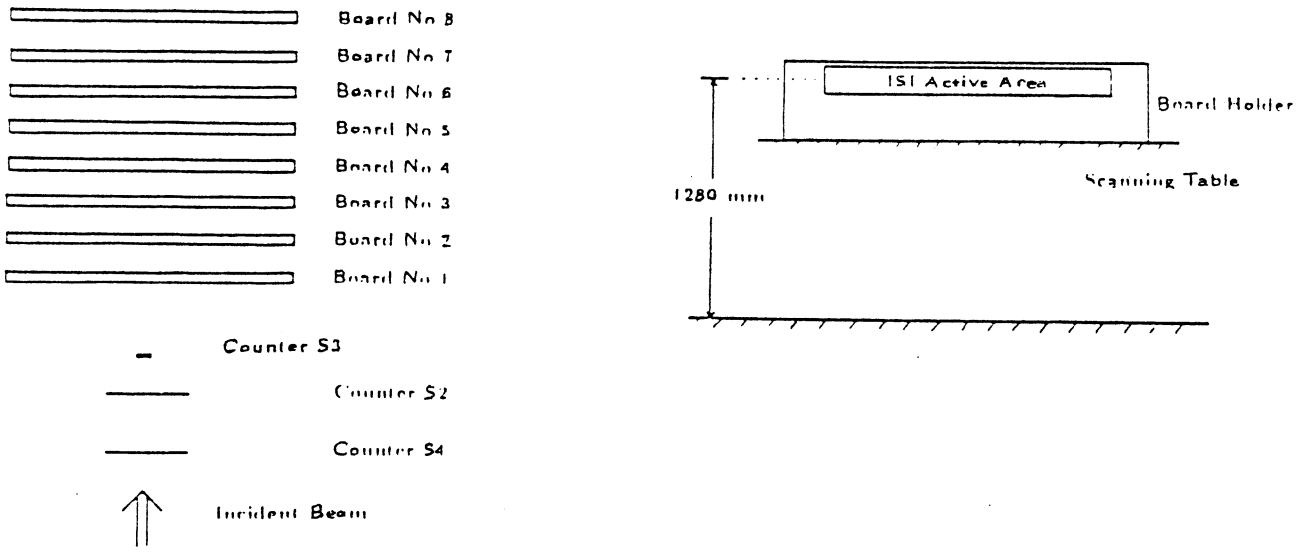

Figure A.1 : The ISI testbeam experimental set-up.

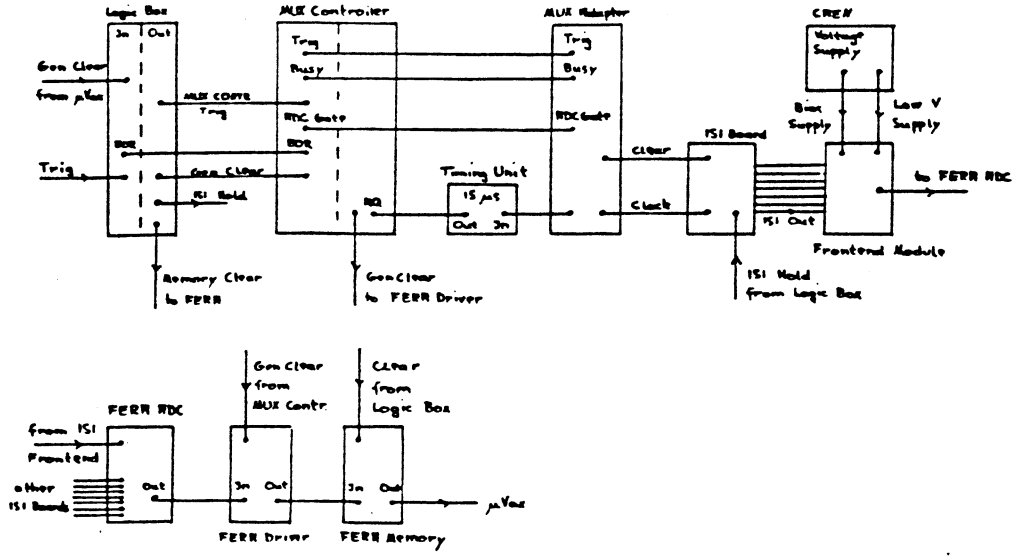

Figure A.2 : The ISI testbeam read-out electronics.

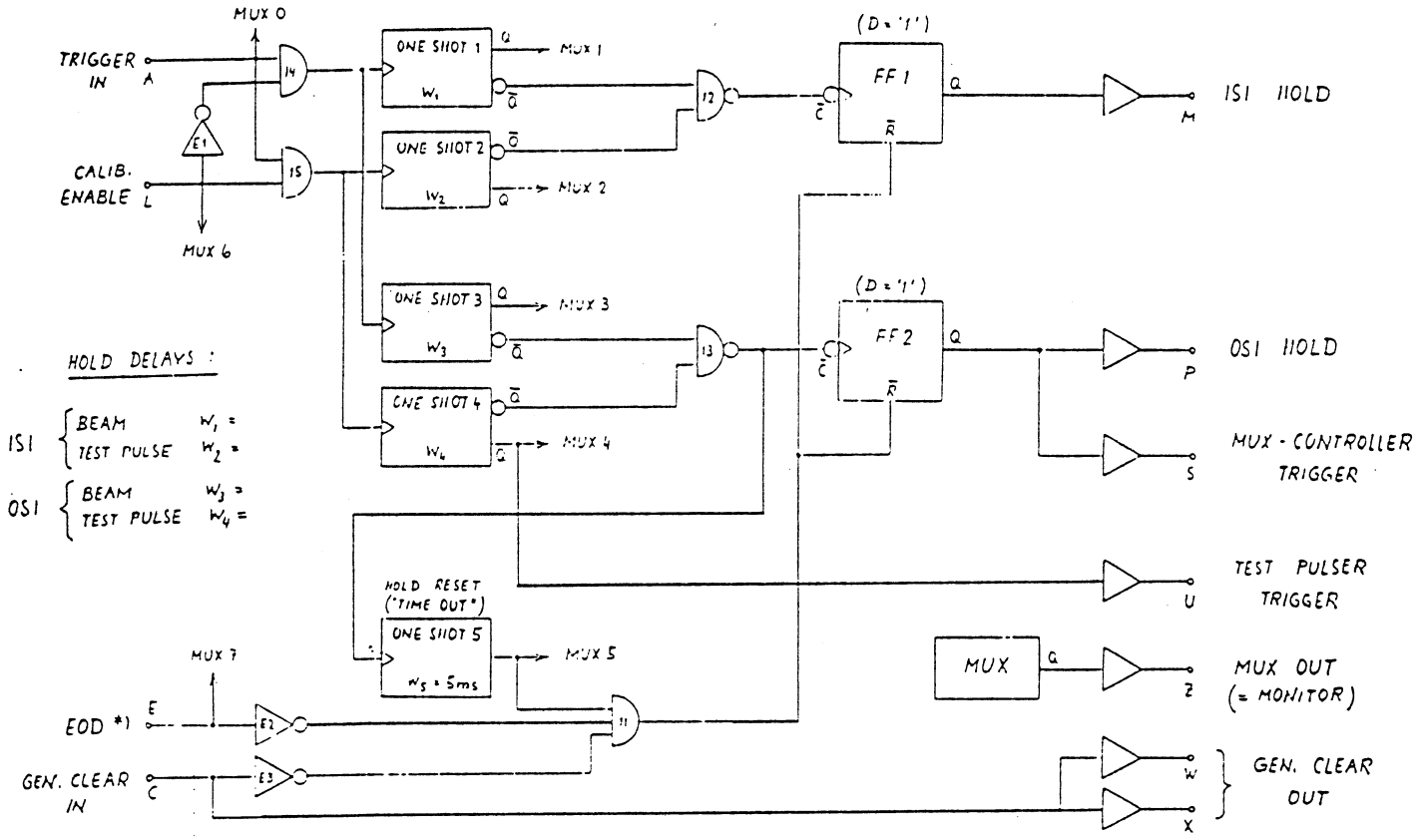

Figure A.3 : Block diagram of the Logic Box.

a board is that of the other boards each having a thickness of $\sim 1.8\%$ r.l.

A valid trigger is defined as the coincidence of the scintillation counters S1, S2, and S3 and initiates the ISI read-out. The trigger pulse takes approximately 400 ns to travel the 35 m from the scintillators to the Logic Box in the counting room. Figure A.3 shows a block diagram of the Logic Box electronics circuit. The Logic Box provides the MUX controller trigger, and the clock, clear and hold pulses for the ISI read-out. The reverse bias voltage supply and the low voltage supply for the AMPLEX chips are provided by a CAEN voltage supply computer-operated. Digitization of the silicon pulse heights is performed with one FERA ADC. The digitized silicon pulse heights, in ADC counts, are stored on tape using a micro-VAX computer for subsequent offline analysis.

Figure A.4 shows the signal timings sent to the AMPLEX chip for reading out a half of an ISI board. From the MUX Adapter 128 clock signals, one for each pad, are sent between clear signals so that half of the ISI board is read out before the clear is set. The first signal on the clock cycle does not activate a channel to be read out. The clear signals clear the MUX controller and FERA MEMORY when either of the two board halves have been read-out. The hold pulse from the Logic Box serves the track-and-hold circuit of the AMPLEX chip and holds the negative silicon signal to within 600 ns of its minimum for it to be digitized. The hold signal, as shown in Figure A.5, is delayed by approximately 570 ns in the counting room before it is sent to the AMPLEX chip.

The FERA ADC unit reads the pulse heights for all the eight boards, one pad after the other, and stores the digitized values in the FERA MEMORY unit which acts an event buffer. When the read-out is completed the data is transferred from the FERA MEMORY unit via the micro-VAX to the tape unit following the last in first out (LIFO) structure of the event buffer. The data written to tape has thus a certain order as depicted in Figure A.6 and each event has a word length of 1025 data words (8 times 128 + word count).

There were two testbeam periods in 1990. In the May period a batch of 8 boards (called Batch 1) were set to the bias voltages shown in Table A.1. Another batch of 8 boards (called Batch 2), were calibrated in the July testbeam period and had the bias voltages and leakage currents as shown in Table A.2. The leakage currents vary by about $\pm 10\%$ during each testbeam period. Each board was calibrated from pads 1 to 256 with approximately 2250 triggers per pad.

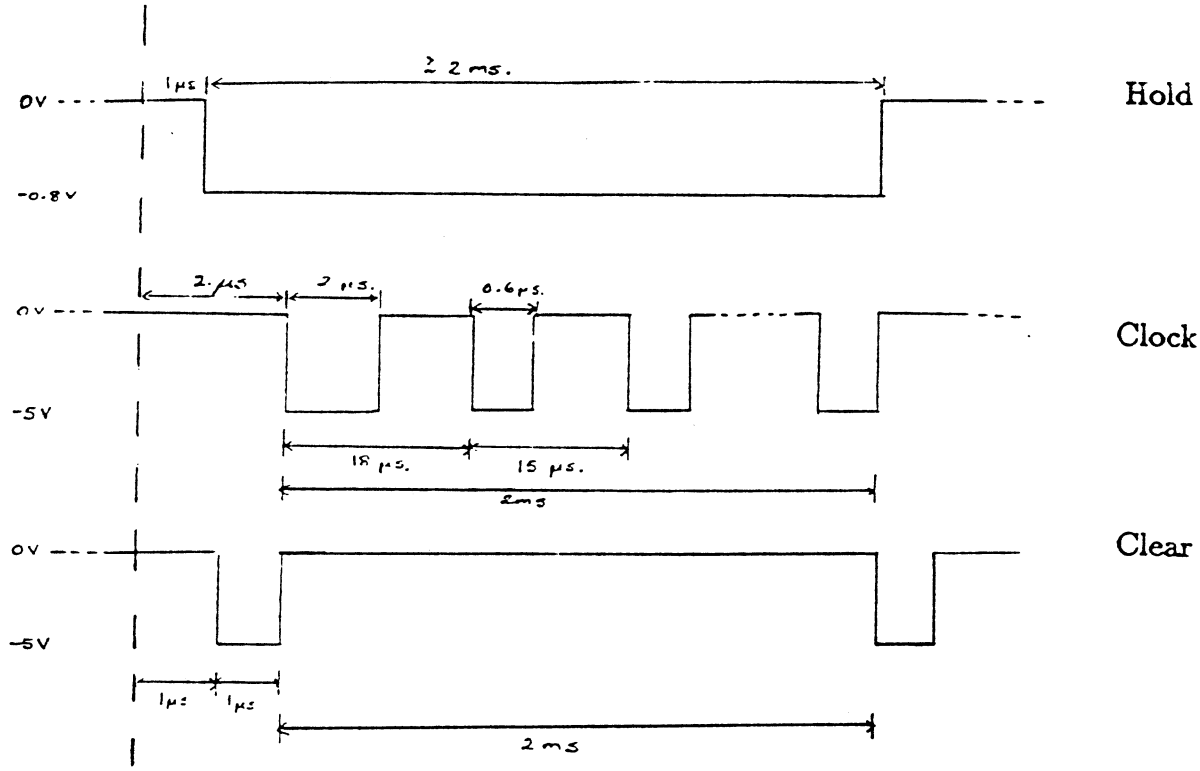

Figure A.4 : Signal timings for the ISI read-out.

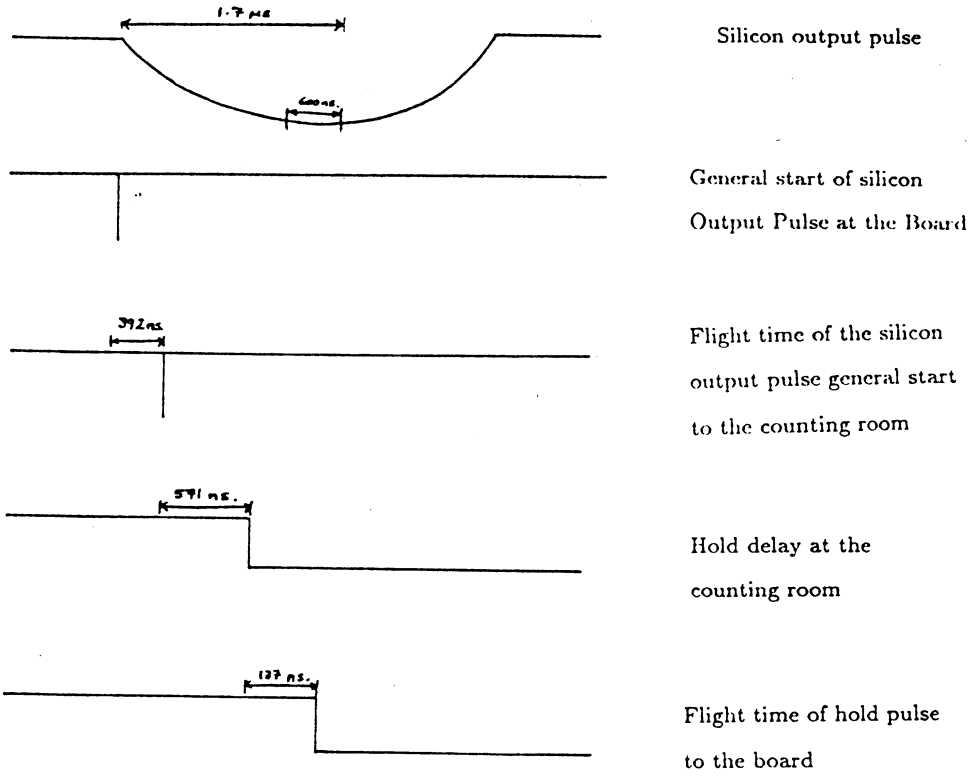

Figure A.5 . Correlation between ISI output pulse and hold signal.

A.2 Analysis of the Testbeam Data

A.2.1 Pedestals Runs

A pedestal is the DC offset in the electronics chain and its width σ_{ped} is a measure of the rms noise from capacitances and leakage currents on the silicon boards. Special runs, called pedestal runs, are taken with the beam trigger inhibited to measure the pedestal values.

The pedestal values for board S5 from Batch 1 are shown in Figure A.7 where the μ and σ are drawn for each pad as well as the distributions of these two variables over the whole board. For board S5 from Batch 1 the μ and σ are similar to those obtained in Batch 2. The two pedestal runs for board S5 are compared in Figure A.8. The good agreement of the two pedestal runs shows that the pedestals are stable and that only one run is needed to produce the pedestal μ and σ that will be used for the pedestal subtraction.

In addition, from σ_{ped} nine noisy pads with a σ_{ped} above 10.0 ADC counts and three dead pads were detected in Batch 2. In Batch 1 five pads were found to be noisy.

A.2.2 Pulser Runs

The pulser runs use the same set-up as the pedestal runs except that a known quantity of charge is injected from a pulse generator into the input of the AMPLEX chip. This produces a response which after pedestal subtraction is used to measure the gain of the electronics.

The fiducial pattern for board S5 from Batch 1 is shown in Figure A.9. The comparison between two pulser runs of Batch 1 is shown in Figure A.10.

A.2.3 Calibration of the Data

The calibration of the ISI is performed by fitting, after pedestal subtraction, the pulse height distribution for each pad with a Landau distribution convoluted with a Gaussian noise of mean and σ taken from the pedestal runs.

Several cuts are made on the data to provide a clean mip sample for the calibration. The first requirement for an event to be included in the

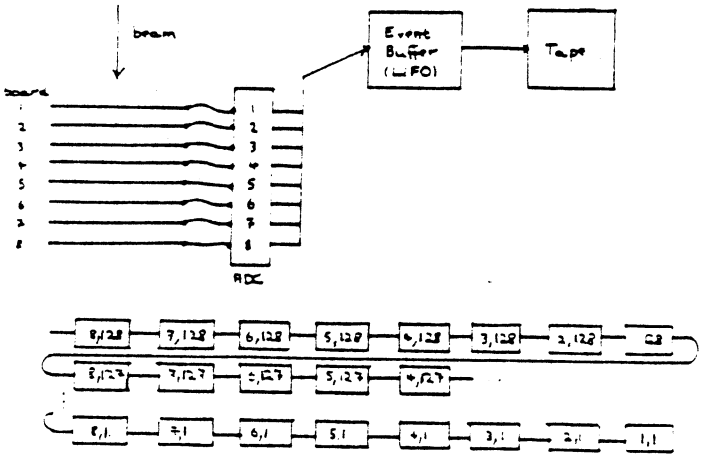

Figure A.6 : Format of data written to tape.

Position	Board	$V_{Bias}(V)$	$I_{Leakage}(\mu A)$
1	S11	40.0	9.9
2	S5	40.0	11.1
3	S7	40.0	7.7
4	S9	40.0	8.0
5	S13	40.0	15.6
6	S15	40.0	9.2
7	S16	40.0	6.1
8	S11	40.0	5.6

Table A.1 : Bias voltages and leakage currents for Batch 1.

Position	Board	$V_{Bias}(V)$	$I_{Leakage}(\mu A)$
1	S3	40.0	36.3
2	S5	40.0	13.3
3	S7	40.0	11.0
4	S9	40.0	4.2
5	S13	40.0	5.5
6	S15	40.0	9.5
7	S16	40.0	9.1
8	S11	40.0	13.7

Table A.2 : Bias voltages and leakage currents for Batch 2.

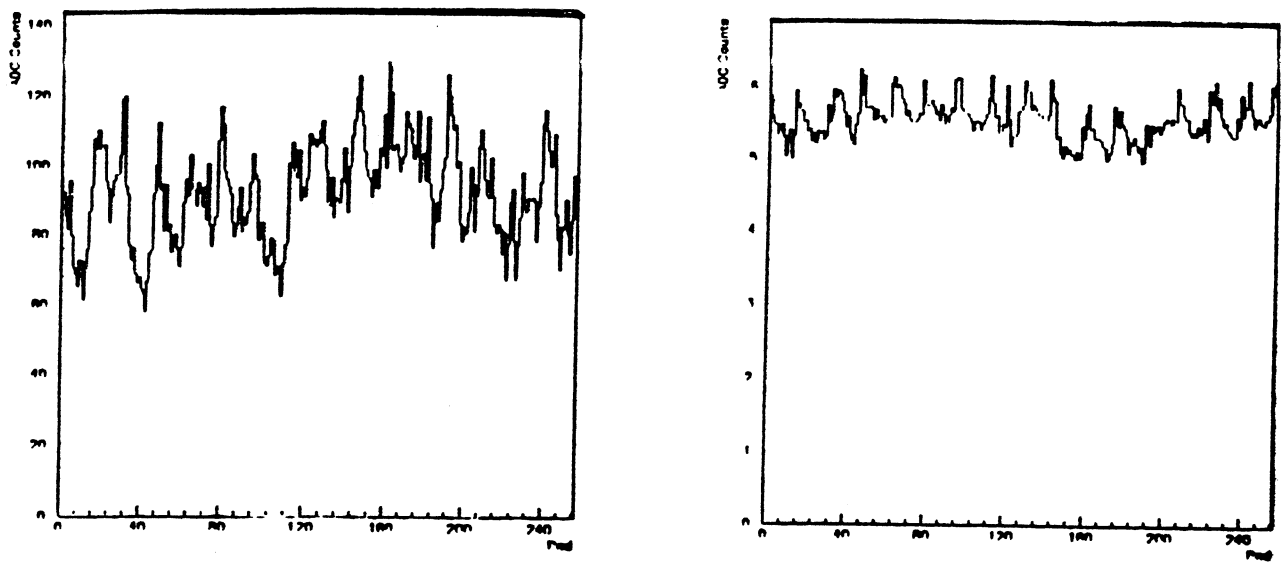

Figure A.7 : Pedestal values for Board S5 from Batch 1.

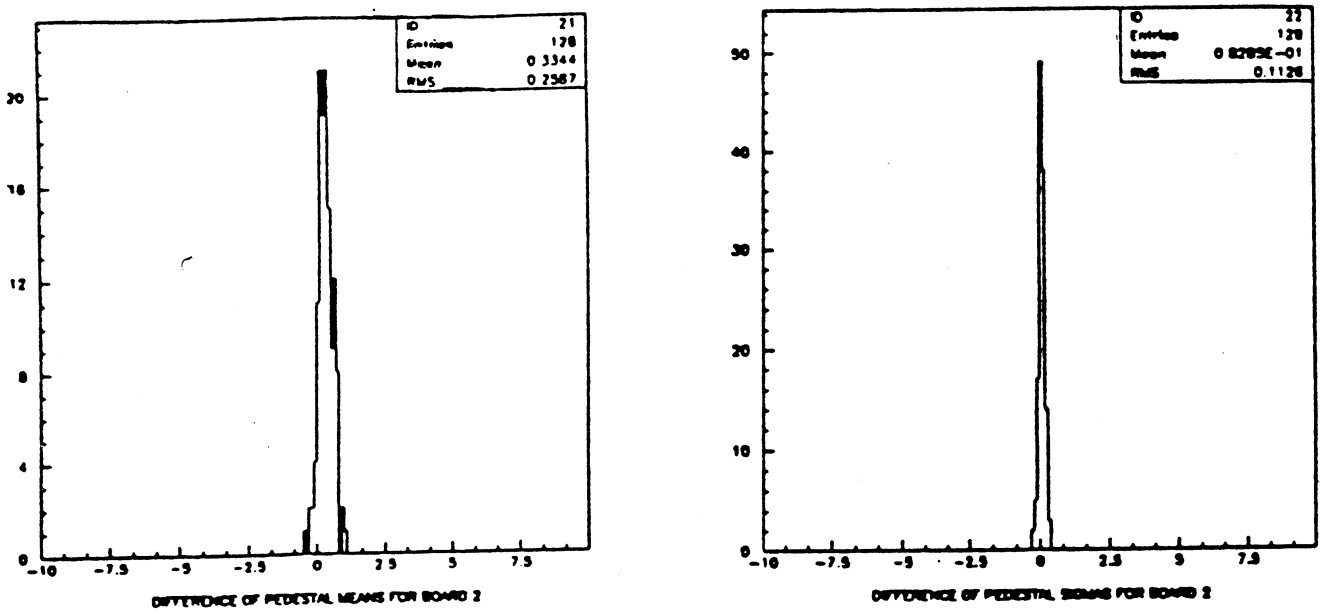

Figure A.8 : Comparison of two pedestal runs.

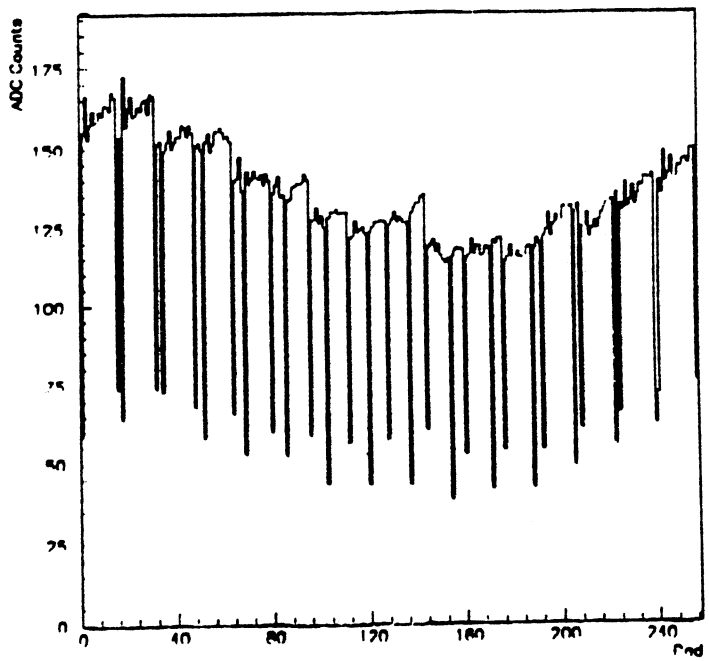

Figure A.9 : Pulser run for Board S5.

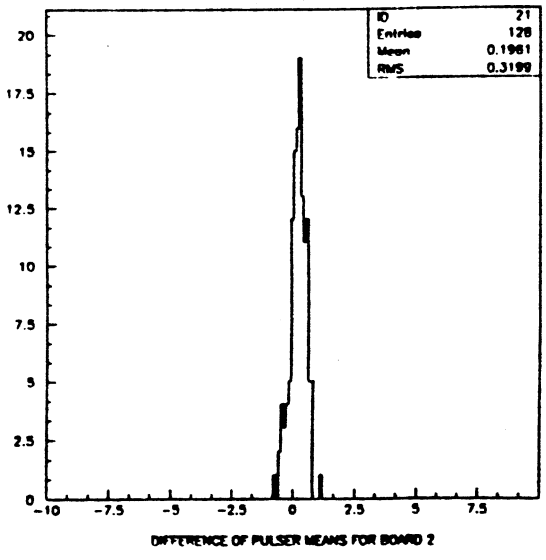

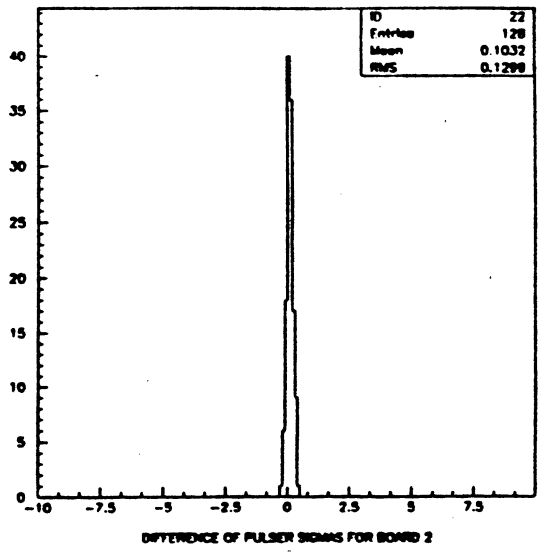

Figure A.10 : Comparison between two pulser runs in Batch 1.

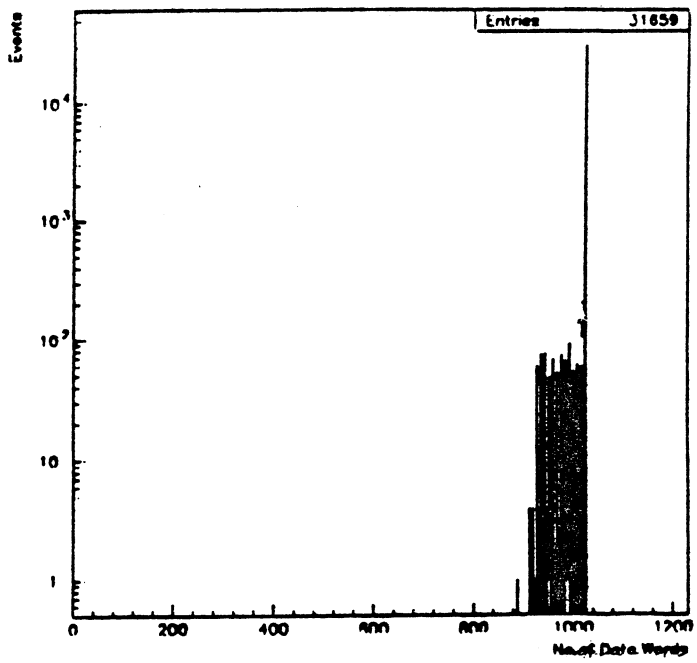

Figure A.11 : Event word length.

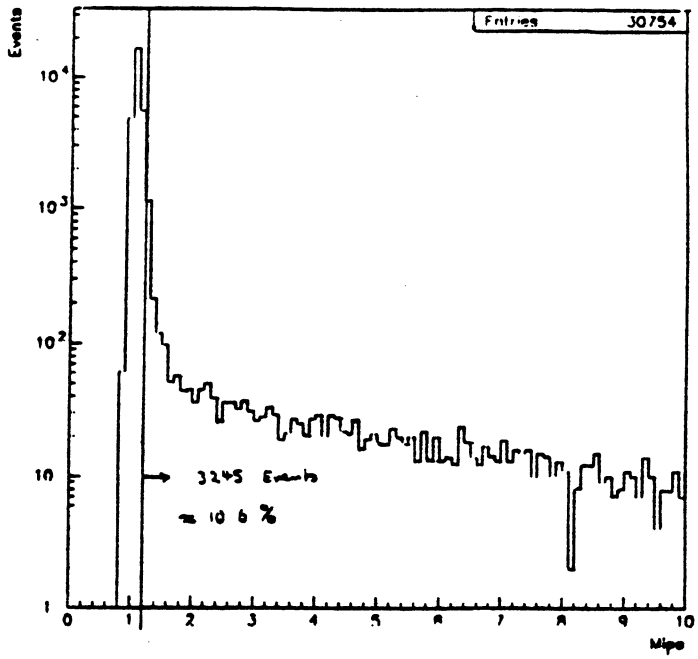

Figure A.12 : Energy distribution in scintillator S6.

calibration is that the correct amount of data has been written to tape for that event. From before, the word length for an event is required to be 1025 words. If this is not the case the event is not included in the data sample. An example of the word length of several events is shown in Figure A.11. This shows that the proportion of events with too few words recorded is $\sim 3\%$. These truncated readouts are caused by timing problems because triggered beam events come too close together in time for the electronics to reset before the next event. This problem does not occur for the pedestal and pulser runs because the clock cycle is configured to avoid this.

In addition, although the beam is nominally a pure 40 GeV pion beam, it is, however, contaminated with electrons at the $\sim 3\%$ level. The electrons have different energy deposition characteristics than pions. Unlike pions, electrons may shower and deposit more energy in the silicon leading to a longer Landau tail resulting in an overestimation of the most probable energy loss. To distinguish between electrons and pions, the scintillation counter S6 is included in the testbeam. The counter is placed behind a lead converter of thickness ~ 1.5 r.l. The electrons, after showering, will deposit a larger signal in the counter than pions. This is shown in Figure A.12 which depicts the response of the counter to both electrons and pions. The pions form a distinct peak around one mip whereas the electrons leave a longer tail. To remove the electrons from the data sample a cut is made on the pulse height of counter S6 so that only events with a response less than 1.2 mips are included in the final data sample. This cut eliminates $\sim 10\%$ of the events.

Thirdly, the pedestal has to be subtracted from the pulse height. The pedestal value to be subtracted is obtained from the pedestal runs taken. All events that have a response less than $3\sigma_{\text{ped}}$ are removed.

Finally, if a pion is incident at the edge of a pad or passes through two pads, the charge produced in such an event will be shared by the two pads. These events will cause the position of the most probable energy deposition in the silicon to be underestimated. Therefore, such events are excluded from the final data sample. This is performed by requiring that the pulse height in the neighbouring pads of the nominally hit pad does not exceed $3\sigma_{\text{ped}}$. This cut rejects $\sim 5\%$ of the events remaining after the pedestal cut.

After all the above cuts have been performed about 1 500 events per pad remain to perform the calibration with ($\sim 67\%$ of the total triggers).

Following the above cuts the pulse height in each pad is fitted with a Landau distribution convoluted with a Gaussian noise resolution. An exam-

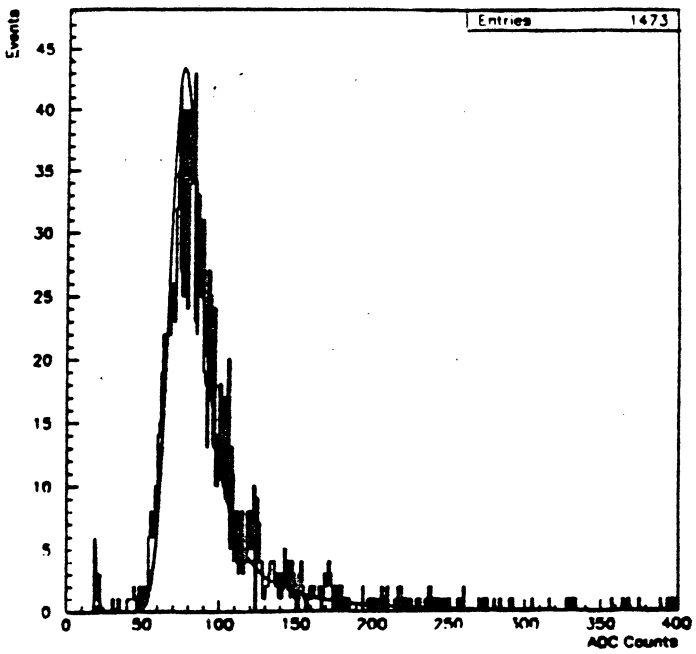

Figure A.13 : Typical fit performed in the calibration process.

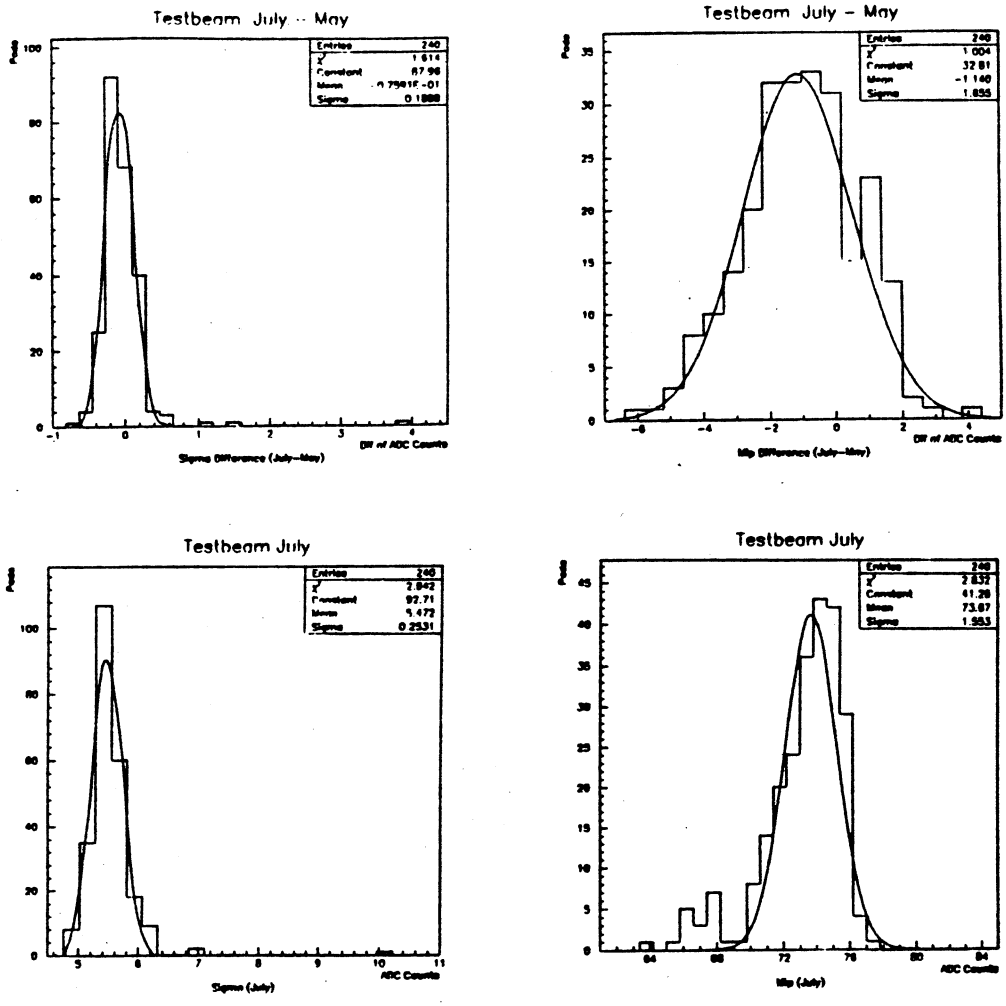

Figure A.14 : Comparison between May and July calibration periods for

ple of such a fit is shown in Figure A.13. The fitting routine gives the most probable energy deposition in the silicon in terms of ADC counts. A typical value of the most probable energy deposition is about 75 ADC counts and ranges from 65 to 80 ADC counts depending on the pad. The typical value of the χ^2 of these fits is approximately 2 to 3 per degree of freedom.

The error on the most probable energy deposition comes from three factors. First, the error from the pedestal position is $\pm 0.5\%$ given by the Gaussian fit to the pedestal. Second, an error of $\pm 0.5\%$ comes from the fitting procedure to the pulse height. Finally, the pedestals have a small fluctuation of about $0.5 \pm 0.5\%$. This implies that there are small deviations over the period taken to collect this data. Therefore, there is an additional error on the pedestal position due to these shifts which amounts to ± 1 ADC count ($\sim \pm 1.5\%$). So, in total the uncertainty in the position of the most probable energy deposition is $\sim \pm 1.7$ %.

Boards S5 and S11 have been calibrated in both the May and July testbeam periods. This allows a comparison between the two calibration values measured. The comparison is performed by calculating the differences in σ_{ped} and the most probable energy loss for each pad in the two testbeam periods. The difference is shown in Figure A.14. These plots show the stability of the calibration values. The σ_{ped} are nearly constant over the two periods and an error of $\pm 2\%$ is assigned to the pedestal stability. The stability of the ADC counts for the most probable energy loss is $\sim \pm 2\%$. This value is comparable to the error assigned to the mip fluctuations from pad to pad. The overall shift in the mip value of -1.1 ADC counts is due to systematic uncertainties arising from the differences in temperature and humidity between the two periods and also because in May S11 was positioned closest to the beam whereas in July it was placed furthest.

Bibliography

[Aac-90] Proc. of the Large Hadron Collider Workshop Vol. I, Aachen 1990, ECFA 90-133 and CERN 90-10

[Ait-89] Aitchinson, I. J. R., Hey, A. J. G., *Gauge Theories in Particle Physics,* Adam Hilger Publishing Company, 1989

[ALE-90a] ALEPH Collaboration, Decamp, D., *et. al.*, Phys. Lett. B236(1990)511

[ALE-90b] ALEPH Collaboration, Decamp, D., *et. al.*, Phys. Lett. B241(1990)623

[Ali-87] Ali, A., van Eijk, B., ten Have, I., Nucl. Phys. B292(1987)1

[Ali-88] Alitti, J., *et. al.*, Nucl. Instr. Meth., A273(1988)135

[Ali-89] Alitti, J., *et. al.*, Nucl. Instr. Meth., A279(1989)364

[Alt-77] Altarelli, G., Parisi, G., Nucl. Phys. B126(1977)298

[Alt-88a] Altarelli, G., *et. al.*, Nucl. Phys. B308(1988)724

[Alt-88b] Altarelli, G., and Franzini, P. J., Z. Phys. C37(1988)37

[Alv-88] Alvarez, T., Leites, A., Ternon, J., Nucl. Phys. B301(1988)1

[Ama-87] Amaldi, U., *et. al.*, Phys. Rev. D36(1987)1385

[Ans-88a] Ansari, R., *et. al.*, Nucl. Instr. Meth., A263(1988)51

[Ans-88b] Ansorge, R., *et. al.*, Nucl. Instr. Meth., A265(1988)33

[Ans-89] Ansari A., *et. al.*, Nucl. Instr. Meth., A279(1989)388

[Apu-92] Appuhn, R-D., and Kolanoski, H., private communication

[APS-91] Grunendahl S., in Proc. of the American Physical Society DPF Conference, Vancouver, August 1991. World Scientific, 1991

[ARG-87] ARGUS Collaboration, Albrecht, H., *et. al.*, Phys. Lett. B192(1987)245

[Bac-88] Bachler, P., *et. al.*, in Proceedings of the Adriatic Conference on the Importance of Digital Microelectronics and Microprocessors on Particle Physics, Trieste 1988. World Scientific, 1989

[Bag-89] Bagnaia, P., *et. al.*, UA2 $p\bar{p}$ Note 565, CERN, March 1989

[Bar-87] Barger, V., Phillips, R., *Collider Physics,* Addison-Wesley Publ. Company, 1987

[Bar-90a] Barger, V., Phillips, R., Phys. Rev. D 41(1990)3421

[Bar-90b] Barger, V., Phillips, R., Phys. Rev. D 41(1990)884

[Bar-90c] Barnett, R. M., Report of the Subgroup on the Top Quark for the Proc. of the 1990 Summer Study on High Energy Physics, Snowmass Colorado, June 1990, ANL-HEP-CP-90-98

[Bea-89] Beauville, E., *et. al.*, CERN/EF/89-89

[Bee-84] Beer A., *et. al.*, Nucl. Instr. Meth., A224(1984)360

[Bel-73] Bell, J. S., Nucl. Phys. B60(1973)427

[Ben-84] Bengtsson H., Computer Physics Comm. 31(1984)323

[Ben-87] Bengtsson H., Sjostrand T., Computer Physics Comm. 46(1987)43

[Ber-89a] Berends, F. A. *et. al.*, Phys. Lett. 224B(1989)237

[Ber-89b] Berends, F. A. *et. al.*, Nucl. Phys. 321B(1989)39

[Ber-90] Bertram, I., Spiwoks, R., and Tsesmelis, E., UA2 $p\bar{p}$ Note 609, CERN, November 1990

[Big-86] Bigi, I., *et. al.*, , Phys. Lett. B 181(1986) 157

[Bjo-76] Bjorken, J. D., *Weak Interactions at High Energies and the Production of New Particles,* 1976 SLAC Summer Institute on Particle Physics

[Bla-88] Blaylock, G., *et. al.*, in Proceedings of the Adriatic Conference on the Importance of Digital Microelectronics and Microprocessors on Particle Physics, Trieste 1988. World Scientific, 1989

[Blu-63] Bludman, S., and Klein, A., Phys. Rev. 131(1963)2364

[Boo-86] Booth, C. N., in Proc of the 6th Topical Workshop on Proton-Antiproton Collider Physics, Aachen 1986. World Scientific, 1987

[Bor-87] Borer A., *et. al.*, Nucl. Instr. Meth., A253(1987)548

[Bor-88] Borer A., *et. al.*, Nucl. Instr. Meth., A273(1988)605

[Bos-89] Bosi, F., *et. al.*, Nucl. Instr. Meth., A283(1989)532

[Bou-72] Bouchiat, C., Iliopoulos, J., Meyer, P., Phys. Lett. B38(1972)519

[Bri-91] Brignole, A, *et. al.*, DFPD/91/TH/28

[Bri-92] Brignole, A, *et. al.*, CERN-TH-6366/92

[Bul-91] Bullock, B. K., *et. al.*, Phys. Rev. Lett. 67(1991)3055

[Bur-90] Buras, A., Krawczyk, P., Lautenbacher, M. E., Salazar, C., Nucl. Phys. B337(1990)284

[Cav-90] Cavalli, D., Costa, G., Cravero, A., Incandela, J., Perini, L., UA2 $p\overline{p}$ Note 605, CERN, July 1990

[Cav-91a] Cavalli, D., Cozzi, L., Incandela, J., Perini, L., Tsesmelis, E., UA2 $p\overline{p}$ Note 624, CERN, September 1991

[Cav-91b] Cavalli, D., Cozzi, L., Incandela, J., Perini, L., Tsesmelis, E., UA2 $p\overline{p}$ Note 626, CERN, November 1991

[CDF-90a] CDF Collaboration, Abe, F., *et. al.*, Phys. Rev. Lett. 65(1990)2243

[CDF-90b] CDF Collaboration, Abe, F., *et. al.*, Phys. Rev. Lett. 64(1990)147

[CDF-90c] CDF Collaboration, Abe, F., *et. al.*, Phys. Rev. Lett. 64(1990)142

[CDF-90d] CDF Collaboration, Abe, F., *et. al.*, Phys. Rev. Lett. 64(1990)152

[CDF-91a] CDF Collaboration, Abe, F., *et. al.*, Phys. Rev. D44(1991)29

[CDF-91b] CDF Collaboration, Abe, F., *et. al.*, Fermilab-Pub-91/356-E,

[CDF-91c] CDF Collaboration, Abe, F., *et. al.*, Fermilab-Pub-91/352-E,

[CDF-91d] CDF Collaboration, Abe, F., *et. al.*, Phys. Rev. D43(1991)2070

[CDF-91e] CDF Collaboration, Abe, F., *et. al.*, Fermilab-Pub-91/280-E,

[CDF-91f] CDF Collaboration, Abe, F., *et. al.*, Phys. Rev. D43(1991)664

[Cia-90] Ciapetti, G., and Di Ciaccio, A., in Proc. of the Large Hadron Collider Workshop Vol. III, Aachen 1990, ECFA 90-133 and CERN 90-10

[CLE-87] CLEO Collaboration, Bean, A., *et. al.*, Phys. Rev. D35(1987)3533

[Com-79] Combridge, B. L., Nucl. Phys. B151(1979)429

[Cor-73] Cornwell, J., M., Levin, D. N., Tiktopoulos, G., Phys. Rev. Lett. 30(1973)1268

[Cor-74] Cornwell, J., M., Levin, D. N., Tiktopoulos, G., Phys. Rev. D10(1974)1145

[Cos-88] Costa, G., *et. al.*, Nucl. Phys. B297(1988)244

[Dar-83] Darriulat, P., UA2 $p\overline{p}$ Note 224, October 1983

[Dar-86] Darriulat, P., UA2 $p\overline{p}$ Note 521, October 1986

[Dar-87] Darriulat, P., and DiLella, L., UA2 $p\bar{p}$ Note 528, January 1987

[DEL-90a] DELPHI Collaboration, Aarnio, P., *et. al.*, Phys. Lett. B242(1990)542

[DEL-90b] DELPHI Collaboration, Abrew, P., *et. al.*, Phys. Lett. B241(1990)449

[Die-88] Diemoz, M., Ferrari, F., Longo, E., Martinelli, G., . Phys. C39(1988)21

[Dil-87a] DiLella L., UA2 $p\bar{p}$ Note 522, CERN, 1987

[Dil-87b] DiLella, L., UA2 $p\bar{p}$ Note 549, CERN, December 1987.

[Dil-89] DiLella, L., UA2 $p\bar{p}$ Note 568, CERN, May 1989.

[Dre-70] Drell, S.D., and Yan, T., Phys. Rev. Lett. 25(1970)316

[Dre-71] Drell, S.D., and Yan, T., Ann. Phys. 66(1971)578

[Dre-91] Drees, M., and Roy; D. P., CERN-TH-6080/91

[Ead-71] Eadie, W. T., *et. al.*, *Statistical Methods in Experimental Physics,* North Holland Publishing Company, Amsterdam 1971

[EAG-92] Jenni, P., Experiment for Accurate Gamma, Lepton and Energy Measurements (EAGLE), Expression of Interest, Evian, March 1992

[ECF-84] Proc. ECFA-CERN Workshop on the Large Hadron Collider in the LEP Tunnel, Lausanne and Geneva, 1984, ECFA 84-85 and CERN 84-10

[EHL-84] Eichten, E., *et. al.*, Rev. Mod. Physics 56(1984)579

[EHL-86] Eichten, E., *et. al.*, Rev. Mod. Physics 58(1986)1065 E

[Ell-85] Ellis, S. D., Kleiss, R., Stirling, W. J., Phys. Lett. 154B(1985)435

[Eng-64] Englert, F., Brout, R., Phys. Rev. Lett. 13(1964)321

[EPS-91a] Carter, J., in Proc. of LP-HEP Conference, Geneva 1991, World Scientific, 1992

[EPS-91b] Ellis, J., in Proc. of LP-HEP Conference, Geneva 1991, World Scientific, 1992

[EPS-91c] Incandela, J., in Proc. of LP-HEP Conference, Geneva 1991, World Scientific, 1992

[Eva-87] Evans, L., *The Proton-Antiproton Collider,* Lecture Delivered at CERN on November 25, 1987

[Fay-90] Fayard, L., and Unal, G., in Proc. of the Large Hadron Collider Workshop Vol. III, Aachen 1990, ECFA 90-133 and CERN 90-10

[Fel-82] Feldman, G. J., *Particles and Fields - 1981,* edited by C. A. Heusch and W. T. Kirk, American Institute of Physics, New York, 1982.

[Fel-90] Felcini, M., in Proc. of the Large Hadron Collider Workshop, Vol III, Aachen 1990, ECFA 90-133 and CERN 90-10

[Fie-78] Field, R. D., Feynman, R. P, Nucl. Phys. 138B(1978)1

[Geo-72] Georgi, H., and Glashow, S. L., Phys. Rev. D6(1972)421

[Geo-78] Georgi, H., Hadronic J. 1(1978)155

[Gil-64] Gilbert, W., Phys. Rev. Lett. 12(1964)713

[Gla-61] Glashow, S. L., Nucl. Phys. A22(1961)579

[Gla-77] Glashow, S. L., and Weinberg, S., Phys. Rev. D15(1977)1958

[Gla-87] Glashow, S. L., and Jenkins, E., Phys. Lett. B196(1987)233

[Glü-90] Glück, M., Reya, E., and Vogt, A., Z. Phys. C48(1990)471

[God-91] Godbole, R. M., Roy, D. P., Phys. Rev. D43(1991)3640

[Gol-61] Goldstone, J., Nuovo Cim., 19(1961)154

[Gol-62] Goldstone, J., Salam, A., Weinberg, S., Phys. Rev. 127(1962)965

[Gos-86] Goessling, C., *et. al.*, IEEE Trans. Nucl. Sci. NS-33(1986)272

[Gos-88] Goessling, C., XXIV International Conf. on High Energy Physics, Munich 1988.

[Gro-72] Gross, D., and Jackiw, R., Phys. Rev. D6(1972)477

[Gun-90a] For a review of the minimal Higgs sector and its extensions see, for example, Gunion, J., Haber, H., Kane, G., and Dawson, S., *The Higgs Hunter's Guide,* Frontiers in Physics Lecture Note Series, Addison-Wesley Publishing Company, 1990 and references therein

[Gun-90b] Gunion, J., Grzadkowski, B., Phys. Lett. B243(1990)301

[Gur-64] Guralnik, G. S., Hagen, C. R., and Kibble, T. W. B., Phys. Rev. Lett. 155(1969)1554

[Hab-85] Haber, H. E., and Kane, G. L., Phys. Rep. 117(1985)75

[Hag-90] Hagiwara, K., Martin, A. D., Zeppenfeld, D., Phys. Lett. B235(1990)198

[Hal-84] Halzen, F., and Martin, A. D., *Quarks and Leptons : An Introductory Course in Modern Particle Physics,* John Wiley and Sons Inc., 1984

[Hew-89] Hewett, J. L., and Rizzo, T. L., Phys. Rep. 183(1989)193

[Hig-64a] Higgs, P. W., Phys. Lett. 12(1964)132

[Hig-64b] Higgs, P. W., Phys. Rev. Lett. 13(1964)508

[Hig-66] Higgs, P. W., Phys. Rev. 145(1966)1156

[Hoo-80] 't Hooft, G., in *Recent Developments in Gauge Theories,* Proc. of the NATO Advanced Summer Institute Congress, 1979, edited by 't Hooft *et. al.*, (Plenum, New York, 1980)

[Inc-88] Incandela, J., Mapelli, L., Stapnes S., UA2 $p\bar{p}$ Note 558, CERN, 1988.

[Inc-91a] Incandela, J., Tsesmelis E., UA2 $p\bar{p}$ Note 623, CERN, September 1991.

[JAD-80] JADE Collaboration, Bartel, W., *et. al.*, Phys. Lett. 91B(1980)142

[Jak-89a] Jakobs, K., UA2 $p\bar{p}$ Note 573, CERN, July 1989.

[Jak-89b] Jakobs, K., UA2 $p\bar{p}$ Note 585, CERN, September 1989.

[Jak-90] Jakobs, K., UA2 $p\bar{p}$ Note 604, CERN, 1990

[Jar-89] Jarron, P., ECFA Workshop on Intrumentation Technology for High Luminosity Colliders, CERN 89-10 (1989)

[Jen-91] Jenni, P., Experiment for Accurate Gamma, Lepton and Energy Measurements (EAGLE), Talk at EAGLE Plenary Meeting, CERN, November 1991

[Jon-86] Jones, E., in 6th Topical Workshop on Proton-Antiproton Collider Physics, Aachen 1986. World Scientific, 1987

[Kan-76] Kang, K., and Kim, J. E., Phys. Lett. B64(1976)93

[Kan-82] Kane, G., and Peskin, M., Nucl. Phys. B195(1982)29

[Kan-87] Kane, G., *Modern Elementary Particle Physics,* Addison - Wesley Publishing Company Inc., 1987

[Kas-66] Kastler, D., Robinson D. W., Swieca, A., Comm. Math. Phys. 2(1966)108

[Kib-67] Kibble, T. W. B., Phys. Rev. 155(1967)1554

[Kur-89] Kurz, N., UA2 $p\bar{p}$ Note 581, September 1989

[Lan-44] Landau, L., J. Phys. (USSR) 8(1944)201

[Lee-72] Lee, B. W., in Proc. of 16th Int. Conf. on High Energy Physics, (Illinois), edited by J. D. Jackson and A. Roberts, Fermilab, Batavia, Illinois, 1972

[Lee-77a] Lee, B. W., Quigg, C., Thacker, G. B., Phys. Rev. Lett. 38(1977)883

[Lee-77b] Lee, B. W., Quigg, C., Thacker, G. B., Phys. Rev. D16(1977)1519

[Lle-73] Llewellyn-Smith, C. H., Phys. Lett. 46B(1973)233

[L3 -90a] L3 Collaboration, Adeva, B., Newman, H., in Proc. of the 25th International Conference on High Energy Physics, Singapore 1990

[L3 -90b] L3 Collaboration, Adeva, B., *et. al.*, Phys. Lett. B252(1990)511

[MAR-79] MARKJ Collaboration, Barber, D. P., *et. al.*, Phys. Rev. Lett. 43(1979)830

[MAR-89] MARK II Collaboration, Abrams, G. S., *et. al.*, Phys. Rev. Lett. 63(1989)2447

[Mor-90] Moreira, P., and Polesello, G., Nucl. Instr. and Meth. A287(1990)417

[Mor-92a] MacFarlane, D., in Proc. of XXVII Rencontres de Moriond - Electroweak Interactions and Unified Theories, Les Arcs, France, March 1992. (To be published).

[Mor-92b] Nash, J., in Proc. of XXVII Rencontres de Moriond - Electroweak Interactions and Unified Theories, Les Arcs, France, March 1992. (To be published).

[Mor-92c] Sherwood, P., in Proc. of XXVII Rencontres de Moriond - Electroweak Interactions and Unified Theories, Les Arcs, France, March 1992. (To be published).

[Mor-92d] Brignole, A., in Proc. of XXVII Rencontres de Moriond - Electroweak Interactions and Unified Theories, Les Arcs, France, March 1992. (To be published).

[Mor-92e] Altarelli, G., in Proc. of XXVII Rencontres de Moriond - Electroweak Interactions and Unified Theories, Les Arcs, France, March 1992. (To be published).

[Mor-92f] Tsesmelis, E., in Proc. of XXVII Rencontres de Moriond - Electroweak Interactions and Unified Theories, Les Arcs, France, March 1992. (To be published).

[MRS-88] Martin, A. D., *et. al.*, , Phys. Rev. D37(1988)1161

[MRS-89] Martin, A. D., *et. al.*, , Mod. Phys. Lett. A4(1989)1135

[Mul-87] Mulvey, J., (editor), in Proc. of Workshop on Physics at Future Accelerators, La Thuile, CERN 87-07

[Mul-88] Mulvey, J., (editor), The Feasability of Experiments at High Luminosity at the LHC, CERN 88-02 Accelerators, La Thuile, CERN 87-07

[Nam-89a] Nambu, Y., *New Theories in Physics,* in Proc. of XI Warsaw Symposium on Elementary Particle Physics, ed. Z. Ajduk *et. al.*, , World Scientific, Singapore, 1989

[Nam-89b] Nambu, Y., in Proc. of 1988 International Workshop on New Trends in Strong Coupling Gauge Theories, ed. M. Bando *et. al.*, , World Scientific, Singapore, 1989

[Nas-87] Nason, P., *et. al.*, Nucl. Phys. B303(1987)607

[Nas-88] Nason, P., *et. al.*, Nucl. Phys. B303(1988)60

[OPA-90a] OPAL Collaboration, Akrawy, M.Z., *et. al.*, B236(1990)364

[OPA-90b] OPAL Collaboration, Akrawy, M.Z., *et. al.*, B242(1990)299

[Pai-86] Paige, F., and Protopopescu, S. D., ISAJET Monte Carlo, BNL 38034 (1986)

[Pas-77] Paschos, E., Phys. Rev. 15(1977)1966

[Pet-83] Peterson, C., Schlatter, D., Schmitt, I., and Zerwas, P., Phys. Rev. D27(1983)105

[PLU-79] PLUTO Collaboration, Berger, C., *et. al.*, Phys. Lett. 86B(1979)418

[PDG-90] Particle Data Group, Review of Particle Properties, Phys. Lett. B Vol. 239, 1990

[Qui-83] Quigg, C., *Gauge Theories of the Strong, Weak and Electromagnetic Interactions,* Frontiers in Physics Lecture Note Series, Benjamin and Cummings Publishing Company, 1983

[Rei-85] Reinders, L. J., Rubinstein, H., Yazaki, S., Phys. Rep. 127(1985)1

[Rey-90] Reya, E., *et. al.*, in Proc. of the Large Hadron Collider Workshop, Vol III, Aachen 1990, ECFA 90-133 and CERN 90-10

[Roy-91a] Roy, D. P., CERN-TH 6274/91

[Roy-91b] Roy, D. P., CERN-TH 6075/91

[Sal-68] Salam, A., *Elementary Particle Theory,* edited by N. Svartholm, Almquist and Wilsell, Stockholm 1968

[SDC-90] Expression of Interest submitted by the Solenoidal Detector Collaboration to the SSC Laboratory, May 1990

[SIT-90] The RD2 Collaboration, A Proposal to Study a Tracking/Preshower Detector for the LHC, CERN/DRDC/90-27, Geneva, August 1990

[SIT-92a] The RD2 Collaboration, Status Report to the DRDC, CERN/DRDC/92-4, Geneva, January 1992

[SIT-92b] The RD2 Collaboration, The Silicon Tracker and Preshower Technical Description, EAGLE INDET Note, SITP-NO-026, CERN, February 1992

[Sjo-88] Sjostrand, T., Int. Journal of Mod. Phys. 3(1988)751

[Sjo-91] Sjostrand, T., private communication

[Sjo-92a] Sjostrand, T., private communication. The PYTHIA parameters PARP(67) and PARP(71) have been varied between 1.0 and 9.0 (their default value is 4.0).

[Sjo-92b] Sjostrand, T., private communication. The JETSET parameters PARJ(41) and PARJ(42) have been varied between 0.0 and 1.0 (their default value is 0.5).

[Spi-92] Spiwoks, R., Diplomarbeit, Universität Dortmund, 1992

[SSS-91] Pepe, M., Talk given at SLAC Summer School, SLAC, August 1991

[Ste-61] Sternheimer, R. M., Methods of Experimental Physics, Vol. 5A. Academic Press, 1961

[Str-65] Streater, R. F., Proc. Roy. Society (London) A287(1965)510

[Sus-79] Susskind, L., Phys. Rev. D20(1979)2619

[Sus-84] Susskind, L., Phys. Rep. 104(1984)181

[TAS-79] TASSO Collaboration, Brandelile, R., *et. al.*, Phys. Lett. 86B(1979)243

[UA1-83] UA1 Collaboration, Arnison, G., *et. al.*, Phys. Lett. 126B(1983)398

[UA1-87] UA1 Collaboration, Arnison, G., *et. al.*, Phys. Lett. 186B(1987)247

[UA1-89] UA1 Collaboration, Albajar, C., *et. al.*, Z. Phys. C44(1989)15

[UA1-90] UA1 Collaboration, Albajar, C., *et. al.*, Z. Phys. C48(1990)1

[UA1-91a] UA1 Collaboration, Albajar, C., *et. al.*, Phys. Lett. 257B(1991)459

[UA1-91b] UA1 Collaboration, Albajar, C., *et. al.*, Phys. Lett. 253B(1991)503

[UA1-91c] UA1 Collaboration, Albajar, C., *et. al.*, Phys. Lett. 253B(1991)506

[UA2-82] UA2 Collaboration, Banner, P., *et. al.*, Phys. Lett. 118B(1982)203

[UA2-83a] UA2 Collaboration, Banner, P., *et. al.*, Phys. Lett. 122B(1983)476

[UA2-83b] UA2 Collaboration, Bagnaia, P., *et. al.*, Phys. Lett. 129B(1983)130

[UA2-83c] UA2 Collaboration, Bagnaia, P., *et. al.*, Z. Phys. C20(1983)117

[UA2-85a] UA2 Collaboration, Appel, J. A. *et. al.*, Phys. Lett. 160B(1985)349

[UA2-85b] UA2 Collaboration, Appel, J. A. *et. al.*, Phys. Lett. 165B(1985)441

[UA2-86a] UA2 Collaboration, Appel, J. A. *et. al.*, Z. Phys. C30(1986)1

[UA2-86b] UA2 Collaboration, Appel, J. A. *et. al.*, Z. Phys. C30(1986)341

[UA2-87a] UA2 Collaboration, Ansari, R. *et. al.*, Phys. Lett. 186B(1987)440

[UA2-87b] UA2 Collaboration, Ansari, R. *et. al.*, Phys. Lett. 186B(1987)452

[UA2-87c] UA2 Collaboration, Ansari, R. *et. al.*, Z. Phys. C36(1987)175

[UA2-87d] UA2 Collaboration, Ansari, R. *et. al.*, Phys. Lett. 195B(1987)613

[UA2-88a] UA2 Collaboration, Ansari, R. *et. al.*, Phys. Lett. 215B(1988)175

[UA2-88b] UA2 Collaboration, Ansari, R. *et. al.*, Z. Phys. C41(1988)395

[UA2-90] UA2 Collaboration, Åkesson, T., *et. al.*, Z. Phys. Ç46(1990)179

[UA2-91a] UA2 Collaboration, Alitti, J. *et. al.*, Z. Phys. C52(1991)209

[UA2-91b] UA2 Collaboration, Alitti, J. *et. al.*, CERN/PPE/91-162 (Submitted to Phys. Lett. B)

[UA2-91c] UA2 Collaboration, Alitti, J. *et. al.*, CERN/PPE/91-163 (Submitted to Phys. Lett. B)

[UA2-92] UA2 Collaboration, Alitti, J. *et. al.*, CERN/PPE/92-13 (Submitted to Phys. Lett. B)

[UA4-84] UA4 Collaboration, M. Bozzo *et. al.*, Phys. Lett. 147B(1984)392

[UA4-87a] UA4 Collaboration, D. Bernard *et. al.*, Phys. Lett. 186B(1987)227

[UA4-87b] UA4 Collaboration, D. Bernard *et. al.*, Phys. Lett. 198B(1987)583

[Vel-77] Veltman, M., Acta Phys. Pol. B8(1977)475

[Vol-90] Volpini, G., UA2 $p\bar{p}$ Note 594, January, 1990

[Wei-67] Weinberg, S., Phys. Rev. Lett. 19(1967)1264

[Wei-79] Weinberg, S., Phys. Rev. D19(1979)1277

[Wil-83] Wilson, E. J. N. (editor), Design Study of an Antiproton Collector for the Antiproton Accumulator (ACOL). CERN Yellow Report 83/10.

[Woo-91] Wood, D., private communication